buildings

Special Issue Reprint

Advanced Building Technologies for Energy Savings and Decarbonization

Edited by
Piljae Im, Yeobeom Yoon and Sungkyun Jung

mdpi.com/journal/buildings

MDPI

Advanced Building Technologies for Energy Savings and Decarbonization

Advanced Building Technologies for Energy Savings and Decarbonization

Editors

Piljae Im
Yeobeom Yoon
Sungkyun Jung

MDPI

Basel • Beijing • Wuhan • Barcelona • Belgrade • Novi Sad • Cluj • Manchester

Editors

Piljae Im
Oak Ridge National Laboratory
Oak Ridge, TN
USA

Yeobeom Yoon
Oak Ridge National Laboratory
Oak Ridge, TN
USA

Sungkyun Jung
Oak Ridge National Laboratory
Oak Ridge, TN
USA

Editorial Office
MDPI AG
Grosspeteranlage 5
4052 Basel, Switzerland

This is a reprint of articles from the Special Issue published online in the open access journal *Buildings* (ISSN 2075-5309) (available at: https://www.mdpi.com/journal/buildings/special_issues/RQS85283H9).

For citation purposes, cite each article independently as indicated on the article page online and as indicated below:

Lastname, A.A.; Lastname, B.B. Article Title. *Journal Name* **Year**, *Volume Number*, Page Range.

ISBN 978-3-7258-2563-9 (Hbk)
ISBN 978-3-7258-2564-6 (PDF)
doi.org/10.3390/books978-3-7258-2564-6

Contents

About the Editors

Piljae Im

Dr. Piljae Im is a senior research and development (R&D) staff member, a group leader for the Integrated Building Deployment and Analysis Group, and the subprogram manager for the Building Energy Modeling program at the US Department of Energy's (DOE's) Oak Ridge National Laboratory (ORNL). He received his PhD and MS in architecture from Texas A&M University. Since he joined ORNL in 2009, Dr. Im has served as principal investigator and co-principal investigator for numerous research projects sponsored by DOE's Building Technologies Office, the US Department of Defense, and domestic and international industry partners. Dr. Im's research has focused on the detailed calibration of building energy simulation models based on field-measured data, the development of prototype building models, validation and uncertainty characterization for energy simulations, advanced controls such as model predictive control, and automated fault detection and diagnosis. He has also led numerous projects for the deployment and demonstration of various energy efficiency measures (EEMs), measurement and verification (M&V), and data analysis. Dr. Im has more than 20 years of experience in building energy simulation modeling and is a user of numerous building energy and daylighting simulation software, such as EnergyPlus, OpenStudio, eQuest, Radiance, and DOE-2.1e. He has authored and co-authored more than a hundred peer-reviewed conference and journal papers. Dr. Im is an active member of the International Building Performance Simulation Association (IBPSA) and the American Society of Heating, Refrigerating and Air-Conditioning Engineers (ASHRAE) and is a voting member of several technical committees, including ASHRAE Standing Standard Project Committee (SSPC) 140 and Guideline Project Committee 45P.

Yeobeom Yoon

Dr. Yeobeom Yoon is an R&D associate staff member in the Integrated Building Deployment and Analysis (IBDA) group at Oak Ridge National Laboratory. He received his Ph.D. degree from North Carolina State University in May 2021, and joined the ORNL in August 2021. In ORNL, Dr. Yoon has been involved in several DOE-funded projects, mainly funded by DOE Building Technologies Office and FEMP. Dr. Yoon's background is in architectural engineering, and his research focuses on building energy simulation modeling and building optimal control to save building energy consumption and reduce CO2 emissions. He has experience in building energy simulation modeling, especially in EnergyPlus and OpenStudio simulation programs.

Sungkyun Jung

Dr. Sungkyun Jung is an R&D associate staff member in the Integrated Building Deployment and Analysis (IBDA) group at Oak Ridge National Laboratory. He specializes in researching building energy performance using simulations and field measurements. His expertise includes building energy modeling, measurement and verification (M&V), and the EMPOWER wall (a smart wall system), as well as fault detection and diagnosis. Dr. Jung obtained his Ph.D. in architecture from Texas A&M University in December 2020. During his time at Texas A&M's Energy Systems Laboratory (ESL), he actively contributed to the Texas Emissions Reduction Program (TERP) project, calculating the reduction in NOx emissions due to renewable energy sources and buildings. He also played a significant role in developing and maintaining the building energy simulation models for the International Code Compliance Calculator (IC3), a software for residential building energy code compliance.

buildings

MDPI

Article

Sensor Incipient Fault Impacts on Building Energy Performance: A Case Study on a Multi-Zone Commercial Building

Yanfei Li [1], Piljae Im [2,*], Seungjae Lee [3], Yeonjin Bae [1], Yeobeom Yoon [2] and Sangkeun Lee [4]

[1] Electrification and Energy Infrastructures Division, Building Technologies Research and Integration Center, Oak Ridge National Laboratory, 1 Bethel Valley Rd, Oak Ridge, TN 37830, USA
[2] Buildings and Transportation Science Division, Building Technologies Research and Integration Center, Oak Ridge National Laboratory, 1 Bethel Valley Rd, Oak Ridge, TN 37830, USA
[3] Department of Civil and Mineral Engineering, University of Toronto, 35 St. George St, Toronto, ON M5S 1A4, Canada
[4] Computer Science and Mathematics Division, Oak Ridge National Laboratory, 1 Bethel Valley Rd, Oak Ridge, TN 37830, USA
* Correspondence: imp1@ornl.gov

Abstract: Existing studies show sensor faults/error could double building energy consumption and carbon emissions compared with the baseline. Those studies assume that the sensor error is fixed or constant. However, sensor faults are incipient in real conditions and there were extremely limited studies investigating the incipient sensor fault impacts systematically. This study filled in this research gap by studying time-developing sensor fault impacts to rule-based controls on a 10-zone office building. The control sequences for variable air volume boxes (VAV) with an air handling unit (AHU) system were selected based on ASHRAE Guideline 36-2018: High-Performance Sequences of Operation for HVAC Systems. Large-scale simulations on cloud were conducted (3600 cases) through stochastic approach. Results show (1) The site energy differences could go −3.3% lower or 18.1% higher, compared with baseline. (2) The heating energy differences could go −66.5% lower or 314.4% higher, compared with baseline. (3) The cooling energy differences could go −11.5% lower or 65.0% higher, compared with baseline. (4) The fan energy differences could go 0.15% lower or 6.9% higher, compared with baseline.

Keywords: building energy; sensor impact; building control; incipient sensor faults

Citation: Li, Y.; Im, P.; Lee, S.; Bae, Y.; Yoon, Y.; Lee, S. Sensor Incipient Fault Impacts on Building Energy Performance: A Case Study on a Multi-Zone Commercial Building. *Buildings* **2023**, *13*, 520. https://doi.org/10.3390/buildings13020520

Academic Editors: Rafik Belarbi and Md Morshed Alam

Received: 13 December 2022
Revised: 19 January 2023
Accepted: 7 February 2023
Published: 14 February 2023

1. Introduction

The building sector consumes 40% of energy consumption and 16% carbon emissions in the United States, based on the 2020 Energy Outlook from the United States Energy Information Administration [1]. It has remained a challenge to reduce building energy consumption and carbon emissions, although many advanced building technologies have been proposed. A few well-known technologies are continually evolving, such as ground source heat pumps [2] and heat pumps in cold climates [3], with the goal of building electrifications and carbon reductions. For any of those building heating/cooling equipment, control loops are an essential part of the system, aiming for optimal operation to reduce energy consumption, power demands, and carbon emissions.

In the past 10 years, building controls have been actively advancing and sensors have not been well studied. Sensors are critical components for controls systems, collecting inputs to controls for subsequent control actions. When sensors work in fault (or unhealthy) conditions, the control benefits will be compromised regardless of the effectiveness of the controls [4]. Buildings are easily operating under fault conditions [5]. For buildings, multiple components directly influence the sensor placement and deployment, such as sensor errors, sensor locations, sensor types, and sensor costs [4].

Sensors are usually calibrated by manufacturers. However, sensor accuracy might drift with time after being installed. There are many reasons for sensor abnormalities, such as harsh environments and manufacturing defects. In such scenarios, sensor reading accuracy might suffer, which is commonly regarded as a sensor fault. Usually, HVAC systems have multiple sensors to assist the controls and multiple sensors might have multiple faults [6]. A study described a total of nine types of sensor fault patterns based on measurement datasets [7]:

- Outlier: usually a small number of isolated sensor readings, unexpectedly far from the majority of normal readings. This reason is usually unknown but could be related to the data logger;
- Spike: a pattern with a much higher rate of change for multiple data points or sensor readings in a short time period. It might be related to battery failure, other hardware failure, or connection issues;
- Stuck-at: a pattern with zero variance or constant sensor readings or data points. The reason is usually associated with hardware malfunction;
- High noise or variance: a pattern with higher variance or noise than historical data suggests or normally expects for sensor readings or data points. The reasons might be associated with hardware failure, environmental conditions, or weakening battery power;
- Calibration: a pattern in which the sensor readings are always offset from ground truth values. It might be related to calibration error or sensor drifting. Often, incipient sensor drift (the amount of drift change with time) is also common in modern sensors;
- Connection or hardware: usually inaccurate sensor readings because of malfunctioning hardware (i.e., hardware dependent). Typical patterns are unusually high/low data readings that are frequently out of normal ranges. The possible reasons might be environment changes, sensor aging, short circuit, or loose wires;
- Low battery: usually inaccurate sensor readings because of low battery power. Typical patterns are unexpected gradient followed by zero variance, or lack of data, or excessive noise;
- Environment out of range: when the environment conditions go beyond what the sensor system can read. Typical examples are extreme high and low temperatures. Patterns might be much higher noise or flattening of the data. Similar patterns occur with improper calibrations;
- Clipping: sensor readings max out. The patterns could be sticking with maximum or minimum readings, perhaps because of environmental conditions.

Multiple sensors (e.g., temperature, flowrate) usually work together as a sensor sets. Sensor sets are different, depending on the HVAC system types and the controls loops. HVAC systems vary based on different building characteristics and functions. For small to medium office buildings, rooftop units (RTUs) are usually used. Typical sensors are air-related [8], such as air temperature, airflow rate, and pressure sensors. For large commercial buildings (e.g., large office buildings), a chiller and cooling tower are usually applied. More sensors are placed on water loops [9], such as water flow rate and water temperature sensors. There are three types of controls: rule-based control, local control, and supervisory control for HVAC systems. Different control strategies might require different sensor sets. Demand control ventilations need zone CO_2 sensors for control actions [8,10]. Occupant control, relying on occupant sensors, is another popular topic attracting attention in the past few years [11,12].

In the context of buildings and HVAC systems, limited studies have investigated sensor fault impacts on HVAC systems. Past studies show that the impact of sensor faults poses a great challenge to optimal performance of advanced control solutions [13,14]. Sensor fault modeling study could be classified into two groups: white-box and black-box [5,15]. The majority of studies applied the white-box method. Black-box method is suitable for fault detection. Due to the severe fault impacts, sensor calibration and fault mitigation become more important. The detailed literature reviews are summarized as:

(1) A study investigated sensor impact on building energy consumption [16], through a small office model in the EnergyPlus platform. Their study proposed a new concept for sensor fault impacts: one-way impact and two-way impact. The one-way impact means that sensor faults cause decreased or increased energy consumption or thermal comfort. The two-way impact means that there could be higher energy consumption for a certain desired energy item (e.g., cooling), and simultaneously lower energy consumption for another desired energy item (e.g., heating). Another recent study proposed the sensor fault impact analysis framework [9] to investigate sensor fault impacts. This framework is based on white-box methods, which opened a door for sensor fault studies on building performance. Their results show that sensors could cause more than double energy consumption. Another study, using white-box modeling platform, demonstrated sensor fault impacts for demand control ventilation (DCV) on building energy consumption [8]. Results show that sensor faults severely downgraded the control performance, leading to increased energy consumption. Another recent study developed a few fault models in the EnergyPlus platform, which were validated through experiments [17,18];

(2) Black-box, or machine learning algorithm, is becoming a new trend in fault detection and diagnostics. This study applied artificial intelligence (AI) algorithms to detect the sensor faults, based on a large dataset. A review study [19] pointed out the biggest issue for black-box method is how to identify the baseline data (data without fault) from the building energy management system;

(3) Sensor fault calibration and mitigation are receiving attention. This study aimed to calibrate the sensor faults [20], to which they applied the virtual in-situ calibration method. Their results showed that the systematic errors of sensors were less than 2% and the random errors were also reduced by as much as 74%. The benefit of such sensor calibration significantly reduced the possibility of abnormal data and enhanced the reliability of sensor measurements. This can effectively eliminate the sensor negative impacts on building energy consumption and thermal comfort. A study [21] applied fault mitigation techniques for sensors (read back for sensor readings and nearest neighbor monitoring for fault sensor correcting), which demonstrated up to 38% improvement in energy consumption and up to 75% improvement in thermal comfort. The sensor faults include stuck-at fault, spike-and-stay (SAS) fault with negative spike, spike-and-stay (SAS) fault with positive spike, single-sample-spike (SSS) fault with negative spike, and single-sample-spike (SSS) fault with positive spike.

However, current literature studies assume sensor fault or errors are constant [5,9,15,22,23]. In real conditions, sensor fault magnitude could evolve or develop over time, which is often observed from field measurements. This is the essence of incipient sensor faults. This is also the main purpose of this study. How to address such an issue is relying on correct modeling of sensor errors. Another research gap is that there was no study proposing a sensor impact evaluation framework. Available studies use their own sensor impact evaluation platform.

The structure of this study is organized as follows: Section 2 summarizes the sensor impact and evaluation framework, which is the methodology; Section 3 describes the surrogate model; Section 4 describes the uncertainty analysis; Section 5 describes the sensitivity analysis; and Section 6 provides conclusions.

2. Methodology

This study aimed to systematically investigate incipient sensor faults for building control performance. The US Department of Energy's Oak Ridge National Laboratory's (ORNL's) two-story Flexible Research Platform (FRP-2) building was used to study the sensor fault impacts. It is a two-floor building with five zones on each floor. The cooling is from rooftop unit (RTU). The heating is from a gas heating coil and VAV electric coils. The control strategy for single-duct variable air volume (VAV) terminal boxes and the air

handling unit (AHU) is implemented based on the control logics from ASHRAE Guideline 36-2018, High-Performance Sequences of Operation for HVAC Systems [24].

A sensor-impact oriented framework is proposed for this purpose. The framework is comprised of (1) a physics-based emulator integrated with sensor faults, control sequences, and building/HVAC models; (2) large-scale simulations for sensor error samplings to the controls on the cloud; (3) a surrogate model development based on cloud simulation results for sensitivity analysis; and (4) sensitivity and uncertainty analyses for the sensors and desired outputs (e.g., energy consumption, thermal comfort).

This study is based on EnergyPlus platform through building energy models. The overall workflow is illustrated in Figure 1. Cloud simulation was used to quicken the 3600 simulation cases, using a stochastic approach. The uncertainty and sensitivity analyses are based on simulation data from cloud simulation. The building model details are not presented here. Interested readers, please refer to the recent publications on the building [25].

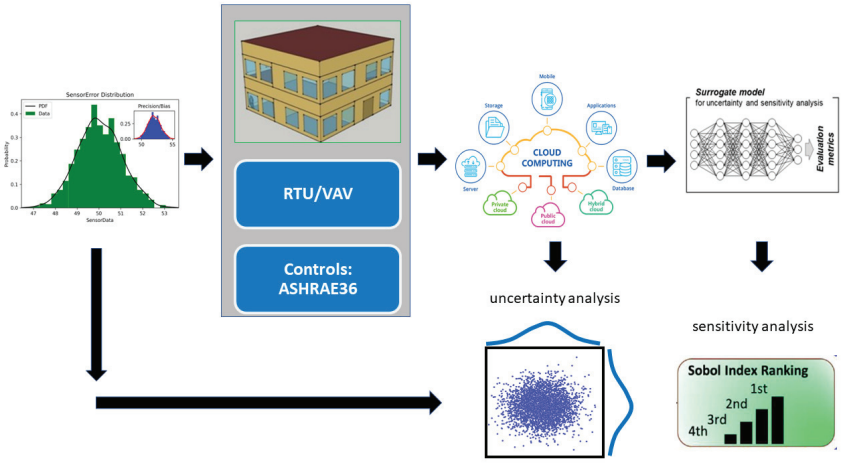

Figure 1. Sensor impact and evaluation framework.

The pseudo code for the sensor fault injection and simulation is shown in Figure 2. The pseudo code follows the basic flowchart in Figure 1, which demonstrates the basic principle of how to implement the sensor impact analysis.

```
for time in range(0, 365*24*60):
    sensor_readings = get_building_states(energyplus_api)
    sensor_err_bias = generate_sensor_err_bias()
    sensor_err_precision = generate_sensor_err_precision()
    sensor_err_tot = sensor_err_bias + sensor_err_precision
    overwrite_sensor_readings(energyplus_api)
    calc_hvac_energy_consumption(energyplus_api)
```

Figure 2. Pseudo code for sensor fault injection and simulation.

2.1. Sensor Sets

Based on extensive literature reviews, 34 sensors were identified. They are typical sensors used to operate RTU and variable air volume (VAV) systems in small to medium office buildings. The sensors were prioritized based on the severity of indoor air (IA) temperature impacts, which can significantly affect energy efficiency and occupant thermal comfort. The identified sensors are frequently used in commercial buildings. They are listed in Table 1.

Table 1. Comprehensive sensor list.

Location	Measurement	Priority	Location	Measurement	Priority
Room	IA temperature	1	RTU	OA CO_2	4
Room	IA humidity	3	RTU	OA flow rate	3
Room	IA CO_2	4	RTU	SA temperature	1
Room	Lighting condition	5	RTU	SA humidity	3
Room	Occupancy	5	RTU	SA CO_2	4
VAV box	SA temperature	1	RTU	SA flow rate	3
VAV box	SA humidity	3	RTU	RA temperature	2
VAV box	SA flow rate	1	RTU	RA humidity	3
Main duct	Static pressure	2	RTU	RA CO_2	4
Exhaust fan	EA temperature	4	RTU	RA flow rate	3
Exhaust fan	EA humidity	4	RTU	MA temperature	2
Exhaust fan	EA flow rate	4	RTU	MA humidity	3
Exhaust fan	EA CO_2	4	RTU	MA CO_2	4
Other	Plug load	5	RTU	MA flow rate	3
Other	Lighting load	5	RTU	Refrigerant temperature	5
RTU	OA temperature	1	RTU	Refrigerant pressure	5
RTU	OA humidity	3	RTU	Refrigerant flow rate	5

SA = supply air; EA = exhaust air; OA = outdoor air; RA = return air; MA = mixing air; IA = indoor air.

Based on the actual HVAC system configuration of the FRP-2 building, five sensor types were selected for the following reasons: (1) Those sensors were closely matching with the selected control logics. Different control logics might need different sets of sensors; (2) the IA temperature is the most important variable to be controlled to meet the heating and cooling set point temperatures; (3) the VAV box supply air (SA) temperature and SA flow rates (SAFs) directly affect the IA temperature from the control perspective; (4) RTU system-level operation also directly affects the VAV box operations; and (5) RTU outdoor air (OA) temperature (OAT) and SA temperature (SAT) are important for determining system-level energy consumption. The sensor types are listed in Table 2. The specification of the selected sensors is described in Table 3.

Table 2. Selected sensor list.

Location	Measurement	Priority	Note
Room	IA temperature	1	IA temperature
VAV box	SAT	1	VAV box SAT
VAV box	SAF	1	VAV box SAF
RTU	OAT	1	OAT
RTU	SAT	1	SAT

Table 3. Specification of the selected sensor.

Measured Data	Range
Outdoor air temperature	−50~100 °C
Indoor air temperature	
Supply air temperature	
Supply airflow rate	0~15.24 m/s

2.2. Sensor Errors

Available literature assumes fixed or constant sensor errors. Here, we proposed the incipient sensor error as bias error and precision (random) error. This research team identified two components for sensor faults [4]: precision and bias. Precision is used to measure how precise the sensor reading is from the true reading because of measuring noise. Bias is used to measure how far the sensor reading is from the true reading because of system bias. Figure 3 shows a diagram for precision and bias. A typical characteristic of incipient faults is that the fault magnitude might change slowly with time and effects on control performance might go unnoticed.

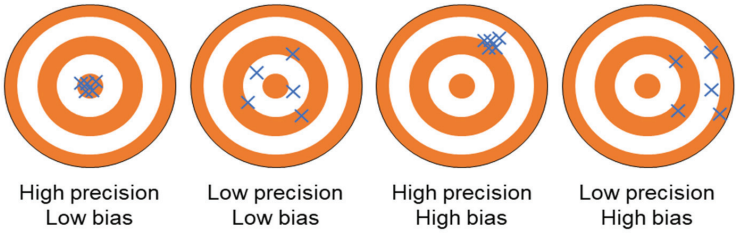

Figure 3. Sensor error component.

For a sensor, an ideal reading (or true reading) exists at a given time step, as shown by the black line in Figure 4. The bias error is the system deviation from the ideal readings, as shown by the green dotted lines in Figure 4. The precision error is the random deviation or noise from the average sensor readings, as shown by the blue dashed lines in Figure 4.

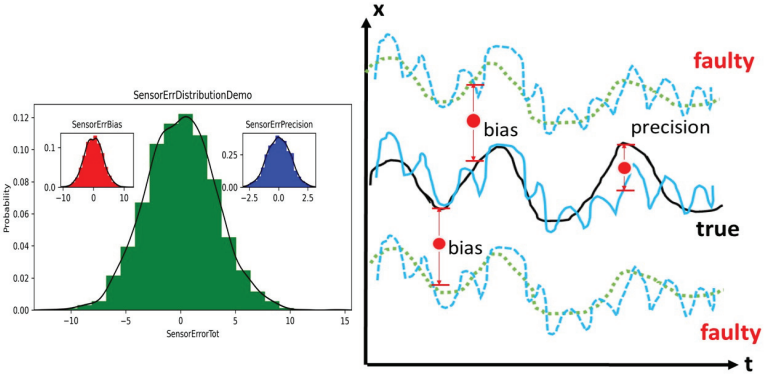

Figure 4. Sensor error diagram.

The mathematical expression of such a fault profile is given as

$$X_f(t) = X_o(t) + X_{bias}(t) + X_{precision}(t) \quad (1)$$

where X_f is the fault reading, X_o is the ideal reading (no fault), X_{bias} is the bias error, and $X_{precision}$ is the precision error.

The bias error is a normal distribution with a certain standard deviation. The expression is given as

$$X_{bias}(t) = N(0, \sigma_{bias}) \quad (2)$$

The precision error is also a normal distribution with a certain standard deviation. The expression is given as

$$X_{precision}(t) = N(0, \sigma_{precision}) \quad (3)$$

where σ_{bias} is the standard deviation of bias error and $\sigma_{precision}$ is the standard deviation of precision error.

The sensor errors were incorporated based on the emulator of EnergyPlus and Python EMS. Due to the technical difficulties from larger airflow sensor errors, the airflow sensor errors need to be within an effective range. The standard deviations for the five types of selected sensors are shown in Table 4.

Table 4. Standard deviation of selected sensor errors.

Location	Measurement	Bias	Precision
Room	IA temperature (°C)	1	0.1
VAV box	SAT (°C)	1	0.1
VAV box	SAF (m^3/s)	0.005	0.0005
RTU	OAT (°C)	1	0.1
RTU	SAT (°C)	1	0.1

2.3. Control Logic for RTU and Single-Duct VAV System (ASHRAE Guideline 36)

The installed HVAC systems in the FRP-2 building are RTUs, in which cooling is from a direct expansion cooling coil and heating is from a gas heating coil. The FRP-2 building has 10 conditioned zones. Each conditioned zone is served by a VAV box with an electricity reheat coil. The air handling unit (AHU) connects all the zone VAV boxes and the RTU. Control logic from ASHRAE Guideline 36-2018, High-Performance Sequences of Operation for HVAC Systems [24], was developed for the RTUs and VAV boxes.

1. AHU: Trim and Respond (T&R) Set Point Logic

The first control logic is the T&R set point logic for the AHU. T&R logic resets set points of the pressure, temperature, or other variables on the AHU or plant side. T&R logic reduces the set point at a fixed rate until the zone thermal comfort is no longer satisfied; then, it generates the request. The set point is increased in response to a sufficient number of requests. By adjusting the importance of each zone's requests, the critical zones will always be satisfied. If there are not a sufficient number of requests, then the set point decreases at a fixed rate.

The term "request" refers to a request to reset a static pressure or temperature set point generated by downstream zones or AHUs. These requests are sent upstream to the AHU or plant that supplies the zone or area that generated the request. For more details of Trim & Respond logic, please refer to the documents of [24,26].

T&R control was used to reset the RTU SA set point temperature in the emulator. When the OAT was higher than the maximum OAT (21 °C), the RTU SAT was set to the minimum RTU SA set point temperature (12 °C). When the OAT was lower than the minimum OAT (16 °C), the RTU SAT was set to the maximum RTU SA set point temperature (18 °C). If the OAT was between the minimum and maximum OAT when the OAT was increased, then the RTU SAT was linearly increased from the minimum RTU SA set point temperature to the maximum RTU SA set point temperature. For T&R control, as ASHRAE Guideline 36 describes, fewer than two requests were ignored.

2. VAV box control logic

The VAV box control is the second control logic applied to the emulator. Figure 5 shows the control logic for the VAV box from ASHRAE Guideline 36. The control logic has three sections, which correspond to the heating mode, cooling mode, and dead-band, and it uses the heating loop demand concept. Heating loop demand is the ratio (as a percentage) of the actual required heating load of the VAV box to the size of the VAV box. Equation (4) describes how to calculate the heating loop demand.

$$Heating\ loop\ demand = \frac{Heating\ load\ of\ the\ VAV\ box}{Capacity\ of\ the\ VAV\ box} \times 100 \quad (4)$$

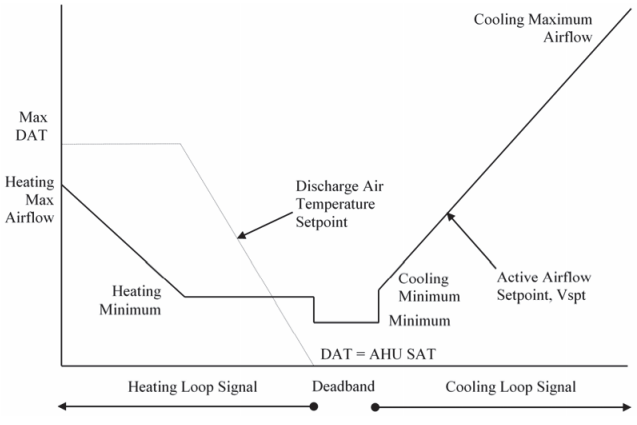

Figure 5. Control logic for VAV box from ASHRAE Guideline 36 [24,26].

The detailed logics are threefold:

a. In the heating mode, when the heating loop is less than or equal to 50%, the discharge air (DA) set point temperature of the VAV box is increased from the RTU SAT to the maximum DA set point temperature of the VAV box, and the minimum SAF is maintained. When the heating loop is greater than 50%, if the DA temperature of the VAV box is greater than the IA temperature plus 3 °C, then the SAF of the VAV box is increased from the minimum SAF to the maximum SAF while maintaining the maximum DA set point temperature of the VAV box;

b. In the cooling mode, the DA temperature of the VAV box is the same as the RTU SAT because no option exists to decrease the SAT using the VAV box. Therefore, VAV box control is linked with T&R control in the cooling season, when the VAV box control must be considered the RTU SAT. The four cooling SA set point temperature reset requests are as follows:

- If the IA temperature exceeds the indoor cooling set point temperature by 3 °C for 2 min and after the suppression period resulting from an RTU SA set point temperature change via the T&R control, then send three requests;
- Else, if the IA temperature exceeds the indoor cooling set point temperature by 2 °C for 2 min and after the suppression period resulting from an RTU SA set point temperature change via the T&R control, then send two requests;
- Else, if the cooling loop is greater than 95%, then send one request until the cooling loop is less than 85%;
- Else, if the cooling loop is less than 95%, then send no request.

In terms of the SAF in the cooling season, the SAF of the VAV box is increased from the minimum SAF to the maximum SAF as the cooling loop is increased;

c. In the dead-band mode, when neither heating nor cooling are needed, the SAF is set to the minimum SAF, and the DA temperature of the VAV box is set to the RTU SAT.

The overall control logic is shown in Figure 6.

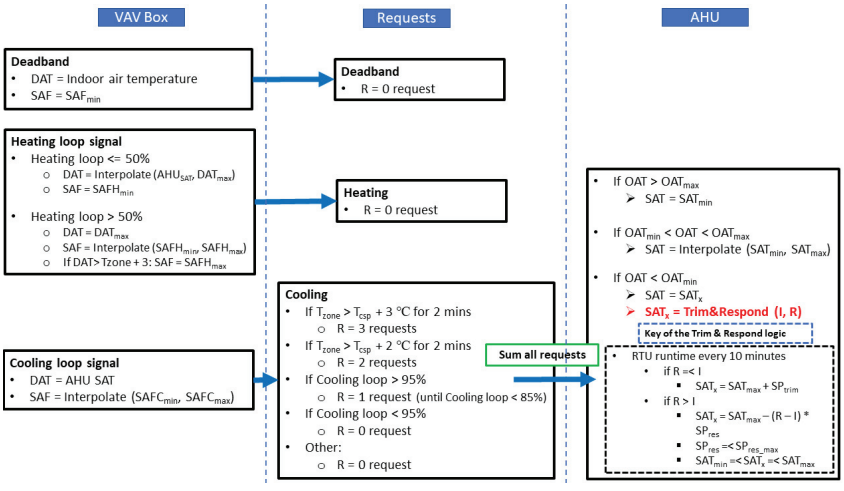

Figure 6. Overall control logic for VAV box and AHU. (DAT: discharge air temperature; SAFH: supply air flow rate for heating; SAFC: supply air flow rate for cooling; R: number of requests; I: ignored responses; SP: respond amount.)

2.4. Large-Scale Simulation

The large-scale simulation was based on a commercial cloud platform, Microsoft Azure. In total, 3600 cases were simulated on the cloud. The inputs were the sensor errors incorporated into the five selected sensors for the FRP-2 building emulator, as shown in Table 2. The sensor errors were obtained using normal distribution samplings. EnergyPlus internal programming limits caused simulation crashes when larger sensor errors were incorporated. The standard deviations of sensor errors were based on multiple trials. The thresholds were based on engineering experience, domain knowledge, and actual RTU- and zone-level sensor ideal readings. The outputs were the target variables for energy consumption and thermal comfort, such as fan electricity consumption and reheat coil electricity energy in the VAV box.

The basic diagram is shown in Figure 7. The basic workflow is as follows:

(1) A Python script was developed to generate 3600 simulation input data files (IDF files). Each IDF file was associated with a Python class of sensor errors through Python EMS. During the simulation, at each time step, a new sensor error (including bias and precision) was injected into the ideal sensor readings from EnergyPlus;
(2) After 3600 cases were generated, they were uploaded to the Azure cloud platform;
(3) In the Azure cloud platform, a bash script selected the appropriate virtual machine configurations (e.g., memory and hard drive, as shown in Table 4) and a number of virtual machines. The team's subscription included 300 nodes (virtual machines);
(4) The Azure cloud provided a job scheduler, which automatically distributed all 3600 cases across 300 nodes;
(5) The simulation ran automatically until all cases were accomplished;
(6) Finally, all the results were selected to set up the data sets (inputs and outputs) to create the black-box models.
(7) The configuration for the cloud is shown in Table 4.

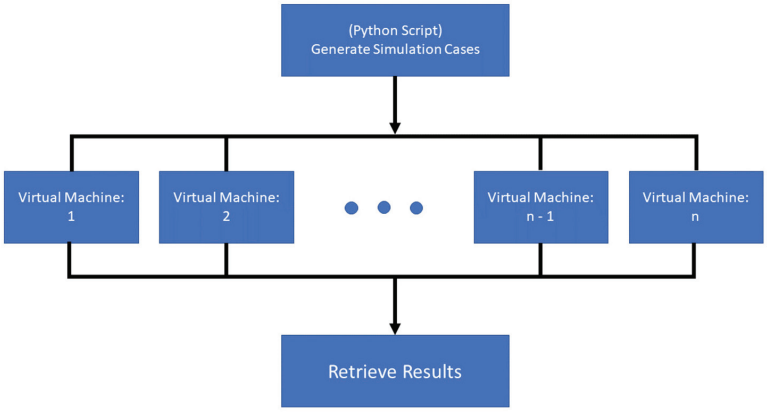

Figure 7. Cloud simulation workflow.

A total of 300 nodes were used for the cloud simulation, in which each node is a standard node: 16 cores, 64 GB memory, and 600 GB storage capacity. The total simulation time is about 9 h.

The sensor errors were sampled using a normal distribution for each time step. The sensor readings from EnergyPlus used the sensor errors to form the faulty sensor readings. The faulty sensor readings were used as inputs to control sequences to calculate new set points. These new set points were used to control the performance of buildings. Ultimately, the simulated energy consumption and thermal comfort were different from the results obtained using the ideal sensor readings.

2.5. Other Aspects

In order to ensure that the simulation results are correct, there are a few extra explanations summarized below.

(1) The baseline model was calibrated with the actual components and systems within the FRP2 building at ORNL campus. The input values for the HVAC system are from the measurement and nameplate values. The simulation results demonstrated the consistency between model and measurements [25];

(2) The simulation cases have a total of 3600 sets. Each case matches with a sensor error module. In each timestep, the sensor error value will be injected into the model following the sensor error components (bias and precision). The energy consumption differences were easily calculated between baseline case and sensor-error case, which was caused by the sensor errors. If sensor errors were made to be zero all through the simulation timesteps, the same energy consumption was obtained with baseline model;

(3) We analyzed the results and see that they are reasonable for sensor errors. For example, (a) when we increase the sensor error to the zone temperature for cooling mode (lower zone temperature than it is supposed to be), we can see the energy consumption increasing. This is because the building model thinks it needs more cooling energy to meet the cooling setpoints. (b) When we increase the sensor error to the zone temperature sensor for heating mode (higher zone temperature than it is supposed to be), we can see the energy consumption decreasing. This is because the building model thinks it needs less heating energy to meet the heating setpoints;

(4) To explain in detail, the sensor error in this study followed the normal distribution (Figure 4) and the sensor error range was calculated by bias sensor error plus precision error. For example, if the standard deviation of sensor error of the temperature sensor is 1 °C, the temperature sensor error range is within −3 °C and +3 °C with a probability of 99.76%. Similarly, the probability of sensor error range between −1 °C and +1 °C is about 68%. The probability of sensor error range within −2 °C and +2 °C is about

95.4%. The extreme cases are within 0.24% of scenarios on the two ends. Therefore, the differences (numbers) mentioned above occur when the sensor error is the largest (either positive or negative values).

3. Surrogate Model

To accomplish sensitivity analysis, the surrogate model was developed based on cloud simulations. The long short-term memory (LSTM) model was selected because it includes previous time step input impacts. These impacts are important because inertia phenomena exist in buildings. The LSTM model internally reflects thermal inertia.

3.1. LSTM Setup

The LSTM model is a neural network model suitable for time-series forecasting. For building energy simulations, the results are time-series variables. The thermal state of buildings at previous time steps has certain impacts on the later time steps. The main purpose of the LSTM model is to find the mapping of inputs and outputs. Figure 8 shows that the input variables were transformed into multiple routes as a way of including previous states' impacts. Detailed mathematics are not included here because the goal was to use the LSTM model to make a black-box model. Many publications already investigated the mathematical details, such as the inventor of LSTM algorithm [27].

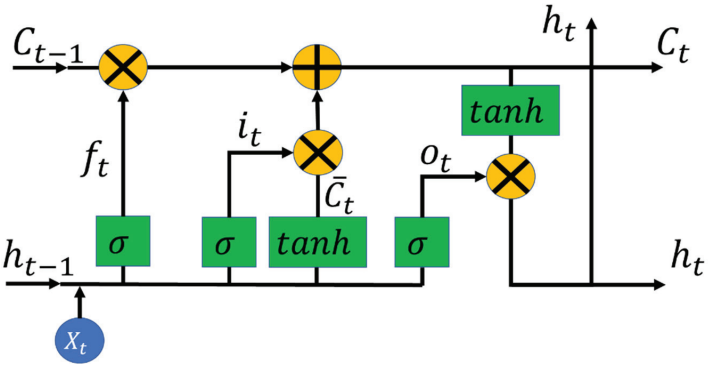

Figure 8. LSTM cell structure.

3.2. Training and Setting

The whole data set was divided into a training data set (80% of total) and a validation data set (20% of total). The training data set was used to learn the weights of input variables to output variables. The validation data set was used to test the accuracy of the surrogate model prediction from the emulator output variables. The data sets were shuffled to avoid the input data internal impacts. The root mean square error was used to quantify the modeling accuracy:

$$RMSE = \sqrt{\frac{\sum_1^N (y_i - \hat{y}_i)^2}{N}} \quad (5)$$

where $RMSE$ is the root mean square error, y_i is the emulator output variable, $\hat{y}_i$ is the surrogate model output variable, and N is the total number of variables in the prediction.

3.3. Input/Output Variables

The surrogate model established the mapping relationship between input and output variables. The input variables were based on the FRP-2 EnergyPlus models. A detailed list of variables is provided in Table 5.

Table 5. Input variables.

Variable Name	Quantity
OAT	1
OA relative humidity	1
OA pressure	1
Wind speed	1
Wind direction	1
Horizontal infrared radiation rate	1
Diffuse solar radiation rate	1
Direct solar radiation rate	1
Lighting energy	1
Internal heat gains: equipment	1
People activity	1
SensorBias: AHU OAT	1
SensorPrecision: AHU OAT	1
SensorTotalError: AHU OAT	1
SensorBias: AHU SAT	1
SensorPrecision: AHU SAT	1
SensorTotalError: AHU SAT	1
SensorBias: zone VAV SAF	10
SensorPrecision: zone VAV SAF	10
SensorTotalError: zone VAV SAF	10
SensorBias: zone VAV SAT	10
SensorPrecision: zone VAV SAT	10
SensorTotalError: zone VAV SAT	10
SensorBias: zone air temperature	10
SensorPrecision: zone air temperature	10
SensorTotalError: zone air temperature	10
Total	107

The output variables were also based on FRP-2 EnergyPlus simulation models. A detailed list of output variables is provided in Table 6.

Table 6. Output variables.

Variable	Quantity
Fan electricity rate (W)	1
Main cooling coil sensible cooling rate (W)	1
Main cooling coil electricity rate (W)	1
Main heating coil heating rate (W)	1
Zone air sensible heating rate (W)	10
Zone air sensible cooling rate (W)	10
Zone air temperature (°C)	10
Zone predicted percentage dissatisfied (%)	10
VAV box reheat energy (W)	10
Total	54

3.4. Workflow for Surrogate Model Training

In total, 3600 simulation cases were simulated on the cloud. Each case generated 1.3 GB of data with 1 min time resolution. A 4.7 TB data set was obtained. To expedite the surrogate model training, a distributed machine learning framework was used. The workflow is shown in Figure 9. Through the cloud, 32-core machines were used. The 3600 cases were divided into 20 groups, or cores, with each group responsible for 180 cases. After all training was completed for each group, the final model parameters were obtained by averaging model parameters from the 20 groups of training.

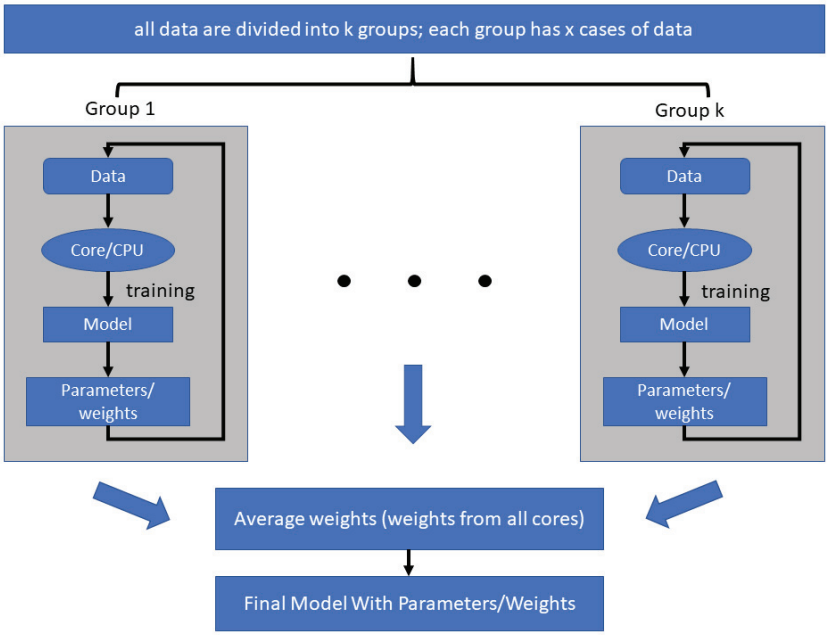

Figure 9. Distributed training of surrogate models.

4. Uncertainty Analysis

4.1. Uncertainty Analysis Setup

Uncertainty analysis assesses the uncertainty of output/target variables in the model in which the inputs are under uncertainty samplings. The purpose of this uncertainty analysis was to identify how output variables were distributed in response to uncertainties of input values. Generally, a wider distribution of output variables corresponds with increased sensitivity of the output variables to the input variables. For this uncertainty analysis, the large-scale simulation (3600 cases) was conducted on a cloud platform. Figure 10 illustrates the overall process of the uncertainty analysis. The standard deviations of input values (sensor errors) of the uncertainty analysis are listed in Table 5 and selected output variables are listed in Table 6. Before the uncertainty analysis, HVAC system controls based on ASHRAE Guideline 36 [24] were applied using the Python EMS function, as described in Section 2.3. Input values for the system control were obtained from the simulation results; then, the total sensor error was added to the HVAC system control. Using the physics-based emulator, 3600 cases were generated. The results are described in Section 4.2.

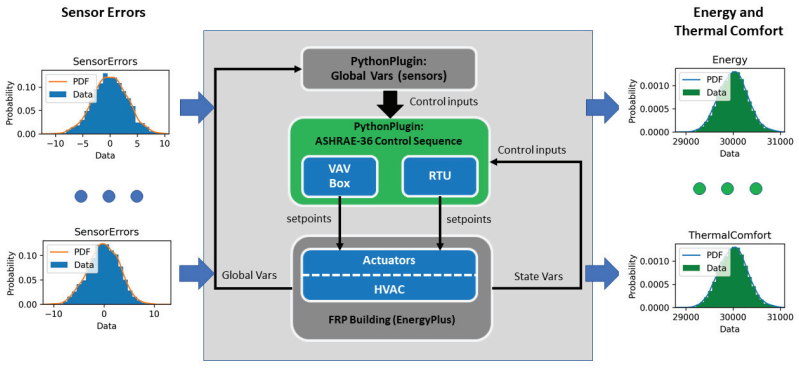

Figure 10. Uncertainty analysis process.

4.2. Uncertainty Analysis Results

For large-scale simulations, each case generated the aggregated energy consumption: site energy, heating energy, cooling energy, and fan energy. The baseline results are 304,083 kBTU (site energy), 60,081 kBTU (heating energy), 105,482 kBTU (cooling energy), and 50,422 kBTU (fan energy). Figure 11 demonstrates the energy distributions under sensor fault and baseline energy items. It shows that the energy consumption varies drastically from the baseline cases, due to the sensor errors.

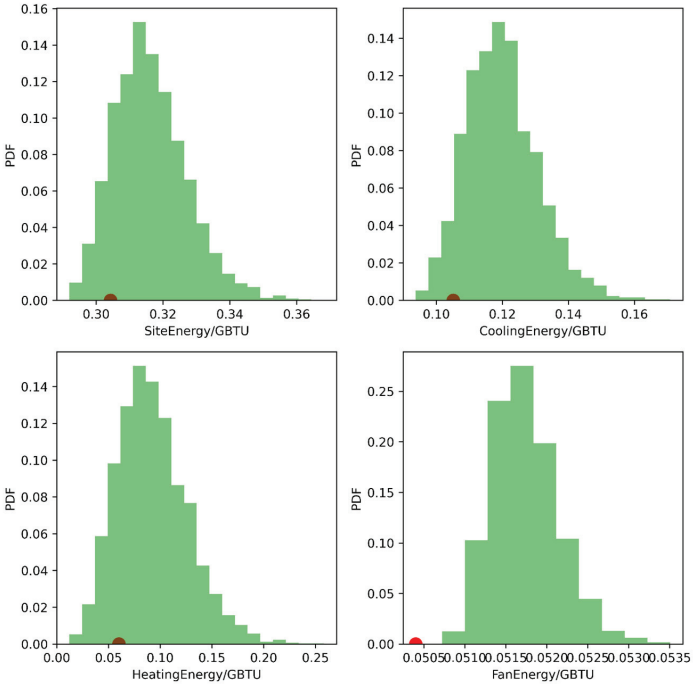

Figure 11. Energy distributions and baseline energy items.

Figure 12 shows the site energy consumption with averaged sensor error distributions. The top left shows the AHU OAT and SAT sensor errors with site energy consumption. The top right shows the VAV box SAT sensor errors and site energy consumption. The bottom left shows the zone temperature sensor errors with site energy consumption.

The bottom right shows the VAV box SAF sensor errors with site energy consumption. From the distributions, the sensor errors show normal distributions instead of a linear relationship. The site energy consumption was 294,000~359,000 kBtu/year based on the distribution of sensor total errors. The change of total site energy consumption was 65,000 kBtu/year, which is 21.4% of the average site energy consumption (340,083 kBtu/year). The site energy impacts could go −3.3% lower or 18.1% higher, compared with baseline. The above energy patterns are a comprehensive demonstration of sensor errors. The underlying logics are: (1) For negative sensor errors under cooling mode, zone temperature sensors would deliver smaller sensor readings to the controls. This could make the control systems call on a larger supply air flow rate or supply air temperature to meet the zone thermal setpoints. This could cause more energy consumption for the cooling coils. (2) For positive sensor errors under cooling mode, zone temperature sensors might deliver higher sensor readings to the controls. This could fool the control system to call on a smaller supply air flow rate or supply air temperature. This will cause the zone to be too hot, subject to thermal comfort issue. (3) For negative sensor errors under heating mode, the zone temperature sensor reading would be smaller, which fools the control system to increase the supply air temperature or supply air flow rate to maintain the zone temperature setpoints. This could cause more heating energy consumption from the heating coils. (4) For positive sensor errors under heating mode, the zone temperature sensor reading would be higher, which leads the control system to decrease supply air temperature or supply air flow rate to maintain the thermal setpoints. This would cause less heating energy demands from the heating coils. Since the sensor errors evolve each time step, this adds more complexity to the control actions, which lead to complicated energy consumption patterns.

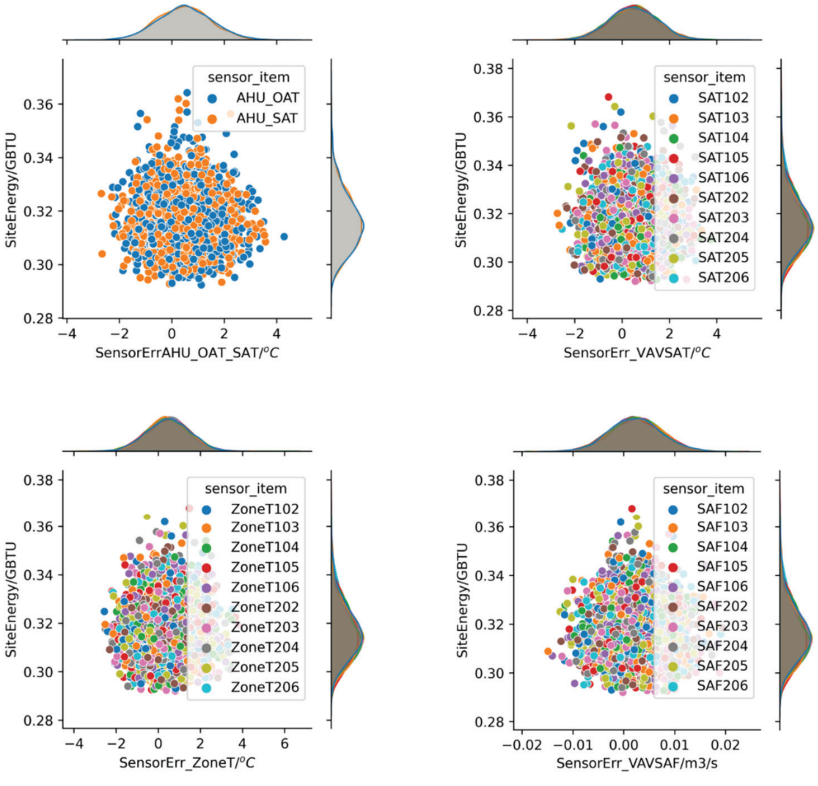

Figure 12. Site energy and sensor errors.

Figure 13 shows the total heating energy consumption with averaged sensor error distributions. The top left shows the AHU OAT and SAT sensor errors with heating energy consumption. The top right shows the VAV box SAT sensor errors and heating energy consumption. The bottom left shows the zone temperature sensor errors with heating energy consumption. The bottom right shows the VAV box SAF sensor errors with heating energy consumption. From the distributions, the sensor errors show normal distributions instead of a linear relationship.

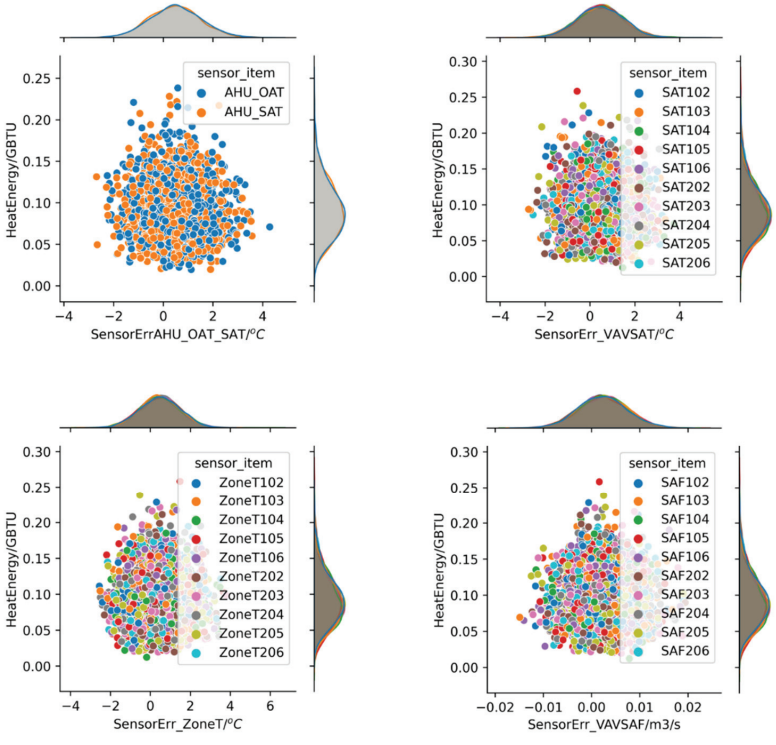

Figure 13. Heating energy and sensor errors.

The heating energy consumption was 20,130~249,000 kBtu/year based on the distribution of sensor total errors. The change of total heating energy consumption was 228,870 kBtu/year, which is 380% of the baseline heating energy consumption (23,265 kBtu/year). The heating energy impacts could go −66.5% lower or 314.4% higher, compared with baseline.

Figure 14 shows the total cooling energy consumption with averaged sensor error distributions. The top left shows the AHU OAT and SAT sensor errors with cooling energy consumption. The top right shows the VAV box SAT sensor errors with cooling energy consumption. The bottom left shows the zone temperature sensor errors with cooling energy consumption. The bottom right shows the VAV box SAF sensor errors with cooling energy consumption. From the distributions, the sensor errors show normal distributions instead of a linear relationship. The cooling energy consumption was 93,320~174,000 kBtu/year based on the distribution of sensor total errors. The range of total cooling energy consumption change was 80,680 kBtu/year, which is 76.5% of the baseline cooling energy consumption (133,660 kBtu/year). The cooling energy impacts could go −11.5% lower or 65.0% higher, compared with baseline.

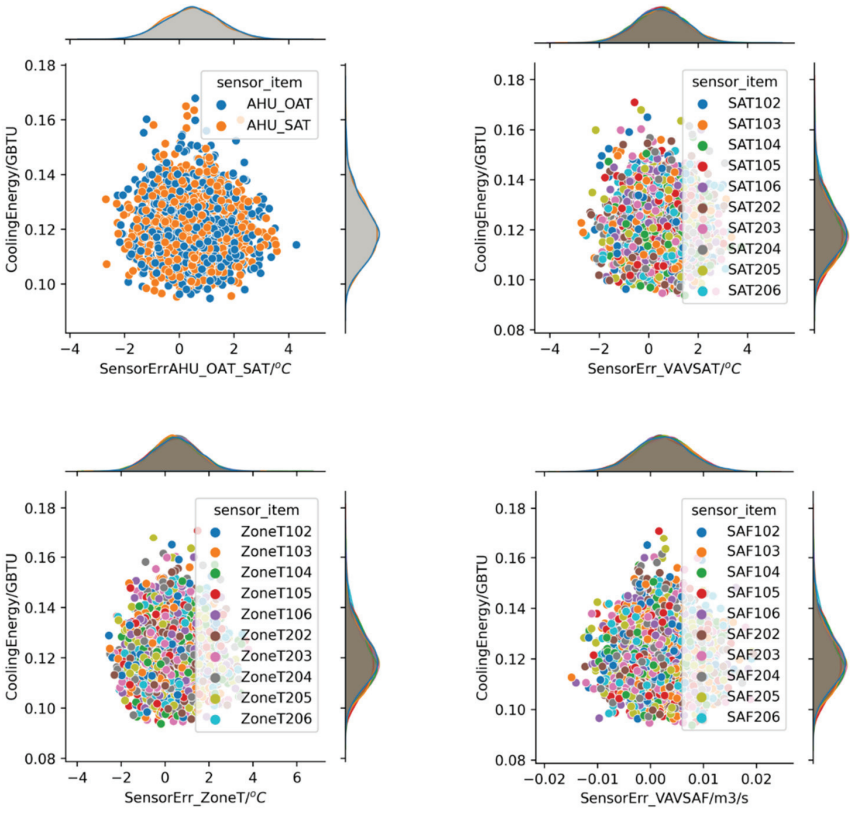

Figure 14. Cooling energy and sensor errors.

Figure 15 shows the total fan energy consumption with averaged sensor error distributions. The top left shows the AHU OAT and SAT sensor errors with fan energy consumption. The top right shows the VAV box SAT sensor errors with fan energy consumption. The bottom left shows the zone temperature sensor errors with fan energy consumption. The bottom right shows the VAV box SAF sensor errors with fan energy consumption. From the distributions, the sensor errors show normal distributions instead of a linear relationship.

The fan energy consumption was 50,501~53,900 kBtu/year based on the distribution of sensor total errors. The change of total fan energy consumption was 3399 kBtu/year, which is 6.7% of the baseline fan energy consumption (50,422 kBtu/year). The fan energy impacts could go 0.15% lower or 6.9% higher, compared with baseline.

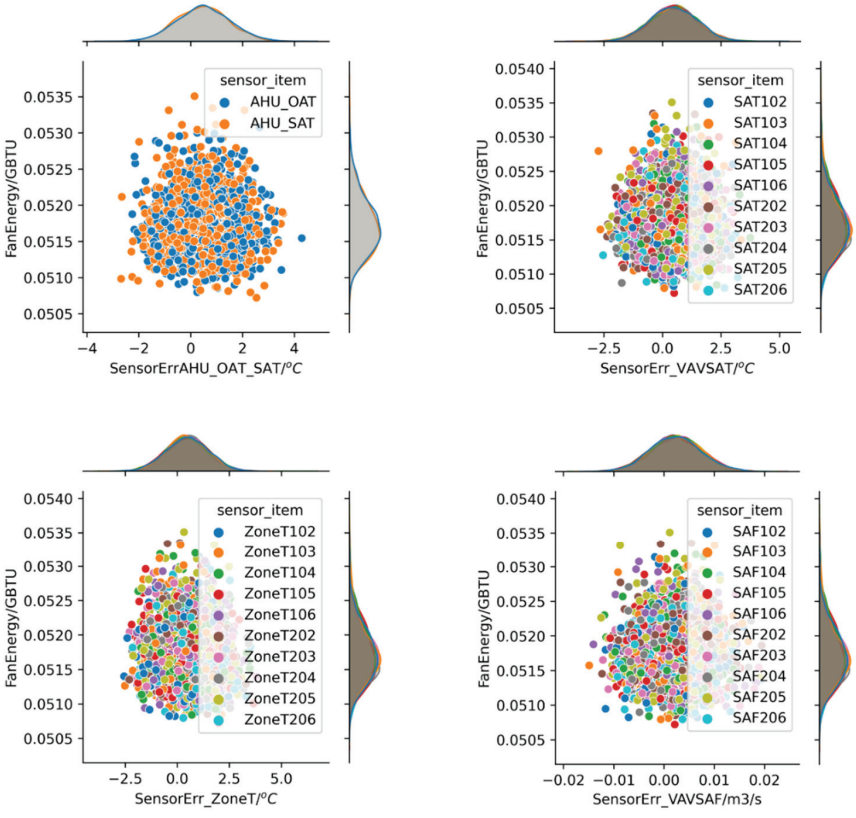

Figure 15. Fan energy and sensor errors.

5. Sensitivity Analysis

5.1. Sensitivity Analysis Principle

The sensitivity analysis identified which sensor errors have stronger impacts on energy consumption and thermal comfort. A ranking of sensor error impacts was obtained using sensitivity analysis index values. Sensitivity analysis can be performed in various ways, including through local and global approaches [28,29]. Different methods have certain strengths and drawbacks. As a preliminary exploration, this project applied the Sobol method [28] to calculate the sensitivity index.

The principle is described as

$$Y = f_0 + \sum_{i=1}^{d} f_i(X_i) + \sum_{i<j}^{d} f_{ij}(X_i, X_j) + \cdots + f_{1,2,\ldots,d}(X_1, X_2, \ldots, X_d) \quad (6)$$

where Y is one of the interested model outputs, X_i is the model input with uncertainty, d is the total number of model inputs with uncertainties, f_0 is the constant, f_i is the function of X_i, and f_{ij} is the function of X_i and X_j.

The sensitivity index is given as

$$S_i = \frac{V_i}{Var(Y)} \quad (7)$$

where V_i is the variance with respect to variable input X_i and $Var(Y)$ is the total variance of the output variable Y.

The definitions of these variances are

$$V_i = Var_{X_i}(E_{X_{\sim i}}(Y|X_i)) \tag{8}$$

$$Var(Y) = \sum_{i=1}^{d} V_i + \sum_{i<j}^{d} V_{ij} + \ldots + V_{12\ldots d} \tag{9}$$

where, $\sim i$ means all the input variables except X_i.

Note that

$$\sum_{i=1}^{d} S_i + \sum_{i<j}^{d} S_{ij} + \ldots + S_{12\ldots d} = 1 \tag{10}$$

The workflow for the sensitivity analysis is shown in Figure 16.

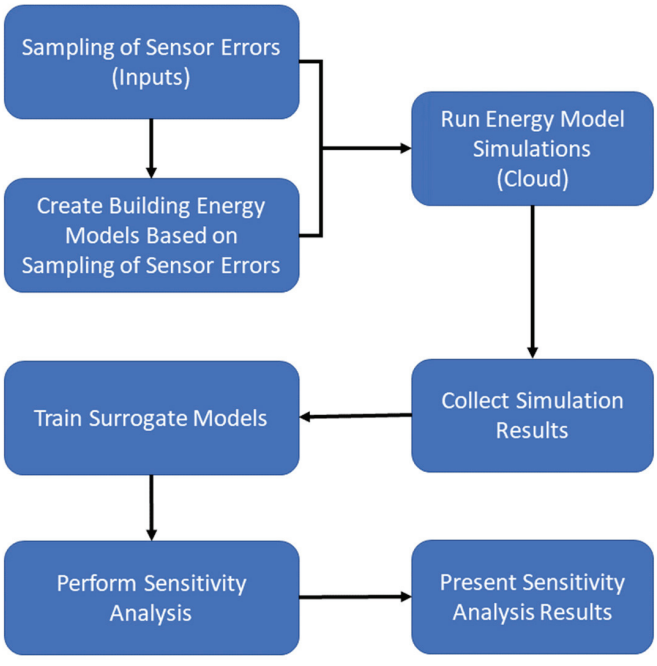

Figure 16. Sensitivity analysis flowchart.

5.2. Sensitivity Analysis Results

Based on the simulation results, AHU- and zone-level sensitivity analyses were performed. The results are presented in the following subsections. For zone-level analysis, there are two floors and each floor has five zones. They have similar patterns in regard to the sensitivity analysis. One zone from each floor (zone 102 and zone 204) was selected to demonstrate the sensitivity analysis.

5.2.1. System SA Analysis

The AHU power consumption was studied. Figure 17 illustrates the sensitivity index for cooling power. The cooling power is sensitive to the random errors of the SAT and OAT sensors, total errors of the SAT and OAT sensors, and bias errors of the SAT and OAT sensors. They have equal impacts on cooling power demands.

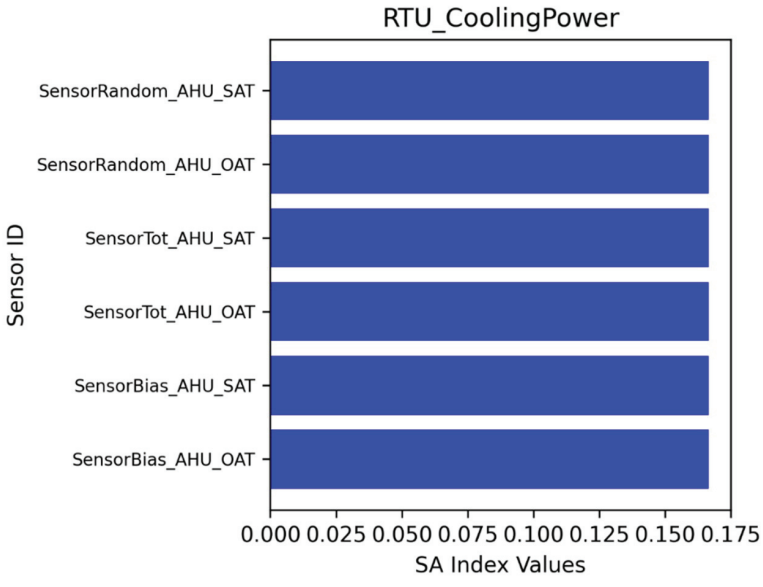

Figure 17. SA for RTU cooling power.

Figure 18 illustrates the sensitivity index for fan power demands. The sensor impacts are similar to the cooling power. Figure 19 illustrates the sensitivity index for main heating coil heating rates. The SAT and OAT sensors are the most dominant sensors.

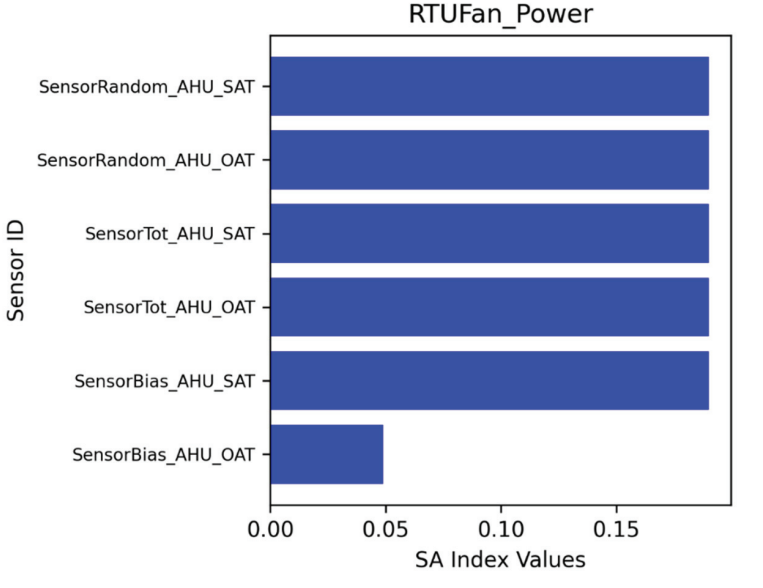

Figure 18. SA for RTU fan power.

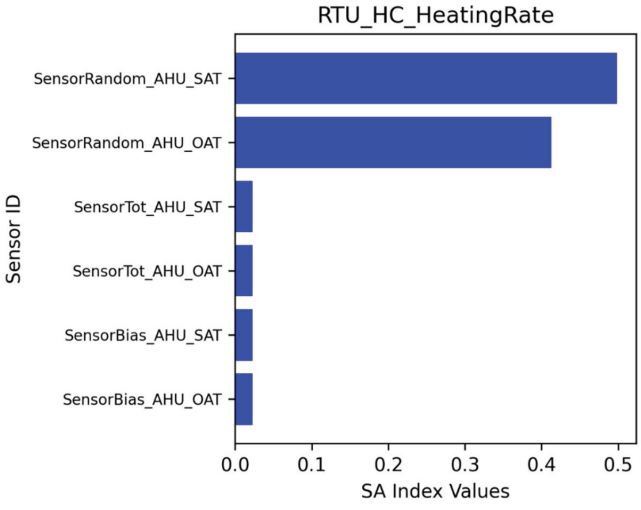

Figure 19. SA for RTU main heating coil heating rate.

5.2.2. Zone 204 SA Analysis

At the zone level, four energy consumption variables (zone temperature, zone sensible heating, zone sensible cooling, and reheat coil energy consumption) and one thermal comfort variable (zone-predicted percentage of dissatisfied occupants [PPD]) were selected. Figure 20 shows the ranking of the sensitivity index for zone air temperature. Overall, the system- and zone-level sensors affected the zone temperature. The sensor with the highest sensitivity index was the zone air temperature sensor with random error. The random errors were the most influential, followed by total errors and then bias errors. Figure 21 shows the ranking of the sensitivity index for zone sensible heating. The zone air temperature sensor with random error had the highest sensitivity index. Figure 22 shows the zone sensible cooling impacts from the sensors. Figure 23 shows the impacts on reheat coil energy. Figure 24 shows the sensitive index ranking for zone thermal comfort (PPD). Across zone 204 outputs, the random errors consistently had stronger impacts.

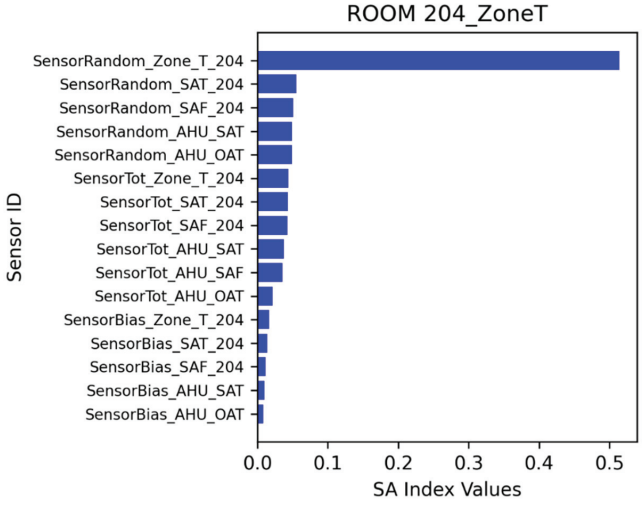

Figure 20. SA for zone 204 air temperature.

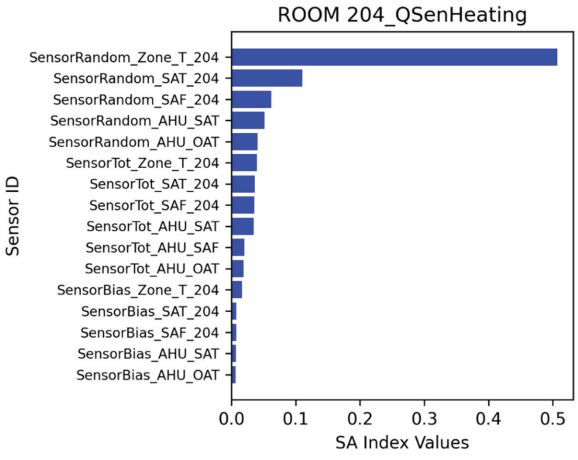

Figure 21. SA for zone 204 sensible heating.

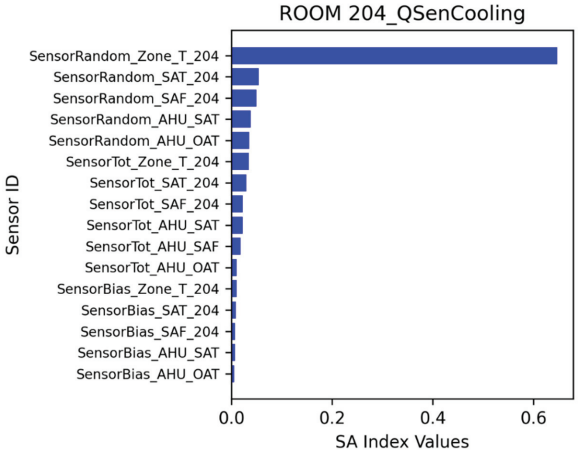

Figure 22. SA for zone 204 sensible cooling.

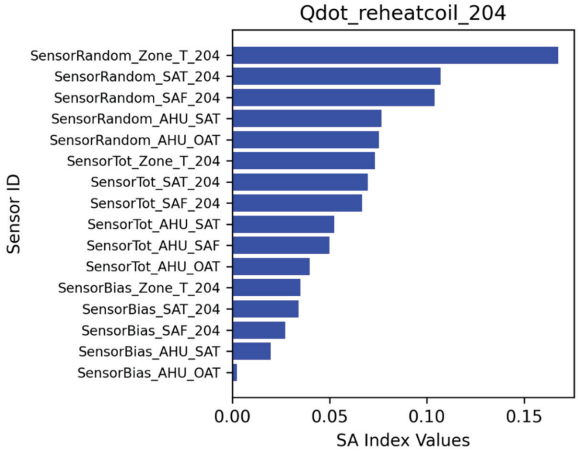

Figure 23. SA for zone 204 reheat coil energy.

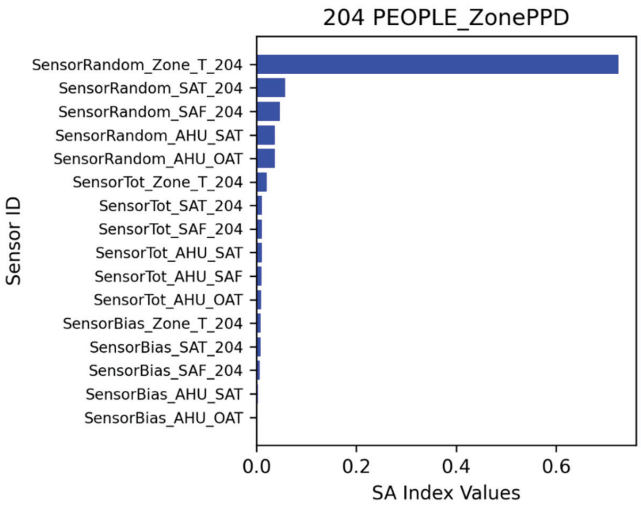

Figure 24. SA for zone 204 PPD.

5.2.3. Zone 102 SA Analysis

Sensitivity analysis for zone 102 was performed similarly to that of zone 204. The impacts of sensor errors on four energy consumption variables (zone temperature, zone sensible heating, zone sensible cooling, and reheat coil energy consumption) and one thermal comfort variable (zone PPD) were demonstrated. Figure 25 shows the ranking of the sensitivity index for zone 102 air temperature. The system-level sensors and zone-level sensors affected the zone temperature. The zone air temperature sensor with random error had the highest sensitivity index. Figure 26 shows the ranking of the sensitivity index for zone sensible heating. The zone air temperature sensor with random error had the highest sensitivity index. Figure 27 shows the zone sensible cooling impacts from the sensors. Figure 28 shows the impacts on reheat coil energy. Figure 29 shows the sensitivity index ranking for zone thermal comfort (PPD). Across zone 102 output variables, random errors consistently had stronger impacts.

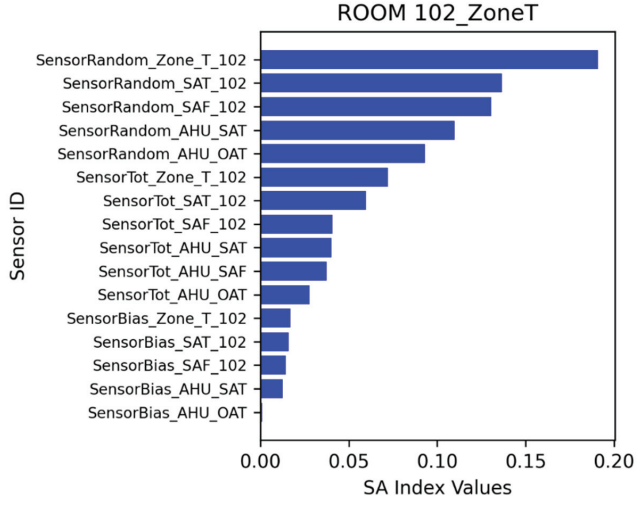

Figure 25. SA for zone 102 air temperature.

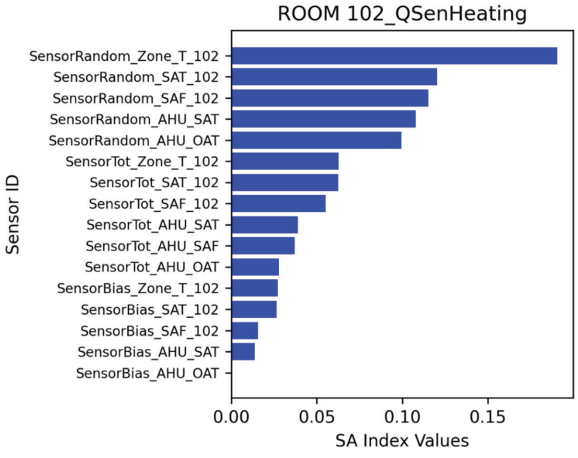

Figure 26. SA for zone 102 sensible heating energy.

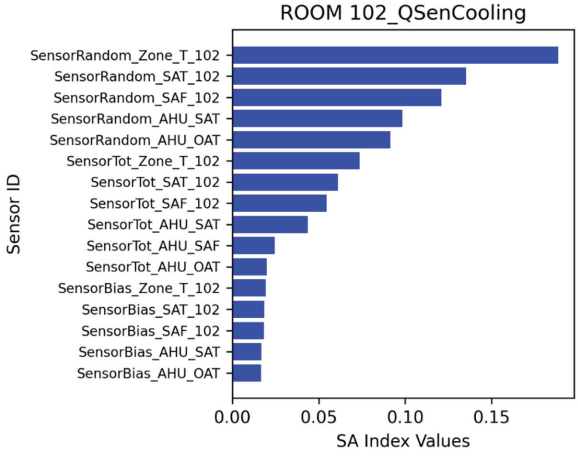

Figure 27. SA for zone 102 sensible cooling energy.

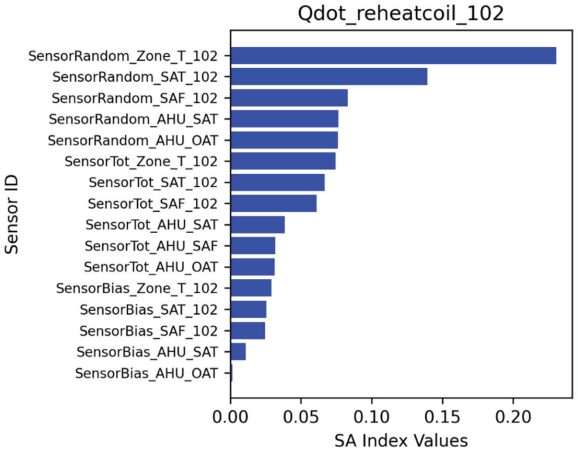

Figure 28. SA for zone 102 reheat coil energy.

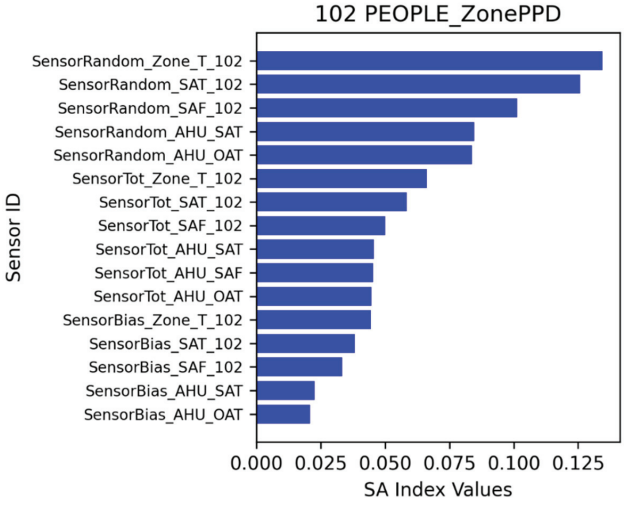

Figure 29. SA for zone 102 PPD.

6. Conclusions

This study investigated the incipient sensor impacts on the ASHRAE Guideline 36 control sequences through sensitivity and uncertainty analyses. The sensor errors had two components: bias error and precision (random) error. The sensor samplings were performed with normal distributions. Cloud simulations were conducted based on the sensor samplings and 3600 simulation cases. The results were collected to train surrogate models for sensitivity analysis.

The energy consumption was classified into system levels (power demands) and zone levels (zone air temperature, zone sensible heating, zone sensible cooling, and zone reheat coil energy). The thermal comfort (PPD) at the zone level was also investigated.

The uncertainty and sensitivity analyses were conducted with respect to sensor errors and energy/thermal comfort variables. The uncertainty analysis showed that the sensor errors and energy consumptions have a nonlinear relationship. The energy consumptions have wide distributions compared with the baseline model with sensor error uncertainties:

- The site energy differences could go −3.3% lower or 18.1% higher, compared with baseline;
- The heating energy differences could go −66.5% lower or 314.4% higher, compared with baseline;
- The cooling energy differences could go −11.5% lower or 65.0% higher, compared with baseline;
- The fan energy differences could go 0.15% lower or 6.9% higher, compared with baseline.

The sensitivity analysis was performed at both system and zone levels. At the system level, the random errors for SAT and OAT sensors had the most significant impacts. At the zone level, the random errors were the most influential, followed by total errors and then bias errors.

In the future, there are a few works worth exploring:

- Other sensitivity analysis methods will be used for comparative analysis;
- Other control strategies or HVAC systems will be used for more demonstrations.

This study clearly demonstrated the severe impacts of incipient sensor faults. The implications for research, policy, and study are: (1) calibrating sensors as recommended by the manufacturer. (2) if calibration is feasible, fault mitigations are recommended.

Author Contributions: Y.L.: Modeling development and simulations, Investigation, Data analysis, Writing—original draft, Writing—review & editing; P.I.: Supervision, Data analysis, Project management, Conceptualization, Investigation, Writing—review & editing, and Funding acquisition; S.L. (Seungjae Lee): Modeling development and simulation, Conceptualization, Investigation; Y.B.: Modeling development and simulation, Conceptualization, and Project management; Y.Y.: Modeling development and simulation, Writing—original draft, and Data analysis; S.L. (Sangkeun Lee): Modeling simulation. All authors have read and agreed to the published version of the manuscript.

Funding: This work was funded by field work proposal CEBT105 under DOE BTO activity nos. BT0302000 and BT0305000.

Acknowledgments: This material is based upon work supported by the US Department of Energy's (DOE's) Office of Science and Building Technologies Office (BTO). This research used resources of Oak Ridge National Laboratory's Building Technologies Research and Integration, which is a DOE Office of Science User Facility. This work was funded by field work proposal CEBT105 under DOE BTO activity nos. BT0302000 and BT0305000. This manuscript has been authored by UT-Battelle LLC under contract DEAC05-00OR22725 with DOE. The US government retains and the publisher, by accepting the article for publication, acknowledges that the US government retains a nonexclusive, paid-up, irrevocable, worldwide license to publish or reproduce the published form of this manuscript, or allow others to do so, for US government purposes.

Conflicts of Interest: The authors declare that they have no known competing financial interests or personal relationships that could have appeared to influence the work reported in this paper.

References

1. Analysis & Projections—U.S. Energy Information Administration (EIA). Available online: https://www.eia.gov/analysis/index.php (accessed on 9 September 2022).
2. Liu, X.; Lu, S.; Hughes, P.; Cai, Z. A comparative study of the status of GSHP applications in the United States and China. *Renew. Sustain. Energy Rev.* **2015**, *48*, 558–570. [CrossRef]
3. Shen, B.; Ally, M.R. Energy and Exergy Analysis of Low-Global Warming Potential Refrigerants as Replacement for R410A in Two-Speed Heat Pumps for Cold Climates. *Energies* **2020**, *13*, 5666. [CrossRef]
4. Bae, Y.; Bhattacharya, S.; Cui, B.; Lee, S.; Li, Y.; Zhang, L.; Im, P.; Adetola, V.; Vrabie, D.; Leach, M.; et al. Sensor impacts on building and HVAC controls: A critical review for building energy performance. *Adv. Appl. Energy* **2021**, *4*, 100068. [CrossRef]
5. Li, Y.; O'Neill, Z. A critical review of fault modeling of HVAC systems in buildings. In Proceedings of the Building Simulation, Cambridge, UK, 11–12 September 2018; Springer: Berlin/Heidelberg, Germany, 2018; Volume 11, pp. 953–975.
6. Basarkar, M.; Pang, X.; Wang, L.; Haves, P.; Hong, T. *Modeling and Simulation of HVAC Faults in EnergyPlus*; Lawrence Berkeley National Lab. (LBNL): Berkeley, CA, USA, 2011.
7. Ni, K.; Ramanathan, N.; Chehade, M.N.H.; Balzano, L.; Nair, S.; Zahedi, S.; Kohler, E.; Pottie, G.; Hansen, M.; Srivastava, M. Sensor network data fault types. *ACM Trans. Sens. Netw. (TOSN)* **2009**, *5*, 1–29. [CrossRef]
8. Lu, X.; O'Neill, Z.; Li, Y.; Niu, F. A novel simulation-based framework for sensor error impact analysis in smart building systems: A case study for a demand-controlled ventilation system. *Appl. Energy* **2020**, *263*, 114638. [CrossRef]
9. Li, Y.; O'Neill, Z. An innovative fault impact analysis framework for enhancing building operations. *Energy Build.* **2019**, *199*, 311–331. [CrossRef]
10. O'Neill, Z.D.; Li, Y.; Cheng, H.C.; Zhou, X.; Taylor, S.T. Energy savings and ventilation performance from CO_2-based demand controlled ventilation: Simulation results from ASHRAE RP-1747 (ASHRAE RP-1747). *Sci. Technol. Built Environ.* **2020**, *26*, 257–281. [CrossRef]
11. Ye, Y.; Chen, Y.; Zhang, J.; Pang, Z.; O'Neill, Z.; Dong, B.; Cheng, H. Energy-saving potential evaluation for primary schools with occupant-centric controls. *Appl. Energy* **2021**, *293*, 116854. [CrossRef]
12. Pang, Z.; Chen, Y.; Zhang, J.; O'Neill, Z.; Cheng, H.; Dong, B. Nationwide HVAC energy-saving potential quantification for office buildings with occupant-centric controls in various climates. *Appl. Energy* **2020**, *279*, 115727. [CrossRef]
13. Maasoumy, M.; Razmara, M.; Shahbakhti, M.; Vincentelli, A. Handling model uncertainty in model predictive control for energy efficient buildings. *Energy Build.* **2014**, *77*, 377–392. [CrossRef]
14. Bengea, S.; Adetola, V.; Kang, K.; Liba, M.J.; Vrabie, D.; Bitmead, R.; Narayanan, S. Parameter estimation of a building system model and impact of estimation error on closed-loop performance. In Proceedings of the 2011 50th IEEE Conference on Decision and Control and European Control Conference, Orlando, FL, USA, 12–15 December 2011; pp. 5137–5143.
15. Chen, J.; Zhang, L.; Li, Y.; Shi, Y.; Gao, X.; Hu, Y. A review of computing-based automated fault detection and diagnosis of heating, ventilation and air conditioning systems. *Renew. Sustain. Energy Rev.* **2022**, *161*, 112395. [CrossRef]
16. Yoon, S.; Yu, Y.; Wang, J.; Wang, P. Impacts of HVACR temperature sensor offsets on building energy performance and occupant thermal comfort. In Proceedings of the Building Simulation, Rome, Italy, 2–4 September 2019; Springer: Berlin/Heidelberg, Germany, 2019; Volume 12, pp. 259–271.

17. Kim, J.; Frank, S.; Braun, J.E.; Goldwasser, D. Representing small commercial building faults in energyplus, Part I: Model development. *Buildings* **2019**, *9*, 233. [CrossRef]
18. Kim, J.; Frank, S.; Im, P.; Braun, J.E.; Goldwasser, D.; Leach, M. Representing small commercial building faults in EnergyPlus, part II: Model validation. *Buildings* **2019**, *9*, 239. [CrossRef]
19. Zhao, Y.; Li, T.; Zhang, X.; Zhang, C. Artificial intelligence-based fault detection and diagnosis methods for building energy systems: Advantages, challenges and the future. *Renew. Sustain. Energy Rev.* **2019**, *109*, 85–101. [CrossRef]
20. Wang, P.; Li, J.; Yoon, S.; Zhao, T.; Yu, Y. The detection and correction of various faulty sensors in a photovoltaic thermal heat pump system. *Appl. Therm. Eng.* **2020**, *175*, 115347. [CrossRef]
21. Gunes, V.; Peter, S.; Givargis, T. Improving energy efficiency and thermal comfort of smart buildings with HVAC systems in the presence of sensor faults. In Proceedings of the 2015 IEEE 17th International Conference on High Performance Computing and Communications, New York, NY, USA, 24–26 August 2015; IEEE: Piscataway, NJ, USA, 2015; pp. 945–950.
22. Zhang, L.; Leach, M.; Bae, Y.; Cui, B.; Bhattacharya, S.; Lee, S.; Im, P.; Adetola, V.; Vrabie, D.; Kuruganti, T. Sensor impact evaluation and verification for fault detection and diagnostics in building energy systems: A review. *Adv. Appl. Energy* **2021**, *3*, 100055. [CrossRef]
23. Cheung, H.; Braun, J.E. Empirical modeling of the impacts of faults on water-cooled chiller power consumption for use in building simulation programs. *Appl. Therm. Eng.* **2016**, *99*, 756–764. [CrossRef]
24. ASHRAE Guideline 36-2018: High-Performance Sequences of Operation for HVAC Systems 2022. Available online: https://www.techstreet.com/ashrae/standards/guideline-36-2018-high-performance-sequences-of-operation-for-hvac-systems (accessed on 9 September 2022).
25. Im, P.; Joe, J.; Bae, Y.; New, J.R. Empirical validation of building energy modeling for multi-zones commercial buildings in cooling season. *Appl. Energy* **2020**, *261*, 114374. [CrossRef]
26. Taylor, S. Resetting setpoints using trim & respond logic. *Ashrae J.* **2015**, *11*, 52–57.
27. Hochreiter, S.; Schmidhuber, J. Long short-term memory. *Neural Comput.* **1997**, *9*, 1735–1780. [CrossRef]
28. Tian, W. A review of sensitivity analysis methods in building energy analysis. *Renew. Sustain. Energy Rev.* **2013**, *20*, 411–419. [CrossRef]
29. Pang, Z.; O'Neill, Z.; Li, Y.; Niu, F. The role of sensitivity analysis in the building performance analysis: A critical review. *Energy Build.* **2020**, *209*, 109659. [CrossRef]

buildings

MDPI

Article

Potential Cooling Energy Savings of Economizer Control and Artificial-Neural-Network-Based Air-Handling Unit Discharge Air Temperature Control for Commercial Building

Yeobeom Yoon [1,2,*,†], Byeongmo Seo [2,†] and Soolyeon Cho [2,*]

[1] Oak Ridge National Laboratory, One Bethel Valley Road, Oak Ridge, TN 37830, USA
[2] College of Design, North Carolina State University, Raleigh, NC 27695, USA
* Correspondence: yoony@ornl.gov (Y.Y.); soolyeon_cho@ncsu.edu (S.C.)
† These authors contributed equally to this work.

Abstract: Heating, ventilation, and air-conditioning (HVAC) systems play a significant role in building energy consumption, accounting for around 50% of total energy usage. As a result, it is essential to explore ways to conserve energy and improve HVAC system efficiency. One such solution is the use of economizer controls, which can reduce cooling energy consumption by using the free-cooling effect. However, there are various types of economizer controls available, and their effectiveness may vary depending on the specific climate conditions. To investigate the cooling energy-saving potential of economizer controls, this study employs a dry-bulb temperature-based economizer control approach. The dry-bulb temperature-based control strategy uses the outdoor air temperature as an indicator of whether free cooling can be used instead of mechanical cooling. This study also introduces an artificial neural network (ANN) prediction model to optimize the control of the HVAC system, which can lead to additional cooling energy savings. To develop the ANN prediction model, the EnergyPlus program is used for simulation modeling, and the Python programming language is employed for model development. The results show that implementing a temperature-based economizer control strategy can lead to a reduction of 7.6% in annual cooling energy consumption. Moreover, by employing an ANN-based optimal control of discharge air temperature in air-handling units, an additional 22.1% of cooling energy savings can be achieved. In conclusion, the findings of this study demonstrate that the implementation of economizer controls, especially the dry-bulb temperature-based approach, can be an effective strategy for reducing cooling energy consumption in HVAC systems. Additionally, using ANN prediction models to optimize HVAC system controls can further increase energy savings, resulting in improved energy efficiency and reduced operating costs.

Keywords: EnergyPlus; artificial neural network; economizer; discharged air temperature; optimal control

Citation: Yoon, Y.; Seo, B.; Cho, S. Potential Cooling Energy Savings of Economizer Control and Artificial-Neural-Network-Based Air-Handling Unit Discharge Air Temperature Control for Commercial Building. *Buildings* **2023**, *13*, 1174. https://doi.org/10.3390/buildings13051174

Academic Editors: Elena Lucchi and Alban Kuriqi

Received: 22 March 2023
Revised: 18 April 2023
Accepted: 25 April 2023
Published: 28 April 2023

1. Introduction

The building sector represents one of the largest consumers in the US [1]. Energy consumption for heating, ventilation, and air-conditioning (HVAC) systems is approximately 50% of the total energy consumption of the building sector [2]. Therefore, to reduce building energy, it is essential to reduce heating and cooling energy consumption. To do so, the American Society of Heating, Refrigerating, and Air-Conditioning Engineers (ASHRAE) continuously improves the insulation performance of buildings by lowering the U-value of walls and windows every three years. However, in the case of enhanced insulation performance, such improvements are introduced through retrofitting or in new buildings. It is important to control the HVAC systems that are already installed in the existing building for building energy savings without retrofitting. However, since most of the existing control methods of the HVAC system are time-based control, optimal control

may not be achieved. Therefore, the existing HVAC control method is difficult to predict for the control of the future state of HVAC systems by simultaneously considering variables that affect building energy consumption [3–5]. To predict and control the future state of the HVAC system, an artificial neural network (ANN)-based HVAC control is required [3–5]. In addition, ANNs enable accurate prediction through adaptability to external changes. They enable accurate and efficient control [5]. Previous studies using predictive models to properly control HVAC systems are described as follows.

Mba et al. predicted indoor air temperature and relative humidity using an ANN to save cooling energy in residential buildings. According to their findings, the correlation coefficient between the outcomes of their developed ANN prediction model and the actual data was 98% [6]. Zhao and Liu proposed a load-predicting method using regression analysis and artificial intelligence [7]. Chae et al. proposed a data-driven forecasting model for one-day-ahead energy consumption of commercial buildings at 15-min resolution. They used a short-term building energy usage forecasting model based on an ANN algorithm [8]. Ding et al. proposed genetic algorithm-based short-term and ultra-short-term prediction models to predict cooling load in office buildings [9]. Luo proposed an ANN model to forecast a day-ahead cooling demand in an office building. The researcher argued that the proposed method can be implemented in the building to predict cooling demand [10]. Nasruddin et al. argued that the ANN-based HVAC control method performed better than the conventional HVAC control method regarding thermal comfort and energy efficiency [11].

Additionally, Yilmaz and Atik used the ANN model for modeling a cooling system with variable cooling capacity [12] and Moon et al. developed an ANN model that can estimate the time needed to restore the indoor temperature from a setback period to the normal set-point temperature in accommodation buildings during the cooling season [13]. Jani et al. used an ANN model for predicting the performance of the hybrid desiccant cooling systems [14].

There have been many studies conducted on the appropriate control of the HVAC system, verification of the accuracy of the predictive model, and HVAC system performance through predictive control to reduce building energy consumption.

However, few studies have dealt with cooling energy savings through the economizer system itself.

An economizer system that has a free-cooling effect while introducing outside air into the room is used to reduce cooling energy and improve indoor air quality. An economizer system is a cooling system that can reduce energy consumption by introducing outdoor air into the building. Depending on the outdoor conditions, such as in humid, dry, hot, or cold regions, control of the economizer should be considered to properly use the economizer. The following outlines previous studies on economizer systems.

Ezzeldin and Rees conducted a performance evaluation of various cooling strategies in office buildings in four climates using the EnergyPlus simulation program. The main results indicated that economizers for free cooling have the advantage of reducing plant energy consumption while maintaining indoor thermal comfort when compared with a typical HVAC system. Furthermore, the application of the economizer needs to be considered in dry climate conditions [15]. Hong et al. proposed an optimal outdoor air fraction using the economizer control to reduce cooling energy consumption in a hospital building. The main result was that 6–14% of the cooling energy consumption could be saved by differential dry-bulb temperature-based control and 17–27% of the cooling energy consumption using differential enthalpy-based control compared to no economizer [16]. Lee and Chen examined the potential cooling energy consumption savings through the free-cooling technology with differential enthalpy control for data centers in 17 climate zones. The results of this study showed that for every 2 °C decrease in the indoor air temperature in the data center, the cooling energy consumption can be reduced by 2.8 to 8.5%, depending on the climate zones. Furthermore, this study revealed significant potential for free cooling in data centers located in mixed-humid, warm-marine, and mixed-marine climate zones [17]. Yao et al. conducted simulation research to reduce cooling energy

consumption by controlling the air-side economizer system in an office building. Dry-bulb temperature-based control operates on a shorter time scale than enthalpy-based control, but can produce more cooling energy savings than enthalpy-based control. However, in the south of China, dry-bulb temperature-based control operates on a longer time scale and saves more cooling energy than economizer-based control systems [18]. Chowdhury and Khan analyzed economizer control strategies using the EnergyPlus simulation program. Measured chiller energy consumption is compared with TRNSYS simulation results, finding that economizer control can save 72 kW/m^2 per month in cooling loads [19]. Wang and Song proposed an optimal AHU supply air set-point temperature to minimize energy consumption while maximizing the economizer effect. Wang and Song accounted for a balance between cooling consumption savings and the increased supply airflow rate when setting a higher supply air set-point temperature [20]. Yiu et al. conducted an experimental study to verify an air-side economizer system in an office building in Hong Kong. The main result was 12.1% of the existing annual cooling energy consumption using the air-side economizer system [21]. Bulut and Aktacir conducted a detailed analysis of economizers in climate conditions present in Turkey. The free-cooling potential of the economizer was determined using actual hourly dry-bulb temperatures. The main result was that the free-cooling potential is dependent on the supply air temperature and season, and significant energy savings were achieved, especially in the transition period [22].

In summary, most of the research on economizer systems has focused on how to control the economizer itself depending on the climatic conditions. Some studies were conducted by combining the air supply temperature and the economizer control, but the air supply temperature was not proposed in consideration of the internal and external environment.

This study aims to confirm the free-cooling effect of the economizer system in office buildings. It also aims to confirm additional energy consumption reduction through ANN-based optimal air-handling unit (AHU)-discharge air temperature (DAT) control. To understand the cooling effect of the economizer and ANN-based optimal AHU-DAT control, a cooling dominant region and differential dry-bulb temperature-based control were selected due to the climate characteristics. To analyze the cooling effect of the economizer system, a prototype office building simulation model was used. To propose the ANN-based optimal AHU-DAT control, the ANN-based load prediction model was established through Python code.

The primary research inquiries addressed in this paper are as follows:

(1) What is the potential cooling energy savings through the use of ANN-based control?
(2) Does ANN-based control result in greater cooling energy savings compared to the current rule-based economizer control?

2. Simulation Method

2.1. Simulation Program

Two software programs are used in this study: EnergyPlus version 9.1 for making simulation models and Python ver. 3.6 for developing the ANN model.

EnergyPlus is a software for building energy simulation, developed by the U.S. Department of Energy (USDOE). It uses the recommended heat balance calculation method from ASHRAE and can analyze simulations using both heat and mass balance calculations, which is not possible in other existing simulation programs [5,23,24]. Using the "Controller: Outdoor air" function in the EnergyPlus simulation program, the economizer system is controlled.

Python is an interpreted language developed by Amsterdam's Guido Van Rossum in 1990. Python has been widely used in many areas of social computing, such as web programming, data analysis, numerical computation, object-oriented programming, graphic user interface programming, and system utility building [5,25].

2.2. Description of the Simulation Model

The simulation model was implemented using the EnergyPlus simulation program. Figure 1 shows the building simulation model. In this study, an office building model, developed based on ASHRAE 90.1-2004, is used as a baseline when analyzing energy consumption, was selected. The size of the building is 52.3 m × 35.2 m (1841 m^2), and the floor-to-floor height is 3.96 m. The building is a three-story office building with a 40% window-to-wall ratio. The space to be analyzed in this study is the core zone on the second floor that is not directly affected by the external environment, and the size of the core zone is 43.7 m × 26.1 m (1140.6 m^2).

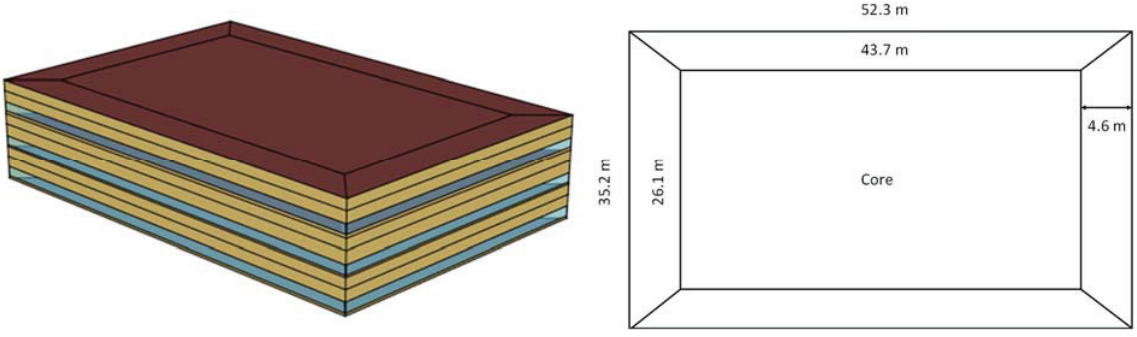

Figure 1. Simulation model.

2.3. Simulation Conditions

Table 1 provides details on the simulation model's construction and material properties, which are based on ASHRAE Standard 90.1-2004 for climate zone 3. The cooling set-point temperature for the model is 26 °C, and Table 2 shows the internal heat gains of the model. The values for material, construction, and internal heat gains are based on ASHRAE 90.1-2004 [26]. For this study, an AHU-based variable air volume (VAV) system commonly used in office buildings [3] was selected as the HVAC system. Figure 2 shows that the HVAC system of the simulation model is an AHU-based VAV system that consists of a hot water coil and reheating coil receiving hot water from a district heating system, and a cooling coil receiving chilled water from a district cooling system. The HVAC system operates from 7 a.m. to 10 p.m.

Table 1. Construction properties.

Construction	U-Value ($W/m^2 \cdot K$)	Visible Transmittance	Solar Heat Gain Coefficient
Exterior Wall	0.704	-	-
Interior Wall	5.68	-	-
Raised Floor	1.74	-	-
Ceiling Slab	1.88	-	-
Roof	0.358	-	-
Exterior window	5.835	0.341	0.340

Table 2. Internal heat gain condition.

Type	Input
People	0.057 person/m^2
Light	10.76 W/m^2
Equipment	10.33 W/m^2
Cooling set-point temperature	26 °C

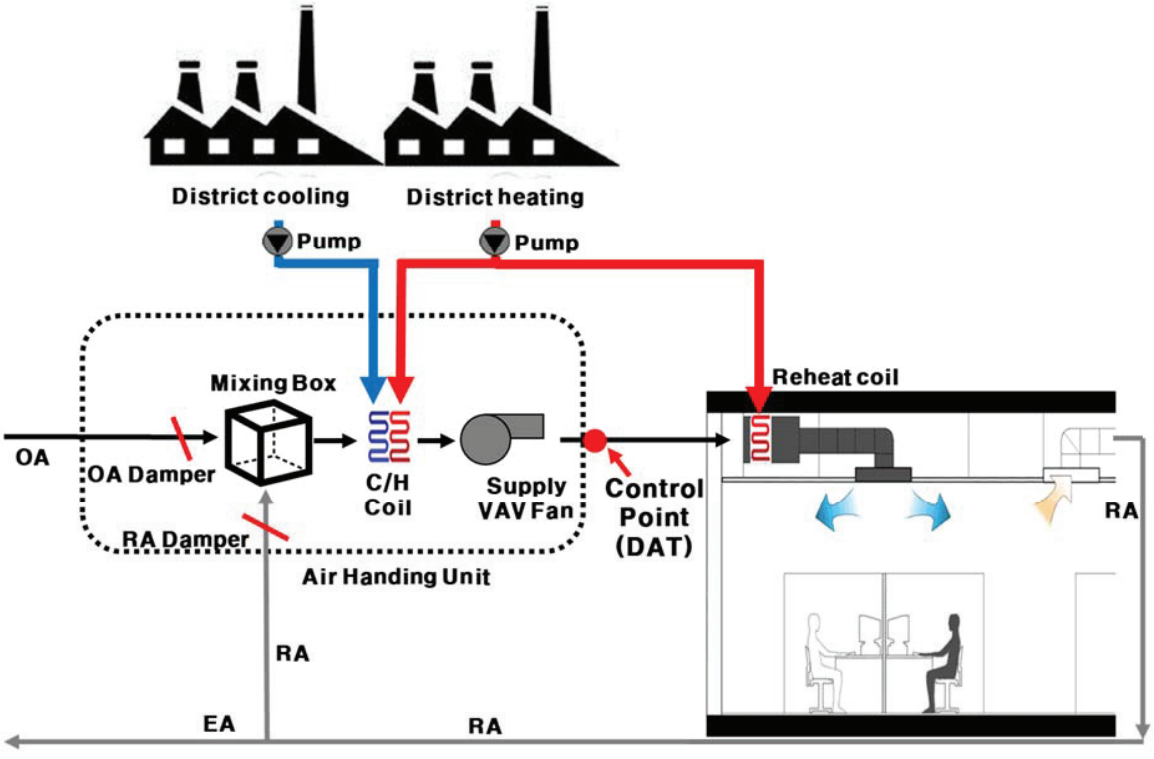

Figure 2. System diagram.

2.4. Economizer System

The economizer system regulates the outdoor air damper located in the mixing box, based on its control type, to introduce outdoor air into the mixing box. By comparing the dry-bulb temperature or enthalpy of the return air from the zone with fresh air from outside, the economizer system can reduce the cooling coil's load while maintaining AHU-DAT. The outdoor air volume is adjusted by an outdoor air damper, depending on the economizer controls, such as dry-bulb temperature, and enthalpy. Dry-bulb temperature-based control is used to determine the outdoor air volume by comparing the outdoor air's dry-bulb temperature with that of the return air from the zone. During cooling periods, such as in the intermediate and summer season, if the outdoor air temperature is lower than the return air temperature, the amount of outdoor air is increased. Conversely, if the outdoor air temperature is higher than the return air temperature, the minimum amount of outdoor air set is applied.

The dry-bulb temperature-based control method only accounts for sensible heat, whereas the enthalpy-based control method considers both sensible and latent heat. In the enthalpy-based control method, the enthalpy of the return air and outdoor air is compared. If the outdoor air enthalpy is lower than the return air enthalpy, the outdoor air volume is increased. Conversely, if the outdoor air enthalpy is higher than the return air enthalpy, the minimum set outdoor air volume is used [27].

2.5. Simulation Cases

This study has three simulation cases. Case 1 is the base case in which the economizer system is not installed, using a fixed AHU-DAT of 12 °C. Case 2 is Case 1 with the economizer system. Case 3 is Case 2 with AHU-DAT control based on an ANN. Cooling energy consumption savings due to the installation of the economizer system can be analyzed

by comparing Case 1 and Case 2. Further cooling energy consumption savings due to ANN-based AHU-DAT control can be analyzed by comparing Case 2 and Case 3.

2.6. Artificial Neural Network (ANN) Modeling

In this study, we used the Numerical Python and Scientific Python libraries of Python to develop an ANN model, following previous research [5]. Two crucial factors when designing the ANN model are the selection of the activation function and the learning method. For the activation function, we used a sigmoid function implemented in non-linear programs such as energy consumption prediction. This function calculates results using input values between 0.00 and 1.00 [5].

Regarding the learning method, we used a supervised learning method, commonly employed in prediction models. This method requires both the input value and the ground truth. The ground truth is used to determine the reliability of the ANN model against the predicted result value from the ANN prediction model. The supervised learning method includes an update process of the weight factors to enhance the ANN model's reliability.

To elaborate, the input value is multiplied by the weight factor, added to each neuron, and passed to the input value of the activation function. If the input values are within the range of a particular threshold, the activation function does not output anything. Conversely, if the input values are outside the threshold range, the neuron is activated to transmit data to the next step. Hence, the ANN generates results by taking into account the data, weight factors, and activation function [5].

2.7. Development Process of the Predictive ANN Model

The predictive ANN model comprises two main components: the ANN component and the control logic component. The ANN component is responsible for predicting output datasets and uses a three-step process, illustrated on the left side of Figure 3 [5].

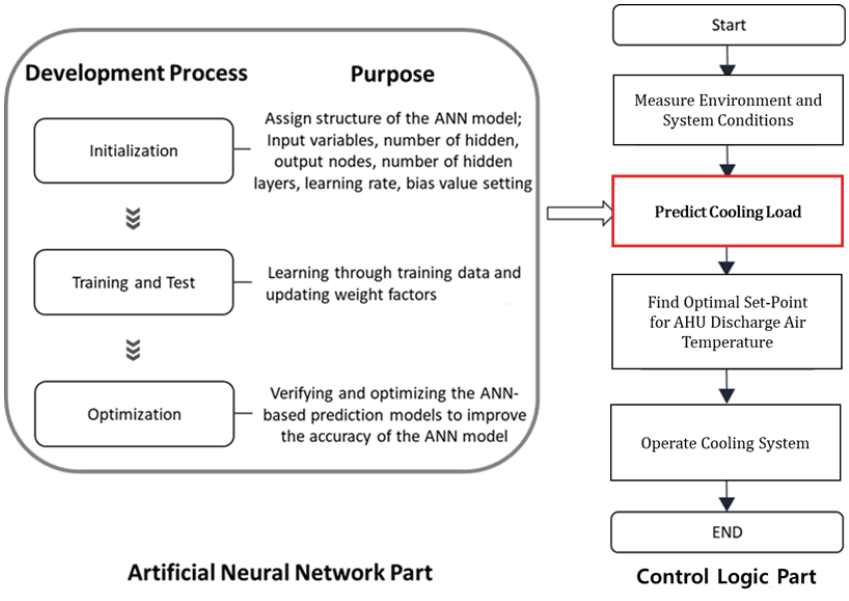

Figure 3. Processes in the predictive ANN model.

The first step involves selecting highly correlated variables with the ground truth. To achieve this, a correlation analysis of variables is performed to identify input variables that are highly correlated with the ground truth, using objective indicators such as r^2. This helps to increase the training efficiency [3–5,28].

The second step is training and testing, when training the ANN, weight factors are initialized and updated during the learning process to minimize the error rate between the ANN output and the simulation results. The activation function is applied to the input data and weight factors to generate a prediction, which is compared to the correct answer to calculate the error rate [3–5]. This process is repeated for a certain number of iterations, called epochs, to obtain the weight factors at which the error rate is minimized. To evaluate the performance of the trained ANN, a separate set of data, called test, or validation data, is used to measure the accuracy of the model [5]. The test data should be new and unseen during the training process to ensure the generalization ability of the model [5,28]. The error rate between the ANN output and the ground truth labels is calculated for the test data, but the weight factors are not updated during this process [28].

Optimizing the ANN involves tuning hyperparameters such as bias, learning rate, number of hidden neurons, and number of hidden layers to minimize error rates [5,25]. This is an iterative process that involves training the model multiple times with different hyperparameters until the desired performance is achieved [5,28].

The coefficient of variance of the root mean square error (cv(RMSE)) is used to ensure the reliability of the ANN model, with lower values indicating better prediction performance. The ASHRAE guideline 14-2014 suggests a tolerance of 30% for the cv(RMSE) value for hourly data [29], and the user should modify the hyperparameter values and repeat the process until the cv(RMSE) value is less than 30%. Equations (1) and (2) display the formulas for RMSE and cv(RMSE), respectively, and Equation (3) shows how to calculate the measurement period average [30]. The control logic sequence comprises four steps, as demonstrated on the right side of Figure 3. The first step is to collect input data through an experimental or simulation study. The second step is to predict the output from the input datasets, which is linked with the ANN part. The output datasets in this research are the cooling coil total cooling loads. The third step is to determine the optimal values for the parameters to be controlled to suggest optimal control after the optimization process concludes. In this research, the parameters to be controlled are the AHU-DAT to lower cooling energy consumption. The final step is to operate the cooling system using the optimal control suggested by the ANN model.

$$RMSE = \sqrt{\frac{\sum (S - M)^2_{interval}}{N_{interval}}} \tag{1}$$

$$cv(RMSE) = \frac{RMSE_{period}}{A_{period}} \tag{2}$$

$$A_{period} = \sqrt{\frac{\sum_{period} M_{interval}}{N_{interval}}} \tag{3}$$

where

S = ANN model prediction value,
M = EnergyPlus simulation results,
$N_{interval}$ = Number of EnergyPlus results, and
A_{period} = Measurement period average.

2.7.1. ANN Model Development

The dataset was partitioned into two distinct sets for different purposes: the training dataset and the test dataset. During the training stage, the ANN model uses the training dataset, while the test dataset is employed for testing. To determine the predictive performance of the ANN model, it is essential to use different datasets for training and testing. In this study, EnergyPlus simulation results from April to October, 5136 h, were randomly shuffled and 70%, 3596 h, were selected as the training data set and 30%, 1540 h, as the test data set.

Seven input variables that displayed a high correlation with the cooling coil's total cooling load were selected for the model. The seven input variables are outdoor air dry-bulb temperature, outdoor air relative humidity, direct solar radiation rate per area, diffuse solar radiation rate per area, occupancy schedule, lights schedule, and electric equipment schedule.

The initial ANN prediction model structure and input values are presented in Figure 4 and Table 3. The ANN model was initialized with seven input nodes, one hidden layer, 10 hidden nodes, and one output node. The learning rate was set to 10%, and the epoch value indicated the number of times learning was repeated. The cv(RMSE) of the initial ANN prediction model was 24.07%, which falls within the acceptable tolerance range of 30% specified in ASHRAE guideline 14-2014 [29].

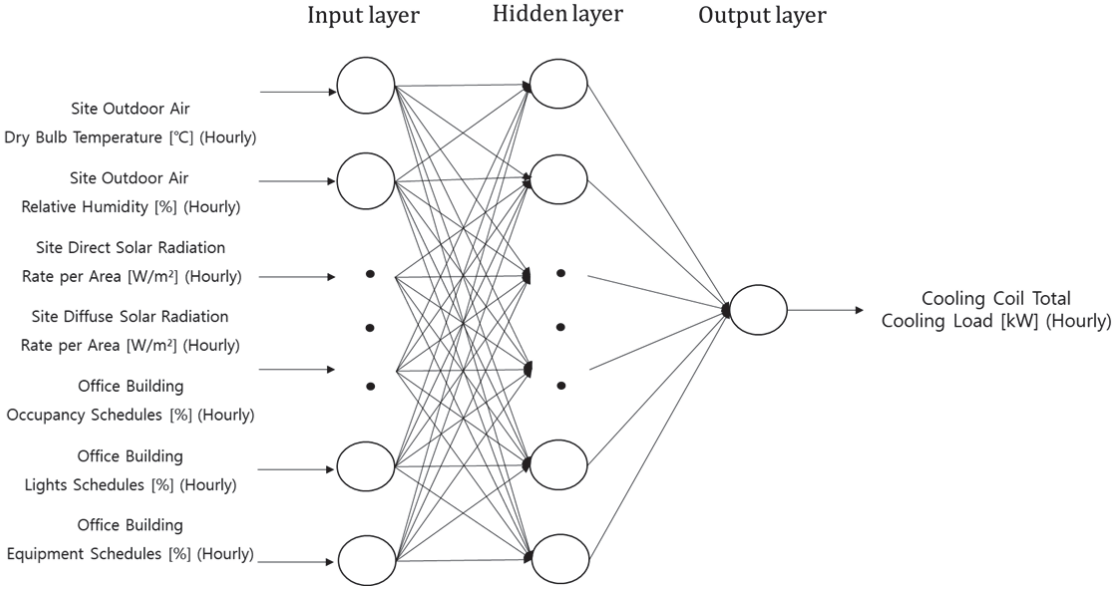

Figure 4. ANN-based predictive model input data list and structure.

Table 3. Initial ANN structure and parameter values.

Division	Range	Initial Values
Number of Hidden Layers	1–n	1
Number of Hidden Neurons	1–n	10
Learning Rate	0.1–1.0	0.1
Epochs	1–n	100

The optimization of the ANN prediction model involves identifying the ideal values for hyperparameters such as learning rate, hidden nodes, epochs, and the number of hidden layers to improve prediction accuracy. Currently, there are no established methods for determining optimal hyperparameter values, and it is best to adjust these values iteratively based on the results. In this study, around 160,000 attempts were made to optimize the ANN prediction model. Python was used to conceptualize the optimization process, and the combination with the lowest cv (RMSE) value was chosen based on a comparison of EnergyPlus simulation results with the cooling coil total cooling load predicted by the ANN model. Table 4 shows the optimized hyperparameter values and their input range, with the cv (RMSE) value decreased from 24.07% to 8.44%. Therefore, it was determined that the optimized ANN prediction model is suitable for HVAC optimal control. Figure 5 shows the

structure of Python programming code for the optimization process and Figure 6 illustrates a comparison of the simulation results and those predicted by the ANN prediction model.

Table 4. Optimal ANN structure and parameter values.

Division	Range	Optimized Values
Number of Hidden Layers	1–n	2
Number of Hidden Neurons Layer 1	1–n	9
Number of Hidden Neurons Layer 2	1–n	8
Learning Rate	0.1–1.0	0.2
Epochs	1–n	267
cv (RMSE) [%]	0~100	8.44%

```
Number of input nodes = 7
Number of hidden nodes = numpy.arange(6, 12, 1)
Number of hidden nodes2 = numpy.arange(6, 12, 1)
Number of output node = 1

Learningrate = numpy.arange(0.1, 1.0, 0.1)
Epochs = numpy.arange(1, 1000, 1)

for i in range(len(hiddennodes)):
    for j in range(len(hiddennodes2)):
        for x in range(len(learningrate)):
            for y in range(len(epochs)):

                n = neuralNetwork(inputnodes, hiddennodes[i], hiddennodes2[j], outputnodes, learningrate[x])
```

Figure 5. Structure of the Python programming code for the optimization process.

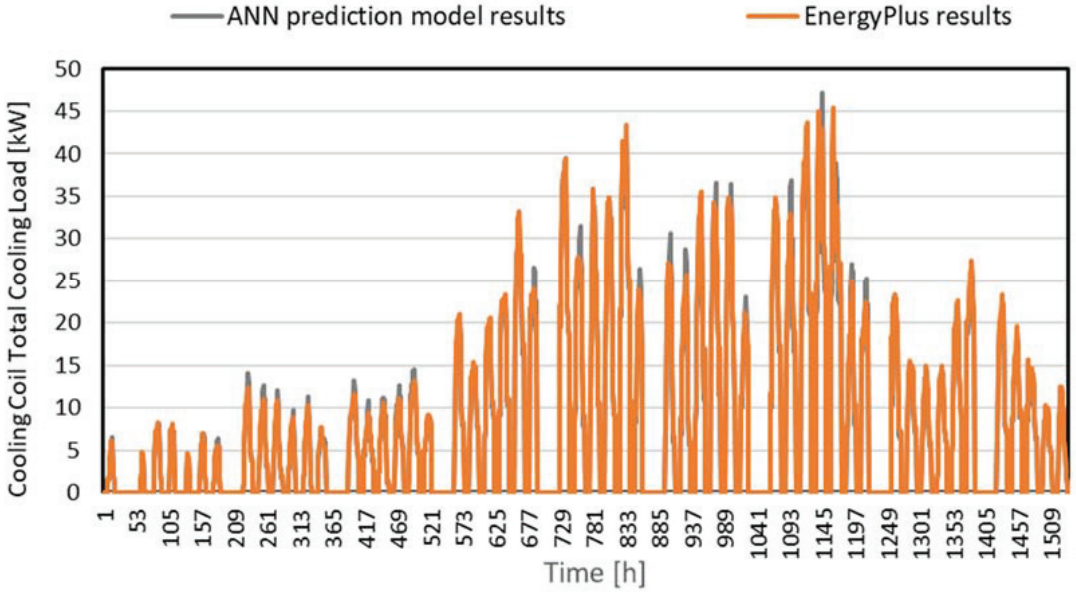

Figure 6. Comparison of simulation data and ANN results.

2.7.2. Initial ANN Model Development Optimized Performance Analysis of the ANN Model Heating, Ventilation, and Air-Conditioning Control Strategy Based on the ANN Results

In this study, a method for determining the appropriate AHU-DAT using the ANN-based cooling coil total cooling load prediction model was developed. The method involves determining an AHU-DAT within the range of 12 to 16 °C through linear interpolation based on the cooling coil total cooling load predicted by the ANN prediction model during the operating hours of the HVAC system. Thus, the predicted cooling coil total cooling load is used to determine the appropriate AHU-DAT when cooling is required.

3. Analysis and Results

3.1. Weather Conditions

This study used weather data provided by EnergyPlus from the Brown Field Municipal Airport, one of the cooling-dominated regions. Brown Field Municipal Airport is in Southern San Diego, CA, USA. The analysis period in this study is the intermediate and cooling seasons, which is from April to October, to understand the free cooling and cooling effect of the economizer. April, May, September, and October are selected as the intermediate season, and June, July, and August are selected as the cooling season. Figure 7 shows the outdoor air dry-bulb temperature and relative humidity in San Diego, CA, USA. The range of the outdoor air dry-bulb temperature during the analysis period is 10.8–31.2 °C, and the range of the outdoor air relative humidity during the analysis period is 7–100%. The analysis period is 5136 h. Observing the outdoor air relative humidity, 4831 h is more than 50% of the outdoor air relative humidity, which is 94% of the total analyzed period.

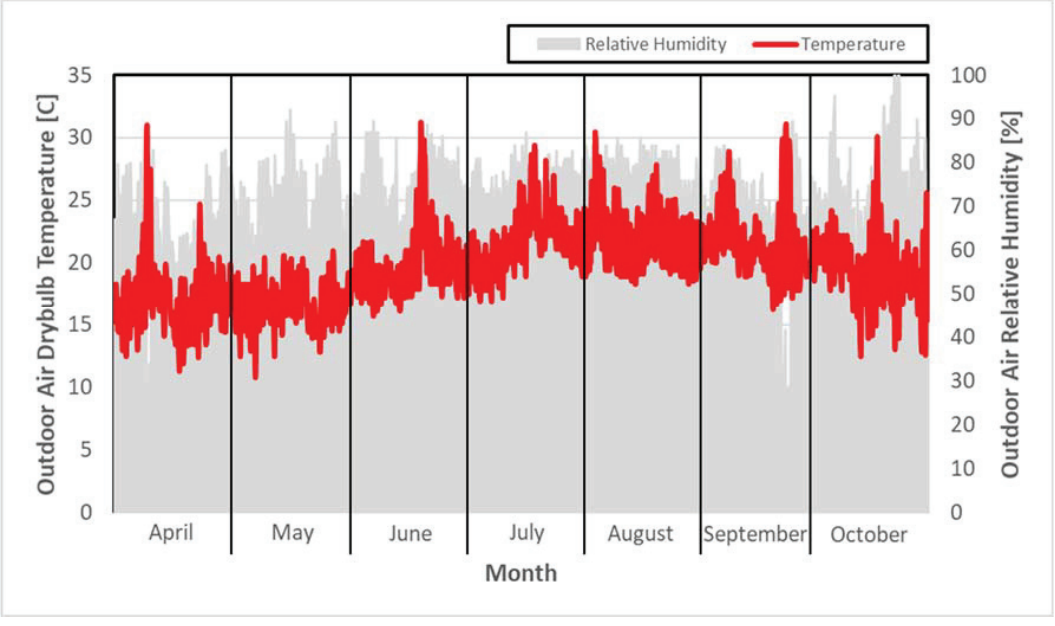

Figure 7. Outdoor air dry-bulb temperature and relative humidity in San Diego, CA, USA.

3.2. Analysis of Representative Days of the Intermediate and Cooling Season

3.2.1. Comparison of the Pattern for Cooling Coil Total Cooling Load and Air-Handling Units with Discharge Air Temperature in the Representative Days of the Intermediate and Cooling Season

This paper uses 15 May as a representative day of the intermediate season and 11 August as a representative day of the cooling season. Representative days were chosen

because they represent the average outdoor air temperature in the intermediate and cooling seasons. Figure 8 shows the change in AHU-DAT according to the cooling coil's total cooling load during the representative days in the intermediate and cooling seasons. The cooling load pattern is similar to outdoor air temperature in all three cases. Since the cooling system operates from 7 a.m. to 10 p.m. in all cases, there is no cooling load from 11 p.m. to 6 a.m. In the case of the AHU-DAT value, it was found that Cases 1 and 2 were tightly controlled at 12 °C regardless of changes in the cooling load, and in Case 3, AHU-DAT is controlled by fluctuating within the range of the maximum of 16 °C to the minimum of 12 °C as the cooling load changes.

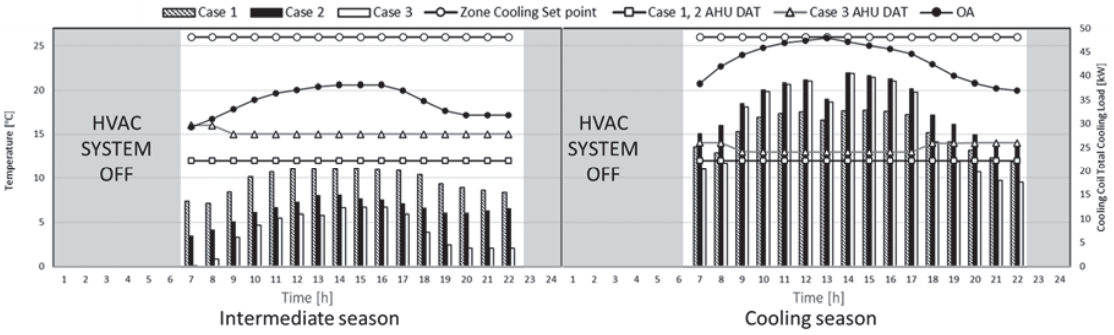

Figure 8. Comparison of the cooling coil total cooling load and AHU-DAT pattern in the representative days.

When comparing the cooling load of each case on the representative day of the intermediate season, compared to Case 1, Case 2 showed a maximum reduction in cooling load of 53% at 7 a.m. when the outside temperature was relatively low, and Case 3 showed 99% less cooling load.

Considering the average daily data, Case 2 showed 35% less cooling load than Case 1, and Case 3 showed 61% less cooling load than Case 1. The explanation of the difference in the cooling load of each case is as follows. In both Cases 1 and 2, the AHU-DAT is the same at 12 °C, but in Case 2, the cooling load is lower than that of Case 1, which introduces only the minimum amount of outdoor air. This is because the economizer system performs free cooling when the outside air temperature is lower than the return air temperature. In addition, in Case 3, free cooling is performed through an economizer in the same manner as in Case 2, but since AHU-DAT is controlled according to the cooling load, less cooling load is required compared to Case 2.

When comparing the cooling load of each case on a representative day in the cooling season, Case 2 required more cooling load than Case 1, contrary to the results of the representative day in the intermediate season. In addition, Case 3 showed a relatively higher cooling load than Case 1 from 9 a.m. to 5 p.m. Comparing this with daily average data, compared to Case 1, Case 2 showed an average of about 18% and Case 3 an average of about 3% more cooling load. This can be explained in Figure 9, which compares the enthalpy of the outdoor air and mixed air of the representative days, where OA is outdoor air, MA is mixed air, and RA is return air. The blue box in Figure 9 is the enthalpy of the outdoor air and mixed air of Cases 2 and 3. The red box in Figure 9 is the enthalpy of the return air from the zone in Case 1, and the grey box is the mixed air of Case 1.

The average value of the outdoor air enthalpy from 7 a.m. to 10 p.m. on the representative day of the intermediate season is about 41 kJ/kg, the return air enthalpy of Case 1 is 48 kJ/kg, and the mixed air enthalpy is 45 kJ/kg. In the case of the representative day in summer, the average value of the outdoor air enthalpy is about 54 kJ/kg, the return air enthalpy of Case 1 is 49 kJ/kg, and the mixed air enthalpy is 45 kJ/kg.

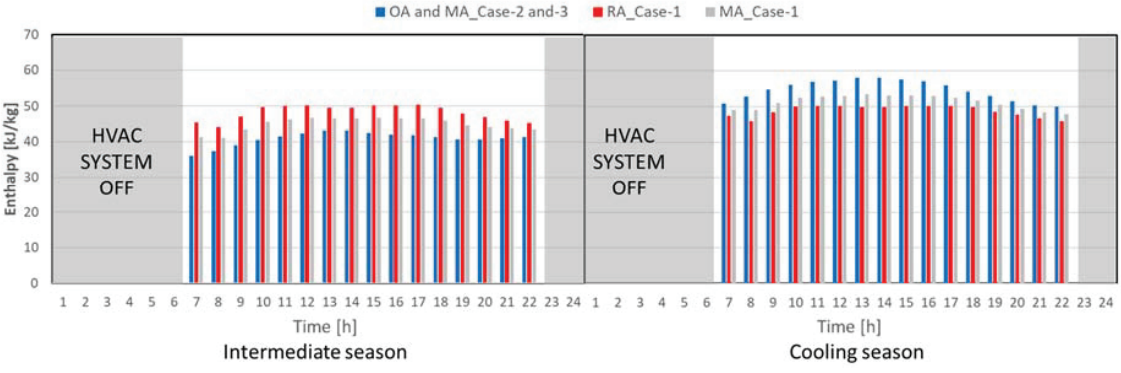

Figure 9. Comparison of the enthalpy in the representative days.

The reason that the enthalpy of the outdoor air and the enthalpy of mixed air of Cases 2 and 3 are similar on the representative day of both intermediate and cooling seasons is that the economizer system performs free cooling because the outdoor air temperature is lower than the cooling set temperature of 26 °C. In addition, the reason the enthalpy of the mixed air in Case 1 is higher than that in the other two cases in the intermediate season is that Case 1 introduces only the minimum outdoor air when cooling is needed. Because the enthalpy of the outside air is relatively lower than that of the return air, the enthalpy of the mixed air in Case 1 is higher than that of the other two cases where 100% outdoor air is introduced.

In contrast, in the case of the cooling season, the economizer system performs free cooling using outdoor air, which has higher enthalpy than that of return air. Even if the AHU-DAT of Case 2 is the same as Case 1, the enthalpy of the mixed air in Case 2 is higher than that of Case 1, in which only the minimum outdoor air is introduced. Due to the higher enthalpy, more cooling load is required in Case 2 compared to Case 1.

In addition, in Case 3, free cooling is performed through outdoor air in the same manner as in Case 2; however, the AHU-DAT of Case 3 is relatively higher than that of Case 2 by controlling the AHU-DAT according to the cooling load. As a result, it is judged that relatively less cooling load is required compared to Case 2.

3.2.2. Comparison of the Fan Flow Mass Rate in the Representative Days of the Intermediate and Cooling Season

Figure 10 shows the fan mass flow rate in each case in the representative days. In all cases, the fan was operated only from 7 a.m. to 10 p.m., when the HVAC system operates. On the representative day of the intermediate season, Cases 1 and 2 showed the same fan mass flow rate of 1.54 kg/s at all times, and Case 3 showed the maximum fan air volume of 2.06 kg/s at 5 p.m., the minimum fan mass flow rate of Case 3 was 1.5393 kg/s, the same as Cases 1 and 2 at 8 a.m. and from 6 p.m. to 10 p.m. Comparing the fan mass flow rate of Case 3 to the other two cases, Case 3 required an average of 19% greater fan mass flow rate per day.

Cases 1 and 2 showed the same fan mass flow rate because the temperature difference between the indoor cooling set-point temperature and AHU-DAT was fixed at 12 °C regardless of the cooling coil's total cooling load. In addition, the reason that the fan mass flow rate was the same at all times is that the outside air temperature was lower than the indoor set temperature of 26 °C due to the characteristics of the intermediate season. That is why the cooling load can be handled with only the minimum fan mass flow rate under the condition that the AHU-DAT is set to 12 °C.

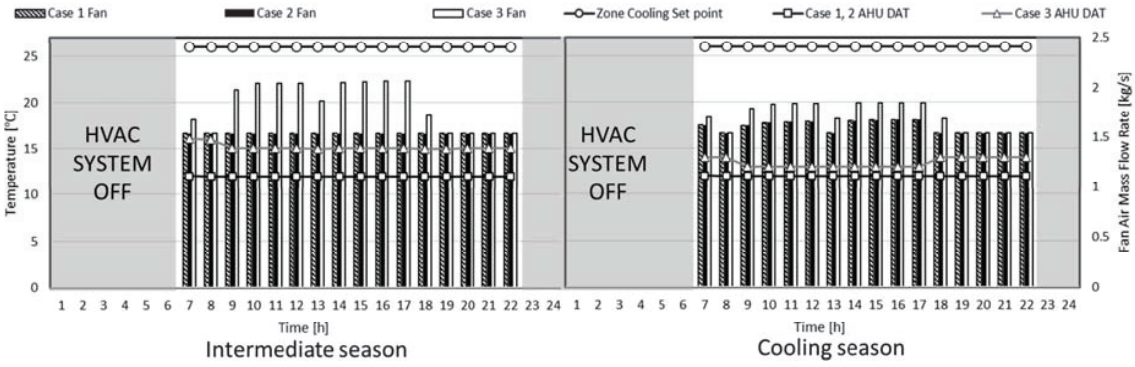

Figure 10. Comparison of the fan flow mass rate in the representative days.

However, in Case 3, the temperature difference between the cooling set-point temperature and the AHU-DAT changes continuously because the AHU-DAT changes according to the cooling coil's total cooling load. In accordance with this, the fan mass flow rate is also increased or decreased to handle the cooling load. Therefore, although the cooling loads of all the cases are the same, a relatively high fan mass flow rate is required because the temperature difference between the AHU-DAT of Case 3 and the cooling set-point temperature is smaller than in the other two cases.

On the representative day of the cooling season, the maximum fan mass flow rate of 1.68 kg/s was reached at 5 p.m. in Case 1 and Case 2, and the minimum fan air volume of 1.54 kg/s at 8 a.m. and from 6 p.m. to 10 p.m. Case 3 showed the maximum fan mass flow rate of 1.85 kg/s at 4 p.m. and the minimum fan air volume of 1.54 kg/s at 8 a.m. and from 7 p.m. to 10 p.m. Comparing the fan mass flow rate of Case 3 to the other two cases, Case 3 required 7% more fan mass flow rate per day.

On the representative day of the cooling season, Case 3 shows that the AHU-DAT is controlled at a lower temperature compared to the intermediate season, as a result of the higher cooling load. Due to the lower temperature provided to the zone, the supply air flow rate is decreased. In addition, the fan mass flow rate of Cases 1 and 2 is increased or decreased according to the cooling load pattern. This is because the outside air temperature in the cooling season is relatively high compared to the intermediate season, which is why the cooling load cannot be handled with only the minimum fan mass flow rate.

3.2.3. Comparison of the Cooling Energy Consumption in the Representative Days

Table 5 shows the cooling energy consumption on the representative days. In the case of the representative day in the intermediate season, Through the installation of the economizer system, fan electric energy is the same as in Case 1 due to the same AHU-DAT; however, electric energy for the chiller and pump is decreased. Additionally, 31.4% of total cooling electric energy can be saved through the installation of the economizer system. By optimal AHU-DAT control, electric energy for the chiller and pump can be reduced; however, fan electric energy is increased due to the higher temperature of the AHU-DAT than that of Case 1 and Case 2: 52.3% of total electric energy for cooling can be saved. In the cooling season, Case 2 consumes 17.0% more cooling energy than Case 1 due to introducing more outdoor air than Case 1. Case 3 consumes less cooling energy than Case 2; however, it still consumes 5.3% more cooling energy than Case 1.

Table 5. Comparison of the cooling energy consumption in each case on the representative days.

	Intermediate Season			Cooling Season		
	Case 1	**Case 2**	**Case 3**	**Case 1**	**Case 2**	**Case 3**
District cooling energy [kWh/day]	287.2	189.1	118.9	457.9	540.2	483.1
Chiller (COP 5) electric [kWh/day]	57.4	37.8	23.8	91.6	108.0	96.6
Fan electric [kWh/day]	4.9	4.9	6.1	5.1	5.1	5.6
Pump electric [kWh/day]	2.0	1.5	0.9	2.8	3.3	2.7
Total cooling energy [kWh/day]	64.3	44.1	30.7	99.5	116.4	104.8

3.3. Analysis of Cooling Energy Consumption in the Intermediate and Summer Seasons

Table 6 shows the cooling energy consumption in each component for each case in the intermediate and cooling seasons. Case 2, with an economizer system with differential dry-bulb temperature-based control, uses 25,292 kWh of district cooling energy and saves 18.9% of district cooling energy compared to Case 1. As analyzed above, even if an economizer is installed, AHU-DAT is equal to 12 °C for Cases 1 and 2. Therefore, since Cases 1 and 2 are the same as the temperature supplied to the room for cooling at 12 °C, the fan electric energy consumption is the same regardless of the presence of an economizer system. Due to the free-cooling effect of the economizer system, the pump electric energy used to circulate chilled water in the cooling coil is 186 kWh, which uses 13.5% less electricity than Case 1. When comparing the total cooling energy, it consumes 10.6% less cooling energy than Case 1 due to the economizer installation. When AHU-DAT is controlled, 45.8% of the district cooling energy can be saved when compared to Case 1, and 33.2% of the district cooling energy can be saved when compared to Case 2. In the case of fans, Case 3 uses more fan electrical energy than the other two cases. This is because a higher air volume is required since AHU-DAT, which is relatively higher than the other two cases, is supplied to the zone. The total amount of electric energy used for cooling is 4088 kWh, which is 41.1% less than Case 1 and 34.2% less than Case 2.

Table 6. Cooling energy consumption in the intermediate and summer seasons.

	Intermediate Season			Cooling Season		
	Case 1	**Case 2**	**Case 3**	**Case 1**	**Case 2**	**Case 3**
District cooling energy [kWh]	31,174	25,292	16,907	30,261	31,057	24,372
Chiller (COP 5) electric [kWh]	6235	5058	3381	6052	6211	4874
Fan electric [kWh]	496	496	600	386	386	444
Pump electric [kWh]	215	186	106	194	202	139
Total cooling energy [kWh]	6945	6211	4088	6632	6799	5458

In the case of the cooling season, the district cooling energy and pump electricity consumption increase due to the installation of the economizer system, unlike during the intermediate season. This is because of the enthalpy of the mixing air, which is described in the analysis of a representative day. As with the intermediate season, the fan electric energy consumption is the same regardless of the economizer system installation. Due to the installation of the economizer, the total electric energy consumption used for cooling is 6799 kWh, which is a 2.5% increase compared to Case 1. In Case 3, only the electric energy used in the fan increases, and the district cooling energy and pump electric energy use decreases, as in the intermediate season. The total electricity consumption used for cooling is reduced by 17.7% when compared to Case 1 and by 19.7% when compared to Case 2.

Figure 11 shows the amount of electric energy used for cooling in the intermediate and cooling seasons. The total amount of electric energy for cooling in Figure 9 is under the assumption that a chiller with a coefficient of performance (COP) of 5 is used. Case 2 consumes 12,539 kWh/year for cooling. Compared with Case 1, installation of the economizer system can save 7.6% of electricity energy. The amount of electric energy in

the cooling season is increased due to the installation of the economizer system, but the free-cooling effect of the economizer system reduces the electric energy in the intermediate season. For this reason, the total electric energy consumption for cooling is reduced. Case 3 consumes 9545 kWh/year of electricity for cooling is used during a year. Compared with Case 1, electric energy of 29.7% can be saved, and compared with Case 2, 23.9% of electric energy can be saved.

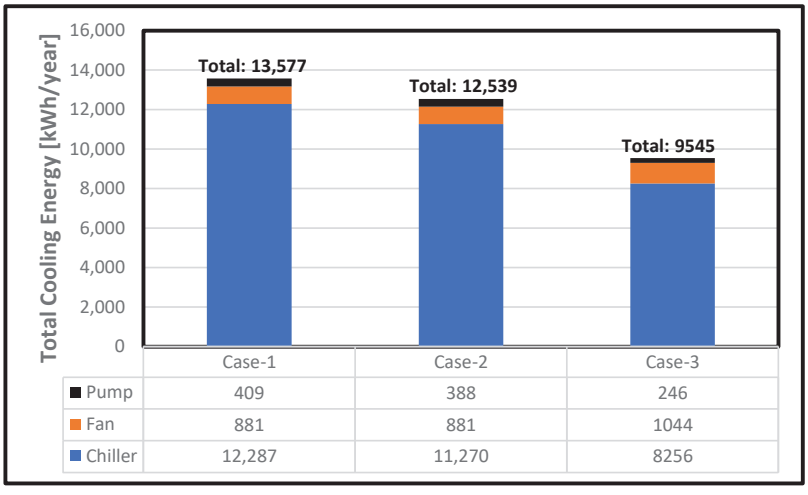

Figure 11. Comparison of the total cooling energy consumption.

Figure 12 shows the cumulative time and hourly average cooling coil total cooling load per hour for each range of AHU-DAT in Case 3. For the analysis of the AHU-DAT in Case 3, the data were divided into five ranges. In Case 3, the AHU-DAT changes according to the cooling coil's total cooling load. The cumulative time when the AHU-DAT is controlled by 15 °C is the maximum, and the cumulative time decreases in the order of 14, 16, 13, and 12 °C. Since AHU-DAT of Case 3 is usually controlled higher than the other two cases whereas AHU-DAT is fixed at 12 °C, the cooling load of the cooling coil is reduced, therefore reducing cooling energy consumption.

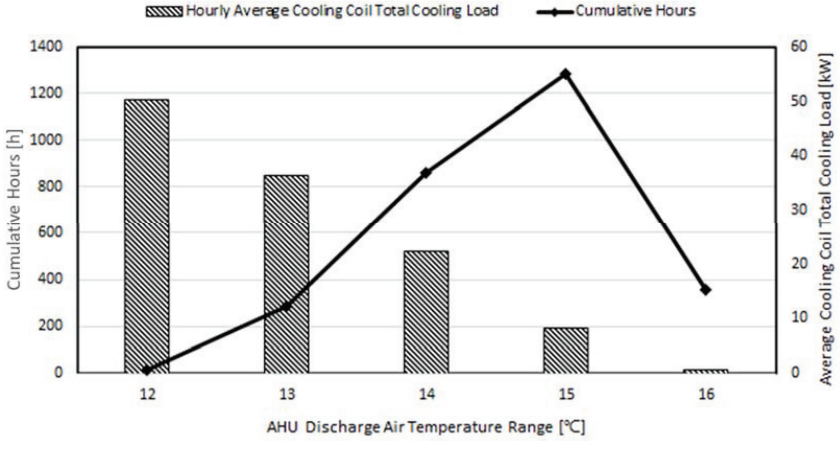

Figure 12. Cumulative operation hours and hourly average cooling coil total cooling load in each AHU-DAT range.

4. Conclusions

In this research, an ANN prediction model is used to propose an optimal AHU-DAT control approach in an office building that implements differential dry-bulb temperature-based economizer control. The results of the study demonstrate that the AHU-DAT optimal control can lead to an additional cooling energy savings of approximately 23.9% in an office building with an economizer control within the temperature range of 12 to 16 °C. The installation of the economizer system showed a reduction in cooling energy consumption due to the free-cooling effect in the intermediate season; however, it resulted in increased cooling energy consumption in the summer season due to the higher enthalpy of the introduced outside air. When comparing the annual cooling energy consumption, the reduction of the cooling energy consumption in the intermediate seasons is larger than the increase in the cooling energy consumption in the summer season, resulting in annual cooling energy savings by installing the economizer system. Moreover, this research confirms that further cooling energy savings can be attained through optimal AHU-DAT control. Although this study focuses on hot and humid climates, future studies aim to analyze the change in cooling energy consumption via the installation of an economizer system and optimal control of AHU-DAT in different climate conditions. Furthermore, a future study will analyze an enthalpy-based economizer with the on/off control strategy.

Author Contributions: Conceptualization, Y.Y.; Methodology, Y.Y. and S.C.; Software, Y.Y. and B.S.; Formal analysis, Y.Y. and B.S.; Investigation, B.S. and S.C.; Writing—original draft, Y.Y. and B.S.; Writing—review & editing, Y.Y., B.S. and S.C.; Visualization, Y.Y.; Supervision, S.C. All authors have read and agreed to the published version of the manuscript.

Funding: This research received no external funding.

Data Availability Statement: Not applicable.

Conflicts of Interest: The authors declare no conflict of interest.

Nomenclature

Abbreviations	
HVAC	Heating, ventilation, and air conditioning
ANN	Artificial neural network
ASHRAE	American Society of Heating, Refrigerating, and Air-Conditioning Engineers
AHU	Air-handling unit-
DAT	Discharge air temperature
USDOE	U.S. Department of Energy
VAV	Variable air volume
cv (RMSE)	Coefficient of variance of the root mean square error
COP	Coefficient of performance
OA	Outdoor air
MA	Mixed air
RA	Return air
Units	
m	Meter
m^2	Square meter
$W/m^2 \cdot K$	Watts per square meter-Kelvin
kg/s	Kilogram per second
person/m^2	Number of people per square meter
W/m^2	Watts per square meter
°C	Degree Celsius
kJ/kg	Kilojoule per kilogram
%	Percentage
kWh	Kilowatt-hour

Symbol	
S	ANN model prediction value,
M	EnergyPlus simulation results
$N_{interval}$	Number of EnergyPlus results
A_{period}	Measurement period average

References

1. EIA. Energy Consumption by Sector. Energy. 2015. Available online: http://www.eia.gov/totalenergy/data/monthly/pdf/sec2_3.pdf (accessed on 28 December 2020).
2. Roth, K.W.; Westphalen, D.; Kieckmann, J. Energy Consumption Characteristics of Commercial Building HVAC Systems Volume III: Energy Savings Potential. In *Building Technologies Program*; TIAX LLC.: Cambridge, MA, USA, 2002.
3. Lee, J.M.; Seo, B.M.; Hong, S.H.; Lee, K.H. Application of Artificial Neural Networks for Optimized AHU Discharge Air Temperature Set-point and Minimized Cooling Energy in VAV System. *Appl. Therm. Eng.* **2019**, *153*, 726–738. [CrossRef]
4. Yeon, S.H.; Yu, B.; Seo, B.M.; Yoon, Y.B.; Lee, K.H. ANN Based Automatic Slat Angle Control of Venetian Blind for Minimized Total Load in an Office Building. *Sol. Energy* **2019**, *180*, 133–145. [CrossRef]
5. Seo, B.M.; Yoon, Y.B.; Song, S.; Cho, S. ANN-based thermal load prediction approach for advanced controls in building energy systems. In Proceedings of the Conference for ARCC 2019 International Conference, Toronto, ON, Canada, 29 May–1 June 2019.
6. Mba, L.; Meukam, P.; Kemajou, A. Application of artificial neural network for predicting hourly indoor air temperature and relative humidity in modern building in humid region. *Energy Build.* **2016**, *121*, 32–42. [CrossRef]
7. Zhao, J.; Liu, X. A hybrid method of dynamic cooling and heating load forecasting for office buildings based on artificial intelligence and regression analysis. *Energy Build.* **2018**, *174*, 293–308. [CrossRef]
8. Chae, Y.T.; Horesh, R.; Hwang, Y.; Lee, Y.M. Artificial neural network model for forecasting sub-hourly electricity usage in commercial building. *Energy Build.* **2016**, *111*, 184–194. [CrossRef]
9. Ding, Y.; Zhang, Q.; Yuan, T. Research on short-term and ultra-short-term cooling load prediction models for office buildings. *Energy Build.* **2017**, *154*, 254–267. [CrossRef]
10. Luo, X.J. A novel clustering-enhanced adaptive artificial neural network model for predicting day-ahead building cooling demand. *J. Build. Eng.* **2020**, *32*, 101504. [CrossRef]
11. Nasruddin; Scholahudin; Satrio, P.; Mahlia, T.M.I.; Giannetti, N.; Saito, K. Optimization of HVAC system energy consumption in a building using artificial neural network and multi-objective genetic algorithm. *Sustain. Energy Technol. Assess.* **2019**, *35*, 48–57.
12. Yilmaz, S.; Atik, K. Modeling of a mechanical cooling system with variable cooling capacity by using artificial neural network. *Appl. Therm. Eng.* **2007**, *27*, 2308–2313. [CrossRef]
13. Moon, J.W.; Kim, K.; Min, H. ANN-based prediction and optimization of cooling system in hotel rooms. *Energies* **2015**, *8*, 10775–10795. [CrossRef]
14. Jani, D.B.; Mishra, M.; Sahoo, P.K. Performance prediction of solid desiccant–vapor compression hybrid air-conditioning system using artificial neural network. *Energy* **2016**, *103*, 618–629. [CrossRef]
15. Ezzeldin, S.; Rees, S.J. The potential for office buildings with mixed-mode ventilation and low energy cooling systems in arid climates. *Energy Build.* **2013**, *65*, 368–381. [CrossRef]
16. Hong, G.; Kim, C.; Hong, J. Energy Conservation Potential of Economizer Controls Using Optimal Outdoor Air Fraction Based on Field Study. *Energies* **2020**, *13*, 5038. [CrossRef]
17. Lee, K.; Chen, H. Analysis of energy saving potential of air-side free cooling for data centers in worldwide climate zones. *Energy Build.* **2013**, *64*, 103–112. [CrossRef]
18. Yao, Y.; Wang, L. Energy analysis on VAV system with different air-side economizers in China. *Energy Build.* **2010**, *42*, 1220–1230. [CrossRef]
19. Chowdhury, A.A.; Rasul, M.G.; Khan, M.M.K. Modelling and Analysis of Air-Cooled Reciprocating Chiller and Demand Energy Savings Using Passive Cooling. *Appl. Therm. Eng.* **2009**, *29*, 1825–1830. [CrossRef]
20. Wang, G.; Song, L. An energy performance study of several factors in aireconomizers with low-limit space humidity. *Energy Build.* **2013**, *64*, 447–455. [CrossRef]
21. Yiu, J.; Wang, S.; Yik, F.W.H. Assessment of practical applications of outdoor air economiser in Hong Kong. *Build. Serv. Eng.* **2000**, *21*, 187–198. [CrossRef]
22. Bulut, H.; Aktacir, M.A. Determination of free cooling potential: A case study for Istanbul, Turkey. *Appl. Energy* **2011**, *88*, 680–689. [CrossRef]
23. The U.S. DOE. Getting Started. In *EnergyPlus, Version 9.1.0 Documentation*; The U.S. DOE: Washington, DC, USA, 2019.
24. The U.S. DOE. EnergyPlus Engineering Reference. In *The Reference to EnergyPlus Calculations, Version 9.1*; The U.S. DOE: Washington, DC, USA, 2019.
25. Seo, B.M.; Lee, K.H. Detailed analysis on part load ratio characteristics and cooling energy saving of chiller staging in an office building. *Energy Build.* **2016**, *119*, 309–322. [CrossRef]
26. OpenStudio Official Hompage. Available online: https://nrel.github.io/OpenStudio-user-documentation/help/finding_model_data/ (accessed on 28 December 2020).

27. Lim, S.H. A Study on the Energy Efficient Control Strategies of Outdoor Air Introduction in Office Building. Ph.D. Thesis, Konkuk University, Seoul, Republic of Korea, 2002.
28. Rashid, T. *Make Your Own Neural Network*; CreateSpace Independent Publishing Platform: North Charleston, SC, USA, 2016.
29. ASHRAE. *Guideline 14-2014*; Measurement of Energy and Demand Savings; American Society of Heating, Refrigerating, and Air Conditioning Engineers: Atlanta, Georgia, 2014.
30. Seo, B.M.; Yoon, Y.B.; Moon, J.H.; Cho, S. Application of Artificial Neural Network for the Optimum Control of HVAC Systems in Double-Skinned Office Buildings. *Energies* **2019**, *24*, 4754. [CrossRef]

buildings

MDPI

Article

Comparative Analysis of ANN and LSTM Prediction Accuracy and Cooling Energy Savings through AHU-DAT Control in an Office Building

Byeongmo Seo [1,†], Yeobeom Yoon [2,†], Kwang Ho Lee [3] and Soolyeon Cho [1,*]

[1] College of Design, North Carolina State University, Raleigh, NC 27695, USA
[2] Buildings and Transportation Science Division, Oak Ridge National Laboratory, Oak Ridge, TN 37830, USA
[3] School of Architecture, Korea University, Seoul 02481, Republic of Korea
* Correspondence: soolyeon_cho@ncsu.edu
† These authors contributed equally to this work.

Abstract: This paper proposes the optimal algorithm for controlling the HVAC system in the target building. Previous studies have analyzed pre-selected algorithms without considering the unique data characteristics of the target building, such as location, climate conditions, and HVAC system type. To address this, we compare the accuracy of cooling load prediction using ANN and LSTM algorithms, widely used in building energy research, to determine the optimal algorithm for HVAC control in the target building. We develop a simulation model calibrated with actual data to ensure data reliability and compare the energy consumption of the existing HVAC control method and the two algorithms-based methods. Results show that the ANN algorithm, with a CV(RMSE) of 12.7%, has a higher prediction accuracy than the LSTM algorithm, CV(RMSE) of 17.3%, making it a more suitable algorithm for HVAC control. Furthermore, implementing the ANN-based approach results in a 3.2% cooling energy reduction from the optimal control of Air Handling Unit (AHU) Discharge Air Temperature (DAT) compared to the fixed DAT at 12.8 °C in a representative day. This study demonstrates that ML-based HVAC system control can effectively reduce cooling energy consumption in HVAC systems, providing an effective strategy for energy conservation and improved HVAC system efficiency.

Keywords: EnergyPlus; artificial neural network; long short-term memory; discharged air temperature; optimal control

Citation: Seo, B.; Yoon, Y.; Lee, K.H.; Cho, S. Comparative Analysis of ANN and LSTM Prediction Accuracy and Cooling Energy Savings through AHU-DAT Control in an Office Building. *Buildings* **2023**, *13*, 1434. https://doi.org/10.3390/buildings13061434

Academic Editor: Gerardo Maria Mauro

Received: 27 April 2023
Revised: 19 May 2023
Accepted: 26 May 2023
Published: 31 May 2023

1. Introduction

1.1. Background

According to the Annual Energy Outlook 2019 published by the U.S. Energy Information Administration (EIA), the building sector accounts for 40% of the total energy consumed in the United States. Commercial buildings constitute about 50% of total energy consumption, of which about 40% is used for heating, ventilating, and air conditioning (HVAC) [1]. The International Energy Agency (IEA) report "The Future of Cooling" affirmed that global energy demand and district cooling and heating demand had increased rapidly over the past decade due to economic development—electricity energy consumption for space cooling accounts for about 20% of total building energy. In addition, the report emphasized that if space cooling systems remain inefficient, global cooling energy demand will be three times higher in 2050 than in 2016 [2].

High-efficiency cooling systems or optimal control of cooling systems should be considered to increase cooling system efficiency. High-efficiency cooling systems are suitable for newly built buildings but are challenging to apply in existing buildings due to the cost and time required for system replacement. Therefore, to increase the efficiency of

cooling systems already installed in existing buildings, the better option is to ensure their optimal control [3].

Various studies on optimal control methods for HVAC systems have used advanced technology, such as machine learning (ML)-based controls [3–5]. Based on their learning method, ML methods are generally categorized into three main types: supervised learning, semi-supervised learning, and unsupervised learning. The selection of the learning method primarily depends on the intended purpose. For tasks involving regression, such as prediction and control, a supervised learning-based algorithm is generally suitable [3–5]. Artificial neural networks (ANNs), particularly those that imitate the human brain, and Long Short-Term Memory (LSTM) algorithms specialized in time series data are widely utilized as the primary algorithms in supervised learning [5–19].

Previous studies have utilized ANN and LSTM algorithms to predict building energy consumption, cooling and heating load, and control HVAC systems. Using an ANN-based prediction model, Lee et al. measured the cooling energy reduction effect during summer according to Air Handling Unit (AHU) optimal temperature control. The research results showed that compared to a conventional control method, the ANN-based predictive control method could reduce cooling energy consumption by approximately 10%. The authors argued that the ANN-based control algorithm could be applied to various forced air systems by taking dynamic operating conditions [5]. Qian et al. asserted that accurate HVAC system load forecasting is required for optimal control and design. They developed an ANN-based load forecasting model and analyzed its accuracy. The proposed model showed 10% more accuracy than the conventional load forecasting method [6].

Moon et al. developed an ANN-based Variable Refrigerant Flow system control algorithm to increase the cost-effectiveness in the heating season. Comparing simulation results with ANN prediction results, they found that the ANN model has a coefficient of variation root mean square error (CV[RMSE]) of 7.42%. The ANN model was embedded in the control algorithm to determine the intermittent operation. They confirmed that the ANN model and the control algorithm could enhance the prediction accuracy and cost-effectiveness of the heating system [7]. Park et al. proposed an ANN-based prediction model to forecast the energy cost for a VRF heating system. In the performance evaluation, the prediction accuracy of the proposed model was within the recommended level, with a coefficient of variation root mean square error of 4.87%. They suggested that the predicted energy cost can be used as a determinant for the control algorithm to reduce operating costs [8]. Mtibaa et al. developed an LSTM-based model predictive control method. The prediction model was used for energy consumption, peak demand, and indoor thermal discomfort during occupied hours. The results showed that the LSTM model reduced energy consumption and indoor thermal discomfort degree [9].

Sendra-Arranz and Gutierrez stated that the HVAC system predictive control is essential to realize demand-side management strategies. They developed an LSTM-based prediction model to forecast a day ahead of the energy consumption of an HVAC system. The model showed outstanding results, supported by a Pearson test correlation coefficient 0.972 and a normalized root mean square error of 0.052 [10]. Mba et al. conducted a study to predict room temperature and humidity in the past using ANN to reduce cooling energy in residential buildings. The ANN model showed 98% accuracy [11]. Zhao and Liu proposed a load-predicting method for office buildings based on regression analysis and artificial intelligence [12]. Afram et al. studied ANN-based HVAC optimal control in residential buildings. They found that HVAC operation costs can be lowered using the proposed ANN-based HVAC control strategy [13]. Jang et al. developed an LSTM-based prediction model to predict the heating energy consumption in daycare centres. They used environmental data and building operation pattern data to train the LSTM model. The optimized LSTM model showed a CV(RMSE) of 17.6% during the winter season [14]. Faid et al. proposed prediction models based on LSTM, support vector regression, and Gaussian process regression to predict the peak electricity usage of a target building. The electricity usage included the electric equipment and HVAC systems energy consumption of the

building. They found that the LSTM model showed the highest accuracy among the three models. However, they cited the need for massive time series data as a drawback of LSTM models [15]. Fang et al. developed an LSTM-based prediction model to determine the accurate indoor temperature for controlling the HVAC system [16]. Bouktif et al. constructed a model for predicting short- and mid-term building electric loads using the LSTM algorithm and established that the proposed LSTM model has high accuracy [17].

Similarly, Somu et al. developed an LSTM model to predict building energy consumption. Their proposed model also showed high accuracy [18]. Peng et al. claimed that their LSTM model demonstrates high efficiency in building load forecasting [19].

In summary, many previous studies have analyzed pre-selected algorithms without considering the data characteristics of the target building. However, many factors influence building loads, such as location, climate conditions, and HVAC system type. It is, therefore, crucial to carefully select an appropriate algorithm that considers the specific characteristics of the target building. Furthermore, ensuring the reliability of the findings was challenging in certain studies because simulations were not calibrated with actual building data. To achieve reliable algorithm-based HVAC control, it is imperative to establish the credibility of the algorithm. Ensuring the reliability of actual HVAC control is crucial, even if predictions are accurate in an ideal environment. The use of unverified data can undermine this reliability. Therefore, utilizing a calibrated model based on the actual data is essential. In this study, we address this concern by developing a calibrated simulation model, which enhances the reliability of the data used.

Our research objective is to determine the optimal algorithm for HVAC system control in the target building. To achieve this, we compare the accuracy of cooling load prediction using two widely utilized algorithms in building energy research: ANN and LSTM. Additionally, we investigate the impact of cooling load prediction accuracy on HVAC control by comparing the patterns of AHU discharge air temperature (DAT) control values. We select the most suitable ML algorithm for the target building based on these comparisons. Furthermore, we evaluate the feasibility of applying ML-based HVAC control by selecting representative dates for analysis.

1.2. Scope

This study aims to find the optimal algorithm for HVAC system control in the target building. We used Python programming to develop prediction models using ANN and LSTM algorithms. To train and test two models, we utilized an EnergyPlus simulation model calibrated by the actual data. We compared the accuracy of the prediction models and then conducted a comparative analysis of AHU-DAT patterns to determine the optimal algorithm for HVAC control in the target building. In addition, we performed a feasibility analysis by analyzing a representative day to assess the potential for ML-based HVAC control in the target building. A visual representation of our process can be found in Figure 1.

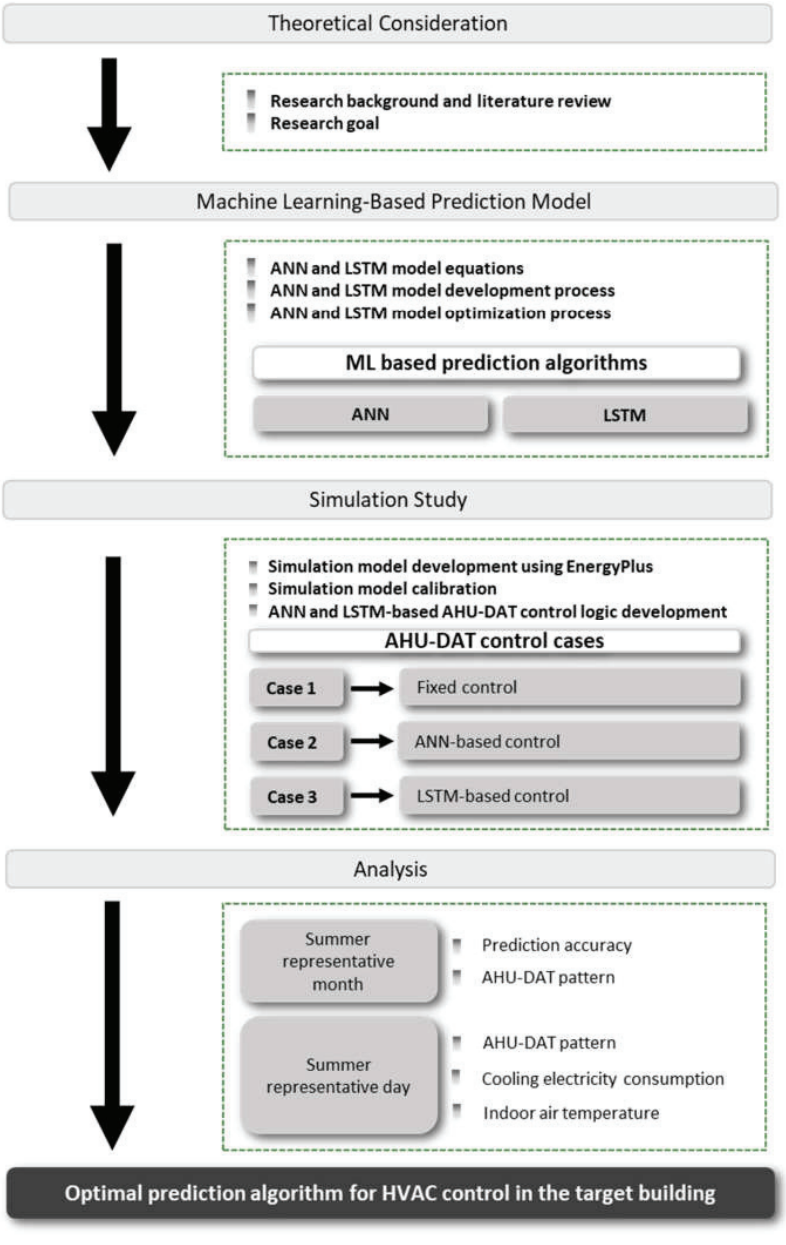

Figure 1. Overview of the research flow.

2. Machine Learning-Based Prediction Model: Concept and Formulation

2.1. Artificial Neural Network

Figure 2 shows the structure of an ANN algorithm with an input layer, a hidden layer, and an output layer. In the following paragraphs, we explain the process and outline the formulas related to the learning method of ANN.

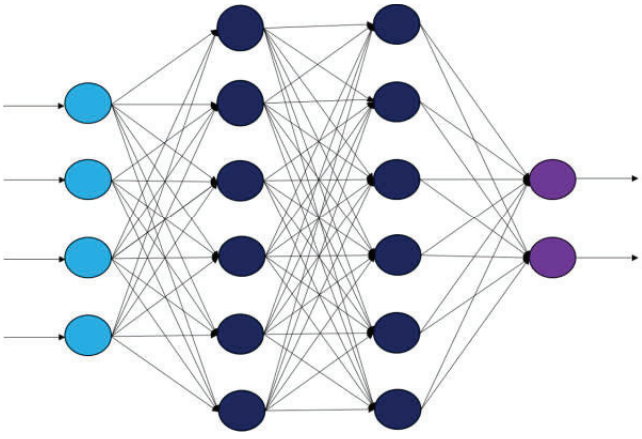

Figure 2. ANN algorithm structure.

The critical advantage of ANN is its robustness to noisy input data. They can learn to generalize from training examples and make accurate predictions even in noise [3–12]. However, a limitation of ANN is that they are not inherently designed to capture temporal dependencies in sequential data. They treat all inputs independently, which can be a drawback in tasks where the order or timing of the data is essential [3–12].

First, ANN prints a predicted value through a certain calculation process in the input, hidden, and output layers based on the input data using feed-forward propagation. After which, it performs an error back-propagation process to identify the error between the predicted value and the correct determined value, which is then reflected in the next learning.

The feed-forward neural network, the basic algorithm of ANN, is transmitted from the input layer and the hidden layer to the output layer. Each layer consists of nodes, and each node is connected. When neurons in the input layer receive an external input, weight factors are applied to input data and output values through the activation function. Equations (1) and (2) [4,20] are the formulas used for data forward propagation in ANN, using sigmoid as an activation function [4,20].

$$y = \sigma(b + \sum_{i=1}^{n} x_i w_i) \tag{1}$$

where

y = output of the node,
σ = sigmoid function,
b = bias,
n = number of nodes in a previous layer connected to the node,
x_i = input values of nodes in a previous layer connected to the node, and
w_i = weight factor of all nodes connected to the node.

$$\sigma = \frac{1}{1 + e^{-x}} \tag{2}$$

where

x = a value obtained by adding a bias to the value multiplied by all input values input to the node and a weight factor.

When an error occurs in the resulting data, updating the weight factor by propagating the error to the previous layer is repeated. This process is called back-propagation. The optimal value is found by updating the weight factor during the back-propagation process by repeating the gradient descent method. This process also minimizes the error rate of the ANN model and increases the prediction accuracy of printed data.

Equations (3)–(6) are the formulas used for updating the weight factor through the gradient descent method [20]. Equation (3) is the final formula for calculating the error function for the weight factor of each node located between the hidden layer and the output layer [20].

$$\frac{\partial E}{\partial w_{ho}} = -(t_o - o_o) \times sigmoid(\sum_h w_{ho} \times o_h)(1 - sigmoid(\sum_h w_{ho} \times o_h)) \times o_h \quad (3)$$

where

$\frac{\partial E}{\partial w_{ho}}$ = slope of the error for the weight factor located between the hidden layer and the output layer,

$t_o - o_o$ = difference between the printed values and the correct answer,

$sigmoid(\sum_h w_{ho} \times o_h)$ = sum of the input values coming in the node located in the output layer, and

o_h = output value of the node located in the hidden layer.

Equation (4) is the formula for updating the weight factor between the hidden and output layers based on the calculated error function [20]. The updated weight factor can be calculated by subtracting the value obtained and multiplying the error slope calculated in Equation (6) by a constant from the previous value of the weight factor. The constant α adjusts the intensity of the change, which is called the learning rate [4,20].

$$New\ (w_{ho}) = Old\ (w_{ho}) - \alpha\ \frac{\partial E}{\partial w_{ho}} \quad (4)$$

where

w_{ho} = weight factor between the hidden layer and the output layer,

α = learning rate, and

$\frac{\partial E}{\partial w_{ho}}$ = slope of the error for the weight factor between the hidden and output layers.

Equation (5) is the final formula for calculating the error function for the weight factor of the nodes between the input and hidden layers [20].

$$\frac{\partial E}{\partial w_{ih}} = -(e_h) \times sigmoid(\sum_i w_{ih} \times o_i)(1 - sigmoid(\sum_i w_{ih} \times o_i)) \times o_i \quad (5)$$

where

$\frac{\partial E}{\partial w_{ih}}$ = slope of the error for the weight factor between the input layer and the hidden layer,

e_h = back-propagation error transmitted to the hidden layer,

$sigmoid(\sum_i w_{ih} \times o_i)$ = sum of the input values from the input layer to the node located in the hidden layer, and

o_i = output of the node in the input layer.

Equation (6) is the formula for updating the weight factor located between the input layer and the hidden layer based on the calculated error function [20].

$$New\ (w_{ih}) = Old\ (w_{ih}) - \alpha\ \frac{\partial E}{\partial w_{ih}} \quad (6)$$

where

w_{ih} = weight factor between the input layer and hidden layer,

α = learning rate, and

$\frac{\partial E}{\partial w_{ih}}$ = slope of the error for the weight factor between the input layer and hidden layer.

2.2. Long Short-Term Memory

Long Short-Term Memory is an algorithm that compensates for the shortcomings of RNN. RNN was introduced in the study of David Rumelhart in 1986. It is a type of

ANN characterized as having an internal circular structure of data [21]. It involves saving previous data and feeding it back when inputting new data so it is not forgotten. Unlike ANN, where all input data are independent, RNN processes input data in its internal memory so that all input values are related [22]. As such, RNN is suitable for learning time series data with temporal correlation [23].

In addition, RNN uses "back-propagation through time" during training, performing back-propagation of errors up to the earliest time step for every time step [24]. If the time step exceeds a certain period of time, gradient vanishing can occur in which the learning rate is not updated, and long-term patterns cannot be learned [23]. To overcome these shortcomings of RNN, Sepp Hochreiter and Jürgen Schmidhuberdm introduced LSTM in 1997 [22]. Figure 3 shows the structure of LSTM.

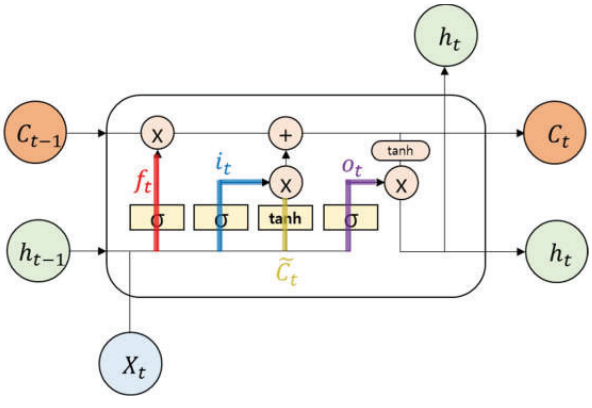

Figure 3. LSTM algorithm structure.

The LSTM structure, as shown in Figure 3, is designed to continuously transmit information necessary for long-term learning by improving the existing RNN structure. Learning is performed on time-dependent data input through a long-term memory device called cell state—the core of LSTM. In LSTM, a forget gate, an input gate, a hidden state, and an output gate are added to the existing RNN memory cell. The role of the forget gate and input gate is to update the value of the cell state. Meanwhile, the hidden state and the output gate's role is to print a predicted value based on the updated cell state value and input value.

LSTM has a key advantage in that it is specifically designed to model and capture long-term dependencies in sequential data [14–19]. With a memory cell that can store information over extended time intervals, LSTM is effective in tasks involving time series analysis, natural language processing, and speech recognition [25]. However, a significant drawback of LSTM is its higher computational cost than ANN [23].

The learning method of LSTM entails several formulas. Equations (7)–(11) calculate the forget gate and input gate to update the cell state [25]. The forget gate calculates a value based on the input data of the current time step and the predicted value of LSTM in the previous time step. The value calculated for the forget gate is then multiplied by the cell state value of the previous time step. The output value of LSTM in the previous time step and the input data in the current time step helps determine if the value of the cell state in the previous time step needs to be reduced through the forget gate.

Equation (7) is the formula for the forget gate [25].

$$f_t = \sigma\left(W_f[h_{t-1}, x_t] + b_f\right) \tag{7}$$

where

f_t = output of the forget gate,

σ = sigmoid function,
W_f = weight factor assigned to the forget gate,
h_{t-1} = output value of LSTM in the previous time step,
x_t = input data in the current time step, and
b_f = bias assigned to the forget gate.

The input gate plays a role in determining how much new information is stored in the cell state. First, the input gate calculates the output value of the input gate using Equation (8) and determines new values that can be added to the cell state using Equations (9) and (10) [25]. After which, Equations (8) and (9) are multiplied to output one value [25]. This value is then added to the updated cell state value through the forget gate to determine the cell state value of the current time step, which is represented in Equation (11) [25].

$$i_t = \sigma\left(W_i[h_{t-1}, x_t] + b_i\right) \tag{8}$$

where
i_t = output of the input gate,
σ = sigmoid function,
W_i = weight factor assigned to the input gate,
h_{t-1} = output value of LSTM in the previous time step,
x_t = input data in the current time step, and
b_i = bias assigned to the input gate.

$$\widetilde{C}_t = tanh\left(W_C[h_{t-1}, x_t] + b_C\right) \tag{9}$$

where
$\widetilde{C}_t$ = new values that can be added to the cell state,
$tanh$ = hyperbolic tangent activation function,
W_C = weight factor assigned to the layer,
h_{t-1} = output value of LSTM in the previous time step,
x_t = input data in the current time step, and
b_C = bias assigned to the cell state.

$$\tanh(x) = \frac{e^{2x} - 1}{e^{2x} + 1} \tag{10}$$

$$C_t = (f_t * C_{t-1}) + \left(i_t * \widetilde{C}_t\right) \tag{11}$$

where
C_t = value of the cell state at this time step determined through the forget gate and input gate,
f_t = output of the forget gate,
C_{t-1} = value of the cell state in the previous time step,
i_t = output of the input gate, and
$\widetilde{C}_t$ = new values that can be added to the cell state.

The output gate plays a role in printing output values of LSTM in the current time step. The output gate uses the calculated value of the output gate in Equation (12) and the updated value of the cell state in Equation (11) to print the predicted output value of LSTM in the current time step using Equation (13) [25].

$$o_t = \sigma\left(W_o[h_{t-1}, x_t] + b_o\right) \tag{12}$$

where
o_t = output of the output gate,
σ = sigmoid function,
W_o = weight factor assigned to the output gate,
h_{t-1} = output value of LSTM in the previous time step,

x_t = input data in the current time step, and
b_o = bias assigned to the output gate.

$$h_t = o_t * tanh(C_t) \quad (13)$$

where
h_t = output value of LSTM in the current time step,
o_t = output of the output gate,
$tanh$ = hyperbolic tangent activation function, and
C_t = value of the cell state at this time step determined through the forget gate and input gate.

As previously shown in Figure 3, both the value of the cell state in Equation (11) for long-term memory and the output value of LSTM in Equation (13) for short-term memory are transferred to the input value of the next time step [25]. Due to this unique structure, LSTM can long-term memory storage of input data without gradient vanishing.

2.3. Development Process of ML Models

In this study, we developed ANN and LSTM models using the Keras library through Python version 3.9.5. Keras is a library for ML written in Python and an ML platform based on TensorFlow. The Keras library offers a significant advantage in ease of implementation and optimization, as the ML and Deep Learning algorithms can be structured simply using the Keras. Layers and Keras.Models modules. It is currently used to build various algorithms, such as ANN, recurrent neural networks, LSTM, and convolutional neural networks [26].

Developing an ML-based prediction model entails three significant steps: input variables selection, algorithm training and testing, and optimization.

The first step in implementing an ML-based predictive model is input variables selection. It is important to select input variables with high correlation, which can be done through correlation analysis of input and output variables. To check the correlation between two linearly related variables, we used the Pearson correlation coefficient, one of the commonly used statistical methods.

The closer $|r|$ is to 1.0, the higher the correlation between variables X and Y. The closer $|r|$ is to 0, the lower the correlation between the variables. In this study, we used Falk and Miller's determination ($r^2 > 0.7$), the criterion for determining the suitability of variables in the engineering field, as the primary criterion [27]. According to previous research, if no variable meets the primary criterion, $|r| > 0.3$ can be used as the secondary criterion to select and determine the appropriateness of the input variable [28].

Table 1 shows the results of the Pearson correlation analysis of input and output variables for the ML-based cooling load prediction model. Among these variables, those that satisfy the primary criterion for judging suitability $r^2 > 0.7$ are lighting schedules (%), people schedules (%), and day and hour types (-) [27]. The remaining five variables do not satisfy the primary criterion but satisfy the secondary criterion $|r| > 0.3$ [28]. Accordingly, all eight variables are considered suitable for use in the ML-based cooling load prediction model.

Table 1. Correlation analysis results.

Correlation Factor with Cooling Load	Outdoor Air Temperature (°C)	Outdoor Air Relative Humidity (%)	Diffuse Solar Radiation (W/m^2)	Direct Solar Radiation (W/m^2)	Lighting Schedules (%)	Electric Equipment Schedules (%)	People Schedules (%)	Day and Hour Type (-)
r	0.5621	−0.5022	0.4737	0.4863	0.8694	0.8353	0.9061	0.9446
r^2	0.3159	0.2522	0.2243	0.2365	0.7558	0.6977	0.8210	0.8923

When developing an ML model, if the same data set is used in the training and validation process, ML can generate good predictions under certain conditions, but it may not sufficiently consider new patterns of data that have not been experienced. Therefore, in this study, we divided the data into two categories: learning data and testing data. Only learning data was used in the learning part, while only testing data was used in the verification part. Simulation data were collected from June to August 2017, a total of 2208 hours. To check the adaptability of ML to a new pattern not experienced during training, the entire data was divided at a ratio of about 66:34, and training and tests were conducted. In this study, 1 June to 31 July was designated as a period for training, while 1 August to 31 August was designated as a period for testing.

The second step in implementing an ML-based predictive model is ML algorithm training and testing. The training aims to obtain the lowest error rate between the ML's output and the answer. To ensure this, learning is repeatedly performed, called an epoch. Unlike the training process, the testing process does not adjust the weighting factor based on the error rate between the ML result and the "correct answer" but checks the predicted accuracy rate of the trained ML model.

The final step is optimization. Optimization means optimizing by changing the hyperparameters of the ML algorithms, such as the number of hidden neurons, hidden layers, and epochs. Optimisation aims to improve the predictive performance and reliability of ML-based predictive models. The statistical term, or the CV(RMSE), is used to confirm the reliability of the ML model. When the CV(RMSE) value exceeds 30%, the user changes the hyperparameter value and repeats it until the CV(RMSE) value is less than 30%.

2.4. A Comparative Method for Evaluating the Accuracy of Prediction Models

This study aims to compare the accuracy of cooling load prediction between ANN and LSTM algorithms widely employed in building energy research to identify the optimal algorithm for HVAC control in the target building. The goal is to select an algorithm that aligns well with the data characteristics of the said building. ANN and LSTM are supervised learning-based algorithms, but they differ in data processing methods, resulting in potential variations in predicted values even when fed with the same input data.

As such, in this study, the optimization of prediction accuracy for both ANN and LSTM algorithms involved selecting variables, such as the number of hidden layers, nodes, and epochs, which are common hyperparameters in both algorithms. Table 2 presents the hyperparameters and their corresponding ranges used to compare ANN and LSTM prediction accuracy in this study.

Table 2. Hyperparameters and ranges.

Division	Hyperparameter Range	
	ANN	**LSTM**
Number of hidden layers [n]	1, 2, 3	
Number of hidden nodes [n]	10~15	
Epochs [n]	100, 200, 300	
Batch size [n]	24	
Optimizer	Adam	
Activation Function	Sigmoid and Rectified linear unit	

Figure 4 shows an example of the optimization of ANN structure. The optimization process involved evaluating the prediction accuracy of various conditions, ranging from 1 hidden layer, ten hidden nodes, and 100 epochs to 3 hidden layers, 15 hidden nodes, and 300 epochs for each algorithm. In total, 774 conditions were compared to identify the optimal structure for predicting the cooling load.

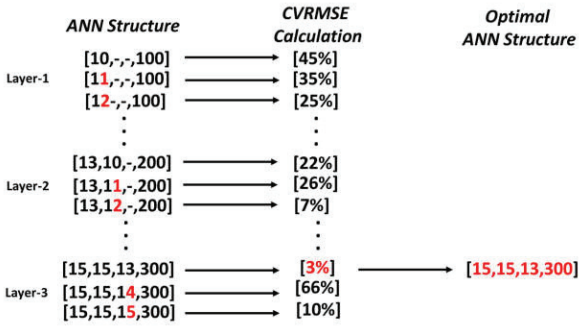

Figure 4. Example of the optimization process.

3. Simulation Study

3.1. Simulation Program

This study used the EnergyPlus simulation program developed by the U.S. Department of Energy (U.S. DOE) to ensure detailed analysis. The EnergyPlus program is a simulation program that combines the advantages of BLAST and DOE-2 and uses the heat balance method recommended by the American Society of Heating, Refrigerating, and Air-Conditioning Engineers (ASHRAE).

For the reliability verification of the EnergyPlus simulation program, simulation tools were developed and verified using ASHRAE Standard 140-2014 [29]. Eighty scenarios were tested and verified in three categories: building air-conditioning load, heating equipment, and cooling equipment. In addition, the EnergyPlus program was further reviewed using the IEA's Building Energy Simulation Test.

In the EnergyPlus program, zone simulation analysis based on the integrated thermal and material equilibrium—the biggest drawback of the DOE-2 program—is possible. In addition, the analysis of flow between multiple zones, the analysis of pollutants generated in buildings, and the analysis of renewable energy systems are supported.

3.2. Target Building and Simulation Model

The Target building in this study is an office built in 2014 in the Research Triangle Park (RTP) area, NC, USA. The three-story structure includes offices, conference rooms, common areas, and storage spaces. The floor area is 4310 m^2, and the window-to-wall ratio is 23.3%. The HVAC system operates from 7 a.m. to 8 p.m. Figure 5 shows an overview of Target Building A.

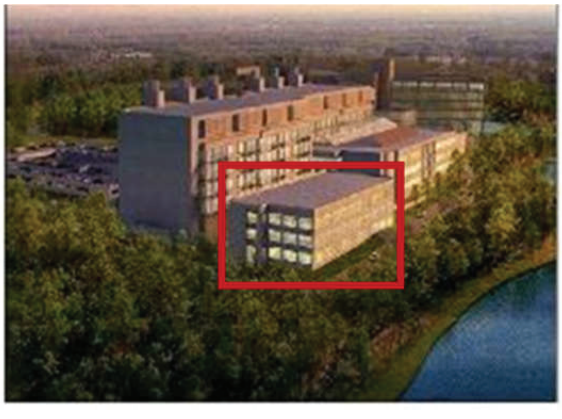

Figure 5. Overview of Target Building A.

The simulation model was developed using EnergyPlus version 9.4. Simulation conditions were mostly taken from real building values. Table 3 shows the people density in each space type in the target building. For example, lighting power density is 8.07 W/m^2, while equipment power density is 10.76 W/m^2. Table 4 provides details on the construction and material properties of the simulation model, which are all based on the target building.

Table 3. Target Building A's people density in each space type.

Zone	People Density (m^2/Person)
Break Room	5.0
Closed Office	12.1
Open Office	12.1
Conference	12.1
IT Room	12.1
Lobby	9.3
Corridor	9.3
Mechanical Room	14.0
Stair	12.1
Rest Room	14.9
Storage	14.0

Table 4. Target Building A's construction properties.

Construction	U-Value (W/m^2 K)	Visible Transmittance	Solar Heat Gain Coefficient
Exterior Wall	0.232	X	X
Interior Wall	2.867	X	X
Roof	0.174	X	X
Exterior window	1.65	0.60	0.31

Three AHUs are installed as the target building's main heating and cooling system. A district heating and cooling system supplies chilled water and hot water to the AHUs for space cooling and heating. The AHUs provide cold or hot air to conditioned zones through the variable air volume fan. The cooling setpoint of the target building is 22.2 °C during office hours between 7 a.m. and 8 p.m. At night, the setback setpoint is 26.6 °C. We also used a throttling range of 1.1 °C for the cooling setpoint. The AHUs discharge air temperature (DAT) is 12.8 °C. For the detailed analysis, we selected the AHU installed on the second floor for the space heating and cooling.

In our research, we utilized a district cooling system. We used Equations (14) and (15) to convert the usage for chilled water (CHW) into the corresponding electricity consumption of the district cooling system. The estimation was based on assuming a Coefficient of Performance (COP) value of 5, equivalent to 0.7 kW/ton [30]. This COP value represents the recommended minimum requirement for Chiller COP, as suggested by the NC Department of Environmental Quality in their Energy Saving Fact Sheet: Chillers report [30].

$$CHW_{electricity} = TOR * COP_{chiller,avg} \quad (14)$$

where

$CHW_{electricity}$ = chilled water electricity consumption (kWh)
TOR = A ton of refrigeration (ton-hour); 1 TOR = 3.5169 kWh
$COP_{chiller,avg}$ = typical COP value of chiller (0.7 kW/ton)

$$TOR = CHW_{ussed} * CF \quad (15)$$

where

TOR = A ton of refrigeration (ton-hour); 1 TOR = 3.5169 kWh
CHW_{used} = chilled water usage (MJ)
CF = MJ to TOR conversion factor; 0.07898476 ton-hour/MJ

3.3. Calibration Process

In the measurement & verification (M&V) standard, the accuracy of the simulation model is assessed by comparing simulation results with actual experimental data. The ASHRAE Guideline 14-2014 [29], the International Performance Measurement and Verification Protocol [31], and the Federal Energy Management Program are representative M&V guides [32] and are indicators for the accuracy of simulation models.

The allowable error rate of the tolerance range varies depending on which of the three M&V guides is used. When we performed a correction with monthly data, the allowable tolerance range differed for each guide. However, when we calibrated the simulation model with hourly data, the tolerance range for all three M&V guides was the same at $\pm$10% for normalized mean bias error (NMBE) and 30% for $cv(RMSE)$ [29,31,32].

In this study, the simulation model was calibrated with hourly data, and the tolerance range was based on NMBE $\pm$ 10% and $cv(RMSE)$ 30%. We used Equations (16) to (18) to calculate NMBE and $cv(RMSE)$.

$$RMSE = \sqrt{\frac{\sum(S-M)^2_{interval}}{N_{interval}}} \tag{16}$$

$$cv(RMSE) = \frac{RMSE_{period}}{A_{period}} \tag{17}$$

$$A_{period} = \sqrt{\frac{\sum_{period} M_{interval}}{N_{interval}}} \tag{18}$$

where

S = ANN model prediction value,
M = EnergyPlus simulation results,
$N_{interval}$ = number of EnergyPlus results, and
A_{period} = measurement period average.

The data collection period for the target building A was from 10 May 2017 to 7 August 2017. Except for periods when there was a system problem, or the system was turned off, all data were normally collected from 4 July 2017 to 7 August 2017. During the periods when data were collected, the simulation model was calibrated, particularly during the hottest week of 17–21 July 2017, as this study aims to propose a control to save cooling energy.

Figures 6–8 show the comparison of field data and simulation results for lighting electricity energy consumption, electric equipment electricity energy consumption, and electrical energy consumption for heating and cooling during the selected week. For lighting electricity energy consumption, NMBE was 1.15%, whereas $cv(RMSE)$ was 23%. For electric equipment electricity energy consumption, NMBE was 8.96%, whereas $cv(RMSE)$ was 18.9%. Finally, regarding electricity energy consumption for heating and cooling, NMBE was 1.13%, whereas $cv(RMSE)$ was 21.3%. Since both NMBE and $cv(RMSE)$ were within the tolerance range described above, the simulation model was considered calibrated.

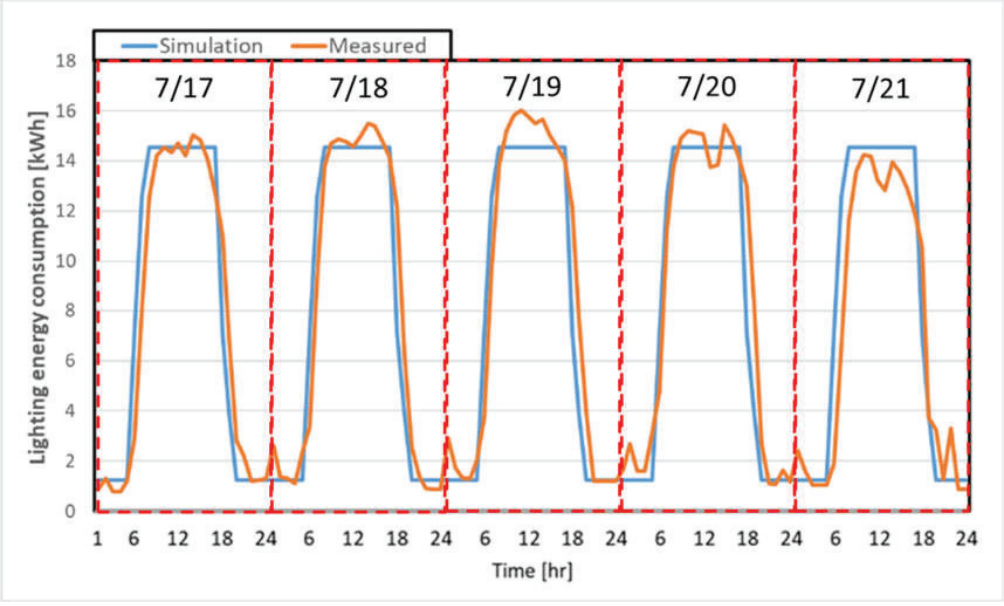

Figure 6. Calibration results for lighting energy consumption.

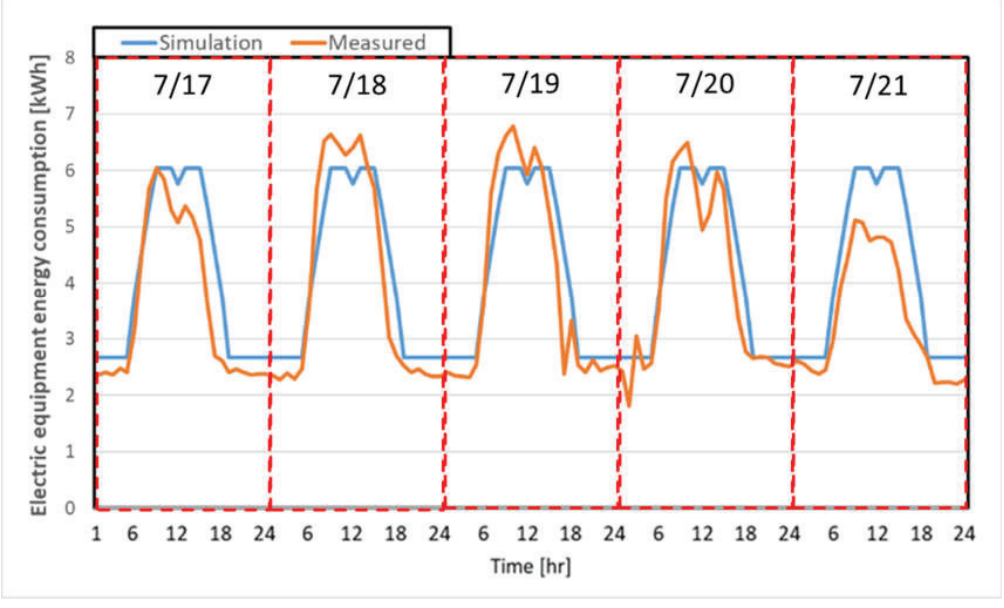

Figure 7. Calibration results for electric equipment energy consumption.

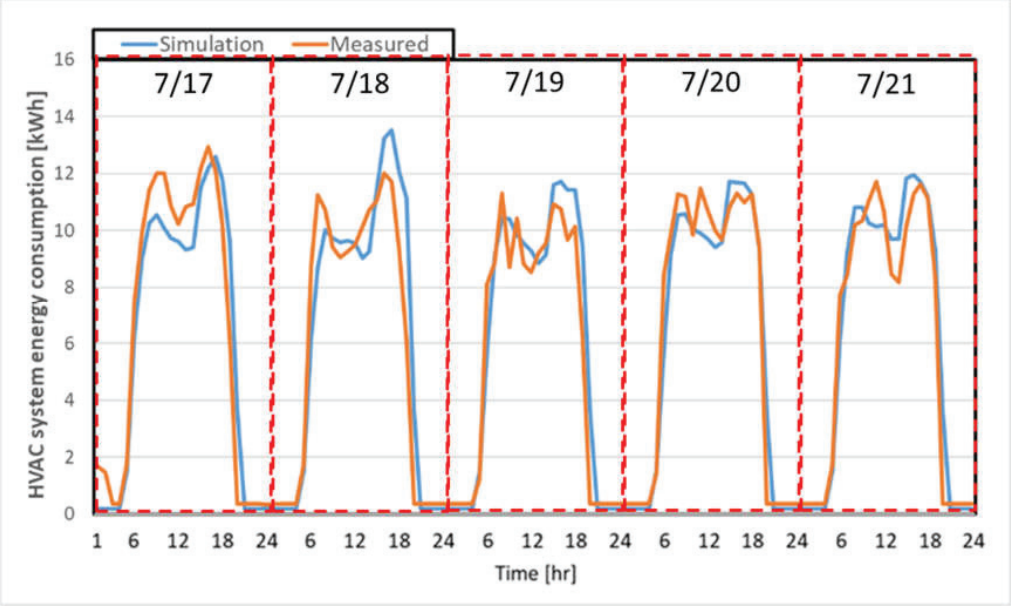

Figure 8. Calibration results for HVAC system energy consumption.

4. Case Study

4.1. Simulation Cases

This study had three simulation cases. In Case 1, the base case, the AHU-DAT was fixed at the actual control value of 12.8 °C for the target building. In Case 2, an optimized ANN-based cooling load prediction model was used to predict and control the AHU-DAT within the range of 12.8 °C to 17.8 °C based on the partial load section. Meanwhile, in Case 3, an optimized LSTM-based cooling load prediction model was used to predict and control the AHU-DAT within the same range. Finally, we compared the cooling electricity consumption on a representative day in a case study for each of the three cases. We evaluated the energy-saving ability of ML-based AHU-DAT control.

4.2. ML-Based HVAC Control Methods

Figure 9 and Table 5 present the AHU-DAT determination method for Cases 1, 2, and 3 based on the part load ratio (PLR) change in this study. In Case 1, the AHU-DAT was fixed at 12.8 °C, the actual AHU-DAT setpoint temperature in the test building. In Cases 2 and 3, the AHU-DAT setpoint temperatures were set within the 12.8 to 17.8 °C range based on the PLR interval predicted by the ANN and LSTM models. We conducted a simulation analysis and selected the temperature range of 12.8 to 17.8 °C, which falls within the allowable range of ±1.1 °C for the indoor cooling set temperature of 22.2 °C during office hours and 26.6 °C during the night. Notably, in Case 1, AHU-DAT was fixed at 12.8 °C regardless of changes in cooling load. In contrast, in Cases 2 and 3, AHU-DAT was controlled at 12.8 °C when the cooling load was predicted to be in the PLR 90–100% range and at 17.8 °C when the cooling load was predicted to be in the PLR 0–10% range to adapt the AHU-DAT control according to the change in cooling load.

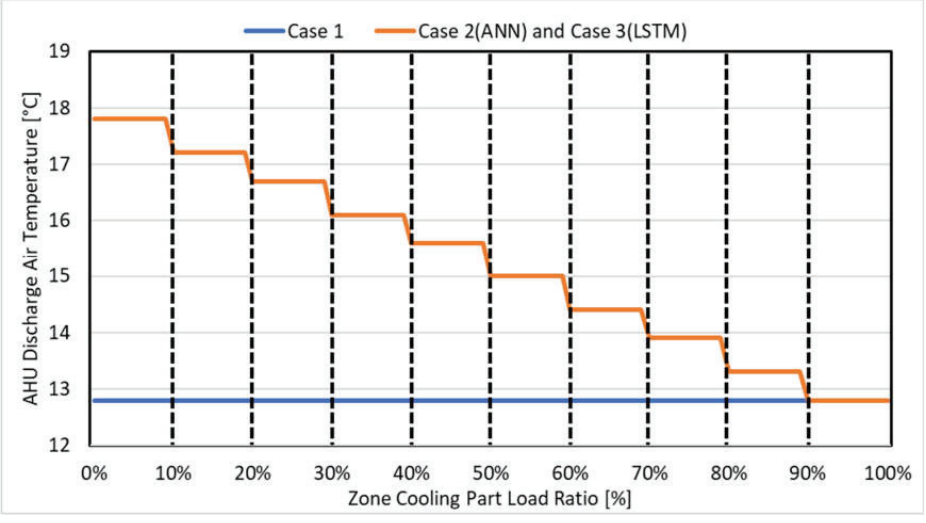

Figure 9. Comparison of AHU-DAT control values by PLR section in each case.

Table 5. AHU-DAT control classes by PLR section in each case.

Class	AHU-DAT (°C)	Case 1 Interval	Class	AHU-DAT (°C)	Cases 2 and 3 Interval
1	12.8	0% ≤ PLR < 10%	1	17.8	0% ≤ PLR < 10%
2	12.8	10% ≤ PLR < 20%	2	17.2	10% ≤ PLR < 20%
3	12.8	20% ≤ PLR < 30%	3	16.7	20% ≤ PLR < 30%
4	12.8	30% ≤ PLR < 40%	4	16.1	30% ≤ PLR < 40%
5	12.8	40% ≤ PLR < 50%	5	15.6	40% ≤ PLR < 50%
6	12.8	50% ≤ PLR < 60%	6	15.0	50% ≤ PLR < 60%
7	12.8	60% ≤ PLR < 70%	7	14.4	60% ≤ PLR < 70%
8	12.8	70% ≤ PLR < 80%	8	13.9	70% ≤ PLR < 80%
9	12.8	80% ≤ PLR < 90%	9	13.3	80% ≤ PLR < 90%
10	12.8	90% ≤ PLR ≤ 100%	10	12.8	90% ≤ PLR ≤ 100%

5. Analysis and Results

5.1. Weather Conditions

Figure 10 presents the outdoor air temperature pattern in Raleigh, North Carolina, where the target building is located. The Raleigh weather file provided by EnergyPlus was modified using actual outdoor air temperature and humidity data collected from the target building in 2017 and total solar radiation collected from Raleigh Durham Airport. The outdoor air dry-bulb temperature range during the analysis period is 13.1–37.4 °C, and the outdoor air relative humidity during the analysis period is 20–100%.

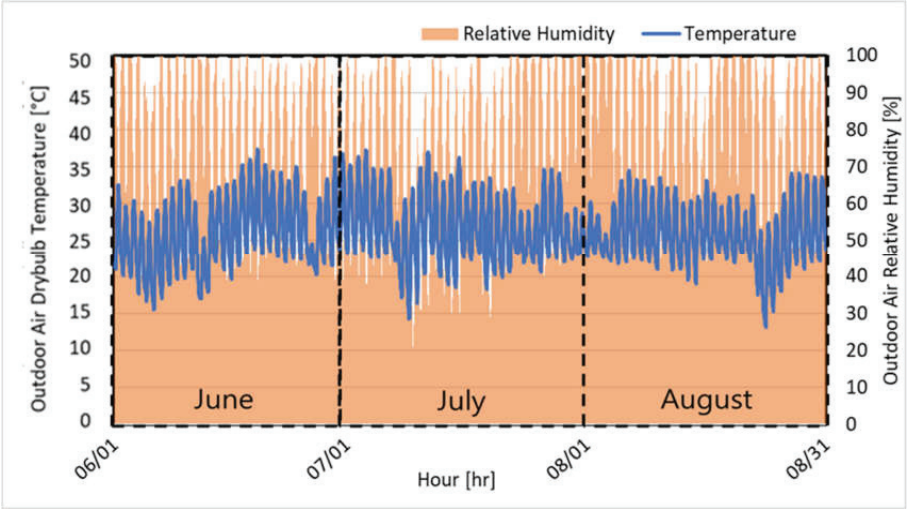

Figure 10. Outdoor air dry-bulb temperature and relative humidity in Raleigh, North Carolina.

5.2. Evaluation of Cooling Load Prediction Model Accuracy

In this study, the hyperparameters (i.e., number of hidden layers, hidden nodes, and epochs) were selected and optimized for ANN and LSTM algorithms to enhance their performance. Figure 11 shows the cooling load prediction accuracy based on the different configurations of hidden nodes, epochs, and several hidden layers in the ANN and LSTM models. We observed that both algorithms achieved the highest prediction accuracy using hidden triple layers and 300 epochs.

The optimized algorithm structures and their corresponding prediction accuracy are presented in Table 6. The prediction accuracy, as indicated by CV(RMSE), was 12.7% for ANN and 17.3% for LSTM, demonstrating a certain level of reliability for both optimized algorithms. However, the ANN algorithm has a higher prediction accuracy than the LSTM algorithm. This result can be attributed to the differences in the characteristics of the two algorithms. For example, LSTM incorporates past output data into the current input data, allowing for time-dependent learning. On the other hand, ANN treats all input data independently without considering the time sequence [3–12]. Due to these algorithm differences, LSTM is relatively more sensitive to patterns in past data than ANN [14–19,23,25].

Table 6. Optimal structure and parameter values.

Division	ANN	LSTM
	Optimized Values	**Optimized Values**
Number of Hidden Layers [n]	3	3
Number of Hidden Neurons Layer 1 [n]	13	12
Number of Hidden Neurons Layer 2 [n]	12	12
Number of Hidden Neurons Layer 3 [n]	11	12
Epochs [n]	300	300
CV(RMSE) [%]	12.7	17.3

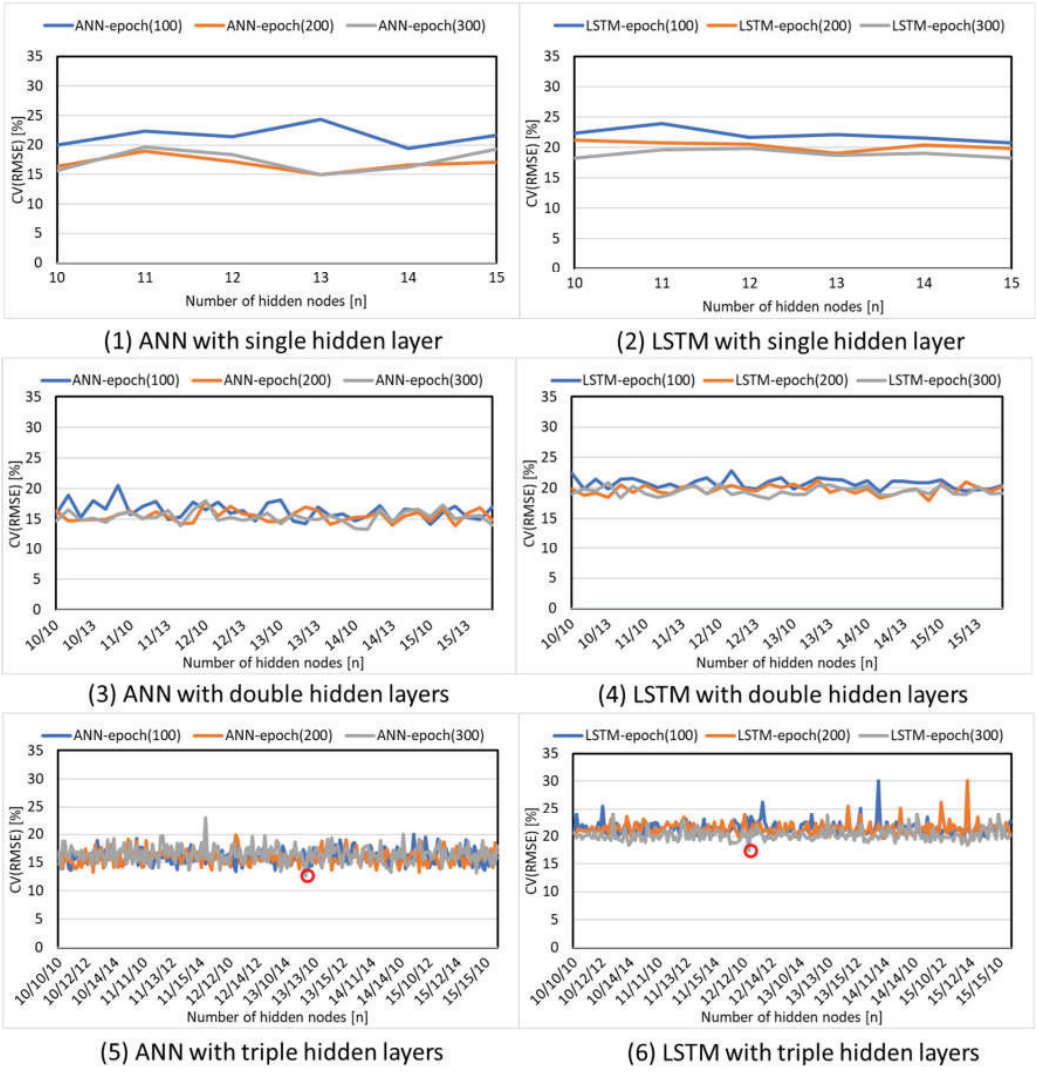

Figure 11. Comparison of the predictive accuracy of the ANN and LSTM models according to hyperparameter changes.

Figure 12 depicts the pattern of outdoor air temperature, which directly impacts the cooling load of the building, among the input data used for training the ANN and LSTM models during June and July 2017. Examining the figure, we observed that the outside air temperature exhibits rapid fluctuations in three sections.

A comparison of the average outdoor air temperature during the building's office hours from 7 AM to 8 PM revealed the following trends: In the first section, the average outdoor air temperature on 11 June was 26.5 °C, which decreased to 22.5 °C on 12 June and subsequently rose to 28.1 °C on 13 June. In the second section, the average outdoor air temperature on 25 June was 29.7 °C, followed by a decrease to 23.5 °C on 26 June and then a rise to 28.1 °C on 27 June. Meanwhile, in the third section, the average outdoor air temperature was 31.4 °C on 6 July but decreased to 24.9 °C on 7 July. Considering the rapid

changes in the data trends that impact the cooling load, we inferred that the learning rate of the LSTM model shows a relatively lower prediction accuracy than that of the ANN model.

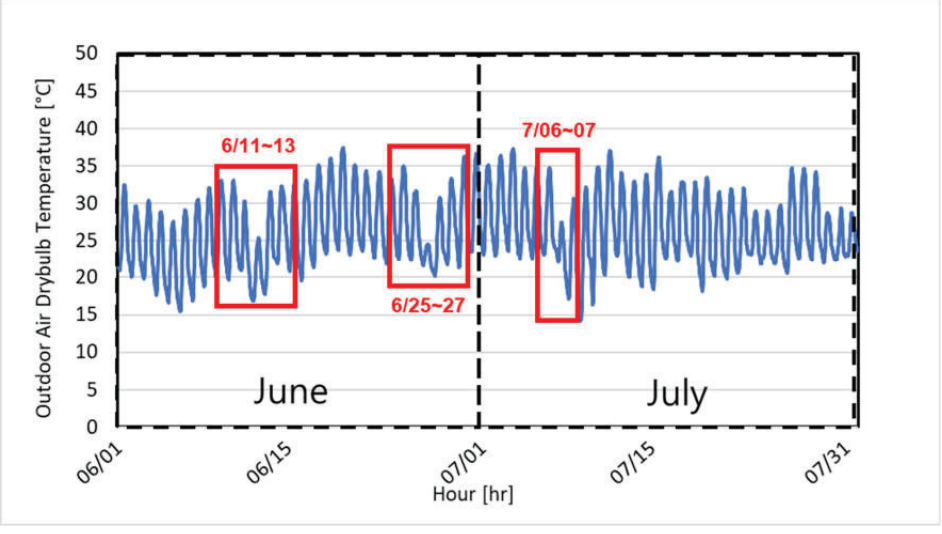

Figure 12. Outdoor air dry-bulb temperature and relative humidity in June and July in Raleigh, North Carolina.

Figures 13 and 14 compare the predicted cooling load generated by the optimized ANN and LSTM algorithms and the actual cooling load obtained from simulations from 1 August to 31 August.

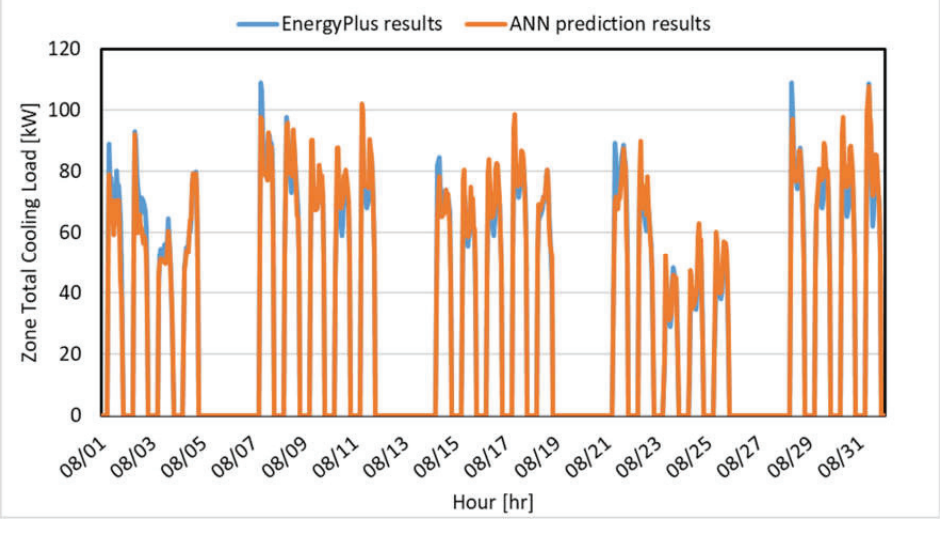

Figure 13. Comparison of simulation data and ANN results.

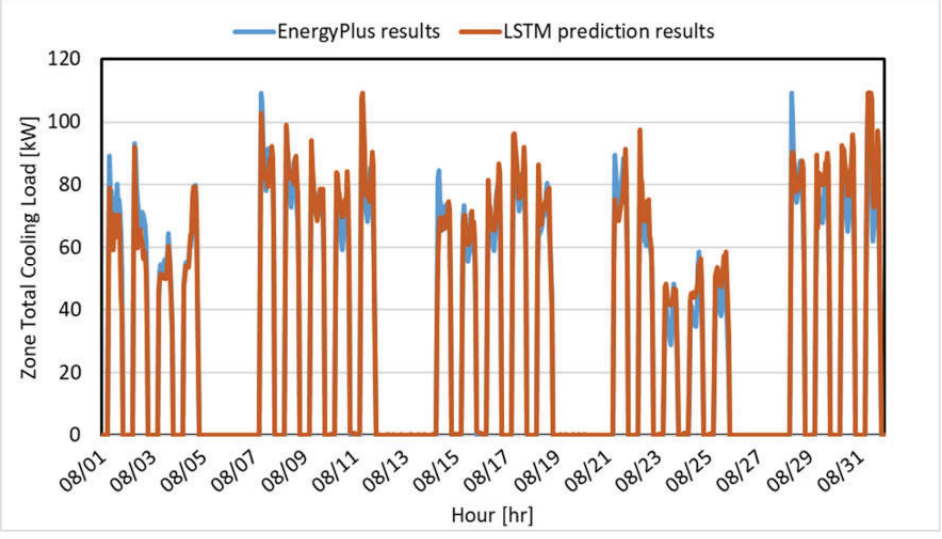

Figure 14. Comparison of simulation data and LSTM result.

5.3. AHU-DAT Operating Scenarios Comparison

Figure 15 and Table 7 present the AHU-DAT operating scenarios for the three cases. We examined the impact of cooling load prediction accuracy on HVAC control by comparing the patterns of AHU-DAT control values. For each case, we constructed the scenarios based on the simulation results for Case 1 and the predicted cooling load for Cases 2 and 3. Additionally, we developed AHU-DAT scenarios for different PLR intervals, as shown in Table 5. The analysis focused on office hours in August.

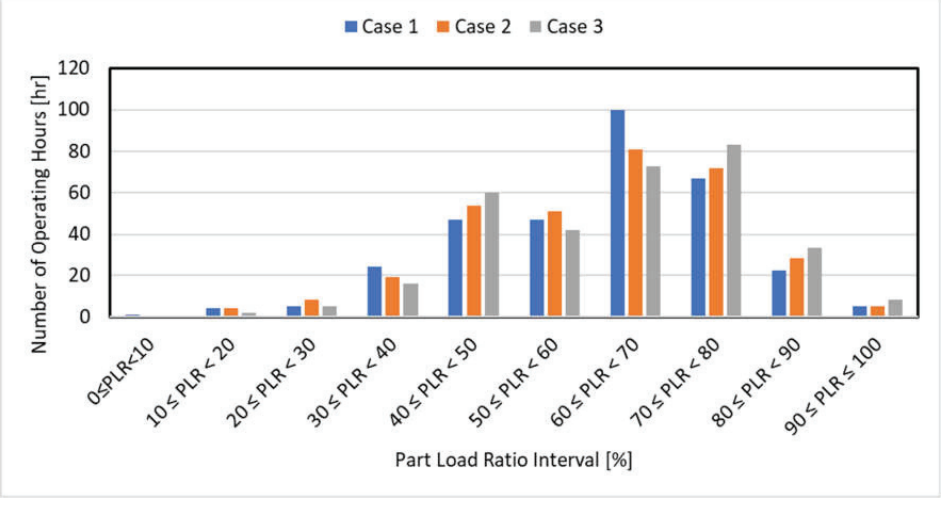

Figure 15. AHU-DAT control scenarios during office hours in August.

Table 7. AHU-DAT operating scenarios during office hours in August.

Class	AHU-DAT (°C)	Case 1		AHU-DAT (°C)	Case 2		Case 3	
		Interval	Number of Hours (h)		Interval	Number of Hours (h)	Interval	Number of Hours (h)
1	12.8	0% ≤ PLR < 10%	1	17.8	0% ≤ PLR < 10%	-	0% ≤ PLR < 10%	-
2	12.8	10% ≤ PLR < 20%	4	17.2	10% ≤ PLR < 20%	4	10% ≤ PLR < 20%	2
3	12.8	20% ≤ PLR < 30%	5	16.7	20% ≤ PLR < 30%	8	20% ≤ PLR < 30%	5
4	12.8	30% ≤ PLR < 40%	24	16.1	30% ≤ PLR < 40%	19	30% ≤ PLR < 40%	16
5	12.8	40% ≤ PLR < 50%	47	15.6	40% ≤ PLR < 50%	54	40% ≤ PLR < 50%	60
6	12.8	50% ≤ PLR < 60%	47	15.0	50% ≤ PLR < 60%	51	50% ≤ PLR < 60%	42
7	12.8	60% ≤ PLR < 70%	100	14.4	60% ≤ PLR < 70%	81	60% ≤ PLR < 70%	73
8	12.8	70% ≤ PLR < 80%	67	13.9	70% ≤ PLR < 80%	72	70% ≤ PLR < 80%	83
9	12.8	80% ≤ PLR < 90%	22	13.3	80% ≤ PLR < 90%	28	80% ≤ PLR < 90%	33
10	12.8	90% ≤ PLR ≤ 100%	5	12.8	90% ≤ PLR ≤ 100%	5	90% ≤ PLR ≤ 100%	8
Total hours (h)		322			322		322	

According to Figure 15 and Table 7, when examining the load pattern of Case 1, a considerable amount of time (i.e., 241 h or 74.8% of the total hours) belonged to the PLR 50% above section. Within this section, the PLR range of 60% to less than 70% accounted for the highest duration, with 100 h. The next highest duration was observed in the PLR range of 70% to less than 80%, totaling 67 h.

In the load pattern of Case 2, a substantial duration of time (i.e., 237 h or 73.6% of the total hours) belonged to the PLR 50% above section. Within this section, the PLR range of 60% to less than 70% accounted for the highest duration, with 81 h. The next highest duration was observed in the PLR range of 70% to less than 80%, totaling 72 h.

In the load pattern of Case 3, a significant portion of the time (i.e., 239 h or 74.2% of the total hours) belonged to the PLR 50% above section. Notably, the PLR range of 60% to less than 70% had the highest duration, with 73 h. The next highest duration was observed in the PLR range of 70% to less than 80%, totaling 83 h.

Comparing the cumulative hours of PLR ranges among the cases, for the PLR range of 60% to less than 70%, Case 2 showed 19% fewer cumulative hours than Case 1. Case 3 exhibited 27% fewer cumulative hours compared to Case 1. Additionally, for the PLR range of 70% to less than 80%, Case 2 showed 7% more cumulative hours than Case 1. In contrast, Case 3 demonstrated 24% more cumulative hours than Case 1. Based on the analysis of the AHU-DAT operating scenarios for the three cases and the evaluation of prediction accuracy conducted in Section 5.2, it has been concluded that the ANN algorithm exhibits superior performance in predicting the load pattern of the target building compared to the LSTM algorithm. Considering the prediction accuracies of both models, it can be determined that the ANN algorithm is the more appropriate choice for controlling the HVAC system of the target building.

5.4. Weather Conditions on the Representative Day

In this study, we conducted a feasibility analysis by analyzing a representative day to evaluate the potential of ML-based HVAC control in the target building. The test period for the ANN and LSTM algorithms was the month of August. Regarding the hottest day, it was difficult to compare the difference in control values by case because the PLR continued to maintain more than 80% most of the time. Therefore, we selected August 15, the median value of the outdoor air temperature, as the representative summer day. Figure 16 shows the outdoor air temperature and humidity variations on the summer representative day. The lowest outdoor air temperature was 19.0 °C, while the highest was 31.0 °C. The lowest outdoor air relative humidity was 46%, whereas the highest outdoor air relative humidity was 98%. Analyzing the characteristics of office hours between 7 a.m. and 8 p.m., we observed that the outdoor air temperature was at its lowest at 22 °C, while the outdoor air

humidity was at its highest at 86% at 7 a.m. The outdoor air temperature peaked at 31 °C, while the outdoor air humidity reached its lowest point of 46% at noon.

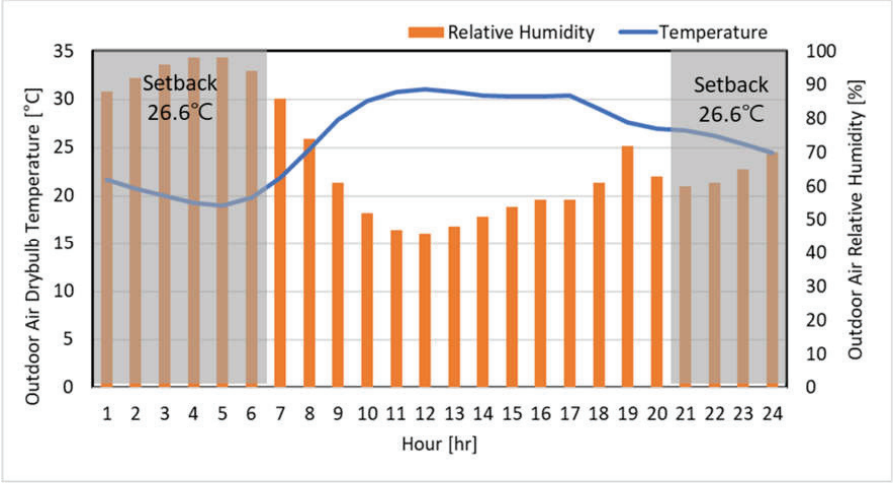

Figure 16. Outdoor air dry-bulb temperature and relative humidity pattern on a representative day.

5.5. Sensitivity Analysis of Zone Mean Air Temperature According to AHU-DAT Change on the Representative Day

Figure 17 illustrates the variation in the average indoor air temperature across all zones connected to the AHU. DAT in the figure means AHU-DAT. The results indicate that the indoor air temperature on a representative day consistently meets the cooling set temperature of 22.2 °C, with a throttling range of 1.1 °C during office hours, regardless of AHU-DAT conditions. Furthermore, during the night, the indoor air temperature does not rise above the designated setback temperature of 26.6 °C, which means there is no need for the cooling system to activate. For this reason, the set temperature range specified for AHU-DAT control in Cases 2 and 3 is deemed suitable for maintaining the indoor cooling set temperature. AHU-DAT control was based on the predicted cooling partial load on a representative day, utilizing ANN and LSTM algorithms with AHU-DAT set in 10 selected temperature ranges.

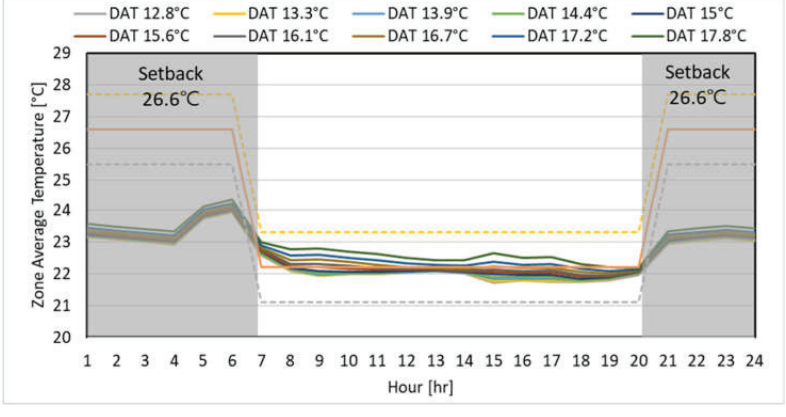

Figure 17. Sensitivity analysis of zone mean air temperature according to AHU-DAT change on a representative day.

5.6. Comparison of AHU-DAT Pattern on the Representative Day

Figure 18 depicts the variation in AHU-DAT based on the PLR on the summer representative day, analyzed by case. The PLR pattern on a representative day increases sharply from 8 a.m. across all cases, decreases around noon, and follows a pattern similar to the change in outdoor air temperature until 8 p.m. This pattern is attributed to the rapid fluctuation in outdoor air temperature from 22 °C at 7 a.m. to 25 °C at 8 a.m. and the consideration of internal heat gain schedules, accounting for reduced building utilization during lunchtime.

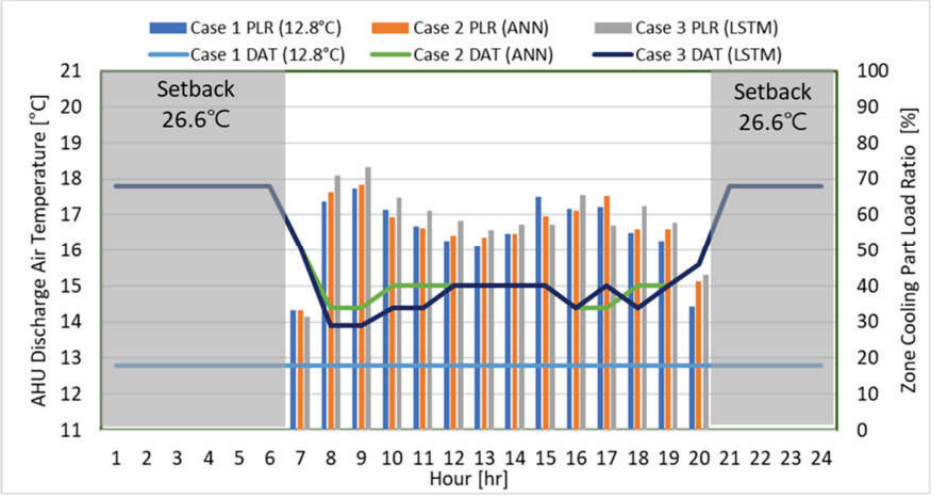

Figure 18. Comparison of the PLR and AHU-DAT pattern on a representative day.

When comparing the PLR in each case, Case 1 served as the base case. It reflected the PLR obtained by dividing the cooling load for each hour, calculated through the EnergyPlus simulation model, by the maximum cooling load during summer. Conversely, in Cases 2 and 3, as explained in Section 3.1, the algorithms learned the cooling load pattern according to the input variables during the learning period, and based on this, they predicted the cooling load on a representative day.

In Cases 2 and 3, the predicted cooling load was divided by the same maximum cooling load value as in Case 1 to determine the PLR for control purposes. Although the same input variables were employed, the predicted cooling PLR in Cases 2 and 3 tended to differ due to variations in prediction accuracy arising from the characteristics of the algorithm.

An examination of the AHU-DAT set values for each case revealed that Case 1 maintained a constant temperature of 12.8 °C irrespective of changes in the PLR. In contrast, Cases 2 and 3 exhibited distinct AHU-DAT values corresponding to the predicted PLR. For example, in Case 2, AHU-DAT was controlled at 16.0 °C at 7 a.m.. As a result, the lowest predicted PLR, and at 14.4 °C around 9 a.m., the highest predicted PLR. Meanwhile, in Case 3, AHU-DAT was controlled at 16.0 °C at 7 a.m., the lowest predicted PLR, and at 13.9 °C around 9 a.m., the highest predicted PLR.

This discrepancy is attributed to the variation in AHU-DAT control values for each 10% interval of the PLR, as illustrated in Figure 9 and Table 5. The predicted PLR at 9 a.m. for Case 2 falls within 60% or more and less than 70%, specifically at 68.4%. Meanwhile, the predicted PLR for Case 3 is 70.9%, which falls within 70% or more and less than 80%. Although the predicted PLR at 9 a.m. for Case 1 is 67.3%, which is not significantly different from that in Cases 2 and 3, differences in AHU-DAT occur as the PLR section changes. However, it was determined that the 4.6% difference in Cases 2 and 3 prediction accuracy was not significant enough to change control of the AHU-DAT at each hour. In this

study, AHU-DAT control was performed by dividing the intervals by PLR at 10% intervals (see Figure 8). Accordingly, we reckoned that there was a limit to control AHU-DAT by sufficiently reflecting the 4.6% difference in prediction accuracy between Case 2 and Case 3.

During the night, the AHU-DAT of Case 2 and 3 was controlled at 17.8 °C because no cooling load was required due to the indoor air temperature not rising above the set temperature of 26.6 °C, as shown in Figure 18.

Figure 19 compares averaged indoor air temperature and relative humidity for each case. It can be observed that all cases met the tolerance of 22.2 ± 1.1 °C for indoor air temperature. Additionally, the indoor relative humidity remained below 70% in all sections. Notably, Cases 2 and 3 exhibited a higher indoor air temperature of 22.2 °C compared to Case 1, as AHU-DAT was controlled at a higher set temperature in these cases.

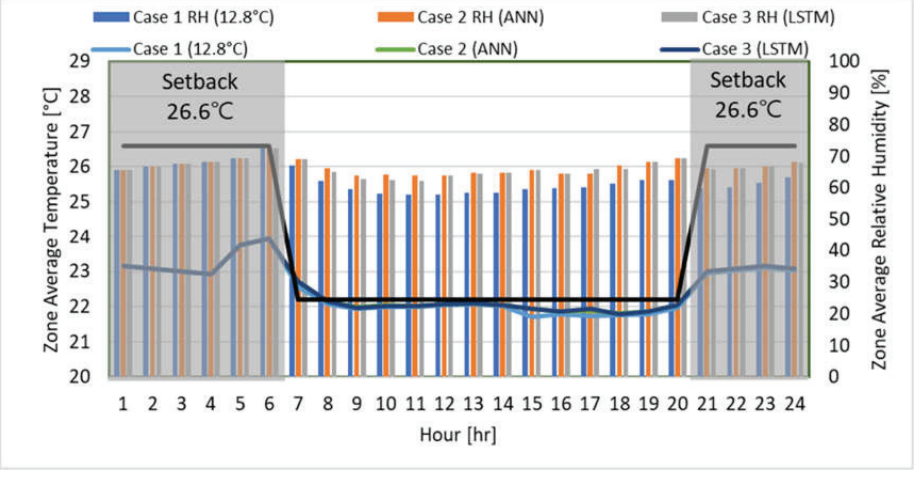

Figure 19. Comparison of the relative humidity and zone average temperature on a representative day.

5.7. Comparison of Total Cooling Energy Consumption on the Representative Day

Figure 20 and Table 8 show the total cooling electricity consumption, including CHW used (MJ/day), TOR (ton-hour/day), CHW electricity consumption (kWh/day), CHW pump electricity consumption (kWh/day), and fan electricity consumption (kWh/day) in each case on the summer representative day. For example, case 1 showed CHW using about 3060.0 MJ/day, while Case 2 showed about 2870.2 MJ/day and 2875.7 MJ/day on the summer representative day. Also, Case 1 consumed a TOR of 241.7 ton-hour/day, whereas Cases 2 and 3 consumed about 226.7 ton-hour/day and 227.1 ton-hour/day, respectively.

Regarding CHW electricity consumption, Case 1 consumed 169.2 kWh/day, while Case 2 and Case 3 consumed 158.7 kWh/day and 159.0 kWh/day, respectively. Comparing the CHW energy consumption of Cases 1 and 2, Case 2 saved 6.2% more CHW energy than Case 1. Meanwhile, Case 3 saved 6.0% more CHW energy than Case 1.

On the summer representative day, Case 1 consumed about 12.3 kWh/day for CHW pump electricity, while Case 2 and Case 3 consumed about 10.7 kWh/day and 10.8 kWh/day, respectively. Comparing the CHW pump electricity consumption of Cases 1 and 2, Case 2 consumed 12.5% less than Case 1. Meanwhile, comparing the CHW pump electricity consumption of Cases 1 and 3, Case 3 consumed 11.8% less than Case 1. Controlling the AHU-DAT through the ANN and LSTM algorithms significantly reduced CHW electricity consumption and CHW pump consumption compared to that of a fixed AHU-DAT.

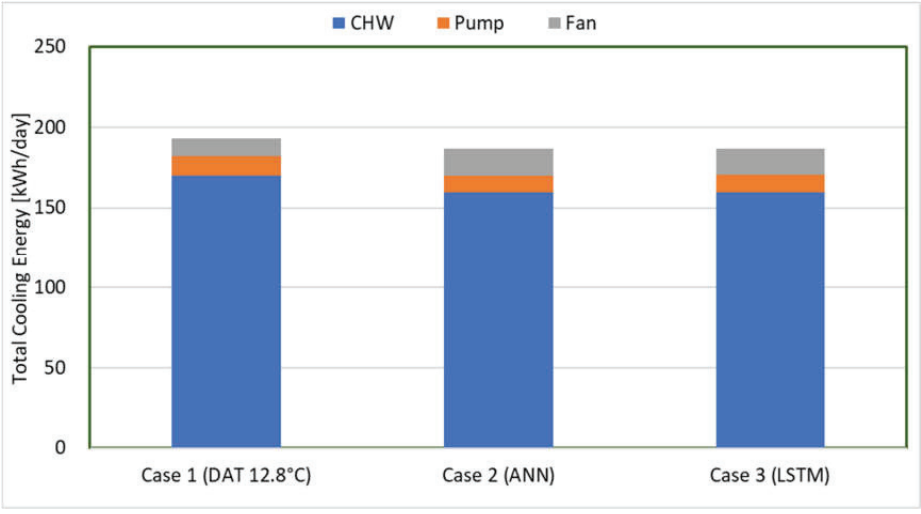

Figure 20. Comparison of the total cooling energy consumption on a representative day.

Table 8. Comparison of the total cooling energy consumption on a representative day.

	Case 1	Case 2	Case 3
CHW used (MJ/day)	3060.0	2870.2	2875.7
TOR (ton-hour/day)	241.7	226.7	227.1
CHW electricity consumption (kWh/day) based on COP 5 (0.7 kW/ton)	169.2	158.7	159.0
CHW Pump electricity consumption (kWh/day)	12.3	10.7	10.8
Fan electricity consumption (kWh/day)	10.8	16.7	16.1
Total cooling electricity consumption (CHW+CHW pump+fan) [kWh/day]	192.3	186.1	185.9

Regarding the supply fan, the fan electricity consumption of Case 1 on the summer representative day was about 10.8 kWh/day, while Case 2 and Case 3 consumed about 16.7 kWh/day and about 16.1 kWh/day, respectively. Comparing the fan electricity consumption of Cases 1 and 2, Case 2 consumed 55.2% more than Case 1. Meanwhile, comparing Cases 1 and 3, Case 3 consumed 49.4% more fan electricity than Case 1.

In Case 1, fan air volume was decreased when the required cooling load was reduced, whereas in Cases 2 and 3, the AHU-DAT was increased in response to the lowered cooling load, resulting in increased fan air volume and decreased CHW flow rate. As a result of this difference, Cases 2 and 3 exhibited lower energy consumption for both CHW and pump but higher fan consumption compared to Case 1. Regarding the combined electricity consumption for CHW, pump, and fan, Case 2 achieved cooling energy savings of 3.2%, while Case 3 showed cooling energy savings of 3.3% compared to Case 1. Through these results, we determined that ML-based AHU-DAT control has the potential to save energy compared to fixed AHU-DAT control.

6. Conclusions

In this study, we aimed to compare the accuracy of cooling load prediction using ANN and LSTM algorithms, widely utilized in building energy research, to determine the optimal algorithm for controlling HVAC systems in the target building.

Based on the comparison of CV(RMSE) values, the ANN algorithm demonstrated higher prediction accuracy than LSTM, with a CV(RMSE) value of 12.7% for ANN and

17.3% for LSTM. We analyzed that the rapid changes in historical data trends of the target building made LSTM relatively less effective. This is because ANN treats all input data independently, while LSTM processes input and output data in its internal memory to relate all input and output values. Furthermore, by analyzing the AHU-DAT operating scenarios for the three cases, we determined that the ANN algorithm exhibits superior performance in predicting the load pattern of the target building compared to the LSTM algorithm. Taking into consideration the prediction accuracies and the AHU-DAT operating scenarios of both models, we concluded that the ANN algorithm is the more suitable choice for controlling the HVAC system in the target building.

Three cases were considered to assess the cooling energy consumption of ML-based HVAC control methods: Case 1 with a fixed AHU-DAT control at 12.8 °C, Case 2 with an ANN-based predictive control, and Case 3 with an LSTM-based predictive control. In addition, this study considered the control strategy of adjusting the AHU-DAT for each 10% interval of the PLR based on the cooling load predictions from Case 2 and Case 3. The results indicated that Case 2 can save cooling energy consumption by 3.2%, while Case 3 can save 3.3% consumption compared to Case 1. Therefore, it was determined that ML-based AHU-DAT control could save energy compared to fixed AHU-DAT control.

However, according to the AHU-DAT pattern of the representative day, the 4.6% difference in Cases 2 and 3 prediction accuracy was not significant enough to change control of the AHU-DAT at each PLR 10% interval. To address this issue in the future, we intend to research predictive control of Air Handling Unit-Discharge Air Temperature (AHU-DAT) by dividing Part Load Ratio (PLR) sections based on the load characteristics of the target building in various scenarios. Instead of dividing sections into 10% intervals, this approach will ensure more precise control. We also plan to conduct a comparative analysis of Fuzzy logic-based HVAC control and ML-based HVAC control methods. Additionally, we will evaluate the energy efficiency of ML-based HVAC control methods by selecting low, medium, and high load days and performing a comparative analysis monthly.

Author Contributions: Conceptualization, B.S.; Methodology, B.S., Y.Y. and S.C.; Software, B.S. and Y.Y.; Formal analysis, B.S. and Y.Y.; Investigation, B.S., K.H.L. and S.C.; Writing—original draft, Y.Y., B.S. and K.H.L.; Writing—review & editing, Y.Y., B.S., K.H.L. and S.C.; Visualization, B.S. and Y.Y.; Supervision, S.C. All authors have read and agreed to the published version of the manuscript.

Funding: This research was funded by the Technology Innovation Program (or Industrial Strategic Technology Development Program, 20014154, Development of EMS with Optimal Control Algorithm for Energy Efficiency Improvement in Commercial Building Using AI and Digital Twin Technology) funded By the Ministry of Trade, Industry & Energy (MOTIE, Republic of Korea).

Informed Consent Statement: Not applicable.

Data Availability Statement: Data will be made available on request.

Conflicts of Interest: The authors declare no conflict of interest.

References

1. U.S Energy Information Administration (EIA). Annual Energy Outlook 2019. 2019. Available online: https://www.eia.gov/todayinenergy/detail.php?id=38112 (accessed on 17 April 2023).
2. International Energy Agency (IEA). The Future of Cooling. 2018. Available online: https://www.iea.org/reports/the-future-of-cooling (accessed on 17 April 2023).
3. Yeon, S.; Yu, B.; Seo, B.; Yoon, Y.; Lee, K.H. ANN based automatic slat angle control of venetian blind for minimized total load in an office building. *Sol. Energy* **2019**, *180*, 133–145. [CrossRef]
4. Seo, B.M.; Yoon, Y.B.; Song, S.; Cho, S. ANN-based thermal load prediction approach for advanced controls in building energy systems. In Proceedings of the Conference for ARCC 2019 International Conference, Toronto, ON, Canada, 29 May–1 June 2019.
5. Lee, J.M.; Hong, S.H.; Seo, B.M.; Lee, K.H. Application of artificial neural networks for optimized AHU discharge air temperature set-point and minimized cooling energy in VAV system. *Appl. Therm. Eng.* **2019**, *153*, 726–738. [CrossRef]
6. Qian, F.; Gao, W.; Yang, Y.; Yu, D. Potential analysis of the transfer learning model in short and medium-term forecasting of building HVAC energy consumption. *Energy* **2020**, *193*, 116724. [CrossRef]

7. Moon, J.W.; Yang, Y.K.; Choi, E.J.; Choi, Y.J.; Lee, K.-H.; Kim, Y.-S.; Park, B.R. Development of a control algorithm aiming at cost-effective operation of a VRF heating system. *Appl. Therm. Eng.* **2019**, *149*, 1522–1531. [CrossRef]
8. Park, B.R.; Choi, E.J.; Hong, J.; Lee, J.H.; Moon, J.W. Development of an energy cost prediction model for a VRF heating system. *Appl. Therm. Eng.* **2018**, *140*, 476–486. [CrossRef]
9. Mtibaa, F.; Nguyen, K.-K.; Dermardiros, V.; Cheriet, M. Context-aware Model Predictive Control framework for multi-zone buildings. *J. Build. Eng.* **2021**, *42*, 102340. [CrossRef]
10. Sendra-Arranz, R.; Gutiérrez, A. A long short-term memory artificial neural network to predict daily HVAC consumption in buildings. *Energy Build.* **2020**, *216*, 109952.
11. Mba, L.; Meukam, P.; Kemajou, A. Application of artificial neural network for predicting hourly indoor air temperature and relative humidity in modern building in humid region. *Energy Build.* **2016**, *121*, 32–42. [CrossRef]
12. Zhao, J.; Liu, X. A hybrid method of dynamic cooling and heating load forecasting for office buildings based on artificial intelligence and regression analysis. *Energy Build.* **2018**, *174*, 293–308. [CrossRef]
13. Afram, A.; Janabi-Sharifi, F.; Fung, A.S.; Raahemifar, K. Artificial neural network (ANN) based model predictive control (MPC) and optimization of HVAC systems: A state of the art review and case study of a residential HVAC system. *Energy Build.* **2017**, *141*, 96–113. [CrossRef]
14. Jang, J.; Han, J.; Leigh, S.-B. Prediction of heating energy consumption with operation pattern variables for non-residential buildings using LSTM networks. *Energy Build.* **2022**, *255*, 111647. [CrossRef]
15. Faiq, M.; Tan, K.G.; Liew, C.P.; Hossain, F.; Tso, C.-P.; Lim, L.L.; Wong, A.Y.K.; Shah, Z.M. Prediction of energy consumption in campus buildings using long short-term memory. *Alex. Eng. J.* **2023**, *67*, 65–76. [CrossRef]
16. Fang, Z.; Crimier, N.; Scanu, L.; Midelet, A.; Alyafi, A.; Delinchant, B. Multi-zone indoor temperature prediction with LSTM-based sequence to sequence model. *Energy Build.* **2021**, *245*, 111053. [CrossRef]
17. Bouktif, S.; Fiaz, A.; Ouni, A.; Serhani, M.A. Optimal Deep Learning LSTM Model for Electric Load Forecasting using Feature Selection and Genetic Algorithm: Comparison with Machine Learning Approaches[†]. *Energies* **2018**, *11*, 1636. [CrossRef]
18. Somu, N.; Ramamritham, G.R.K. A deep learning framework for building energy consumption forecast. *Renew. Sustain. Energy Rev.* **2021**, *137*, 110591.
19. Peng, C.; Tao, Y.; Chen, Z.; Zhang, Y.; Sun, X. Multi-source transfer learning guided ensemble LSTM for building multi-load forecasting. *Expert Syst. Appl.* **2022**, *202*, 117194. [CrossRef]
20. Rashid, T. *Make Your Own Neural Network*; CreateSpace Independent Publishing Platform: North Charleston, SC, USA, 2016.
21. Rumelhart, D.E.; Hinton, G.E.; Williams, R.J. Learning representations by back-propagating errors. *Nature* **1986**, *323*, 533–536. [CrossRef]
22. Mittal, A. Understanding RNN and LSTM. 2019. Available online: https://towardsdatascience.com/understanding-rnn-and-lstm-f7cdf6dfc14e (accessed on 17 April 2023).
23. Zarzycki, K.; Lawrynczuk, M. LSTM and GRU Neural Networks as Models of Dynamical Processes Used in Predictive Control: A Comparison of Models Developed for Two Chemical Reactors. *Sensors* **2021**, *21*, 5625. [CrossRef] [PubMed]
24. Olah, C. Understanding LSTM Networks. 2015. Available online: https://colah.github.io/posts/2015-08-Understanding-LSTMs/ (accessed on 17 April 2023).
25. Jung, M.; Mendes, P.R.d.C.; Önnheim, M.; Gustavsson, E. Model Predictive Control when utilizing LSTM as dynamic models. *Eng. Appl. Artif. Intell.* **2023**, *123*, 106226. [CrossRef]
26. Keras. Available online: https://keras.io/about/ (accessed on 17 April 2023).
27. Falk, R.F.; Miller, N.B. *A Primer for Soft Modeling*; University of Akron Press: Akron, OH, USA, 1992.
28. Schober, P.; Boer, C.; Schwarte, L.A. Correlation Coefficients: Appropriate Use and Interpretation. *Anesth Analg.* **2018**, *126*, 1763–1768. [PubMed]
29. ASHRAE. *Guideline 14-2014. 2014. Measurement of Energy and Demand Savings*; American Society of Heating, Refrigerating, and Air Conditioning Engineers: Atlanta, GA, USA, 2014.
30. North Carolina Environmental Quality, Energy Saving Fact Sheet: Chillers. 2010. Available online: https://www.deq.nc.gov/environmental-assistance-and-customer-service/ias-energy-efficiency/opportunities/chillers/download (accessed on 26 April 2023).
31. International Performance Measurement & Verification Protocol (IPMVP). Concepts and Options for Determining Energy and Water Savings. Volume 1, Section 3.4.4.2. 2002. Available online: https://www.nrel.gov/docs/fy02osti/31505.pdf (accessed on 26 April 2023).
32. Federal Energy Management Program (FEMP). M&V Guidelines: Measurement and Verification for Performance-Based Contracts Version 4.0, Section 4.5.3. 2015. Available online: https://www.energy.gov/femp/articles/mv-guidelines-measurement-and-verification-performance-based-contracts-version-40 (accessed on 26 April 2023).

buildings

MDPI

Article

Development of Building Design Optimization Methodology: Residential Building Applications

Yeonjin Bae [1,*,†], Donghun Kim [2] and William Travis Horton [3]

[1] Building Technologies Research and Integration Center, Oak Ridge National Laboratory, Oak Ridge, TN 37830, USA
[2] Building Technology and Urban System Division, Lawrence Berkeley National Laboratory, Berkeley, CA 94720, USA
[3] School of Civil Engineering, Purdue University, West Lafayette, IN 47907, USA
* Correspondence: baey@ornl.gov
† Yeonjin's work was done while she was at Purdue University.

Abstract: Building design optimization is a highly complex problem, requiring long computational running processes because of the many options that exist when a building is being designed. This paper introduces an integrated approach through which to perform this optimization within an acceptable time frame. The approach includes the methods of variable selection, model simplification, and a sequential optimization process. Using singular value decomposition, a large number of design variables is reduced to a smaller subset that can be solved more quickly through the optimization algorithm. To expedite the variable selection process, a modeling approach that quickly simulates annual energy consumption was developed to replace full annual energy simulations. The developed methodology was applied to two residential buildings in the US, and the results are discussed herein. To assess the accuracy of the integrated optimization methodology, the optimized life cycle costs are compaa variables demonstrating the strongest contributions in the optimization study were identified. The proposed methodology significantly shortened the time requirements for the optimization processes of the two case studies by 74% and 84%; the optimized life cycle costs were within 0.05% and 0.06%, respectively, of the optimum point.

Keywords: building design optimization; energy simulation; variable selection; life cycle cost

Citation: Bae, Y.; Kim, D.; Horton, W.T. Development of Building Design Optimization Methodology: Residential Building Applications. *Buildings* **2024**, *14*, 107. https://doi.org/10.3390/buildings14010107

Academic Editor: Danny Hin Wa Li

Received: 25 October 2023
Revised: 14 November 2023
Accepted: 20 November 2023
Published: 31 December 2023

1. Introduction

According to energy usage data from the US Energy Information Administration, residential and commercial buildings contribute approximately 40% of energy consumption and 16% of energy-related carbon emissions in the US [1,2]. Over the past 25 years, residential energy use has increased by approximately 7.0%, and that of commercial buildings has increased by about 10.4% [3]. As energy consumption in the US continues to increase and as energy-related carbon emissions need to be reduced, energy simulation tools have been incorporated more regularly into the building design process for high-performance buildings. Energy-efficient design optimization techniques for buildings are undoubtedly important to reducing building energy consumption and its associated costs, which have been active research topics [4].

Ideally, to find an optimal building design point that minimizes an objective function, such as energy consumption or building life cycle cost (LCC), building energy simulation software, such as EnergyPlus [5] and TRNSYS [6], can be coupled with an optimization algorithm for accurate energy consumption calculations. However, such optimization studies are usually prohibitive because of their very long calculation times, owing to large numbers of design variables, and their relatively long simulation times related to the software used to predict annual energy consumption at each iteration of the optimization process.

A lot of research has been carried out on reducing the long computational times associated with the optimization process. The primary focus of previous research has been to develop simplified energy consumption models that can replace detailed energy simulation software using, for example, neural networks and regression models. Magnier and Haghighat [7], as well as Gossard et al. [8], used a genetic algorithm with an artificial neural network model to optimize thermal comfort and energy consumption in a residential house. Ghiaus [9] applied robust regression (an alternative of the least squares regression method that is effective when outliers exist) to predict the heating load as a function of outdoor temperature. Catalina et al. [10] used a quadratic polynomial regression model to predict heating demand with multiple independent variables, such as shape factor, building time constant, and more. To generate the database for creating the model, 18,144 simulations were performed. Hygh et al. [11] used EnergyPlus to build a multivariate regression model with 27 parameters; 20,000 full annual simulation datasets were generated to predict heating and cooling loads. Assuming each simulation takes 30 s to 1 min, the process of generating the dataset alone requires 166 to 332 h. The cooling regression model has a high value for the coefficient of determination (R^2) that indicates how well the data fit the model; however, the heating regression model has a low value for R^2 from 0.498 to 0.816. Ghiaus [9] used the concept of balance point temperature to construct a regression model. Hygh et al. [11] used a fixed 18 °C balance temperature to predict energy consumption, and Krarti [12] estimated the exact balance temperature. Eisenhower [13] developed an analytical metamodel that fit the building simulation data and then performed the optimization. Although a simplified modeling approach is capable of carrying out the building design optimization process with little computational effort, it essentially requires a tremendous number of pre-energy simulation results to obtain a reliable model, which is the major disadvantage of this approach. Consequently, regenerating the database is necessary when changing the design variables to create a simplified model.

Another approach through which to accelerate the optimization process involves employing variable selection methods to choose a subset of variables from the entire set of variables. Bettonvil [14] applied a group screening method to detect important factors by applying sequential bifurcation to a building energy model. Rahni [15] partitioned building parameters into multiple groups and tested which groups make more significant contributions to building energy performance. Corrado and Mechri [16] used the Morris method to reduce the parameter dimensions from 129 to 10. Brohus et al. [17] used an analysis of variance-based analysis to identify significant variables of residential building energy consumption, and identified the 10 most important parameters out of a total of 57.

An alternative approach is using sensitivity analysis. In previous studies, sensitivity analyses were employed in either the pre- or postoptimization phases or to efficiently select a subset of variables significantly affecting the objective function, thus streamlining the optimal design process with reduced effort compared with full optimization. Gunay et al. [18] used sensitivity analysis to identify the key operational parameters of office buildings, and Cheng et al. [19] used the Morris one-at-a-time method to design a sustainable housing community. Østergård et al. [20] used sensitivity analysis to inform the decision-making process in the early building design process. Sensitivity analysis is easy to use and is a valuable tool for assessing model behavior and identifying critical input parameters; therefore, it is frequently used in building simulation research. However, sensitivity analysis becomes more challenging as the dimensionality of the input space increases, and the interactions between variables can become complex, making it difficult to isolate the effect of an individual variable [21].

To speed up building design optimization, the two approaches of simplified modeling and variable reduction can naturally be combined. However, despite many previous studies, it is hard to find studies testing the integrated optimization approach. Additionally, the computational time needed to generate a reduced-order model or a variable selection process is often neglected. Therefore, it is not clear how much the integrated approach is able to accelerate building design optimization.

This paper presents an integrated optimization methodology to tackle the building design optimization problem. The developed methodology can be used for any residential building design optimization process, including for the early design and engineering design stages. Also, the developed methodology is not limited to any specific design variables for the optimization process. A novel variable selection method is proposed and adopted for the optimization problem to reduce the high dimensionality of the design variables. To overcome the long computational time required to generate sufficient data that can be used during the variable selection process, a new, simplified modeling approach is developed to replace the full annual energy simulation for residential buildings. A strategy through which to approach the true optimal point is also introduced. The integrated methodology is applied to two case studies of typical residential buildings in the US, and comparisons of the results with those of the full optimization processes for the entire design spaces are presented.

2. Overall Methodology

To derive an accurate but computationally efficient methodology for building design optimizations, two main problems need to be solved: (1) reduce the number of optimization variables and (2) reduce the amount of computational time consumed by the energy simulation software. To overcome these problems, the following process shown in Figure 1 is proposed.

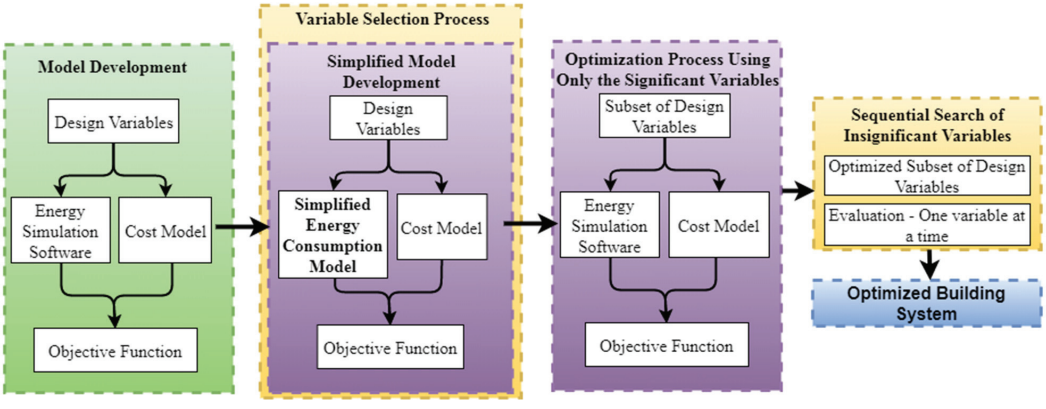

Figure 1. Building optimization process.

The first step, shown in the green box, is to define a building design optimization problem by specifying appropriate design variables and their corresponding constraints, along with the objective function (e.g., the minimization of LCC for residential buildings in this paper). To evaluate energy costs accurately during the optimization process, detailed building energy simulation software is incorporated rather than the simplified models that are typically used in other research approaches. The second step is to reduce the number of design variables using a variable selection method, which identifies subvariables that have a significant influence on the objective function. To accelerate this process, which requires a large number of annual building energy simulations, a simplified modeling strategy is adopted. Then, an optimization algorithm is coupled to the building energy software, which searches for the optimum point only in a reduced dimension of the design space as defined by the variable selection method. In this approach, the simplified energy consumption models are only used during the variable selection process (the second block of Figure 1), and high-fidelity models are used in the actual optimization process (the third block of Figure 1). The last step is to reduce the optimization error that is inherited from the approximation approach (i.e., the variable selection algorithm) by sequentially adjusting the insignificant variables.

3. Variable Selection Algorithm and Optimization Process

In this section, each step shown in Section 2 is described in detail. Section 3.1 provides the details of the variable selection algorithm, and Section 3.2 shows how this variable selection algorithm is applied to an optimization problem. Section 3.3 shows the simplified energy consumption model used for residential building applications that will be used only in the variable selection process, and Section 3.4 shows the optimization process, with the variables selected from the variable selection process and postoptimization process.

3.1. Variable Selection Algorithm Using Singular Value Decomposition

Consider a differentiable function, denoted as $f : (x_1, x_2, \cdots, x_n) \mapsto y$, where $y \in \mathcal{R}$, $x_i \in \mathcal{D}_i, \forall i \in \{1, 2, \cdots, n\}$, and $\mathcal{D}_i \subset \mathcal{R}$ is a feasible set for a variable x_i. The task here is to select the important subvariables out of $(x_1, x_2, \cdots, x_n)$, which influence y most significantly. Selecting a metric that quantifies the magnitude of importance or significance of a variable is the key step. We define the following operator L:

$$L(v) := \frac{1}{\iint_{\mathcal{D}} dx} \iint_{\mathcal{D}} | < \nabla f(x), v > |^2 dx, \tag{1}$$

where $\mathcal{D} = \mathcal{D}_1 \times \cdots \times \mathcal{D}_n$, $\nabla f(x_1, x_2, \cdots, x_n) = \sum_{i=1}^{n} e_i \frac{\partial f}{\partial x_i}(x_1, x_2, \cdots, x_n)$, e_i is the natural basis corresponding to x_i, $< \cdot, \cdot >$ is the inner product, and $v (\in \mathcal{R}^n)$ is a unit vector. Operator L measures the spatial average of the directional derivate of f over $\mathcal{D}$ in the direction of v. When $L(v) = 0$, y does not change in the direction of v. When $L(v_1) >> L(v_2)$, y varies more significantly in the direction of v_1 than that of v_2 in the spatial average sense. Therefore, employing L as a measure to gauge the significance or importance of a variable is a rational choice.

The following example is provided for further clarity. Let $y = {x_1}^2 + 0.01{x_2}^2$, and assume that x_1 and x_2 are well-scaled such that $-1 \leq x_1, x_2 \leq 1$. Variable x_1 clearly influences the output variable y more significantly than it does x_2. The L values for $e_1 = \begin{bmatrix} 1 \\ 0 \end{bmatrix}$ and $e_2 = \begin{bmatrix} 0 \\ 1 \end{bmatrix}$, which correspond to x_1 and x_2, respectively, are

$$L(e_1) = \iint_{-1 \leq x_i \leq 1} < \begin{bmatrix} 2x_1 \\ 0.02x_2 \end{bmatrix}, \begin{bmatrix} 1 \\ 0 \end{bmatrix} >^2 dx_1 dx_2 = \iint_{-1 \leq x_i \leq 1} 2^2 {x_1}^2 dx_1 dx_2 = 2^2 \times \frac{2}{3} \times 2 \text{ and}$$

$$L(e_2) = \iint_{-1 \leq x_i \leq 1} < \begin{bmatrix} 2x_1 \\ 0.02x_2 \end{bmatrix}, \begin{bmatrix} 0 \\ 1 \end{bmatrix} >^2 dx_1 dx_2 = \iint_{-1 \leq x_i \leq 1} 0.02^2 {x_2}^2 dx_1 dx_2 = 0.02^2 \times \frac{2}{3} \times 2.$$

For these L values, $L(e_1) >> L(e_2)$. This example shows that the operator L provides a measure of the contribution of a variable to an output variable.

For practical applications, Equation (1) can be approximated as

$$L(v) \approx \frac{1}{N} \sum_{k=1}^{N} \Big| < \nabla f(x_k), v > |^2, \tag{2}$$

where N is a total number of samples of x_k over a feasible domain $\mathcal{D} = \mathcal{D}_1 \times \cdots \times \mathcal{D}_n$. With this metric, the most important variable is represented by

$$\arg\max_{||v||=1} L(v). \tag{3}$$

The maximizer can be obtained by performing singular value decomposition (SVD) of the matrix JJ^T, where $J = \begin{bmatrix} \nabla f(\boldsymbol{x}_1) & \nabla f(\boldsymbol{x}_2) & \cdots & \nabla f(\boldsymbol{x}_N) \end{bmatrix} (\in \mathcal{R}^{n \times N})$. We denote the resulting form of the singular value decomposition as

$$JJ^T = V \Sigma V^T = \begin{bmatrix} V_1 & V_2 \end{bmatrix} \begin{bmatrix} \Sigma_1 & \\ & \Sigma_2 \end{bmatrix} \begin{bmatrix} V_1^T \\ V_2^T \end{bmatrix}, \tag{4}$$

where $V_1(\in \mathcal{R}^{n\times r}), V_2(\in \mathcal{R}^{n\times(n-r)}), \Sigma_1 \in \mathcal{R}^{r\times r}, \Sigma_2 \in \mathcal{R}^{(n-r)\times(n-r)}$ are submatrices of V and Σ, and

$$\Sigma_1 = \begin{bmatrix} \sigma_1 & & \\ & \ddots & \\ & & \sigma_r \end{bmatrix}, \Sigma_2 = \begin{bmatrix} \sigma_{r+1} & & \\ & \ddots & \\ & & \sigma_n \end{bmatrix}.$$

The diagonal matrix Σ contains magnitudes of L in descending order corresponding to each column vector of V. The first column vector of V maximizes the metric L (i.e., the maximizer of Equation (3)), and the second column vector of V maximizes the metric L over a space perpendicular to the first column vector of V. Consequently, the last column vector has a minimum value of L. Therefore, primary coordinates can be selected out of V in which y varies significantly by looking at the values of Σ; these coordinates can denote V_1 as the primary component. The criteria can be set to select V_1 so that the cumulative sum of the percentage of Σ_1 is at least 99.5%, which means that 99.5% of the magnitudes of L can be explained by primary component V_1, and Σ_2 is negligible [15].

3.2. Application to an Optimization Problem

Consider an optimization problem,

$$\begin{aligned} &\min_{x\in\mathcal{R}^n} f(\boldsymbol{x}) \\ &s.t. A\boldsymbol{x} \leq b, \end{aligned} \tag{5}$$

where f is a differentiable function for $\forall x \in \mathcal{R}^n$. We define new variables of z such that $z = V^T x$. The ith element of z is the projection of x onto the ith column vector of V. Note that x can be expressed as $x = V_1 z_1 + V_2 z_2$ because $V = \begin{bmatrix} V_1 & V_2 \end{bmatrix}$ and V is orthonormal. Because $L(V_1) >> L(V_2)$, the optimization problem can be searched over a subspace spanned by the column vectors of V_1 rather than over the entire $\mathcal{R}^n$ space. In other words, neglecting the influence of z_2 in the optimization problem becomes possible because the magnitudes of the directional derivatives along the column vector of V_2 are small. The new optimization problem in a lower dimension then becomes

$$\begin{aligned} &\min_{z_1\in\mathcal{R}^r} f(V_1 z_1) \\ &s.t. (AV_1) z_1 \leq b. \end{aligned} \tag{6}$$

For some cases, it is worthwhile to retrieve the important variables in the original design space from z_1 because z_1 is a linear combination of design variables; thus, z_1 may not have a direct physical meaning. The significant design variables in the original space can be retrieved by examining the column vectors of V_1. For example, when the jth component of a column vector of V_1 is more predominant than the others, it means that the jth component of x contributes to the output significantly. The retrieving process may increase the dimension of the design space from r to $m(\geq r)$.

The final optimization problem with the selected m variables in the original design space becomes

$$\begin{aligned} &\min_{\boldsymbol{x}\in E} f(\boldsymbol{x}) \\ &s.t. A\boldsymbol{x} \leq b, \end{aligned} \tag{7}$$

where $E \subset R^m$.

The proposed method is very similar to that of principle component analysis (PCA). PCA is also a dimensionality reduction technique commonly used in statistic and machine learning. The method aims to reduce the data's dimensionality while retaining as much relevant information as possible [22]. However, it differs significantly because (1) the matrix to be composed by SVD contains information of the output variable, and PCA does not, and (2) the proposed method is developed from deterministic points of view, and PCA is based on random variables. It also differs from the partial least squares method (PLS). PLS is a multivariate statistical technique used for modeling the relationship between

a set of independent variables and a set of dependent variables [23]. PLS is commonly used in regression analysis and classification tasks to establish predictive models, but it assumes a linear relationship between input and output variables. In contrast, SVD does not inherently assume linearity. Additionally and more importantly, our proposed method can be applied to an optimization process as described here, and PCA and PLS cannot [24,25].

3.3. Simplified Energy Consumption Modeling Approach

The introduced variable selection algorithm requires calculating the Jacobian matrix of the objective function at multiple points in a design space (see Equation (4)). This method would take a tremendous time with approximately (n variables) $\times$ (N design points) $\times$ (T annual simulation times per a design point). To reduce the time required for generating the series of Jacobian matrices, the modified degree day method is proposed. The degree day method is easy to implement and requires only basic weather data, but it has limitations because it assumes a linear relationship between temperature and energy use, and other factors such as insulation level, building design, and occupant behavior can also significantly affect energy use. Given the robust correlation between degree day data and energy consumption in residential buildings, and coupled with the relatively limited influence of occupant behavior, the degree day method continues to be a valuable and straightforward tool for energy modeling in the residential sector. The proposed method is based on the following assumptions and modifications to the existing degree day method, and the detailed process is shown in Figure 2:

- The actual degree day varies with the chosen design variables. Consequently, the balance temperature must be calculated for each design combination;
- The modified ANAGRAM method is used to shift the diagonal linear regression models to the origin based on daily average degree days to separately predict heating, cooling, and fan energy consumption;
- To find an appropriate number of data samples to yield an accurate regression model, the recursive least square (RLS) algorithm is used;
- A simplified model is constructed specifically to replace energy simulation software during the variable selection phase. This model is employed for the sole purpose of identifying which variables significantly influence the output. Therefore, the model must be sufficiently accurate to discern these influential trends.

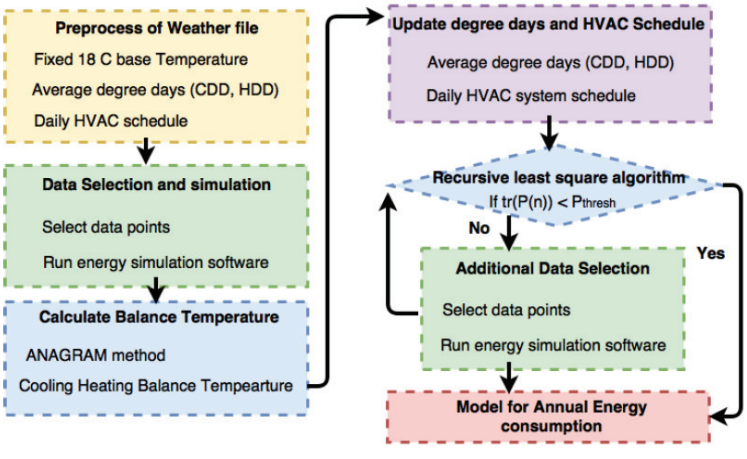

Figure 2. Process of the simplified energy consumption model's development.

Suppose we want to evaluate annual energy consumption y for a residential building at a design point x, which consists of building design parameters. The role of building an energy simulation model, denoted as f, that maps x to y, is $y = f(x, w)$, where w represents any other inputs that influence y, such as weather data. The goal is to find a function that approximates f. We adopt the degree day method for its simplicity and widespread use in predicting energy consumption for a long time period for residential buildings. More precisely, it can be represented as the following relationship over a heating season, for example:

$$\begin{gathered} y_P \approx \alpha \times DD_P \\ DD_P = \int_{t_0}^{t_0+P} (T_\mathrm{b} - T_\mathrm{a}(\tau))d\tau, \end{gathered} \tag{8}$$

where y_P is the heating energy consumption for the period of $[t_0, t_0 + P]$, and α is a building-specific coefficient. The variable DD_P is the number of heating degree days for the period, and $(T_\mathrm{a}, T_\mathrm{b})$ are the ambient and balance temperatures of the building, respectively. Note that once α and T_b are identified, the annual energy consumption for heating can be easily predicted by only considering the weather data. In other words, when α and T_b are known, annual heating energy consumption can be predicted without simulating a detailed building energy model. The time-invariant parameters of α and T_b depend on $\boldsymbol{x}$. To estimate them, a regression approach is used with samples of y_P obtained from building energy simulations for selected days. The final form of our simplified model is

$$y_P \approx \hat{\alpha}(x) \int_{t_0}^{t_0+P} \left(\hat{T}_\mathrm{b} - T_\mathrm{a}(\tau)\right) d\tau, \tag{9}$$

where $\hat{\alpha}$ and $\hat{T}_\mathrm{b}$ are the estimated values of α and T_b at a design point of $\boldsymbol{x}$**.** After the simulation studies for residential buildings, a day is selected as P (i.e., $P = 1$ day). A natural question regards the selection of an appropriate sample size to accurately estimate the parameters; that is, the question of how many daily simulations are needed to accurately estimate α and T_b. This problem can be handled by employing the RLS method because it calculates confidence intervals for estimated parameters as each sample is updated. Because the original model, Equation (8), is a nonlinear function with respect to the parameters, it was reformulated as follows:

$$y_P = \theta_1 DD_{P,18} + \theta_2, \tag{10}$$

where $\theta_1 = \alpha$, and $\theta_2 = \alpha P(T_\mathrm{b} - 18)$. The equation $DD_{P,18} = \int_{t_0}^{t_0+P} (18 - T_\mathrm{a}(\tau))d\tau$ represents the number of degree days with the assumption of an 18 °C balance temperature [9].

The model structure, shown in Equation (10), can be readily used with the RLS method because of its linearity. Once the parameters of θ_1 and θ_2 are estimated, the balance temperature can be retrieved by $T_\mathrm{b} = 18 + \frac{1}{P}\frac{\theta_2}{\theta_1}$.

As an initial dataset, 6 days from the weather file are selected and simulated; these include the heating design day as well as 5 other days, which are uniformly distributed and are found by preprocessing a typical meteorological year file at the location. Next, θ_1 and θ_2 are calculated from the six samples. Then, they are inserted into the RLS method as the initial guess. Another day simulation is implemented, and those parameters are updated. This process is repeated until the parameter covariance goes below a threshold. For a description of the RLS method, refer to Appendix A. Because heating energy, cooling energy, and fan energy consumption need to be considered to predict total annual energy consumption, separate models for heating, cooling, and fan energies are developed using the same methodology as used here. For brevity, in this paper, the equations for cooling and fan energy are omitted.

To calculate $\partial f / \partial x_i(x)$**,** two simplified models at two design points of $(x, x + \Delta x_i)$ are constructed. The process is repeated for each variable and each data point to construct a series of Jacobian matrices (shown in Equation (4)).

3.4. Optimization with the Significant Variables and Sequential Search Method

After identifying significant variables using the variable selection method with the simplified modeling approach, an optimization routine can be implemented with those variables while fixing the remaining variables, which are insignificant, to reference values. In the current case study, a discrete binary version of the particle swarm optimization (PSO) methodology [26] is adopted. This algorithm is selected based on its ability to efficiently explore the design space and arrive at an optimal solution to overcome the problems of the continuous version that cannot handle discrete variables. To prevent fast convergence to a local optimum, the inertia PSO version [27] is used. The results that are discussed in Section 4 demonstrate that it is possible to get close to the optimum point when using only those significant variables that were identified using the variable selection method. Once an optimal point is found with the significant variables, there may still be a chance to get closer to the true optimum point by perturbing the insignificant variables, although their contributions are expected to be small. One point of clarification is that the variables that are identified as insignificant are not necessarily unimportant; they just do not demonstrate a significant contribution within the scope of the optimization study, which is why they are excluded in that phase. However, to further improve the final result, a sequential one-dimensional optimization approach is used. This approach optimizes the first variable in the group of insignificant variables while fixing the others. Once the process is terminated, the second variable in that group is optimized while fixing those that remain. This process is repeated until the last variable is optimized. The order of the sequential search approach may be important because variables are sorted according to their contributions to the cost function. Therefore, the order of variables in the sequential search approach follows that determined in the variable selection process.

4. Case Studies

To validate the developed methodology, two cases studies for residential buildings were selected. Two representative residential building types in the US were chosen, and design variables were selected from typical variables that are often considered in the engineering design stage.

4.1. Descriptions of Case Study Buildings

To develop detailed building models, the energy simulation software EnergyPlus was used. The buildings are a typical slab-on-grade residential house and a house with a heated basement. They were referenced from the Pacific Northwest National Laboratory residential prototype [28] and were assumed to be located in Indianapolis, Indiana. Figure 3 shows the model dimensions of the houses.

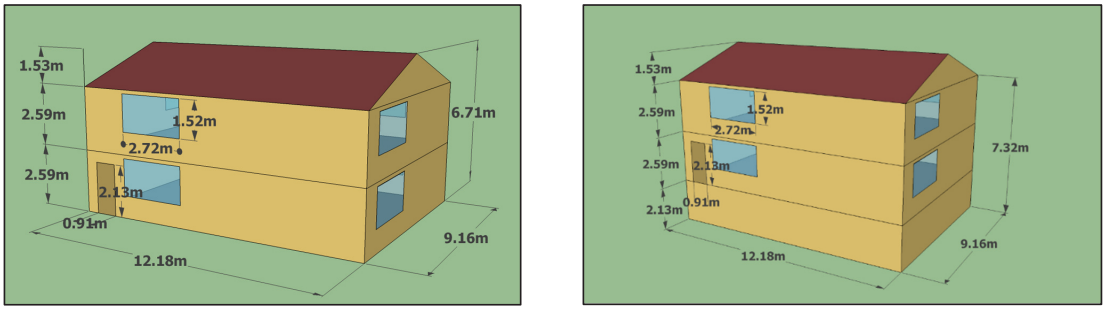

Figure 3. Dimensions of the case study houses.

The first house has a gross floor area of 334.6 m^2 with two different spaces, which include a living space and attic. The living space is the only conditioned zone, and the net conditioned area is 223.1 m^2. The entry doors are located on the south and north sides of the

building, and two windows are placed on each side of the building. The house is assumed to have three bedrooms and three bathrooms. The second house has a gross floor area of 446.1 m^2. The house has a living space, attic, and heated basement. The prototype complies with the 2012 International Energy Conservation Code with modified construction layers for optimization purposes. The living space is the only conditioned zone, and the net conditioned area is 334.6 m^2. The house has four bedrooms and four bathrooms, and the basement is placed completely below the ground level.

4.2. Defining Design Variables for Optimization

To compare the results of the proposed method with those of the full optimization, we chose a relatively small number of design variables in this paper. The following considerations were made in defining the design variables for the case studies: select elements that may have (1) a high impact on building energy consumption, (2) a strong influence in the construction cost, and (3) energy-saving or cost-saving benefits, but whose influence is not strictly known beforehand. Based on these considerations, 12 different construction design variables were selected to investigate their effect on the LCC of the residential building. The first eight variables were related to the building envelope, and the remaining variables were associated with the heating, ventilation, and air-conditioning (HVAC) system.

Commercially available products associated with those design variables are listed in Table 1. For example, for roofing material, one can take either asphalt shingles, a metal surface, or a concrete tile roof. Design variables of the wall core can be a given stud dimension and filled with any type of insulation shown in the table. Structural insulated panels or insulated concrete forms with various thicknesses were also considered to be different wall core materials for this study. The under-floor insulation was used only for case study 1, and the foundation wall insulation was used only for case study 2. The total number of possible combinations, $\prod_{i=1}^{n} N_i$, is around 60 million for each case, where N_i is the number of options for the ith variable. Notably, it can be reduced significantly to $\prod_{i=1}^{r} N_i$ through variable selection, because the reduced dimension r is generally much smaller than the original dimension n. For the case studies, $n = 12$, $r = 5$ (see the later discussion), and, thus, the total number of combinations was reduced to around 700.

Table 1. Design variables and values.

Design Variables (Number of Options)	Available Values
Roofing Material (3)	Asphalt shingles, metal surface, concrete tile roof
Roof Eave Overhang Depth (3)	305 mm (12 in.), 457 mm (18 in.), 610 mm (24 in.)
Attic Insulation Material (12)	Loose fill cellulose: R3.3 (IP [1]-R19), R4.4 (IP-R25), R5.3 (IP-R30), R6.7 (IP-R38), R8.6 (IP-R49), R10.6 (IP-R60)
	Fiberglass batting: R3.3 (IP-R19), R4.4 (IP-R25), R5.3 (IP-R30), R6.7 (IP-R38), R8.6 (IP-R49), R10.6 (IP-R60)
External Wall Siding Material (4)	Vinyl siding, wood siding, fiber cement siding, brick
Wall Core (16)	Stud: 38 × 89 mm (2 × 4 in.) studs at 400 mm (16 in.), 38 × 140 mm (2 × 6 in.) studs at 600 mm (24 in.) on center, 38 × 184 mm (2 × 8 in.) studs at 600 mm (24 in.) on center Insulation: filled with fiberglass batting insulation, sprayed-on foam insulation, loose-fill cellulose insulation
	Structural insulated panels: 114 mm (3 5/8 in.), 165 mm (5 5/8 in.), 210 mm (7 3/8 in.), 260 mm (9 3/8 in.)
	Insulated concrete forms: 228 mm (9 in.), 278 mm (11 in.), 328 mm (13 in.)

Table 1. *Cont.*

Design Variables (Number of Options)	Available Values
External Foam Board Insulation (6)	Board insulation: 12.7 mm (0.5 in.), 25.4 mm (1 in.), 38.1 mm (1.5 in.), 50.8 mm (2 in.), 63.5 mm (2.5 in.), 76.2 mm (3 in.)
Under-Floor Insulation or Foundation Wall Insulation (8)	Extruded polystyrene: 25.4 mm (1 in.), 50.8 mm (2 in.), 76.2 mm (3 in.), 101.6 mm (4 in.)
	Expanded polystyrene: 25.4 mm (1 in.), 50.8 mm (2 in.), 76.2 mm (3 in.), 101.6 mm (4 in.)
Window Type (2)	Double-pane window, triple-pane window
Air Conditioner Speed (2)	Single-speed, multispeed
Heat Recovery Type (2)	None, sensible heat recovery
Seasonal Coefficient of Performance (Air Conditioner SEER [2]) (6)	3.81 (SEER 13), 4.10 (SEER 14), 4.40 (SEER 15), 4.69 (SEER 16), 4.98 (SEER 17), 5.28 (SEER18)
Natural Gas Furnace Efficiency (4)	80%, 85%, 90%, 95%

[1] IP stands for imperial units; [2] SEER represents Seasonal Energy Efficiency Ratio.

4.3. Optimization Objective Function

We considered an LCC over a 20-year time horizon as the objective function, as shown in Equation (11). To estimate realistic construction costs, the material cost, labor, overhead, and profit were all considered. The primary tool used for estimating construction costs is RSMeans [29]. RSMeans is a construction cost database that is widely used and respected in the United States. It provides comprehensive, up-to-date, and reliable information related to construction costs, materials, labor, and equipment cost. To account for regional variations in construction costs, a location influence factor (I_f) is used, and the I_f of 92.5% (applicable for Indianapolis) is multiplied by the national average cost. HVAC equipment costs were modeled using multiple linear regression to fit cost data taken from online equipment suppliers relative to both system capacity and efficiency. The discount rate was assumed to be 3%, and the modified uniform present value (UPV^*) factors were taken from the annual supplement to the NIST Handbook [30]. The UPV^* factors are energy price projections for different fuel types based on the US Department of Energy/US Energy Information Administration regional projections.

$$LCC = I_f C_{\text{Con}} + C_{\text{HVAC}} + C_{\text{Elec}} UPV^*_{\text{Elec}} + C_{\text{NG}} UPV^*_{\text{NG}} \quad (11)$$

Here, the following pertains:

LCC—incremental LCC of given building system;
I_f—influence factor of the location;
C_{Con}—construction cost;
C_{HVAC}—HVAC equipment cost;
C_{Elec}—electricity cost;
C_{NG}—natural gas cost;
UPV^*_{Elec}—UPV* factor for electricity cost;
UPV^*_{NG}—UPV* factor for natural gas cost.

5. Case Study Results

5.1. Validation Methodology

To validate and compare the accuracy and efficiency of the proposed methodology, a full optimization with all design variables was first performed. The full optimization was intended to minimize the LCC using all 12 variables. Following the full optimization study, the proposed methodology was implemented. The required data size, N in Equation (4), may be automatically selected by tracking the convergence behavior of singular values as

N increases. However, for the feasibility study of the proposed method, a fixed size of data (i.e., 100 data points) was generated to identify significant variables.

After finding the significant variables using the variable selection method, the remaining variables were fixed to the cheapest material, and the optimization process was carried out on the significant variables. For more detailed information about the initial setting of variables, refer to Appendix B. Finally, the best values of the remaining insignificant variables were determined using a sequential search method.

The inertia weight version of the binary PSO algorithm was used for both full and proposed optimizations. Based on the suggestions of Parsopoulos and Vrahatis [31], the swarm size for the PSO algorithm and the neighborhood size of a von Neumann topology were set as 64 and 8, respectively, for the full optimization, and were 36 and 6, respectively, for the proposed method.

5.2. Variable Selection Results

Figure 4 shows the singular values of the Gramian matrix (see Equation (4)) in descending order. The singular values are scaled with respect to the sum of all singular values. For both case studies, the first four coordinates are selected based on the fact that their cumulative sum of singular values is at least 99.49% and 99.46% with respect to the sum of all singular values. In other words, using only the first four coordinates, 99.49% and 99.46% of data can be captured for case studies 1 and 2. Because the variables are discrete, it is convenient to find the significant parameters in the original design space using Equation (7).

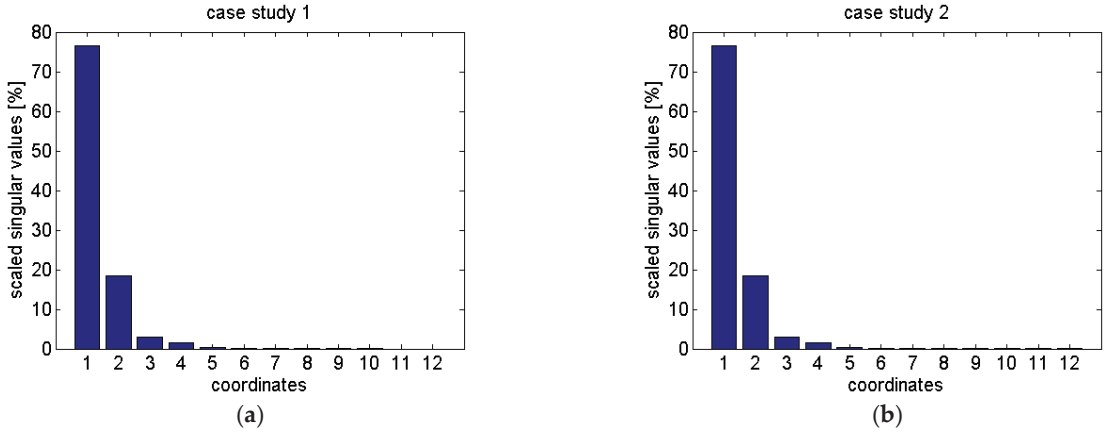

Figure 4. (**a**) Result of singular values in case study 1. (**b**) Result of singular values in case study 2.

Table 2 displays the singular vectors of the first four coordinates with the higher values shown in bold, indicating the variables that significantly contribute to the corresponding coordinates. For example, external wall siding material and wall core type make the strongest contributions to the first and second singular vectors, and roofing materials, air-conditioning (AC) speed, and heat recovery type are the primary contributors to the third singular vector. Through this process, 5 out of the 12 design variables, including roofing material, external wall siding material, wall core, AC speed, and heat recovery, were identified as significant variables in both case studies. Although the same five design variables are selected for both case studies, this choice does not necessarily imply that these five design variables are significant variables for all cases. The results will vary based on the specified design parameter values and regional factors, including construction cost and equipment cost, as well as weather conditions.

Table 2. Singular vectors. [3]

Case Study Building 1	**Coordinate 1**	**Coordinate 2**	**Coordinate 3**	**Coordinate 4**
Roofing Material	−0.012	0.024	0.401	−0.910
Roof Eave Overhang Depth	0.000	−0.001	−0.030	0.003
Attic Insulation Material	−0.006	−0.006	0.014	0.101
External Wall Siding Material	**0.999**	0.028	0.017	−0.005
External Foam Board	0.000	−0.005	−0.041	−0.010
Wall Core	−0.028	**0.999**	−0.008	0.023
Foundation Wall Insulation	−0.003	−0.009	−0.021	−0.069
Window Type	−0.002	0.001	0.125	0.053
AC Speed	−0.004	−0.001	**0.274**	0.118
Heat Recovery Type	−0.012	−0.002	**0.847**	**0.367**
Air Conditioner Seasonal Coefficient of Performance	−0.001	0.000	0.041	0.018
Natural Gas Furnace Efficiency	−0.003	−0.002	0.163	0.071
Case Study Building 2	**Coordinate 1**	**Coordinate 2**	**Coordinate 3**	**Coordinate 4**
Roofing material	−0.012	0.024	**0.416**	**−0.903**
Roof Eave Overhang Depth	0.000	−0.001	−0.030	0.003
Attic Insulation Material	−0.006	−0.006	0.013	0.101
External Wall Siding Material	**0.999**	0.028	0.017	−0.004
External Foam Board	0.000	−0.006	−0.041	−0.011
Wall Core	−0.028	**0.999**	−0.009	0.023
Under-floor Wall Insulation	−0.002	−0.009	−0.023	−0.074
Window Type	−0.002	0.001	0.130	0.057
AC Speed	−0.004	−0.001	**0.271**	0.122
Heat Recovery Type	−0.012	−0.002	**0.837**	**0.379**
Air Conditioner Seasonal Coefficient of Performance	−0.001	0.000	0.040	0.018
Natural Gas Furnace Efficiency	−0.003	−0.002	0.176	0.080

[3] Significant variables in both case studies are highlighted in blue in the first column.

5.3. Simplified Energy Consumption Model

To ensure that the simplified modeling approach is sufficiently accurate for the purpose of the variable selection, the variable selection algorithm is also implemented using the full annual energy model for comparison. Then, the first four singular vectors obtained from the simplified model, denoted as $V_s = [v_{s,1}, v_{s,2}, v_{s,3}, v_{s,4}]$, and from the full model, denoted as $V_f = [v_{f,1}, v_{f,2}, v_{f,3}, v_{f,4}]$, are compared. Table 3 shows the matrix of $V_s^T V_f$ for the case 1 and 2 buildings. If the simplified modeling approach is accurate, ${v_{s,i}}^T v_{f,j} \approx \pm\delta_{i,j}$ where $\delta_{i,j}$ is the Kronecker delta. That is, the diagonal elements of $V_s^T V_f$ must be close to either 1 or −1, and the off-diagonal elements must be close to 0. Notably, the 0 property arises because of the orthonormal characteristic of singular vectors. The results satisfy the criteria, which demonstrates that the resulting significant variables from the simplified modeling approach are very similar to those of the full model for both case studies.

Table 3. Correlation matrices between singular vectors obtained from detailed and simplified models [4].

Case 1				**Case 2**			
−1.00	−0.08	−0.02	0.02	−0.99	−0.11	−0.05	0.02
−0.08	0.99	0.05	0.04	−0.11	0.99	−0.01	−0.04
−0.02	−0.05	1.00	−0.07	0.05	0.00	−0.99	0.14
−0.02	0.04	−0.07	−0.99	−0.01	−0.04	−0.14	−0.97

[4] Diagonal elements of $V_s^T V_f$ are shown in grey.

5.4. Optimization Result Comparison

To compare the accuracy of the integrated optimization methodology, the optimized LCCs were compared with the full optimizations, and they are shown in Table 4. Because it is of interest to see the improvement resulting from incorporating the sequential search method, the optimization results with only the selected variables (i.e., without the sequential method) were also included.

Table 4. Comparison of optimized LCC. [5]

Case Study Building 1	**Optimized LCC (USD)**	**Percentage Difference (%)**
Optimization with the Significant Variables	53,062	4.19
Optimization with the Significant Variables and Sequential Search	50,956	0.05
Optimization with All Design Variables	50,929	-
Case Study Building 2	**Optimized LCC (USD)**	**Percentage Difference (%)**
Optimization with the Significant Variables	57,818	4.60
Optimization with the Significant Variables and S Search	55,308	0.06
Optimization with All Design Variables	55,273	-

[5] This cost does not include construction and HVAC costs in Equation (11) that are not associated with design variables.

The results show that the minimal LCC errors arising from only using the subset of design variables were around 4% for both case studies. By further employing the sequential search method, the errors were brought to within 0.05% (USD 27) and 0.06% (USD 35) for a 20-year horizon.

Table 5 shows a comparison of the optimized designs using full optimization and the proposed methodology. In case study 1, the difference was caused only by the roof eave overhang depth and attic insulation material. For case study 2, roof eave overhang depth and air conditioner seasonal energy efficiency ratio (SEER) rating caused the difference. As expected from the variable selection algorithm, the variables are insignificant in both cases.

All numerical experiments were run on a desktop computer with a 6 core 3.10 GHz CPU, 6 GB RAM, and Windows (64-bit) operating systems. For both cases, the variable selection process took a majority of the total optimization time. However, the variable selection process without introducing the simplified modeling approach took 13.5 for case study building 1 and 9.98 h for case study building 2. This time demonstrates the efficiency of the proposed modeling methodology. The full optimization process required approximately 33 and 29 h, and the proposed methodology required 8.7 and 5.7 h for each case. In other words, the proposed optimization approach achieved 74% and 84% computational time savings. These significant reductions were mainly because of the reduced design space and the number of evaluations requested by the optimization algorithm.

Table 5. Comparison of optimal design. [6]

Case Study Building 1	**Optimal Design with Full Optimization**	**Optimal Design with the Proposed Method**
Roofing Material	F12 asphalt shingles	F12 asphalt shingles
Roof Eave Overhang Depth	305 mm (12 in.)	457 mm (18 in.)
Attic Insulation Material	Attic loose fill—R3.3 (IP-R19)	Attic loose fill—R4.4 (IP-R25)
External Wall Siding Material	F11 wood siding	F11 wood siding
External Foam Board	12.7 mm (0.5 in.)	12.7 mm (0.5 in.)
Wall Core	38 × 140 mm (2 × 6 in.) studs at 600 mm (24 in.) on center filled with loose fill cellulose insulation	38 × 140 mm (2 × 6 in.) studs at 600 mm (24 in.) on center filled with loose fill cellulose insulation

Table 5. *Cont.*

Case Study Building 1	**Optimal Design with Full Optimization**	**Optimal Design with the Proposed Method**
Foundation Wall Insulation	Expanded polystyrene 50.8 mm (2 in.)	Expanded polystyrene 50.8 mm (2 in.)
Window Type	Triple-pane window	Triple-pane window
AC Speed	Multispeed	Multispeed
Heat Recovery Type	Sensible	Sensible
Seasonal Coefficient of Performance (Air Conditioner SEER)	5.28 (SEER 18)	5.28 (SEER 18)
Natural Gas Furnace Efficiency	0.95	0.95
Case Study Building 2	**Optimal Design with Full Optimization**	**Optimal Design with the Proposed Method**
Roofing Material	F12 asphalt shingles	F12 asphalt shingles
Roof Eave Overhang Depth	305 mm (12 in.)	457 mm (18 in.)
Attic Insulation Material	Attic loose fill—R4.4 (IP-R25)	Attic loose fill—R4.4 (IP-R25)
External Wall Siding Material	F11 wood siding	F11 wood siding
External Foam Board	12.7 mm (0.5 in.)	12.7 mm (0.5 in.)
Wall Core	38 × 140 mm (2 × 6 in.) studs at 600 mm (24 in.) on center filled with loose fill cellulose insulation	38 × 140 mm (2 × 6 in.) studs at 600 mm (24 in.) on center filled with loose fill cellulose insulation
Under-Floor Insulation	Expanded polystyrene 25.4 mm (1 in.)	Expanded polystyrene 25.4 mm (1 in.)
Window Type	Triple-pane window	Triple-pane window
AC Speed	Multispeed	Multispeed
Heat Recovery Type	Sensible	Sensible
Seasonal Coefficient of Performance (Air Conditioner SEER)	4.98 (SEER 17)	5.28 (SEER 18)
Natural Gas Furnace Efficiency	0.95	0.95

[6] The differences are shown in blue rows in the table.

6. Conclusions

To make building design optimization feasible, a novel integrated approach is presented in this paper. This work includes a method to reduce the dimensionality of a design space, which aims to identify only a few significant variables that need to be considered as optimization variables. The method formally defines a measure of significance and uses the SVD to order variables based on the metric using sample data. A simplified modeling methodology to reduce the time needed to generate samples for the variable selection process is introduced. The developed methodology is applied to case studies for residential buildings, and the results are compared with those of the full optimization process over the entire design space.

In summary:

- Using the variable selection process, significant variables (5 out of 12) that demonstrate the strongest contribution to the optimization study are identified;
- The proposed methodology significantly shortens the time requirement for the optimization process in the two case studies of 74% and 84%, and the optimized LCC is within 0.05% and 0.06%, respectively, of the optimum point.

These findings not only validate the effectiveness of the integrated approach, but also highlight its potential to streamline and expedite the design optimization process while maintaining a high degree of accuracy in the results.

Author Contributions: Y.B.: Model development and simulation, data analysis, writing—original draft, writing—review and editing. D.K.: model development, writing—original draft. W.T.H.:

project administration, writing—review and editing, supervision. All authors have read and agreed to the published version of the manuscript.

Funding: This work was partially funded by field work proposal CEBT105 under DOE BTO activity no. BT0302000 and BT0305000.

Data Availability Statement: The data presented in this study are available on request from the corresponding author. The data are not publicly available due to privacy.

Acknowledgments: This manuscript was authored by UT-Battelle LLC under contract DEAC05-00OR22725 with DOE. The publisher, by accepting the article for publication, acknowledges that the US government retains a nonexclusive, paid-up, irrevocable, worldwide license to publish or reproduce the published form of this manuscript, or allow others to do so, for US government purposes. DOE will provide public access to these results of federally sponsored research in accordance with the DOE Public Access Plan (https://www.energy.gov/doe-public-access-plan (accessed on 18 September 2023)).

Conflicts of Interest: The authors declare no conflicts of interest.

Appendix A

To find an appropriate number of data samples to yield an accurate regression model, the regression least square (RLS) algorithm is used. The RLS gives an advantage related to computational efficiency by immediately acquiring coefficients of a_j with the current data sample without storing past observation data [32]. In addition to this advantage, the required number of data samples can be determined based on the confidence of parameters.

Suppose a true model has the following general linear form:

$$y(k) = a_0 + a_1 x_1(k) + a_2 x_2(k) + \cdots a_m x_m(k) + e(k), \tag{A1}$$

where $y(k) \in \mathcal{R}$ and $x(k) \in \mathcal{R}^m$ are the outputs and inputs, respectively. Variable $e(k) \in \mathcal{R}$ is a mean zero random variable. The coefficients of a_j are the true parameters. Equation (A1) can be rewritten as follows:

$$y(k) = \phi^T(k)\theta_T + e(k). \tag{A2}$$

Let θ be candidate parameters for θ_T, and define model error as $\epsilon(k;\theta) := y(k) - \phi^T(k)\theta$. For a single-output system, the least squares estimator tries to minimize $\frac{1}{n}\sum_{k=1}^{n} \epsilon\left(k;\theta\right)^2$. In other words, the least square problem is $\min_{\theta} \frac{1}{n}\sum_{k=1}^{n}\Big(y(k) - \phi^T(k)\theta)^2$, where n is the number of data points. Let the optimal solution with data length n be $\hat{\theta}_n$. The least squares solution is given by

$$\hat{\theta}_n = (\frac{1}{n}\sum_{k=1}^{n} \phi(k-1)\phi(k-1)^T)^{-1}\frac{1}{n}\sum_{k=1}^{n} \phi(k-1)y(k).$$

The RLS algorithm tries to find $\hat{\theta}_{n+1}$ from $\hat{\theta}_n$ iteratively without re-solving the optimization problem as the data size increases. The iteration is given by [32,33].

$$\hat{\theta}(n) = \hat{\theta}(n-1) + K(n-1)(y(t) - \phi(n-1)^T\hat{\theta}(n-1)), \tag{A3}$$

$$P(n-1) = P(n-2) - K(n-1)\phi(n-1)^T P(n-2), \text{ and} \tag{A4}$$

$$K(n-1) = P(n-2)\phi(n-1) \times (1 + \phi(n-1)^T P(n-2)\phi(n-1))^{-1}. \tag{A5}$$

Here, the notation was switched to $\hat{\theta}(n)$ rather than $\hat{\theta}_n$, which is the least square solution. This switch is intended to distinguish the solutions of the least square and the RLS because of an initial condition of the RLS problem. A remark can made on P in Equation (A4). It is well-known that $P(n-1)$ is proportional to $E(\tilde{\theta}_n\tilde{\theta}_n^T)$, where $\tilde{\theta}_n = \theta_T - \hat{\theta}_n$, which is the covariance of the error associated with estimated parameters.

In other words, it is the uncertainty of parameters estimated with data size of n. Therefore, by tracking $tr(P(n-1))$, the required data size can be determined. More precisely, the optimal data size, denoted as n_{opt}, is determined by the following criteria:

$$n_{\text{opt}} = \min \{n | tr(P(n)) \leq p_{\text{thresh}}, n \in \mathcal{N}\}, \tag{A6}$$

where p_{thresh} is the threshold for determining the number of the data size of n. In this paper, we set the initial condition of P, P_0 as 10^5 and p_{thresh} as 10^{-1} based on a simulation study.

Appendix B

Table A1 displays the initial variable values for both the full optimization and optimization with the significant variables for case study buildings 1 and 2. Variables that are not included in the optimization with significant values are set to the cheapest material, and these variables are determined via the sequential search approach.

Table A1. Initial variable values used for optimization.

Case Study Building 1	**Full Optimization**	**Optimization with the Significant Variables**
Roofing Material	F12 asphalt shingles	F12 asphalt shingles
Roof Eave Overhang Depth	305 mm (12 in.)	-
Attic Insulation Material	Attic loose fill—R3.3 (IP-R19)	-
External Wall Siding Material	Vinyl siding	Vinyl siding
External Foam Board	12.7 mm (0.5 in.)	-
Wall Core	38 × 89 mm (2 × 4 in.) studs at 400 mm (16 in.) on center filled with loose fill cellulose insulation	38 × 89 mm (2 × 4 in.) studs at 400 mm (16 in.) on center filled with loose fill cellulose insulation
Foundation Wall Insulation	Extruded polystyrene 25.4 mm (1 in.)	-
Window Type	Double-pane window	-
Air Conditioner Speed	Single-speed	Single-speed
Heat Recovery Type	None	None
Seasonal Coefficient of Performance (Air Conditioner SEER)	3.81 (SEER 13)	-
Natural Gas Furnace Efficiency	0.80	-
Case Study Building 2	**Full Optimization**	**Optimization with the Significant Variables**
Roofing Material	F12 asphalt shingles	F12 asphalt shingles
Roof Eave Overhang Depth	305 mm (12 in.)	-
Attic Insulation Material	Attic loose fill—R3.3 (IP-R19)	-
External Wall Siding Material	Vinyl siding	Vinyl siding
External Foam Board	12.7 mm (0.5 in.)	-
Wall Core	38 × 89 mm (2 × 4 in.) studs at 400 mm (16 in.) on center filled with loose fill cellulose insulation	38 × 89 mm (2 × 4 in.) studs at 400 mm (16 in.) on center filled with loose fill cellulose insulation
Under-Floor Insulation	Extruded polystyrene 25.4 mm (1 in.)	-
Window Type	Double-pane window	-
Air Conditioner Speed	Single-speed DX	Single-speed DX
Heat Recovery Type	None	None
Seasonal Coefficient of Performance (Air Conditioner SEER)	3.81 (SEER 13)	-
Natural Gas Furnace Efficiency	0.80	-

References

1. Li, Y.; Im, P.; Lee, S.; Bae, Y.; Yoon, Y.; Lee, S. Sensor Incipient Fault Impacts on Building Energy Performance: A Case Study on a Multi-Zone Commercial Building. *Buildings* **2023**, *13*, 520. [CrossRef]
2. Huang, H.; Wang, H.; Hu, Y.-J.; Li, C.; Wang, X. The development trends of existing building energy conservation and emission reduction—A comprehensive review. *Energy Rep.* **2022**, *8*, 13170–13188. [CrossRef]
3. EIA. *March 2015 Monthly Energy Review*; U.S. Energy Information Administration: Washington, DC, USA, 2015.
4. Ruparathna, R.; Hewage, K.; Sadiq, R. Improving the energy efficiency of the existing building stock: A critical review of commercial and institutional buildings. *Renew. Sustain. Energy Rev.* **2016**, *53*, 1032–1045. [CrossRef]
5. Crawley, D.B.; Lawrie, L.K.; Winkelmann, F.C.; Buhl, W.F.; Huang, Y.J.; Pedersen, C.O.; Strand, R.K.; Liesen, R.J.; Fisher, D.E.; Witte, M.J.; et al. EnergyPlus: Creating a new-generation building energy simulation program. *Energy Build.* **2001**, *33*, 319–331. [CrossRef]
6. Klein, S.A.; Beckman, W.A.; Mitchell, J.W.; Duffie, J.A.; Duffie, N.A.; Freeman, T.L.; Mitchell, J.C.; Braun, J.E.; Evans, B.L.; Kummer, J.P.; et al. *TRNSYS 16—A TRaNsient System Simulation Program, User Manual*; Solar Energy Laboratory, University of Wisconsin-Madison: Madison, WI, USA, 2004.
7. Magnier, L.; Haghighat, F. Multiobjective optimization of building design using TRNSYS simulations, genetic algorithm, and Artificial Neural Network. *J. Affect. Disord.* **2010**, *45*, 739–746. [CrossRef]
8. Gossard, D.; Lartigue, B.; Thellier, F. Multi-objective optimization of a building envelope for thermal performance using genetic algorithms and artificial neural network. *Energy Build.* **2013**, *67*, 253–260. [CrossRef]
9. Ghiaus, C. Experimental estimation of building energy performance by robust regression. *Energy Build.* **2006**, *38*, 582–587. [CrossRef]
10. Catalina, T.; Virgone, J.; Blanco, E. Development and validation of regression models to predict monthly heating demand for residential buildings. *Energy Build.* **2008**, *40*, 1825–1832. [CrossRef]
11. Hygh, J.S.; DeCarolis, J.F.; Hill, D.B.; Ranjithan, S.R. Multivariate regression as an energy assessment tool in early building design. *J. Affect. Disord.* **2012**, *57*, 165–175. [CrossRef]
12. Krarti, M. *Energy Audit of Building Systems: An Engineering Approach*; CRC Press: Boca Raton, FL, USA, 2020.
13. Eisenhower, B.; O'neill, Z.; Narayanan, S.; Fonoberov, V.A.; Mezić, I. A methodology for meta-model based optimization in building energy models. *Energy Build.* **2012**, *47*, 292–301. [CrossRef]
14. Bettonvil, B.; Kleijnen, J.P. Searching for important factors in simulation models with many factors: Sequential bifurcation. *Eur. J. Oper. Res.* **1997**, *96*, 180–194. [CrossRef]
15. Rahni, N.; Ramdani, N.; Candau, Y.; Dalicieux, P. Application of group screening to dynamic building energy simulation models. *J. Stat. Comput. Simul.* **1997**, *57*, 285–304. [CrossRef]
16. Corrado, V.; Mechri, H.E. Uncertainty and Sensitivity Analysis for Building Energy Rating. *J. Build. Phys.* **2009**, *33*, 125–156. [CrossRef]
17. Brohus, H.; Heiselberg, P.; Simonsen, A.; Sørensen, K.C. Uncertainty of energy consumption assessment of domestic buildings. In *E-Nova Internationaler Kongress 2009: Null Emissions Gebäude: Gebäude, Gebäudeteile, Anlagen, Anlagenkomponenten, Energie-und Gebäudekonzepte, Proceedings of the E-Nova Internationaler Kongress, Pinkafeld, Austria, 19–20 November 2009*; Fachhochschulstudiengänge Burgenland: Eisenstadt, Austria, 2009; pp. 31–38.
18. Gunay, H.B.; Ouf, M.; Newsham, G.; O'Brien, W. Sensitivity analysis and optimization of building operations. *Energy Build.* **2019**, *199*, 164–175. [CrossRef]
19. Cheng, L.; Bae, Y.; Horton, W.T. A system-level approach for designing multi-family sustainable and energy-efficient housing communities. *Sustain. Cities Soc.* **2019**, *44*, 183–194. [CrossRef]
20. Østergård, T.; Jensen, R.L.; Maagaard, S.E. Early Building Design: Informed decision-making by exploring multidimensional design space using sensitivity analysis. *Energy Build.* **2017**, *142*, 8–22. [CrossRef]
21. Saltelli, A.; Tarantola, S.; Campolongo, F.; Ratto, M. *Sensitivity Analysis in Practice: A Guide to Assessing Scientific Models*; Wiley: New York, NY, USA, 2004; Volume 1.
22. Bro, R.; Smilde, A.K. Principal component analysis. *Anal. Methods* **2014**, *6*, 2812–2831. [CrossRef]
23. Mehmood, T.; Liland, K.H.; Snipen, L.; Sæbø, S. A review of variable selection methods in partial least squares regression. *Chemom. Intell. Lab. Syst.* **2012**, *118*, 62–69. [CrossRef]
24. Bae, Y.; Horton, W.T. An Efficient and Accurate Building Optimization Strategy Using Singular Value Decomposition. In Proceedings of the International High Performance Buildings Conference, West Lafayette, IN, USA, 11–14 July 2016; Paper 199.
25. Bae, Y.J. Integrated Design Tool of Building System Optimization for Building Life Cycle Cost. Ph.D. Thesis, Purdue University, West Lafayette, IN, USA, 2016.
26. Kennedy, J.; Eberhart, R.C. A discrete binary version of the particle swarm algorithm. In Proceedings of the IEEE International Conference on Systems, Man, and Cybernetics. Computational Cybernetics and Simulation, Orlando, FL, USA, 12–15 October 1997; Volume 5, pp. 4104–4108.
27. Kennedy, J. Swarm intelligence. In *Handbook of Nature-Inspired and Innovative Computing: Integrating Classical Models with Emerging Technologies*; Springer: Boston, MA, USA, 2006; pp. 187–219.
28. PNNL Residential Prototype Building Models. Available online: https://www.energycodes.gov/development/residential/iecc_models (accessed on 30 July 2013).

29. RSMeans. RSMeans Residential Cost Data 2013. Available online: http://www.rsmeans.com (accessed on 30 July 2013).
30. Rushing, A.S.; Kneifel, J.D.; Lippiatt, B.L. *Energy Price Indices and Discount Factors for Life-Cycle Cost Analysis-2013: Annual Supplement to NIST Handbook 135 and NBS Special Publication 709*; National Institute of Standards and Technology: Gaithersburg, MD, USA, 2013.
31. Parsopoulos, K.E.; Vrahatis, M.N. Recent approaches to global optimization problems through Particle Swarm Optimization. *Nat. Comput.* **2002**, *1*, 235–306. [CrossRef]
32. Ljung, L.; Söderström, T. *Theory and Practice of Recursive Identification*; MIT Press: Cambridge, MA, USA, 1983.
33. Goodwin, G.C.; Sin, K.S. *Adaptive Filtering Prediction and Control*; Courier Corporation: Chelmsford, MA, USA, 2014.

buildings

MDPI

Article

Achieving Energy Self-Sufficiency in a Dormitory Building: An Experimental Analysis of a PV–AWHP-ERV Integrated System

Su-Kwang Yang [1,†], Yul-Ho Kang [2,†] and Young-Chull Ahn [1,*]

[1] School of Architectural Engineering, Pusan National University, Busan 46241, Republic of Korea; didtnrhkd@pusan.ac.kr
[2] Research Institute for Future Wind Energy Technology, Pusan National University, Busan 46241, Republic of Korea; kyh@pusan.ac.kr
* Correspondence: ycahn@pusan.ac.kr; Tel.: +82-51-510-2492
† These authors contributed equally to this work.

Abstract: In this study, we investigated the performance of air-to-water heat pump (AWHP) and energy recovery ventilator (ERV) systems combined with photovoltaics (PV) to achieve the energy independence of a dormitory building and conducted an analysis of the energy independence rate and economic feasibility by using energy storage devices. Our data were collected for 5 months from July to November, and the building energy load, energy consumption, and system performance were derived by measuring the PV power generation, purchase, sales volume, AWHP inlet and outlet water temperature, and ERV outdoor, supply, and exhaust temperature. When analyzing representative days, the PV–AWHP integrated system achieved an energy efficiency ratio (EER) of 4.49 and a coefficient of performance (COP) of 2.27. Even when the generated electrical energy exceeds 100% of the electricity consumption, the energy self-sufficiency rate remains at 24% due to the imbalance between energy consumption and production. The monthly average energy self-sufficiency rate changed significantly during the measurement period, from 20.27% in November to 57.95% in September, highlighting the importance of energy storage for self-reliance. When using a 4 kWp solar power system and 4 kWh and 8 kWh batteries, the annual energy self-sufficiency rate would increase to 67.43% and 86.98%, respectively, and our economic analysis showed it would take 16.5 years and more than 20 years, respectively, to become profitable compared to the operation of an AWHP system alone.

Keywords: photovoltaic; energy storage system; air-to-water heat pump; energy self-sufficiency; dormitory building

Citation: Yang, S.-K.; Kang, Y.-H.; Ahn, Y.-C. Achieving Energy Self-Sufficiency in a Dormitory Building: An Experimental Analysis of a PV–AWHP-ERV Integrated System. *Buildings* **2024**, *14*, 882. https://doi.org/10.3390/buildings14040882

Academic Editor: Ricardo M. S. F. Almeida

Received: 29 February 2024
Revised: 17 March 2024
Accepted: 22 March 2024
Published: 25 March 2024

1. Introduction

The global climate crisis has underscored the urgent need to reduce carbon emissions from energy use, making this a key objective across various industries. In the construction sector, one promising strategy to achieve this goal is the adoption of zero-energy buildings (ZEBs) [1–3]. These buildings are designed to produce as much energy as they consume over the course of a year, effectively eliminating their carbon footprint. The push for ZEBs has become more pronounced due to concerns about energy security and the impact of energy price volatility on the global economy [4,5]. To achieve ZEB status, buildings must significantly reduce their energy consumption and meet any remaining energy needs with renewable sources. This involves improving the insulation performance of buildings, enhancing the efficiency of heating, ventilation, and air conditioning (HVAC) systems, and integrating renewable energy sources like photovoltaic (PV) panels. Research is underway to improve the efficiency of PV panels, particularly in terms of thermal performance, and to explore the potential of photovoltaic–thermal (PV/T) systems that can simultaneously generate electricity and heat [6–10]. As the electrification of major energy sources becomes

more widespread, the use of solar energy is expected to increase significantly [11]. Additionally, heat pumps, which are powered by electricity, are being increasingly utilized in various applications [12–15]. However, the performance of heat pumps can vary based on factors such as technology, geographic location, and energy source [16,17]. Therefore, it is crucial to analyze the performance characteristics of HVAC systems, including heat pumps, PV generation facilities, and energy storage facilities, based on specific building conditions. Recent studies have shown promising results. For instance, Long et al. [18] conducted a simulation to evaluate the performance of solar–air source heat pump (SASHP) heating systems in a low-humidity Tibetan region. Their simulation results showed that initially, the solar heat could handle the entire heating load, but the overall proportion over the entire period was only 42.79%. Therefore, their performance should be improved through the optimization of the solar collector area, angle, and water tank capacity. Kong et al. [19] presented the appropriate number of PV/T modules through a performance analysis and an economic comparison of PV/T–cascade heat pumps for cooling and heating periods in tropical climates. Bae et al. [20] found that a PV/T–ASHP system installed in a small building improved heating and cooling performance coefficients by 52% compared to an ASHP system used alone. They also demonstrated that the electricity generated by the PV/T modules during certain periods exceeded the system's power consumption, making it possible to achieve a fully zero-energy building [21]. Dementzis et al. [22] monitored a 16 kWp solar panel and a 74 m^2 solar collector, along with a 58 kW heat pump, for four years. They found that the PV system generated 6% more electrical energy than the heat pump consumed. Additionally, the solar collector produced 20% more heat per unit area than the heat pump powered by the PV system. Shono et al. [23] conducted a time-resolution analysis of BIPV in large-scale commercial buildings, confirming that 33% of their energy demand could be met by PV modules installed on exterior walls and 15% by rooftop modules. Building on this, Perwez et al. [24] assessed the combined impact on the overall decarbonization potential of buildings, including building-integrated photovoltaics (BIPV). Their results indicate that implementing all measures simultaneously could lead to an 84% reduction in annual CO_2 emissions. BIPV emerged as a significant contributor, fulfilling 8–16% and 34–63% of the electricity demand when considering threshold constraints and the full utilization of the building surface, respectively. Sigounis et al. [25] investigated the feasibility of achieving zero-energy implementation in library buildings through the integration of BIPV/T, ERV, and AWHP systems. Their analysis revealed that controlling the heat flow with BIPV/T can satisfy the heating demand and reduce energy consumption for ventilation by up to 37%.

Other studies have focused on the integration of PV generation facilities and energy storage systems. Aneli et al. [26] found that when a 4.8 kWp solar PV generator and a 10 kW heat pump were connected, an energy independence of about 34% could be achieved. Perrella et al. [27] showed that when a heat pump, an 18 kWp PV panel, and a 24 kWh battery were used together, 76% of the heat and electricity demand could be met. Nicoletti et al. [28] conducted a study on the optimal capacity design of air-to-water heat pump (AWHP), PV, and ESS systems considering their economic feasibility for a 20-year driving period. They performed building energy simulations based on the climate of five regions in Italy. Their results showed that the appropriate PV capacity depends on the building's energy usage independently of the solar source for each region, while the battery size is significantly dependent on the climate characteristics and PV size. A sensitivity analysis of initial costs confirmed a strong interdependence between AWHP, PV, and battery sizes. As the capacities of PV generation facilities and energy storage systems increase, the energy independence rate also increases. However, initial installation costs are high, necessitating a sensitivity analysis of various capacities and prices [29]. Additionally, Yang et al. [30] analyzed various scenarios using a real option model to explore the impact on optimal investment decisions for residential PV–ESS installation projects. Their findings suggest that it could be feasible to apply such installations to all local projects if the initial investment

cost is reduced by 50% or the CO_2 price is increased by about 33 times. Nonetheless, they also indicate limitations to commercialization under the current circumstances.

Previous studies have been conducted to predict the performance and economic feasibility of systems through mathematical models and energy simulations, as shown in Table 1. In order to accurately evaluate the feasibility of the integrated system, the actual building load and environmental conditions should be considered. Therefore, this study aims to analyze the performance of a system integrating PV, AWHP, and energy recovery ventilation (ERV) in a dormitory building. We analyzed the building load usage patterns during the summer and winter periods, assessed the surplus and shortage of power generation due to PV generation, and evaluated the energy independence rate considering the performance of AWHP systems. Additionally, we performed an economic analysis of the AWHP system alone to propose appropriate capacities considering the energy independence rate and economic feasibility. By understanding the performance characteristics of these integrated systems under actual operating conditions, we hope to provide valuable insights for the design and implementation of ZEBs and renewable energy systems in buildings.

Table 1. Literature review for the photovoltaic–heat pump integrated system.

Authors	System Description	Analytical Approach	Evaluation Method		
			Performance	Economic	Energy Self-Sufficiency
Long et al. [18]	PVT/ASHP/HST	Simulation	o	x	x
Kong et al. [19]	PVT/ASHP/HST	Simulation	x	o	x
Bae et al. [20]	PVT/ASHP/HST	Simulation	o	x	o
Bae et al. [21]	PVT/ASHP/HST	Experiment	o	o	x
Aneli et al. [21]	PV/ASHP/HST/EES	Simulation	o	x	o
Perrella et al. [24]	PV/AWHP/HST/EES	Simulation	x	x	o
Nicoletti et al. [25]	PV/AWHP	Simulation	o	o	o
This work	PV/AWHP/ERV/HST /EES	Experiment Simulation	o	o	o

The objectives of this study are as follows: (1) to analyze the building load usage patterns during the summer and winter periods; (2) to assess the surplus and shortage of power generation due to PV generation; (3) to evaluate the energy independence rate considering the performance of the AWHP systems; and (4) to perform an economic analysis of the AWHP system alone to propose appropriate capacities considering the energy independence rate and economic feasibility.

2. Methodology

2.1. Building and System Description

The building is located in Cheonan Asan, Republic of Korea (36°46′12.7″ N, 126°59′30.9″ E). The climate zone is classified according to ASHRAE 90.1-2007 as hot and humid in the summer and cold and dry in the winter (4A and 4B). Figure 1 shows the average monthly outdoor temperature and solar radiation. The highest and lowest outdoor temperatures are −2.2 C and 26.2 C, respectively. The monthly average solar radiation is 299.95 W/m^2 in May, which is the highest, and 88.69 W/m^2 in December, which is the lowest. The building is used as a dormitory, with two people staying in each room, and each person occupies an area of 16.25 m^2.

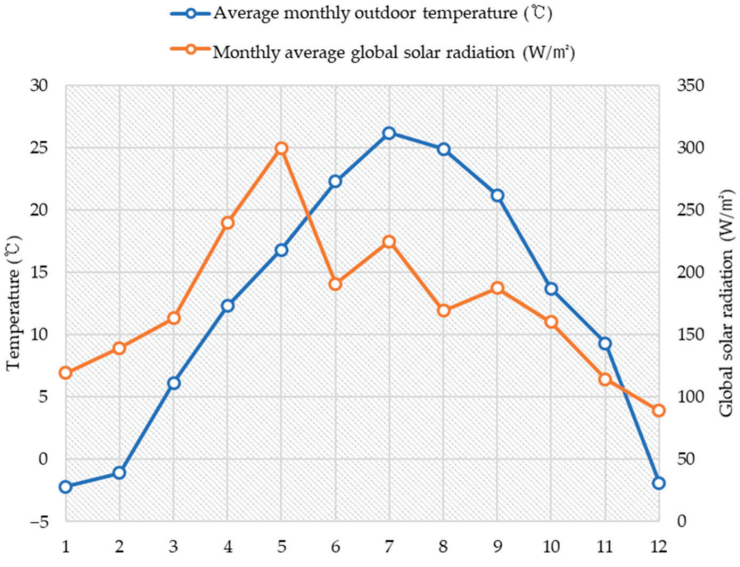

Figure 1. Average monthly outdoor temperature and global solar radiation.

Through the remodeling of the existing building, a renewable energy (PV) and integrated air conditioning system were installed. The integrated energy system (IES) constructed connects two rooms to IES_A and three rooms to IES_B, each responsible for handling the load, as shown in Figure 2. This system can analyze the energy consumption, reflecting the characteristics of the building load as all the loads required for the building are used in the form of electrical energy, and can suggest the appropriate capacity design for renewable energy. The system components include solar panels, power conversion system (PCS), ERV, and AWHP as depicted in Figure 3, and the configuration and specifications of each system are shown in Table 2. The direct current generated by PV is supplied through PCS to operate ERV and AWHP and is connected to the external power grid to sell excess power generated by the system or purchase power when the amount is insufficient. The capacity of AWHP and the storage tank is designed based on ASHRAE Standard 90.1 [31], and floor heating is used for heating, while ceiling-mounted FCUs are used for cooling. For hot water supply, hot water at 65 °C is supplied to the storage tank, and the temperature inside the storage tank is controlled to always be above 50 °C.

Table 2. HVAC system configuration and specifications of the building.

Component		Specification
AWHP	Model	HM051MR U44
	Capacity	5 kW × 2EA
	Refrigerant	R32 (1.4 kg)
HST	Capacity	220 L
ERV	Air volume	250 CMH
PV Panel	Capacity	4.44 kW (370 W × 12 EA)
PCS	AC	5 kW
	Power conversion efficiency	96%
LED	Power consumption	50 W × 5 EA13 W × 5 EA

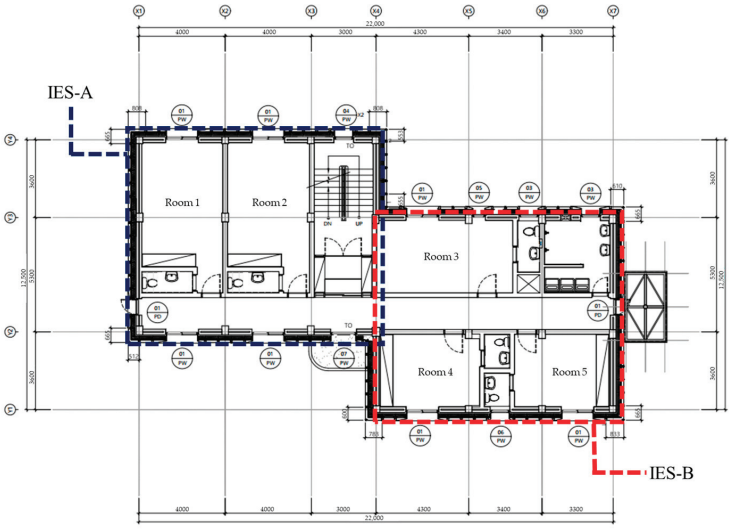

Figure 2. Drawing of the building layout and integrated energy system classification.

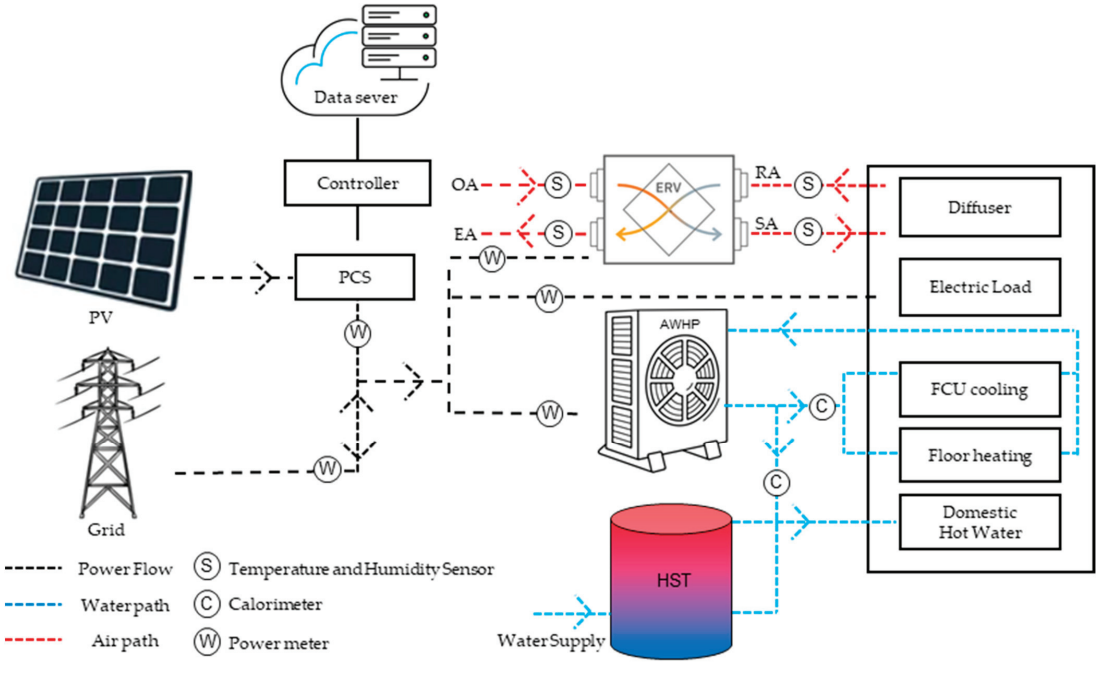

Figure 3. Energy flow diagram of integrated energy system.

2.2. Experimental Conditions

Throughout the five-month period from July to November, meticulous data collection was conducted. Indoor and outdoor temperature and humidity were monitored using sensors, while solar radiation was gauged utilizing an SR-05 solar radiation meter. The cooling and heating loads were quantified through the utilization of an RCN8 ultrasonic heat meter, which measured both inlet and outlet temperatures alongside flow rates. Furthermore, the efficiency of the ERV was assessed using the QAF 3160 apparatus in accordance with

ISO 5222-1 standards [32]. This involved meticulous measurement of temperature and humidity at various points including outdoor air inlet (OA), supply air inlet (SA), and exhaust air outlet (RA), facilitating a comprehensive evaluation of ERV performance.

For quantifying the performance of the PV system and related energy dynamics, an EM415 power meter was employed. This meter facilitated the precise measurement of the amount of PV power generation, power purchased from the grid, power sold, and power consumption by auxiliary systems such as the AWHP and ERV. The collected data, spanning minute intervals, were promptly transmitted to a centralized data server for analysis.

The reliability of the measurement equipment utilized in this study is detailed in Table 3, ensuring confidence in the accuracy of the obtained data. Additionally, the precise locations of our measurements are depicted in Figure 3, providing insight into the spatial distribution of data collection points.

Table 3. Measuring equipment and specifications.

Equipment	Metrics	Specification
RCN8 Ultrasonic Heat Meter	Heat and flow rate	Accuracy class 2 (European EN1434) Temperature sensor: Pt1000
EM415	Power meter	Accuracy Class B
SR-05	Solar radiation	ISO second class pyranometer Uncertainty < 1.8%
QFA3160	Temperature and humidity	Accuracy: 0.8 K (15~35 °C) 1 K (−35~50 °C)

Given the significant influence of climate data on system performance, specific days representing peak energy consumption during summer and winter periods were selected for in-depth analysis. Notably, August 7th and November 27th were identified as representative days for comparison and analysis. Through comprehensive examination of trends in PV generation, integrated system energy consumption, and power transactions with the external grid, a nuanced understanding of system behavior was attained, facilitating informed decision-making and optimization strategies.

2.3. Key Performance Indicators

The heating and cooling capacity (Q_h and Q_c) of an air-to-water heat pump (AWHP) is determined by Equations (1) and (2), and the coefficient of performance (*COP*) and energy efficiency ratio (*EER*) are calculated using Equations (3) and (4).

$$Q_h = \dot{m} \times c_{p,w} \times (T_{w,i} - T_{w,o}) \tag{1}$$

$$Q_c = \dot{m} \times c_{p,w} \times (T_{w,o} - T_{w,i}) \tag{2}$$

where $\dot{m}$ and $c_{p,w}$ are mass flow rate of water (kg/s) and specific heat capacity of water (kJ/kg°C). $T_{w,i}$ and $T_{w,o}$ are the water temperatures at the inlet and outlet of the condenser (°C).

$$COP = \frac{Q_h}{P_{AWHP}} \tag{3}$$

$$EER = \frac{Q_c}{P_{AWHP}} \tag{4}$$

where P_{AWHP} is the power usage of the AWHP (kW).

The energy saved by operating an energy recovery ventilator (Q_{saved}) is calculated using Equation (5), and the energy saving efficiency of the ERV is calculated using Equation (6).

$$Q_{saved} = \eta_t \times \rho \times c_{p,a} \times G \times (T_{OA} - T_{RA}) \tag{5}$$

$$\eta_t \frac{T_{OA} - T_{SA}}{T_{OA} - T_{RA}} \times 100 \quad (6)$$

where η_t is the efficiency of the ERV. ρ and $c_{p,a}$ are the density of air (kg/m^3) and specific heat capacity of air (kJ/kg°C). G is the indoor and outdoor ventilation amount per sec (m^3/s). T_{OA}, T_{SA}, and T_{RA} are the outdoor air temperature, supply air temperature, and indoor air temperature (°C), respectively.

2.4. Building Energy Self-Sufficiency Rate

The building energy self-sufficiency rate is an indicator of the percentage of energy used in the entire building that can be covered by renewable energy. As shown in Equation (7), the building energy self-sufficiency rate was calculated by dividing the total power generated by renewable energy by the total energy consumption.

$$Energy\ self-sufficiency\ rate = \frac{\sum Renewable\ energy\ generation\ system}{Total\ energy\ consumption} \times 100 \quad (7)$$

2.5. Economic Analysis

The initial investment (I) includes the cost of purchasing and installing the AWHP, PV, and ESS. The annual operating cost (AOC) includes the cost of electricity to run the AWHP and the cost of maintaining the system. Annual savings (AS) come from the energy generated by the PV and ESS. Initial investment, annual operating cost, and annual savings can be calculated according to Equations (8)–(10).

$$I = C_{AWHP} + C_{PV} + C_{ESS} \quad (8)$$

$$AOC = E_{AWHP} \times P_{electricity} + M_{AWHP} \quad (9)$$

$$AS = (E_{PV} + E_{ESS}) \times P_{electricity} \quad (10)$$

where C_{AWHP}, C_{PV}, and C_{ESS} are the cost of AWHP, PV, and ESS. E_{AWHP} is the annual energy consumption of the AWHP (kWh). $P_{electricity}$ is the annual energy consumption per kWh. M_{AWHP} is the annual maintenance cost of the AWHP.

The net present value (NPV) is the difference between the present value of the benefits and the present value of the costs. Payback period (PP) is the time it takes for the system to pay for itself. Net present value and payback period can be calculated as Equations (11) and (12).

$$NPV = \sum_{t=0}^{n} \frac{AS_t - AOC_t}{(1+r)^t} - I \quad (11)$$

$$PP = \frac{I}{AS - AOC} \quad (12)$$

where AS_t is the annual savings in year t, and AOC_t is the annual operating cost in the year t. r and n are the discount rate and number of years.

3. Result and Discussion

3.1. Representative Day Analysis

3.1.1. System Performance Analysis

To accurately understand the system's operational characteristics and assess the suitability of its PV generation capacity, the days with the highest energy consumption during the entire measurement period are selected as representative days. Specifically, 8 July and 27 November are chosen as representative days for the summer and winter seasons, respectively. During the entire cooling operation of the AWHP system, the average energy consumption per hour was 0.64 kWh, and the EER was 4.49. However, there is a tendency

for the cooling EER to decrease during the transition period when the system switches to hot water operation at around 7 A.M. and 7 P.M. The hourly load and energy consumption of the AWHP system are shown in Figure 4. During the heating operation of the AWHP system from 12 P.M. to 7 P.M., there is almost no heating load due to the absence of occupants. The average energy consumption per hour during the heating operation is 2.25 kWh, and the COP is 2.27. The heating COP and cooling EER of the systems proposed in previous studies range from 1.2 to 5.3 and 3.31 to 16, respectively, and the performance of the AWHP system used in this study falls within this range. If the ventilation frequency is satisfied once per hour, it is possible to reduce the ventilation load by an average of 87 W in the summer and 650 W in the winter compared to natural ventilation. The ERV efficiency and load reduction are calculated using Equations (5) and (6). The outdoor temperature and hourly load reduction are shown in Figure 5.

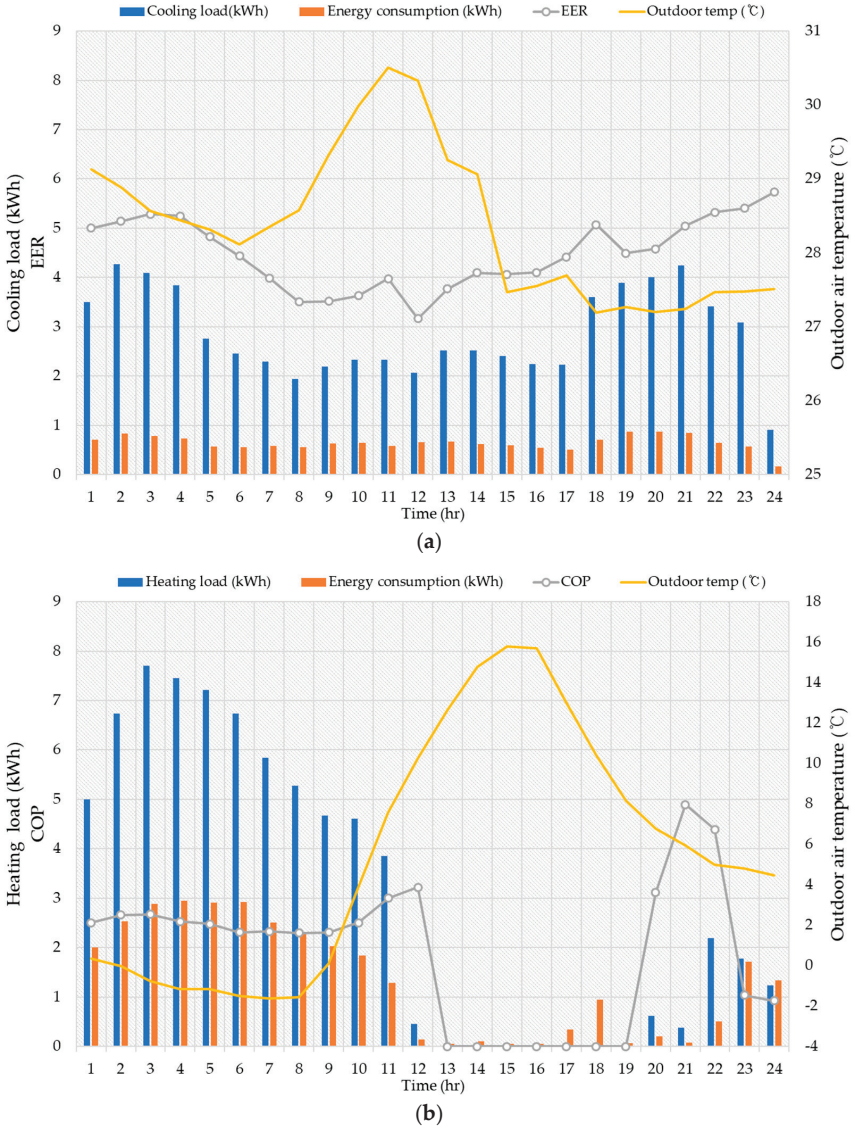

Figure 4. Cooling and heating performance of AWHP: (**a**) summer period; (**b**) winter period.

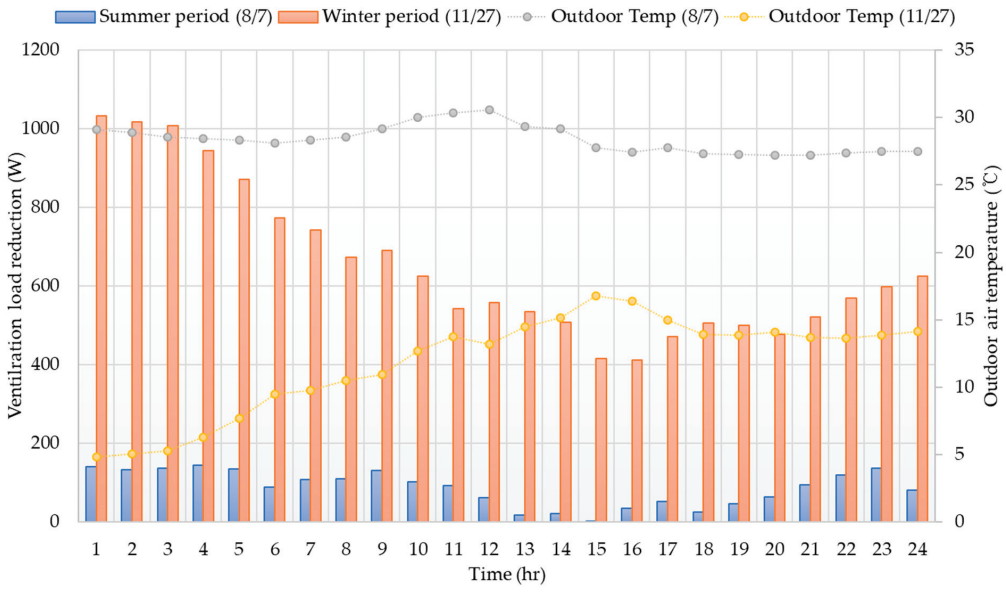

Figure 5. Energy savings using energy recovery ventilator.

3.1.2. PV Generation and Power Flow Analysis

On the representative summer day, the daily PV generation is 15.29 kWh, and the energy consumption is 33.05 kWh. The energy self-sufficiency rate is 46.3%. However, due to the imbalance in energy demand, 12.8% of the renewable energy generation, which is 1.96 kWh, is sold to the external grid, and 80.7% of the energy consumption, which is 26.68 kWh, is purchased from the external grid. On the representative winter day, the daily PV generation is 9.74 kWh, and the energy consumption is 48.74 kWh. The renewable energy production ratio is 19.97% compared to the energy consumption, and due to the imbalance in energy demand, 33.25% of the renewable energy generated, which is 3.24 kWh, is sold to the external grid, and 98.18% of the energy consumed, which is 47.86 kWh, is purchased from the external grid. The hourly power flow on the representative days is shown in Figure 6.

3.2. Building Energy Independence Analysis

The daily average value of the energy self-sufficiency rate, determined by Equation (7), varied throughout the period from July to November: 47% in July, 39.2% in August, 57.95% in September, 55.94% in October, and 20.27% in November. Notably, the presence of solar power generation significantly elevated the energy self-sufficiency rate, particularly during the mid-term, summer, and winter periods. The average solar radiation levels—214.75, 179.27, 219.83, 201.28, and 147.87 W/m^2—were identified as a primary contributing factor to this self-sufficiency. Concurrently, our analysis of the average energy sold to the external grid revealed percentages of 47.78, 36.22, 57.47, 55.94, and 53.22%, underscoring the impact of energy demand imbalances on the energy independence rate. These relationships between the average solar radiation, renewable energy sales ratio, and energy independence rate are visually represented in Figure 7 below.

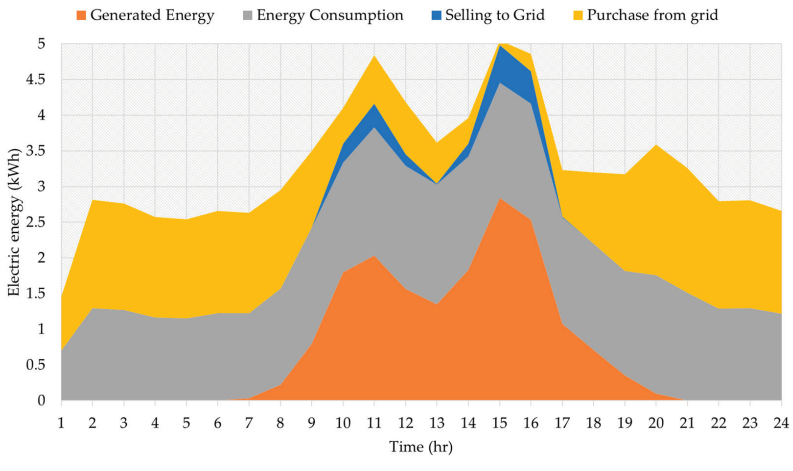

(**a**)

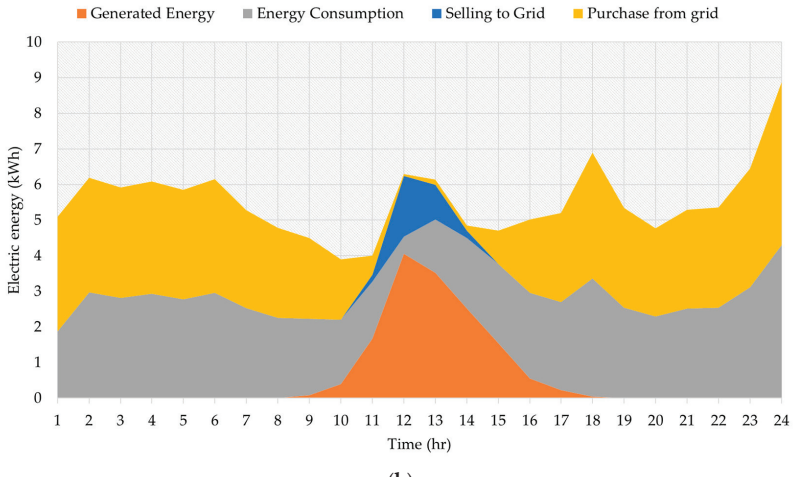

(**b**)

Figure 6. Electrical energy flow; (**a**) summer (7 August) (**b**) winter (27 November).

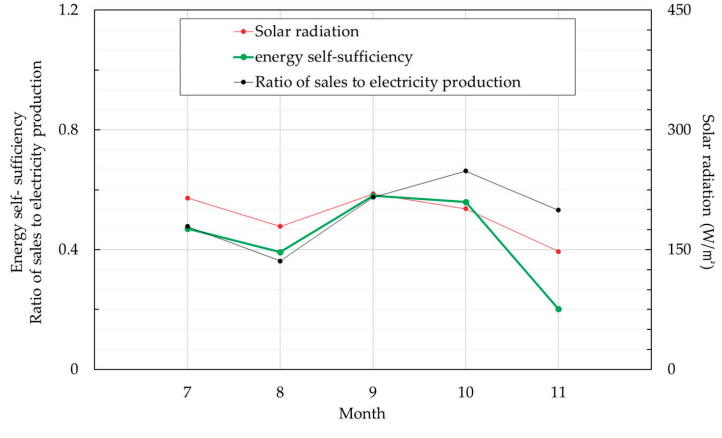

Figure 7. Relationship between solar radiation, electricity sales, and energy self-sufficiency.

The distribution of the energy self-sufficiency rates by outdoor temperature is shown in Figure 8a. In this study, since there were no batteries, the excess power generated from the PV was not stored and was sold to the grid. Although revenue can be expected from selling electricity, the energy self-sufficiency is reduced because electricity needs to be purchased and used during non-generating hours. As shown in Figure 8b, even when the energy self-sufficiency rate is close to 100%, a significant portion of the load required for the HVAC system needs to be purchased from the grid, highlighting the need for ESS installation to improve the building's energy self-sufficiency. Figure 8c shows the difference between daily PV generation and energy consumption, and it was observed that in the winter, the PV energy generated was not enough to be stored. The daily power production, purchase and sales volume, and energy consumption during the measurement period are shown in Figure 9.

3.3. Energy Independence Analysis by PV–ESS Capacity

Through a building energy simulation, the annual load demand of a building with the same insulation performance, floor area, and AWHP capacity as the building taken as our subject was calculated. The power consumption required for heating and cooling loads was calculated based on the AWHP performance coefficient, and the energy self-sufficiency rate was analyzed for different PV–ESS capacities, as shown in Table 4. When the PV capacity is 4 kW and the ESS capacity is 2, 4, and 8 kWh, the building's energy self-sufficiency rates are 55.84%, 67.43%, and 86.98%, respectively. As the PV and ESS capacities increase, the energy self-sufficiency rate naturally increases. However, it was observed that the rate of increase significantly decreases as the capacity increases excessively. Therefore, it is necessary to compare energy self-sufficiency and economic feasibility to select an appropriate capacity.

Table 4. Energy self-sufficiency rate according to PV–ESS capacity.

		PV Capacity (kW) (%)							
		1	**2**	**3**	**4**	**5**	**6**	**7**	**8**
ESS Capacity (kWh)	1	27.74	43.62	47.68	49.97	51.71	53.03	54.09	55.02
	2	27.76	48.13	53.45	55.84	57.65	58.95	60.02	60.94
	3	27.77	51.57	58.99	61.68	63.52	64.87	65.94	66.87
	4	27.79	53.81	64.00	67.43	69.36	70.76	71.86	72.79
	5	27.80	55.08	68.47	73.06	75.19	76.61	77.75	78.70
	6	27.82	55.50	72.44	78.41	80.93	82.42	83.58	84.50
	7	27.84	55.56	75.78	83.28	86.28	87.66	88.65	89.44
	8	27.85	55.57	78.11	86.98	90.61	91.98	92.76	93.37

3.4. Economic Analysis of PV–ESS System

Through Equations (8)–(10), the initial investment cost and annual operating cost were compared and analyzed for scenarios in which the energy production limit cost for the AWHP system alone is used and that of the PV–ESS system with different capacities is used. Compared to using the AWHP system alone without a PV–ESS system, the period required to make a profit is 14 years for a 4 kW–2 kWh PV–ESS capacity, 16.5 years for a 4 kW–4 kWh PV–ESS capacity, and 20 years for a 4 kW–8 kWh PV–ESS capacity. However, since an energy self-sufficiency of 87% is possible, it may be a better choice than using the AWHP system alone when considering carbon emissions reductions. Focusing on an energy self-sufficiency of over 90% and an 8 kWh battery capacity, an economic analysis was performed for PV capacities of 4, 5, 6, and 7 kW. The results showed that the difference in energy cost reductions was negligible in each case due to the large initial investment cost. Figure 10a shows the annual operating cost of 4 kW PV–2, 4, and 8 kWh ESS, and Figure 10b shows the annual operating cost of 4, 5, 6, and 7 kW PV–8 kWh ESS.

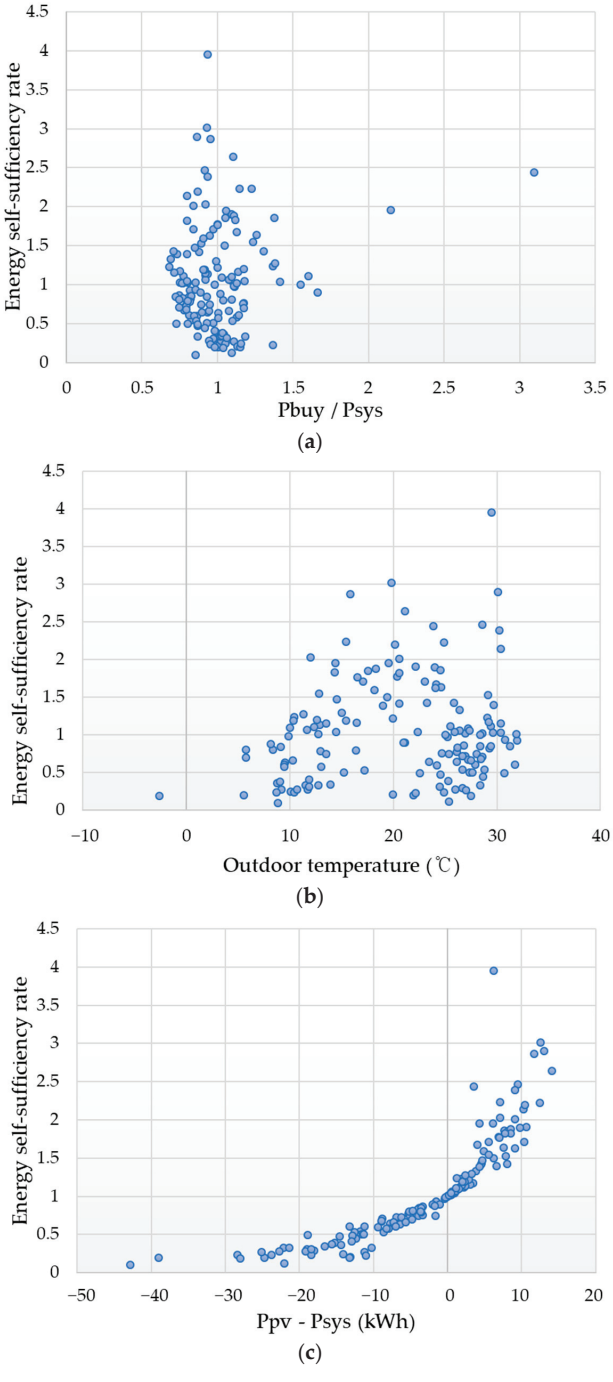

Figure 8. Renewable energy rate distribution. (**a**) Energy self-sufficiency rate for outdoor temperature; (**b**) Energy self-sufficiency rate based on ratio of power purchase amount to system energy consumption; (**c**) Energy self-sufficiency rate for difference in power production and energy consumption.

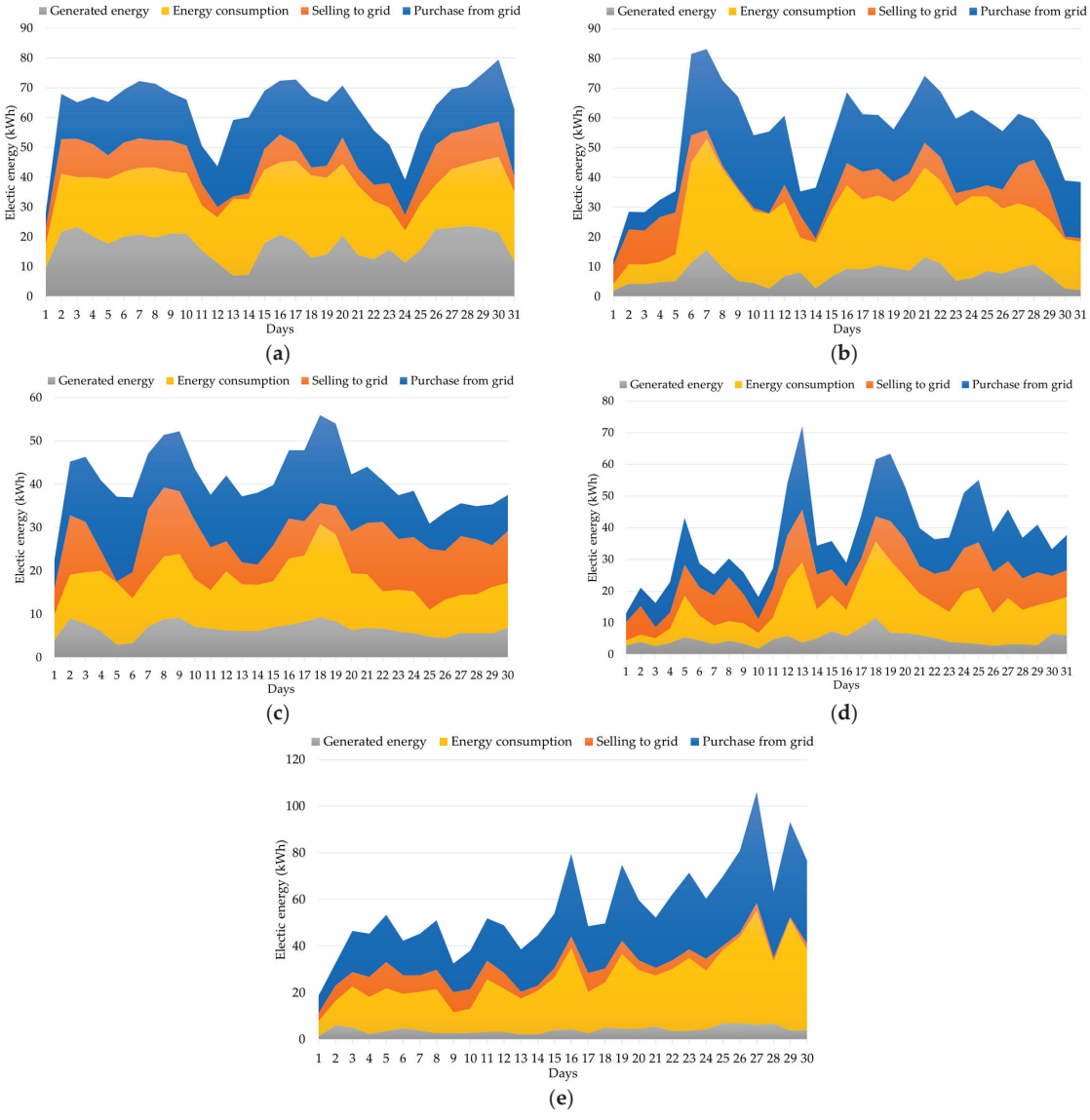

Figure 9. Electrical energy flow of integrated energy system. (**a**) July; (**b**) August; (**c**) September; (**d**) October; (**e**) November.

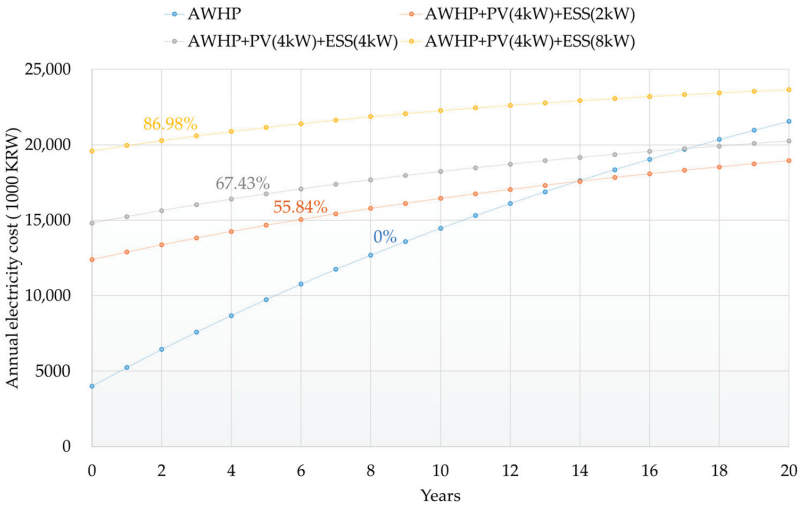

(**a**)

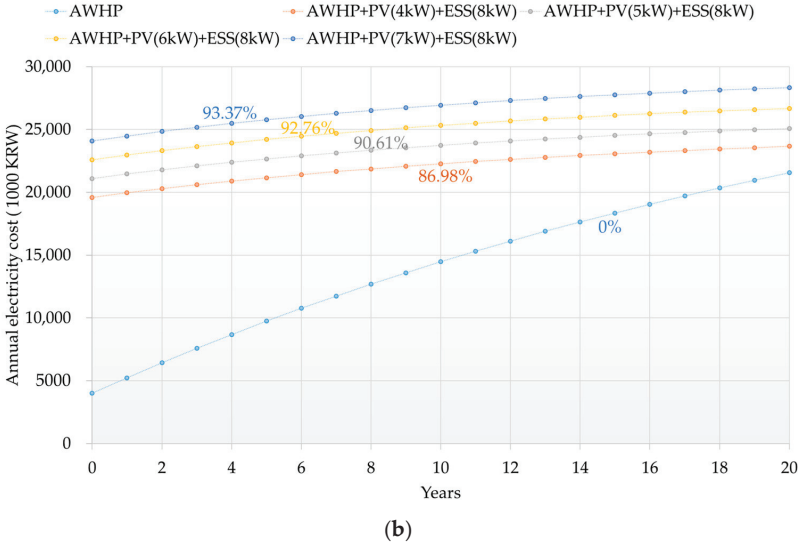

(**b**)

Figure 10. Annual electricity cost according to PV–ESS capacity. (**a**) PV capacity changes; (**b**) ESS capacity changes.

4. Conclusions

This study investigated the potential of a building-integrated air-to-water heat pump system coupled with photovoltaics to achieve energy independence. We analyzed the energy independence rate and economic feasibility based on different PV–ESS capacities. The integrated PV–AWHP system shared indoor electrical loads with the building's energy recovery ventilator. The AWHP system achieved an average cooling EER of 4.49 and a heating COP of 2.27. The energy independence rate varied significantly during the measurement period, ranging from 20.27% in November to 57.95% in September. This finding underscores the critical role of energy storage systems in enhancing self-sufficiency by storing surplus PV power for later use. With a 4 kW PV capacity, an energy independence of 67.43% was achieved with a 4 kWh battery and 86.96% with an 8 kWh battery. However,

it is crucial to note that while increasing PV and ESS capacities might lead to a higher self-sufficiency, a cost/benefit analysis remains essential to determine the optimal capacity for both energy and economic efficiency. Compared to using AWHP alone, the payback period when combined with PV–ESS takes 14 years for a 4 kW–4 kWh system and over 20 years for a 4 kW–8 kWh system. Implementing an ESS remains an attractive option despite the longer payback period compared to that of a standalone AWHP system, considering its potential for carbon emissions reductions. Future research could explore optimizing the sizing of PV and ESS systems for a balance between energy self-sufficiency and economic feasibility. Additionally, integrating smart energy management systems could further optimize their energy use and improve their cost-effectiveness.

Author Contributions: Conceptualization, S.-K.Y. and Y.-H.K.; Data curation, S.-K.Y. and Y.-H.K.; Validation, S.-K.Y. and Y.-C.A.; Formal analysis, S.-K.Y. and Y.-H.K.; investigation, S.-K.Y. and Y.-H.K. Resources, S.-K.Y. and Y.-C.A.; writing—original draft preparation, S.-K.Y. and Y.-H.K.; writing—review and editing, S.-K.Y. and Y.-C.A. All authors have read and agreed to the published version of the manuscript.

Funding: This research was supported by the Basic Science Research Program through the National Research Foundation of Korea (NRF), funded by the Ministry of Education (2021R1I1A3048346).

Data Availability Statement: Data are available upon request due to privacy or ethical restrictions.

Conflicts of Interest: The authors declare no conflicts of interest.

References

1. European Parliament. Smarter and More Energy-Efficient Buildings in the EU by 2050. Available online: https://www.europarl.europa.eu (accessed on 26 February 2024).
2. European Commission. *Horizon Europe Work Programme 2023–2024 Climate, Energy and Mobility*; European Commission: Brussels, Belgium, 2023.
3. Korol, E.; Shushunova, N. Analysis and Valuation of the Energy-Efficient Residential Building with Innovative Modular Green Wall Systems. *Sustainability* **2022**, *14*, 6891. [CrossRef]
4. IEA. *Tracking Buildings 2020*; IEA: Paris, France, 2020.
5. IEA. Energy Efficiency. *The First Fuel of a Sustainable Global Energy System.* 2022. Available online: https://www.iea.org/topics/energy-efficiency (accessed on 26 February 2024).
6. Zheng, Y.; Miao, J.; Yu, H.; Liu, F.; Cai, Q. Thermal Analysis of Air-Cooled Channels of Different Sizes in Naturally Ventilated Photovoltaic Wall Panels. *Buildings* **2023**, *13*, 3002. [CrossRef]
7. Ma, T.; Kazemian, A.; Habibollahzade, A.; Salari, A.; Gu, W.; Peng, J. A comparative study on bifacial photovoltaic/thermal modules with various cooling methods. *Energy Convers. Manag.* **2022**, *263*, 115555. [CrossRef]
8. Prakash, K.B.; Almeshaal, M.; Pasupathi, M.K.; Chinnasamy, S.; Saravanakumar, S. Hybrid PV/T Heat Pump System with PCM for Combined Heating, Cooling and Power Provision in Buildings. *Buildings* **2023**, *13*, 1133. [CrossRef]
9. Li, H.; Sun, Y. Operational Performance Study on a Photovoltaic Loop Heat Pipe/Solar Assisted Heat Pump Water Heating System. *Energy Build.* **2018**, *158*, 861–872. [CrossRef]
10. James, A.; Srinivas, M.; Mohanraj, M.; Raj, A.K.; Jayaraj, S. Experimental Studies on Photovoltaic-Thermal Heat Pump Water Heaters Using Variable Frequency Drive Compressors. *Sustain. Energy Technol. Assess.* **2021**, *45*, 101152. [CrossRef]
11. United Nations Climate Change. *Net Zero by 2050: A Roadmap for the Global Energy Sector—A Special Report by the International Energy Agency*; United Nations Climate Change: New York, NY, USA, 2021.
12. Schreurs, T.; Madani, H.; Zottl, A.; Sommerfeldt, N.; Zucker, G. Techno-economic analysis of combined heat pump and solar PV system for multi-family houses: An Austrian case study. *Energy Strategy Rev.* **2021**, *36*, 100666. [CrossRef]
13. Allouhi, A. Techno-economic and environmental accounting analyses of an innovative power-to-heat concept based on solar PV systems and a geothermal heat pump. *Renew. Energy* **2022**, *191*, 649–661. [CrossRef]
14. Martorana, F.; Bonomolo, M.; Leone, G.; Monteleone, F.; Zizzo, G.; Beccali, M. Solar-assisted heat pumps systems for domestic hot water production in small energy communities. *Sol. Energy* **2021**, *217*, 113–133. [CrossRef]
15. Baggio, P.; Bee, E.; Prada, A. Demand-side management of air-source heat pump and photovoltaic systems for heating applications in the italian context. *Environments* **2018**, *5*, 132.
16. Bee, E.; Prada, A.; Baggio, P.; Psimopoulos, E. Air-source heat pump and photovoltaic systems for residential heating and cooling: Potential of self-consumption in different European climates. *Build. Simul.* **2019**, *12*, 453–463. [CrossRef]
17. Zhou, C.; Liang, R.; Zhang, J.; Riaz, A. Experimental Study on the Cogeneration Performance of Roll-Bond-PVT Heat Pump System with Single Stage Compression during Summer. *Appl. Therm. Eng.* **2019**, *149*, 249–261. [CrossRef]

18. Long, T.; Qiao, Z.; Wang, M.; Li, Y.; Lu, J.; Li, W.; Zeng, L.; Huang, S. Performance Analysis and Optimization of a Solar-Air Source Heat Pump Heating System in Tibet, China. *Energy Build.* **2020**, *220*, 110084. [CrossRef]
19. Kong, R.; Deethayat, T.; Asanakham, A.; Kiatsiriroat, T. Performance and Economic Evaluation of a Photovoltaic/Thermal (PV/T)-Cascade Heat Pump for Combined Cooling, Heat and Power in Tropical Climate Area. *J. Energy Storage* **2020**, *30*, 101507. [CrossRef]
20. Bae, S.; Chae, S.; Nam, Y. Performance Analysis of Integrated Photovoltaic-Thermal and Air Source Heat Pump System through Energy Simulation. *Energies* **2022**, *15*, 528. [CrossRef]
21. Bae, S.; Chae, H.; Nam, Y. Experimental analysis of an integrated system using photovoltaic–thermal and air source heat pump for real applications. *Renew. Energy* **2023**, *217*, 119128. [CrossRef]
22. Dermentzis, G.; Ochs, F.; Franzoi, N. Four years monitoring of heat pump, solar thermal and PV system in two net-zero energy multi-family buildings. *J. Build. Eng.* **2021**, *43*, 103199. [CrossRef]
23. Shono, K.; Yamaguchi, Y.; Perwez, U.; Ma, T.; Dai, Y.; Shimoda, Y. Large-scale building-integrated photovoltaics installation on building façades: Hourly resolution analysis using commercial building stock in Tokyo, Japan. *Sol. Energy* **2023**, *253*, 137–153. [CrossRef]
24. Perwez, U.; Shono, K.; Yamaguchi, Y.; Shimoda, Y. Multi-scale UBEM-BIPV coupled approach for the assessment of carbon neutrality of commercial building stock. *Energy Build.* **2023**, *291*, 113086. [CrossRef]
25. Sigounis, A.; Vallianos, C.; Athienitis, A. Model predictive control of air-based building integrated PV/T systems for optimal HVAC integration. *Renew. Energy* **2023**, *212*, 655–668. [CrossRef]
26. Aneli, S.; Arena, R.; Tina, G.M.; Gagliano, A. Improvement of energy self-sufficiency in residential buildings by using solar-assisted heat pumps and thermal and electrical storage. Sustain. *Energy Technol. Assess.* **2023**, *60*, 103446.
27. Perrella, S.; Bisegna, F.; Bevilacqua, P.; Cirone, D.; Bruno, R. Solar-Assisted Heat Pump with Electric and Thermal Storage: The Role of Appropriate Control Strategies for the Exploitation of the Solar Source. *Buildings* **2024**, *14*, 296. [CrossRef]
28. Nicoletti, F.; Cucumo, M.A.; Arcuri, N. Cost optimal sizing of photovoltaic-battery system and air–water heat pump in the Medi-terranean area. *Energy Convers. Manag.* **2022**, *270*, 116274. [CrossRef]
29. Liu, X.; Zhang, P.; Pimm, A.; Feng, D.; Zheng, M. Optimal design and operation of PV-battery systems considering the interdependency of heat pumps. *J. Energy Storage* **2019**, *23*, 526–536. [CrossRef]
30. Yang, C.; Fu, Y.; He, L.; Jiang, Q.; Cui, Y. Real options analysis for regional investment decisions of household PV-ESS in China. *Energy* **2024**, *293*, 130725. [CrossRef]
31. *ANSI/ASHRAE Standard 90.2—2007*; Energy Efficient Design for Low-Rise Residential Buildings. ASHRAE: Atlanta, GA, USA, 2007.
32. *ISO 5222-1:2023*; Heat Recovery Ventilators and Energy Recovery Ventilators: Testing and Calculating Methods for Seasonal Performance Factor. ISO: Geneva, Switzerland, 2023.

buildings

MDPI

Article

Impact of Insulation Strategies of Cross-Laminated Timber Assemblies on Energy Use, Peak Demand, and Carbon Emissions

Mikael Salonvaara * and André Desjarlais

Oak Ridge National Laboratory, Oak Ridge, TN 37830, USA; desjarlaisa@ornl.gov
* Correspondence: salonvaaramh@ornl.gov

Abstract: Cross-Laminated Timber (CLT) panels have many structural benefits but do not have much thermal resistance. We have developed a solution to insulate CLT structures that uses high-performance insulation panels that provide R-values up to R40/inch. The CLT panels are made of layers of wood laminates (three, five, seven or more). The solution replaces some of the wood laminates in the CLT production with the insulation panels in a staggered fashion so that the wood laminates maintain contact throughout the panel, ensuring the CLT panel's structural integrity. The insulated CLT panels have factory-installed water-resistive barriers reducing the installation time by eliminating installing insulation and water-resistive barriers on site. Per simulations, the CLT/insulation panel achieved code-required insulation levels with commonly available insulation materials. The significance of the thermal mass of CLT/insulation hybrid building envelopes was quantified by comparing the whole building energy performance and peak demand of traditional low mass and CLT wall assemblies resulting in up to 7% reduction in peak demand for cooling in Knoxville, TN, in a multifamily building. Buildings contribute over 40 percent of carbon emissions. The proposed CLT/insulation hybrid building envelope addresses both operational and embodied carbon by having high thermal resistances due to the embedded insulation sections and eliminating the use of high embodied carbon materials such as steel and concrete. The carbon benefit is estimated.

Keywords: cross-laminated timber; insulation; thermal performance

Citation: Salonvaara, M.; Desjarlais, A. Impact of Insulation Strategies of Cross-Laminated Timber Assemblies on Energy Use, Peak Demand, and Carbon Emissions. *Buildings* **2024**, *14*, 1089. https://doi.org/10.3390/buildings14041089

Academic Editor: Antonio Caggiano

Received: 1 March 2024
Revised: 7 April 2024
Accepted: 10 April 2024
Published: 13 April 2024

1. Introduction

Cross-laminated timber (CLT) has gained significant traction in the building construction industry for several reasons, ranging from environmental benefits to structural performance. There are multifaceted reasons behind the increasing popularity of CLT in building construction, such as its sustainability, efficiency, versatility, and positive impact on the construction process and the built environment. The prefabrication of CLT panels off-site allows for quicker assembly times on construction sites, significantly reducing the overall build time of projects. This efficiency translates to cost savings and minimizes the environmental impact and disruption typically associated with construction activities. Compared to traditional construction materials, the lightweight nature of CLT further reduces transportation and handling costs, contributing to the economic and environmental efficiency of construction projects. This paper discusses an innovative product that further reduces construction times while providing a compact, thermally insulated CLT panel.

In April 2024, the U.S. Department of Energy released the first-ever federal blueprint to decarbonize America's buildings sector [1]. The blueprint is designed to cut greenhouse gas emissions from U.S. buildings by 65% by 2035 and by 90% by 2050, compared to levels in 2005, focusing on fairness and community advantages. It establishes three overarching goals related to fairness, cost-effectiveness, and resilience, aimed at ensuring that the transition to low-carbon buildings aids underserved communities, lowers energy expenses, and enhances the resilience of communities to stressors. Additionally, the blueprint outlines

four key strategic objectives, each with defined performance goals, to facilitate the overall reduction in emissions: Increase building energy efficiency, accelerate onsite emissions reductions, transform the grid edge, and minimize embodied life cycle emissions. Compared with steel and concrete construction, CLT is a low-impact material with a much lower carbon footprint. Using a material such as CLT offers carbon benefits through the sequestered carbon throughout the lifetime of the timber, and unlike concrete and steel, it is a regenerative material.

In their comprehensive literature review, Cabral and Blanchet [2] highlight the significant energy efficiency advantages of mass timber and hybrid construction systems, despite the current scarcity of specific design codes and standards for these innovative building methods. They particularly emphasize the potential of Cross-Laminated Timber (CLT) to outperform traditional construction materials like concrete and light steel frames, with possible energy savings reaching up to 40%. A notable advantage of CLT lies in its ability to minimize thermal bridging, thereby facilitating achieving stringent energy performance benchmarks. Moreover, the inherent airtightness of CLT structures contributes to further energy conservation by reducing uncontrolled ventilation and enhancing the operational energy efficiency of buildings. Salonvaara et al. [3] studied the benefits of mass timber in buildings, demonstrating notable reductions in annual energy use and peak demand, alongside improved thermal comfort, compared to conventional lightweight wall systems. The laboratory tests and simulation research revealed mass timber's ability to shift heating and cooling energy demand away from peak hours, resulting in a 30–50% reduction in peak demand and enhancing thermal comfort by reducing uncomfortable hours by up to 46%. The thermal mass of CLT contributes to energy efficiency, maintaining stable indoor temperatures and reducing the need for mechanical heating and cooling. Setter et al. [4] showed a 38% reduction in annual heating energy in Minneapolis, MN, and a 17% reduction in annual cooling energy in Phoenix, AZ, with simulations. These findings advocate for integrating mass timber as an effective energy efficiency and thermal management strategy in various climate zones. In their comprehensive review within the context of Cross-Laminated Timber (CLT) development and application, Ren et al. [5] assert that CLT emerges as a superior building material when evaluated against criteria such as energy consumption, environmental impact, and structural integrity as corroborated by the majority of sources referenced in their study. They forecast that future research in CLT could pivot around several areas, such as the innovation of non-adhesive CLT solutions to eliminate reliance on chemical binders, enhancements in CLT logistics aimed at optimizing energy efficiency, advancements in the design and functionality of edge connections, mass CLT elements, and the investigation into the airtightness of CLT structures and their energy performance.

Past research on combining insulation with CLT panels is available. Santos et al. [6] focused on a sandwich wall-panel solution based on CLT, aiming to improve thermal insulation and reduce weight by combining wood with a low-density core layer. They presented a Life-Cycle Analysis (LCA) study about the product's environmental impact. The layout of the new panel is like that of a five-layer CLT panel, but they replaced the inner layer with rigid polyurethane foam. In a follow-up paper [7], they explored the new panel layout named Cross-Insulated Timber (CIT), which uses polyurethane (PUR) rigid foam instead of timber for the inner layer to improve thermal insulation and reduce weight for acoustic and thermal behavior. The CIT panel included four layers of solid wood lamellae with one solid rigid insulation layer in the middle.

Reducing wood content inside the CLT panels impacts its acoustical and structural performance and fire rating. Huang et al. [8] showed that the hollow cores have little effect on the static bending stiffness of the CLT panels. However, there were indications that the hollow cores could degrade the floor dynamic bending stiffness.

This manuscript's investigation exclusively concentrates on thermal performance aspects. The novel method, replacing pieces of wood boards inside the CLT panel in a staggered fashion, provides a compact, readily insulated CLT panel. The paper constitutes a

preliminary analysis, emphasizing the steady-state thermal behavior and the thermal delay characteristics of heat flow through the assembly. Should this foundational examination prove satisfactory, subsequent investigations will encompass fire safety, structural integrity, and other pertinent parameters.

2. Materials and Methods

In this study, we enhanced the thermal performance of Cross-Laminated Timber (CLT) by integrating insulation within its structure and devising an innovative insulated CLT panel. Traditional CLT comprises multiple layers of lumber, with each layer's wood grain oriented perpendicularly to adjacent ones. Our modification involved substituting a portion of the wood with insulation material in two or three layers, thereby creating partially insulated lamellae within the CLT matrix.

The standard configuration of the CLT used in our experiments was a five-ply structure, with each ply measuring 34.9 mm in thickness, culminating in a total panel thickness of 174.6 mm. To assess the impact of varying insulation properties, we experimented with insulation materials offering a range of thermal conductivity, including 0.0036 W/m·K (vacuum insulation panel) and extending up to 0.11 W/m·K (typical of wood), representing a broad spectrum of thermal conductivity.

A key variable in our study was the 'insulation ratio', which refers to the proportion of insulation substituted for wood in the partially insulated layers. Values range from 30% to 70%. This parameter allowed us to explore the structural integrity and thermal performance balance.

We compared the thermal efficiency of our modified CLT panels against a conventional insulation strategy, termed the '1D-assembly'. This conventional model consists of a solid wood panel paired with a continuous layer of insulation, maintaining the same overall thickness but lacking the integrated approach of the insulated CLT. The volumes of the wood and insulation materials are identical in the 1D assembly and the insulated CLT.

Our analysis included two configurations: (1) one with insulation replacing wood in two CLT layers and (2) another with three middle layers substituted with insulation. We employed the COMSOL Multiphysics® software v6.2 [9] for our simulations, enabling detailed modeling and calculating the effective surface-to-surface R-value, thereby quantifying the thermal performance enhancements achieved through our insulated CLT design.

3. Results

The simulations for heat transfer through the CLT panels with varying degrees of insulation were carried out for a panel size mimicking one that would be used in a heat flow meter apparatus. The panel size was 0.61 m × 0.61 m with an overall thickness of 175 mm for a five-ply CLT with 35 mm layers.

The thermal properties of the wood used in the simulations for the CLT were

- Density 500 kg/m^3
- Specific heat capacity 1880 J/kg·K
- Thermal conductivity 0.11 W/m·K

Staggering the insulation layers in the CLT was created in the test sample by placing the insulation layers at 0.61 m on-center distance from each other, creating a symmetric boundary condition on the sides.

3.1. Staggered Insulation in Two Lamellae of CLT

An insulated CLT assembly was created by replacing some pieces of wood in two layers of a CLT assembly with insulation (Figure 1). Both layers had the same percentage of insulation in the total area.

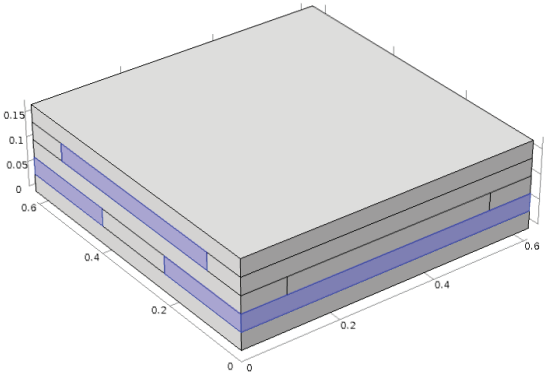

Figure 1. Staggered insulation layers in two lamellae of CLT.

The assembly is a five-ply CLT with the layers listed in Table 1.

Table 1. The material arrangement in the CLT with two insulated layers.

Layer	Materials
1	Wood only
2	Wood (1.0-insulation ratio *), insulation (insulation ratio *)
3	Wood only
4	Wood (1.0-insulation ratio *), insulation (insulation ratio *)
5	Wood only

* Insulation ratio = area of insulation/total area in a layer.

The resulting effective R-values as a function of insulation's R-value and area coverage are shown in Table 2. The insulation ratio is the same for each partially insulated layer (2 and 4).

Table 2. Assembly R-values for a staggered two-layer system and a one-dimensional (1D) assembly with average material thicknesses.

k, W/m·K	0.0036	0.0180	0.0240	0.0288	0.0400	0.0500	0.1100		
Insulation ratio			**R-value (m^2, K/W): Staggered two layers**						
0.3	2.60	2.13	2.02	1.96	1.85	1.78	1.59		
0.4	3.50	2.44	2.25	2.14	1.96	1.86	1.59		
0.5	5.06	2.81	2.51	2.34	2.08	1.94	1.59		
0.6	6.82	3.15	2.74	2.52	2.19	2.01	1.59		
0.7	8.32	3.44	2.94	2.68	2.30	2.08	1.59		
								Homogeneous thickness as a single layer	
			R-value (m^2, K/W): 1D-assembly					**d-wood, mm**	**d-ins, mm**
0.3	7.22	2.56	2.27	2.12	1.92	1.82	1.59	153.7	21.0
0.4	9.09	2.89	2.50	2.30	2.03	1.89	1.59	146.7	27.9
0.5	10.97	3.21	2.73	2.48	2.14	1.97	1.59	139.7	34.9
0.6	12.85	3.53	2.95	2.66	2.25	2.04	1.59	132.7	41.9
0.7	14.72	3.86	3.18	2.84	2.37	2.12	1.59	125.7	48.9
				R-value ratio (-): Staggered/1D-assembly					
0.3	36%	83%	89%	92%	96%	98%	100%		
0.4	38%	84%	90%	93%	97%	98%	100%		
0.5	46%	88%	92%	94%	97%	98%	100%		
0.6	53%	89%	93%	95%	97%	98%	100%		
0.7	56%	89%	93%	94%	97%	98%	100%		

Figures 2 and 3 demonstrate that the overall R-value of the partially insulated CLT panel depends linearly on the insulation ratio in the two-layer staggered system. The impact of thermal bridging between the insulation layers is less than 12% when the insulation's thermal conductivity is higher or equal to 0.018 W/m·K. The thermal bypasses in the system with vacuum insulation, 0.0036 W/m·K, reduce the overall R-value to half that of a system with continuous insulation when the insulation ratio is 0.3 and the volume of the insulation material is the same. The higher the insulation ratio, the smaller the impact of thermal bridging on the overall R-value.

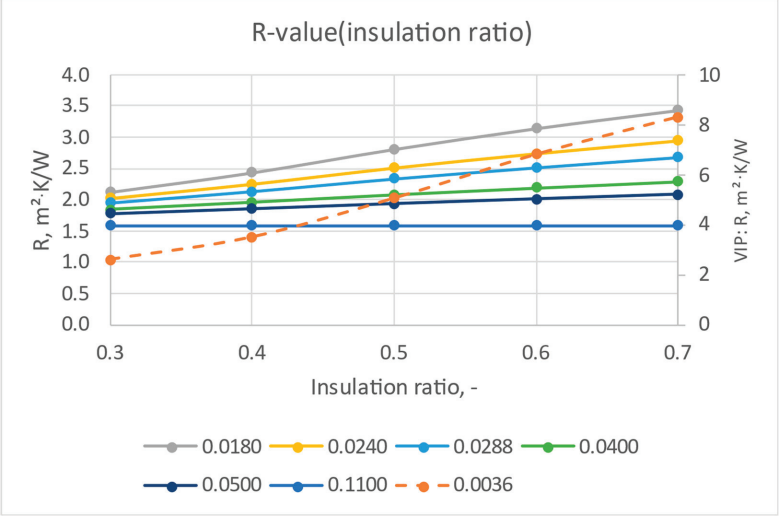

Figure 2. Effective R-value of the five-ply CLT with varying degrees of insulation in two layers (layers 2 and 4). Results for insulation materials with thermal conductivity ranging from 0.0036 to 0.11 W/m·K. The dotted line is for the vacuum-insulated panel (VIP).

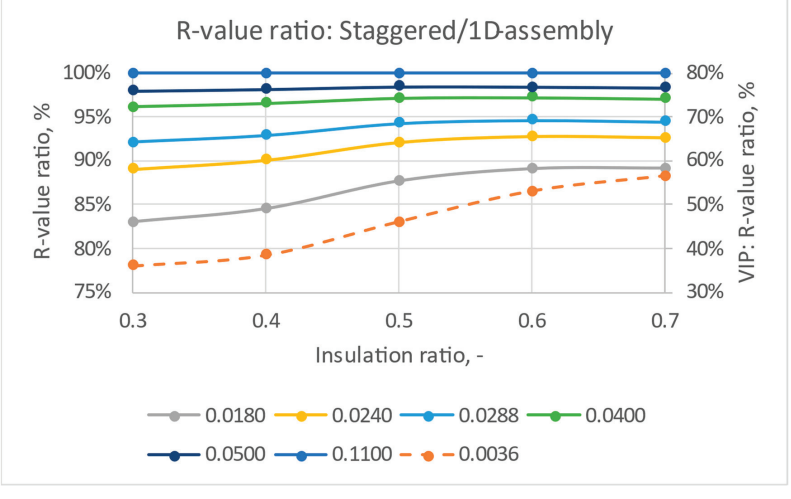

Figure 3. R-value ratio (%) in the five-ply CLT with varying degrees of insulation in two layers (layers 2 and 4) compared to a solid CLT with a homogeneous insulation layer. Results for insulation materials with thermal conductivity ranging from 0.0036 to 0.11 W/m·K. The dotted line is for the vacuum-insulated panel (VIP).

3.2. Staggered Insulation in Three Lamellae of CLT

The insulated CLT system with insulation in two lamellas of CLT was further improved by adding insulation in the third lamellae (Figure 4). This layer runs perpendicular to the other two layers with insulation. All three layers had the same percentage of insulation in the total area.

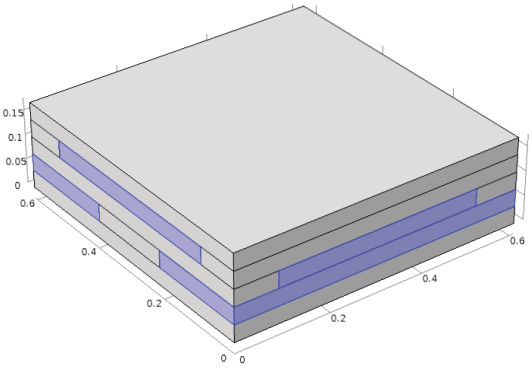

Figure 4. Staggered insulation in three lamellae of a five-ply CLT.

The assembly is a five-ply CLT with the lamellae listed in Table 3.

Table 3. Material arrangement in the CLT with staggered insulation in three lamellae.

Layer	Materials
1	Wood only
2	Wood (1.0-insulation ratio *), insulation (insulation ratio *)
3	Wood (1.0-insulation ratio *), insulation (insulation ratio *)
4	Wood (1.0-insulation ratio *), insulation (insulation ratio *)
5	Wood only

* Insulation ratio = area of insulation/total area in a layer.

The resulting effective R-values as a function of the insulation's R-value and area coverage are shown in Table 4. The insulation ratio is the same for each partially insulated layer (2, 3, and 4).

Table 4. Assembly R-values for a staggered three-layer system and 1D assembly with average material thicknesses.

k, W/m K	0.0036	0.0180	0.0240	0.0288	0.0400	0.0500	0.1100		
Insulation ratio		**R-value (m^2, K/W): Staggered three layers**							
0.3	3.26	2.41	2.25	2.15	1.98	1.87	1.59		
0.4	4.84	2.89	2.59	2.41	2.14	1.99	1.59		
0.5	7.63	3.44	2.97	2.71	2.32	2.11	1.59		
0.6	11.01	3.97	3.33	2.99	2.49	2.22	1.59		
0.7	14.31	4.46	3.67	3.25	2.66	2.34	1.59		
								Homogeneous thickness as a single layer	
		R-value (m^2, K/W): 1D-assembly						**d-wood, mm**	**d-ins, mm**
0.3	10.03	3.05	2.61	2.39	2.09	1.93	1.59	143.2	31.4
0.4	12.85	3.53	2.95	2.66	2.25	2.04	1.59	132.7	41.9
0.5	15.66	4.02	3.29	2.93	2.42	2.16	1.59	122.2	52.4
0.6	18.48	4.51	3.64	3.20	2.59	2.27	1.59	111.8	62.9
0.7	21.29	5.00	3.98	3.47	2.75	2.39	1.59	101.3	73.3

Table 4. *Cont.*

R-value ratio (-): Staggered/1D-assembly							
0.3	32%	79%	86%	90%	95%	97%	100%
0.4	38%	82%	88%	91%	95%	97%	100%
0.5	49%	86%	90%	92%	96%	98%	100%
0.6	60%	88%	91%	93%	96%	98%	100%
0.7	67%	89%	92%	94%	96%	98%	100%

Figures 5 and 6 demonstrate that the overall R-value of the partially insulated CLT panel depends linearly on the insulation ratio in the two-layer staggered system.

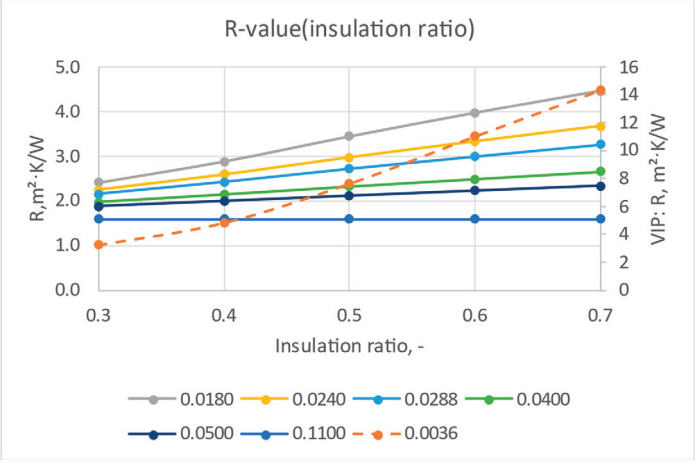

Figure 5. Effective R-value of the five-ply CLT with varying degrees of insulation in three layers (layers 2, 3, and 4). Results for insulation materials with thermal conductivity ranging from 0.0036 to 0.11 W/m·K. The dotted line is for the vacuum-insulated panel (VIP).

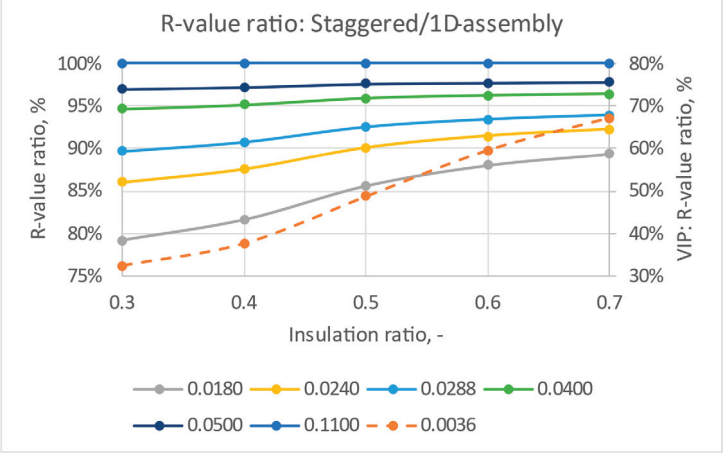

Figure 6. R-value ratio (%) in the five-ply CLT with varying degrees of insulation in three layers (layers 2, 3, and 4) compared to a solid CLT with a homogeneous insulation layer. Results for insulation materials with thermal conductivity ranging from 0.0036 to 0.11 W/m·K. The dotted line is for the vacuum-insulated panel (VIP).

In a two-layer insulated system, the impact of thermal bridging between the insulation layers is less than 17% when the insulation's thermal conductivity is equal to or higher than 0.018 W/m·K. The thermal bypasses in the system with vacuum insulation, 0.0036 W/m·K, reduce the overall R-value by 64% of that of a system with continuous insulation when the insulation ratio is 0.3 and the volume of the insulation material is the same. Comparing these results to the three-layer insulation system, we notice that the impact of thermal bridges is higher in the three-layer system, up to 21% with k = 0.018 W/m·K insulation and 68% with k = 0.0036 W/m·K. The higher the insulation ratio, the smaller the impact of thermal bridging on the overall R-value.

3.3. Comparing the Two- and Three-Layer Staggered Insulation CLTs

Figure 7 compares the two- and three-layer staggered insulated systems with thermal conductivity values of 0.0036 and 0.024 for the insulation. The three-layer staggered system provides a better R-value than the two-layer system with the same insulation ratio. However, the three-layer insulation system uses more insulation at the same ratio. Table 5 shows the volume percentage of insulation when the insulation is placed in two or three layers of the CLT. Comparing the two systems at the same volume of insulation used, we can take, for example, an insulation ratio of 0.5 for the two-layer system and 0.33 for the three-layer system. In this case, both systems have one full layer of insulation out of five in the CLT. The two-layer system with R-40 per inch insulation (k = 0.0036 W/m·K) achieves an R-value of 5.1 m^2K/W, whereas the three-layer system achieves only 3.8 m^2/K/W. Therefore, the arrangement in the two-layer system is more efficient in recovering the R-value of a continuous insulation layer.

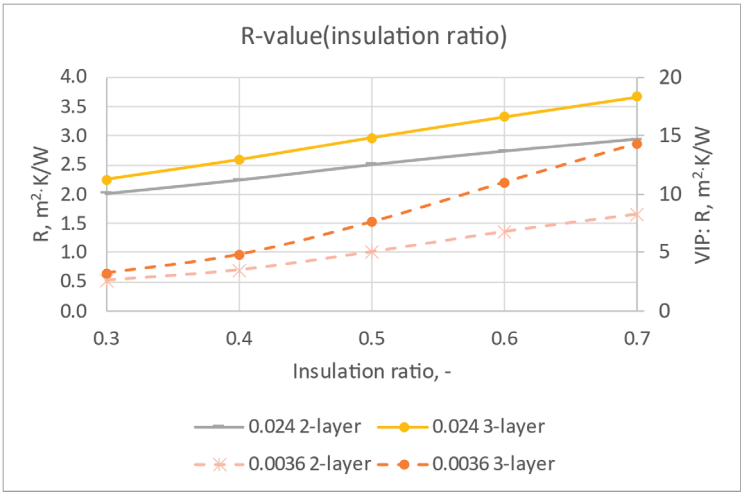

Figure 7. Comparison of the system R-value with k = 0.0036 W/m·K and k = 0.024 W/m·K insulation staggered in CLTs' two and three insulation lamellae.

Table 5. Volume fraction of insulation (%) in the insulated CLTs.

	Volume Percentage of Insulation, %	
Insulation Ratio, -	**2-Ply**	**3-Ply**
0.3	12%	18%
0.4	16%	24%
0.5	20%	30%
0.6	24%	36%
0.7	28%	42%

3.4. Validating Simulations with an Experimental Test

Simulations can provide theoretical values that are not necessarily replicated in real assemblies due to imperfections such as gaps between components. To validate that the simulations mimic reality, we tested one assembly with insulation in three lamellae of a five-ply CLT in a heat flow meter apparatus for a sample size of 610 mm × 610 mm. The assembly had three solid 203 mm wide wood layers of 16.7 mm thick on top and bottom. Out of the three 19.1 mm middle layers, the top and middle layers had 33% insulation in a staggered fashion (insulation ratio = 0.33) (Figure 8). The bottom 19.1 mm layer has 2/3 insulation of the total area. The total thickness of the assembly was 90.5 mm.

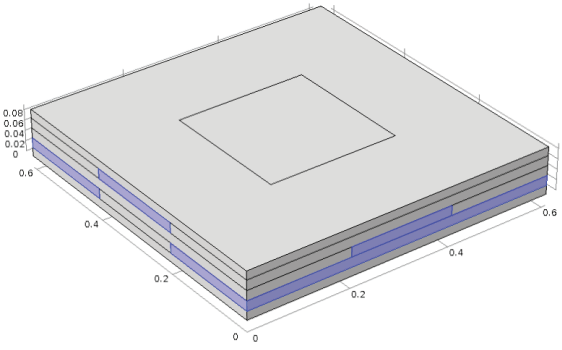

Figure 8. The assembly for comparing the effective R-value based on heat flow meter results to simulated performance. The top square area shows where heat flux is measured and outputted in the simulation for comparison.

The insulation's thermal conductivity was measured in the heat flow meter and was found to be 0.033 W/m·K. The thermal conductivity of the wood was not measured but assumed to be 0.11 W/m·K. The materials and assembly were tested using a FOX 600 heat flow meter with an absolute thermal conductivity accuracy of ±1% and reproducibility of ±0.5%. The heat flow meter measures the heat flow in the center of the surfaces in an area of 254 mm × 254 mm (Figure 8). The tested and simulated steady-state results are shown in Table 6 for a temperature difference of 22.2 K at an average temperature of 23.9 °C. The difference between the simulated and tested results is small, less than 2%, indicating that the simulations provide accurate predictions.

Table 6. Simulated and tested heat flow meter results for an insulated CLT panel.

Area	Measured Heat Flux W/m^2	Simulated Heat Flux W/m^2	Difference between Simulated and Measured
Top 254 mm × 254 mm	14.42	14.68	+1.8%
Bottom 254 mm × 254 mm	15.27	15.57	+1.9%
Total area 0.61 m × 0.62 m		17.00	N/A
Overall R-value for 0.61 m × 0.61 m area		1.31	N/A

3.5. Dynamic Calculations

The thermal mass inherent in construction materials facilitates the absorption and storage of heat, adapting to fluctuating environmental conditions. The integration of heat capacity and thermal conductivity modulates the heat transfer rate through the material, thereby attenuating the intensity of peak thermal fluxes. The effect of thermal mass is well characterized in homogeneous material layers. The insulated CLT panels have staggered internal layers, and the dynamic performance is not as easy to estimate without advanced modeling. We simulated the transient response of the uninsulated and insulated CLT panels of the same thickness to show the impact of the insulation on the time delay and magnitude

of the heat flux on the interior side when the panel was exposed to sine wave temperature on the exterior side. The sine wave had a 24 h cycle, which could be expected in natural weather exposure in buildings. The exterior and interior surface had a convection heat transfer coefficient of 10 W/m^2K.

The simulations were conducted for the staggered two-layer insulation system with an insulation ratio of 0.5 and a thermal conductivity of insulation 0.024 W/m·K. Five systems were simulated with the same overall thickness of 175 mm:

1. Solid CLT panel
2. Staggered two-layer insulated CLT panel
3. CLT panel with continuous insulation on the exterior side
4. CLT panel with continuous insulation in the middle of the panel
5. CLT panel with continuous insulation on the interior side

Figure 9 shows how the insulation layers in the CLT panel lower the heat flux through the panel while still providing the same long time delay for the peak (~12 h). Shifting the peak heat flux from the daytime to night reduces energy use during peak demand hours, typically in the afternoon and evening hours for cooling climates.

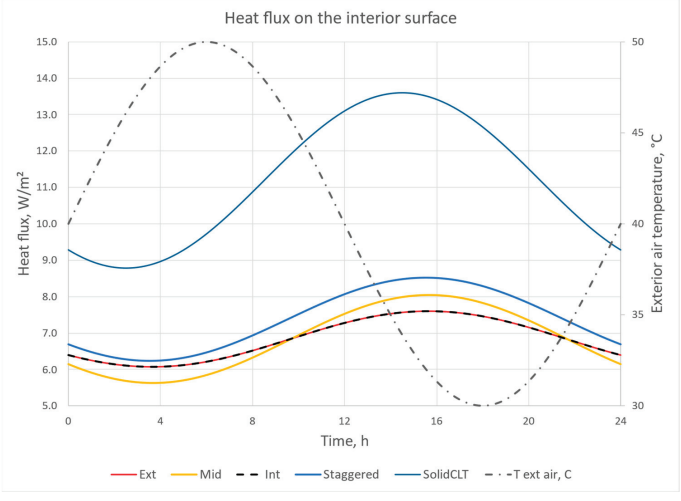

Figure 9. Heat flux on the interior surface under dynamic conditions for the uninsulated and insulated CLT panels.

3.6. Targeted Thermal Performance

The integration of insulation within Cross-Laminated Timber (CLT) panels represents a significant advancement in construction technology. It aligns with rigorous building codes for thermal performance without necessitating additional insulation applications on-site. Our study evaluates the compatibility of these innovative hybrid CLT panels with the 2021 International Residential Code (IRC) [10], focusing on the mandated insulation R-value and U-value requirements across diverse International Energy Conservation Code (IECC) climate zones (Table 7).

According to the IRC, walls possessing a thermal mass exceeding 123 $kJ/m^2 \cdot K$ are classified as mass walls within the thermal envelope of a building. The IECC standards for commercial buildings set this threshold at 103 $kJ/m^2 \cdot K$ for materials weighing under 1900 kg/m^3. Our analysis indicates that 175 mm thick CLT panels, comprised of solid wood, have a thermal mass of 164 $kJ/m^2 \cdot K$, qualifying them as mass walls. Notably, embedding insulation up to 25% by volume within these panels does not affect their classification as mass walls in residential constructions. However, this percentage might vary depending on the wood used in the CLT panels.

Table 7. Thermal requirements for mass walls in IRC 2021 [10] (Tables R402.1.3 and R402.1.2) and in IECC 2021 Table C402.1.4 for commercial buildings Group R (residential) [11]. Dual units are given to show original content as written in the building codes. The SI units have been converted from IP.

Climate Zone	Mass Wall R-Value * $ft^2 \cdot °F \cdot h/Btu$ ($m^2 \cdot K/W$)	Mass Wall U-Value $Btu/ft^2 \cdot °F \cdot h$ ($W/m^2 \cdot K$)	Frame Wall U-Value $Btu/ft^2 \cdot °F \cdot h$ ($W/m^2 \cdot K$)	Commercial Buildings Mass Wall U-Value, Group R $Btu/ft^2 \cdot °F \cdot h$ ($W/m^2 \cdot K$)
0	3/4 (0.53/0.70)	0.197 (1.12)	0.084 (0.47)	0.151 (0.86)
1	3/4 (0.53/0.70)	0.197 (1.12)	0.084 (0.47)	0.151 (0.86)
2	4/6 (0.70/1.06)	0.165 (0.94)	0.084 (0.47)	0.123 (0.70)
3	8/13 (1.41/2.29)	0.098 (0.56)	0.060 (0.34)	0.104 (0.59)
4 except marine	8/13 (1.41/2.29)	0.098 (0.56)	0.045 (0.26)	0.104 (0.59)
5 and marine 4	13/17 (2.29/2.99)	0.082 (0.47)	0.045 (0.26)	0.080 (0.45)
6	15/20 (2.64/3.52)	0.060 (0.34)	0.045 (0.26)	0.071 (0.04)
7	19/21 (3.35/3.70)	0.057 (0.32)	0.045 (0.26)	0.071 (0.04)
8	19/21 (3.35/3.70)	0.057 (0.32)	0.045 (0.26)	0.037 (0.21)

* The second R-value applies when more than 50% of insulation is on the interior of the mass wall.

From a thermal performance standpoint, a 175 mm thick uninsulated CLT panel, with a thermal conductivity of 0.11 W/m·K, achieves an R-value of 1.6 $m^2 \cdot K/W$. This results in a U-value of 0.63 $W/m^2 \cdot K$, meeting the IECC requirements for climate zones 0 to 2. Thus, the superior thermal efficiency of wood is underscored.

Further analysis of insulated CLT configurations, such as a two-layer staggered arrangement with 20% insulation volume of k = 0.024 W/m·K insulation, revealed an R-value of 2.5 $m^2 \cdot K/W$. A similar three-layer configuration yielded an R-value of 2.4 $m^2 \cdot K/W$, with the two-layer system's improved thermal efficiency mainly due to reduced thermal bridging. The U-value for the two-layer insulated system was calculated at 0.40 $W/m^2 \cdot K$, demonstrating that hybrid CLT panels can meet building code requirements across a broad range of climate zones.

Including additional layers, such as gypsum boards and exterior sidings, along with surface resistances, can further enhance thermal resistance by at least R-0.35 $m^2 \cdot K/W$, leading to a U-value of 0.34 $W/m^2 \cdot K$. This is adequate for meeting the thermal requirements of climate zone 6 for mass walls and zones 0 to 3 for frame walls. Increasing the insulation ratio to 28% of the total volume, with an insulation thermal conductivity of 0.024 W/m·K, results in a U-value of approximately 0.30 $W/m^2 \cdot K$, fulfilling the insulation criteria for all climate zones for mass walls.

While traditional rigid foam insulations provide thermal conductivity down to 0.024 W/m·K, advanced materials like vacuum insulation panels offer higher insulation properties. However, these materials require protection from mechanical damage to maintain their insulating effectiveness. Embedding such panels within CLT structures can safeguard them, ensuring the durability and performance of the insulation.

3.7. Impact of CLT on Peak Demand

The impact of thermal mass on peak demand and annual energy use for heating and cooling was predicted by using a whole-building simulation model, EnergyPlus [12]. EnergyPlus™ is a comprehensive building energy simulation program developed with contributions from several national labs and organizations under the funding and guidance of the U.S. Department of Energy (DOE). Since its inception in 1997, EnergyPlus has been subject to continuous updates and enhancements, reflecting the latest in building energy modeling research and technology.

DOE has created prototype building models for EnergyPlus for different types of buildings [13]. For the simulations, we chose a three-story multifamily building (Figure 10) with a heat pump for heating and cooling in Knoxville, TN. Of the total building area, 3623 m^2, 2007 m^2 is conditioned. The base model has features, such as the exterior wall construction, per the International Energy Conservation Code 2021. The base model with

the lightweight wall assembly was modified by replacing the wood-frame structure with an insulated CLT assembly while maintaining the U-value of 0.271 W/m^2·K. No other changes were made to the model inputs except changing the location and weather file to Knoxville, TN. Thus, all the equipment, internal loads, occupancy schedules, and set points were preserved. The wall layers and their properties are listed in Table 8. Note that EnergyPlus treats wall assemblies as one-dimensional components. The two-dimensional staggered system must be simplified to a three-layer setup with half the thickness of CLT on each side of an insulation layer. Columns LW and CLT show which layers are part of the lightweight and CLT wall assemblies.

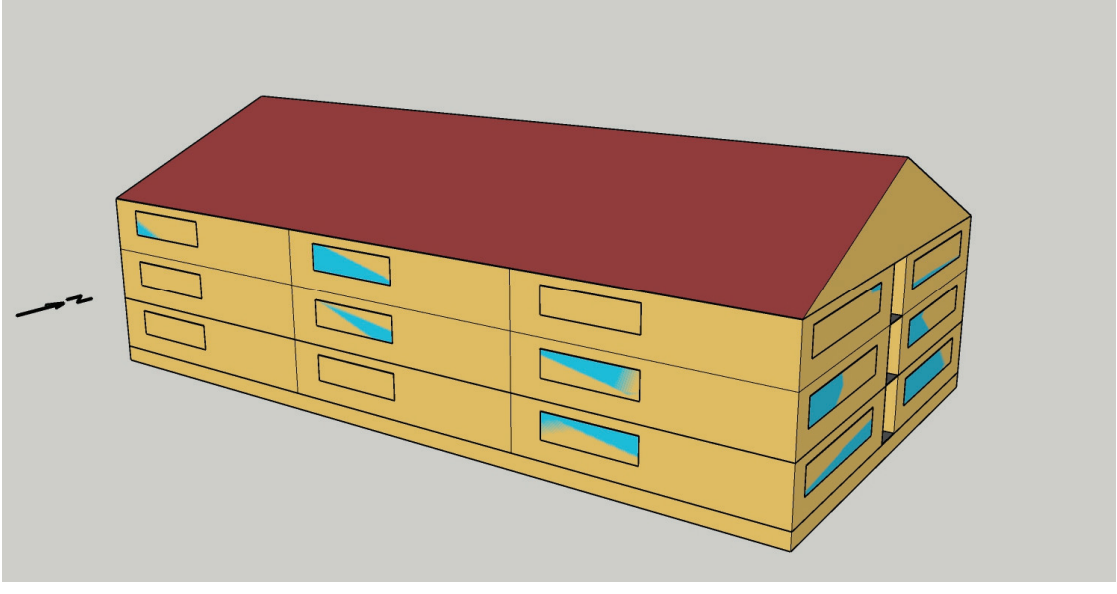

Figure 10. Multifamily building as modeled in EnergyPlus software.

Table 8. Wall assembly details for the base case (lightweight wall) and the mass wall (insulated CLT) with effective layer properties, including thermal bridges.

Layer from Outside to Inside	LW	CLT	Thickness (mm)	Density (kg/m^3)	Specific Heat Capacity (J/kg·K)	Thermal Conductivity (W/m·K)
Synthetic stucco	X	X	3	400	879	0.087
Insulation	X		31	20	1465	0.035
Oriented StrandBoard	X		11	545	1213	0.116
Half CLT		X	67	500	1880	0.110
Insulation		X	40	20	1200	0.018
Half CLT		X	67	500	1880	0.110
Wood Framed Cavity	X		140	121	1036	0.057
Gypsum Board	X	X	13	801	1089	0.16

The annual energy consumption for heating and cooling exhibited a reduction of 2.4% when employing the Cross-Laminated Timber (CLT) wall assembly, compared to the lightweight construction. Specifically, the building outfitted with CLT walls recorded an electricity usage of 53,215 kWh, whereas the structure with lightweight walls accounted for 54,500 kWh. Figure 11 delineates the diurnal heating demand, identifying a morning peak where the CLT wall assembly facilitates a 5.2% decrease in heating requirements

compared to its lightweight counterpart. Figure 12 illustrates the cooling demand patterns during August, pinpointing the peak cooling load. Notably, in August, the CLT wall assembly demonstrated a 7.1% reduction in peak cooling demand relative to the lightweight construction, underscoring its efficiency in thermal management.

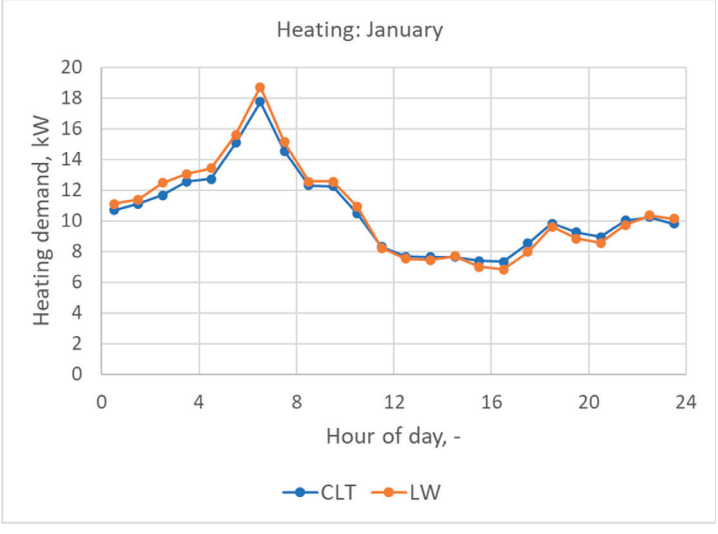

Figure 11. Heating demand on average for each hour in January.

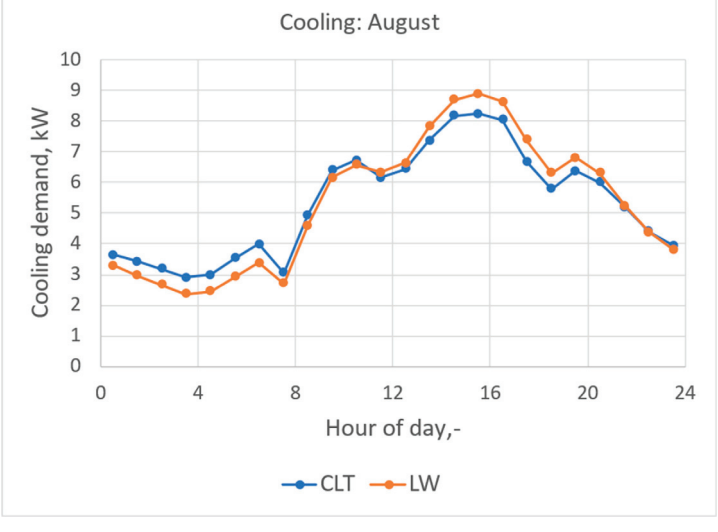

Figure 12. Cooling demand on average for each hour in August.

The results show that the CLT wall assembly dampens the heat flows through the exterior wall and flattens the heating and cooling demand between night and day. For example, the CLT building has higher cooling demand at night but lower in the afternoon and evening.

3.8. Carbon Benefits of the Insulated CLT

Considering sequestered carbon in the embodied carbon calculations for mass timber and Cross-Laminated Timber (CLT) is a topic of ongoing debate within the sustainability and construction communities. Trees absorb carbon dioxide from the atmosphere as they grow, known as carbon sequestration. When trees are harvested and used in building materials like mass timber and CLT, that carbon is effectively stored in the built environment, potentially for decades or centuries. Including sequestered carbon in embodied carbon calculations acknowledges this benefit and can show mass timber and CLT as more sustainable options than materials like steel or concrete, which have higher embodied carbon and do not sequester carbon.

Accounting for sequestered carbon adds complexity to embodied carbon calculations due to the need to consider factors like the source of the timber, forest management practices, and the likelihood of the carbon being released back into the atmosphere at the end of the product's life (e.g., through decay or combustion). These factors can vary widely and introduce uncertainty into the calculations. There is a risk that the same sequestered carbon could be counted multiple times in different products or accounting systems, leading to overestimating the actual carbon benefits. For example, if the carbon sequestered by a forest is counted in national carbon inventories, counting it again in the embodied carbon of timber products could lead to double counting. The carbon stored in mass timber and CLT will eventually be released back into the atmosphere when the material decomposes or is burned at the end of its life. Unless there are guarantees that the material will be reused, recycled, or permanently sequestered, including sequestered carbon in embodied calculations could give a misleading impression of the material's long-term environmental impact.

The impact of internally insulated CLT on carbon released to the atmosphere is multifaceted, involving considerations of operational and embodied carbon, carbon sequestration, construction efficiency, and end-of-life scenarios. The overall impact will depend on factors such as the choice of insulation materials, the energy sources used during the building's operation, and the practices for managing the building materials at the end of their life. Substituting some wood layers with insulation material will alter the embodied carbon of the CLT panels. The net effect on embodied carbon will depend on the type of insulation material used. If the insulation is made from materials with low embodied carbon, the overall embodied carbon of the insulated CLT panels may be lower than standard CLT panels. Conversely, if the insulation material has high embodied carbon (e.g., certain foams or plastics), it could increase the total embodied carbon of the panels. The pre-installation of water-resistive barriers and the integration of insulation can streamline the construction process, reducing the time and potentially the energy required on-site. This efficiency can lead to lower carbon emissions associated with construction activities.

Improved energy efficiency in buildings can reduce the overall energy demand, potentially leading to decreased carbon emissions at a larger scale within the energy grid, assuming a mix of fossil fuels and renewable energy sources.

On a negative note, non-wood materials (like insulation and water-resistive barriers) within the CLT panels could complicate recycling or reuse at the end of the building's life, potentially leading to higher carbon emissions associated with waste processing or disposal. However, the impact could be mitigated if these materials are selected for recyclability or systems are in place for recovery.

4. Discussion

This paper presents a novel method for enhancing the thermal efficiency of Cross-Laminated Timber (CLT) panels, which are traditionally characterized by their low thermal resistance. By embedding high-performance insulation within the CLT framework in a staggered arrangement, this approach not only preserves the structural integrity of the CLT panels but also significantly boosts their thermal insulation capabilities. This innovative technique streamlines the construction process by diminishing the need for additional

insulation and water-resistive barriers to be applied on-site. The research assesses the impact of this integrated CLT-insulation system on the building's energy performance and carbon footprint, juxtaposing it with conventional construction materials. The findings underscore the dual benefits of this system in enhancing energy efficiency during the building's operational phase and reducing embodied carbon, thereby underscoring its potential to advance more ecologically responsible construction methodologies.

This study highlights the potential of hybrid CLT panels with integrated insulation to streamline construction processes and enhance thermal performance, aligning with energy conservation goals outlined in building codes. Future work will involve detailed species-specific analysis to further optimize this innovative building solution. Additionally, the structural and fire performance requirements must be evaluated to comply with the code referenced ANSI/APA PRG 320: Standard for Performance-Rated Cross-Laminated Timber to allow the use of novel products in buildings [14].

5. Conclusions

This paper explored the development and performance evaluation of partially insulated Cross-Laminated Timber (CLT) panels, integrating high-performance insulation within the panel structure to enhance thermal efficiency without compromising structural integrity. Through a comprehensive literature review, we identified a gap in existing research regarding the thermal optimization of CLT panels. We addressed this by proposing an innovative configuration incorporating hollow or insulated core layers. Experimental results demonstrated that these modified CLT panels meet and exceed current thermal performance standards, offering a viable solution for energy-efficient, sustainable construction. The discussion highlighted the broader implications of our findings for the construction industry, particularly in terms of meeting stringent energy codes and sustainability goals. Our conclusions underline the potential of insulated CLT panels to revolutionize building practices, emphasizing the need for further research into long-term performance, cost analysis, and adaptability to various climatic conditions. This study contributes to the growing body of knowledge on sustainable building materials and paves the way for future innovations in green construction.

Author Contributions: Conceptualization, M.S. and A.D.; methodology, M.S.; validation, M.S.; formal analysis, M.S.; investigation, M.S. and A.D.; resources, M.S. and A.D.; data curation, M.S.; writing—original draft preparation, M.S.; supervision, A.D. All authors have read and agreed to the published version of the manuscript.

Funding: This manuscript has been authored in part by UT-Battelle, LLC, under contract DE-AC05-00OR22725 with the US Department of Energy (DOE). The publisher acknowledges the US government license to provide public access under the DOE Public Access Plan (http://energy.gov/downloads/doe-public-access-plan, accessed on 12 April 2024).

Data Availability Statement: Data are contained within the article.

Acknowledgments: Jonathan Cole's efforts to do the testing are greatly appreciated.

Conflicts of Interest: The funders had no role in the design of the study; in the collection, analyses, or interpretation of data; in the writing of the manuscript; or in the decision to publish the results.

References

1. U.S. Department of Energy. Decarbonizing the U.S. Economy by 2050. Office of Energy Efficiency & Renewable Energy. Available online: https://www.energy.gov/eere/articles/decarbonizing-us-economy-2050 (accessed on 4 April 2024).
2. Cabral, M.R.; Blanchet, P. A state of the Art of the Overall Energy Efficiency of Wood Buildings—An Overview and Future Possibilities. *Materials* **2021**, *14*, 1848. [CrossRef] [PubMed]
3. Salonvaara, M.; Iffa, E.; Desjarlais, A.O.; Atchley, J. *Impact of Mass Wood Walls on Building Energy Use, Peak Demand, and Thermal Comfort*; Oak Ridge National Laboratory (ORNL): Oak Ridge, TN, USA, 2022.
4. Setter, L.; Smoorenburg, E.; Wijesuriya, S.; Tabares-Velasco, P.C. Energy and hygrothermal performance of cross laminated timber single-family homes subjected to constant and variable electric rates. *J. Build. Eng.* **2019**, *25*, 100784. [CrossRef]

5. Ren, H.; Bahrami, A.; Cehlin, M.; Wallhagen, M. Literature Review on Development and Implementation of Cross-Laminated Timber. In Proceedings of the 5th International Conference on Building Energy and Environment. COBEE 2022. Environmental Science and Engineering, Montreal, QC, Canada, 25–29 July 2022; Wang, L.L., Ge, H., Zhai, Z.J., Qi, D., Ouf, M., Sun, C., Wang, D., Eds.; Springer: Singapore, 2023. [CrossRef]
6. Santos, P.; Correia, J.R.; Godinho, L.; Dias, A.M.P.G.; Dias, A. Life cycle analysis of cross-insulated timber panels. *Structures* **2021**, *31*, 1311–1324. [CrossRef]
7. Santos, P.; Sousa, L.; Godinho, L.; João, R.; Correia, A.M.P.G. Dias, Acoustic and thermal behaviour of cross-insulated timber panels. *J. Build. Eng.* **2021**, *44*, 103309. [CrossRef]
8. Huang, H.; Lin, X.; Zhang, J.; Wu, Z.; Wang, C.; Wang, B.J. Performance of the hollow-core cross-laminated timber (HC-CLT) floor under human-induced vibration. *Structures* **2021**, *32*, 1481–1491. [CrossRef]
9. *COMSOL Multiphysics®*, version 6.2; COMSOL AB: Stockholm, Sweden, 2023. Available online: www.comsol.com (accessed on 1 December 2023).
10. International Code Council. *2021 International Residential Code (IRC)*; International Code Council: Falls Church, VA, USA, 2021.
11. International Code Council. *2021 International Energy Conservation Code (IECC)*; International Code Council: Falls Church, VA, USA, 2021.
12. National Renewable Energy Laboratory (NREL); Lawrence Berkeley National Laboratory (LBNL); Oak Ridge National Laboratory (ORNL). *EnergyPlus, Version 23.1*; U.S. Department of Energy: Washington, DC, USA, 2023. Available online: https://energyplus.net/ (accessed on 1 May 2023).
13. U.S. Department of Energy. Prototype building models. Building Energy Codes Program. Available online: https://www.energycodes.gov/prototype-building-models (accessed on 4 April 2024).
14. *2018 ANSI/APA PRG 320*; Standard for Performance-Rated Cross-Laminated Timber. American National Standard Institute: Washington, DC, USA, 2018. Available online: https://www.apawood.org/ansi-apa-prg-320 (accessed on 15 March 2024).

buildings

MDPI

Article

Energy Efficiency Analysis of Building Envelope Renovation and Photovoltaic System in a High-Rise Hotel Building in Indonesia

Leni Sagita Riantini [1], Rossy Armyn Machfudiyanto [1,*], Titi Sari Nurul Rachmawati [1], Mochamad Daffa Alfiansyah Rachman [1], Reza Fachrizal [2] and Farshid Shadram [3]

[1] Department of Civil and Environmental Engineering, Faculty of Engineering, Universitas Indonesia, Depok 16424, Indonesia; lsagita@eng.ui.ac.id (L.S.R.); titisarinurul@ui.ac.id (T.S.N.R.); daffaalfiansyah99@gmail.com (M.D.A.R.)
[2] Future Energy Center, Mälardalen University, Universitetsplan 1, 72220 Västerås, Sweden; reza.fachrizal@mdu.se
[3] Division of Civil Engineering and Built Environment, Department of Civil and Industrial Engineering, Uppsala University, 75237 Uppsala, Sweden; farshid.shadram@angstrom.uu.se
* Correspondence: rossyarmyn@eng.ui.ac.id

Abstract: The development of high-rise buildings worldwide has given rise to significant concerns regarding their excessive electricity consumption. Among the various categories of high-rise structures, hotels used for business and conferences stand out as particularly extravagant in their energy use. The consequence arising from excessive energy usage is an escalation in carbon emissions, which is a primary driver of global warming. Therefore, this study aims to investigate the energy use intensity (EUI) of a hotel building located in Jakarta, Indonesia. In order to improve energy performance, this study explored various options for renovating the building envelope, such as incorporating insulation and a roof covering, as well as implementing building-integrated photovoltaics (BIPV). The building envelope renovations demonstrated a notable reduction in energy use by 15.8–27.7% per year. BIPV, such as curtain walls and double-skin façades, generated an energy use reduction of 4.8–8.6% per year. Remarkably, by combining the two approaches (i.e., adding insulation and a roof covering in the building envelope and adopting BIPV as double-skin façades), the potential reduction in energy use reached up to 32.2% per year. The findings can assist decision-makers in developing building renovation strategies for high-rise buildings while considering energy conservation.

Keywords: building integrated photovoltaics; energy use intensity; energy analysis; BIM

Citation: Riantini, L.S.; Machfudiyanto, R.A.; Rachmawati, T.S.N.; Rachman, M.D.A.; Fachrizal, R.; Shadram, F. Energy Efficiency Analysis of Building Envelope Renovation and Photovoltaic System in a High-Rise Hotel Building in Indonesia. *Buildings* **2024**, *14*, 1646. https://doi.org/10.3390/buildings14061646

Academic Editors: Sungkyun Jung, Piljae Im and Yeobeom Yoon

Received: 26 April 2024
Revised: 27 May 2024
Accepted: 30 May 2024
Published: 3 June 2024

1. Introduction

Buildings use a significant amount of energy, comprising approximately 40% of overall energy usage [1]. The 2021 United Nations Climate Change Conference (COP 26) highlighted the crucial role of buildings in climate action, emphasizing the requirement to cut emissions by 50% by the year 2030 through building energy efficiency [2]. In particular, high-rise buildings require enormous electricity consumption throughout operational periods, which increases carbon emissions, leading to environmental issues [3]. Among the various types of high-rise buildings, hotels are ranked as the highest energy-intensive structures, alongside shopping centers and office buildings [4]. As hotels use more energy compared to other commercial buildings [5], it is essential to improve energy performance in hotels to minimize their environmental impacts.

Two main strategies that can be implemented for such buildings are building envelope renovation and building-integrated photovoltaics (BIPV) installation. Building envelope renovation aims to reduce the energy demands of buildings, while BIPV installation aims to provide additional opportunities for energy generation. BIPV has the potential to transform the hotel industry by lowering energy expenses; enhancing hotels' sustainable image,

giving them a competitive edge; and contributing additional value towards achieving green building certification

Typically, the evaluation standard for investigating building energy use is the Energy Use Intensity (EUI) value, which is the ratio of energy used to the building's gross floor area [3]. The EUI value, expressed in units of (kWh/(m^2·year)), quantifies the annual energy used (kWh) per square meter of building area (m^2) [6]. The impact of both strategies on influencing the EUI value is commonly assessed using building information modeling (BIM) tools such as Revit for building modeling and Insight 360 for EUI value analysis [7]. BIM enables the rapid analysis of energy performance across numerous design alternatives, proving particularly advantageous during the initial design phase of new buildings or the retrofitting design phase of existing buildings [8].

The approaches of these two renovation strategies differ significantly, with building envelope renovations focusing on enhancing thermal performance to resist heat transfer between the warmer and colder environments within a building [9], while BIPV installation hinges on the self-generation of renewable energy. These two strategies can function independently or in combination. As per Ochoa and Capeluto [10], integrating both passive building envelope renovations and BIPV strategies can yield a reliable energy reduction ranging from 50% to 55%, surpassing the savings achieved by implementing individual active features or passive design strategies alone. Therefore, this study aims to explore the potential for reducing EUI values by considering building envelope renovation and BIPV strategies independently and in combination.

1.1. Building Envelope Renovation Strategies

A building envelope consists of elements such as the walls, fenestration, foundations, roof, shading devices, etc., which separate indoor and outdoor environments [11]. The building envelope plays a vital role in regulating the temperature within indoor spaces [12]. Among the modifiable components of a building envelope, insulation stands out as the most effective and primary contributor to energy savings [13,14].

Correct utilization of thermal insulation within the building envelope proves to be the most efficient approach in diminishing the heat transmission rate and lowering energy consumption for heating and cooling internal spaces [15]. Adequate thermal insulation can notably decrease the annual cooling load and peak cooling demands for buildings situated in hot regions (both dry and humid) [16]. The factors considered in choosing insulation materials include material properties, material thickness, availability, ease of application, life-cycle cost, climate condition, and energy-saving rate [17].

The properties that influence insulation materials include thermal conductivity, thermal resistance, thermal transmittance, etc. [18]. The U-value (thermal transmittance), measured in W/m^2·K, represents the overall heat flow coefficient, indicating the rate of heat transfer through one square meter of a building component with a 1-degree Kelvin temperature gradient. On the other hand, the R-value (unit: m^2·K/W), the thermal resistance, is the inverse of the U-value and is crucial in insulation selection [19]. To be effectively integrated and operate efficiently within the building's design, it is essential to attain low U-values in the building envelope [20].

In tropical climates, thermal insulation can be advantageous by maintaining cooler indoor temperatures through the reduction of heat transfer from the outside to inside [21]. Insulation helps in reducing the load on cooling systems, leading to energy savings. This is particularly relevant in regions with hot climates where air conditioning is commonly used [22].

Currently, there are many types of insulation materials on the market, each with distinct thermal properties, material composition, and associated costs. Their application methods vary depending on the overall structures of walls and roofs. Some studies conducted analysis using various insulation materials in tropical climate [23–25]. A study conducted in Maldives examined the potential for cost savings and emission reductions through the installation of various insulation materials at the optimal thickness in building

walls [23]. The research revealed that using fiberglass (rigid) and fiberglass urethane (roof deck) at their ideal thicknesses could decrease fuel consumption by over 77%. Another study explored the application of extruded polystyrene (XPS) in two common wall structures, concrete blocks and compressed stabilized earth blocks, in Cameroon [24]. The research revealed that the orientation of the walls significantly influenced the optimal insulation thickness, consequently impacting energy savings.

A research project in Malaysia assessed the impact of ten different thermal insulation materials, including urethane, fiberglass, and XPS, on air-conditioning energy consumption for cooling purposes, considering the tropical climate [25]. The findings showed that energy savings ranged from 85 to 92%/m^2 depending on the insulation material at its optimal thickness. Finally, a study carried out in Iran focused on optimizing the thicknesses of various insulation materials and assessing them through life-cycle cost analysis [26]. Despite Iran not being situated in a tropical region, buildings in the country face substantial cooling demands. The study determined that as the thermal resistance of the insulation material increased, the cost of insulation also increased, but the cooling expenses decreased.

Roof technologies, alongside insulation, play a significant role in enhancing energy efficiency. Recent innovations, such as cool roofs and green roofs, have been employed in roof design to reduce cooling needs in buildings [27]. These strategies not only aid in conserving energy but also contribute to providing thermal comfort for occupants. One current approach suggests an optimum combination of surface reflectivity and insulation to maximize energy savings in buildings [28]. Among the various cool roof technologies and methods are reflective coatings, light-colored roofing materials, metal roofs, asphalt shingles, and roof ventilation.

1.2. BIPV Strategies

BIPV is an energy efficiency strategy that complements primary electrical energy with electricity generated from solar panels through energy conversion, which can reduce the use of fossil fuels and greenhouse gas emissions [29,30]. In its installations, BIPV integrates solar panels into building envelope components such as façades, roofs, and shading devices, rather than using separate mounting materials and spaces [31]. BIPV functions not only as an on-site electricity generator but also as an envelope material that can decrease the room temperature and save energy consumption for indoor lighting [32]. BIPV may act as additional layer, providing shading which therefore lowers the building's cooling demand [33].

Currently, semi-transparent BIPV modules are frequently employed to curtain walls and façades to allow sunlight into the building interior while still fulfilling their role in generating electricity [34]. Semi-transparent BIPV curtain walls and BIPV double-skin façades (DSF) are two examples of BIPV. Apart from preserving the amount and intensity of natural light that goes in, semi-transparent solar panels also increase the aesthetic value of buildings. Semi-transparent BIPV can be accomplished either by using transparent thin film or spacing opaque solar modules [35]. BIPV modules are comprised of PV cells arranged with gaps between them, enabling a portion of solar radiation to penetrate. This feature proves particularly valuable in situations where there is a need for decreased or filtered sunlight [36].

The use of BIPV on building envelopes has been proven to reduce building energy consumption. Several studies have incorporated BIPV into the curtain wall. Chen et al. [37] presented evidence that the incorporation of BIPV into building windows could mitigate cooling loads, resulting in substantial energy savings of up to 63.71%. An et al. [38] showed that BIPV on building windows reduced the heating and cooling load by 18.2% when compared to double-layer windows.

Regarding BIPV DSF, some studies have investigated its energy performance. Peng et al. [39] provided evidence demonstrating that implementing a BIPV double-skin façade (DSF) featuring semi-transparent PV modules resulted in a significant reduction (of approximately 50%) in net electricity usage. Additionally, Peng et al. [40] illustrated that a BIPV

DSF comprising a translucent amorphous silicon (a-Si) PV module and inward-opening windows offers a low solar heat gain coefficient (SHGC). Furthermore, Italos et al. [41] analyzed the energy performance pre- and post- an energy renovation that incorporated a BIPV DSF. The BIPV system contributed to around 26,706 kWh of electricity generation annually, covering 63% of the building's projected energy use. Lastly, a study by Aguacil et al. [42] evaluated a combination of passive, active, and BIPV strategies for energy saving using a multi-criteria evaluation approach. This research revealed that the combined implementation of these strategies achieved energy savings of over 89%.

1.3. Aims and Scope

Few studies have focused on the impact of retrofitting strategies for high-rise hotel buildings, which are among the most energy-intensive buildings worldwide. One novel aspect of this research is that it addresses the existing gap in the literature, focusing specifically on the relatively limited retrofit studies of hotels. Another novel aspect of this study is the hotel building's location and Indonesia's unique climatic conditions as an equatorial country. In such regions, due to the consistent cooling demands throughout the year, the potential to minimize energy use through retrofitting strategies (both passive and active) is underrepresented in the existing literature. This makes the research a valuable contribution to reducing the energy demand in buildings located in equatorial countries. Therefore, this study aims to investigate the potential for reducing EUI in a high-rise hotel building in Indonesia through building envelope renovation and BIPV strategies. Three strategies were defined: (1) building envelope renovation by adding insulation materials to walls and roof; (2) semi-transparent BIPV installation in the form of curtain walls and double-skin façades; and (3) the combination of the first and second strategies.

Each strategy was subdivided into multiple sub-scenarios, with slight variations introduced in each of the sub-scenarios. The results of this study are expected to assist designers in planning the optimum building envelope renovation strategies for high-rise buildings while attaining the ideal EUI value for low-carbon buildings.

The structure of this paper is outlined as follows: Section 2 includes data from a hotel building case study along with the process of developing building envelope and BIPV installation strategies. Section 3 presents the resulting EUI values for each scenario and their comparison. Section 4 discusses the results and possibilities for future studies. Section 5 presents the conclusions of the research.

2. Methodology

2.1. Case Study Hotel

Indonesia, situated in Southeast Asia, possesses a tropical rainforest climate characterized by consistent high temperatures, humidity, and abundant rainfall throughout the year. The temperature typically ranges from 23 °C to 32 °C. Due to the hot and humid conditions, a significant portion of electricity, approximately 50–60%, is consumed for cooling and ventilation purposes [43]. Urban areas such as Jakarta heavily rely on heating, ventilation, and air conditioning (HVAC) systems, which contribute substantially to electricity consumption.

The selected case study is a high-rise hotel located in Jakarta, Indonesia, which was chosen due to Jakarta having 11% of the total hotel units in Indonesia [44]. Figure 1 shows the hotel from front and rear views. The selected hotel consisted of 21 floors, and the total building area of 9320 m^2 (44.4 m in length and 26.35 m in width) served as a suitable representative of Indonesian hotels. The guest rooms, lobby, and convention hall of the hotel were designed to use a centralized air conditioning system for temperature control convenience. The remaining spaces utilized a single-mounted or exhaust fan due to lower population density, making a targeted cooling approach more feasible and effective.

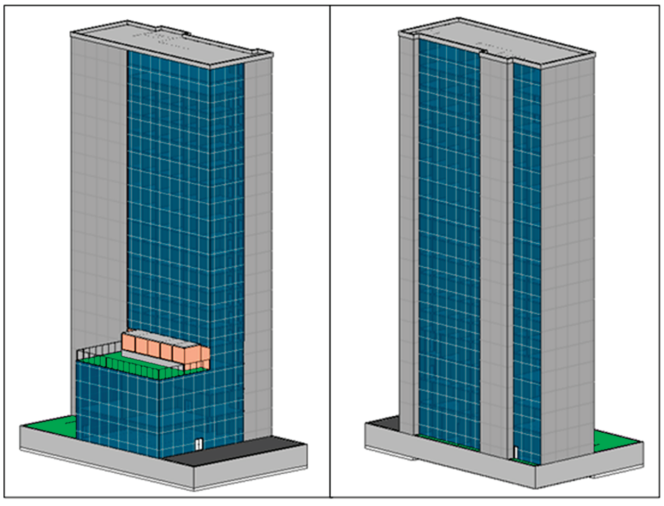

Figure 1. 3D view of building model in Autodesk Revit: (**a**) front view; (**b**) rear view.

The initial modeling of the case study was referred to as the base case, representing the existing condition without any improvement. The building components of the hotel were assembled in Revit using the default settings, with slight adjustments made to comply with Indonesia's standards. Table 1 presents the characteristics of the building components of the case study.

Table 1. Initial characteristics of building components of the case study.

No.	Building Part	Building Products
1	Basement wall	Cement plaster 15 mm Cast in situ 400 mm
2	Interior walls	Light brick 100 mm Cement plaster 15 mm Frame partition with 19 mm gypsum board Adding soft board for both inner coverings
3	Exterior walls	Lightweight concrete 200 mm—no insulation Cement plaster 15 mm Adding aluminium composite panel for outer coverings panel and soft board for inner coverings
4	Curtain wall	Double glazed with reflective coating 30 mm
5	Ceilings	Lightweight concrete 200 mm—no insulation Cement plaster 15 mm Frame partition with 19 mm gypsum board
6	Flat roof deck	Cement plaster 15 mm 100 mm lightweight concrete-no insulation
7	Room floor	Cement plaster 15 mm 100 mm lightweight concrete—no insulation Adding ceramic tile and carpet tile

2.2. Research Framework

The framework of this study is outlined in Figure 2. The workflow consists of three steps: (1) model preparation of initial design, (2) development of renovation scenarios related to passive building envelope and BIPV strategies, (3) combination scenario of

passive and BIPV strategies. In the first step, the base case was built using BIM software (Autodesk Revit 2023.1). Material type and thickness, building dimension, building location, and weather data were obtained from the existing data of the hotel building study case. After the BIM model was developed, the EUI of the initial design was calculated using Insight 360. Then, renovation scenarios were developed, which were denoted as Scenarios A, B, and C for passive renovation strategies and Scenario D for BIPV installation. Scenario A emphasized adding building envelope insulation to walls, Scenario B focused on the addition of a roof covering, Scenario C was a combination of Scenarios A and B, and Scenario D was the implementation of BIPV installation. Lastly, optimal passive strategies were combined with BIPV application to obtain the maximum possible EUI reduction. This combination strategy was referred to as Scenario E.

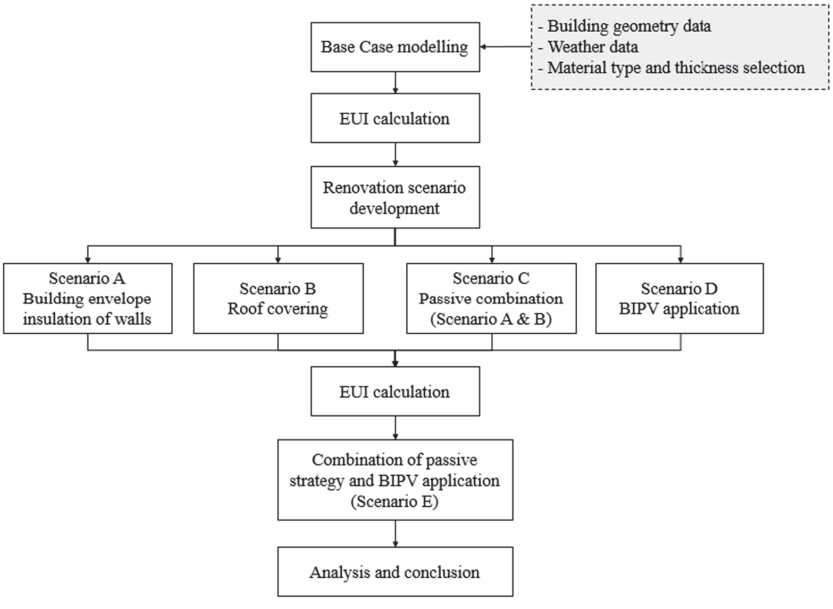

Figure 2. Research methodology.

2.3. Scenario Development

As mentioned earlier, the developed scenarios for this study are the base case, four individual scenarios, and one combination scenario. The EUI calculation for the base case was conducted in three phases: modelling, zone setting, and EUI calculation. In the modelling phase, the model was built based on existing data for the hotel building (see Table 1) and also from studies conducted by Fitriani et al. [45] and Berawi et al. [46]. In the zone setting phase, each room (or thermal zone) in the building was defined by its type, such as guest room, meeting room, etc. In the third phase, the EUI calculation was performed using Insight 360.

Scenarios A, B, and C were related to building envelope renovation, whereas Scenario D was related to BIPV application. Scenario A involved the addition of insulation to the building envelope, where the building envelope was modified by incorporating an additional insulation layer with three different material types (all having the same thickness): A1, A2, and A3. These insulations were 50 mm of polyurethane foam (PU), fiberglass batt, and extruded polystyrene (XPS) for A1, A2, and A3, respectively. The thickness of 50 mm was chosen to maintain the thickness of the existing wall. If the insulator was thicker than 50 mm, it would reduce the room size. Furthermore, in Scenario A, the previous curtain wall was replaced with triple energy-efficient glazing to improve energy performance.

Scenario B concentrated on building envelope renovation through the addition of roof coverings. Two types of renovation were developed in Scenario B: the application of reflective white paint and the incorporation of asphalt, designated as Scenarios B1 and B2, respectively. Meanwhile, Scenario C was a combination of Scenarios A and B, which entailed the installation of building envelope insulation and improvement of the roof coverings. As a result of Scenarios A and B being integrated, six distinct renovation configurations (3 × 2) were obtained in Scenario C.

Scenario D involved the application of an integrated solar panel system, referred to as BIPV, at two distinct building parts, namely the southeast (SE) and northeast (NE) sides of the hotel. BIPV was only modeled on the SE and NE sides of the building due to surrounding buildings that had been built on the west side of the building. The calculation of PV generation was performed using the solar analysis feature of Revit. A 13.3% panel efficiency was set due to the use of semi-transparent solar panels. The average efficiency value of 13.3% is derived from the efficiencies reported in two studies: 12.4% in the study by Zhao et al. [47] and 14.3% in the study by Wong et al. [48]. Lastly, the average for solar radiation was set to 2–6 kWh/m^2 [49].

Scenario D encompassed two primary configurations: semi-transparent BIPV integrated within curtain wall panels and semi-transparent BIPV employed as a double-skin façade, designated as Scenarios D1 and D2, respectively. Within Scenario D2, an aluminum mullion frame was utilized as the second façade layer, assuming its robust capacity to sustain the semi-transparent solar panels, which were attached to the glazing panels. Both D1 and D2 utilized the exact same dimensions of semi-transparent solar panels, measuring 1 m × 2 m. Moreover, Scenarios D1 and D2 shared an equivalent installation area of 882 m^2 for the NE side and 360 m^2 for the SE side. The depiction of BIPV installation for Scenarios D1 and D2 is shown in Figure 3.

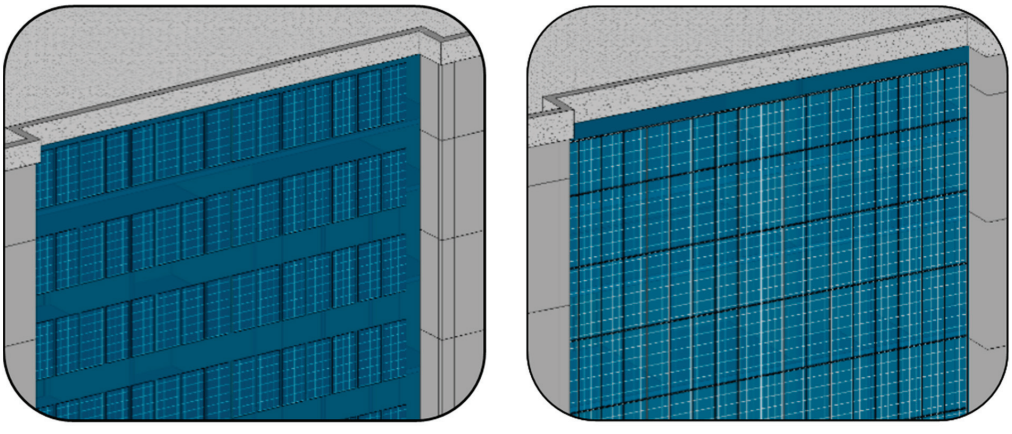

Figure 3. (**a**) Scenario D1 with BIPV integrated within curtain wall panels; (**b**) Scenario D2 with BIPV as double-skin façade.

Finally, the best passive strategies (from Scenario A to Scenario C) were merged with the most effective BIPV strategies (Scenario D) to form a combined scenario, called Scenario E.

2.4. EUI Calculation

For the renovation scenarios of the building envelope (Scenarios A, B, and C), the final EUI is obtained by conducting simulation in Insight 360 3.0. The software directly displays the final EUI results by doing calculations as shown in Equation (1). Equation (1) achieves

EUI calculation (kWh/m^2·year) by considering annual energy use (kWh/year) and total area of building (m^2).

$$EUI_{scenario} = \frac{Annual\ Energy\ Use}{Area} \quad (1)$$

For the analysis, EUI percentage reduction is calculated by comparing the EUI results from each scenario with the EUI value of the base case. The calculation is conducted by dividing the difference between the EUI of each scenario and the EUI of the base case by the EUI of the base case, as shown in Equation (2).

$$EUI_{\%\ reduction} = \frac{EUI_{base\ case} - EUI_{scenario}}{EUI_{base\ case}} \times 100\% \quad (2)$$

Meanwhile, EUI calculation for Scenario D, which implements BIPV, requires several steps. The first step is to determine the building's electricity consumption after installing solar panels, which might differ from the EUI of the base case. The calculation is performed using Equation (1). The second step is finding the production of solar panels. Equation (3) shows PV output (kWh/m^2·year) considering energy production (kWh/year) and area of building (m^2).

$$PV_{output} = \frac{Energy_{production}}{Area_{building}} \quad (3)$$

Third, the final EUI of the BIPV scenario was obtained by subtracting the building's electricity consumption from the solar panel production, as shows in Equation (4). Finally, the reduction percentage compared to the base case was calculated as shown in Equation (2).

$$EUI_{final} = EUI_{initial} - PV_{output} \quad (4)$$

3. Results

After establishing the baseline condition, the simulation outcomes for the base case yielded an EUI value of 336.7 kWh/m^2·year. This value acted as a base value for the EUI reduction percentage of the four analyzed scenarios (Scenarios A–D).

Scenario A involved the addition of building insulation material, with 50 mm PU foam in A1, fiberglass batt in A2, and XPS in A3. The thermal conductivity (unit: W/m·K) of these insulation materials is considered to be 0.022 [50], 0.032 [51], and 0.036 [52,53], respectively.

The EUI results, calculated using Equation (1) by dividing the annual energy consumption by the total building area, are shown in Insight 360 and summarized in Table 2. The selected hotel has a total building area of 9320 m^2. From Scenario A, Scenario A1 (addition of 50 mm PU foam) achieved the lowest EUI value (275.8 kWh/m^2·year). Using Equation (2) to compare the EUI value with the EUI of the base case, Scenario A1 achieved the highest percentage reduction in EUI, which was 18.1%. This suggests that the use of PU foam, which has the lowest thermal conductivity value, produced the lowest EUI value among other scenarios related to building wall renovation. The low thermal conductivity of PU foam enables the minimization of transmission losses and thus results in a lower U-value, even when using the exact same thickness. Scenario A1, A2, and A3 yielded a U-value of 0.155, 0.199, and 0.213 W/m^2·K, respectively.

The roof coverings used in Scenario B were a reflective coating in B1 and asphalt shingle in B2. The results of the EUI calculation for scenario B are summarized in Table 3. The thermal conductivity (unit: W/m·K) of these roof coverings is 0.63 [54] for reflective coating and 1.594 for asphalt shingle [55]. The EUI value for Scenario B1 demonstrated the reflective capabilities of using a reflective coating, efficiently deflecting heat from sunlight. Meanwhile, the asphalt layer in Scenario B2 tended to absorb solar heat due to its higher emissivity compared to Scenario B1. This indicates that energy demand is affected not only by material thickness and thermal conductivity but also by the material's capacity to reflect solar heat. As a result, the reflective coating from Scenario B1 yielded a lower EUI

value and a higher EUI percentage reduction than the asphalt shingle from Scenario B2. Furthermore, Scenario B1 yielded a U-value of 0.549 W/m^2·K, while Scenario B2 showed a U-value of 0.553 W/m^2·K. Consistently with Scenario A, a lower U-value for roof coverings also resulted in a higher EUI reduction.

Table 2. Thermal conductivity, U-value, and EUI calculation results of Scenario A.

Scenario	Material	Thermal Conductivity (W/m·K)	U-Value (W/m^2·K)	Annual Energy Use (kWh/year)	EUI Value (kWh/m^2·year)	EUI Reduction to Base Case (%)
A1	Polyurethane foam	0.022	0.155	2,570,456	275.8	18.1%
A2	Fiberglass batt	0.032	0.199	2,582,572	277.1	17.7%
A3	Extruded Polystyrene (XPS)	0.036	0.213	2,585,368	277.4	17.6%

Table 3. Thermal conductivity, U-value, and EUI calculation results of Scenario B.

Scenario	Material	Thermal Conductivity (W/m·K)	U-Value (W/m^2·K)	Annual Energy Use (kWh/year)	EUI Value (kWh/m^2·year)	EUI Reduction to Base Case (%)
B1	Reflective coating	0.630	0.549	2,595,154	278.45	17.3%
B2	Asphalt shingle	1.594	0.553	2,644,643	283.76	15.8%

Scenario C is the combination of Scenarios A and B; the results are summarized in Table 4. There was no notable difference in the EUI values between Scenarios A and B. However, combining Scenarios A and B into Scenario C resulted in a significantly reduced final EUI value when compared to the base case's EUI value. Scenario C1, which was the combination of PU foam insulation on the walls and roof and a reflective coating, produced the lowest EUI of 243.4 kWh/m^2·year and an EUI reduction percentage of 27.7%. This was due to both materials having the lowest thermal conductivity.

Table 4. EUI calculation results for Scenario C.

Scenario	Description	Annual Energy Use (kWh/year)	EUI Value (kWh/m^2/year)	EUI Reduction to Base Case (%)
C1	PU foam + reflective coating	2,268,488	243.4	27.7%
C2	PU foam + asphalt	2,280,604	244.7	27.3%
C3	Fiberglass + reflective coating	2,307,632	247.6	26.5%
C4	Fiberglass + asphalt	2,311,360	248.0	26.4%
C5	XPS + reflective coating	2,315,088	248.4	26.2%
C6	XPS + asphalt	2,326,272	249.6	25.9%

In Scenario D, BIPV was implemented as curtain walls (Scenario D1) and as double-skin façades (Scenario D2); the results are summarized in Table 5. The PV output results for both scenarios are the same because they use the same type of panels and the same area of coverage. The BIPV system generated 142 MWh annually. Dividing this by the building's area (9320 m^2) yields a PV output of 15.24 kWh/m^2·year. The distinction between Scenarios D1 and D2 lies in their initial EUI values. Scenarios D1 and D2 yield initial EUI values of 335.6 and 322.9 kWh/m^2·year, respectively. The lower initial EUI value in Scenario D2 is due to the shading caused by the solar panels acting as façades being more impactful compared to the solar panels acting as curtain walls. The final EUI values for the BIPV scenarios were calculated by considering the initial EUI value and the energy generated from BIPV, as outlined in Equation 4. Therefore, Scenarios D1 and D2 yielded final EUI

values of 320.3 kWh/m^2·year and 307.6 kWh/m^2·year, respectively. This corresponds to EUI reductions of 4.8% for D1 and 8.6% for D2 compared to the base case.

Table 5. EUI calculation results of Scenario D.

Scenario D	Description	PV Output (kWh/m^2·year)	Initial EUI Value (kWh/m^2·year)	Final EUI Value (kWh/m^2·year)	EUI Reduction to Base Case (%)
D1	BIPV as curtain walls	15.24	335.6	320.3	4.8%
D2	BIPV as double-skin façades	15.24	322.9	307.6	8.6%

The EUI values for Scenario C can be further reduced with the implementation of BIPV, as demonstrated by the results of Scenario D. To achieve the maximum EUI reduction, this study combined the optimum scenarios from both passive building envelope strategies and BIPV strategies. Specifically, the optimal among the passive strategies is Scenario C, particularly Scenario C1, while the best among the BIPV strategies is Scenario D2. In the calculation of the combined scenario, named Scenario E, the final EUI value of Scenario C1 was adjusted with the PV output from Scenario D2, resulting in 228.16 kWh/m^2·year. When compared to the EUI value of the base case (336.73 kWh/m^2·year), this equates to a 32.2% reduction in energy use.

Figures 4 and 5 display the compilation of EUI values and the percentage reduction in EUI from Scenarios A–E compared to the base case's EUI value. From Figures 4 and 5, it is evident that renovating building walls or roof coverings individually has a more significant impact on reduction of EUI than installing BIPV alone. However, when these efforts are combined in Scenario E, the maximum reduction in energy use is achieved. This phenomenon can be attributed to several factors. Firstly, renovating the building envelope can address all sides of the building, whereas BIPV installations are limited to the NE and SE sides due to the proximity of adjacent buildings. Secondly, given the extensive building area of 9320 m^2, the energy production from BIPV, when divided by the total building area, results in a PV output of 15.24 kWh/m^2·year. This output does not significantly offset the hotel's high energy demand.

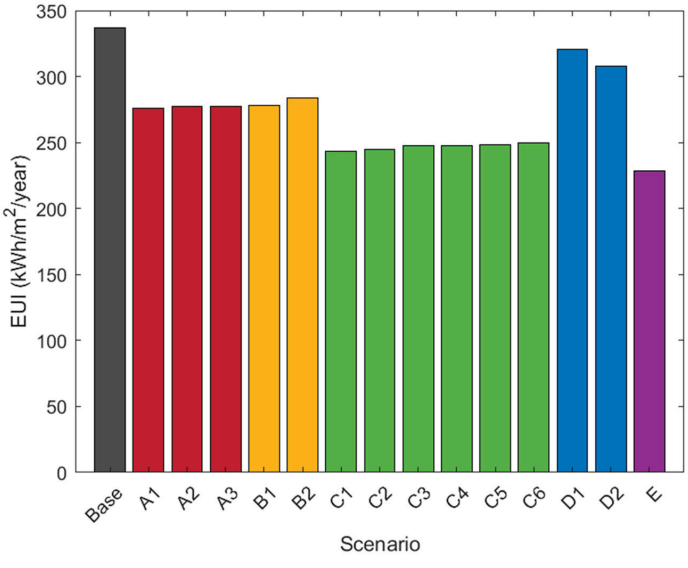

Figure 4. Compilation of EUI values of the base case and Scenarios A–D.

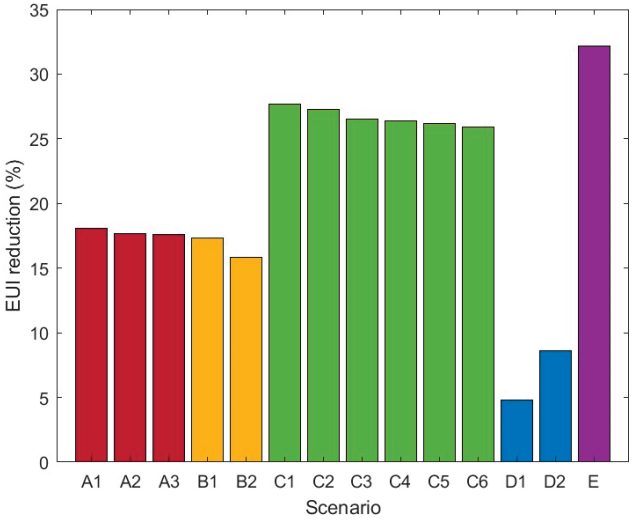

Figure 5. Compilation of EUI reduction (in percentage) from Scenarios A–E compared to the base case's EUI value.

4. Discussion

The energy analysis results showed differences in approaches between passive envelope renovation strategies and BIPV implementation in reducing EUI values in a high-rise hotel building in Indonesia. Passive renovation minimizes heat transfer and, thus, energy use through wall insulation and roof coverings. Additionally, insulating the building envelope can mitigate structural damage risks from moisture, reduce material waste, and extend building lifespan, as shown by Cusenza et al. [56]. Meanwhile, integrating PV systems into a building not only generates clean energy and reduces electricity usage but also enhances property value and elevates architectural appeal, as demonstrated by Polo López et al. [57]. The combination of passive strategies and BIPV implementation, as explored in this study, yielded the most significant EUI reduction. Specifically, integrating 50 mm PU foam insulation into the building envelope, applying a reflective coating on the roof, and implementing BIPV as a double-skin façade emerged as the most effective strategy, achieving up to a 32.2% reduction in EUI.

A direct relationship was observed between the thermal properties of materials and EUI reduction. Thermal properties influence U-values, which regulate heat transfer and, consequently, lower EUI. In Scenario A, PU foam stood out for its heat transfer control, leading to a considerable EUI reduction. Scenario B benefited from reflective coating that, due to low emissivity, effectively reflected heat. As a result, the combination of PU foam insulation in the building envelope and a reflective coating on roof in Scenario C showed the most substantial EUI reduction, though this finding requires experimental validation. Future research could thus include prototype testing to evaluate the performance of various insulation materials and roof coverings.

Incorporating a PV system into the northeast and southeast of the building, as seen in Scenarios D1 and D2, contributed to a reduction in the building's EUI. BIPV, by efficiently generating electricity, present a practical alternative to conventional energy sources. Specifically, in Scenario D2, utilizing BIPV as a double-skin façade (DSF) was more effective in lowering EUI than its application on the curtain wall in Scenario D1. The enhanced efficiency observed in Scenario D2 is primarily due to the shading conferred by the additional layer of BIPV as double-skin façade, which effectively mitigates solar heat gain, thereby lowering the building's cooling demands. In contrast, Scenario D1, featuring BIPV on the curtain wall, fails to offer sufficient shading, which could have contributed to a reduction

in cooling and energy demands. Thus, utilizing a BIPV double-skin façade in Scenario D2 leads to a more significant reduction in EUI, despite using the same solar panels and the same area for installation.

Nonetheless, installing BIPV on all sides of a building poses significant financial considerations. Solar panel initiatives demand substantial investment, as reported by Hajir et al. [58], who spent approximately 635 million IDR on 80 solar panel modules for a manufacturing facility. Based on this investment, the current study, which used nearly 600 semi-transparent panel modules, would face renovation expenses of around 4.7 billion IDR for BIPV installation. Additionally, Gholami et al. [59] highlighted the lengthy payback period for BIPV projects, which can extend up to 22 years. Given that the PV output from BIPV fell short of meeting the building's energy demands, the main challenge with BIPV lies in its high investment costs and a prolonged payback period. Hence, further research is required to explore the life-cycle cost–benefits of BIPV as well as the combined life-cycle cost–benefits of integrating passive strategies with BIPV.

5. Conclusions

This study highlights the advantages of BIPV applications and building envelope renovations that use insulation materials and roof coverings to reduce energy use for a high-rise hotel building in Indonesia. Scenarios A1–A3 explored different insulation materials, including PU foam, fiberglass batt, and XPS, while Scenarios B1–B2 investigated roofing materials such as reflective coatings and asphalt shingle. The findings indicated that PU foam (used in Scenario A) was the most effective insulation material for building envelopes for minimizing heat transfer, and reflective coating (used in Scenario B) was identified as the optimal roofing material due to its high sunlight reflectivity. U-values, significantly affected by thermal properties and material emissivity, were key in determining EUI outcomes. The study found that combining 50 mm PU foam in the building envelope with a reflective coating on the roof yielded the lowest EUI value for the building case in Scenario C. Regarding renewable strategies, the study analyzed the integration of PV systems on the building's curtain wall in Scenario D1 and as a double-skin façade in Scenario D2. The results demonstrated that while both scenarios produced the same amount of energy (15 kWh/m^2.year), integrating BIPV as a double-skin façade achieved a more substantial reduction in EUI value (8.6%) compared to the curtain wall BIPV. This significant reduction was attributed to the shading benefits provided by the double-skin façade BIPV, which effectively minimized solar heat gain and, consequently, the building's cooling demand. Finally, to explore the maximum EUI reduction for the case study building, the most effective passive strategy from Scenario C was combined with the leading renewable strategy from Scenario D. This synergistic strategy involved incorporating 50 mm PU foam insulation into the building envelope, applying a reflective coating on the roof, and installing BIPV as a double-skin façade on the building's northeast and southeast faces. This holistic approach led to a significant EUI reduction of 32.2%.

Author Contributions: Conceptualization, L.S.R., R.A.M., T.S.N.R. and M.D.A.R.; methodology, M.D.A.R.; software, M.D.A.R.; validation, T.S.N.R., R.F. and F.S.; formal analysis, M.D.A.R. and T.S.N.R.; investigation, M.D.A.R. and T.S.N.R.; writing—original draft preparation, M.D.A.R. and T.S.N.R.; writing—review and editing, R.F. and F.S.; visualization, M.D.A.R., T.S.N.R. and R.F.; supervision, L.S.R., R.A.M., R.F. and F.S.; project administration, L.S.R. and R.A.M.; funding acquisition, L.S.R. and R.A.M. All authors have read and agreed to the published version of the manuscript.

Funding: This research was funded by the Directorate of Research and Development, Universitas Indonesia, under Hibah PUTI Q2 (Grant No. NKB-821/UN2.RST/HKP.05.00/2023).

Data Availability Statement: The original contributions presented in the study are included in the article, further inquiries can be directed to the corresponding authors.

Conflicts of Interest: The authors declare no conflicts of interests.

References

1. Cao, X.; Dai, X.; Liu, J. Building Energy-Consumption Status Worldwide and the State-of-the-Art Technologies for Zero-Energy Buildings during the Past Decade. *Energy Build.* **2016**, *128*, 198–213. [CrossRef]
2. World Green Building Council. Accelerating Deep Collaboration: 26 Built Environment Climate Action Initiatives Announced at COP26—World Green Building Council. 2022. Available online: https://worldgbc.org/article/accelerating-deep-collaboration-26-built-environment-climate-action-initiatives-announced-at-cop26/ (accessed on 31 March 2024).
3. Mahiwal, S.G.; Bhoi, M.K.; Bhatt, N. Evaluation of Energy Use Intensity (EUI) and Energy Cost of Commercial Building in India Using BIM Technology. *Asian J. Civ. Eng.* **2021**, *22*, 877–894. [CrossRef]
4. Gong, X.; Li, Y.; Cai, J.; Ma, Z.; He, S.; Pan, B.; Lei, X. A Statistical Analysis of Energy Consumption Survey of Public Buildings in a Hot Summer and Cold Winter Coastal Zone of China. *Buildings* **2023**, *13*, 2685. [CrossRef]
5. Pérez-Lombard, L.; Ortiz, J.; Pout, C. A Review on Buildings Energy Consumption Information. *Energy Build.* **2008**, *40*, 394–398. [CrossRef]
6. Wang, J.C. Analysis of Energy Use Intensity and Greenhouse Gas Emissions for Universities in Taiwan. *J. Clean. Prod.* **2019**, *241*, 118363. [CrossRef]
7. Maglad, A.M.; Houda, M.; Alrowais, R.; Khan, A.M.; Jameel, M.; Rehman, S.K.U.; Khan, H.; Javed, M.F.; Rehman, M.F. Bim-Based Energy Analysis and Optimization Using Insight 360 (Case Study). *Case Stud. Constr. Mater.* **2023**, *18*, e01755. [CrossRef]
8. Sanhudo, L.; Ramos, N.M.M.; Poças Martins, J.; Almeida, R.M.S.F.; Barreira, E.; Simões, M.L.; Cardoso, V. Building Information Modeling for Energy Retrofitting—A Review. *Renew. Sustain. Energy Rev.* **2018**, *89*, 249–260. [CrossRef]
9. Al-Saadi, S.N.J.; Budaiwi, I. Performance-based envelope design for residential buildings in hot climates. In Proceedings of the Building Simulation 2007: 10th Conference of IBPSA, Beijing, China, 27–30 July 2009.
10. Ochoa, C.E.; Capeluto, I.G. Strategic Decision-Making for Intelligent Buildings: Comparative Impact of Passive Design Strategies and Active Features in a Hot Climate. *Build. Environ.* **2008**, *43*, 1829–1839. [CrossRef]
11. Verma, R.; Rakshit, D. Comparison of Reflective Coating with Other Passive Strategies: A Climate Based Design and Optimization Study of Building Envelope. *Energy Build.* **2023**, *287*, 112973. [CrossRef]
12. Mohammad, S.; Shea, A. Performance Evaluation of Modern Building Thermal Envelope Designs in the Semi-Arid Continental Climate of Tehran. *Buildings* **2013**, *3*, 674–688. [CrossRef]
13. Dylewski, R.; Adamczyk, J. Economic and Environmental Benefits of Thermal Insulation of Building External Walls. *Build. Environ.* **2011**, *46*, 2615–2623. [CrossRef]
14. Al-Homoud, M.S. Performance Characteristics and Practical Applications of Common Building Thermal Insulation Materials. *Build. Environ.* **2005**, *40*, 353–366. [CrossRef]
15. Thani, S.K.S.O.; Mohamad, N.H.N.; Idilfitri, S. Modification of Urban Temperature in Hot-Humid Climate through Landscape Design Approach: A Review. *Procedia—Soc. Behav. Sci.* **2012**, *68*, 439–450. [CrossRef]
16. Wagner, I.; Zalewski, M. Ecohydrology as a Basis for the Sustainable City Strategic Planning: Focus on Lodz, Poland. *Rev. Environ. Sci. Bio/Technol.* **2009**, *8*, 209–217. [CrossRef]
17. Mirrahimi, S.; Mohamed, M.F.; Haw, L.C.; Ibrahim, N.L.N.; Yusoff, W.F.M.; Aflaki, A. The Effect of Building Envelope on the Thermal Comfort and Energy Saving for High-Rise Buildings in Hot–Humid Climate. *Renew. Sustain. Energy Rev.* **2016**, *53*, 1508–1519. [CrossRef]
18. Schiavoni, S.; D'Alessandro, F.; Bianchi, F.; Asdrubali, F. Insulation Materials for the Building Sector: A Review and Comparative Analysis. *Renew. Sustain. Energy Rev.* **2016**, *62*, 988–1011. [CrossRef]
19. Choi, D.S.; Ko, M.J. Analysis of Convergence Characteristics of Average Method Regulated by ISO 9869-1 for Evaluating In Situ Thermal Resistance and Thermal Transmittance of Opaque Exterior Walls. *Energies* **2019**, *12*, 1989. [CrossRef]
20. Jannat, N.; Hussien, A.; Abdullah, B.; Cotgrave, A. A Comparative Simulation Study of the Thermal Performances of the Building Envelope Wall Materials in the Tropics. *Sustainability* **2020**, *12*, 4892. [CrossRef]
21. Fang, Z.; Li, N.; Li, B.; Luo, G.; Huang, Y. The Effect of Building Envelope Insulation on Cooling Energy Consumption in Summer. *Energy Build.* **2014**, *77*, 197–205. [CrossRef]
22. Ahmadzadehtalatapeh, M. Determination of Optimum Insulation Thickness for Building Walls in Iran Using Life Cycle Cost Analysis. *J. Energy Eng. Manag.* **2021**, *10*, 30–43.
23. Mahlia, T.M.I.; Iqbal, A. Cost Benefits Analysis and Emission Reductions of Optimum Thickness and Air Gaps for Selected Insulation Materials for Building Walls in Maldives. *Energy* **2010**, *35*, 2242–2250. [CrossRef]
24. Kameni Nematchoua, M.; Ricciardi, P.; Reiter, S.; Yvon, A. A Comparative Study on Optimum Insulation Thickness of Walls and Energy Savings in Equatorial and Tropical Climate. *Int. J. Sustain. Built Environ.* **2017**, *6*, 170–182. [CrossRef]
25. Mahlia, T.M.I.; Ng, H.M.; Olofsson, T.; Andriyana, A.; Hasanuddin, I. Energy and cost savings of optimal thickness for selected insulation materials and air gaps for building walls in tropical climate. *Energy Educ. Sci. Technol. Part A-Energy Sci. Res.* **2012**, *29*, 549–662.
26. Rawat, M.; Singh, R.N. A Study on the Comparative Review of Cool Roof Thermal Performance in Various Regions. *Energy Built Environ.* **2022**, *3*, 327–347. [CrossRef]
27. Saafi, K.; Daouas, N. A Life-Cycle Cost Analysis for an Optimum Combination of Cool Coating and Thermal Insulation of Residential Building Roofs in Tunisia. *Energy* **2018**, *152*, 925–938. [CrossRef]

28. Aguacil, M.S.; Lufkin, S.; Rey, E. Influence of energy-use scenarios in Life-Cycle Analysis of renovation projects with Building Integrated Photovoltaics—Investigation through two case studies in Neuchâtel (Switzerland). In Proceedings of the International Conference for Sustainable Design of the Built Environment 2017, London, UK, 20–21 December 2017.
29. Fachrizal, R.; Lindberg, O.; Kinasih, A.D.S.; Muntean, A.; Widén, J.; Munkhammar, J. Residential Building with Rooftop Solar PV System, Battery Storage and Electric Vehicle Charging: Environmental Impact and Energy Matching Assessments for a Multi-Family House in a Swedish City. In Proceedings of the 21st Wind & Solar Integration Workshop (WIW 2022); Institution of Engineering and Technology: Hybrid Conference, The Hague, The Netherlands, 12–14 October 2022; pp. 565–572.
30. Putri, R.K.; Widhi Astuti, Y.D.R.; Wardhany, A.K.; Hudaya, C. Building Integrated Photovoltaic for Rooftop and Facade Application in Indonesia. In Proceedings of the 2018 2nd International Conference on Green Energy and Applications (ICGEA), Singapore, 24–26 March 2018; pp. 171–175.
31. Li, D.H.W.; Lam, T.N.T.; Chan, W.W.H.; Mak, A.H.L. Energy and Cost Analysis of Semi-Transparent Photovoltaic in Office Buildings. *Appl. Energy* **2009**, *86*, 722–729. [CrossRef]
32. Martín-Chivelet, N.; Kapsis, K.; Wilson, H.R.; Delisle, V.; Yang, R.; Olivieri, L.; Polo, J.; Eisenlohr, J.; Roy, B.; Maturi, L.; et al. Building-Integrated Photovoltaic (BIPV) Products and Systems: A Review of Energy-Related Behavior. *Energy Build.* **2022**, *262*, 111998. [CrossRef]
33. Yu, G.; Yang, H.; Luo, D.; Cheng, X.; Ansah, M.K. A Review on Developments and Researches of Building Integrated Photovoltaic (BIPV) Windows and Shading Blinds. *Renew. Sustain. Energy Rev.* **2021**, *149*, 111355. [CrossRef]
34. Chung, M.H.; Park, B.R.; Choi, E.J.; Choi, Y.J.; Lee, C.; Hong, J.; Cho, H.U.; Cho, J.H.; Moon, J.W. Performance Level Criteria for Semi-Transparent Photovoltaic Windows Based on Dye-Sensitized Solar Cells. *Sol. Energy Mater. Sol. Cells* **2020**, *217*, 110683. [CrossRef]
35. Abojela, Z.R.K.; Desa, M.K.M.; Sabry, A.H. Current Prospects of Building-Integrated Solar PV Systems and the Application of Bifacial PVs. *Front. Energy Res.* **2023**, *11*, 1164494. [CrossRef]
36. Kruglov, O. Design Methodology and Experimental Investigation of a Multiple-Inlet BIPV/T System in a Curtain Wall Facade Assembly and Roof Application. Master's Thesis, Concordia University, Montreal, QC, Canada, November 2018.
37. Chen, L.; Zheng, X.; Yang, J.; Yoon, J.H. Impact of BIPV Windows on Building Energy Consumption in Street Canyons: Model Development and Validation. *Energy Build.* **2021**, *249*, 111207. [CrossRef]
38. An, H.; Yoon, J.; An, Y.; Heo, E. Heating and Cooling Performance of Office Buildings with A-Si BIPV Windows Considering Operating Conditions in Temperate Climates: The Case of Korea. *Sustainability* **2018**, *10*, 4856. [CrossRef]
39. Peng, J.; Curcija, D.C.; Lu, L.; Selkowitz, S.E.; Yang, H.; Zhang, W. Numerical Investigation of the Energy Saving Potential of a Semi-Transparent Photovoltaic Double-Skin Facade in a Cool-Summer Mediterranean Climate. *Appl. Energy* **2016**, *165*, 345–356. [CrossRef]
40. Peng, J.; Lu, L.; Yang, H. An Experimental Study of the Thermal Performance of a Novel Photovoltaic Double-Skin Facade in Hong Kong. *Sol. Energy* **2013**, *97*, 293–304. [CrossRef]
41. Italos, C.; Patsias, M.; Yiangou, A.; Stavrinou, S.; Vassiliades, C. Use of Double Skin Façade with Building Integrated Solar Systems for an Energy Renovation of an Existing Building in Limassol, Cyprus: Energy Performance Analysis. *Energy Rep.* **2022**, *8*, 15144–15161. [CrossRef]
42. Aguacil, S.; Lufkin, S.; Rey, E. Architectural design scenarios with building-integrated photovoltaic solutions in renovation processes: Case study in Neuchâtel (Switzerland). In Proceedings of the International Conference on Passive and Low Energy Architecture. "PLEA 2016—Cities, Buildings, People: Towards Regenerative Environments, Proceedings of the 32nd International Conference on Passive and Low Energy Architecture", Los Angeles, CA, USA, 11–13 July 2016.
43. Katili, A.; Boukhanouf, R.; Wilson, R. Space Cooling in Buildings in Hot and Humid Climates—A Review of the Effect of Humidity on the Applicability of Existing Cooling Techniques. In Proceedings of the 14th International Conference on Sustainable Energy Technologies—SET 2015, Nottingham, UK, 25–27 August 2015.
44. Number of Accommodations, Rooms, and Beds Available in Classified Hotel 2020–2022. Available online: https://www.bps.go.id/id/statistics-table/2/MzA3IzI=/number-of-accommodations--rooms--and-beds-available-in-classified-hotel.html (accessed on 1 April 2024).
45. Fitriani, H.; Rifki, M.; Foralisa, M.; Muhtarom, A. Investigation of energy saving using building information modeling for building energy performance in office building. *Civ. Eng. Archit.* **2022**, *10*, 1280–1292. [CrossRef]
46. Berawi, M.A.; Sari, M.; Salsabila, A.A.; Susantono, B.; Woodhead, R. Utilizing Building Information Modelling in the Tax Assessment Process of Apartment Buildings. *Int. J. Technol.* **2022**, *13*, 1515. [CrossRef]
47. Zhao, Y.; Zhu, Y.; Cheng, H.-W.; Zheng, R.; Meng, D.; Yang, Y. A Review on Semitransparent Solar Cells for Agricultural Application. *Mater. Today Energy* **2021**, *22*, 100852. [CrossRef]
48. Wong, P.W.; Shimoda, Y.; Nonaka, M.; Inoue, M.; Mizuno, M. Semi-Transparent PV: Thermal Performance, Power Generation, Daylight Modelling and Energy Saving Potential in a Residential Application. *Renew. Energy* **2008**, *33*, 1024–1036. [CrossRef]
49. Climate Information for the Energy Sector. Available online: https://iklim.bmkg.go.id/bmkgadmin/storage/brosur/Leaflet%20Matahari.pdf (accessed on 27 May 2024).
50. Zhang, H.; Fang, W.-Z.; Li, Y.-M.; Tao, W.-Q. Experimental Study of the Thermal Conductivity of Polyurethane Foams. *Appl. Therm. Eng.* **2017**, *115*, 528–538. [CrossRef]

51. Cai, S.; Cremaschi, L.; Ghajar, A.J. Pipe Insulation Thermal Conductivity under Dry and Wet Condensing Conditions with Moisture Ingress: A Critical Review. *HVACR Res.* **2014**, *20*, 458–479. [CrossRef]
52. Jelle, B.P. Traditional, State-of-the-Art and Future Thermal Building Insulation Materials and Solutions—Properties, Requirements and Possibilities. *Energy Build.* **2011**, *43*, 2549–2563. [CrossRef]
53. Aksit, M.; Zhao, C.; Klose, B.; Kreger, K.; Schmidt, H.-W.; Altstädt, V. Extruded Polystyrene Foams with Enhanced Insulation and Mechanical Properties by a Benzene-Trisamide-Based Additive. *Polymers* **2019**, *11*, 268. [CrossRef] [PubMed]
54. Ligati, S.; Ohayon-Lavi, A.; Keyes, J.; Ziskind, G.; Regev, O. Enhancing Thermal Conductivity in Graphene-Loaded Paint: Effects of Phase Change, Rheology and Filler Size. *Int. J. Therm. Sci.* **2020**, *153*, 106381. [CrossRef]
55. Pan, P.; Wu, S.; Hu, X.; Liu, G.; Li, B. Effect of Material Composition and Environmental Condition on Thermal Characteristics of Conductive Asphalt Concrete. *Materials* **2017**, *10*, 218. [CrossRef] [PubMed]
56. Cusenza, M.A.; Gulotta, T.M.; Mistretta, M.; Cellura, M. Life Cycle Energy and Environmental Assessment of the Thermal Insulation Improvement in Residential Buildings. *Energies* **2021**, *14*, 3452. [CrossRef]
57. Polo López, C.S.; Troia, F.; Nocera, F. Photovoltaic BIPV Systems and Architectural Heritage: New Balance between Conservation and Transformation. An Assessment Method for Heritage Values Compatibility and Energy Benefits of Interventions. *Sustainability* **2021**, *13*, 5107. [CrossRef]
58. Hajir, N.; Haddin, M.; Suprajitno, A. Analysis of solar power rooftop generation planning with hybrid system at PT. *Koloni Timur Elektr.* **2022**, *14*, 20–25.
59. Gholami, H.; Nils Røstvik, H.; Manoj Kumar, N.; Chopra, S.S. Lifecycle Cost Analysis (LCCA) of Tailor-Made Building Integrated Photovoltaics (BIPV) Façade: Solsmaragden Case Study in Norway. *Sol. Energy* **2020**, *211*, 488–502. [CrossRef]

buildings

MDPI

Article

Research on the Current Situation and Calculation Method of Carbon Emissions Assessment for Building Curtain Walls

Xichen Zhang [1,2], Xiangqiu Fu [1,2,*], Xiuchun Zheng [2], Shunmou Li [1,2], Qian Zhao [2] and Jinjie Lin [2]

[1] State Key Laboratory of Building Safety and Built Environment, China Academy of Building Research, Beijing 100013, China; zhangxichen@cabr-bctc.com (X.Z.); lishunmou@cabr-bctc.com (S.L.)
[2] Jianke EET Co., Ltd., Beijing 100013, China; zhengxiuchun@cabr-bctc.com (X.Z.); zhaoqian@cabr-bctc.com (Q.Z.); linjinjie@cabr-bctc.com (J.L.)
* Correspondence: fuxiangqiu@cabr-bctc.com; Tel.: +86-188-1134-3143

Abstract: Curtain wall systems stand out as a pivotal domain within the construction sector's endeavors towards energy efficiency and carbon mitigation. To refine the evaluation framework for carbon emissions within this industry, this paper explores the calculation and assessment method for building curtain walls. The article first reviews the current research status regarding carbon emissions from materials and the impact of curtain walls on buildings in the operational stage. Based on lifecycle theory, the carbon emissions from building curtain walls are divided into six stages: material acquisition, processing and production, installation and construction, transportation, use and maintenance, and dismantling. On this basis, this paper proposes a method for calculating carbon emissions from building curtain walls. Following that, a case study is conducted using a specific glass curtain wall project for illustrative analysis. The results indicate that the carbon emissions from the material acquisition stage constitute approximately 90% of the total, serving as the primary source of carbon emissions for glass curtain walls. Furthermore, the scientific application of photovoltaics can significantly reduce the carbon emission levels of building curtain walls. Finally, an analysis was conducted on the current issues existing in the evaluation of carbon emissions.

Keywords: building curtain walls; building energy conservation; calculation method of carbon emission; life cycle theory; carbon emission evaluation

Citation: Zhang, X.; Fu, X.; Zheng, X.; Li, S.; Zhao, Q.; Lin, J. Research on the Current Situation and Calculation Method of Carbon Emissions Assessment for Building Curtain Walls. *Buildings* **2024**, *14*, 1647. https://doi.org/10.3390/buildings14061647

Academic Editors: Sungkyun Jung, Piljae Im and Yeobeom Yoon

Received: 28 April 2024
Revised: 26 May 2024
Accepted: 30 May 2024
Published: 3 June 2024

1. Introduction

To restrain global climate change and its negative impacts, 178 contracting parties worldwide jointly signed the Paris Agreement in 2015, which sets long-term goals that will guide all nations to achieve carbon neutrality [1,2]. The United States and the European Union plan to achieve carbon neutrality in 2050 [3,4]. China plans to reach a carbon peak before 2030 and carbon neutrality before 2060 [5]. The construction industry is one of the primary contributors to carbon emissions. In China, the total carbon emissions from the entire process of construction nationwide amounted to 40.7 billion tCO_2, accounting for 38.2% of the country's total carbon emissions in 2021 [6]. Worldwide, the building sector accounts for almost 38% of global energy-related carbon emissions, with at least 20% of these coming from the materials production industry [7].

Curtain walls are an important component of building carbon emissions, especially for public buildings. On the one hand, aluminum alloy and silicate glass, as the primary materials for building curtain walls, have high carbon emission factors. On the other hand, compared to the minimum service life of the main structure, which is usually around 50 years, the design lifespan of curtain walls is typically 25 years, implying the need for at least one retrofitting. According to research by the World Business Council for Sustainable Development on carbon emissions from different types of buildings, the embodied carbon emissions of external envelope structures account for approximately 10% to 31% of the total construction carbon emissions [8]. Therefore, the calculation and

evaluation of carbon emissions from building curtain walls are of significant importance to the construction industry.

Currently, two main types of commonly used carbon accounting methods exist. The first one is the "bottom-up" model, which is based on process analysis and is also known as Life Cycle Assessment (LCA). It serves as the core theory for calculating and evaluating carbon emissions in the construction field. The second is the "up-bottom" model, which is based on input-output analysis and is mainly applicable to the economic sector. The LCA method has garnered recognition with several high-profile accounting standards. Examples include the first global accounting standard, the *Greenhouse Gas Protocol*, developed by the World Resources Institute (WRI), and the *IPCC Guidelines for National Greenhouse Gas Inventories* by the Intergovernmental Panel on Climate Change (IPCC). These standards have contributed to the formation of two widely influential life cycle assessment theoretical frameworks: SETAC and ISO. In recent years, many scholars have conducted research on the accounting and analysis of the complete lifecycle of carbon emissions of buildings using methods such as input-output analysis [9,10] or LCA [11–13]. In 2019, China released the national standard GB/T 51366-2019 *Standard for Calculation of Building Carbon Emissions* [14], which divides building carbon emissions into the operational stage, the construction and dismantling stage, and the building materials production and transportation stage. The standard specifies detailed calculation methods to guide carbon emission calculations in the construction sector. However, for non-structural components such as curtain walls, there are still many gaps in carbon emission calculations.

As non-structural components, curtain walls differ significantly from the main structure in terms of construction methods, material usage, and engineering calculations. Firstly, the weight of the non-structural curtain wall components is relatively small compared to the main structural system, while the area is large. Therefore, area-based units are more appropriate than mass-based units for carbon emission calculations. Secondly, carbon emissions from the main structural system mainly consider major materials such as steel and concrete, making it difficult to account for small components within curtain walls, which are crucial for the curtain wall industry. Additionally, the carbon emission calculation for the main structural system makes it difficult to compare carbon emissions for different types of curtain walls. Therefore, there is a lack of specific carbon emission calculation methods for building curtain walls.

To fill the gap in carbon emission calculation methods for building curtain walls and guide the development of carbon emission evaluation and reduction strategies, this study summarizes the current status of carbon emissions from building curtain walls. Based on the LCA theory and the GB/T 51366-2019 *Standard for Calculation of Building Carbon Emissions* [14], a method for calculating carbon emissions from building curtain walls was proposed, in which the carbon emission was divided into six stages: material acquisition, processing and production, transportation, installation and construction, use and maintenance, and dismantling. For the convenience of application in curtain walls, the carbon emission calculation method in this paper uses area (m^2) as the benchmark unit. Then, a glass curtain wall project was analyzed as a case study, detailing the process of a carbon emission calculation. Finally, the main issues in the current research and evaluation work were analyzed in this paper, and suggestions were made for addressing these problems and proposing directions for future development.

2. Research Status of Carbon Emissions from Building Curtain Walls

2.1. Material Carbon Emissions

During the operational phase of buildings, curtain walls contribute negligibly to carbon emissions. Therefore, the contribution of building curtain walls to carbon emissions primarily occurs during the construction phase, especially due to the embodied carbon emissions of building materials. Categorized by panel materials, curtain walls encompass glass, metal, stone, and artificial board varieties. The construction of curtain walls varies

in accordance with the architectural form, necessitating the determination of material quantities specific to each project.

Currently, the curtain wall market is still predominantly occupied by glass curtain walls. These mainly comprise aluminum alloy framework profiles, insulating tempered glass panels, and sealing materials. According to rough estimates provided by the U.S. Department of Energy [15], the embodied energy of a standard aluminum alloy-framed glass curtain wall stands at 734.5 kWh/m^2, with a corresponding embodied CO_2 emission of 322.7 kg/m^2. Furthermore, scholars have extensively investigated the production processes and carbon emission levels associated with the frame materials of glass curtain walls [16,17], which include wood, aluminum, PVC, wood–aluminum composites, fiberglass, and others. By comparing glass curtain wall systems with different frame materials but identical specifications, Azari and Kim [18] found the carbon emission levels of frame curtain wall systems, from low to high, as follows: wood frame, steel frame, and aluminum alloy. The production of aluminum and its alloys, recognized as a high-energy and high-emission industry, emits greenhouse gases per unit product at rates 12.4 and 2.3 times higher than steel and copper [19], respectively. Aluminum alloy profiles remain predominant in glass curtain wall frameworks. Over 90% of their carbon emissions throughout the lifecycle originate from the production phase, specifically from ore to aluminum ingot, with surface corrosion treatments accounting for approximately 5%. Statistics indicate that China's carbon emission factor for electrolytic aluminum is around 11,200 kgCO_2e/t, significantly higher than Russia's at about 3300 kgCO_2e/t and the United States' at approximately 6900 kgCO_2e/t. As a comparison, the carbon emission factor of concrete C30 in building materials is 295 kgCO_2e/t, and the carbon emission factor of steel is 2050 kgCO_2e/t in China [14]. This substantial difference in carbon emission factors is attributed to the energy structure of aluminum production, with China relying mainly on thermal power and Russia on hydropower. Additionally, the process of extruding aluminum metal into aluminum profiles for glass curtain walls results in carbon emissions of approximately 11,131.04 kgCO_2e/t in China [20].

The carbon emissions throughout the lifecycle of glass panels mainly stem from the energy consumption in the production process, particularly from sand to float glass production, accounting for 80%. The deep processing process of tempered glass contributes 15%, while the remaining emissions arise from the assembly process of hollow glass. Yan et al. [21] investigated over 300 flat glass production lines in China and, based on 2015 production conditions, found that the carbon emissions per unit weight of boxed glass were approximately 52.46 kg, equivalent to 1049 kgCO_2e/t. Additionally, Yu et al. [22], based on extensive research data, determined that the carbon emissions for flat glass were 1130 kgCO_2e/t, tempered glass emissions were 1530 kgCO_2e/t, and laminated glass emissions were 1280 kgCO_2e/t. In addition to controlling carbon emissions during the production process, the recycling and utilization of materials are also effective ways to reduce glass carbon emissions. Statistics show that when the glass recycling rate reaches 50%, production process carbon emissions can be reduced by 42%, and when the recycling rate reaches 90%, production process carbon emissions can be reduced by 75% [23]. The efficiency of material recycling and reuse, in addition to the recycling rate, also depends on the quantity of raw materials produced, which is another major factor influencing the implicit carbon emission levels of building curtain walls. In 2019, China's waste flat glass production was 98.67 million tons, with a recovery of 59.16 million tons, yielding an almost 60% recovery rate, higher than the international level of 35%. Unfortunately, due to the lack of data on carbon emissions from the process of sand to glass liquid in glass production, it is difficult to estimate the contribution of glass recycling to carbon emission reduction.

Sealant, including silicone structural sealant, weather-resistant sealant, and secondary sealant for insulating glass, is another material widely used in glass curtain walls. According to industry data [24], Ethylene Propylene Diene Monomer emits 2670 kgCO_2e/t, while silicone sealant emits 2910 kgCO_2e/t. Despite their high carbon emission factors, sealant materials significantly improve curtain wall performance in energy conservation.

Compared to carbon dioxide released during production, silicone resin provides an average benefit nearly nine times higher before the end of its service life, with applications in insulating glass showing benefits exceeding 27 times.

In comparison to glass curtain walls, metal curtain walls exhibit a similarly significant level of carbon emissions. Industry data [24] suggests that 2 mm aluminum veneer emits around 159.6 $kgCO_2e/m^2$, equivalent to 29,600 $kgCO_2e/t$. In contrast, stone curtain walls have relatively lower carbon emissions. Zhao et al. [25] calculated that the carbon emissions during the production stage of 30 mm stone panels were only 18.75 $kgCO_2e/t$ when converted, owing to the low energy consumption inherent in the mechanical processing of stone materials. In recent years, the rapid development of artificial panel curtain walls, such as porcelain panels, ceramic panels, PC panels, and UHPC panels, has been observed. The carbon emissions during the production stage of UHPC panels are approximately 1245.84 $kgCO_2eq/m^3$, which is 1.58 times that of ordinary concrete. Despite the relatively high carbon emissions, artificial panel materials typically offer superior performance advantages. However, due to significant differences in the production processes of artificial panels, current carbon emission data remains incomplete.

The evaluation of embodied carbon emissions in building curtain walls should encompass not only the emissions generated during the material production phase but also integrate considerations of material longevity and recyclability. Currently, in China, the design lifespan of building curtain walls is 25 years, primarily limited by factors such as the surface corrosion resistance level of frame materials, the aging limit of sealants for insulating glass panels, and the fatigue performance of hardware systems in opening parts. Especially for organic sealant materials serving as sealing or structural connection functions, the industry generally recognizes a lifespan ranging from 10 to 25 years, directly determining the lifespan of building curtain wall systems. However, with technological advancements, the international community has been researching and achieving breakthroughs in the goal of achieving a 50-year lifespan for sealant materials [26]. Considering current engineering practices and technological levels, the requirement for building curtain wall materials to have the same lifespan as the system is realistic and feasible. This requirement can significantly reduce the carbon emission levels of building curtain walls caused by their lifespan.

According to the standards in China [14,24], the carbon emission data, which were mainly from comprehensive industry surveys, and crucial carbon emission factor data pertaining to primary materials have been scrutinized and compiled for the benefit of the industry, as delineated in Table 1.

Table 1. Carbon Emission Factors for Main Materials of Building Curtain Walls.

	Materials	Values	Units
Profile	Electrolytic aluminum	20,300	$kgCO_2e/t$
	Ordinary carbon steel	2050	$kgCO_2e/t$
	Hot-rolled carbon steel small-profiled sections	2310	$kgCO_2e/t$
	Hot-rolled medium-sized carbon steel profiles	2365	$kgCO_2e/t$
	Hot-rolled medium-thick carbon steel plates	2400	$kgCO_2e/t$
	Hot-rolled carbon steel H-beams	2350	$kgCO_2e/t$
	Hot-rolled carbon steel rebars	2340	$kgCO_2e/t$
	Hot-rolled carbon steel seamless pipes	3150	$kgCO_2e/t$
	Cold-drawn carbon steel seamless pipes	3680	$kgCO_2e/t$
	Timber	310	$kgCO_2e/t$
Panel	Flat glass	1130	$kgCO_2e/t$
	Aluminum sheet and strip	28,500	$kgCO_2e/t$
	Copper sheet	218	$kgCO_2e/m^2$
	Carbon steel hot-dip galvanized sheet/coil	3110	$kgCO_2e/t$
	Carbon steel electro-galvanized sheet/coil	3020	$kgCO_2e/t$
	Aluminum-plastic composite panel	8.06	$kgCO_2e/m^2$
	Copper-plastic composite panel	37.1	$kgCO_2e/m^2$

Table 1. *Cont.*

Materials		Values	Units
Fireproof insulation materials	Rockwool board	1980	$kgCO_2e/t$
Sealing materials	Ethylene Propylene Diene Monomer sealing strip	2670	$kgCO_2e/t$
	Silicone sealant	2910	$kgCO_2e/t$
	Polyurethane foam	4330	$kgCO_2e/t$
Fasteners and hardware materials	Mild steel	2050	$kgCO_2e/t$
	Carbon steel	1960	$kgCO_2e/t$
	Stainless steel	6800	$kgCO_2e/t$
	Galvanized steel	2487	$kgCO_2e/t$
Packaging materials	Plastic film	2570	$kgCO_2e/t$
	Corrugated paper	1230	$kgCO_2e/t$
Other materials	Tap water	0.168	$kgCO_2e/t$
	High-density polyethylene	2620	$kgCO_2e/t$
	Low-density polyethylene	2810	$kgCO_2e/t$
	Polyvinyl chloride	7300	$kgCO_2e/t$
	Linear low-density polyethylene	1990	$kgCO_2e/t$

2.2. Impact of Carbon Emissions on Construction Operation Phase

In the operational phase of buildings, curtain walls contribute negligibly to direct carbon emissions. However, the energy-saving performance of curtain walls significantly affects the carbon emissions of buildings. Curtain walls facilitate thermal exchange between indoor and outdoor environments through mechanisms such as conduction, radiation, and convection, due to solar radiation and temperature differentials. To maintain indoor comfort, heating and air conditioning systems are necessary, the energy consumption of which is significantly influenced by the energy performance of curtain walls.

Based on experiments, theoretical analyses, and simulation software such as Energy Plus 8.2.0, PKPM V3.1, and DeST3.0, the insulation [27–29], air tightness [30–32], and shading performance [33–35] on building energy consumption of building curtain wall have been extensively investigated. The results underscore the pivotal role of curtain walls in building energy consumption. In 2021, China implemented the mandatory general specification GB55015-2021, titled *General Specification for Building Energy Conservation and Utilization of Renewable Energy* [36], which stipulates that the carbon emission intensity of newly constructed residential and public buildings should be reduced by an average of 40% compared to the energy-saving design standards implemented in 2016. Additionally, it requires that the carbon emission intensity should be reduced by an average of at least 7 $kgCO_2/(m^2 \cdot a)$. To ensure the achievement of the target, it is crucial to enhance the energy efficiency of building curtain wall systems, which account for over 50% of energy consumption. Globally, the potential for energy savings from the construction of high-performance buildings and energy retrofitting of existing building envelope structures exceeds the total energy consumption of all G20 countries in 2015, with an accumulated energy saving of approximately 330 EJ by 2060.

However, due to the complexity of energy consumption during the operational stage of buildings, it is challenging to contain the carbon emissions of this part within the curtain walls. Therefore, it is usually considered in carbon emissions of the whole building. Similarly, the calculation method proposed in this paper only considers the implicit carbon emissions. It should be noted that when evaluating the carbon emissions of building curtain walls, it should be based on the same performance standards. Curtain wall types with lower emissions but inferior performance may not necessarily have an advantage in actual carbon emission levels. This aspect requires further in-depth research for reasonable consideration.

3. Calculation Method of Carbon Emissions of Curtain Walls

3.1. Framework and System Boundaries

Referring to the calculation method for building carbon emissions and considering the engineering characteristics of building curtain walls, the life cycle of building curtain walls is divided into six stages, consisting of material acquisition, processing and production, installation and construction, transportation, use, and dismantling; this includes the entire life cycle from raw materials to waste disposal, as shown in Figure 1. In practical engineering, various response measures may be taken in retrofitting, including minor repairs, energy-saving renovations, safety improvements, and overall refurbishments. Considering the uncertainty of renovation, the carbon emission calculation method proposed in this paper adopts a conservative approach, treating the carbon emissions caused by renovation as if it were a complete refurbishment. Considering that the area is commonly used as the engineering measurement unit in the design, construction, and budgeting of building curtain wall projects and to meet the habits of the industry and facilitate comparisons under different engineering conditions, the carbon emission calculation method in this paper uses area (m^2) as the benchmark unit.

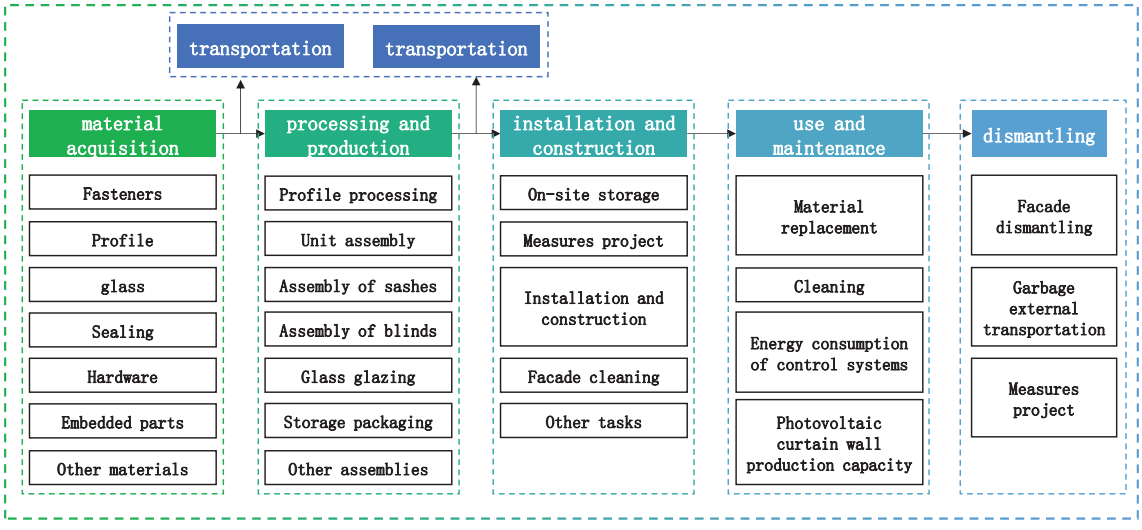

Figure 1. Framework of carbon emissions from building curtain walls.

Due to differences in energy consumption pathways, it is challenging to quantify which portion of this carbon emission reduction originates from the curtain wall. In contrast, with photovoltaic curtain walls, the contribution to reducing carbon emissions from the curtain wall can be clearly identified. Therefore, in the carbon emission calculation method proposed in this paper, the influence of curtain walls on building carbon emissions during the operational phase is not considered, and photovoltaic curtain walls are treated separately.

3.2. Calculation Method

Based on the different materials of curtain wall panels, they can be roughly categorized into glass curtain walls, metal curtain walls, stone curtain walls, and artificial board curtain walls. Due to the significant differences in materials and construction methods among different types of curtain walls and the possibility of multiple types of curtain walls being used in the same project, the carbon emissions are calculated separately for each type of

curtain wall in this paper. Then, the total carbon emissions of the entire curtain wall project are obtained by adding up the emissions from each type as follows:

$$GHG_{\mathrm{cw,all}} = \sum_{j}^{n} GHG_{\mathrm{cw},j} A_j (N_j + 1). \quad (1)$$

In the equation, $GHG_{\mathrm{cw,all}}$ represents the total carbon emissions of curtain walls over the lifespan of a single building or buildings in $kgCO_2e$; $GHG_{\mathrm{cw},j}$ represents the carbon emissions per unit area of the j-th type of curtain wall in $kgCO_2e$; A_j represents the area of the j-th type of the curtain wall in m^2; N_j represents the number of replacements of the j-th type of curtain wall over the entire lifespan.

According to the delineation of different stages within the boundary of the building of the curtain wall, the carbon emissions per unit area of different types of curtain wall can be represented as follows:

$$GHG_{\mathrm{cw},j} = GHG_{\mathrm{gain},j} + GHG_{\mathrm{proc},j} + GHG_{\mathrm{tran},j} + GHG_{\mathrm{cons},j} + GHG_{\mathrm{use},j} + GHG_{\mathrm{aban},j}, \quad (2)$$

In the equation, $GHG_{\mathrm{gain},j}$ represents the carbon emissions per unit area of the curtain wall during the material acquisition stage, $GHG_{\mathrm{proc},j}$ represents the carbon emissions per unit area of the curtain wall during the processing and production stage, $GHG_{\mathrm{tran},j}$ represents the carbon emissions per unit area of curtain wall during the transportation stage, $GHG_{\mathrm{cons},j}$ represents the carbon emissions per unit area of the curtain wall during the installation and construction stage, $GHG_{\mathrm{use},j}$ represents the carbon emissions per unit area of curtain wall during the use and maintenance stage, and $GHG_{\mathrm{aban},j}$ represents the carbon emissions per unit area of the curtain wall during the dismantling stage. For building curtain walls, the carbon emissions at different stages can be categorized into three parts: materials, energy consumption, and combustion of fossil fuels, where the combustion of fossil fuels refers to the generation of greenhouse gases.

Considering the differing statistical practices across various stages of engineering, no uniform calculation formula has been established. Therefore, each stage is computed separately. The carbon emissions during the material acquisition stage of the unit area curtain wall can be represented as follows:

$$GHG_{\mathrm{gain},j} = \sum_{i=1}^{n} G_{i,j} M_i. \quad (3)$$

In the equation, $G_{i,j}$ denotes the consumption per unit area of a specific material i for a given curtain wall j, in kg/m^2 or m^2/m^2, while M_i represents the carbon emission factor of material i, in $kgCO_2e/kg$ or $kgCO_2e/m^2$. Building curtain wall materials encompass profiles, glass, stone, aluminum panels, fireproof insulation materials, sealing materials, fasteners, embedded parts, hardware materials, packaging materials, etc. Typically, the manufacturers provide the carbon emission factors of materials.

The processing and production stage of curtain walls mainly includes the processing of profiles, assembly of unit modules, assembly of opening fans, assembly of sun shading louvers, glass gluing, and storage packaging processes. During the processing and production process, materials such as packaging, cleaning, and auxiliary materials are involved, as well as energy consumption from equipment operation and on-site transportation. The carbon emission intensity of curtain wall processing and production per unit area can be expressed as follows:

$$GHG_{\mathrm{proc},j} = \sum_{i=1}^{n} G_{i,j} M_i + \sum_{i=1}^{n} P_{i,j} E_i + GHG_{\mathrm{comb},j}. \quad (4)$$

In the equation, $P_{i,j}$ represents the consumption per unit area of a specific energy i for curtain wall j, in $(kW{\cdot}h)/m^2$ or L/m^2 or kg/m^2, where energy types may include electricity,

petroleum, coal, etc.; E_i represents the carbon emission factor of energy i, measured in $kgCO_2e/(kW{\cdot}h)$, $kgCO_2e/L$, or $kgCO_2e/kg$; $GHG_{comb,j}$ represents the carbon emissions per unit area generated by the combustion of fossil energy i for curtain wall j, which can be calculated using the following formula:

$$GHG_{comb,j} = \sum_{i=1}^{n} \left(FC_{i,j} \times NCV_i \times CC_i \times OF_i \times \frac{44}{12} \right). \quad (5)$$

In the equation, $FC_{i,j}$ represents the consumption per unit area of a specific type of fossil energy i for curtain wall j, in L/m^2 or kg/m^2; NCV_i represents the average lower heating value of fossil energy type i, in GJ/L or GJ/kg; CC_i represents the carbon content per unit heat value of fossil energy type i, in kgC/GJ; OF_i represents the carbon oxidation rate of fossil energy type i, in %.

The transportation stage of building curtain walls primarily involves two parts: transporting the acquired materials to the processing workshop and then transporting them to the construction site after processing. Transportation within the workshop or site, as well as the external transportation of waste during the dismantling phase, are not included. Unlike other stages, carbon emissions during transportation are typically calculated based on different transportation methods and distances. The carbon emissions of curtain wall transportation per unit area can be expressed as follows:

$$GHG_{tran,j} = \sum_{k=1}^{m} \sum_{i=1}^{n} Q_{k,i,j} D_{k,i,j} F_k, \quad (6)$$

In the equation, $Q_{k,i,j}$ denotes the quantity per unit area of the material i for transportation mode k of the curtain wall j, in kg/m^2; $D_{k,i,j}$ represents the transportation distance of the material i for transportation mode k of the curtain wall j, in km; F_k signifies the carbon emission factor of the transportation mode k, in $kgCO_2e/(kg{\cdot}km)$.

The calculation of carbon emissions $GHG_{cons,j}$ during the installation and construction phase of unit-area curtain wall construction relies on Equations (4) and (5), encompassing measures such as the on-site storage of components, on-site transportation, auxiliary installation of scaffolding, installation processes, and curtain wall cleaning.

Similarly, the calculation of carbon emissions $GHG_{use,j}$ during the use and maintenance phase of the unit-area curtain wall is also based on Equations (4) and (5). The stage involves activities such as replacing aged materials, repairing faulty components, daily cleaning of curtain walls, and energy consumption of control systems like electric sunshades. When the photovoltaic curtain wall is applied, $P_{i,j}$ in Equation (4) should include the electricity generation resulting from the photovoltaic, with a negative value indicating carbon reduction due to photovoltaic capacity.

The calculation of carbon emissions $GHG_{aban,j}$ during the dismantling phase of a unit-area curtain wall is likewise based on Equations (4) and (5), primarily including the material and energy consumption from dismantling and auxiliary measures during the dismantling process, as well as carbon emissions from waste transportation.

3.3. Case Study

A specific aluminum-glass curtain wall is considered, comprising both framed and photovoltaic curtain walls. The building is designed to endure for 50 years. The area of the framed glass curtain wall is 8000 m^2, with a designated service life of 25 years, while the photovoltaic curtain wall spans 1000 m^2, similarly engineered for a 25-year period. The design drawing for the curtain wall section is shown in Figure 2.

The material quantities and carbon emission factors during the material acquisition phase of the curtain wall are outlined in Table 2. When calculating the consumption of materials, material loss should be considered and converted based on the service life of the

materials and the projects. Utilizing Equation (3), the carbon emissions $GHG_{gain,j}$ during the material acquisition phase of the curtain wall were calculated to be 310.9 $kgCO_2e/m^2$.

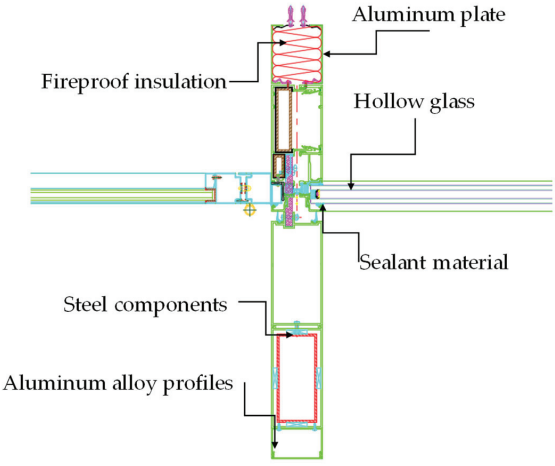

Figure 2. Framework of carbon emissions from building curtain walls.

Table 2. Activity level data and carbon emission factors during the material acquisition stage.

Materials	Technical Specifications	Material Quantity		Carbon Emission Factors	
		Values	Units	Values	Units
Aluminum alloy profiles	Thermal break, powder coating	10	kg/m^2	20.3	$kgCO_2e/kg$
Hollow glass 1	Low-E float glass 10 mm + 12Air + Tempered glass 10 mm, homogenization treatment	0.36	m^2/m^2	57.9	$kgCO_2e/m^2$
Hollow glass 2	Low-E float glass 6 mm + 12Air + Tempered glass 6 mm, homogenization treatment	0.64	m^2/m^2	34.7	$kgCO_2e/m^2$
Aluminum plate	2 mm, powder coating	0.29	m^2/m^2	159.6	$kgCO_2e/m^2$
Fireproof insulation	100 mm thick rock wool insulation, density 100 kg/m^3	2.90	kg/m^2	1.98	$kgCO_2e/kg$
Steel components	Hot-dip galvanized steel	0.9	kg/m^2	2.4	$kgCO_2e/kg$
Sealant material 1	Ethylene Propylene Diene Monomer	1.6	kg/m^2	2.67	$kgCO_2e/kg$
Sealant material 2	Silicone sealant	1.8	kg/m^2	2.91	$kgCO_2e/kg$
Fasteners	Stainless steel fasteners	0.15	kg/m^2	6.8	$kgCO_2e/kg$
Auxiliary materials	Polyethylene foam rods	0.04	kg/m^2	2.81	$kgCO_2e/kg$

The material and energy consumption, as well as the carbon emission factors during the processing and production stage of the curtain wall, are delineated in Table 3. These factors primarily encompass the electricity consumption of processing machinery and packaging materials. Based on Equations (4) and (5), the carbon emissions $GHG_{proc,j}$ during this stage were calculated to be 1.13 $kgCO_2e/m^2$.

Table 3. Activity level data and carbon emission factors during the processing and production stage.

Materials and Energy	Purpose	Material Quantity		Carbon Emission Factors	
		Values	Units	Values	Units
Electricity	Operation of machinery, on-site transportation, etc.	0.9	$(kW{\cdot}h)/m^2$	0.9419	$kgCO_2e/(kW{\cdot}h)$
Corrugated paper	Packaging materials, etc.	0.2	kg/m^2	1.41	$kgCO_2e/kg$

Table 4 presents the materials, energy consumption, and carbon emission factors for the transportation phase of the curtain wall. Usually, aluminum alloy profiles and glass materials are sourced from manufacturing companies, resulting in longer transportation distances. Steel components can be purchased from the market, allowing for sourcing from nearby locations. Semi-finished products typically come from processing plants near the construction site, thus minimizing transportation distances.

Table 4. Activity level data and carbon emission factors during the transport stage.

Product	Purpose	Values (kg/m^2)	Distance (km)	Transportation Mode	Carbon Emission Factors ($kgCO_2e/(kg \cdot km)$)
Materials	Aluminum alloy profiles	10	500	Medium-sized diesel trucks (Load capacity of 8 tons)	0.179×10^{-3}
	glass	50	400	Medium-sized diesel trucks (Load capacity of 8 tons)	0.179×10^{-3}
	Steel components	0.9	300	Small-sized diesel trucks (Load capacity of 2 tons)	0.286×10^{-3}
	Other materials	10	300	Small-sized diesel trucks (Load capacity of 2 tons)	0.286×10^{-3}
Semi-finished products	-	60	80	Large-sized diesel trucks (Load capacity of 10 tons)	0.162×10^{-3}

Considering the carbon emissions during the return journey of the transportation vehicle, the transportation distance needs to be calculated twice. Consequently, employing Equation (6) yielded the carbon emissions $GHG_{\text{tran},j}$ for the transportation phase as 12.38 $kgCO_2e/m^2$.

The materials, energy consumption, and carbon emission factors during the installation and construction stage of the curtain wall are detailed in Table 5. The carbon emissions primarily encompass the energy consumption during the construction process and the utilization of non-recyclable auxiliary materials. The average low-heat NCV_i of diesel, essential for calculation purposes, stands at 42.652×10^{-3} GJ/kg. Correspondingly, the carbon content per unit calorific CC_i is estimated to be 20.2 kgC/GJ, with a carbon oxidation rate of 99%. Consequently, the carbon emissions $GHG_{\text{cons},j}$ of the curtain wall installation and construction stage were derived through the application of Equations (4) and (5), resulting in 4.37 $kgCO_2e/m^2$.

Table 5. Activity level data and carbon emission factors during the installation and construction stage.

Materials and Energy	Purpose	Material Quantity		Carbon Emission Factors	
		Values	Units	Values	Units
Electricity	Operation of machinery, on-site transportation, etc.	2	$(kW \cdot h)/m^2$	0.9419	$kgCO_2e/(kW \cdot h)$
Diesel fuel	On-site transportation, etc.	0.36	kg/m^2	0.3383	$kgCO_2e/kg$
Carbon steel	Carbon structural steel, Q235B, Hot-dip galvanizing	0.6	kg/m^2	2.05	$kgCO_2e/kg$
Tap water	Building water supply	0.03	kg/m^2	0.168×10^{-3}	$kgCO_2e/kg$

Table 6 presents the annual material and energy consumption, along with carbon emission factors during the usage phase of the curtain wall. With a service life of 25 years, the carbon emissions $GHG_{\text{use},j}$ resulting from the consumption of materials or energy during this stage amounted to 17.02 $kgCO_2e/m^2$, calculated using Equations (4) and (5).

Table 6. Activity level data and carbon emission factors during the using stage (annually).

Materials and Energy	Purpose	Material Quantity		Carbon Emission Factors	
		Values	Units	Values	Units
Electricity	Maintenance and upkeep Power consumption of control systems	0.5 0.01	$(kW \cdot h)/m^2$	0.9419	$kgCO_2e/(kW \cdot h)$
Tap water	Building water supply	1.5	kg/m^2	0.168	$kgCO_2e/kg$
Cleaning agent	Glass cleaner	0.1	kg/m^2	2.0	$kgCO_2e/kg$

The material and energy consumption, as well as the carbon emission factors during the dismantling phase of the curtain wall, are presented in Table 7. The activity level data and carbon emission factors during the transportation process are shown in Table 8. Based on Equations (4)–(6), the carbon emissions $GHG_{aban,j}$ during the dismantling phase of the curtain wall were calculated to be 5.43 $kgCO_2e/m^2$.

Table 7. Activity level data and carbon emission factors during the dismantling stage.

Materials and Energy	Purpose	Material Quantity		Carbon Emission Factors	
		Values	Units	Values	Units
Electricity	Dismantling machinery	1.8	$(kW \cdot h)/m^2$	0.9419	$kgCO_2e/(kW \cdot h)$
Diesel fuel	Dismantling machinery	0.35	kg/m^2	0.3383	$kgCO_2e/kg$
Mild carbon steel	Carbon structural steel, Q235B, Hot-dip galvanizing	0.3	kg/m^2	2.05	$kgCO_2e/kg$

Table 8. Activity level data and carbon emission factors during garbage transportation.

Product	Purpose	Values (kg/m^2)	Distance (km)	Transportation Mode	Carbon Emission Factors ($kgCO_2e/(kg \cdot km)$)
Demolition waste	From the demolition site to the waste disposal facility	61	80	Medium-sized diesel trucks (Load capacity of 8 tons)	0.179×10^{-3}
	From the waste disposal facility to the recycling center	14	20	Small-sized diesel trucks (Load capacity of 2 tons)	0.286×10^{-3}

Based on the cumulative analysis, the carbon emissions per unit area of the framed glass curtain wall for this building project amounted to 351.23 $kgCO_2e/m^2$. The photovoltaic curtain wall of the project generates approximately 100 kWh/m^2 of electricity annually. The design lifespan realistic with photovoltaic products is 25 years. Utilizing the electricity carbon emission factor from Table 6, the carbon reduction during its usage phase was calculated to be $-100 \times 25 \times 0.9419 = -2354.75$ $kgCO_2e/m^2$. Apart from the usage phase of electricity generation, other phases' configurations were similar to the framed glass curtain wall, with negligible differences. Referring to the carbon emission calculation results of the framed glass curtain wall, the cumulative carbon emissions per unit area of the photovoltaic curtain wall in this building project were $-2354.75 + 351.23 = -2003.52$ $kgCO_2e/m^2$.

The total carbon emissions $GHG_{cw,all}$ of the building curtain wall over its lifecycle amounted to 1612.640 tCO_2e, calculated according to Equation (1). The carbon emissions data for different stages are illustrated in Figure 3. Insights from the case study reveal the following: (1) Excluding photovoltaic components, the material acquisition stage contributes nearly 90% of carbon emissions, serving as the primary source of emissions for glass curtain walls. Consequently, mitigating emissions should primarily focus on material reduction; (2) The scientific application of photovoltaic curtain walls can significantly reduce the carbon emissions associated with building curtain walls.

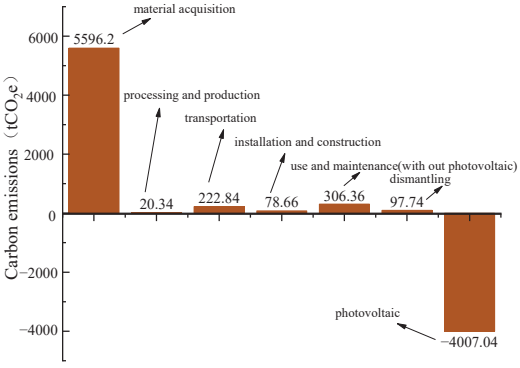

Figure 3. Calculation of carbon emission results at different stages.

4. Carbon Reduction Pathways for Building Curtain Walls

Carbon emissions in building curtain walls primarily encompass embodied carbon emissions from the materials and operation stage. The reduction of this in the operation stage can be facilitated through the application of photovoltaics. As for the materials, the methods for carbon reduction can be categorized into three main aspects:

(1) Optimizing structures to reduce material usage: For instance, curtain wall frame and panel strength designs are considered unfavorable positions, leading to similar construction and material usage for both lower and upper levels in buildings, which may lead to redundancy on the low floor of the building. Therefore, by improving and optimizing the structural forms of curtain walls while ensuring no reduction in performance, the carbon emissions of these structures can be reasonably reduced. Actually, through the analysis of the frame mechanical performance, the optimization of wall thickness and dimensions based on different application positions, such as using thicker and larger profiles for high-rise and high-wind pressure areas while using the thinner and smaller profiles for low-rise and low-wind pressure areas, can effectively reduce the carbon emissions of frame materials. In addition, developing energy-saving and material-saving panel materials and promoting new insulation materials, such as vacuum glass, low-emissivity glass, and aerogel-filled materials, are equally effective;

(2) Material recycling and substitution: With the advancement of carbon emission assessment for building curtain walls, there is a growing emphasis on materials with low implicit carbon emissions, high recyclability, and long lifespans, such as bamboo, wood, and plant-based framing materials which inherently store carbon, offering significant carbon reduction advantages. Traditional frame materials like aluminum alloy and steel profiles, with similar lifespans and recyclability as buildings, can fully leverage their advantages through enhanced surface anti-corrosion treatment techniques. As for glass, addressing the improvement of aging resistance in sealing materials for assembled hollow glass and refining the recycling processes for raw glass are necessary;

(3) Reducing carbon emissions during the production process: Considering the technological characteristics of curtain wall materials and the energy structure of factories, the technical pathways for reducing carbon emissions may include: (1) Optimizing product production processes by prioritizing the use of state-encouraged advanced technology processes and advocating for green production concepts; (2) Constructing distributed photovoltaic systems using unused roofs of factories for photovoltaic power generation to improve the sustainability of enterprise operations and reduce the use of non-renewable energy sources; (3) Applying air-source heat pumps and ground-source heat pumps to replace externally purchased thermal energy and split

air conditioning systems; (4) Establishing smart energy island systems by enhancing factory energy data collection, upgrading control systems.

In fact, in addition to reducing carbon emissions from the perspective of building curtain wall engineering, it is equally crucial to establish a unified standard and evaluation method for calculating carbon emission levels from policy and market perspectives. This is also the objective of the work presented in this paper. Relevant standards can regulate the carbon emission levels of curtain walls, while the evaluation system can incentivize enterprises to reduce this through market competition.

5. Current Existence of Problems

While the assessment and calculation of carbon emissions have become a focal point in the curtain wall industry, there are still many pressing practical issues that need to be addressed, as follows:

(1) Inadequate database of carbon emission factors: The building curtain wall sector lacks a comprehensive database for carbon emission factors associated with key materials, including glass, profiles, hardware, and sealing materials. This deficiency hinders the selection of materials based on accurate data, leading to uncertainty in assessments. Additionally, considering that recycling and reuse have a significant impact on balancing the carbon emission levels of raw materials, the lack of sufficient data on recycling and reuse rates can lead to overestimated results in the final evaluation;

(2) Lack of unified assessment methodology for carbon emissions: There is no standardized system specifically for assessing carbon emissions in building curtain walls. The diverse construction forms of building curtain walls in real projects introduce complexities to carbon emission assessments. In the absence of a unified evaluation technique, the evaluation results provided by different evaluation agencies and personnel may lack scientific data collection, be incomplete in the evaluation process, or be based on different sources of calculation. These issues result in evaluation outcomes that lack objective comparability;

(3) Lack of correlation research between curtain wall performance and carbon emissions of buildings during the operation phase: Building envelope structures are significant pathways for building energy consumption, with doors and windows accounting for over 40% of total energy consumption and building curtain walls sometimes exceeding 80%. Therefore, the question of how to consider the carbon emissions caused by the operational stage of buildings attributed to curtain walls is a question that requires further research.

6. Conclusions

Based on the analysis of the current research status of carbon emissions from curtain walls, this paper proposes a carbon emission calculation method based on the entire life cycle. Through the analysis of a glass curtain wall case study, the following conclusions are drawn:

(1) High-carbon-emission materials such as aluminum profiles, glass panels, and sealing agents are commonly utilized in architectural curtain walls, significantly contributing to the overall carbon emissions of buildings. At the same time, the impact of curtain wall energy efficiency on the operational carbon emissions of buildings cannot be overlooked;

(2) Findings from a case study on a glass curtain wall project indicate that the material acquisition stage constitutes nearly 90% of the total carbon emissions associated with glass curtain walls. In addition, the scientific application of photovoltaics presents a viable approach to substantially reducing the carbon footprint of architectural curtain walls.

Overall, the calculation method for curtain wall carbon emissions plays a crucial role in promoting the application of green and low-carbon building materials and advancing

the construction of carbon emission standard systems. However, challenges persist in the current evaluation of carbon emissions in the curtain wall field, including severe deficiencies in the database of material carbon emission factors, a lack of uniformity in carbon emission level calculation and evaluation methods, and the need for further research on the correlation between curtain wall performance and carbon emissions of buildings during the operation phase.

Author Contributions: Conceptualization, X.Z. (Xichen Zhang); methodology, X.Z. (Xichen Zhang); investigation, X.F. and X.Z. (Xiuchun Zheng); writing—original draft preparation, S.L. and Q.Z.; writing—review and editing, S.L. and J.L. All authors have read and agreed to the published version of the manuscript.

Funding: This research was funded by the Research Fund of *China Academy of Building Research*, grant number 20220112330730010; 2022 Science and Technology Project of *Ministry of Housing and Urban Rural Development*, grant number 2022-K-146.

Data Availability Statement: The original contributions presented in the study are included in the article, further inquiries can be directed to the corresponding authors.

Conflicts of Interest: All authors were employed by the company Jianke EET Co., Ltd. Authors declare that the research was conducted in the absence of any commercial or financial relationships that could be construed as a potential conflict of interest.

References

1. Röck, M.; Saade, M.; Balouktsi, M.; Rasmussen, F.; Birgisdottir, H.; Frischknecht, R. Embodied GHG emissions of buildings—The hidden challenge for effective climate change mitigation. *Appl. Energy* **2020**, *258*, 114107. [CrossRef]
2. Schleussner, C.F.; Rogelj, J.; Schaeffer, M.; Lissner, T.; Licker, R.; Fischer, E.M.; Knutti, R.; Levermann, A.; Frieler, K.; Hare, W. Science and policy characteristics of the Paris Agreement temperature goal. *Nat. Clim. Chang.* **2016**, *6*, 827–835. [CrossRef]
3. American Government. Executive Order on Tackling the Climate Crisis at Home and Abroad. Available online: https://www.whitehouse.gov/briefing-room/presidential-actions/2021/01/27/executive-order-on-tackling-the-climatecrisis-at-home-and-abroad/ (accessed on 5 June 2022.).
4. European Commission. European Climate Law. Available online: https://ec.europa.eu/clima/policies/eu-climate-action/law_en (accessed on 5 June 2022.).
5. The Government of China. The Outline of the 14th Five-Year Plan (2021–2025) for National Economic and Social Development and the Long-Range Objectives through the Year 2035. Available online: http://www.gov.cn/xinwen/2021-03/13/content_5592681.htm (accessed on 5 June 2023.).
6. China Association of Building Energy Efficiency, Institute of Urban-rural Construction and Development, Chongqing University. *Research Report on Building Energy Consumption and Carbon Emissions in China (2023). Constr. Archit.* **2024**, *2*, 46–59.
7. WGBC—World Green Building Council, Bringing Embodied Carbon Upfront. 2019. Available online: https://worldgbc.s3.eu-west-2.amazonaws.com/wp-content/uploads/2022/09/22123951/WorldGBC_Bringing_Embodied_Carbon_Upfront.pdf (accessed on 5 June 2022.).
8. Hunziker, R.; Carroll, C. *Net-Zero Buildings: Where Do We Stand?* World Business Council for Sustainable Development: Geneva, Switzerland, 2021.
9. Gao, H.; Wang, X.K.; Wu, K.; Zheng, Y.; Wang, Q.; Shi, W.; He, M. A Review of Building Carbon Emission Accounting and Prediction Models. *Buildings* **2023**, *13*, 1617. [CrossRef]
10. Wang, P.F.; Li, H.B.; Huang, Z.B. The inter-provincial trade inequality in China: An assessment of the impact of changes in built-up land and carbon storage. *Ecol. Econ.* **2023**, *206*, 107749. [CrossRef]
11. Chau, C.K.; Leung, T.M.; Ng, W.Y. A review on Life Cycle Assessment, Life Cycle Energy Assessment and Life Cycle Carbon Emissions Assessment on buildings. *Appl. Energy* **2015**, *143*, 395–413. [CrossRef]
12. Marsh, E.; Allen, S.; Hattam, L. Tackling uncertainty in life cycle assessments for the built environment: A review. *Build. Environ.* **2023**, *231*, 109941. [CrossRef]
13. Zhao, Y.; Liu, L.; Yu, M. Comparison and analysis of carbon emissions of traditional, prefabricated, and green material buildings in materialization stage. *J. Clean. Prod.* **2023**, *232*, 110045. [CrossRef]
14. *GB/T 51366-2019*; Standard of Carbon Emission Calculation for Building. China Architecture & Building Press: Beijing, China, 2019.
15. Kibert, C.J. *Sustainable Construction-Green Building Design and Delivery*, 3rd ed.; John Wiley & Sons Ltd.: Hoboken, NJ, USA, 2010.
16. Citherlet, S.; Guglielmo, F.D.; Gay, B. Window and advanced glazing systems life cycle assessment. *Energy Build.* **2000**, *32*, 225–234. [CrossRef]
17. Salazar, J.; Sowlati, T. Life cycle assessment of windows for the North American residential market: Case study. *Scand. J. For. Res.* **2008**, *23*, 121–132. [CrossRef]

18. Azari, R.; Kim, Y.-W. A Comparative Study on Environmental Life Cycle Impacts of Curtain Walls. In *Construction Research Congress 2012*; ASCE: Reston, VA, USA, 2012; pp. 1610–1619.
19. Das, S. Achieving carbon neutrality in the global aluminum industry. *JOM* **2012**, *64*, 285–290. [CrossRef]
20. Zhang, Y. Carbon Footprint Analysis of Typical Aluminum Alloy Profile Products. Metal Composite Materials Branch of China Building Materials Federation. In *Proceedings of the Special Issue of the 2018 Metal Composite Materials Annual Conference*; China Testing & Certification International Group Co., Ltd.: Hangzhou, China, 18 April 2018; p. 3.
21. Yan, Y.; Liu, J.; Ding, N.; Yan, L. Investigation on CO_2 emissions from flat glass production in China. *Acta Sci. Circumstantiae* **2017**, *37*, 3213–3219.
22. Yu, H.; Zeng, J.; Zhao, M. Life-Cycle Energy Consumption and Carbon Emission of Typical Decoration Materials. *Build. Sci.* **2014**, *30*, 21–25.
23. *Analysis of Competitive Strategies and Market Demand Forecast for China's Waste Glass Industry from 2022 to 2028: R980721*; Intelligence Research Group: Beijing, China, 2022.
24. *T/CECS 1525-2024*; Standard for Evaluating of Carbon Footprint of Windows and Doors in Building. China Association for Engineering Construction Standardization: Beijing, China, 2024.
25. Zhao, B.; Zhang, J.; Liu, H.; Wei, W. Study on carbon emissions of the granite of garden pavement. *J. Nanjing For. Univ.* **2016**, *40*, 101–106.
26. Wolf, A.T.; Recknagel, C.; Wenzel, N.; Sitte, S. Structural Silicone Glazing: Life Expectancy of more than 50 Years? In Proceedings of the Glass Performance Days 2017 Conference, Tampere, Finland, 28–30 June 2017.
27. Yang, C.; Yu, S.; Cao, Y. Design optimization of office building envelope by developed farmland fertility algorithm for energy saving. *Heliyon* **2024**, *10*, e23387. [CrossRef] [PubMed]
28. Joo, N.Y.; Song, S.Y. Improvement of thermal insulation performance of precast concrete curtain walls for apartment buildings. *Energy Build.* **2023**, *296*, 113350. [CrossRef]
29. Altaf, M.; Alalaoul, W.S.; Musarat, M.A.; Abdelaziz, A.A.; Thaheem, M.J. Optimisation of energy and life cycle costs via building envelope: A BIM approaches. *Environ. Dev. Sustain.* **2024**, *26*, 7105–7128. [CrossRef]
30. Yang, Y. Energy Consumption of Windows Caused by Air Permeability in Const ruction Engineering. *Build. Energy Effic.* **2016**, *44*, 42–44.
31. Yan, Z.; Chengwen, Y.; Jian, Y.; Wenhong, Z. The Influence of External Window's Air Tightness on Residential Building's Energy Consumption. *J. Ningbo Univ.* **2007**, *20*, 248–250.
32. Wang, X.; Xu, J.; Wang, Y. Experimental Study on the Effect of Air Permeability for Building External Windows and Doors to Thermal Insulation. *Build. Energy Effic.* **2017**, *45*, 35–37.
33. Sümer-Haydaraslan, K.; Dikmen, N. Investigation of the effects of curtain wall angle on energy consumption in buildings. *J. Fac. Eng. Archit. Gazi Univ.* **2024**, *39*, 315–325.
34. Tao, Q.H.; Li, Z.R.; Jiang, F.J.; Hu, L.Z. Necessity of shading on north curtain wall and optimal selection of shading device. *J. Chongqing Univ.* **2013**, *36*, 151–158.
35. Liu, Y.; Wang, W.; Huang, Y.; Song, J.; Zhou, Z. Energy Performance Analysis and Study of an Office Building in an Extremely Hot and Cold Region. *Sustainability* **2024**, *16*, 572. [CrossRef]
36. *GB 55015-2021*; General Code for Energy Efficiency and Renewable Energy Application in Buildings. China Architecture & Building Press: Beijing, China, 2021.

buildings

MDPI

Article

Fault Diagnosis of Centrifugal Chiller Based on Extreme Gradient Boosting

Yaxiang Liu [1], Tao Liang [1], Mengxin Zhang [2], Nijie Jing [2], Yudong Xia [2] and Qiang Ding [2,*]

[1] Shandong Electric Power Engineering Consulting Institute Co., Ltd., Jinan 250013, China
[2] Institute of Energy Utilization and Automation, Hangzhou Dianzi University, Hangzhou 310018, China
* Correspondence: dingqiang@hdu.edu.cn; Tel.: +86-571-86919133

Abstract: Centrifugal chillers have been widely used in medium- and large-scale air conditioning projects. However, equipment running with faults will result in additional energy consumption. Meanwhile, it is difficult to diagnose the minor faults of the equipment. Therefore, the Extreme Gradient Boost (XGBoost) algorithm was used to solve the above problem in this article. The ASHRAE RP-1043 dataset was employed for research, utilizing the feature splitting principle of XGBoost to reduce the data dimension to 23 dimensions. Subsequently, the five important parameters of the XGBoost algorithm were optimized using Multi-swarm Cooperative Particle Swarm Optimization (MSPSO). The minor fault diagnosis model, MSPSO-XGBoost, was established. The results show that the ability of the proposed MSPSO-XGBoost model to diagnose eight different states is uniform, and the diagnostic accuracy of the model reaches 99.67%. The accuracy rate is significantly improved compared to that of the support vector machine (SVM) and back propagation neural network (BPNN) diagnostic models.

Keywords: centrifugal chillers; fault diagnosis; extreme gradient boosting; MSPSO-XGBoost

Citation: Liu, Y.; Liang, T.; Zhang, M.; Jing, N.; Xia, Y.; Ding, Q. Fault Diagnosis of Centrifugal Chiller Based on Extreme Gradient Boosting. *Buildings* **2024**, *14*, 1835. https://doi.org/10.3390/buildings14061835

Academic Editors: Sungkyun Jung, Piljae Im and Yeobeom Yoon

Received: 9 April 2024
Revised: 8 June 2024
Accepted: 11 June 2024
Published: 17 June 2024

1. Introduction

Centrifugal chillers have the characteristics of a high energy efficiency ratio and large single-machine capacity, which makes them the most used model in medium and large air-conditioning systems. Due to the continuous improvements in modern industrial levels, the structure and system of centrifugal chillers have become more complex [1]. This will increase energy consumption by 20% to 50% for the centrifugal chillers without timely troubleshooting [2]. Therefore, it is critical to use the micro-fault diagnosis technology in the early fault diagnosis of chillers. It can determine the type of fault occurrence quickly and accurately and shorten the maintenance time effectively. It plays a role in guaranteeing refrigeration efficiency, reducing equipment loss, and saving energy [3].

The minor fault diagnosis techniques may be classified into three types, namely engineering experience, mechanisms, and data-driven models. Profiting from the large data technology industry, fault diagnosis with data-driven models has become the mainstream method. Data-based fault diagnosis is essentially a search for the mapping relationship between the monitoring data and the unit state without relying on a priori knowledge of the system. However, for complex systems such as chillers, there is no simple correspondence between monitoring data and unit status [4]. In addition, the operating conditions of chiller units are varied, and certain operating parameters are highly similar in the micro-fault state and the no-fault state in incipient faults [5]. Due to the complexity and uncertainty of the system, machine learning algorithms like Artificial Neural Networks (ANNs) [6] and support vector machines (SVMs) [7] were applied to the diagnosis of minor faults, and some results have been achieved. In the study of chiller fault diagnosis, study [8] used an ANN to diagnose various faults in chillers and found that the diagnosis of system faults is more difficult than local faults. An SVM is used in chiller fault diagnosis with information

from factory-installed sensors. And, the experimental results show that the information from eight sensors can satisfy the needs of the diagnosis task [9].

SVMs [10] are based on statistical learning theory [11] and skilled in different classes of the small sample dataset by finding the optimal hyperplane. However, SVMs are not appropriate for training large sample datasets because they cannot manage the complicated nonlinear correlations that large-scale datasets—especially those with high dimensionality—present in the high-dimensional space [12]. ANNs [8,13] have strong robustness and flexibility, learning complex nonlinear relationships between data by adjusting the connection weights between neurons. However, ANNs usually obtain sub-optimal solutions and often obtain non-global minimum values, which means that during the training process, they may fall into local optima. Therefore, in order to obtain a suitable model, ANNs need a lot of data for training. ANNs are generally used for classification problems in the form of data such as images, text, etc., and are not optimal for dealing with the problem of classifying discrete table data.

To address the above problems, integrated learning algorithms can be used in the fields of fault diagnosis and signal classification [14]. In integrated learning algorithms, the type of data can be detected and classified by a weak classifier with the advantages of a fast training speed and the ease of adjusting parameters; however, the accuracy is not high. A strong classifier is constructed by combining multiple weak classifiers, thus improving the overall generalization performance. Typical integrated learning algorithms include Random Forest (RF) and Extreme Gradient Boosting (XGBoost). XGBoost is proposed by Chen [15] on the basis of a Boosting algorithm based on GBDT. XGBoost has better modelling capabilities, higher computational accuracy, and faster training speed [16], and is suitable for the classification of table data, compared to other data types such as images and signals. XGBoost has been popular in fields such as statistics, data mining, and machine learning since its release. As a typical representative of Boosting technology in ensemble learning, XGBoost can effectively handle large-scale machine learning tasks. Since the introduction of XGBoost, it has been widely used in various research fields, such as cancer diagnosis [17], credit risk assessment [18], and macro genomics [19], due to its performance advantages and affordable time and memory complexity. However, the predictive performance of XGBoost without parameter optimization is often unsatisfactory due to its low fit with the dataset, resulting in poor generalization and adaptability. Its predictive performance highly depends on the tuning of hyper-parameters. Therefore, it is necessary to propose an efficient method to optimize these hyper-parameters [20].

However, there is little research on using the XGBoost method in the fault diagnosis of chillers [21]. This research aims to study the XGBoost algorithm and its parameter optimization. For seven typical minor faults in centrifugal chillers, this paper builds an XGBoost diagnostic framework and analyzes the impact of hyper-parameters on model performance. It implements the optimization of the hyper-parameters using the MSPSO algorithm, thus establishing the MSPSO-XGBoost diagnostic model. Consequently, the MSPSO-XGBoost model is further compared and analyzed with the SVM and BPNN models to verify the effectiveness of the proposed method in the micro-fault diagnosis of chillers.

The paper is organized as follows. Firstly, a description of the principle content for the research process is introduced in Section 2. Then, the description of the implementation and validation process of fault diagnosis is introduced in Section 3. Finally, the main contributions of the current study are summarized in Section 4.

2. Basic Principles

2.1. XGBoost

The core idea of the Boosting framework is to form a stronger classifier by combining multiple weak classifiers. The weak classifier chosen by XGBoost is Classification and Regression Trees (CARTs).

As shown in Figure 1, XGBoost belongs to a type of boosting tree model. Initially, a tree independently predicts a value based on the actual value and then obtains the deviation

between the actual and forecast values. After that, the deviation is used as the actual value of the second tree, and new deviations are continuously obtained. When t trees are added,

$$\hat{y}_i^{(t)} = \hat{y}_i^{(t-1)} + \eta f_t(x_i), 0 < \eta < 1 \tag{1}$$

where $f_t(x_i)$ is the discriminant function of the t-th tree for the i-th datapoint, $\hat{y}_i^{(t)}$ is the discriminant result of the strong model integrated by t decision tree models, and η is the learning rate.

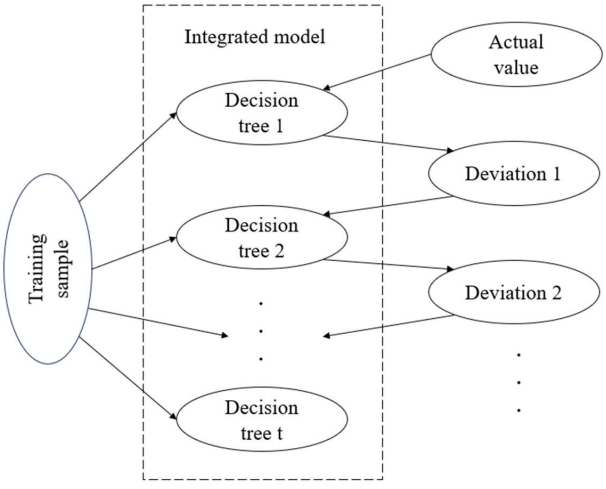

Figure 1. XGBoost principle.

The essence of CART is to construct a binary tree to divide the feature space; training CART is to find an optimal binary tree structure to make the minimum objective function. Similarly, the XGBoost objective function is defined as follows:

$$Obj(t) = \sum_{i=1}^{n} l(y_i, \hat{y}_i) + \sum_{i=1}^{t} \Omega(f_i) \tag{2}$$

The first term on the right side of the formula is the deviation between the actual value and the predicted value, where n is the number of training samples. The last term on the right side of the formula is the regularization term, which mainly serves to suppress model complexity.

$$\Omega(f) = \gamma T + \frac{1}{2}\lambda \|\omega\|^2 \tag{3}$$

where T is the depth of the current subtree and ω is the node value of the leaf node. γ represents the node segmentation threshold and λ is the L2 regularization coefficient.

According to the objective function, the optimal output obtained is as follows:

$$Obj^* = -\frac{1}{2}\sum_{j=1}^{T} \frac{G_j^2}{H_j + \lambda} + \gamma T \tag{4}$$

$$G_j = \sum_{i \in I_j} \partial_{\hat{y}_i^{(t-1)}} l(y_i, \hat{y}_i^{(t-1)}) \tag{5}$$

$$H_j = \sum_{i \in I_j} \partial^2_{\hat{y}_i^{(t-1)}} l(y_i, \hat{y}_i^{(t-1)}) \tag{6}$$

Equation (4) is the rating function of the tree, with smaller values indicating better structure. XGBoost relies on the greedy strategy of recursive node splitting to generate sub-model trees. Equation (7) is the expression of the splitting profit Gain. When selecting the optimal splitting Gain, the feature with the largest difference in *Obj** values before and after splitting is considered, and the feature with the largest Gain value is used as the splitting point to construct a CART.

$$Gain = \frac{1}{2}\left[\frac{G_L^2}{H_L+\lambda} + \frac{G_R^2}{H_R+\lambda} - \frac{(G_L+G_R)^2}{H_L+H_R+\lambda}\right] - \gamma \tag{7}$$

The index L represents the optimal value of the objective function when the value is divided into the left subtree, and the index R represents the optimal value of the objective function when the value is divided into the right subtree.

When generating XGBoost models, it is possible to count the instances in which features engage in splitting, thereby establishing a ranking of feature contribution, because the process of developing CART adheres to inference rules and has practical physical significance and interpretability. Then, the top-ranked features are selected to construct low-dimensional training samples, which can reduce feature redundancy and improve model training speed.

2.2. Principles of MSPSO-XGBoost

The XGBoost algorithm is an efficient classification algorithm. The performance of the XGBoost model is highly dependent on the optimization of the hyper-parameters, and it has a large number of parameters. Hence, it is difficult to adjust using the empirical method and cannot achieve the global optimum [22]. Based on the basic principles of XGBoost and existing studies [22,23] on optimizing XGBoost parameters, five parameters were chosen that affect the classification accuracy significantly, as listed in Table 1.

Table 1. XGBoost algorithm partial parameter information table.

Parameter	Range	Describe
eta	[0, 1]	Learning rate: η, reducing the weight of each step. If a learning rate is too high or too low, it is impossible to find the position of the minimum loss function.
gamma	[0, ∞]	Gain threshold: γ, gamma specifies the loss reduction which is necessary to split tree nodes rightly in a loss function. In other words, it is a parameter that contributes to making an algorithm conservative.
max_depth	[0, ∞]	The maximum depth of the tree; the larger the max_depth value is, the more a model learns a very characteristic relation for a particular sample. The parameter is used to adjust over-fitting.
min_child_weight	[0, ∞]	The minimum weight of leaf nodes; when the value is large, the model can avoid learning the local optimal solution.
n_estimators	[100, 500]	The number of sub-model trees; if the value is too small, the problem of model underfitting will occur, and if the value is too large, the calculation amount will be greatly increased.

PSO [24] is a commonly used heuristic optimization algorithm that has the characteristics of a simple implementation mechanism, strong interpretability, and fast convergence speed. Its speed and position update formulas are as follows:

$$V_i^{t+1} = \omega V_i^t + c_1 r_1 (P_g^t - X_i^t) + c_2 r_2 (P_i^t - X_i^t) \tag{8}$$

$$X_i^{t+1} = X_i^t + V_i^{t+1} \tag{9}$$

where c_1 and c_2 are the learning factors, r_1 and r_2 are the random factors, ω is the inertia weight coefficient, V_i^t and X_i^t are the velocity and position of the particle at the current time, V_i^{t+1} and X_i^{t+1} are the updated velocity and position, P_i^t is the historical optimal position of the *i*-th particle, and P_g^t is the optimal particle position of all the particles.

When facing complex problems, reducing ω according to inertia can easily trap the algorithm into local optima. Based on the literature [23,25,26], and inspired by the idea of group decision-making, MSPSO is employed to address this issue. The particle swarm is divided into multiple subgroups, each of which independently seeks optimization. After each iteration, the optimal particle information for each subgroup is shared, and the most adaptable particle is selected as the global guiding particle. When updating the speed, the global guide particles guide all particles, and the formula for updating the speed is as follows:

$$V_i^{t+1} = \omega V_i^t + c_1 r_1 (P_g^t - X_i^t) + c_2 r_2 (P_i^t - X_i^t) + c_3 r_3 (P_G^t - X_i^t) \tag{10}$$

where c_3 is the learning factor for the *i*-th particle to learn the global guide particle, r_3 is a random factor with values in the [0, 1] interval, and P_G^t is the optimal position for the global guide particle.

The steps to optimize XGBoost using MSPSO are the following:

Step 1: First, initialize, set the number of particles to N, divide them equally into S subgroups, set the particle dimension to D, and iterate T times;

Step 2: Calculate the fitness value of particles at time t = 0, that is, the accuracy of each particle's corresponding model;

Step 3: S subgroup updates speed and position in parallel according to Equations (9) and (10);

Step 4: Process boundary constraints and calculate the fitness value of particles at time t + 1;

Step 5: Determines whether the current iteration count has reached its maximum setting. If so, end the optimization and output the model; otherwise, jump to step 3.

2.3. Evaluation Indicators and Model Establishment Process

The multi-classification confusion matrix is shown in Table 2. A to I show classification number (for example, B represents the number of misclassified datapoints in C1 to C2). Based on the confusion matrix, the accuracy rate (AR), precision rate (PR), and recall rate (RR) are defined.

Table 2. Confusion matrix.

		Diagnosed Faults		
	Category	**C1**	**C2**	**C3**
True Faults	C1	A	B	C
	C2	D	E	F
	C3	G	H	I

Define *AR* to measure the overall classification performance of diagnostic models:

$$AR = (A + E + I)/(A + B + C + D + E + F + G + H + I) \tag{11}$$

Taking C1 as an example, define *PR* and *RR* to measure the diagnostic model's ability to separate and identify different fault states:

$$PR = A/(A + \mathrm{D} + \mathrm{G}) \tag{12}$$

$$RR = A/(A + \mathrm{B} + \mathrm{C}) \tag{13}$$

Figure 2 shows the flowchart for training a fault diagnosis model, which includes two parts: data preprocessing and the optimization of the model. Data preprocessing includes reading data from a database, adding labels, feature selection, and dataset splitting. In the model optimization, the training set and particle positions are used to establish the model, while the test set is input into the model to obtain the confusion matrix, which can evaluate the model. Based on the overall diagnostic accuracy of the model, the performance is evaluated. The evaluation indicators of the model are taken as the fitness function of the particles and the particle positions are adjusted according to Equations (9) and (10). The particle positions are repeatedly updated to establish the diagnostic model until the maximum number of iterations stops training; then, the diagnostic model is output.

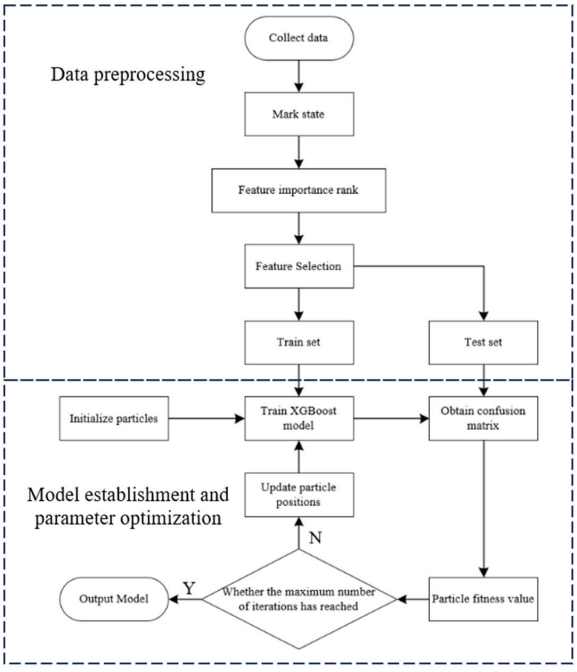

Figure 2. Model training flowchart.

3. Examples of Fault Diagnosis for Chiller Units

The minimum classification loss function is chosen as the penalty function for the diagnostic model. This model is based on the Python 3.6.15 platform and references the Numpy 1.19.5, Scikitlearn 0.17.1, Pandas 1.2.4, Matplotlib 3.4.3, and Seaborn 0.12.2 [27] scientific computing packages.

3.1. Fault Sample Information

The dataset used in this article comes from the ASHRAE RP-1043 chiller fault simulation experiment [28], and the system sketch is shown in Figure 3.

In Figure 3, a centrifugal chiller with a capacity of 90 refrigeration tons can be used to simulate the cooling effect of the cooling tower by exchanging heat between tap water and cooling water. Steam and hot water are used to simulate user load, and 64 parameters are recorded, including 48 measured parameters and 16 calculated parameters such as compressor efficiency and heat exchanger efficiency. The parameters are numbered 0–7 in the order shown in Table 3 according to reference [28]. The experiment simulated four types of local faults and three types of system faults and simulated four degradation levels from small to large for these seven faults to obtain operational data. In order to explore the

diagnostic ability of minor faults in chillers, seven types of minimum simulated monitoring data with different fault levels were selected as the research samples for this article. The fault description is detailed in Table 3, and the percentage after the unit status description text in the table represents the degree of change compared to the normal state.

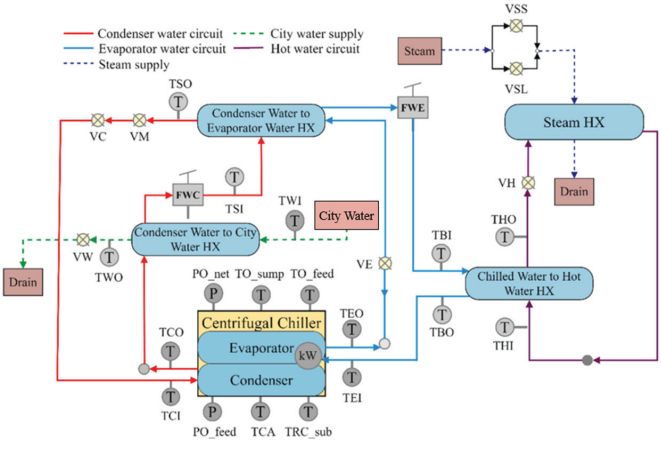

Figure 3. RP-1043chiller system fault simulation experimental device schematic diagram.

Table 3. RP-1043 fault information.

Type of Fault	Unit Status	Abbreviation	Label
——	Normal state	Normal	0
partial fault	Reduced condenser water flow (−10%)	FWC	1
	Reduced evaporator water flow (−10%)	FWE	2
	Condenser fouling (12%)	CF	3
	Non-condensable gas in refrigerant (1%)	NC	4
system fault	Refrigerant leak (−10%)	RL	5
	Refrigerant overcharge (+10%)	RO	6
	Excess oil (+14%)	EO	7

The experimental period for each state is up to 14 h, and the data collection interval is 10 s. Due to the drastic fluctuations in some parameters during the brief moments of starting and stopping the chiller unit, the data validity is not high. Therefore, this part of the data is removed when selecting the dataset. In the remaining data, 4000 samples are uniformly extracted for each of the eight states mentioned in Table 3. This forms a training sample set of 32,000 × 64 dimensions, ensuring a balanced number of samples among different classes.

3.2. Data Preprocessing

Among the 64 parameters, the calculated parameters are all obtained from the measured parameters, and the parameters numbered 0–8 are repeated measurements of temperature parameters related to the condenser and evaporator using a Resistance Temperature Detector (RTD) and thermistors. In addition, the complex nonlinear relationship between the parameters of the refrigeration system results in a highly coupled situation among the 64 parameters. The contribution degree is defined as the ratio of the splitting times of a feature participating in the decision tree to the total splitting times of the model. All features are ranked in order to lower the input feature dimension of the training set. Table 4 shows that the cumulative contribution is the sum of the current feature contribution and all feature contributions before the current feature ranking. The accuracy is the overall

accuracy of the XGBoost model classification under the current cumulative contribution, and then the optimal feature dimension is determined together with the training time.

Table 4. Original data feature parameter contribution analysis.

Number	Contribution Degree	Ranking	Accumulated Contribution	Accuracy	Training Time/s
56	18.42%	1	18.42%	26.87%	6.28
25	14.11%	2	32.53%	39.76%	7.56
24	10.64%	3	43.17%	48.04%	9.14
47	8.66%	4	51.83%	73.17%	12.03
4	5.31%	5	57.14%	79.28%	13.12
45	4.08%	6	61.22%	83.67%	14.99
58	3.74%	7	64.96%	85.71%	16.17
27	3.14%	8	68.10%	87.19%	16.81
48	2.66%	9	70.76%	88.46%	17.93
28	2.42%	10	73.18%	89.35%	20.20
39	2.31%	11	75.49%	90.02%	24.43
33	2.11%	12	77.60%	90.12%	26.51
3	1.86%	13	76.69%	90.39%	26.99
20	1.73%	14	79.46%	90.81%	28.80
30	1.62%	15	79.97%	91.18%	30.42
49	1.51%	16	81.08%	91.61%	32.51
9	1.39%	17	82.47%	91.82%	33.69
7	1.31%	18	83.78%	92.01%	33.99
46	1.26%	19	85.04%	92.43%	34.48
36	1.23%	20	86.27%	92.54%	35.34
11	1.18%	21	87.45%	92.89%	38.86
16	1.09%	22	88.54%	93.15%	39.21
18	1.00%	23	89.54%	93.35%	42.75
52	0.96%	24	90.50%	93.23%	43.93
32	0.87%	25	91.37%	92.11%	45.41
			...		
63	0%	64	100%	93.51%	79.16

Table 4 shows that as the number of features increases, the model training time continues to increase, with accuracy first increasing and then decreasing. The cumulative contribution reaches 89.54% with the feature number at 23, and the XGBoost model has the best accuracy rate of 93.35%. Considering that the original feature parameters, such as pressure and temperature, belong to slowly changing process parameters, and the training time is 41.75 s, which meets the practical requirements of engineering applications, the top 23 features ranked in contribution are selected to form a new low-dimensional learning sample.

The set of training samples after dimensionality reduction is a matrix of 32,000 × 23. Based on the size of the sample and the perspective of statistical learning, cross-validation is adopted and the samples are randomly and evenly divided into a training set of 24,000 × 23 and a test set of 8000 × 23 in a 3:1 ratio. First, the training set data were input into the given algorithm to train the fault diagnosis model, then the test set data were input into the trained diagnostic model and the confusion matrix and other evaluation indicators were used to evaluate the performance of fault diagnosis models.

3.3. XGBoost Parameter Optimization

Table 5 shows the optimization results of XGBoost parameters using MSPSO and PSO, respectively. Figure 4 shows the accuracy curves of XGBoost optimized via both methods. As shown in Figure 4, the PSO algorithm has a faster convergence speed in the early stages but it falls into a local optimum at 20 iterations and is unable to escape. The classification accuracy of the XGBoost algorithm optimized using PSO increased from 93.35% to 97.71% after 50 iterations. The MSPSO algorithm has a slow convergence speed in the early stages

but particles search for the optimal solution through multi-group cooperation, which can effectively prevent the local optima [29]. The accuracy of the XGBoost optimized using MSPSO can be considerably enhanced when compared to the PSO-optimized version. The classification accuracy of the MSPSO-optimized XGBoost algorithm is now 99.67%, up from 93.35% previously.

Table 5. Model parameter optimization results.

Parameter	Default	PSO	MSPSO
Learning rate (η)	0.3	0.12	0.033
Gain threshold (γ)	0	0.11	0.02
The maximum depth of the tree	6	4	3
Minimum weight of leaf nodes	1	2	3
Number of sub-model trees	100	345	203

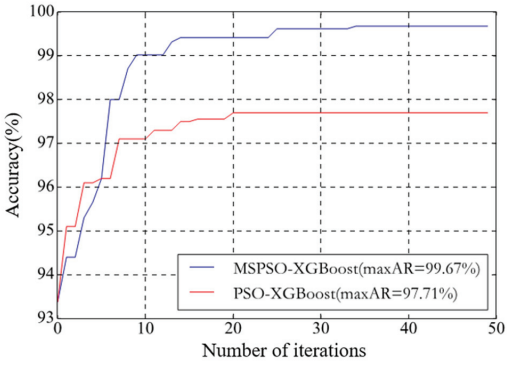

Figure 4. MSPSO and PSO optimize the XGBoost accuracy curve.

3.4. Diagnostic Results and Analysis

Figure 5 illustrates the diagnostic accuracy of fault models that were trained using the same dataset with the SVM, back propagation neural network (BPNN), XGBoost, PSO-XGBoost, and MSPSO-XGBoost algorithms for eight distinct states. The SVM and the BPNN parameter sets are shown, and the parameters are listed in Tables 6 and 7. The AR in Figure 5 represents the overall diagnostic accuracy of the five models.

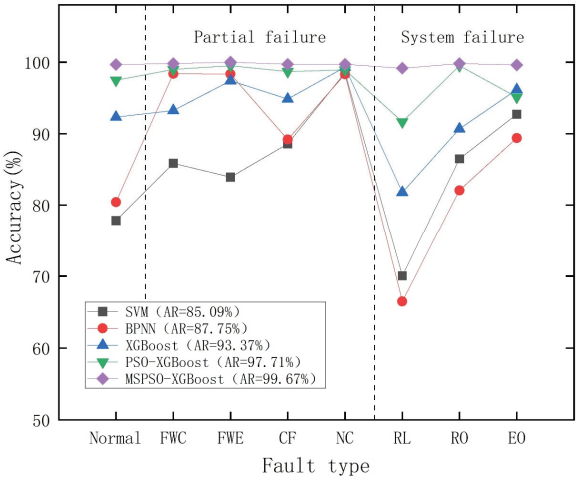

Figure 5. The precision rate of the diagnosis of 8 states using 5 algorithms.

Table 6. SVM parameter values.

Kernel Function Type	Kernel Function Parameters (γ)	Penalty Factor (C)
Gaussian kernel	0.6	32

Table 7. BPNN parameter values.

Hyper-Parameters	Value
Number of input layer neurons	23
Number of hidden layers	3
Number of neurons per hidden layer	12
The activation function of the hidden layer	sigmoid
Number of output layer neurons	8

From Figure 5, some results can be concluded.

1. The performance of the local fault diagnosis is superior to that of system fault diagnosis, indicating that the difficulty of diagnosing local faults is lower than that of system faults in the minor faults of chillers. The reason for this phenomenon is that local faults can usually be judged with a small number or even a single parameter change, while system faults often require more parameter changes to be judged comprehensively. From the perspective of engineering practice, for example, FWC failure is usually based on the chilled water flow and cooling water flow changes can be relatively accurate judgements, while the RL failure needs to be combined with the degree of subcooling, chilled water flow, cooling water flow, compressor operating power, the condenser temperature, the evaporator temperature, condensing pressure, oil supply temperature, oil pressure temperature, and oil supply pressure parameter changes to make a comprehensive diagnosis decision;
2. According to the literature [30,31], it can be concluded that BPNNs are superior to SVMs in the diagnosis of local faults, but inferior to SVMs in the diagnosis of system faults. Except for slightly lower diagnostic accuracy in FWC and FWE faults compared to BPNNs, XGBoost outperforms BPNNs and SVMs in diagnostic accuracy in other faults. In terms of overall accuracy ratio (AR), XGBoost is better than BPNNs and SVMs for chiller micro-fault diagnosis;
3. Compared with XGBoost, the PSO-XGBoost has improved diagnosis accuracy of all faults except EO; the accuracy of MSPSO-XGBoost diagnosis in eight states is better than XGBoost. The diagnosis performance of the MSPSO-XGBoost is prior to PSO-XGBoost in three types of system faults and normal states, demonstrating that MSPSO-XGBoost is more capable of diagnosing micro-faults in chillers than PSO-XGBoost.
4. Compared to SVMs and BPNNs, the AR of MSPSO-XGBoost is improved by 14.58% and 11.92%, respectively. The gap in diagnostic performance for various types of faults is narrowed by XGBoost after parameter optimization.

Tables 8–12 show the confusion matrices of SVMs (Gaussian kernel), BPNNs, XGBoost, PSO-XGBoost, and MSPSO-XGBoost. The confusion matrix is partitioned into nine parts with four black dashed lines according to the three levels of normal, local, and systematic faults, which is known as the nine-grid. In this case, the middle part of the nine-grid (4×4 matrix) represents the classification results of local faults, while the bottom-right corner (3×3 matrix) represents the classification results of systematic faults.

Table 8. SVM (Gaussian kernel) confusion matrix.

	Number	True Faults								Precision Rate	Recall Rate
		0	**1**	**2**	**3**	**4**	**5**	**6**	**7**		
Diagnosed Faults	0 Normal	752	42	57	0	0	64	6	45	77.84%	78.08%
	1 FWC	39	850	12	2	1	46	23	17	85.85%	85.00%
	2 FWE	89	11	808	0	1	21	11	22	83.90%	87.06%
	3 CF	7	4	5	875	0	54	22	21	88.56%	92.59%
	4 NC	0	3	3	3	1002	0	6	0	98.52%	99.30%
	5 RL	46	71	28	39	0	746	88	47	70.04%	71.93%
	6 RO	6	13	9	25	5	71	883	9	86.48%	84.98%
	7 EO	24	6	6	1	0	35	0	918	92.72%	85.07%

Table 9. BPNN confusion matrix.

	Number	True Faults								Precision Rate	Recall Rate
		0	**1**	**2**	**3**	**4**	**5**	**6**	**7**		
Diagnosed Faults	0 Normal	777	2	37	0	0	105	5	40	80.43%	79.12%
	1 FWC	2	974	1	2	5	3	3	0	98.38%	98.58%
	2 FWE	10	0	947	0	1	2	0	3	98.33%	94.22%
	3 CF	3	0	0	881	5	57	29	13	89.17%	86.54%
	4 NC	0	2	0	5	1000	0	9	1	98.32%	98.23%
	5 RL	151	4	10	66	0	708	89	37	66.47%	69.54%
	6 RO	13	6	2	54	7	88	838	13	82.07%	85.67%
	7 EO	26	0	8	10	0	55	6	885	89.39%	89.21%

Table 10. XGBoost confusion matrix.

	Number	True Faults								Precision Rate	Recall Rate
		0	**1**	**2**	**3**	**4**	**5**	**6**	**7**		
Diagnosed Faults	0 Normal	892	22	0	0	2	28	17	5	92.33%	88.84%
	1 FWC	47	923	0	0	2	7	9	2	93.23%	96.44%
	2 FWE	13	5	938	0	0	2	1	4	97.40%	99.57%
	3 CF	0	0	2	937	1	30	15	3	94.83%	99.57%
	4 NC	0	0	2	2	1010	0	1	2	99.31%	99.51%
	5 RL	29	4	0	2	0	871	126	33	81.78%	86.66%
	6 RO	8	2	0	0	0	58	927	26	90.69%	83.49%
	7 EO	15	1	0	0	0	9	13	952	96.16%	92.69%

Table 11. PSO-XGBoost confusion matrix.

	Number	True Faults								Precision Rate	Recall Rate
		0	**1**	**2**	**3**	**4**	**5**	**6**	**7**		
Diagnosed Faults	0 Normal	937	2	0	4	0	21	1	1	96.99%	99.26%
	1 FWC	0	979	0	0	9	0	1	1	98.89%	99.69%
	2 FWE	0	0	958	2	0	0	0	3	99.48%	100.00%
	3 CF	0	1	0	975	12	0	0	0	98.68%	99.19%
	4 NC	1	0	0	2	1004	0	10	0	98.72%	97.95%
	5 RL	4	0	0	0	0	976	80	5	91.64%	97.80%
	6 RO	1	0	0	0	0	0	1015	5	99.41%	88.26%
	7 EO	1	0	0	0	0	1	43	945	95.45%	97.72%

Table 12. MSPSO-XGBoost confusion matrix.

	Number	True Faults								Precision Rate	Recall Rate
		0	**1**	**2**	**3**	**4**	**5**	**6**	**7**		
Diagnosed Faults	0 Normal	963	0	0	1	0	1	0	1	99.68%	99.27%
	1 FWC	0	988	0	0	0	0	1	1	99.79%	99.89%
	2 FWE	0	0	963	0	0	0	0	0	100.00%	100.00%
	3 CF	0	1	0	985	2	0	0	0	99.69%	99.69%
	4 NC	1	0	0	2	1013	0	1	0	99.70%	99.80%
	5 RL	4	0	0	0	0	1056	1	4	99.15%	99.81%
	6 RO	1	0	0	0	0	0	1019	1	99.80%	99.51%
	7 EO	1	0	0	0	0	1	2	986	99.59%	99.29%

From Table 8, it can be found that the diagnostic accuracy of NC is significantly better than the other faults in the table, while the diagnostic accuracies of NC faults in Tables 8–12 are quite close to each other. From the perspective of refrigeration principles, the variables that will be affected first are analyzed when an NC fault occurs. It is found that they coincide with the four variables listed in the top five contributions in Table 4. The raw data feature parameter numbers, namely 56, 25, 24, and 4, are the VE, FWE, FWC, and TWEO variables in the RP-1043 dataset, respectively. This phenomenon indicates that the key features have a greater impact on the fault diagnosis performance compared to the diagnostic model. It is also found that for NC faults XGBoost, PSO-XGBoost, and MPSO-XGBoost diagnostic performance gradually and slightly decreases. It can be concluded that the overall diagnostic performance index of the model will be improved by optimizing the model parameters, but it may not necessarily be improved for certain types of faults.

As can be seen from Table 10, the XGBoost diagnostic model is prone to confuse normal with the three system-level faults of RL, RO, and EO due to the fact that in the early stage of the occurrence of the tiny faults, the monitoring data of the system faults are coupled with the monitoring data of the normal state, which results in the difficulty of the diagnosis and the existence of a high rate of misclassification. From the comparison between Tables 8 and 9, it is obvious that in the BPNN and SVM diagnostic models, there is a coupling between the normal state and system faults, as well as a certain coupling with the local faults of FWC and FWE. Table 10 shows that the XGBoost diagnostic easily confuses normal with the three system-level faults of RL, RO, and EO. The reason is that in the early stages of micro-faults, the monitoring data of system faults are coupled with the monitoring data of normal states, resulting in high diagnostic difficulty and a high misclassification rate. It can be concluded that the normal state is coupled with other faults, possibly due to the fact that experiments on fault-free data are conducted intermittently between various fault experiments. Various faults can cause changes in the physical properties of the chiller unit, resulting in a constantly changing physical state of the fault-free state, which is coupled with other fault states. Therefore, the diagnosis of minor faults at the system level of chillers is difficult.

In analyzing Tables 8–12, it was found that compared to SVMs and BPNNs, XGBoost has the highest overall correctness for local fault diagnosis, with improved recall and precision for each system fault diagnosis. PSO-XGBoost has shown considerable improvement in the diagnosis of most fault categories, but it still needs to be improved in some system faults, like RL and EO. The recall and accuracy of FWE for local faults under the MSPSO-XGBoost composite model diagnosis are 100%, and the classification performance of other local faults is likewise optimal. For system failures, the recall and accuracy rates of the three types of failures have been improved, with the accuracy rate of RL increasing to 99.81% and the recall rate of RO increasing to 99.51%. Therefore, MSPSO-XGBoost can significantly enhance the accuracy of minor fault diagnosis in chillers and facilitate timely detection.

Table 13 shows the comparison of the research of this work and the references; it can be concluded that the MSPSO-XGBoost method has a significant improvement in diagnosis, compared to the SVM and BPNN models.

Table 13. Comparative analysis of present work with other references.

Reference	Classifier	Sample Size	Ratio of Training Set to Test Set	0 Normal	1 FWC	2 FWE	3 CF	4 NC	5 RL	6 RO	7 EO	Accuracy (Minor Grade)
[32]	SVM	41,528	4:1	0.924	0.998	0.998	0.994	0.947	0.949	0.922	0.929	95.8%
[33]	BPNN	12,000	2:1	0.9243	0.9634	0.9981	0.9899	0.9922	0.9153	0.9482	0.9025	95.50%
Present Work	XGBoost	32,000	3:1	0.9233	0.9233	0.9740	0.9483	0.9931	0.8178	0.9069	0.9616	93.37%
Present Work	MPSO-XGBoost	32,000	3:1	0.9968	0.9979	1.000	0.9969	0.9970	0.9915	0.9980	0.9959	99.67%

4. Conclusions

A minor fault diagnosis model for centrifugal chillers based on the XGBoost algorithm was proposed in this paper. Five important parameters of the XGBoost algorithm were optimized using MSPSO. The minor fault diagnosis model (MSPSO-XGBoost) was established. By comparing and analyzing the diagnostic results of the XGBoost, PSO-XGBoost, MSPSO-XGBoost, BPNN, and SVM models, the following conclusions are drawn:

1. The cumulative contribution reaches 89.54% with the feature number at 23. The XGBoost model has the best accuracy rate of 93.35%;
2. The MSPSO algorithm is a good choice for optimizing XGBoost parameters. Compared to PSO, it may effectively prevent the local optimal solution, while MSPSO has a slower initial convergence speed;
3. For chillers, the high similarity of the data between minor faults and the normal state leads to distinguishing difficulty. Therefore, system-level minor faults are more difficult to distinguish compared to local minor faults;
4. The diagnostic ability of the proposed MSPSO-XGBoost model on the eight different states is uniform. The diagnostic accuracy of the model reaches 99.67%. The classification performance of MSPSO-XGBoost is superior to the SVM and BPNN diagnostic models;
5. Critical features have a greater impact on fault diagnosis performance compared to the diagnostic model. Optimizing the model parameters will improve the overall diagnostic performance metrics of the model, but it may not necessarily improve for certain types of faults.

Author Contributions: Conceptualization, Q.D.; methodology, Y.L.; software, Y.X.; validation, Y.X.; formal analysis, N.J. and Q.D.; investigation, T.L., M.Z. and N.J.; resources, M.Z.; data curation, T.L.; writing—original draft preparation, Y.L. All authors have read and agreed to the published version of the manuscript.

Funding: This research received no external funding.

Data Availability Statement: The original contributions presented in the study are included in the article, further inquiries can be directed to the corresponding author.

Conflicts of Interest: Authors Yaxiang Liu and Tao Liang were employed by the company Shandong Electric Power Engineering Consulting Institute Co., Ltd. The remaining authors declare that the research was conducted in the absence of any commercial or financial relationships that could be construed as a potential conflict of interest.

References

1. Dou, H.; Zmeureanu, R. Detection and diagnosis of multiple-dependent faults (MDFDD) of water-cooled centrifugal chillers using grey-box model-based method. *Energies* **2022**, *16*, 210. [CrossRef]
2. Singh, V.; Mathur, J.; Bhatia, A. A comprehensive review: Fault detection, diagnostics, prognostics, and fault modeling in HVAC systems. *Int. J. Refrig.* **2022**, *144*, 283–295. [CrossRef]
3. Zhao, Y.; Zhang, C.; Zhang, Y.; Wang, Z.; Li, J. A review of data mining technologies in building energy systems: Load prediction, pattern identification, fault detection and diagnosis. *Energy Built Environ.* **2020**, *1*, 149–164. [CrossRef]
4. Wang, Z.; Dong, Y.; Liu, W.; Ma, Z. A novel fault diagnosis approach for chillers based on 1-D convolutional neural network and gated recurrent unit. *Sensors* **2020**, *20*, 2458. [CrossRef] [PubMed]
5. Li, G.; Yao, Q.; Fan, C.; Zhou, C.; Wu, G.; Zhou, Z.; Fang, X. An explainable one-dimensional convolutional neural networks based fault diagnosis method for building heating, ventilation and air conditioning systems. *Build. Environ.* **2021**, *203*, 108057. [CrossRef]
6. Thango, B.A. On the Application of Artificial Neural Network for Classification of Incipient Faults in Dissolved Gas Analysis of Power Transformers. *Mach. Learn. Knowl. Extr.* **2022**, *4*, 839–851. [CrossRef]
7. Gao, T.; Yang, J.; Jiang, S. A novel incipient fault diagnosis method for analog circuits based on GMKL-SVM and wavelet fusion features. *IEEE Trans. Instrum. Meas.* **2020**, *70*, 3502315. [CrossRef]
8. Wang, Z.; Guo, J.; Zhou, S.; Xia, P. Performance Evaluation of Chiller Fault Detection and Diagnosis Using Only Field-Installed Sensors. *Processes* **2023**, *11*, 3299. [CrossRef]
9. Fan, Y.; Cui, X.; Han, H.; Lu, H. Feasibility and improvement of fault detection and diagnosis based on factory-installed sensors for chillers. *Appl. Therm. Eng.* **2020**, *164*, 114506. [CrossRef]
10. Han, H.; Cui, X.; Fan, Y.; Qing, H. Least squares support vector machine (LS-SVM)-based chiller fault diagnosis using fault indicative features. *Appl. Therm. Eng.* **2019**, *154*, 540–547. [CrossRef]
11. Vapnik, V.N. An overview of statistical learning theory. *IEEE Trans. Neural Netw.* **1999**, *10*, 988–999. [CrossRef] [PubMed]
12. Gong, W.; Chen, H.; Zhang, Z.; Zhang, M.; Wang, R.; Guan, C.; Wang, Q. A novel deep learning method for intelligent fault diagnosis of rotating machinery based on improved CNN-SVM and multichannel data fusion. *Sensors* **2019**, *19*, 1693. [CrossRef]
13. Kukreja, H.; Bharath, N.; Siddesh, C.S.; Kuldeep, S. An introduction to artificial neural network. *Int. J. Adv. Res. Innov. Ideas Educ.* **2016**, *1*, 27–30. [CrossRef] [PubMed]
14. Mienye, I.D.; Sun, Y. A Survey of Ensemble Learning: Concepts, Algorithms, Applications, and Prospects. *IEEE Access* **2022**, *10*, 99129–99149. [CrossRef]
15. Chen, T.; Guestrin, C. Xgboost: A scalable tree boosting system. In Proceedings of the 22nd ACM Sigkdd International Conference on Knowledge Discovery and Data Mining, ACM, San Francisco, CA, USA, 13–17 August 2016; pp. 785–794. [CrossRef]
16. Grinsztajn, L.; Oyallon, E.; Varoquaux, G. Why do tree-based models still outperform deep learning on typical tabular data? *Adv. Neural Inf. Process. Syst.* **2022**, *35*, 507–520. [CrossRef]
17. Wang, C.W.; Lee, Y.C.; Calista, E.; Zhou, F.; Zhu, H.; Suzuki, R.; Cheng, S.P. A benchmark for comparing precision medicine methods in thyroid cancer diagnosis using tissue microarrays. *Bioinformatics* **2018**, *34*, 1767–1773. [CrossRef] [PubMed]
18. Wang, W.; Lesner, C.; Ran, A.; Rukonic, M.; Xue, J.; Shiu, E. Using small business banking data for explainable credit risk scoring. *Proc. AAAI Conf. Artif. Intell.* **2020**, *34*, 13396–13401. [CrossRef]
19. Wassan, J.T.; Wang, H.; Browne, F.; Zheng, H. A comprehensive study on predicting functional role of metagenomes using machine learning methods. *IEEE/ACM Trans. Comput. Biol. Bioinform.* **2018**, *16*, 751–763. [CrossRef] [PubMed]
20. Qiu, C.; Zhang, L.; Li, M.; Zhang, P.; Zheng, X. Elevator Fault Diagnosis Method Based on IAO-XGBoost under Unbalanced Samples. *Appl. Sci.* **2023**, *13*, 10968. [CrossRef]
21. Zhang, S.; Zhu, X.; Anduv, B.; Jin, X.; Du, Z. Fault detection and diagnosis for the screw chillers using multi-region XGBoost model. *Sci. Technol. Built Environ.* **2021**, *27*, 608–623. [CrossRef]
22. Wang, Y.; Ni, X.S. A XGBoost risk model via feature selection and Bayesian hyper-parameter optimization. *arXiv* **2019**, arXiv:1901.08433. [CrossRef]
23. Kaligambe, A.; Fujita, G.; Tagami, K. Indoor Room Temperature and Relative Humidity Estimation in a Commercial Building Using the XGBoost Machine Learning Algorithm. In Proceedings of the 2022 IEEE PES/IAS PowerAfrica, Kigali, Rwanda, 22–26 August 2022; IEEE: Piscataway, NJ, USA, 2022; pp. 1–5. [CrossRef]
24. Jain, M.; Saihjpal, V.; Singh, N.; Singh, S.B. An overview of variants and advancements of PSO algorithm. *Appl. Sci.* **2022**, *12*, 8392. [CrossRef]
25. Gad, A.G. Particle swarm optimization algorithm and its applications: A systematic review. *Arch. Comput. Methods Eng.* **2022**, *29*, 2531–2561. [CrossRef]
26. Yang, X.; Li, H.; Yu, X. A dynamic multi-swarm cooperation particle swarm optimization with dimension mutation for complex optimization problem. *International J. Mach. Learn. Cybern.* **2022**, *13*, 2581–2608. [CrossRef]
27. Hao, J.; Ho, T.K. Machine learning made easy: A review of scikit-learn package in python programming language. *J. Educ. Behav. Stat.* **2019**, *44*, 348–361. [CrossRef]
28. Comstock, M.C.; Braun, J.E. Development of analysis tools for the evaluation of fault detection and diagnostics for chillers. In *ASHRAE Research Project 1043-RP, HL 99-20, Report #4036-3*; Purdue University: West Lafayette, IN, USA, 1999.

29. Gu, K.; Wang, J.; Qian, H.; Su, X. Study on intelligent diagnosis of rotor fault causes with the PSO-XGBoost algorithm. *Math. Probl. Eng.* **2021**, *2021*, 9963146. [CrossRef]
30. Ren, Z.; Han, H.; Cui, X.; Qing, H.; Ye, H. Application of PSO-LSSVM and hybrid programming to fault diagnosis of refrigeration systems. *Sci. Technol. Built Environ.* **2021**, *27*, 592–607. [CrossRef]
31. Sun, S.; Li, G.; Chen, H.; Huang, Q.; Shi, S.; Hu, W. A hybrid ICA-BPNN-based FDD strategy for refrigerant charge faults in variable refrigerant flow system. *Appl. Therm. Eng.* **2017**, *127*, 718–728. [CrossRef]
32. Sun, X.; Yan, K.; Zhou, X. Fault detection and diagnosis of chillers with s&d convolutional neural network. In Proceedings of the 2020 International Conferences on Internet of Things (iThings) and IEEE Green Computing and Communications (GreenCom) and IEEE Cyber, Physical and Social Computing (CPSCom) and IEEE Smart Data (SmartData) and IEEE Congress on Cybermatics (Cybermatics), Rhodes, Greece, 2–6 November 2020; IEEE: Piscataway, NJ, USA, 2020; pp. 829–836. [CrossRef]
33. Liang, Q.; Han, H.; Cui, X.; Qing, H.; Fan, Y. Comparative study of probabilistic neural network and back propagation network for fault diagnosis of refrigeration systems. *Sci. Technol. Built Environ.* **2018**, *24*, 448–457. [CrossRef]

buildings

MDPI

Article

Investigation of the Temperature Distribution and Energy Consumption of an Integrated Carbon Fiber Paper-Embedded Electric-Heated Floor

Chengjian Huang [1,2,*], Neng Li [1,2], Sheng He [1,2], Xiang Weng [3], Yi Shu [1,2], Guang Yang [4] and Yongjie Bao [1,2,*]

[1] China National Bamboo Research Center, Hangzhou 310012, China; lineng8657@sina.com (N.L.); hesheng_cbrc@163.com (S.H.); sunlee6789@hotmail.com (Y.S.)
[2] Key Laboratory of High Efficient Processing of Bamboo of Zhejiang Province, Hangzhou 310012, China
[3] College of Mathematics and Computer Science, Zhejiang A&F University, Hangzhou 311300, China; woodweng@zafu.edu.cn
[4] Harbin Institute of Forestry Machinery, State Forestry and Grassland Bureau, Harbin 150086, China; heyyangguang@gmail.com
* Correspondence: hcj5236@yeah.net (C.H.); baoyongjie1@126.com (Y.B.)

Abstract: This study examined spatial and temporal thermal performance and energy consumption. The temperature distribution in the running period was monitored in test rooms with integrated electric- and hot water-heated floors. The short- and long-term energy consumption of the two heating systems were recorded and compared. The results indicated that the integrated electric heating system generated higher temperatures for indoor air and on the exterior surface of the wooden floor than the hot water heating system; meanwhile, the difference in the mean temperatures of the exterior and rear surfaces of the electric-heated floor was 2.44 °C, while that of the hot water-heated test room was 13.25 °C. The efficient structure of the integrated electric heating system saved 22.97% energy compared to the hot water system after short-term (7 h) charging and reaching a dynamic balance, and it efficiently increased the energy utilization rate to 11.81%. After long-term charging, the daily energy consumption of the integrated electric heating system consumed much less energy than the hot water system every month. The integrated electric heating system saved 62.55% and 34.30% of energy in May and January, respectively, and consumed less than half of the energy the hot water system consumed in the less cold months. Therefore, a high-efficiency and energy-saving integrated electric-heated floor could be a potential indoor heating solution.

Keywords: radiant heating; energy saving; indoor thermal environment; carbon fiber paper

Citation: Huang, C.; Li, N.; He, S.; Weng, X.; Shu, Y.; Yang, G.; Bao, Y. Investigation of the Temperature Distribution and Energy Consumption of an Integrated Carbon Fiber Paper-Embedded Electric-Heated Floor. *Buildings* **2024**, *14*, 2097. https://doi.org/10.3390/buildings14072097

Academic Editors: Sungkyun Jung, Piljae Im and Yeobeom Yoon

Received: 24 May 2024
Revised: 3 July 2024
Accepted: 4 July 2024
Published: 9 July 2024

1. Introduction

Indoor thermal environments are increasingly popular as they involve human health [1], comfort [2,3], environmental pollution [4], and energy consumption [5]. Given the current increasingly strong awareness of energy conservation, energy conservation research of indoor heating has been vitally important in developing energy consumption [5].

Bojić et al. compared the performance of different radiant heating systems on walls, ceilings, and floors and reported that floor heating involved the lowest energy and operation costs [6], which was consistent with Fabrizio's study [3]. Using energy substitution technology, Zhang et al. proposed that the radiant floor heating system is highly efficient and environmentally protective [7]. The earliest radiant floor heating systems used hot gases and were termed "kang" and "dikang", which were used in China in the 11th century BC [8]. The modern fluid-based systems began with the circulating hot water patent from Europe in 1839. Since then, the circulating hot water-based radiant floor heating system has improved and developed into a widely used indoor heating system in residential buildings [9,10]. Rohdin et al. investigated energy-conservation strategies for improving the hot water floor heating system, such as a proportional flux modulation strategy and

a two-parameter on–off control strategy [11]. Cho explored a predictive control strategy involving the intermittently heated radiant floor heating system and reported that 10–12% of energy could be saved [12]. However, the disadvantages of hot water floor heating systems were as apparent as the advantages. Hu et al. [13] summarized the practical application of the radiant floor heating system in mainland China, where the long response time of the hot water floor heating systems was a drawback. A compared simulation analysis of low-temperature hot water floor radiant heating and electrical floor radiant heating by Qi et al. [14] indicated a more uniform floor surface temperature distribution of electrical radiant floor heating. While the hot water system warming is time-consuming and the temperature is inhomogeneous, the system is still widely used in many residential buildings. Thus, the hot water heating system must be used as a reference in electrical radiant floor heating system analysis.

Various forms of electrical radiant floor heating systems have been developed. In the mid-20th century, radiant heating using concrete-embedded copper pipes was extensively applied in the first large-scale multi-building project in New York, the United States [9]. After that, energy-saving and thermal performance improvement strategies were researched. The 1970s marked the early phase of radiant floor heating system research and application. For example, steel wire fabric was used to form an electrical loop in concrete floors for storing heat [15]. The structure of the cable-embedding matrix material might influence temperature transformation and distribution [16,17]. Yan et al. [18] compared the thermal performance of cable radiant heating floors in three different structures and reported that the ready-made thin structure had relatively good thermal and mechanical properties. Similarly, heating system structures significantly affect thermal performance [19]. Furthermore, the aforementioned report involved energy saving and reported that electrically heated floors shifted 84% of the building load to nighttime, which saved costs based on off-peak electricity prices [19].

Based on the above literature review, embedded structures generally conduct much more heat loss to the ground and consume more energy, while the heating unit of wire-like materials causes temperature inhomogeneity on the floor surface. Fontana [20] placed a thick aluminum sheet above the electrical heater to reduce the surface temperature non-uniformity. However, this action might complicate the structures, which is not conducive to manufacturing. A heating unit that uses advanced materials converts wire-like materials (cables) to facet materials (carbon crystal membrane, carbon black mortar slabs, and carbon fiber paper (CFP)). Carbon fiber is an advanced high-strength material with an efficient electro-thermal conversion efficiency approach nearing 100% [21,22], from which integrated electric floor heating was developed. Carbon fiber is blended with plant fiber [23] to produce CFP [24,25], which is generally used in high-performance capacitors [26] and fuel cells as electrodes [27,28]. CFP has substantial potential for indoor thermal application due to its prominent advantages of electro-thermal conversion efficiency > 97% [29] and emission of health-beneficial infrared rays of 8~15 μm [30].

Electric-heated floors consist of three layers [30,31]: a wooden facial layer [32], a heating unit [33], and a wooden matrix layer, and they are connected to the energy source using two electrodes at both ends of the floorboards [31]. Compared with the wire-like heating unit (electric cables and water pipes), CFP has a much greater heating area and uniform temperature distribution as a facet heating unit. While the properties of wooden electric heating composites were comparatively well investigated, investigations of the performance of electric floor heating as compared with the conventional heating system remain indispensable to researchers and consumers.

The literature review indicates that the radiant floor heating system is a highly efficient and energy-saving indoor heating system. Furthermore, the application of advanced materials is an inevitable trend due to their high performance and as a solution to surface temperature non-uniformity. However, previous works mainly focused on theoretical and trial sample experimental studies of wooden electric heating composites, which cannot

represent its performance as a radiant heating system in practical projects, including its energy-saving and thermal performance attributes.

This study developed an electric heating system with the CFP integrated in a wooden floor which could be used directly on electricity, and two identical experimental rooms were used for short- and long-term energization experiments with the electric heating system and the hot water heating system. A comparative study was conducted to investigate the temperature distribution, energy consumption and energy utilization of the two heating systems and aimed to visually demonstrate the indoor temperature and energy efficiency of the designed electric heating system. The authors intended to propose a high-efficiency and energy-saving radiant floor heating system.

2. Materials and Methods

2.1. Materials

Figure 1a demonstrates that the integrated electric-heated floor consisted of a wooden floor, heating unit, power cables, and a temperature controller. The CFP was obtained in accordance with the methodology outlined in reference [34], and its volume resistivity was found to range 10^{-1}~10^{4} Ω·cm. The front board was constructed from red oak, while the matrix board was made from eucalyptus composite board.

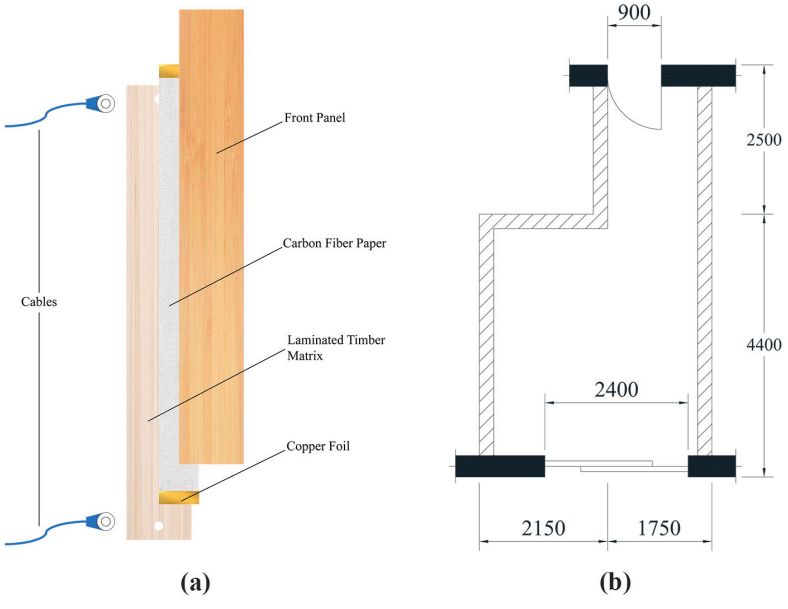

Figure 1. Schematic sketch of (**a**) integrated electric-heated floor and (**b**) test room. Author's drawings.

2.2. Methods of Preparing Integrated Electric Floor and Test Room

As shown in Figure 2, the heating unit (CFP with two electrodes pasted on two sides) was embedded in wood veneers with glue between the front board and matrix board. The hot water floor heating system involved water pipes embedded in a cement matrix, placed on concrete, and covered by a wood floor. A temperature regulatory controlled the temperature approaches of the two systems. In this study, both systems used electricity as the energy source. The wooden floor in the integrated electric heating system was directly connected to the electricity power supply. In the hot water heating system, water was heated by an electric boiler with 98% conversion efficiency, flowed cyclically, and was turned into the indoor heat source.

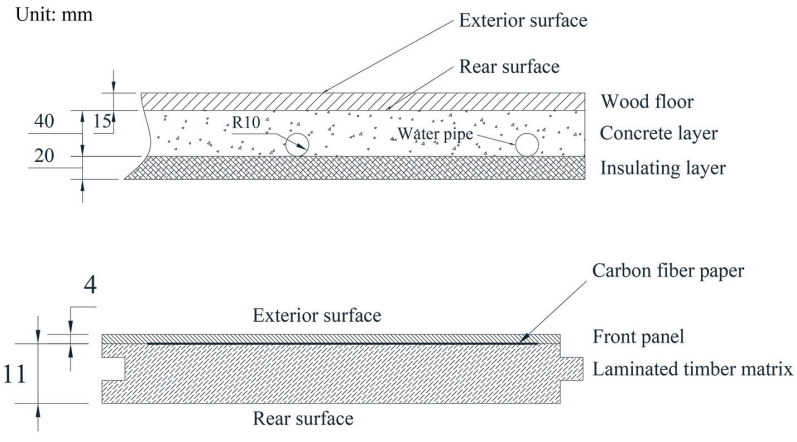

Figure 2. Schematic sketch of heating unit distribution in the two systems. Author's drawings.

The two systems were tested in two adjacent empty rooms in an experimental base of China National Bamboo Research Center, which was the new laboratory building, located at Jieruo Village, Huzhou City, Zhejiang Province. Figure 1b displays that the test rooms covered approximately 22 m^2 and were 3.70 m high indoors. The walls of the rooms are constructed of 240 mm brick walls covered with layers of cement, putty, and paint. The original floor is composed of poured cement. Each test room contained a south-facing window (2400 mm wide × 2800 mm high) opposite a north-facing door.

Figure 2 presents that the integrated electric-heated floor was laid on floor joists as a standard floor. However, the floor joists in the integrated electric-heated floor were filled with thermal insulation materials and covered with a reflective film. The electric cables were linked to the back of the floor with a pair of fasteners. A series connection was used for the power supply between floorboards. The hot water floor heating system consisted of a wooden floor layer, cement matrix layer, and insulating layer, which were laid on the concrete layer of the structure. The cement matrix layer was 40 mm high and laid on the 20 mm thick insulating layer. The electric boiler was set up on the veranda with no exposed pipes.

2.3. Methods of Temperature Distribution Test

Based on human foot and chest comfort zones [35], the temperature test experiment was conducted by establishing eight test points at eight evenly distributed locations within the test room. The aforementioned points were positioned vertically at the rear surface of the floorboard, on the exterior surface of the floorboard, and at 100 mm and 1100 mm above the floorboard, respectively. The temperature data were collected in real time by a 64-channel portable temperature tracker mentioned in the reference [32], which has an accuracy of 0.1 °C. The power was shut off when the temperature reached equilibrium.

2.4. Methods of Energy Consumption Computation

Both heating systems used electricity as the energy source, which was convenient for comparative analysis of energy consumption. Water in the hot water system was heated using an electric boiler, and the integrated electric system used CFP as the electro-thermal conversion unit. During the experiment, the doors, windows and other channels connected to the outside of the two experimental rooms were all closed and sealed in order to exclude the interference of external factors and to ensure that the data collected by fixed temperature sensors was as accurate as possible. In order to carry out the relevant calculations, the airflow in the experimental rooms was set to be purely natural convection.

Based on the law of energy balance, the heat balance of the system was calculated using the following equation:

$$\Phi_T = \Phi_a + \Phi_l \tag{1}$$

where Φ_T is the heat supply by CFP under charging or water, Φ_a is the heating capacity for heating the air in the test room, and Φ_l is the heat loss from the entire heating system. The heat supply by CFP under charging or hot water, Φ, was calculated as follows:

$$\Phi_T = WT \cdot \eta \tag{2}$$

where W is the electric power, T is the charging duration, and η is the heat efficiency. The heating capacity for heating the air in the test room, Φ_a, was calculated as follows:

$$\Phi_a = h_{tot} A (t_s - t_a) \tag{3}$$

where A is the floor surface area, t_s and t_a are the wooden floor surface and room air temperatures, respectively, and h_{tot} is the total heat transfer rate of the wooden floor surface, which consisted of the convective heat transfer coefficient h_c and radiant heat transfer coefficient h_r. The h_c was calculated as follows according to recommendations in the literature [36]:

$$N_u = 0.15(G_r P_r)^{1/4},\ 10^7 \le G_r P_r \le 10^{11} \tag{4}$$

$$G_r = \frac{g \alpha_V \Delta t l^3}{v^2} \tag{5}$$

$$P_r = \frac{v}{a} \tag{6}$$

$$h_c = \frac{N_u \lambda}{l} \tag{7}$$

where N_u, G_r, and P_r are the Nusselt, Grashor, and Prandtl numbers, respectively. α_V, v, a, and λ are the coefficient of cubical expansion, kinematic viscosity, thermal diffusivity, and thermal conductivity of air, respectively. l is the characteristic length calculated by *A/P* (surface area divided by perimeter) [36,37]. The values of each parameter in the aforementioned equation, as calculated in this paper, are presented in Table 1, which was sourced from reference [36]. The h_r was calculated as follows as described previously [36]:

$$h_r = \varepsilon \sigma \left(T_s^2 + T_a^2 \right) (T_s + T_a) \tag{8}$$

where ε is the floor surface emissivity with the value of 0.81 [36], and σ is the Stefan–Boltzmann constant with the value of 5.67 E^{-8} W m^{-2} K^{-4} [37]. The energy utilization rate was defined as the percentage of the heating capacity for heating air in the heat supply and was calculated as follows:

$$c = \frac{\Phi_a}{\Phi_T} \times 100\% \tag{9}$$

Table 1. Parameters in the calculation formula [36].

Parameters	g m s^{-2}	v m^2 s^{-1}	a m^2 s^{-1}	λ W m^{-1} K^{-1}	l m
Value	9.8	15.06×10^{-6}	21.4×10^{-6}	2.59×10^{-2}	1.2

3. Results

3.1. Temperature Distribution

The vertical temperature curves of the two test rooms according to time and height over 20 h are depicted in Figure 3 and were measured at 8:00 a.m. to 12:00 p.m. the following

day. Both the floor's exterior surface and rear surface reached their set temperature at the fastest rate and maintained equilibrium. Nevertheless, the vertical temperature of the integrated electric heated floor exhibited a rapid increase to its maximum value, after which it remained stationary.

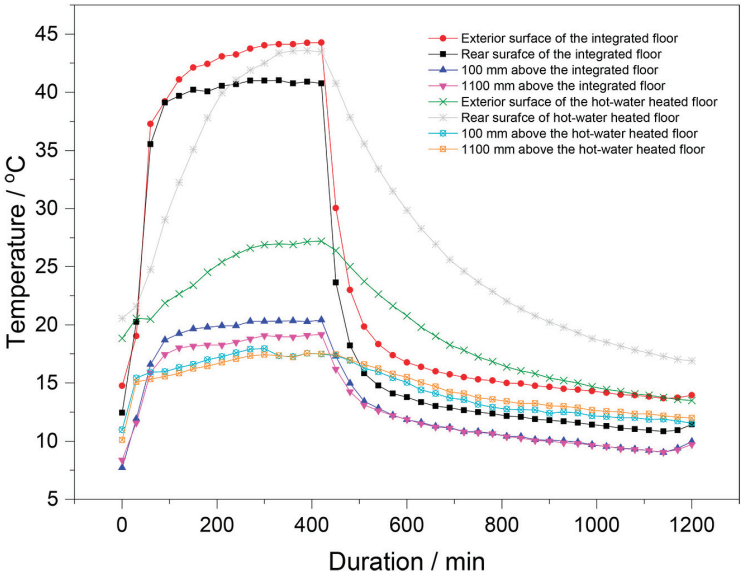

Figure 3. Temperature distribution of the two test rooms. Author's drawings.

The vertical temperatures in both rooms were stratified. Both heating systems employed a process whereby heat radiated from the floor to the air, thus providing a means of heating. Table 2 presents the temperature distribution in the vertical direction. The average temperature of the exterior surface of the electric heating system was 42.55 °C, which was higher than the average temperature of the rear surface, which was 40.11 °C. This is in contrast to the hot water heating system, where the exterior surface temperature was lower than the rear surface temperature. In terms of vertical distribution, the indoor air temperature was observed to be higher at a height of 100 mm above the floor surface than at 1100 mm above the floor surface for both systems. However, at the same height, the electric heating system was observed to be hotter than the water heating system. The average temperature under dynamic balance status was 18.37 °C at the 1100 mm measurement point in the electric-heated room, which reached 18 °C indoor air temperature and led to the lowest energy consumption rate according to Koca et al. [38], while of the hot water-heated room was 16.75 °C. The electric-heated room felt warmer under the feet as the temperature was 40–45 °C on the wooden floor exterior surface.

Table 2. Statistical analysis data (mean value M, standard deviation SD and coefficient of variation CV) of temperature under dynamic balance status in the test rooms.

Statistic	Integrated Electric-Heated Floor Test Room				Hot Water-Heated Floor Test Room			
	Exterior Surface	Rear Surface	100 mm	1100 mm	Exterior Surface	Rear Surface	100 mm	1100 mm
M	42.55	40.11	19.68	18.37	25.09	38.34	17.10	16.75
SD	2.17	1.49	1.05	0.90	2.29	6.23	0.68	0.78
CV	5.10%	3.71%	5.35%	4.88%	9.12%	16.25%	3.98%	4.65%

Both heating systems radiated heat from the floor to the air for the purposes of heating. However, the average temperature of the surface plate in an electric heating system is 42.55 °C, which is higher than the temperature of the back plate, which is 40.11 °C. This is in contrast to the water heating system, where the temperature of the surface plate is lower than that of the back plate. The indoor air temperature of both systems is found to be higher at a depth of 100 mm than at a depth of 1100 mm. However, it is observed that the temperature is higher at the same depth in the electric underfloor heating system.

Figure 4 depicts that the exterior and rear surface temperatures were measured in the coldest winter months. In the integrated electric heating systems, the temperature of the exterior surface was found to be higher than that of the rear surface, whereas in the hot water heating system, the temperature of the exterior surface was lower than that of the rear surface. The temperature discrepancy of the exterior and rear surfaces of the electric-heated floor was significantly small. The difference in the mean temperatures of the exterior and rear surfaces of the electric-heated floor was 2.44 °C, while that of the hot water-heated test room was 13.25 °C.

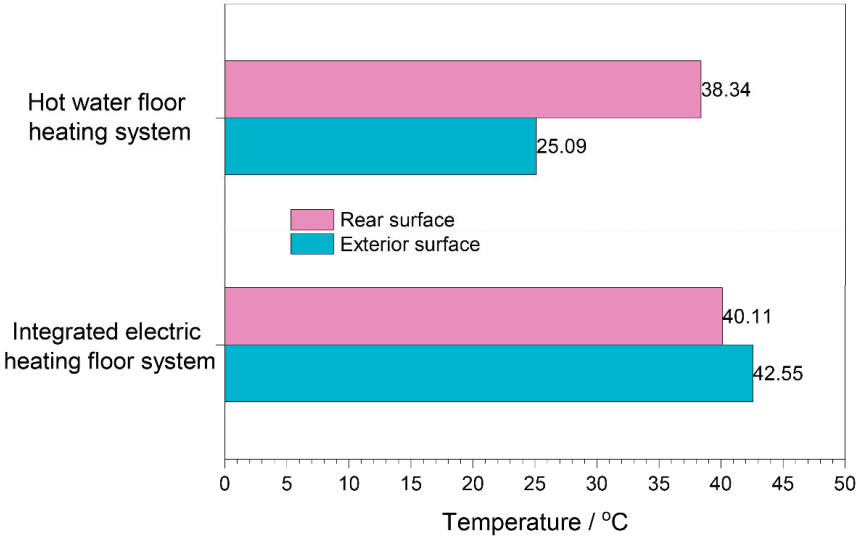

Figure 4. Floor surface temperature distribution of the two heating systems. Author's drawings.

3.2. Energy Consumption

The energy consumption of the two heating systems for 7 h was calculated after reaching dynamic balance. Figure 5 presents that the energy consumption value (Φ) of the integrated electric-heated floor and the hot water-heated floor test rooms were 31.70 and 41.16 kW h^{-1}, respectively. The integrated electric heating system used 22.97% less energy than the hot water heating system.

The thermal mass transferred from the wooden floor exterior surface to the indoor air in the two systems presented different energy utilization rates (c) based on the calculations of Equation (9). The energy utilization rate of the hot water system was 2.79%, while it was 9.02% higher in the integrated electric system (11.81%).

The average daily power consumption of the two heating systems per month was computed after long-term operation in the warm spring months and cold winter months (Figure 6). The systems consumed much more energy when the weather became colder. Specifically, the integrated electric system consumed less than half of the energy the hot water system consumed in the less cold months of May and November. The integrated electric heating system saved 62.55% and 34.30% of energy in May and January, respectively.

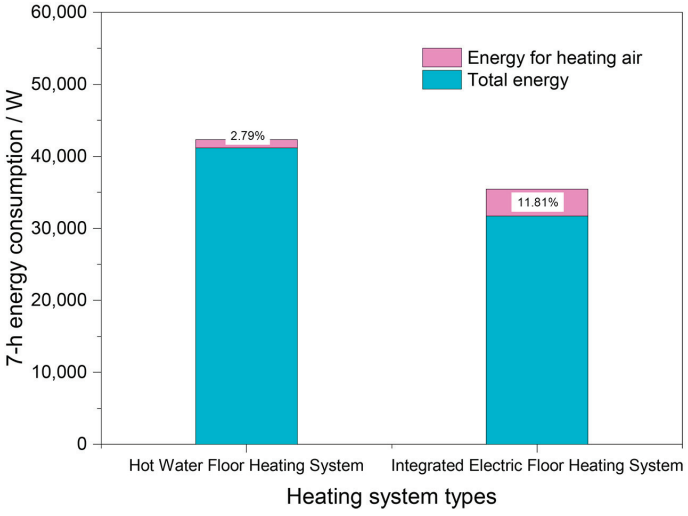

Figure 5. Dynamic balance of 7 h energy consumption. Author's drawings.

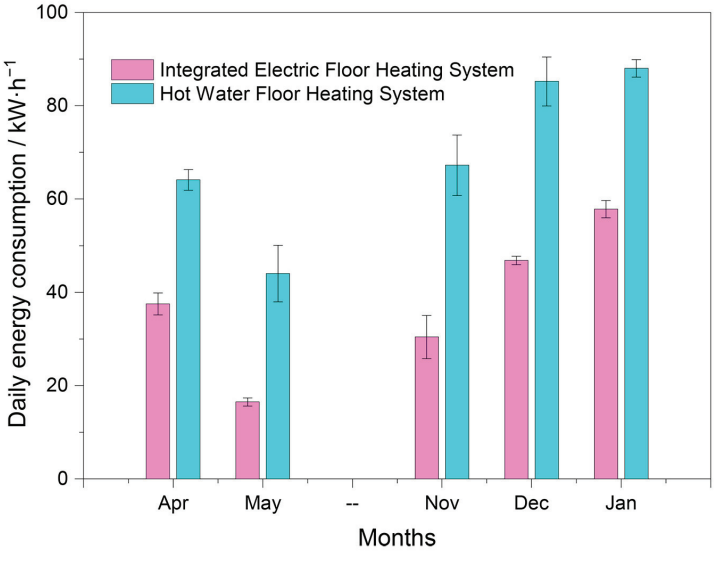

Figure 6. Long-term test of average daily power consumption. Author's drawings.

4. Discussion

4.1. Temperature Distribution

Radiant floor heating may be conceptualized as a process of natural convection in a large space with a horizontal thermal surface oriented upwards. Convective and radiative heat transfer occurred from the heated wooden floor to the air, resulting in the gradual heating of the air above the wooden floor from near to far as the feature length. Therefore, the air temperature disparity of the test rooms was caused by the disparate wooden floor exterior surface temperatures. Nevertheless, the transfer of heat between the wooden floor and the heating unit occurred via thermal conduction. The location of the heat-generating unit has a significant impact on the efficiency of heat transfer and utilization. Meanwhile, wood has a low thermal conductivity; for example, pine has a thermal conductivity of

0.15 W m^{-2} K^{-4} [35], which makes heat transfer inefficient. Therefore, it is necessary to reduce the obstruction of the heat conduction process by the wooden floor in order to improve the heat transfer efficiency.

Figures 2 and 4 manifest that the wooden floor exterior surface of the integrated electric heating system benefitted from the effective structure as its temperature was much higher than the rear surface, which was opposite to the hot water-heated floor. The CFP is the heating unit of electric-heated floors [31,33] and has an efficient conversion of ~97% [29]. The CFP was placed between the front panel and wood laminated timber matrix [32] (Figure 2), resulting in a 4 mm distance to the exterior surface and efficient heat transfer. Furthermore, CFP instantly heats while charging [31,33], resulting in more energy transfer to the indoor air. Figure 4 indicates that the temperature of the exterior surface of the electric-heated floor reached 40 °C in 30~60 min. Contrastingly, the hot water heating floor system required ~4 h to reach dynamic balance.

The disparity in temperature of the exterior surface and rear surface between the integrated electric heating floor and the hot water heating floor could be attributed to the distinct structural characteristics of each. As illustrated in Figure 2, the heating unit of the integrated electric heating floor was embedded directly in the floor, a mere 4 mm below the floor surface. During the charging process, heat was transferred directly from the heating unit (CFP) to the floor surface. Due to the low thermal conductivity of wood and the aforementioned fact that the thickness from CFP to the rear surface was much less than that to the exterior surface, the exterior surface temperature of the floor was higher than that of the rear surface of the floor in the integrated electric heating floor system. In contrast, the heat unit of the hot water heating floor system was situated beneath the floor, as illustrated in Figure 2. The transfer of heat from the hot water occurs via the concrete layer to the rear surface of the wooden floor, subsequently reaching the exterior surface of the wooden floor, which resulted in a higher temperature at the rear surface than at the exterior surface of the wooded floor.

4.2. Energy Consumption

The utilization of high-efficiency heating units is a significant contributing factor to the energy efficiency of radiant floor heating. According to the literature [21,22], the efficient electro-thermal conversion efficiency of carbon fiber approached nearing 100%, and CFP, which is manufactured from carbon fiber, exhibits an electro-thermal conversion efficiency of greater than 97% [29]. The rationale behind the utilization of CFP as a heat-generating unit in this study is to enhance the efficiency of electro-thermal conversion. The use of CFP allowed the integrated electric heating floor system to function as an instantaneous electric radiation heating floor system, thereby demonstrating the effect of energy saving, which was consistent with Cho's research [12].

Conversely, the reliability of structural design is a contributing factor to the enhancement of energy efficiency in radiant floor heating. The integrated electric heating floor system saved energy and achieved higher energy efficiency than the hot water heating floor system, which was primarily due to structural improvements, as the heating units were relocated to a higher position. In contrast to the heating unit of the hot water heating floor system embedded in the concrete matrix layer, the closer the heating unit of the integrated electric heating floor system was to the surface, the lower the heat lost to the underground, thus allowing for a greater transfer of heat to the indoor air, which is essential for the purpose of heating. Consequently, the enhancement of the electric heating floor system structure in this study represents an efficacious energy-saving strategy and indoor heating solution.

5. Conclusions

In terms of vertical distribution, the average temperature of the indoor air decreased with increasing height in both radiant heating systems. However, the average temperature of the exterior surface of the electric heating system was higher than that of the rear

surface, which was in contrast to the hot water heating system. The smaller temperature discrepancy between the exterior and rear surfaces led to the high rate of temperature rise of the integrated electric floor heating system, which addressed the shortcomings of the long reaction time of the water heating system proposed in reference [13].

The integrated electric floor heating system saved 22.97% energy compared to the hot water heating system for 7 h charging after reaching dynamic balance and efficiently increased the energy utilization rate to 11.81%. The long-term charging demonstrated that the integrated electric heating consumed much less energy daily than hot water heating every month. Furthermore, the integrated electric heating system consumed less than half of the energy consumed by the hot water system in the less cold months. This corroborates the efficacy of radiant floor heating systems, as described in the literature, as a highly efficient and energy-saving indoor heating system.

The results indicated that integrated electric floor heating was a more efficient and energy-saving radiant floor heating system for indoor heating. Generally, the integrated electric floor heating system is a potential solution for efficient and energy-saving indoor heating.

Author Contributions: Conceptualization, Y.S. and C.H.; methodology, C.H. and X.W.; validation, Y.B. and G.Y.; formal analysis, Y.B. and N.L.; resources, S.H.; data curation, Y.B. and C.H.; writing—original draft preparation, C.H. and Y.B.; writing—review and editing, X.W., Y.B. and C.H.; visualization, X.W. and N.L.; supervision, S.H. and G.Y.; project administration, Y.S.; funding acquisition, C.H. All authors have read and agreed to the published version of the manuscript.

Funding: This study was supported by the Fundamental Research Funds for the Central Non-profit Research Institution of Chinese Academy of Forestry, CAFYBB2020MB009, CAFYBB2016ZD008.

Data Availability Statement: The data presented in this study are available on request from the corresponding authors.

Conflicts of Interest: The authors declare no conflicts of interest.

Nomenclature

A	Area, m^2
c	Energy utilization rate
G_r	Grashor number
h_{tot}	Total heat transfer rate, W m^{-2} K^{-1}
h_c	Convective heat transfer coefficient, Wm^{-2} K^{-1}
h_r	Radiant heat transfer coefficient, W m^{-2} K^{-1}
N_u	Nusselt number
P_r	Prandtl number
T	Time, h
t	Temperature, °C
W	Electric power, kW h^{-1}
Greek symbols	
Φ	Energy, W
η	Heat efficiency
ε	Floor surface emissivity
σ	Stefan–Boltzmann constant, W m^{-2} K^{-4}
υ	Kinematic viscosity of air, m^2 s^{-1}
α_V	Coefficient of cubical expansion of air, m^2 s^{-1}
α	Thermal diffusivity of air, m^2 s^{-1}
λ	Thermal conductivity of air, W m^{-1} K^{-1}
ι	Characteristic length
Subscripts	
s	Wooden floor surface
a	Indoor air
l	Heat loss

References

1. Ji, P.; Rhoads, W.J.; Edwards, M.A.; Pruden, A. Impact of water heater temperature setting and water use frequency on the building plumbing microbiome. *ISME J.* **2017**, *11*, 1318–1330. [CrossRef] [PubMed]
2. Chen, Q. Comfort and energy consumption analysis in buildings with radiant panels. *Energy Build.* **1990**, *14*, 287–297. [CrossRef]
3. Fabrizio, E.; Corgnati, S.P.; Causone, F.; Filippi, M.D. Numerical comparison between energy and comfort performances of radiant heating and cooling systems versus air systems. *HVAC&R Res.* **2012**, *18*, 692–708.
4. Leivo, V.; Prasauskas, T.; Du, L.; Turunen, M.; Kiviste, M.; Aaltonen, A.; Martuzevicius, D.; Haverinen-Shaughnessy, U. Indoor thermal environment, air exchange rates, and carbon dioxide concentrations before and after energy retro fits in Finnish and Lithuanian multi-family buildings. *Sci. Total Environ.* **2018**, *621*, 398–406. [CrossRef] [PubMed]
5. MacNaughton, P.; Cao, X.; Buonocore, J.; Cedeno-Laurent, J.; Spengler, J.; Bernstein, A.; Allen, J. Energy savings, emission reductions, and health co-benefits of the green building movement. *J. Expo. Sci. Environ. Epidemiol.* **2018**, *28*, 307–318. [CrossRef]
6. Bojić, M.; Cvetković, D.; Marjanović, V.; Blagojević, M.; Djordjević, Z. Performances of low temperature radiant heating systems. *Energy Build.* **2013**, *61*, 233–238. [CrossRef]
7. Zhang, L.; Cao, B. Design and analysis of a floor radiant heating system based on energy substitution technology. *Appl. Sci.* **2018**, *8*, 491. [CrossRef]
8. Bean, R.; Olesen, B.W.; Kim, K.W. Part 1 History of Radiant Heating & Cooling Systems. *Ashrae J.* **2010**, *52*, 40–47.
9. Bean, R.; Olesen, B.W.; Kim, K.W. Part 2 History of Radiant Heating & Cooling Systems. *Ashrae J.* **2010**, *52*, 50–55.
10. Roberts, W.J.; Mears, D.R.; James, M.F. Floor Heating of Greenhouses. *Acta Hortic.* **1981**, 259–268. [CrossRef]
11. Cho, S.H.; Zaheer-uddin, M. An experimental study of multiple parameter switching control for radiant floor heating systems. *Energy* **1999**, *24*, 433–444. [CrossRef]
12. Cho, S.H.; Zaheer-uddin, M. Predictive control of intermittently operated radiant floor heating systems. *Energy Convers. Manag.* **2003**, *44*, 1333–1342. [CrossRef]
13. Hu, R.; Niu, J.L. A review of the application of radiant cooling & heating systems in Mainland China. *Energy Build.* **2012**, *52*, 11–19.
14. Qi, H.B.; He, F.Y.; Wang, Q.S.; Li, D.; Lin, L. Simulation Analysis of Heat Transfer on Low Temperature Hot-Water Radiant Floor Heating and Electrical Radiant Floor Heating. *Appl. Mech. Mater.* **2012**, *204–208*, 4234–4238. [CrossRef]
15. Armstrong, T.B. Wire Mesh Floor Heating Systems. *IEEE Trans. Ind. Appl.* **1978**, *IA-14*, 498–505. [CrossRef]
16. Jeong, Y.-S.; Jung, H.-K. Thermal Performance Analysis of Reinforced Concrete Floor Structure with Radiant Floor Heating System in Apartment Housing. *Adv. Mater. Sci. Eng.* **2015**, *2015*, 1–7. [CrossRef]
17. Obata, Y.; Takeuchi, K.; Kawazoe, M.; Kanayama, K. Design of Functionally Graded Wood-Based Board for Floor Heating System with Higher Energy Efficiency. *Mater. Sci. Forum* **2003**, *423–425*, 819–824. [CrossRef]
18. Yan, Q.Y.; Jin, L.L. Numerical Simulation of the Thermal Performance of Cable Radiant Heating Floors with Different Structure. *Adv. Mater. Res.* **2012**, *512–515*, 3047–3050. [CrossRef]
19. Thieblemont, H.; Haghighat, F.; Moreau, A. Thermal Energy Storage for Building Load Management: Application to Electrically Heated Floor. *Appl. Sci.* **2016**, *6*, 194. [CrossRef]
20. Fontana, L. Thermal performance of radiant heating floors in furnished enclosed spaces. *Appl. Therm. Eng.* **2011**, *31*, 1547–1555. [CrossRef]
21. Kim, T.; Chung, D.D.L. Carbon fiber mats as resistive heating elements. *Carbon* **2003**, *41*, 2436–2440. [CrossRef]
22. Shi, Y.Z.; Wang, B. Mechanical properties of carbon fiber/cellulose composite papers modified by hot-melting fibers. *Prog. Nat. Sci.-Mater.* **2014**, *24*, 56–60. [CrossRef]
23. Li, H.B.; Fang, G.G.; Deng, Y.J.; Shen, K.Z.; Shi, Y.Q.; Ding, L.B.; Han, S.M.; Jiao, J. The preparation of carbon fiber paper and its formation characterization. *China Pulp Pap. Ind.* **2015**, *36*, 6–9. (In Chinese)
24. Jabbour, L.; Chaussy, D.; Eyraud, B.; Beneventi, D. Highly conductive graphite/carbon fiber/cellulose composite papers. *Compos. Sci. Technol.* **2012**, *72*, 616–623. [CrossRef]
25. Zhou, J.; Wu, L.; Lan, X.Z.; Zhang, Q.L.; Chen, X.Y.; Zhao, X.C. Research on Electrothermal Properties of a Composite Carbon Fiber Paper. *Mater. Sci. Forum* **2012**, *724*, 420–424. [CrossRef]
26. Yang, L.; Cheng, S.; Ding, Y.; Zhu, X.; Wang, Z.L.; Liu, M. Hierarchical network architectures of carbon fiber paper supported cobalt oxide nanonet for high-capacity pseudo-capacitors. *Nano Lett.* **2012**, *12*, 321–325. [CrossRef] [PubMed]
27. Zhang, X.; Shen, Z. Carbon fiber paper for fuel cell electrode. *Fuel* **2002**, *81*, 2199–2201. [CrossRef]
28. Kong, D.; Wang, H.; Lu, Z.; Cui, Y. CoSe2 Nanoparticles Grown on Carbon Fiber Paper: An Efficient and Stable Electrocatalyst for Hydrogen Evolution Reaction. *J. Am. Chem. Soc.* **2014**, *136*, 4897–4900. [CrossRef]
29. Song, J.B.; Yuan, Q.; Liu, X.; Wang, D.; Fu, F.; Yang, W. Combination of Nitrogen Plasma Modification and Waterborne Polyurethane Treatment of Carbon Fiber Paper Used for Electric Heating of Wood Floors. *BioResources* **2015**, *10*, 5820–5829. [CrossRef]
30. Song, J.B.; Hu, H.B.; Zhang, M.X.; Huang, B.; Yuan, Z.H. Thermal Aging Properties and Electric Heating Behaviors of Carbon Fiber Paper-based Electric Heating Wood Floors. *Bioresources* **2017**, *12*, 9466–9475. [CrossRef]
31. Huang, C.J.; Bao, Y.J.; Li, N.; Xiao, R.C.; Wu, Z.X.; Chen, Y.H. Adhesives used to make bamboo/wood composite electro-thermal plywood. *J. Zhejiang A&F Univ.* **2017**, *34*, 369–373. (In Chinese)

32. Xiao, R.C.; Chen, Y.H.; Bao, Y.J.; Huang, C.J. Electrifying Aging Performance of Bamboo-wood Thermoelectric Composites. *China Wood Industry* **2017**, *31*, 19–23. (In Chinese)
33. Yuan, Q.P.; Fu, F. Application of Carbon Fiber Paper in Integrated Wooden Electric Heating Composite. *BioResources* **2014**, *9*, 5662–5675. [CrossRef]
34. Bao, Y.J.; Huang, C.J.; Chen, Y.H.; Dai, Y.P. Longitudinal scale effect of electro-thermal effectiveness of front panel of the integrated wooden electric heating composite based on carbon fiber paper. *Acta Mater. Compos. Sin.* **2020**, *37*, 3214–3219. (In Chinese)
35. *ANSI/ASHRAE Standard 55-2013*; Standard 55-2013 User's Manual: Thermal Environmental Conditions for Human Occupancy. ASHRAE Research: Atlanta, GA, USA, 2016.
36. Yang, S.; Tao, W. *Heat Transfer*, 4th ed.; Higher Education Press: Beijing, China, 2006. (In Chinese)
37. Zhou, G.; He, J. Thermal performance of a radiant floor heating system with different heat storage materials and heating pipes. *Appl. Energy* **2015**, *138*, 648–660. [CrossRef]
38. Koca, A.; Gemici, Z.; Bedir, K.; Böke, E.; Kanbur, B.B.; Topaçoğlu, Y. Thermal Comfort Analysis of Novel Low Exergy Radiant Heating Cooling System and Energy Saving Potential Comparing to Conventional Systems. In *Progress in Exergy, Energy, and the Environment*; Springer: Berlin/Heidelberg, Germany, 2014; pp. 435–445.

buildings

MDPI

Article

A Systematic Approach to Developing Sustainable Post-Disaster Shelters in the Southern Region of the United States

Alka Khadka [1], Soojin Yoon [2,*], Richard G. Walker [3], Amy King Lewis [2] and Yeonjin Bae [4]

[1] Intertek-PSI, 1137 S Jupiter Rd, Garland, TX 75042, USA; alka.khadka@intertek.com
[2] Division of Engineering Technology, Oklahoma State University, 511 Engineering North, Stillwater, OK 74078, USA; amyking.lewis@okstate.edu
[3] College of Civil and Environment Engineering, Oklahoma State University, 511 Engineering North, Stillwater, OK 74078, USA; grant.walker@okstate.edu
[4] Building Technologies Research and Integration Center (BTRIC), Oak Ridge National Laboratory, 1 Bethel Valley Rd, Oak Ridge, TN 37830, USA; baey@ornl.gov
* Correspondence: syoon@okstate.edu

Abstract: This study aims to propose a sustainable shelter design involving energy savings, less environmental impact, and rapid construction. The structural design of the shelter is based on 3D-printing technology. Sustainability assessments, including life cycle analysis (LCA), life cycle energy assessment (LCEA), and energy justice of the designed shelter, were conducted to prove the sustainable shelter design. The outcomes of this study for several scenarios will not only allow decision-makers to design permanent shelters with maximized utilization of limited resources but also help local communities strengthen their ability to recover with minimal outside assistance post-disaster. Furthermore, residents can utilize the sustainable shelter to maintain critical functions, including business continuity and local business in emergencies.

Keywords: shelter design; sustainability; life cycle assessment (LCA); life cycle energy analysis (LCEA); energy justice

Citation: Khadka, A.; Yoon, S.; Walker, R.G.; Lewis, A.K.; Bae, Y. A Systematic Approach to Developing Sustainable Post-Disaster Shelters in the Southern Region of the United States. *Buildings* **2024**, *14*, 2536. https://doi.org/10.3390/buildings14082536

Academic Editors: Apple L.S. Chan and Antonio Caggiano

Received: 19 April 2024
Revised: 1 July 2024
Accepted: 30 July 2024
Published: 17 August 2024

1. Introduction

Natural hazards result in an average of 45,000 deaths yearly [1]. The 2004 Sumatra tsunami caused between 200,000 and 310,000 deaths, while Hurricane Katrina, which struck the US Gulf Coast in August 2005, resulted in the deaths of 1833 people and caused property damage valued at USD 81 billion [2]. Moreover, Hurricane Katrina damaged 200,000 homes in New Orleans, of which 41,000 were rental homes for low-income families [3]. The impacts of such disasters extend to housing instability, especially among low-income families who face significant challenges in coping with the aftermath [4]. Disaster shelters play a crucial role in providing temporary accommodation, but existing solutions often lack adequate space, protection, and amenities. Additionally, currently provided temporary shelters are made of nylon, polyester wool, and fiber-reinforced mylar, which are unsustainable in terms of cost and environmental impact [5,6]. Therefore, addressing the shelter needs of disaster-affected populations requires a coordinated and comprehensive approach involving pre-disaster planning, immediate response, and long-term rehabilitation efforts [7].

The primary purpose of this study is to propose a sustainable permanent shelter design involving energy savings, reduced environmental impact, rapid construction, and cost-effectiveness, which will contribute to the resilience of local communities and positively affect business continuity post-disaster. This study considers the availability of energy to power a 3D printer onsite and adequate road conditions for transporting heavy precast modules to create alternative solutions post-disaster. The proposed methodology consists of five steps: (1) structural design, (2) construction method, (3) scenario development, (4) sustainability assessments, and (5) decision-making for the shelter design. The structural

design of the shelter is developed with disaster-resistant construction materials and a shape that enhances resilience. Three-dimensional printing (3DP) printing technology is rapidly being applied in the construction field. Due to its quick construction and design flexibility, the market value of concrete 3D printing was expected to reach USD 56.4 million by 2021 [8]. Three-dimensional printing technology is utilized for the rapid construction method of the shelter. The sustainability assessment includes a life cycle assessment (LCA), life cycle energy assessment (LCEA), and energy justice assessment. Various scenarios are created based on onsite 3DP, insulation types, and HVAC (Heating, Ventilation, and Air Conditioning) systems. Therefore, the proposed shelter design scenario would provide a permanent shelter design pre- and post-disaster for resilience, promoting sustainability in terms of the environment, energy consumption, and the economy. The designed shelter also offers commercial uses, which can uplift the economic conditions of the local community after the transition of the victims to their habitat.

2. Background and Related Studies

2.1. Current Research in Sustainability

In the construction sector, there is a growing recognition that sustainable development must address the goals of environmental quality, well-being, and social justice. To assess and promote sustainability in building practices, Building Industry Reporting and Design for Sustainability (BIRDS) has introduced a new measurement system [9]. This system encompasses three essential components: environmental performance (assessed through LCA), energy performance (evaluated through LCEA), and economic performance (analyzed using life cycle cost analysis—LCCA). Current research in the construction sector demonstrates a significant focus on utilizing LCA, LCEA, and LCCA for studying building and infrastructure projects.

Ashworth et al. [10] stated that LCA and LCCA assist stakeholders in making well-informed decisions during the early design phase of buildings and infrastructure. In addition, they discussed the promising benefits of integrating life cycle tools with Building Information Modeling. Researchers have utilized this integration to compare different solutions and select sustainable options that prioritize both environmental well-being and user well-being. Choosing a method for decision-making can greatly increase the effectiveness and implementation of a project, such as the many methods shown by [11]. Similarly, LCA and LCCA were applied in the study to evaluate the use of phase change materials (PCMs) in office buildings considering environmental and economic performance. The results revealed that while the overall environmental impact was reduced, the cost of the construction stage increased significantly [12]. Vasishta et al. [13] aimed to understand the environmental impacts and costs over the complete life cycle for precast and cast-in-place building systems and found that precast building systems have lower life cycle environmental impacts and life cycle costs compared to cast-in-place building systems. Liang et al. [14] conducted LCA and LCCA to compare a mass timber building and a concrete building to contribute more information to building developers and policy makers. The study concluded that the mass timber building has less environmental impact than concrete construction. The authors of [15] compared the eco-efficiency of 3D printing technology to conventional construction methods using LCA and LCCA techniques, and the results revealed that 3D-printed buildings are environmentally favorable, and the cost of construction is reduced by 78%.

Utama and Gheewala [16] performed LCEA to determine the energy consumption of buildings considering envelope materials. They showed that double-wall envelopes have almost two times less energy consumption than single-wall envelopes in the long run. Similarly, ref. [17] compared the embodied energy and operational energy of concrete- and steel-framed structures using the LCEA method. The results show that concrete has the highest influence on embodied energy for concrete-framed structures, while beams represent the largest component of embodied energy for steel-framed structures, with no significant differences in operational energy between the two structures. An integrated

assessment (LCA, LCEA, and LCCA) was performed to compare the environmental impacts, energy use, and economics of a green roof against a built-up roof. The environmental impact analysis indicates that the built-up roof has 3 times more environmental emissions, 2.5 times more energy, and 50% higher costs than the green roof over the building life span when considering the material acquisition life stage, use stage, and maintenance stage. The authors of [18,19] found that LCA, LCCA, and LCEA are mostly carried out for advanced building designs but rarely in traditional buildings.

2.2. Shelter for Disaster Relief

Emergency shelters provide natural disaster victims with safety, security, support, and their own place to cope with the destruction during disaster recovery [20]. Table 1 outlines the current state of emergency shelters that are provided to refugees and disaster survivors.

Table 1. Current disaster relief shelters.

Authors	Shelter Name	Material Used	Cost	Construction Duration	Total Area
[21]	WeatherHyde, 2013	Nylon, polyester wool, fiber-reinforced mylar	USD 199	15 min	2.69 m^2
[22]	Better Shelter, 2015	Polyolefin panels and galvanized steel, woven high-density polyethylene fibers	USD 1260	4–6 h	17.47 m^2
[23]	Hexyurt, 2011	Cloth, wood, plastic, Polyiso insulation, OSB, sandwich panels, cardboard	USD 229.71	4 h	3.8–25.64 m^2
[24]	Emergency Smart Pod, 2015	Aluminum panels and steel frame	USD 195K–USD 485K	20 min	36.98 m^2
[25]	MTS DOMO Systems, 2014	Aluminum, polyester PVC tarpaulin, cotton	USD 4625	25 min	23.4 m^2

As shown in Table 1, WeatherHyde was designed by Parsoon Kumar to solve homelessness targeted at people in Southeast Asia. This temporary shelter can be ready in 15 min and is made of nylon, polyester wool, and fiber-reinforced mylar. The total area of the shelter is 2.69 m^2 and costs USD 199 [21]. Better Shelter [22], constructed with polyolefin panels and galvanized steel, along with high-density polyethylene fibers, costs USD 1260. The construction duration is about 4–6 h, and its total area is 17.47 m^2 [22]. The temporary shelter Hexyurt (2011) is the modern adaptation of a Yurt (a tent used by nomads for a hundred years), and its design is less susceptible to the winds. It varies in size from 3.8 to 25.64 m^2, can be built in 4 h, and costs approximately USD 229.71. The materials used are cloth, wood, plastic, Polyiso insulation, OSB, sandwich panels, and cardboard [23]. The Emergency Smart POD (2015) is constructed of all metal with a steel frame covered in aluminum, making it the most durable and permanent option. This comes with the fastest erection time of 20 min and the largest area, but it is also the most expensive at USD 195K–USD 485K. The MTS DOMO System [25] offers similar features to the Hexyurt with a Yurt dome-like structure but offers a slightly more durable design with higher-grade materials, with the biggest difference being its lack of insulation. This also comes with a faster erection time of just 25 min but also a much higher cost of USD 4625. Though the current temporary shelters provided are fast to construct, they lack space, protection, sanitation, and reusability after people move back to their homes.

2.3. The 3D Printing of Structures

One of the emerging technologies in the construction sector is 3D printing. Along with rapid construction, 3D printing involves less waste production due to construction and design flexibility [8]. Specifically, there has been a significant expansion of concrete 3D printing, with a projected value of USD 56.4 million in 2021 due to the increasing number

of innovative construction projects being planned [8]. Table 2 showcases notable examples of concrete 3D-printed buildings from around the world. One such example is the WinSun ten 3D-printed house, which was unveiled in 2014. These houses were constructed using offsite 3D printing, and each took just one hour to print. With an area of 18.58 m^2, the cost of these houses amounted to USD 4800 [26]. Another noteworthy project is the onsite 3D-printed home by SQ4D, located in New York. This home, with an area of 12.91 m^2, was printed in just two days and is currently available for sale at USD 3 million [27]. The 3D-printed community by ICON and Lennar, with homes costing over USD 470K and measuring around 148 m^2, exemplifies strong and energy-efficient construction. From Table 2, it becomes evident that 3D printing requires less time for the printing process, whereas offsite 3D printing offers the advantage of lower construction costs.

Table 2. Three-dimensional-printed houses.

Authors	Building Name	Printed Onsite/Offsite	Construction Cost	Printing Durations	Total Area
[26]	WinSun ten 3D-printed house	Offsite	USD 4800	1 Day	18.58 m^2
[28]	Dubai 3D-printed Commercial Building	Offsite	USD 140K	17 Days	22.48 m^2
[29]	Belgium onsite 3D-printed house	Onsite	-	3 Weeks	8.36 m^2
[30]	SQ4D 3D-printed house	Onsite	USD 299.99K	2 Days	12.91 m^2
[31]	Netherland 3D-printed house	Offsite	USD 946/month	2 Days	8.73 m^2
[32]	East 17 Street Residencies	Onsite	USD 450K and above	7 Days/home	8.36–17.19 m^2

3. Methodology

This research proposes an optimal design of a shelter considering sustainability with five steps, as shown in Figure 1. The first step is (1) structural design, focusing on disaster-resistant shelters with modular features to facilitate multipurpose usage. Next, step (2) is the construction method employing concrete 3D printing, a rapid and efficient method during an emergency, and step (3) is scenario development, with six options based on the insulation and HVAC system used. Then, step (4) is evaluating sustainability in the six proposed scenarios by conducting LCA, LCEA, and energy justice assessment. Depending on the results of the sustainability assessment, this step will provide an optimal decision for the shelter design.

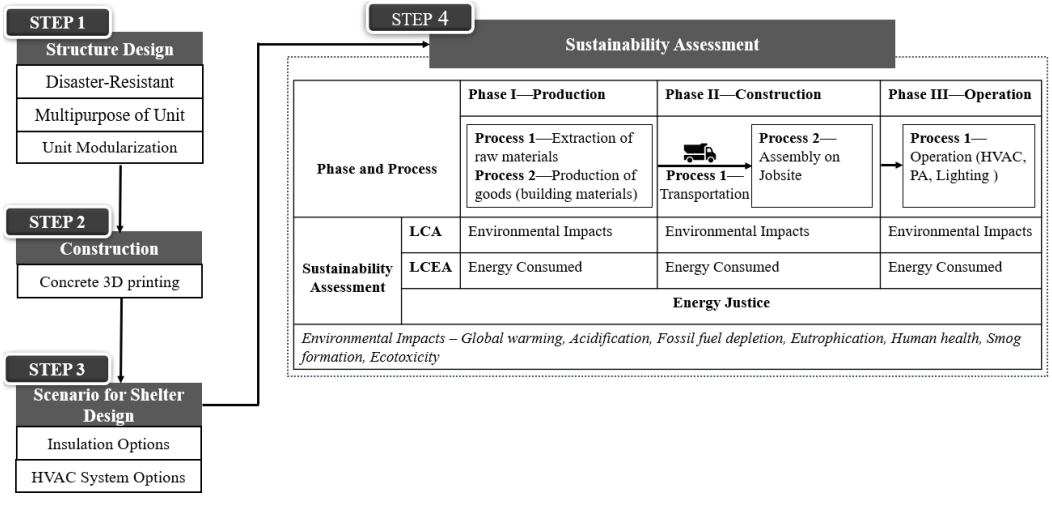

Figure 1. Research methodology.

3.1. Step 1: Structural Design

The objective of step 1 is to provide a structural design of a permanent shelter by considering key performance criteria: (1) disaster resistance, (2) multipurpose functionality of the unit, and (3) unit modularization. To achieve this, we have conducted a comprehensive literature review focusing on exemplary buildings that have withstood disasters and analyzed their construction materials.

One such remarkable building is Alma Hall, which is made of concrete, brick, wood, and metal structural beams and withstood the Johnstown Flood (1889). It was built in 1884 and is capable of housing 264 people [33]. Another notable example is the UST Main Building, known as the first EQ resistance building in Asia, which was built in 1927 and faced major earthquakes in 1937, 1968, 1970, and 1990. The construction materials of the building are concrete, bricks, wood, metals, and aggregates [34]. Similarly, the Sand Palace built in 2017 survived the powerful Hurricane Michael that occurred in the year 2018. The construction materials for the building are concrete, rebar, and steel cables [35]. It can be observed that concrete as the construction or structural element in the above buildings is the major cause of disaster resistance. Furthermore, we can learn valuable insights from the East Pagoda at Yakushiji Temple in Japan, which was built 1300 years ago and has endured various earthquakes. It is believed that its central core pillar is the major reason behind its resistance to earthquakes. During an earthquake, the central core pillar acts as a vibration suppression element [36]. This vibration suppression absorbs and minimizes ground vibrations. When the shelter shakes during an earthquake, the overall shaking is countervailed and minimized by the core that shakes out of sync within the building [36].

3.2. Step 2: Construction Method

Three-dimensional printing has been a big buzz in the construction sector over the past decade. Like every method, 3D printing has its own pros and cons. Its benefits are fast construction, design flexibility, reduced human error, and waste reduction, whereas the disadvantages are high cost and a lack of qualified labor [8]. Different types of 3D printers are available for sale in the market [37]. Table 3 lists the 3D printers that are available for sale in the market and their features.

Table 3. Specifications of 3D printers.

Authors	System Name	Print Speed (cm/s)	Print Dimensions (L × W × H) (m)	Type
[38]	ICON Vulcan II	12.7–25.4	∞ × 11.1 × 3.2	Gantry
[39]	COBOD BOD2	Up to 100	∞ × 14.6 × 14.6	Gantry
[40]	Total Kustom StroyBot 6.2 A	1–24.9	10 × 15 × 5.8	Gantry

ICON Vulcan II can build within the dimensions ∞ × 11.1 m × 3.2 m and has a printing speed range of 12–25 cm per second [38]. Similarly, COBOD BOD2 constructs the structure in gantry style with a speed limit of 1 m per second. It can print dimensions up to 14.62 m × 50.52 m × 8.14 m [39]. All of the 3D printing systems shown in the table use gantry-style printing. A gantry in 3D printing is the frame structure that supports the printer while moving along the X/Y-axis as the printer head moves around to print the part on the build platform [41]. A gantry-type printer can print both large and small buildings. The hopper in a gantry-type printer increases the possibility of controlling the material flow for non-continuous printing. Gantry printers are mobile and can be used for onsite as well as offsite printing [41]. A sulfur concrete mix is considered for this study. The component materials of the mix are silica sand, gravel, sulfur, air, and polypropylene, and their content by volume is 44%, 34%, 20%, 1%, and 1%, respectively. The mix yields a comprehensive strength of 40 MPa without the addition of polypropylene fibers. The addition of fibers to the mix is assumed to increase the comprehensive strength and create a self-reinforced printable mix [16,42–44].

3.3. Step 3: Scenario for Shelter Design

Insulation and HVAC systems play a significant role in the energy consumption of the house [45]. Scenarios for the design of a shelter were developed considering insulation types and HVAC systems. The insulation types are an air cavity and expanded polylactic acid (E-PLA); the HVAC systems are Packaged Terminal Heat Pump (PTHP), Rooftop Unit (RTU), and variable refrigerant flow (VRF) systems. Figure 2 shows that six different scenarios are derived from the insulation types and HVAC systems. In scenario A-PTHP, the exterior wall has air cavity insulation, and the HVAC system is a PTHP. Similarly, in E-PTHP, the exterior wall uses E-PLA insulation, with the HVAC system being a PTHP.

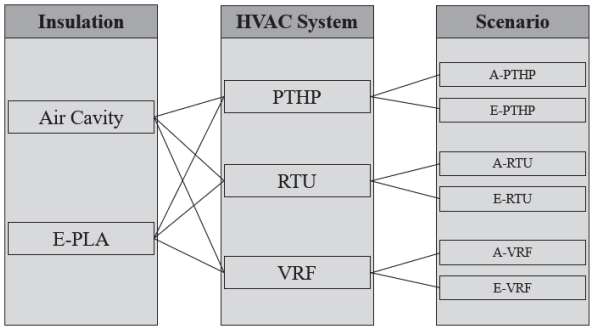

Figure 2. Scenario tree.

In building techniques, the thermal transmittance value can be improved by incorporating air gaps or layers of insulation between the components of building elements. The use of 3D printing technology offers designers the flexibility to create printing layouts with air cavities that meet both thermal and structural requirements. The arrangement of these cavities significantly affects the thermal transmittance value of hollow concrete blocks, as it involves the simultaneous occurrence of conduction, convection, and radiation heat transfer processes. By utilizing different cavity configurations, it is possible to reduce thermal transmittance by approximately 20% [46]

In situations where the desired thermal transmittance values cannot be achieved through the configuration of air cavities, it is recommended to utilize cavity-filling materials instead of adding additional insulation layers. These cavities can be filled with insulation materials possessing specific thermal properties, which aid in achieving the target U-value. In the conducted study, hollow brick activities were tested with three different filling materials: dry sand, polystyrene, and polyurethane. The introduction of these fillings resulted in a significant reduction in thermal transmittance. In particular, the sand filling led to a reduction of 54.3%, while polystyrene and polyurethane fillings achieved a reduction of 80.4% [47]. One promising alternative to expanded polystyrene is expanded polylactic acid (E-PLA), which is characterized by a low density, sustainability, and an environmentally friendly nature. E-PLA exhibits thermal properties like expanded polystyrene and can be effectively used as a replacement in various applications [48]. Regarding the material properties, E-PLA has a density of 30 kg/m^3, a thermal conductivity of 0.03 W/m·K, and a specific heat of 1.483 J/g·K. Meanwhile, the air cavity has an ideal gas density, a thermal conductivity of 0.0242 W/m·K, a specific heat of 1.00643 J/g·K, and a viscosity of 1.7894×10^{-5} kg/m·s. The material properties of the air cavity and E-PLA are sourced from [42].

HVAC System Options

The HVAC system plays a crucial role in maintaining a comfortable indoor environment for buildings. Selecting the appropriate HVAC system is important for achieving optimal energy efficiency, occupant comfort, and indoor air quality [45]. Among the various options available, the three suitable HVAC systems for this shelter design are the Packaged

Terminal Heat Pump (PTHP), Rooftop Unit (RTU), and VRF systems. The choice of an HVAC system depends on factors like the building size, occupancy level, geographical location, and climate zone. Figure 3 provides an overview of the specifications, advantages, and disadvantages of PTHP, RTU, and VRF systems. An appropriate HVAC system is selected with the careful consideration of these factors to operate the building comfortably.

Types	**Packaged terminal heat Pump (PTHP)[a]**	**Rooftop Unit (RTU)[b]**	**Variable refrigerant flow (VRF)[c]**
Specification	-Heating and cooling in a single unit. -Hotels, apartments, and commercial buildings. - 208/230V single-phase power. -Mounted in walls. -Capacity of 7.39 to 17.93 MJs -Electric and water source models.	-Heating and cooling functions. -Installed on roof. -Large commercial buildings. -Capacity ranges from 2 to 200 tons. - 208/230V or 460 V three-phase power. - Gas-fired and electric models.	-Heating and cooling using refrigerant. -Capacity ranges from 6 to 48 tons. - 208/230V or 460V three-phase power. -Commercial and residential buildings.
Advantages	-Minimum space. -Easy to install -Highly energy efficient. -Greater control and customization.	-Options such as economizer, humidity control, and variable speed drives. - Individual temperature control to different zones within the building.	-Individual temperature control. -Quiet operation. -VRF systems are flexible and easily reconfigured. - Advanced features such as humidity controls and air purification systems.
Disadvantages	-Expensive -Not suitable for larger buildings. -May not be effective for spaces that are located far from the unit. -Significant amount of noise.	-Expensive to install. -May not be suitable for buildings with limited roof space -Significant amount of noise.	-Expensive to purchase and install. -Struggles to maintain consistent temperatures in extreme climates. -Complex to install -Installation of refrigerant piping might be challenging.
Figure	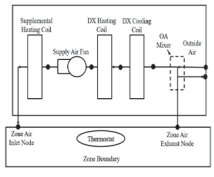	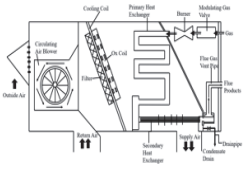	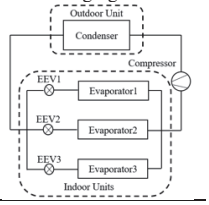

Figure 3. Types of HVAC systems. [a] [49], [b] [50], [c] [51].

3.4. Step 4: Sustainability Assessment

3.4.1. Life Cycle Energy Analysis (LCEA)

Life cycle energy assessment (LCEA) is an approach to the identification and quantification of all energy input to a building in its life cycle. Buildings consume energy directly or indirectly in all phases of their life cycle from start to end (i.e., cradle to grave); hence, they are analyzed from the life cycle point of view [18]. The system boundaries of LCEA include the energy use in three phases of the building life cycle; these are the manufacturing phase, operation phase, and demolition phase, which can be seen in Figure 4 [30,52]. The manufacturing phase encompasses the production and transportation of the building materials to the site, the installation or construction of new buildings, and the renovation of existing buildings. The operation phase includes all of the activities that occur during the use of the buildings throughout their life span. The demolition phase consists of the

destruction of existing buildings and the transportation of the demolished materials to the landfill or recycling plants.

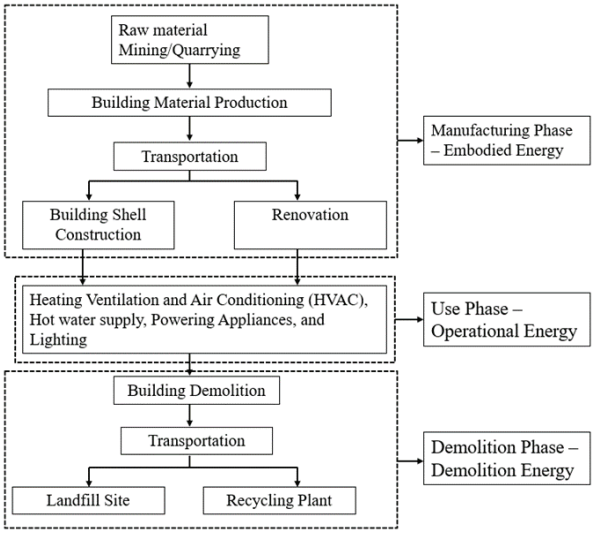

Figure 4. Framework of LCEA.

The corresponding energy required in these three phases is embodied energy, operational energy, and demolition energy. Embodied energy is related to the energy required for the extraction of raw materials, the production of construction materials from raw materials, the transportation of these materials to the construction site, and the construction and renovation of the building. Operational energy is the energy required to operate the building comfortably for the occupants over its life span and includes the energy consumed by HVAC and appliances. Demolition energy is the energy required to demolish and transport the dismantled materials.

3.4.2. Life Cycle Assessment (LCA)

A technique for assessing environmental aspects and potential environmental impacts associated with the development of a product and its potential impact throughout its life from the cradle to the grave, including raw material acquisition, processing, manufacturing, use, and finally, disposal, is called life cycle assessment (LCA) [53]. The framework of LCA consists of four phases, i.e., (1) goal and scope definition; (2) life cycle inventory analysis; (3) life cycle impact assessment; and (4) life cycle interpretation. The goal and scope define the objectives, system boundaries, and functional units for the study. Life cycle inventory (LCI) analysis deals with the collection of the data, the selection of the data source for the assessment, and the compilation of inputs and outputs of each stage of the life cycle. Impact assessment aims to determine the contribution of each selected material to the environment. The impact can be measured using different impact categories. The last step is the interpretation of the observed results through an impact assessment and the determination of better alternatives if the results are negative [53].

3.4.3. Energy Justice

Energy justice serves as a conceptual framework for promoting the fair distribution of benefits and costs for energy services and facilitating impartial decision-making in the energy sector [53]. Fetanat et al. [54] and Sovacool and Dworkin [55] evaluate energy justice using four criteria: availability and affordability, rights, social aspects, and environmental issues. Availability emphasizes the provision of sufficient energy services of high quality to

all individuals. Affordability, on the other hand, advocates for equitable access to energy as cheap as possible, especially to disadvantaged groups, so that there will be no issues with energy needs. Rights include intragenerational equity, due process, and intergenerational equity. Intragenerational equity focuses on the right of all people to fairly access energy services, whereas intergenerational equity centers on the right of future generations to enjoy a good life undisturbed by our energy activities. Due process relates to energy activities performed with respect to due process and human rights. Social aspects have three sub-criteria: resistance, transparency and accountability, and intersectionality. The social aspects criterion evaluates the resistance of a scenario to challenges, the transparency and accountability in providing information and making decisions, and the attention given to the diverse social groups and vulnerable sections of society in the decision-making process. Sustainability and Responsibility are two sub-criteria of environmental issues. This criterion examines the effects on existing energy sources and addresses concerns related to water and soil pollution, toxic emissions, climate change, and global warming. It concerns understanding the impact of a scenario on the maintenance of alternative energy sources and evaluates its potential consequences on environmental pollution, emissions, and long-term climate patterns [54,55]. Much of this decision-making needs to ensure balance, and to maintain the most objective balance of needs, the use of decision-making methods can also be utilized in complex situations [56].

4. Outcomes

4.1. Structural Design

4.1.1. Disaster-Resistant

In support of our literature review, we have recognized the pivotal role of concrete as a construction material and central core pillar for disaster-resistant structures. Therefore, in our shelter design, we have chosen to incorporate concrete as a construction material and concrete central core pillar to resist potential disasters. In designing the structure, particular attention was paid to the literature review and what has shown the best performance in various locations and conditions in search of the most universal design. The proposed design was created by this team and based on a mixture of existing structures and current shelter designs to offer the best design for optimal performance and constructability in any location. Autodesk Revit 2023 was used for the comprehensive design of the shelter, which is illustrated in Figure 5. Its dimensions include a height of 2.4 m and nearly equal lengths and breadths of approximately 19.8 m. The 3D-printed exterior wall has a width of 50.8 in, while partition walls measure 10 cm each. The depicted shelter is configured to accommodate four suites, each comprising a kitchen space (KS), living space (LS), two bedrooms (BDs), a restroom equipped with a washer and dryer, and a storage room (S). The shelter's shape resembles an octagon for a more stable configuration to resist disasters.

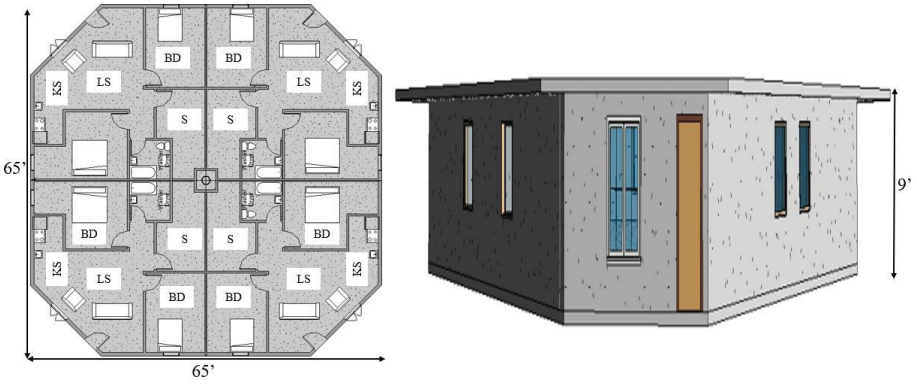

Figure 5. Proposed floor plan and elevation of designed shelter (Revit 2023).

4.1.2. Multipurpose

The proposed designed shelter can be used for both commercial and residential purposes. Figure 5 showcases its residential functionality. In a commercial context, the shelter can be utilized as a medical facility, collaborative workspace, and storage area. This adaptability to multiple purposes and the reusability of the proposed shelter design provide an opportunity for the local community to improve their economic conditions once the affected individuals return to their homes. The ability to repurpose also contributes to long-term sustainability as shelters can continue to serve the evolving needs of the community, ensuring their ongoing usefulness beyond the initial emergency phase. Multipurpose disaster shelters offer a comprehensive solution that addresses immediate needs while supporting long-term recovery and development in disaster-affected areas.

4.1.3. Unit Modularization

Figure 6 showcases the modular nature of the designed shelter, highlighting its expandability, stackability, and accessibility. This modularity offers several significant advantages in disaster scenarios. First, the ability of the shelter to expand and adjust its size allows for efficient space utilization. In situations where space is limited, this feature ensures that a large number of victims can be accommodated within a confined area and that housing solutions are provided for a greater number of individuals. Second, the stackable design of the shelter enables the vertical utilization of space, where multiple units can be stacked on top of each other without compromising safety and stability. This vertical expansion maximizes the use of available land and further increases the capacity of the shelter to accommodate more victims. The shelter's accessibility features play a crucial role in ensuring the safety, security, and well-being of its occupants by considering easy and equal access to occupants. Moreover, the convenient modularization of the shelter facilitates its rapid multiplication and deployment. The standardized components and assembly methods enable the quick replication of shelter units to meet the immediate needs of the affected population. The modularity not only optimizes space utilization but also promotes safety, security, and a homey atmosphere for individuals experiencing emotional and mental distress due to a disaster.

Figure 6. Modularity of designed shelter.

4.2. Construction Method

The designed shelter is constructed utilizing the COBOD BOD2 3D printer. The printer operates by adding layers of prepared mortar through a nozzle. The 3D printer is supported by software COBOD Slice converts 3D models from any CAD/ BIM software for printing preparation. The printer operates on 3 A, 400 V three-phase power. Each printed layer has a width of 7.6 cm and a height of 3 cm [39]. Figure 7 provides details of the printer's configuration for the exterior walls, including the cavity walls and a side view of the printed walls.

For printing the exterior walls of the shelter, the speed is set to 63 cm per second, allowing the walls to be printed in approximately 7.34 h for 1 unit. Tables 4 and 5 present the sulfur concrete mix quantities of each material and properties of the 3D-printed exterior walls, respectively, which were determined based on the literature review for a unit.

Furthermore, it is noted that the transportation of construction materials from suppliers to the site covers a distance of 1000 km.

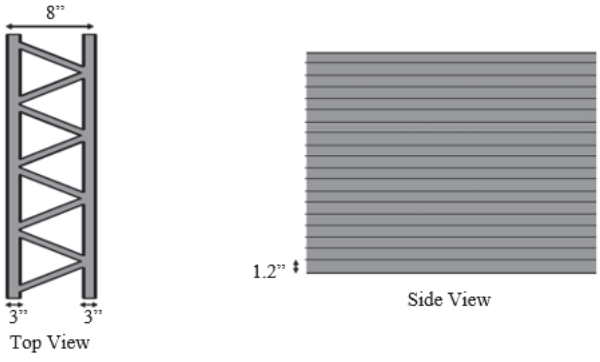

Figure 7. Configuration of 3D-printed exterior walls.

Table 4. Properties of 3D-printed wall [2].

Wall Type	Density (kg/m^3)	Thermal Conductivity (W/m.K)	U-Value (W/m^2.K)	Specific Heat (J/g.K)
Air Cavity	1254.24	0.4114	1.87	0.803
E-PLA	1254.24	0.121	0.55	0.803

Table 5. Inventory for construction of 3D-printed exterior wall of one unit.

Dimension	Variable
3D-printed external wall [a]	17.197 m^3
Silica sand	9235.4 kg
Gravel	9237.15 kg
Sulfur	3784 kg
Polypropylene	160.82 kg
Insulation E-PLA [a,b]	509.037 kg
Energy [c]	94.011 kWh
Transportation	1000

[a] [42], [b] [57], [c] [39].

4.3. Sustainability Assessment

4.3.1. LCEA for Shelter Design

The embodied energy of construction materials, from production to the site, was calculated using the available embodied energy coefficients from various studies. These coefficients, measured in megajoules per kilogram (MJ/kg), were multiplied by the respective material quantities of the sulfur concrete mix to determine the embodied energy of each material in megajoules (MJ). The specific values can be found in Table 6. Upon analysis, it is observed that the embodied energy for material production required for the exterior air cavity wall is approximately 16,368.68 MJ. In contrast, the exterior wall with E-PLA insulation has a higher total embodied energy of approximately 75,926.36 MJ because it also includes the energy required for the production of E-PLA. The energy required for the construction of the designed shelter was specifically calculated for the printing of the exterior wall. The total energy consumption for this process was found to be 338 MJ. These calculations were performed considering the power required to operate the COBOD BOD2 for a duration of 7.34 h.

Table 6. Embodied energy coefficients of materials used for construction of shelter.

Material	Embodied Energy Coefficient (MJ/kg)	Thermal Conductivity (W/m.K)	Specific Heat (J/g.K)
Silica sand	0.039 [a]	9235.4	360.18
Gravel	0.16 [b]	9237.15	1477.94
Sulfur	1.12 [c]	3784	4238.08
Polypropylene fiber	64 [a]	160.82	10,292.48
Insulation (EPLA)	117 [a]	509.04	59,557.68

[a] [58], [b] [11], [c] [31].

Figure 8 illustrates the embodied energy required for printing the exterior walls of one unit of the shelter. The *x*-axis and *y*-axis represent the types of walls and the energy required in megajoules (MJ), respectively. The embodied energy for the production of air cavity wall materials is 16,707.12 MJ, whereas the embodied energy for the E-PLA-insulated wall is 76,264.8 MJ. The figure reveals a significant difference in the energy required for the production, transportation, and construction of insulated walls; it is almost seven times higher for E-PLA walls than for air cavity walls, and the major reason behind this difference is the energy required for the production of the E-PLA material.

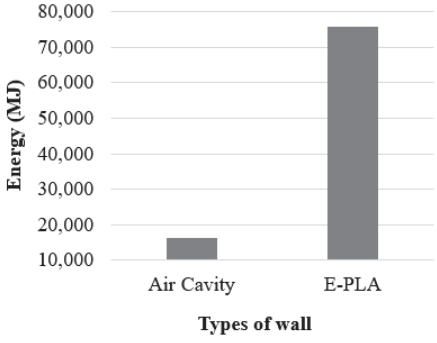

Figure 8. Embodied energy for air-cavity- and E-PLA-filled 3D-printed walls.

Openstudio®, along with Sketchup Pro 2021, was used to determine the operational energy of the shelter. Lighting, building occupancy, the HVAC system, and relevant equipment are considered for the operation state of the shelter. A few considerations are made for the energy analysis in Openstudio®. The building type of the single-unit shelter is considered a large hotel, the 90.1-2010 template is used, and ASHRAE 169-2006-3A (Stillwater, OK, USA) is the climate zone [59]. The surface type, different space types (highlighted by like colors in Figure 9b), and thermal zones (highlighted by different colors to show separation but share no relation to Figure 9c) considered for a single unit can be seen in Figure 9. Similarly, in accordance with Bae et al. [60], occupancy schedules, along with lighting and equipment schedules, are set up for operational energy use analysis.

Table 7 represents the annual energy consumption for the operation of the 3D-printed shelter, considering various HVAC systems and wall insulation types. Six different scenarios have been created, and the operational energy is predicted in gigajoules (GJ). The source energy is then compared to ensure a fair assessment across different energy sources. All of the scenarios use electricity as the energy source, but A-RTU and E-RTU use natural gas for heating along with electricity for cooling. A-RTU has a source energy of 368.52 GJ (electricity) and 92.65 MJ (natural gas); similarly, E-RTU's source energy is 344.25 GJ (electricity) and 74.66 GJ (natural gas). From the table, it can be concluded that the source energy required for insulated walls with E-PLA and the PTHP system is less than in other

scenarios, whereas air cavity walls with a VRF system require the most energy. The best alternative to E-PTHP seems to be either air cavity walls with a PTHP system or insulated walls with a VRF system.

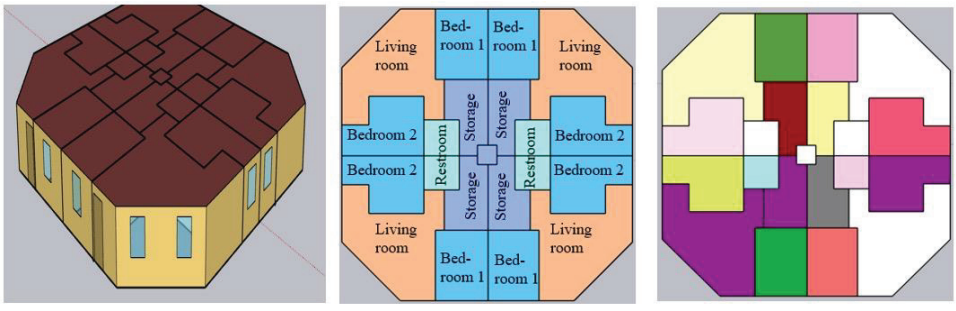

Figure 9. Rendered images (**a**) by surface type, (**b**) by space type, and (**c**) by thermal zone.

Table 7. Operational energy for different scenarios.

Scenario	Operational Energy (GJ)
A-PTHP	409.85
E-PTHP	372.52
A-RTU	461.17
E-RTU	418.91
A-VRF	454.38
E-VRF	413.99

Figure 10 illustrates the total energy required in all three phases of the 3D-printed shelter, i.e., production and transportation, construction, and operation, for different scenarios. The *x*-axis in the figure shows the different scenarios formed depending on the types of walls and HVAC system, whereas the *y*-axis represents the total energy required in gigajoules. From the figure, it is clear that E-RTU requires the most energy when considering all three phases. Although the operational energy required for E-PTHP is low during the operation state, the total energy required for A-PTHP is the lowest among all scenarios. Considering the total energy, the air cavity wall is better than the insulated wall with every HVAC system due to the energy required for the production of insulated walls.

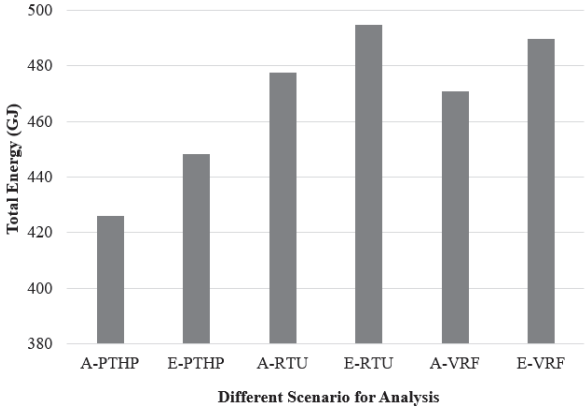

Figure 10. Total energy for different scenarios.

4.3.2. LCA for Shelter Design

The goal of this study is to determine the environmental impacts of designed shelters. Figure 11 shows the system boundaries of the examined systems, including material production, the transportation of materials and equipment, construction, operation, and maintenance. The end-of-life phase is excluded from the study due to the lack of available data. The input data related to the shelter were gathered from the literature review and Ecoinvent database.

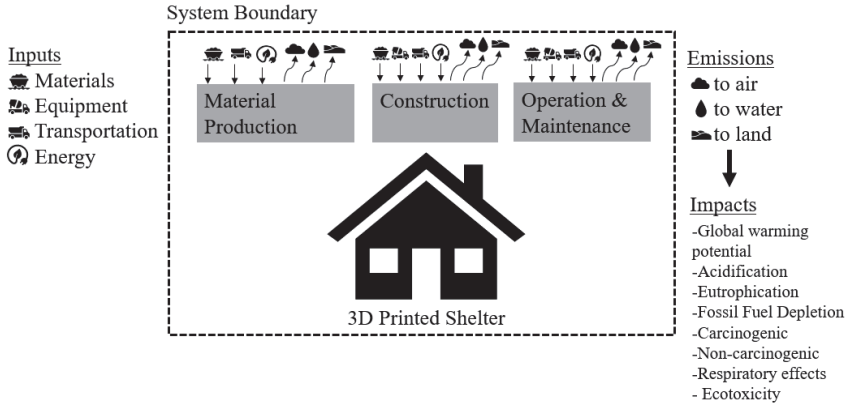

Figure 11. System boundaries of LCA.

The technical data include the quantities of materials, transportation, and energy consumption for construction and operation. The environmental impacts of the designed shelter were estimated using TRACI 2.0. The method represents the impacts of a global representative and addresses nine impact categories: ozone depletion (kgCFC-11eq), global warming potential (kgCO2eq), smog (kgO3eq), acidification (kgSO2eq), eutrophication (kgNeq), fossil fuel depletion (MJ Surplus), carcinogenic effects (CTUh), non-carcinogenic effects (CTUh), respiratory effects (kgPM2.5eq), and ecotoxicity (CTUe) [61]. The software SimaPro (SimaPro PhD) was used to evaluate the environmental impacts associated with the 3D-printed shelter. Figure 12 shows the environmental impacts caused by the production and transportation of construction materials and the construction of 3D-printed exterior walls onsite. Ten different categories of environmental impacts were measured based on the quantities provided, and these categories can be found on the *x*-axis of the figure. The *y*-axis represents the normalized value in percentage for the two different types of walls. The figure shows that insulated walls have higher environmental impacts compared to air cavity walls. Insulated walls seem to have 50% higher environmental impacts compared to air cavity walls, except for acidification, respiratory effects, and fossil fuel depletion. This suggests that E-PLA has less impact on these categories compared to others.

The environmental impacts of the operation phase of different scenarios can be seen in Table 8. From the table, it can be concluded that the source energy required for insulated walls with E-PLA and a PTHP system is less than in other scenarios, whereas air cavity walls with a VRF system require the most energy. The best alternative to E-PTHP, which has the lowest operational energy, is an air cavity wall with a PTHP system (37.33 greater GJ) or an insulated wall with a VRF system (41.47 greater GJ) to improve operational energy consumption.

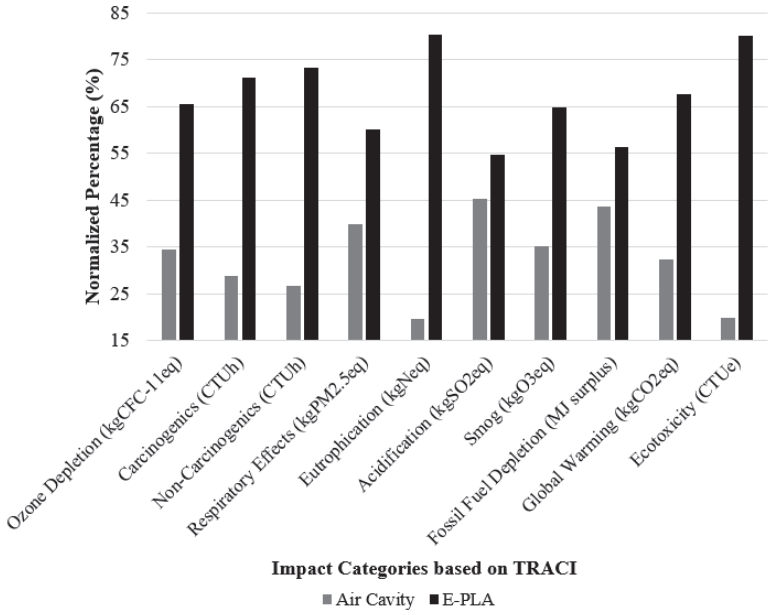

Figure 12. Environmental impacts of production, transportation, and construction of 3D-printed exterior wall.

Table 8. Environmental impacts of operation of 3D-printed shelter for different scenarios.

Impact Categories	A-PTHP	E-PTHP	A-RTU	E-RTU	A-VRF	E-VRF
Ozone depletion (kgCFC-11eq)	0.003934	0.003576	0.004143	0.003792	0.004362	0.003974
Carcinogenic effects (CTUh)	0.004201	0.003819	0.003829	0.003571	0.004658	0.004244
Non-carcinogenic effects (CTUh)	0.013913	0.012646	0.012622	0.011776	0.015425	0.014054
Respiratory effects (kgPM2.5eq)	118.7023	107.8907	107.3047	100.1644	131.5993	119.9014
Eutrophication (kgNeq)	332.9282	302.6044	299.9802	280.1439	369.1007	336.2912
Acidification (kgSO2eq)	155.8035	141.6126	146.0823	135.693	172.7314	157.3773
Smog (kgO3eq)	1570.31	1427.283	1496.777	1387.319	1740.924	1586.172
Fossil fuel depletion (MJ surplus)	59,960.3	54,498.99	69,752.93	63,126.77	66,474.95	60,565.97
Global warming (kgCO2eq)	56,700.18	51,535.81	56,964.53	52,445.37	62,860.62	57,272.92
Ecotoxicity (CTUe)	567,314.1	515,641.9	514,214.1	479,821.7	628,952.5	573,044.7

To calculate the overall environmental impacts of each scenario, the environmental impacts of each phase were identified and then aggregated. Figure 13 presents the total environmental impacts of each scenario for three different phases of the considered shelter unit. The figure clearly illustrates that the E-RTU scenario exhibits lower environmental impacts compared to the others, except for ozone depletion, global warming, and fossil fuel depletion. And, this suggests that the operational energy is more significant than that used for production and construction. Notably, the E-RTU and A-RTU scenarios have similar impacts in terms of eutrophication, but E-RTU outperforms the other scenarios in all other impact categories, demonstrating its superior environmental performance.

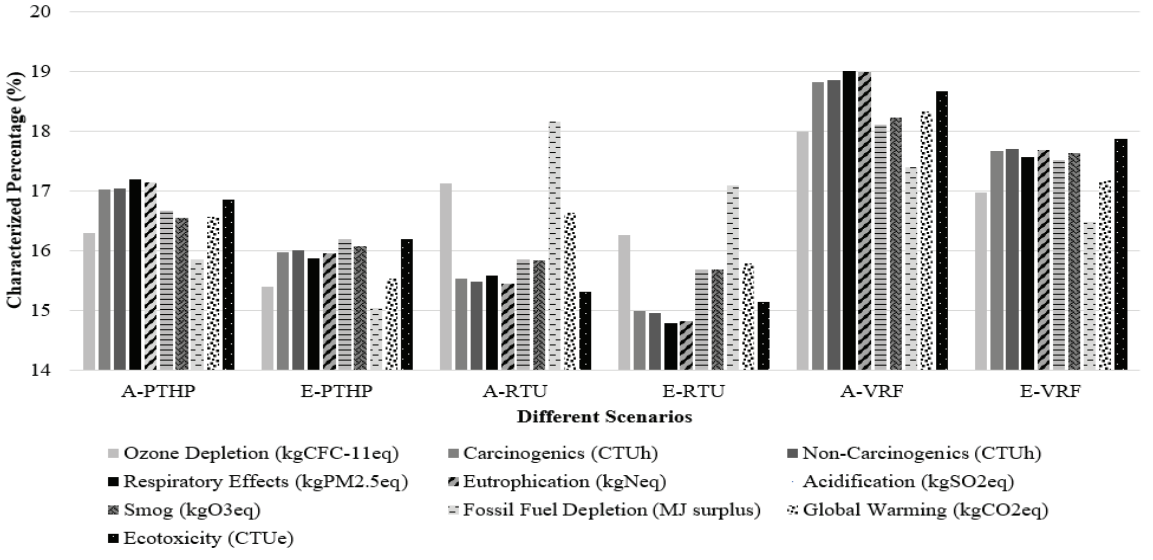

Figure 13. Environmental impacts of production, transportation, construction, and operation of 3D-printed exterior walls.

4.3.3. Energy Justice

In order to identify more favorable options in light of energy justice, the scenarios were carefully analyzed. The analysis employed the linguistic energy justice theory and utilized the Analytical Network Process (ANP) methodology. Figure 14 visually presents the ANP layout, which serves as a framework for evaluating and determining the best scenario in terms of energy justice. Within this framework, the energy justice decision-making theory classifies the criteria, sub-criteria, and scenarios into different levels. Specifically, the criteria are categorized as level 2, the sub-criteria as level 3, and the scenarios as level 4. LCEA and LCA are also taken into consideration as independent variables in decision-making. These variables play a significant role in the analysis, providing valuable insights into the energy justice implications associated with each alternative.

Table 9 shows the supermatrix derived from the eigenvector of criteria and independent variable. The initial eigenvector was constructed by comparing criteria with each other based on the goal. Subsequently, a comparison was made between criteria and independent variables, and vice versa. The supermatrix was column-stochastic and was raised to a sufficiently large power until convergence occurred [55]. Given the irreducible supermatrix, it is raised to the power 2K + 1 and converges if k tends to infinity [62]. In the current study, convergence was stable at W12. Table 10 shows the final weights of the criteria.

Table 9. Supermatrix.

Type	Scope	2A	RIG	SCLA	EI	LCEA	LCA
Scope	0	0	0	0	0	0	0
2A	0.512	0	0	0	0	0.845	0.155
RIG	0.081	0	0	0	0	0.167	0.833
SCLA	0.072	0	0	0	0	0.760	0.240
EI	0.335	0	0	0	0	0.111	0.889
LCEA	0	0.530	0.105	0.050	0.315	0	0
LCA	0	0.046	0.105	0.159	0.602	0	0

Table 10 illustrates the process of determining the final weights of sub-criteria by evaluating each sub-criterion in relation to its respective criterion. This involves multiplying the eigenvectors obtained from the comparison with the final weights of the criteria. The table also displays the limiting values, which represent the final weights of the criteria. Additionally, it presents the relative weights of the sub-criteria derived from the comparison and the resulting final weights of the sub-criteria.

Table 10. Final weights of sub-criteria.

Sub-Criterion	Final Weight of Criterion	Relative Weight of Sub-Criterion	Final Weight of Sub-Criterion
AVA	0.22	0.500	0.110
AFF		0.500	0.110
INTERE	0.161	0.106	0.017
DP		0.634	0.102
INTRAE		0.260	0.042
RES	0.12	1.357	0.163
T&A		0.251	0.030
INTERS		0.743	0.089
SUS	0.499	0.500	0.250
RES		0.500	0.250

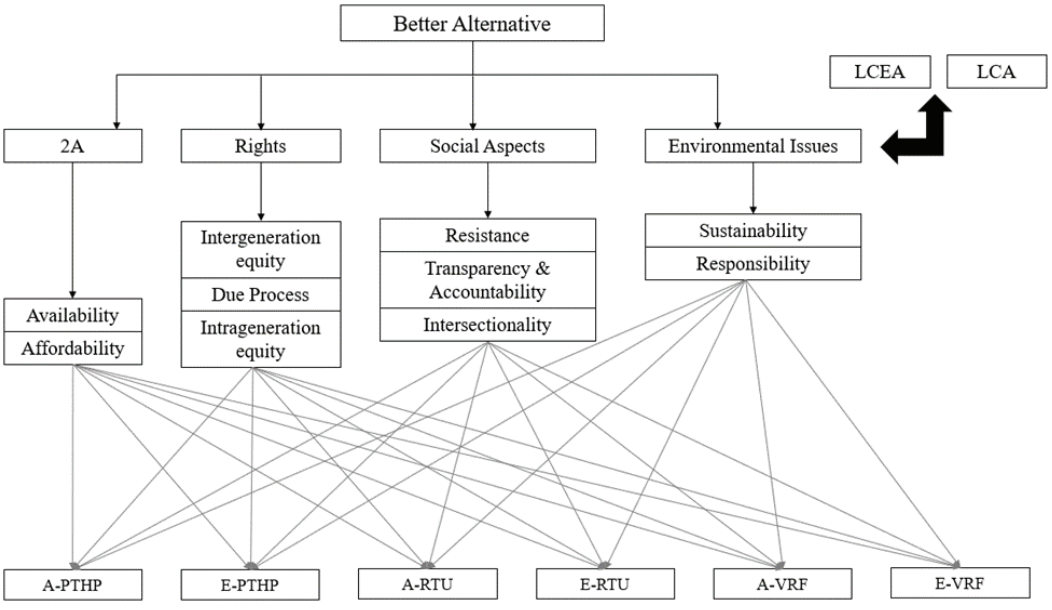

Figure 14. ANP Layout for energy justice assessment.

Table 11 presents the eigenvector, which is obtained by comparing each alternative or scenario according to sub-criteria and the final outcome. The final outcome is determined by multiplying the scenario's eigenvector with the final weights of the sub-criteria. The results indicate that the value for the E-RTU scenario is significantly higher (0.3690) than the others, suggesting that it is the most favorable scenario in terms of energy justice.

Table 11. Comparison of alternatives and findings of ANP.

Type	AVA	AFF	INTERE	DP	INTRAE	RES	T&A	INTRES	SUS	RES	Result
A-PTHP	0.0923	0.2700	0.2023	0.2752	0.0932	0.1667	0.1667	0.0943	0.0943	0.1015	0.1639
E-PTHP	0.1348	0.4216	0.4444	0.3431	0.1554	0.1667	0.1667	0.1753	0.1753	0.1656	0.2383
A-RTU	0.2494	0.0825	0.1044	0.1291	0.2846	0.1667	0.1667	0.2587	0.2400	0.2512	0.2412
E-RTU	0.4435	0.1460	0.1537	0.1646	0.3926	0.1667	0.1667	0.3864	0.4284	0.3798	0.3690
A-VRF	0.0282	0.0267	0.0357	0.0301	0.0285	0.1667	0.1667	0.0324	0.0310	0.0344	0.0623
E-VRF	0.0517	0.0534	0.0595	0.0580	0.0457	0.1667	0.1667	0.0537	0.0537	0.0674	0.0875

4.4. Decision-Making for Shelter Design

From the findings of the three analyses, a decision-making table, Table 12, has been created. Table 12 incorporates the results of LCEA, including various environmental impacts, such as carcinogenic effects, global warming, and smog from LCA, as well as the outcomes of the energy justice assessment. The second column is for LCEA, which is obtained based on the embodied energy required for insulation and operational energy. For instance, LCEA (426.144) for A-PTHP shows a total operational energy of 409.85 GJ and an embodied energy of 16,707 MJ for air cavity insulation. The third–fifth columns are generated based on the environmental impact required for the production of materials, transportation, and the construction of the 3D-printed exterior walls from Figure 12 and the operation of the shelter from Table 8.

Table 12. Decision-making based on sustainability assessment for scenarios.

Scenario	Sustainability Assessment				
	LCEA	LCA			Energy Justice
		Carcinogenic	Global Warming	Smog	
A-PTHP	426.144	0.004285	58,110.5	1681.977	0.1639
E-PTHP	448.372	0.004024	54,492.45	1633.418	0.2383
A-RTU	477.464	0.003913	58,374.85	1608.444	0.2412
E-RTU	494.762	0.003776	55,402.02	1593.453	0.3690
A-VRF	470.674	0.004741	638,410.5	1852.591	0.0623
E-VRF	489.842	0.004449	611,222.3	1792.307	0.0875

As can be seen in Table 12, the LCA result of A-PTHP for carcinogenic impacts is 0.004285. This value is the sum of 0.004201 from the environmental impacts of operation and 0.000081 from the environmental impacts of production, transportation, and the construction of the 3D-printed exterior wall shelter. According to the LCEA results, scenario A-PTHP requires 426.144 GJ less total energy than other scenarios across all three phases. On the other hand, when considering LCA, scenario E-RTU is preferred due to its lower impact values in all categories, except for smog. Furthermore, in terms of energy justice, scenario E-RTU outperforms the other scenarios with a higher value of 0.3690, indicating greater fairness and equity in energy distribution. Therefore, there is no single ideal scenario, but if we prioritize LCA and energy justice, scenario E-RTU is the preferred choice for constructing the shelter. However, if the focus is solely on LCEA, scenario A-PTHP would be the recommended option.

5. Conclusions

To address the issues related to existing disaster shelters, this study proposes a permanent shelter design that incorporates rapid construction technology and focuses on reducing environmental impacts and energy consumption and offering multipurpose functionality. The designed shelter features an octagonal shape, utilizes concrete as the primary construction material, and incorporates a central core pillar. Its multipurpose nature allows for variable uses, such as housing, a medical center, a collaborative space, or a storage area during and after a disaster. Onsite 3D printing technology is adopted for the exterior

walls, enabling a quick response to resilience demands. Various scenarios were created considering different combinations of cavity filling for the exterior walls and HVAC systems. Six scenarios were formed considering insulation options (air cavity or E-PLA) and HVAC systems (PTHP, RTU, or VRF). Sustainability assessments were conducted using life cycle analysis (LCA), life cycle energy assessment (LCEA), and energy justice assessment. According to the results of these assessments, scenario E-RTU (exterior wall with E-PLA insulation and RTU HVAC system) emerges as the best choice in terms of LCA and energy justice. However, if the decision is based solely on LCEA, scenario A-PTHP (air cavity with PTHP system) is the most favorable. It is important to note that these results may vary depending on different building types, sizes, and climate zones.

This study's outcomes have provided a shelter design considering sustainability that will allow decision-makers and stakeholders to perform a systematic decision-making process, which will ensure maximum utilization of limited resources to reach out to a larger number of people post-disaster. The proposed methodology will help local communities to uplift the economic conditions through business continuity after people move back to their own homes. In addition, the developed sustainability assessments can be applied in public buildings, including public libraries, universities, government buildings, etc.

For further studies, analysis can also include 3D-printed roofs or floors for sustainability assessments. Having focused on the southern region of the United States, this study is meant to act as a guide through the process of determining the optimal shelter design for a needed area. Adding life cycle cost analysis as one of the sustainability measurement techniques would be beneficial for some stakeholders, as cost plays a major role in decision-making. Sensitivity analysis can be performed based on different transportation distances of construction materials and equipment, construction materials, and construction methods (onsite/offsite), which would give a more concise scenario.

6. Limitations and Future Work

This study focuses on the sustainable design of shelters post-disaster in the southern region of the United States. However, its applicability to other parts of the United States is limited due to differences in weather, building materials, and LCA and energy justice criteria. Therefore, it is noted that a generalized approach is needed in future work. Additionally, sensitivity analysis will be conducted in future work to understand the impacts of different assumptions made in the calculations.

Furthermore, it is necessary to consider a power supply and energy management system in the sustainability assessment. A building may be well designed, but if it requires excessive amounts of energy for its use, it can become problematic. In many emergency situations, it is not possible to have enough energy to power air conditioning. Therefore, the system should be versatile and capable of accommodating less energy-intensive air-conditioning systems or, in some cases, functioning without them. Future research will integrate plant engineering to ensure that the design is truly reliable and applicable in various contexts.

Author Contributions: A.K.: Formal Analysis, Investigation, Writing-original draft, S.Y.: Methodology, Supervision, Project administration, and validation, R.G.W.: Designing, Writing, Review/Editing, Y.B.: Resources, Software, Writing-review & editing, A.K.L.: Review/Editing, Conceptualization and Supervision. All authors have read and agreed to the published version of the manuscript.

Funding: This work was partially funded by field work proposal CEBT105 under DOE BTO activity no. BT0302000 and BT0305000.

Data Availability Statement: The raw data supporting the conclusions of this article will be made available by the authors on request.

Acknowledgments: This manuscript has been authored by UT-Battelle, LLC, under contract DE-AC05-00OR22725 with the US Department of Energy (DOE). The US government retains and the publisher, by accepting the article for publication, acknowledges that the US government retains a nonexclusive, paid-up, irrevocable, worldwide license to publish or reproduce the published form

of this manuscript, or allow others to do so, for US government purposes. DOE will provide public access to these results of federally sponsored research in accordance with the DOE Public Access Plan (https://www.energy.gov/doe-public-access-plan (accessed on 18 June 2024).

Conflicts of Interest: Author Alka Khadka was employed by the company Intertek-PSI. The remaining authors declare that the research was conducted in the absence of any commercial or financial relationships that could be construed as a potential conflict of interest.

References

1. Data, W. Natural Disasters—Our World in Data. 2022. Available online: https://ourworldindata.org/natural-disasters (accessed on 15 May 2022).
2. Janbb, B. The Five Most Destructive Natural Disasters of the Past 10 Years—Owlcation. 2022. Available online: https://owlcation.com/stem/Worlds-worst-natural-disasters (accessed on 13 March 2023).
3. National Coalition for the Homeless. The Effects of Hurricane Katrina on New Orleans Housing. In *Natural Disasters and Homelessness*; National Coalition for the Homeless: Washington, DC, USA, 2008.
4. Guthier, T. The Devastating Effects of Climate Change on US Housing Security—The Aspen Institute. 2021. Available online: https://www.aspeninstitute.org/blog-posts/the-devastating-effects-of-climate-change-on-us-housing-security/ (accessed on 5 September 2022).
5. Félix, D.; Branco, J.M.; Feio, A. Temporary housing after disasters: A state of the art survey. *Habitat Int.* **2013**, *40*, 136–141. [CrossRef]
6. Kim, M.; Kim, K.; Kim, E. Problems and Implications of Shelter Planning Focusing on Habitability: A Case Study of a Temporary Disaster Shelter after the Pohang Earthquake in South Korea. *Int. J. Environ. Res. Public Health* **2021**, *18*, 2868. [CrossRef] [PubMed]
7. Bashawri, A.; Garrity, S.; Moodley, K. An Overview of the Design of Disaster Relief Shelters. *Procedia Econ. Finance* **2014**, *18*, 924–931. [CrossRef]
8. Elis, G. 3D Printing in Construction: Growth, Benefits, and Challenges. 2020. Available online: https://constructionblog.autodesk.com/3d-printing-construction/ (accessed on 19 October 2022).
9. Rear, O.; Landfield, A. "Building Industry Reporting and Design for Sustainability (BIRDS) Neutral Environment Software Tool (NEST) Technical Manual". 1976. Available online: https://nvlpubs.nist.gov/nistpubs/TechnicalNotes/NIST.TN.1976.pdf (accessed on 26 September 2021).
10. Ashworth, S.; Meslec, M.; Druhmann, C. Integrating Life Cycle Sustainability Analysis with BIM. In Proceedings of the European Facility Management Conference (EFMC), Sofia, Bulgaria, 5–8 June 2018.
11. Ndiaye, D.; Bernier, M.; Zmeureanu, R. Evaluation of the embodied energy in building materials and related carbon dioxide emissions in senegal. In Proceedings of the 2005 World Sustainable Building Conference, Tokyo, Japan, 27–29 September 2005.
12. Konstantinidou, C.A.; Lang, W.; Papadopoulos, A.M.; Santamouris, M. Life cycle and life cycle cost implications of integrated phase change materials in office buildings. *Int. J. Energy Res.* **2019**, *43*, 150–166. [CrossRef]
13. Vasis, T. Comparative Life Cycle Assesment (LCA) and Life Cycle Cost Analysis (LCCA) of Precast and Cast-in-Place Buildings in United States. Master's Thesis, Colorado State University, Fort Collins, CO, USA, 2020.
14. Liang, S.; Gu, H.; Bergman, R. Environmental Life-Cycle Assessment and Life-Cycle Cost Analysis of a High-Rise Mass Timber Building: A Case Study in Pacific Northwestern United States. *Sustainability* **2021**, *13*, 7831. [CrossRef]
15. Abdalla, H.; Fattah, K.P.; Abdallah, M.; Tamimi, A.K. Environmental Footprint and Economics of a Full-Scale 3D-Printed House. *Sustainability* **2021**, *13*, 11978. [CrossRef]
16. Bretz, T.E., Jr. Properties of Sulfur Concrete. Master's Thesis, Air Force Institute of Technology, Fairborn, OH, USA, 1981.
17. Ngo, T.; Raghavender, B.; Mirza, A.; Gammampila, R.; Aye, L.; Crawford, R.; Mendis, P. Life Cycle Energy of Steel and Concrete Framed Commercial Buildings Embodied Energy Analysis of Prefabricat ed Reusable Building Modules for a Multi-Residential . . . A Holistic Model for Designing and Optimising Sustainable Prefabricated Modular Build. . .. 2009. Available online: https://www.academia.edu/download/41597626/Life_cycle_energy_of_steel_and_concrete_20160126-26875-n7m2n.pdf (accessed on 26 September 2021).
18. Cabeza, L.F.; Rincón, L.; Vilariño, V.; Pérez, G.; Castell, A. Life cycle assessment (LCA) and life cycle energy analysis (LCEA) of buildings and the building sector: A review. *Renew. Sustain. Energy Rev.* **2014**, *29*, 394–416. [CrossRef]
19. Muga, H.; Mukherjee, A.; Mihelcic, J. An Integrated Assessment of the Sustainability of Green and Built-up Roofs. *J. Green Build.* **2008**, *3*, 106–127. [CrossRef]
20. CDP. Emergency and Interim Shelter—Center for Disaster Philanthropy. 2022. Available online: https://disasterphilanthropy.org/resources/shelter/ (accessed on 18 October 2022).
21. Cooke, L. Reversible Weather HYDE Tent Saves Lives in Extreme Weather. 2017. Available online: https://inhabitat.com/reversible-weatherhyde-tent-saves-lives-in-extreme-weather/ (accessed on 1 November 2021).
22. Better Shelter. Where We Work: Better Shelter. Available online: https://bettershelter.org/where-we-work/ (accessed on 1 November 2021).
23. Gupta, V. "Hexayurt Design and Construction". 2012. Available online: http://files.howtolivewiki.com/hexayurt.com/MaketheHexayurtv071202.pdf (accessed on 26 September 2021).

24. Baylor College of Medicine. Smart Pod. Available online: https://www.bcm.edu/community/global-outreach/global-health/innovation-center/smart-pod (accessed on 1 November 2021).
25. Domo. DOMO-System-DOMO-SYSTEM. 2021. Available online: https://www.domo-system.org/our-story-1 (accessed on 1 November 2021).
26. Kira. WinSun's 3D Printed Houses, Villa and Appartment. 3ders. 2015. Available online: http://www.3ders.org/articles/20150118-winsun-builds-world-first-3d-printed-villa-and-tallest-3d-printed-building-in-china.html (accessed on 26 September 2021).
27. Olick, D. 3D Printed House on Sale. CNBC Telev. 2021. Available online: https://www.youtube.com/watch?v=bj8kZ3llS5E&ab_channel=CNBCTelevision (accessed on 26 September 2021).
28. Mohan, R. 3D Printed Commercial Building. Econ. Times | Panache. 2020. Available online: https://economictimes.indiatimes.com/magazines/panache/print-to-build-worlds-first-3d-printed-commercial-building-is-here/articleshow/76490308.cms?from=mdr (accessed on 26 September 2021).
29. Carlson, C. Kamp C Completes Two-Storey House 3D-Printed in One Piece. Deezen. 2020. Available online: https://www.dezeen.com/2020/12/22/kamp-c-completes-two-storey-house-3d-printed-one-piece-onsite/ (accessed on 26 September 2021).
30. Omrany, H.; Soebarto, V.; Zuo, J.; Sharifi, E.; Chang, R. What leads to variations in the results of life-cycle energy assessment? An evidence-based framework for residential buildings. *Energy Built Environ.* **2021**, *2*, 392–405. [CrossRef]
31. Pahlavan, R.; Omid, M.; Akram, A. Modeling and sensitivity analysis of energy inputs for greenhouse cucumber production. *J. Agric. Technol.* **2011**, *7*, 1509–1521.
32. Englefield, J. 3D-Printed Houses from Disaster-Proof Concrete. Dezeen. 2021. Available online: https://www.dezeen.com/2021/03/16/icon-3d-printed-houses-austin-texas/ (accessed on 26 September 2021).
33. JAHA. Survivor Stories—Johnstown Area Heritage Association. 2022. Available online: https://www.jaha.org/attractions/johnstown-flood-museum/flood-history/survivor-stories/ (accessed on 11 October 2022).
34. Santos, T. Is UST Ready for the 'Big Quake'? | The Varsitarian. 2008. Available online: https://varsitarian.net/news/20081117/is_ust_ready_for_the_big_quake (accessed on 25 October 2021).
35. Levenson, E. This 'Sand Palace' on Mexico Beach Survived Hurricane Michael. That's No Coincidence. | CNN. 2018. Available online: https://www.cnn.com/2018/10/15/us/mexico-beach-house-hurricane-trnd/index.html (accessed on 25 October 2021).
36. Hi-Tech. Tokyo Skytree, Supported by 1300-Year-Old Technology—Hi-Tech—Kids Web Japan—Web Japan. 2016. Available online: https://web-japan.org/kidsweb/hitech/16/skytree.html (accessed on 4 November 2021).
37. Cherdo, L. Ultimate Guide to Construction 3D Printers in 2022 (Concrete 3D Printing). 2022. Available online: https://www.aniwaa.com/buyers-guide/3d-printers/house-3d-printer-construction/ (accessed on 19 October 2022).
38. ICON Vulcan. Vulcan | ICON. 2022. Available online: https://www.iconbuild.com/vulcan (accessed on 9 November 2022).
39. COBOD. CONTENT 1. 2022. Available online: https://www.cobod.com (accessed on 9 November 2022).
40. StroyBot 6.2. Rudenko 3D Concrete Printers. 2022. Available online: http://www.totalkustom.com/3d-concrete-printers.html (accessed on 9 November 2022).
41. White Clouds. Gantry in 3D Printers | WhiteClouds—WhiteClouds. 2022. Available online: https://www.whiteclouds.com/3dpedia/gantry/ (accessed on 25 October 2022).
42. Alkhalidi, A.; Hatuqay, D. Energy efficient 3D printed buildings: Material and techniques selection worldwide study. *J. Build. Eng.* **2019**, *30*, 101286. [CrossRef]
43. Hager, I.; Golonka, A.; Putanowicz, R. 3D Printing of Buildings and Building Components as the Future of Sustainable Construction? *Procedia Eng.* **2016**, *151*, 292–299. [CrossRef]
44. Labonnote, N.; Rønnquist, A.; Manum, B.; Rüther, P. Additive construction: State-of-the-art, challenges and opportunities. *Autom. Constr.* **2016**, *72*, 347–366. [CrossRef]
45. EPA. Heating, Ventilation and Air-Conditioning Systems, Part of Indoor Air Quality Design Tools for Schools | US EPA. 2023. Available online: https://www.epa.gov/iaq-schools/heating-ventilation-and-air-conditioning-systems-part-indoor-air-quality-design-tools (accessed on 14 May 2023).
46. US DOE. Insulation | Department of Energy. 2023. Available online: https://www.energy.gov/energysaver/insulation (accessed on 14 May 2023).
47. Henrique dos Santos, G.; Fogiatto, M.A.; Mendes, N. Numerical analysis of thermal transmittance of hollow concrete blocks. *J. Build. Phys.* **2017**, *41*, 7–24. [CrossRef]
48. Parker, K.; Garancher, J.P.; Shah, S.; Fernyhough, A. Expanded polylactic acid—An eco-friendly alternative to polystyrene foam. *J. Cell. Plast.* **2011**, *47*, 233–243. [CrossRef]
49. The Building Energy Exchange (BE-Ex). *Packaged Terminal HeatPumps (PTHPs)*; The Building Energy Exchange (BE-Ex): Manhattan, NY, USA, 2019; pp. 1–4.
50. Team, S. "Rooftop Unit". 2021. Available online: https://www.skillcatapp.com/post/packaged-rooftop-units-everything-you-need-to-know-is-here-part-1#:~:text=A (accessed on 14 May 2023).
51. Wicoff, P.; Keen, J. Air-to-air variable refrigerant flow systems. In Proceedings of the AEI 2011: Building Integration Solutions, Oakland, CA, USA, 30 March–2 April 2011; pp. 244–251. [CrossRef]
52. Utama, A.; Gheewala, S.H. Life cycle energy of single landed houses in Indonesia. *Energy Build.* **2008**, *40*, 1911–1916. [CrossRef]
53. The International Standards Organisation. International standard assessment—Requirements and guilelines. *Int. J. Life Cycle Assess.* **2006**, *7*, 652–668.

54. Fetanat, A.; Mofid, H.; Mehrannia, M.; Shafipour, G. Informing energy justice based decision-making framework for waste-to-energy technologies selection in sustainable waste management: A case of Iran. *J. Clean. Prod.* **2019**, *228*, 1377–1390. [CrossRef]
55. Sovacool, B.K.; Dworkin, M.H. Energy justice: Conceptual insights and practical applications. *Appl. Energy* **2015**, *142*, 435–444. [CrossRef]
56. Mohammadnazari, Z.; Mousapour Mamoudan, M.; Alipour-Vaezi, M.; Aghsami, A.; Jolai, F.; Yazdani, M. Prioritizing post-disaster reconstruction projects using an integrated multi-criteria decision-making approach: A case study. *Buildings* **2022**, *12*, 136. [CrossRef]
57. Teamaralingam, T.; Upasiri, I.; Gatheeshgar, P.; Pologanathan, K.; Nagaratnam, B.; Santos, P.; Rajanayagam, H. Energy performance of 3d-printed concrete walls: A numerical study. *Buildings* **2021**, *11*, 3–6. [CrossRef]
58. Victoria University. *Embodied Energy Coefficients*; Victoria University: Melbourne, Austrilia, 2017; p. 14.
59. Addendum, A.; Standard, A. Climatic data for building design standards. *ASHRAE Stand.* **2013**, *8400*, 404–636.
60. Bae, Y.; Yoon, Y.; Jung, S.; Malholtra, M.; Im, P. Development of an Occupancy Schedule for OpenStudio Prototype College Building Model. In Proceedings of the 2022 Building Performance Analysis Conference and SimBuild, Chicago, IL, USA, 14–16 September 2022. [CrossRef]
61. Bare, J. TRACI 2.0: The tool for the reduction and assessment of chemical and other environmental impacts 2.0. *Clean Technol. Environ. Policy* **2011**, *13*, 687–696. [CrossRef]
62. Overbeeke, V.B. First Resident of 3D-Printed Concrete House in Eindhoven Receives Key. TU/e. 2021. Available online: https://www.tue.nl/en/our-university/departments/electrical-engineering/department/news/news-overview/30-04-2021-first-resident-of-3d-printed-concrete-house-in-eindhoven-receives-key/#top (accessed on 26 September 2021).

buildings

MDPI

Article

Efficacy of Accelerated Carbonation Curing and Its Influence on the Strength Development of Concrete

Akarsh Padmalal [1,2], Kishor S. Kulkarni [1,*], Pradeep Rawat [1] and H. K. Sugandhini [2]

[1] Architecture, Planning and Energy Efficiency, CSIR-Central Building Research Institute, Roorkee 247667, Uttarakhand, India; akarsh.padmalal1273@gmail.com (A.P.); pradeeprawat630@gmail.com (P.R.)
[2] Department of Civil Engineering, Manipal Institute of Technology, Manipal 576104, Karnataka, India; sugandhini.hk@manipal.edu
* Correspondence: kishorsk@cbri.res.in

Abstract: The building sector is figuring out how to lower its embodied CO_2 in a sustainable way. The technology, known as Carbon Capture, Utilization, and Storage (CCUS), offers a possible remedy for this issue. Accelerated carbonation is one method of sequestering CO_2 in concrete. In this study, an M25 grade of concrete is made using Ordinary Portland Cement with 0–30% replacements of Class F fly ash. The specimens were exposed to accelerated carbonation curing for 6 h, 24 h, and 72 h, and then the specimens were tested for their compressive strength, carbonation depth, and pH. The CO_2 uptake was measured by Thermogravimetric analysis (TGA), and the occurrence of carbonation was confirmed using X-ray diffraction (XRD) and Scanning Electron Microscopy (SEM). The results of the study indicate a significant improvement in the compressive strength with a percentage increase of 70.46%, 111.28%, 30.36%, and 36.69%, respectively, for 0%, 10%, 20%, and 30% fly ash contents in concrete samples subjected to 72 h of accelerated carbonation curing without affecting its alkalinity. The study reiterated that accelerated carbon curing is an advisable method for countries like India that are undergoing rapid economic developments.

Keywords: global warming; accelerated carbonation; compressive strength; CO_2 uptake; carbonation depth

Citation: Padmalal, A.; Kulkarni, K.S.; Rawat, P.; Sugandhini, H.K. Efficacy of Accelerated Carbonation Curing and Its Influence on the Strength Development of Concrete. *Buildings* **2024**, *14*, 2573. https://doi.org/10.3390/buildings14082573

Academic Editors: Piljae Im, Yeobeom Yoon and Sungkyun Jung

Received: 12 May 2024
Revised: 19 June 2024
Accepted: 16 August 2024
Published: 21 August 2024

1. Introduction

The current environmental landscape is marked by a series of unprecedented challenges, and global warming has emerged as a critical issue threatening the planet's future, especially its biological richness and diversity. The scientific consensus is unequivocal: human activities, particularly the emission of greenhouse gases, are driving an alarming rise in global temperatures [1,2]. While several industries contribute to this environmental crisis, the construction industry stands out as a prime sector that demands heightened scrutiny [3]. The construction industry is widely considered as a vital contributor to social and economic development, playing an important role in shaping the environment. As buildings rise and infrastructure expands, the construction industry's reliance on resource-intensive processes and materials becomes increasingly evident and more pressing than even before. From energy-intensive construction methods to the production of emissions, this sector's carbon footprint extends far beyond the completed structures it leaves in its wake [4].

Cement is an indispensable component of the construction industry, with widespread use around the globe. However, the production of cement is also known to be one of the most carbon-intensive processes in the lifecycle of concrete [5,6]. Current estimates indicate that global cement plants are accountable for about 8% of annual CO_2 emissions. The emission of about 1 tonne of carbon dioxide (CO_2) into the environment is a consequence of producing 1 tonne of Ordinary Portland Cement (OPC), and kiln operation is responsible for 50% of CO_2 emissions, which result from the combustion of fossil fuel [7–9]. This

underscores the urgent need for the industry to explore more sustainable production methods and to reduce its environmental impact. Carbon Capture, Utilization, and Storage (CCUS) has become an excellent means to address the problems of rising temperatures and carbon dioxide emissions related to the construction industry. The technique has become well-known recently as a way to lessen greenhouse gas emissions and the effects of climate change [10]. Accelerated Carbonation Curing (ACC) presents a viable method for the construction industry to implement CCUS. By leveraging the inherent properties of CO_2, ACC offers the potential to reduce carbon emissions and promote sustainable practices within the sector [11].

Accelerated Carbonation Curing stands out as a highly efficient curing method for precast concrete, offering the dual benefit of sequestering CO_2 and aligning with global sustainability goals. Its application not only aids in reducing carbon footprints but also enhances the mechanical and durability properties of concrete, establishing it as a superior option [10,12]. Initially investigated in the early 1970s, ACC did not gain traction due to the high costs associated with CO_2 capture [13,14]. However, recent decades have witnessed significant technological advancements in CO_2 capture, making it more economical and feasible. This has reignited interest worldwide, prompting researchers to explore ACC as a viable alternative to steam curing in the concrete precast industry. The newfound availability of captured CO_2 on a large scale has further propelled investigations into construction materials' potential to sequester CO_2 in a stable form [11].

Accelerated Carbonation Curing during concrete production has the ability to capture CO_2 within a short span of time, ranging from a few hours to a few days. Studies have indicated that this method can enhance the strength and durability of concrete products by modifying their chemical composition and microstructure [15,16]. The literature indicates that adding a high concentration of CO_2 to cement-based materials during their initial hydration process can improve those materials' mechanical qualities, hardening rate, and resistance to a variety of environmental conditions, including sulphate attack, acid erosion, wetting and drying, and freeze-thaw cycles. As such, adopting ACC technology is a viable means of reducing carbon emissions and enhancing the overall performance of these materials [17,18]. Equations (1)–(4) depict the reaction taking place during ACC [19].

$$3(3CaO \cdot SiO_2) + (3 - x)CO_2 + yH_2O \rightarrow xCaO \cdot SiO_3 \cdot yH_2O + (3 - x)CaCO_3 \quad (1)$$

$$2(2CaO \cdot SiO_2) + (2 - x)\,CO_2 + yH_2O \rightarrow xCaO \cdot SiO_2 \cdot yH_2O + (2 - x)CaCO_3 \quad (2)$$

$$Ca(OH)_2 + CO_2 \rightarrow CaCO_3 + H_2O \quad (3)$$

$$3CaO \cdot 2SiO_2 \cdot 3H_2O + 3CO_2 \rightarrow 2SiO_2 + 3CaCO_3 + 3H_2O \quad (4)$$

It is axiomatic that the level of relative humidity in concrete-based products has a significant impact on the degree of carbonation. Reduced levels of relative humidity can expedite the carbonation process, as a dry environment allows greater CO_2 diffusion in the concrete. Both experimental and modelling data suggest that, to attain carbonation, the referred relative humidity range of 50% to 70% is required [20]. At this level, the concrete is neither too dry to restrict carbonation reactions, nor too damp for capillary pores to be fully saturated, which limits CO_2 diffusion [21]. Another prime variable that affects the amount of carbon absorbed during carbonation curing is the length of time exposed to CO_2. According to earlier research, most carbonation reactions seem to happen in the first 6 h of curing. However, this result may vary depending on the concrete mixture design and curing settings [22].

Although many studies related to ACC have been carried out in the world, studies using cementitious products in Indian conditions are meagre. Therefore, the present study has been undertaken to understand the efficiency of ACC over other conventional methods.

Thus, the study delves into the efficacy of ACC as a curing method and its influence on the strength development of concrete, considering varied cementitious contents with fly ash replacements. The parameters scrutinized incorporate compressive strength, carbonation depth, pH analysis, and carbonation uptake.

2. Materials and Methods

2.1. Material

Grade 43 OPC conforming to IS:8112-2013 [23] and Class F fly ash in accordance with IS:3812-2003 [24] were utilized. The cement has a fineness of 327 m^2/kg and a specific gravity of 3.15, while the fly ash has a fineness of 290 m^2/kg and a specific gravity of 2.20. Chemical properties of both binders are detailed in Table 1.

Table 1. Chemical composition of cement and fly ash.

Oxide	CaO	SiO_2	Al_2O_3	Fe_2O_3	MgO
Cement	63.50	21.70	6.60	4.60	2.40
Fly ash	3.13	62.57	27.40	5.92	0.98

River sand from zone II, as specified by IS:383-2016 [25], served as the fine aggregates. Coarse aggregates were composed of crushed granite gravels with nominal sizes of 20 mm and 12.5 mm, blended in a ratio of 3:2. The specific gravities of the fine and coarse aggregates were 2.70 and 2.65, respectively. Figure 1 depicts the grading curve of coarse aggregate and fine aggregate used for the present study.

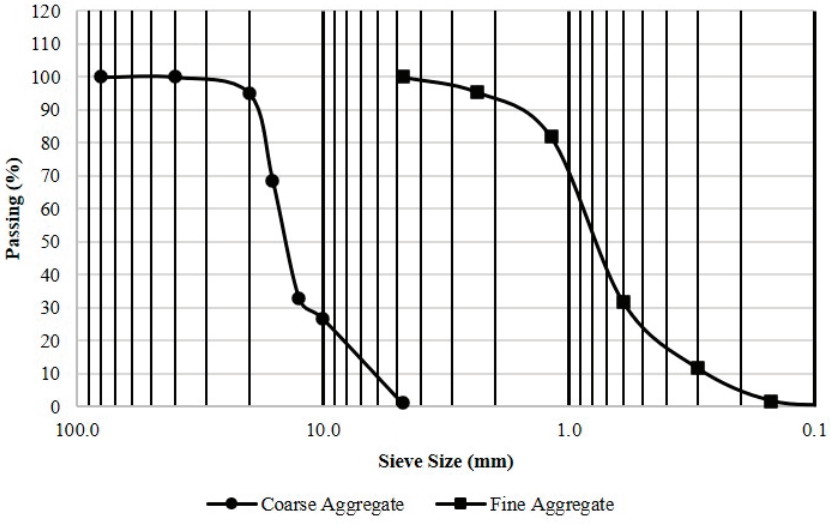

Figure 1. Particle-size distribution curve of aggregates.

2.2. Concrete Mixtures

The study considered four different concrete mixtures with different cementitious materials. The first mixture, abbreviated as M1, was prepared using Ordinary Portland Cement (OPC) as the cementitious material. In the second, third, and fourth mixtures, a blend of fly ash and OPC was used, and these concrete mixtures were represented as M2, M3, and M4, respectively. To prepare one cubic meter of concrete mixtures, the constituent materials' weights are shown in Table 2. A water-to-cementitious material ratio of 0.45 was used to maintain a zero slump for each of these mixtures.

Table 2. Mix proportioning for 1 m^3 of concrete mixture.

Materials	M1	M2	M3	M4
OPC	375	337.5	300	262.5
Fly ash	-	37.5	75	112.5
Fine Aggregate	672.06	672.06	672.06	672.06
Coarse Aggregate	1157.57	1157.57	1157.57	1157.57
Water	168.75	168.75	168.75	168.75

2.3. Experimental Setup for Carbonation

The arrangement depicted in Figure 2a,b illustrates the configuration for Accelerated Carbonation Curing of concrete samples. The valve and pressure regulator assembly located on the CO_2 gas cylinder are connected to the inlet pipe of the chamber. To regulate relative humidity and temperature within the system, a water tank and heating mechanism are included. Additionally, a computerized system facilitates data collection and adjustment of humidity, temperature, and CO_2 levels within the chamber.

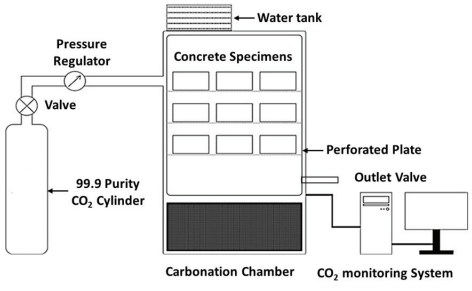

(**a**)

(**b**)

Figure 2. (**a**) Basic setup for Accelerated Carbonation Curing. (**b**) Accelerated Carbonation Chamber.

2.4. Preparation and Curing of Sample

All the ingredients were mixed, and then water was added to make a consistent mixture. Three layers of concrete were poured into moulds, and the voids were eliminated by vibrating the material. After 24 h of casting, the samples of all four concrete samples were taken out of the moulds, and each set of the four concrete mixtures was divided into two groups. One group of samples was treated with ACC for 6, 24, and 72 h at 10% CO_2 concentration, at 35 °C temperature, and at 70% relative humidity, while the other group was water-cured for the same amount of time as the ACC. For the concrete sample ACC, 99.9% pure CO_2 was used from a gas cylinder with pressure regulation. Figure 3a,b shows the preparation and curing of samples.

(**a**) (**b**)

Figure 3. (**a**) Preparation of samples and (**b**) curing.

2.5. Testing of Specimens

To examine the alteration in the concrete matrix with ACC, assessments were carried out after 6, 24, and 72 h of ACC. Additionally, a batch of water-curing specimens was tested for comparison at the same intervals. Compressive strength analysis was utilized to gauge the mechanical robustness of the concrete. To investigate any significant pH variations resulting from the consumption of $Ca(OH)_2$ during the ACC process, the pH of the concrete was measured. This was done to assess any potential impact on the formation of the passivation layer on the rebar. To conduct this measurement near the surface, a sample was collected. Three grams of powdered sample were taken from the desired location and dissolved in 10 mL of distilled water. The mixture was stirred automatically for 15 min, followed by filtration using Whatman filter paper. The pH of the resulting solution was then measured using a digital pH meter following previous studies [10,19]. In order to find the carbonation depth, phenolphthalein solution was applied to the specimen's cross-section. To understand changes in mineralogical compositions, XRD, TGA, and SEM were performed on samples collected from the near surface of concrete. Before testing, samples were immersed in acetone to stop further hydration. XRD was recorded on a RIGAKU D-Max 2000 X-ray diffractometer (Make: Rigaku Corporation, Osaka, Japan) equipped with a Gobel mirror for Cu-Kα radiation. The measurements were carried out in a 2θ range from 5–70° with a step of 0.02° and counting time of 5 s/step. The Xpert High Score Plus programme was used to match the obtained peaks with the ICDD reference database. Measurements were also made of the mass loss within a specific temperature range and the CO_2 uptake by carbonated specimens using TGA data. The mass loss in a specific temperature range was measured and correlated to $Ca(OH)_2$ and $CaCO_3$ that formed during the curing process. A TGA test was conducted using an INSEIS STA PT 1600 analyzer. A part of the powder sample was heated in a nitrogen atmosphere between 50 and 900 °C at a heating rate of 10 °C per minute. Morphological analysis of the specimens utilising SEM images taken using a TESCAN MIRA3 microscope was performed. The specimens underwent an ion sputter procedure to cover them in gold before imaging.

3. Results and Discussion

3.1. Compressive Strength

The mechanical performance of concrete at 6, 24, and 72 h after ACC was examined in the study in relation to water curing. 100-mm cube specimens were examined to assess the compressive strength of the concrete. Figure 4a–d shows the results of compressive strength

at different hours of carbonation curing and compared with water-cured specimens. The data suggest that the compressive strength of the ACC specimens was higher than that of the water-cured specimens with a percentage increase of 70.46%, 111.28%, 30.36%, and 36.69% for the M1, M2, M3 and M4 sample, respectively, after 72 h. Furthermore, mixes M1 and M2 during 72 h of carbonation cure reached the desired strength. Previous researchers reported that enhanced strength development is due to the higher rate of carbonation reaction, which turns C_2S and C_3S into $CaCO_3$ and C-S-H gel; thus, ACC specimens have better strength development [19]. Furthermore, the hydration event that yields $Ca(OH)_2$ is transformed into thermodynamically stable $CaCO_3$ by the carbonation reaction that occurs during ACC.

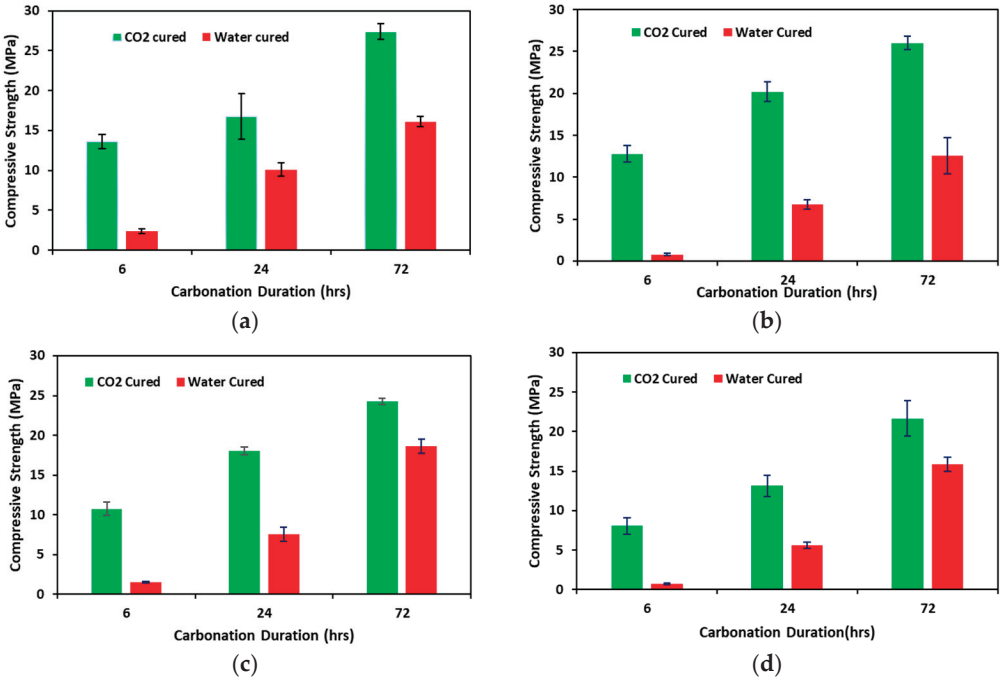

Figure 4. Compressive strength of (**a**) M1, (**b**) M2, (**c**) M3, and (**d**) M4 mixes.

3.2. Carbonation Depth and pH Analysis

Figure 5 shows the image of a typical phenolphthalein-stained concrete specimen after ACC. During the phenolphthalein test for the calculation of carbonation depth, it is observed that the carbonation depth of all the samples is below 5 mm. Carbonation depth was calculated using Equation (5) [26]. So, the chance of carbonation-induced corrosion is negligible. This statement is verified using pH analysis. pH results are depicted in Figure 6. In the pH analysis, even though there is a drop in the pH of ACC samples compared to water-cured samples, it is well above 10, which is in the tolerable limit to avoid deterioration of passivating film over the rebar [10,11,27].

$$\text{Carbonation Depth} = \frac{D1 + D2 + D3 + D4}{4} \quad (5)$$

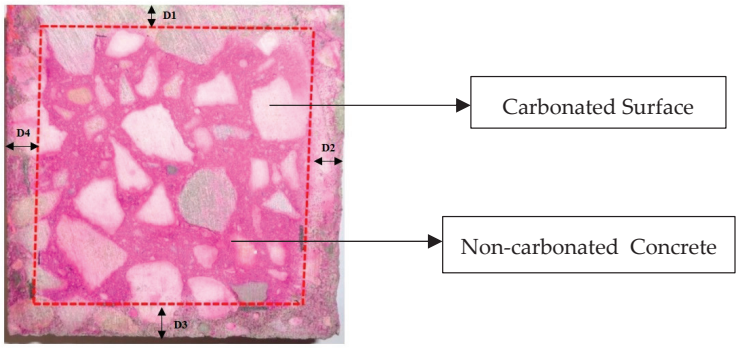

Figure 5. Phenolphthalein-stained concrete specimen after ACC.

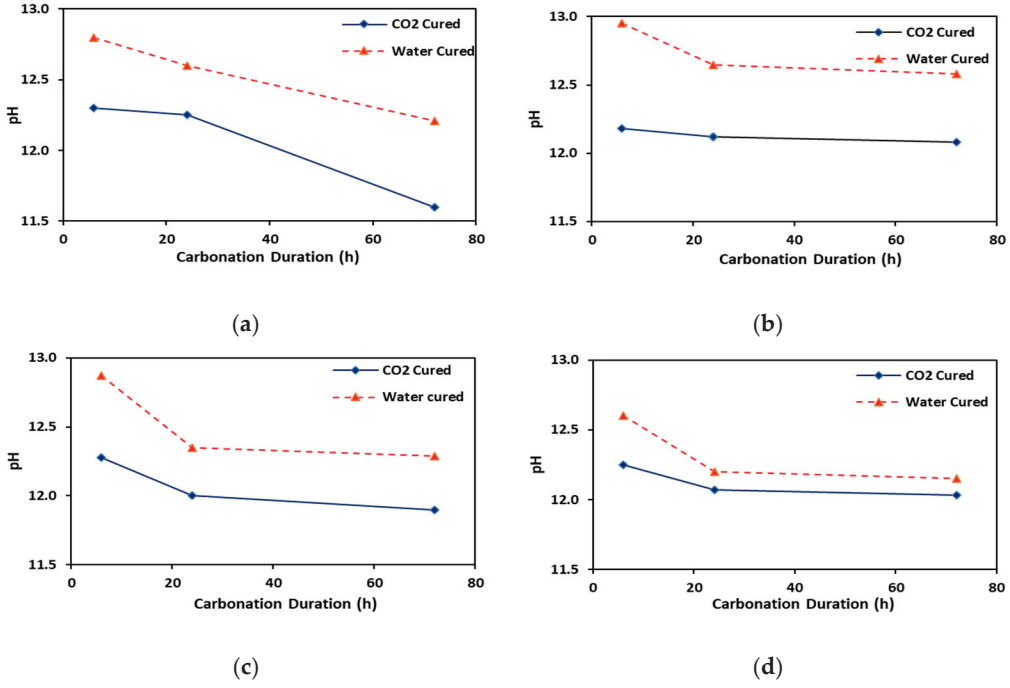

Figure 6. pH Analysis results of (**a**) M1, (**b**) M2, (**c**) M3, and (**d**) M4 mixes.

3.3. Microstructural Study

Curing of the concrete undergoes various physical and chemical reactions. Therefore, microstructural study of the concrete is necessary for understanding the physiochemical changes taking place in different curing regimes. Three different methods were employed to analyze the microstructure of the concrete in this research, namely XRD, TGA, and SEM.

3.3.1. XRD Analysis

XRD is a crucial technique for analyzing hydrated cement concrete samples in both quantitative and qualitative ways. This analysis can detect the mineralogical changes, if any, that can occur due to carbonation. By studying XRD patterns of carbonated and non-carbonated concrete samples, it is possible to determine the extent of carbonation. Bragg's law is the foundation of XRD. By analyzing the results of the XRD test, the angle at

which the wave was diffracted and the intensity of the X-ray can be determined [28]. In Figure 7, the XRD patterns of the M1 and M2 samples subjected to accelerated carbonation curing and water curing are depicted. The graphs reveal a notable increase in the peaks corresponding to $CaCO_3$ and a decrease in those related to $Ca(OH)_2$ following carbonation curing. This phenomenon can be attributed to the reaction between cement hydration products and CO_2.

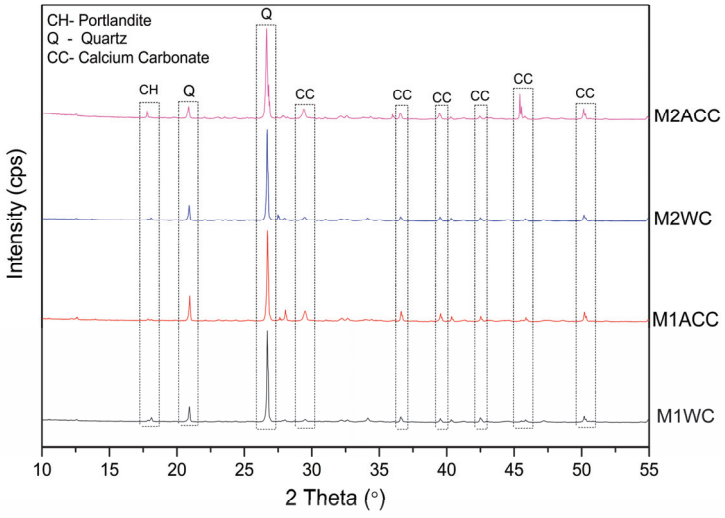

Figure 7. XRD of M1 and M2 accelerated carbonation-cured and water-cured mixes.

3.3.2. TGA and CO_2 Uptake

Understanding the environmental impact of concrete structures and evaluating their potential as carbon sinks requires the measuring of carbonation, which can be quantified through the CO_2 uptake in concrete. The decomposition of $Ca(OH)_2$ can be inferred from the mass loss between the temperature range of 400–460 °C, while the decomposition of $CaCO_3$ occurs between 600–800 °C. Thus, the CO_2 content of the samples after ACC was investigated using TGA. The analysis of CO_2 uptake in concrete can be elucidated through the assessment of mass loss during TGA, as outlined in Equation (6), where the cement mass in the original sample could be calculated by multiplying the original mass of the concrete powder sample by the cement ratio derived from the mix design [29]. Figure 8 shows the TGA-DTG curve for mixes of M1 and M2 carbonation cured for 6 h and 72 h, and the mass loss obtained are 3.94%, 5.83%, 2.67%, and 5.48%, respectively. Figure 9 illustrates the CO_2 uptake trends for the four concrete mixtures, namely M1, M2, M3, and M4. Notably, the observed CO_2 uptake exhibits a direct correlation with the duration of curing, indicating that longer curing periods result in increased CO_2 uptake. Conversely, a negative correlation is observed between CO_2 uptake and the proportion of fly ash replacement in the concrete mixture. This implies that higher levels of fly ash substitution led to decreased CO_2 uptake; this may be due to the fact that the fly ash is unreactive with CO_2.

$$CO_2 \text{ Uptake } (\%) = \frac{\text{Sample mass at } 600\ ^\circ\text{C} - \text{Sample mass at } 800\ ^\circ\text{C}}{\text{Cement mass in orginal sample}} \times 100 \quad (6)$$

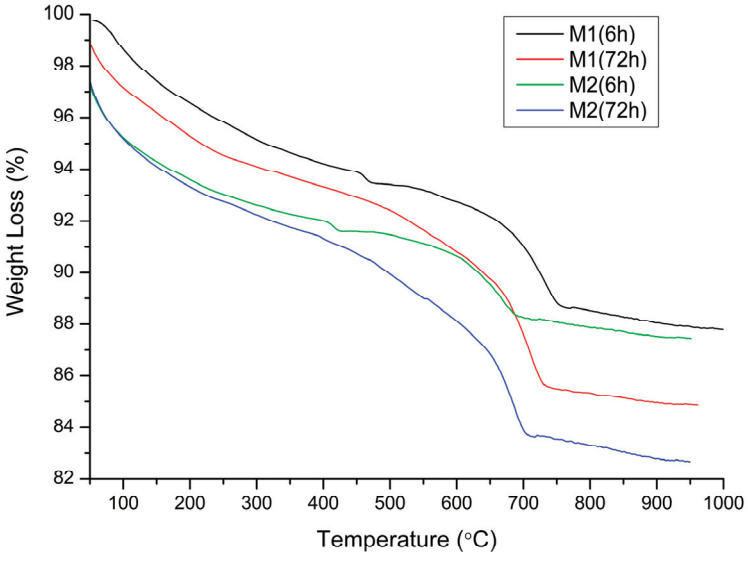

(**a**)

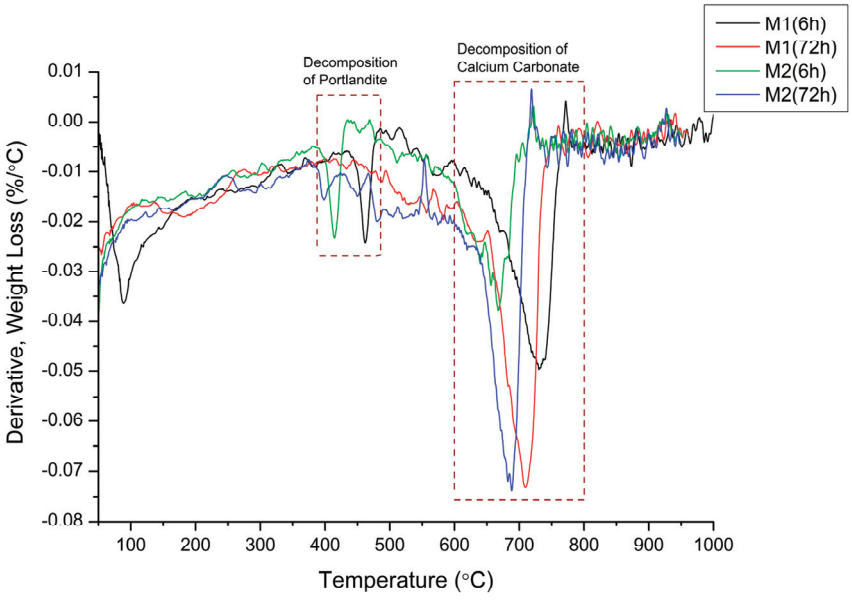

(**b**)

Figure 8. (**a**) TGA (**b**) DTG analysis of carbonation cured M1 and M2 sample for 6 h and 72 h.

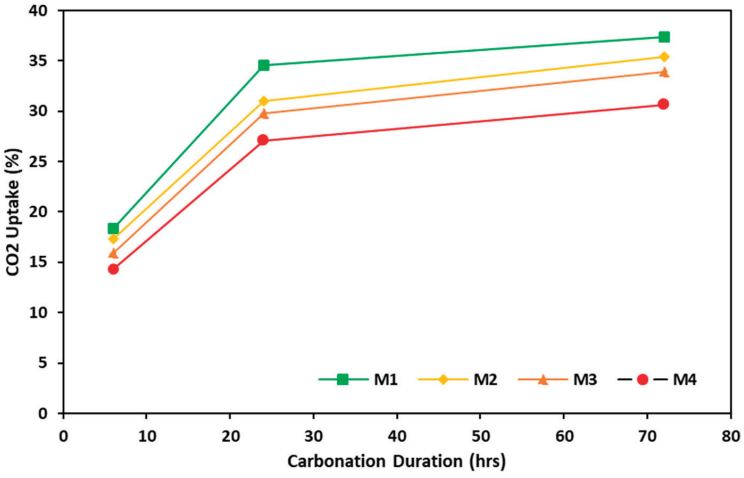

Figure 9. CO_2 uptake of the samples at different time durations.

3.4. SEM

In the SEM image of water-cured concrete (Figure 10a,c), the microstructure shows the well-hydrated cement particles surrounded by a dense matrix of hydrated cement paste. The images display a uniform distribution of voids. The calcium hydroxide and calcium silicate hydrate gel formed as a result of hydration appear under the higher-magnification SEM images [30]. In contrast, Figure 10b,d concrete subjected to carbonation curing exhibit alterations in its microstructure due to the ingress of CO_2. Carbonation leads to the dissolution of $Ca(OH)_2$ and the formation of $CaCO_3$, resulting in a decrease in voids due to $CaCO_3$ precipitation within the pores, leading to a reduction in porosity and an increase in concrete density [31]. This outcome is consistent with the previous research findings. The $CaCO_3$ crystals that formed occupy the voids and the small fractures within the interfacial transition zone (ITZ), which in turn can help to minimize the imperfections of the ITZ [28,29].

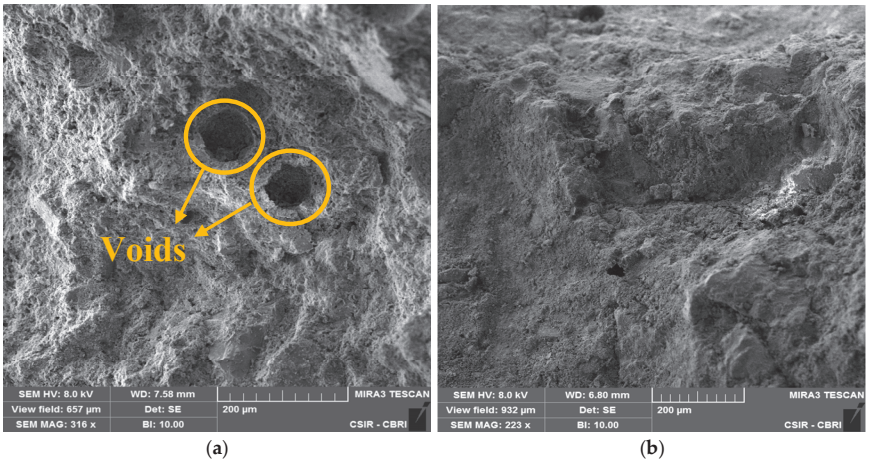

(**a**) (**b**)

Figure 10. *Cont.*

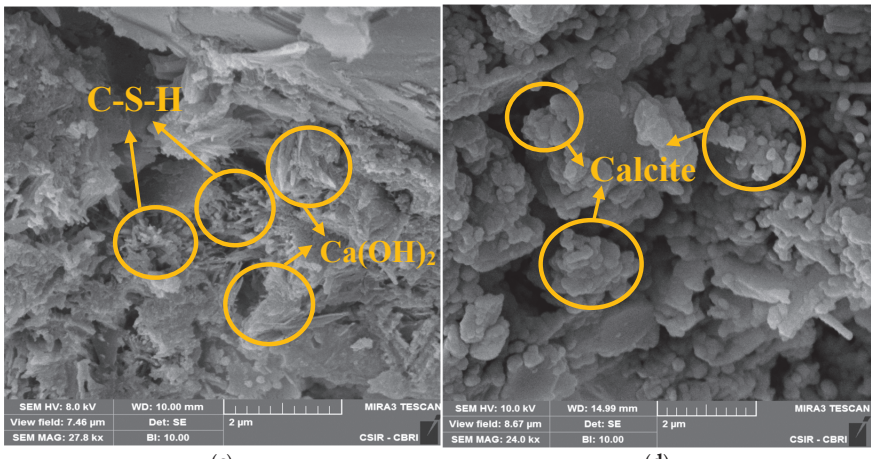

(**c**) (**d**)

Figure 10. SEM images of concrete samples cured at different curing regimes: (**a**) M1 water cured (200 µm), (**b**) M1 CO_2 cured (200 µm), (**c**) M1 water cured (2 µm), and (**d**) M1 CO_2 cured (2 µm).

3.5. Statistical Analysis

The compressive strength of concrete depends on the presence of Flyash Content (FAC) and Carbonation Duration (CD). This study uses the statistical technique Analysis of variance (ANOVA) to evaluate the effect of Carbonation Duration (CD) and Flyash Content (FAC) on compressive strength, pH, and CO_2 uptake of concrete. To determine the significance factor of experimental parameters of carbonated concrete, the ANOVA and F-test were performed. The F-test, originally introduced by Dr. Fisher, serves as a supplementary method to evaluate the primary factors at play [32]. ANOVA helps to quantify the dominance of the control factor and justify the effects of input changes on experimental responses.

The characteristics of compressive strength, pH, and CO_2 uptake are always positive, and the higher the value, the better the performance of concrete. To achieve optimal conditions, the "larger is better (LB)" loss function was chosen, as it takes into account the importance of having larger values for compressive strength, pH, and CO_2 uptake in concrete performance. The loss function Lij of LB performance characteristics is expressed as:

$$L_{ij} = \frac{1}{n}\sum_{k=1}^{n}\frac{1}{y_{ijk}^2} \quad (7)$$

where, "L_{ij}" is the loss function of the ith performance characteristics in the jth experiment, "n" is the number of tests, and "y_{ijk}" is the experimental value of the i-th performance characteristics in the j-th experiment at the k-th test. The loss function is further transformed into a signal-to-noise (S/N) ratio for determining the performance characteristics deviating from the desired value. The S/N ratio n_{ij} for the i-th performance characteristics in the j-th experiment is expressed as:

$$n_{ij} = -10\log(L_{ij}) \quad (8)$$

Table 3 displays the outcomes of ANOVA, which is employed for statistical analysis using Minitab 15 software.

Table 3. Results of ANOVA.

Response Factor	Control Factor	DF	SS	MS	F-Level	Contribution (%)	*p*-Level
Compressive Strength	FAC	3	53.6	17.87	11.95	12.4	0.006
	CD	2	369.37	184.69	123.47	85.5	0
	Error	6	8.98	22.55		2.1	
pH	FAC	3	0.43	0.14	10.7	59.72	0.008
	CD	2	0.21	0.1	7.72	29.16	0.022
	Error	6	0.08	0.01			
CO_2 uptake	FAC	3	4.47	1.49	12.5	21.3	0.005
	CD	2	15.29	7.89	66.23	75.26	0
	Error	6	0.72	0.012		3.44	

From Table 3 it is observed that Carbonation Duration has great importance on compressive strength (85.50%) and CO_2 uptake (75.26%) than Flyash Content, whereas the pH of concrete was highly dependent on Flyash Content (59.72%) than Carbonation Duration. The analysis indicates that the experimental error was very low-level. The larger F value indicates that the variation of the control parameters makes a big change in the performance characteristics. The *p*-Level value is less than 0.05, which indicates that both the Flyash Content and Carbonation Duration and retention period are significant. Figure 11 shows the variation of means of the S/N ratio with levels of input parameters.

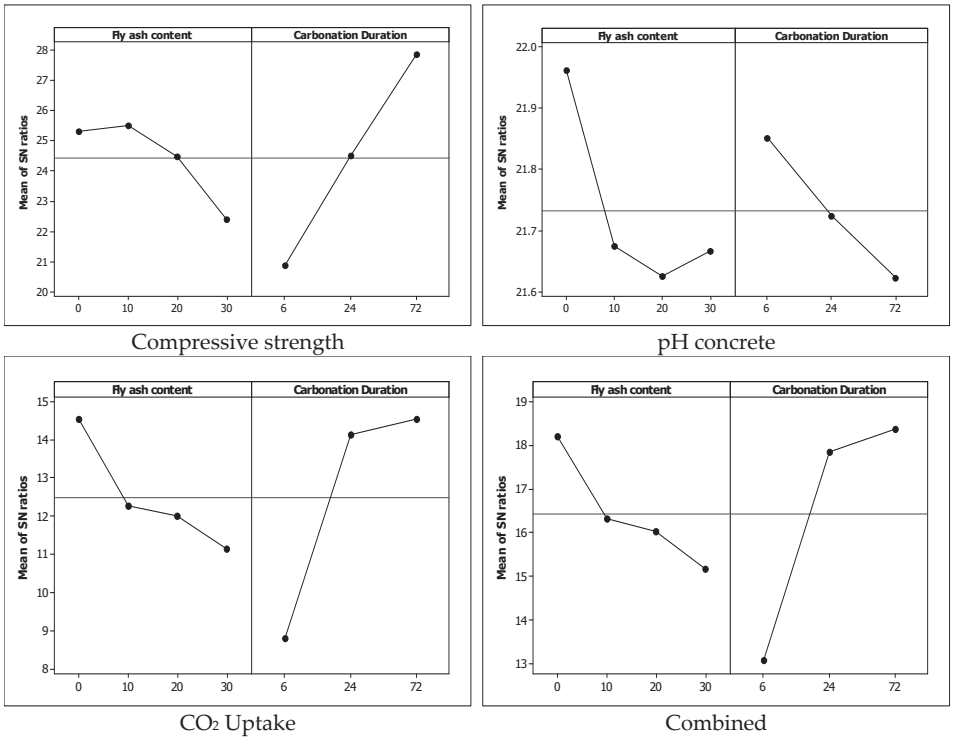

Figure 11. S/N graphs of experimental parameters.

Minitab software was utilized to develop models for the response surface. Response surface methodology consists of a series of mathematical and statistical techniques that are valuable for modeling and analyzing situations where a response of interest is influenced

by various variables. Experimental data was employed to propose predictions for the compressive strength and CO_2 uptake of concrete exposed to carbonation. Table 4 displays the individual coefficients for compressive strength and CO_2 uptake response surface models.

Table 4. Interferences about the individual coefficient of the response surface models.

Input Term	Output Parameters					
	Compressive Strength			CO_2 Uptake		
	Coefficient	T	*p*	Coefficient	T	*p*
Constant	10.5182	8.373	0.000	2.91796	7.725	0.000
FAC	0.1227	1.045	0.336	−0.11938	−3.382	0.015
CD	0.3916	5.121	0.002	0.18037	7.845	0.000
FAC × FAC	−0.0094	−2.656	0.038	0.00185	1.738	0.133
CD × CD	−0.0023	−2.600	0.041	−0.0019	−7.029	0.000
FAC × CD	−0.0003	−0.248	0.813	0.00040	1.183	0.282
Standard Deviation	1.22673			0.36883		
R Sq. (%)	97.9			96.11		

Note: FAC-Flyash Content, CD-Carbonation Duration.

4. Conclusions

Based on the ACC procedure utilized for the concrete mixture examined in this research, the following conclusions can be made:

(1) Carbonation curing leads to accelerated strength development and densification of the concrete surface, resulting in improved durability over conventional water-curing methods.
(2) The process of carbonation curing allows concrete to absorb CO_2, offering potential benefits for reducing greenhouse gas emissions and mitigating global warming.
(3) There is a significant improvement in the compressive strength with a percentage increase of 70.46%, 111.28%, 30.36%, and 36.69%, respectively, for 0%, 10%, 20%, and 30% fly ash contents in concrete samples subjected to 72 h of accelerated carbonation curing.
(4) Longer durations of carbonation result in higher compressive strength gains, with 72-h durations showing the most significant improvement. Additionally, substituting fly ash with 10% in the mix can achieve comparable strength to conventional water-cured concrete.
(5) While the pH of carbonated concrete is lower than water-cured concrete, it remains within safe limits to prevent reinforcement corrosion. Additionally, the average carbonation depth is minimal, reducing the risk of CO_2-induced corrosion.
(6) The use of carbonation curing with industrial waste fly ash not only creates eco-friendly concrete but also contributes to CO_2 sequestration efforts, promoting sustainability in construction practices.

Author Contributions: Conceptualization K.S.K. and H.K.S.; formal analysis A.P., K.S.K. and P.R.; methodology K.S.K., H.K.S. and A.P.; software, K.S.K. and A.P.; investigation, K.S.K., A.P. and P.R.; supervision K.S.K. and H.K.S.; visualization K.S.K., A.P. and P.R.; writing—original draft preparation, A.P. and K.S.K.; writing—review and editing, K.S.K. and H.K.S.; Funding acquisition K.S.K. All authors have read and agreed to the published version of the manuscript.

Funding: This work was supported by the Council of Scientific and Industrial Research—Central Building Research Institute (CSIR–CBRI) under the project HCP 48.

Institutional Review Board Statement: Not applicable.

Informed Consent Statement: Not applicable.

Data Availability Statement: Data are contained within the article.

Conflicts of Interest: The authors declare no conflict of interest.

References

1. Yoro, K.O.; Daramola, M.O. CO_2 emission sources, greenhouse gases, and the global warming effect. In *Advances in Carbon Capture*; Elsevier: Amsterdam, The Netherlands, 2020; pp. 3–28. [CrossRef]
2. Worrell, E.; Price, L.; Martin, N.; Hendriks, C.; Meida, L.O. Carbon dioxide emissions from the global cement industry. *Annu. Rev. Energy Environ.* **2001**, *26*, 303–329. [CrossRef]
3. Huang, L.; Krigsvoll, G.; Johansen, F.; Liu, Y.; Zhang, X. Carbon emission of global construction sector. *Renew. Sustain. Energy Rev.* **2018**, *81*, 1906–1916. [CrossRef]
4. Chen, J.; Wang, Y.; Shi, Q.; Peng, X.; Zheng, J. An international comparison analysis of CO_2 emissions in the construction industry. *Sustain. Dev.* **2021**, *29*, 754–767. [CrossRef]
5. Ye, J.; Liu, S.; Zhao, Y.; Li, Y.; Fang, J.; Zhang, H.; Guan, X. Development of Ultrafine Mineral Admixture from Magnesium Slag and Sequestration of CO_2. *Buildings* **2023**, *13*, 204. [CrossRef]
6. Davidovits, J. Global Warming Impact on the Cement and Aggregates Industries. *World Resour. Rev.* **1994**, *6*, 263–278.
7. Huntzinger, D.N.; Eatmon, T.D. A life-cycle assessment of Portland cement manufacturing: Comparing the traditional process with alternative technologies. *J. Clean. Prod.* **2009**, *17*, 668–675. [CrossRef]
8. Meyer, C. The greening of the concrete industry. *Cem. Concr. Compos.* **2009**, *31*, 601–605. [CrossRef]
9. Pasupathy, K.; Sanjayan, J.; Rajeev, P. Evaluation of alkalinity changes and carbonation of geopolymer concrete exposed to wetting and drying. *J. Build. Eng.* **2021**, *35*, 102029. [CrossRef]
10. Guleria, H.; Sharma, D.; Goyal, S. Long term performance of concrete using accelerated carbonation curing: An effective CCUS technique. *Eur. J. Environ. Civ. Eng.* **2023**, *28*, 2138–2159. [CrossRef]
11. Goyal, S.; Sharma, D. *CO_2 Sequestration on Cement*; Elsevier: Amsterdam, The Netherlands, 2020. [CrossRef]
12. Rostami, V.; Shao, Y.; Boyd, A.J. Carbonation Curing versus Steam Curing for Precast Concrete Production. *J. Mater. Civ. Eng.* **2012**, *24*, 1221–1229. [CrossRef]
13. Berger, R.L.; Young, J.F.; Leung, K. Acceleration of Hydration of Calcium Silicates by Carbon Dioxide Treatment. *Nat. Phys. Sci.* **1972**, *240*, 16–18. [CrossRef]
14. Berger, R.L. Stabilization of silicate structures by carbonation. *Cem. Concr. Res.* **1979**, *9*, 649–651. [CrossRef]
15. Rostami, V.; Shao, Y.; Boyd, A.J.; He, Z. Microstructure of cement paste subject to early carbonation curing. *Cem. Concr. Res.* **2012**, *42*, 186–193. [CrossRef]
16. Liu, Y.; Zhuge, Y.; Chow, C.W.; Keegan, A.; Li, D.; Pham, P.N.; Huang, J.; Siddique, R. Properties and microstructure of concrete blocks incorporating drinking water treatment sludge exposed to early-age carbonation curing. *J. Clean. Prod.* **2020**, *261*, 121257. [CrossRef]
17. Jang, J.; Kim, G.; Kim, H.; Lee, H. Review on recent advances in CO_2 utilization and sequestration technologies in cement-based materials. *Constr. Build. Mater.* **2016**, *127*, 762–773. [CrossRef]
18. Zhang, D.; Ghouleh, Z.; Shao, Y. Review on carbonation curing of cement-based materials. *J. CO_2 Util.* **2017**, *21*, 119–131. [CrossRef]
19. Sharma, D.; Goyal, S. Effect of accelerated carbonation curing on near surface properties of concrete. *Eur. J. Environ. Civ. Eng.* **2020**, *26*, 1300–1321. [CrossRef]
20. Papadakis, V.G.; Vayenas, C.G.; Fardis, M.N. A reaction engineering approach to the problem of concrete carbonation. *AIChE J.* **1989**, *35*, 1639–1650. [CrossRef]
21. Zhan, B.J.; Poon, C.S.; Shi, C.J. Materials characteristics affecting CO_2 curing of concrete blocks containing recycled aggregates. *Cem. Concr. Compos.* **2016**, *67*, 50–59. [CrossRef]
22. Xuan, D.; Zhan, B.; Poon, C.S. Development of a new generation of eco-friendly concrete blocks by accelerated mineral carbonation. *J. Clean. Prod.* **2016**, *133*, 1235–1241. [CrossRef]
23. *IS: 8112—2013*; Specification for 43 Grade Ordinary Portland Cement. Bureau of Indian Standard (BIS): Delhi, Indian, 2013; p. 17.
24. *IS:3812 (Part-1)*; Pulverized Fuel Ash—Specification. Part 1: For use as Pozzolana in cement, Cement Mortar and Concrete (Second Revision). Bureau of Indian Standards: New Delhi, India, 2013; pp. 1–14.
25. *IS 383 (2016)*; Coarse and Fine Aggregate for Concrete-Specification. Bureau of Indian Standard: New Delhi, India, 2016; p. 110002.
26. Assaggaf, R.; Adekunle, S.K.; Ahmad, S.; Maslehuddin, M.; Al-Amoudi, O.S.B.; Ali, S. Mechanical properties, durability characteristics and shrinkage of plain cement and fly ash concretes subjected to accelerated carbonation curing. *J. S. Afr. Inst. Civ. Eng.* **2019**, *61*, 73–81. [CrossRef]
27. Rostami, V.; Shao, Y.; Boyd, A.J. Durability of concrete pipes subjected to combined steam and carbonation curing. *Constr. Build. Mater.* **2011**, *25*, 3345–3355. [CrossRef]
28. Reddy, P.N.; Naqash, J.A. Experimental study on TGA, XRD and SEM analysis of concrete with ultra-fine slag. *Int. J. Eng. Trans. B Appl.* **2019**, *32*, 679–684. [CrossRef]
29. Xian, X.; Zhang, D.; Lin, H.; Shao, Y. Ambient pressure carbonation curing of reinforced concrete for CO_2 utilization and corrosion resistance. *J. CO_2 Util.* **2022**, *56*, 101861. [CrossRef]
30. Horn, L. Targeted/Emerging Therapies for Metastatic Non–Small Cell Lung Cancer. *J. Natl. Compr. Cancer Netw.* **2015**, *13*, 676–678. [CrossRef]

31. Scrivener, K.L.; Kirkpatrick, R.J. Innovation in use and research on cementitious material. *Cem. Concr. Res.* **2008**, *38*, 128–136. [CrossRef]
32. Douglas, C.M. *Design and Analysis of Experiments*; John Wiley & Sons, Inc.: New York, NY, USA, 2012.

buildings

MDPI

Review

A Comprehensive Review of Thermal Transmittance Assessments of Building Envelopes

Ahhyun Song [1], Yeeun Kim [1], Sangjun Hwang [2], Minjae Shin [3,*] and Sanghyo Lee [4,*]

[1] Department of Architectural Engineering, College of Engineering Sciences, Hanyang University, Ansan 15588, Republic of Korea; sahhyun22@hanyang.ac.kr (A.S.); dpdms4046@hanyang.ac.kr (Y.K.)
[2] Department of Smart City Engineering, College of Engineering Sciences, Hanyang University, Ansan 15588, Republic of Korea; hs971001@naver.com
[3] Division of Architecture and Architectural Engineering, College of Engineering Sciences, Hanyang University, Ansan 15588, Republic of Korea
[4] Division of Smart Convergence Engineering, College of Engineering Sciences, Hanyang University, Ansan 15588, Republic of Korea
* Correspondence: mshin@hanyang.ac.kr (M.S.); mir0903@hanyang.ac.kr (S.L.)

Abstract: Improving the energy efficiency of buildings is an important element of the effort to address global warming. The thermal performance of building envelopes is the most important thermal and physical property affecting energy performance. Therefore, identifying the thermal performance of a building envelope is essential to applying effective energy-saving measures. The U-value is a quantitative indicator of the thermal performance of the building envelope quantitatively. Methods for determining the U-value are largely classified into passive methods, which use building information without measurement campaigns, and active methods, which conduct in situ measurements. This paper reviews and evaluates the most commonly used methods and experimental results of previous studies to determine the actual U-value of a building envelope. Accordingly, this paper focuses solely on field measurement studies, excluding laboratory measurements. Comparing the existing methods used to determine the U-value can help researchers choose appropriate field measurement methods and future research directions.

Keywords: thermal transmittance; U-value; building envelope; passive measurement; active measurement

Citation: Song, A.; Kim, Y.; Hwang, S.; Shin, M.; Lee, S. A Comprehensive Review of Thermal Transmittance Assessments of Building Envelopes. *Buildings* **2024**, *14*, 3304. https://doi.org/10.3390/buildings14103304

Academic Editor: Francesca Stazi

Received: 23 September 2024
Revised: 10 October 2024
Accepted: 16 October 2024
Published: 18 October 2024

1. Introduction

Due to global warming and other manifestations of climate shifts, reducing greenhouse gas emissions has become a critical responsibility. According to the International Energy Agency (IEA) [1], buildings are responsible for a significant share of global greenhouse gas (GHG) emissions [2] and consume 37% of global energy. The energy consumption of buildings and the activities within them is expected to rise by an average of 1.5% annually from 2012 to 2040, potentially doubling or even tripling by 2050 compared to 2010 levels [3–5]. As new construction activity surges and current building inventories continue to show inefficiencies globally, GHG emissions from buildings are projected to rise in the future [6]. Nevertheless, when compared to the transportation and industry sectors, buildings offer the greatest potential for contributing to sustainability strategies [6]. Many countries and municipalities have proposed goals to reduce GHGs in the construction sector and have prepared appropriate measures [7–10].

To reduce GHGs in the building sector, it is crucial to minimize energy consumption in buildings by improving overall energy efficiency. Improving the insulation quality of the building envelope is one method to reduce heat absorption or loss, thereby enhancing overall energy efficiency [11–13]. Enhancing the insulation performance of the building envelope is a crucial aspect of this approach because walls have the greatest exposure to the external environment, leading to higher energy losses through them compared to other

parts of the outer shell. The IEA anticipates substantial energy savings (around 6 EJ in total) to be achieved through improved building envelope technologies by 2050 [14].

To enhance a building's energy efficiency, it is essential to assess the performance of the insulation in its outer shell. Among the quantitative indicators of insulation effectiveness for a building envelope, the representative indicator is the U-value [15–18]. As shown in Figure 1, the U-value of the building envelope can be calculated according to the presence or absence of measurements. Passive methods use data sheets or information from comparable buildings without field measurements. On the other hand, active methods measure environmental variables such as wall temperature, indoor and outdoor temperature, and wind speed.

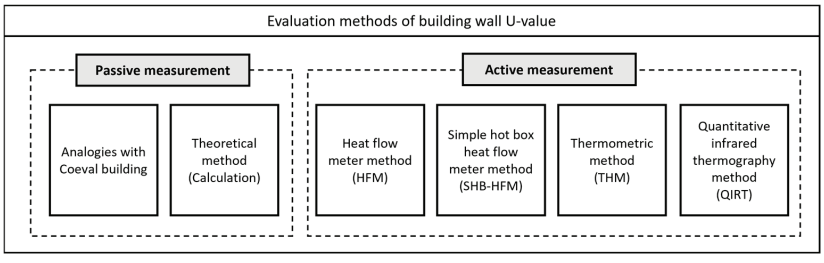

Figure 1. U-value assessment methodologies for building envelopes.

Applying a U-value, which can be derived by the methods shown in Figure 1, requires an understanding of the theory, strengths, and limitations of each method. Previous reviews have covered the determination of thermal transmittance to some extent. Kirimtat and Ondrej [19], Lucchi [20], and Tardy [21] published reviews involving U-values based on infrared cameras. However, methods that do not use infrared cameras were not discussed. Teni et al. [22] and Bienvenido-Huertas et al. [23] published reviews of field measurements of U-values. However, a method that does not rely on field measurements has not been discussed. In practical situations, collecting field measurements may not always be feasible, creating a demand for a method to assess the U-value without physical measurements. In this paper, basic information regarding the thermal characteristics of the building envelope and various methods of diagnosing its thermal performance are reviewed.

The methods reviewed in this study are the most widely used of several published options. In the passive method of diagnosing without measurements, a method involving analogous coeval buildings, and a theoretical method are reviewed. Active methods involving measurements and diagnoses in the field, including the standardized heat flow meter (HFM) method, the simple hot box (SHB-HFM) method, the so-called thermometer (THM) method, and the quantitative infrared thermography (QIRT) approach, are reviewed. This paper provides a summary of the significance of assessing the thermal performance of buildings and the techniques employed to calculate U-values. The purpose of this paper is to evaluate each U-value diagnostic method using findings from existing studies, summarize their limitations, and propose areas for further research.

2. Methodology

We first conducted a comprehensive literature review of approaches to calculating U-values for assessing the thermal performance of building envelopes, focusing on the measurement methodology. The objectives of this study were to (1) present essential concepts and definitions related to the thermal performance of building envelopes; (2) summarize the existing methods of evaluating the U-value and experimental results; (3) investigate the limitations of each conventional method; and (4) propose future research directions and highlight the potential significance of new methods for U-value assessment in building envelopes. The literature review was conducted utilizing the academic search engines Google Scholar, Scopus, and Mendeley, with "Building U-value", "Building R-value", "Estimation

U-value", "Building envelope thermal performance", "U-value measurement", "U-value assessment", "In-situ U-value", and "Building envelope assessment" as the primary keywords. Additionally, research articles, textbooks, and standards covering U-values, as well as the relevant definitions, methodologies, and applications, were reviewed.

This review is structured into seven sections. Section 1 offers an overview and background on the significance of the U-value in evaluating the thermal performance of building envelopes. Section 2 explains the comprehensive methodology employed in conducting this study. Section 3 covers the basic concepts and background of the thermal performance of a building envelope. Section 4 summarizes a literature review on methods of evaluating U-values without field measurements, and Section 5 includes a literature review of commonly used U-value field evaluation methods. Section 6 presents the review results and a discussion of the limitations of existing methods. Conclusions are presented in Section 7.

3. Building Envelope Thermal Transmittance

The thermal transmittance of the building envelope is a critical thermal and physical property that affects energy performance [15–18] and has a significant impact on annual energy requirements. The efficiency of heating and cooling systems, along with occupant comfort, is largely influenced by the thermal resistance of the building envelope [15]. Two parameters describe the thermal performance of a building envelope: the U-value, which describes thermal transmittance, and the R-value, which describes thermal resistance.

The U-value [24] is obtained by dividing the heat flow rate, or flux (Φ), under steady-state conditions by the area (A) and the temperature difference between the interior and exterior of a system ($T_i - T_e$). In Equation (1), Φ represents the value obtained by dividing the amount of heat (dQ) transferred to or from the system by the time (dt). The reciprocal of the U-value is the sum (R_{tot}) of the thermal resistance (R) and the internal ($R_{s,in}$) and external ($R_{s,out}$) air film resistance of each material comprising the envelope. The R-value of the building envelope is defined [24] as the temperature difference ($T_i - T_e$) under steady-state conditions divided by the density (q) of the heat flow rate. In Equation (2), the heat flux density (q) is calculated by dividing the amount of heat ($d\Phi$) transferred to or from the system by the area (dA). Equation (1) calculates the U-value, and Equation (2) the R-value.

$$U - value = \frac{\Phi}{(T_i - T_e)A} = \frac{\frac{dQ}{dt}}{(T_i - T_e)A} = \frac{1}{R_{tot}} = \frac{1}{R_{s,out} + R + R_{s,in}} [\mathrm{W/m^2K}] \quad (1)$$

$$\mathrm{R} - value = \frac{(T_{si} - T_{se})}{q} = \frac{(T_{si} - T_{se})}{\frac{d\Phi}{dA}} = \frac{(T_{si} - T_{se})dA}{d\Phi} [\mathrm{m^2K/W}] \quad (2)$$

The ISO 7345 [24] defines the U-value, or thermal transmittance of a building envelope, as the product of the heat flow rate under steady-state conditions to the product of the area and the temperature difference between the internal and external sides of the system. ISO 6946 [25] calculates the thermal transmittance as the inverse of the total thermal resistance of the material comprising the envelope.

As per the ASHRAE Terminology [26], thermal transmittance refers to the amount of heat transmitted in a unit of time through the unit area of a material or construction and the boundary air layers due to the temperature differential between the inside and outside of the material. Also known as the U-factor or total coefficient of heat transport, thermal transmittance is measured in Btu/h·ft2·°F (W/m^2 K).

The Plant Engineer's Reference Book [27] defines thermal transmittance (U-value) as the ability of an element of structure to transmit heat under steady-state conditions. It measures the quantity of heat transfers through a unit area per unit time for each unit of temperature difference between the inside and outside of a structure. It is calculated by taking the inverse of the sum of the resistances of each component part of the structure, including the resistance of any air space or cavity, as well as the inside and outside surfaces. It is expressed as W/m^{2}K.

In summary, the thermal transmittance, commonly referred to as the U-value, represents the rate of heat transfer through the building envelope divided by the temperature difference across the entire structure. It is inversely proportional to the R-value, which indicates the material's effectiveness at resisting heat transfer. The unit of the U-value is W/m^2K, and a lower U-value indicates better thermal performance of the envelope. This means that the U-value has a fairly high value when the insulation material of the envelope is deteriorated or not properly installed. Therefore, in order to renovate the energy performance of an aging building, it is necessary to understand the U-value of the existing building. In the next section, various methods currently used to determine the U-value are described and evaluated.

4. Passive Measurement (In-Office)

This section describes passive methods, which can diagnose the thermal performance of the building envelope without measurement. These methods can save costs and time because they diagnose the thermal performance of the building envelope without measurements. In addition, this method can be used when actual measurements of the building are not feasible. However, using this method requires a reliable technical document (e.g., a detail drawing) or database for the building. The methods in this category include the following:

- Analogies with coeval buildings;
- Theoretical method (calculation).

4.1. Analogies with Coeval Buildings

This approach generally applies to existing and historical buildings and is commonly used when specific details about building's structures or materials are lacking [28,29]. The U-value of a building is derived by referring to data from other buildings of a similar age, function, shape, thermal characteristics, and texture [30–32] (Figure 2). In addition to U-values, the database used in this approach includes building types, building years, structural information, and energy use. Field measurements and data collection are essential for building a database containing such information [33,34]. The following section summarizes the research results regarding the evaluation of building thermal performance through the collection of actual field data.

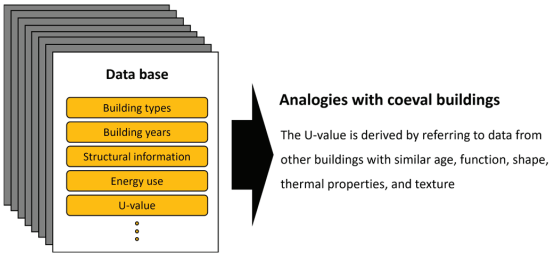

Figure 2. Schematic of analogies with coeval buildings.

Cesaratto and De Carli [35] conducted an analysis of different methods of estimating thermal transmittance (*C*) values using data from a measurement campaign of the walls of buildings in northeastern Italy between 2006 and 2010. The estimated *C* value was compared with the measurement results. The field measurement value was 20% higher than the estimated value, *C*. The authors confirmed that the actual thermal transmittance leads to an increase in the net energy demand for heating of approximately 12%. Their study suggests that the thermal properties of buildings are not only characteristics of the outer shell but also of the construction and maintenance. To verify this, measurement investigations in different locations and periods for the same factors will be needed in the future.

Aksoezen et al. [36] analyzed approximately 20,000 buildings using chi-square automatic interaction detection by integrating data from various administrative agencies in Basel City. They discovered a significant relationship between energy consumption and the construction period and confirmed that the energy-saving potential varied greatly by building age. They used various building data (e.g., building type, building year, area, heating system type, and hot water supply type), but the heat perfusion rate (U-value) was not evaluated.

Ballarini et al. [37] presented a method for identifying reference buildings in accordance with the IEE-TABULA Project (2009–12) [38] for "European building types". In the TABULA project [38], which was carried out between 2009 and 2012, building types in 13 European countries (i.e., Germany, Greece, Slovenia, Italy, France, Ireland, Belgium, Poland, Austria, Bulgaria, Sweden, Czech Republic, and Denmark) were characterized and classified according to location related to climate, construction period, and size and shape of buildings. The authors show that basic energy measures through the analysis of identified scenarios can achieve an average energy saving of more than 40% in residential buildings. However, no studies that quantitatively derive the thermal performance of the buildings have been conducted.

Basaglia et al. [39] presented a new procedure for defining building subtypes in the CARTIS database. CARTIS is a data collection form used to gather information on residential buildings in Italian municipalities since 2014. The authors also shared the MATLAB code for deriving building subtypes, which is expected to help derive the U-value of buildings at the local level. However, studies to determine the U-value using the database have not yet been conducted.

In this section, several studies evaluating the approach through regional and national databases of building information are reviewed. This approach is used primarily when implementing national and local energy planning measures or policies, as it is the fastest way to thermally characterize large numbers of buildings. This method is fast and inexpensive, but various factors may influence the reliability of the results: (1) misinformation about the building year [35,40]; (2) texture and thickness of the wall [35,41–44]; (3) the degree of aging of the building envelope material affecting thermal performance [41,42,45,46]; (4) state of building repair [46–48]; and (5) moisture content affecting energy performance [35,41,42]. If a database that considers these factors is used, it will be easy to evaluate the U-value when on-site measurements are impossible or when a large number of buildings must be thermally characterized. Several studies have been performed to evaluate energy performance using the database, but relatively few quantitatively evaluated the U-value of a building. Therefore, it is necessary to quantitatively evaluate the U-value of a building envelope using the database.

4.2. Theoretical Method (Calculation)

This approach is widely used in the design stage. Thermal transmittance is determined from the dimension and thermal conductivity of each wall material and the thermal resistance of the inside and outside surfaces of the wall, as defined by ISO 6946 [25]. It assumes that each component of the assembly obstructs heat transfer in the same way a resistor impedes current flow in an electrical circuit [49]. Thermal transmittance can be calculated using Equation (3),

$$\mathrm{U} = \frac{1}{R_{tot}} = \frac{1}{R_{s,out} + \sum_{i=1}^{n} \frac{s_i}{\lambda_i} + R_{s,in}} [\mathrm{W/m^2K}] \quad (3)$$

where s_i and λ_i are the thickness and thermal conductivity, respectively, of each wall layer, and $R_{s,in}$ and $R_{s,out}$ are the internal and external thermal resistances of the surface. The resistances are determined from values provided by ISO 6946 [25] and are based on specific boundary conditions related to convective and radiative heat transfer. Equation (3) is typically used to estimate the U-value during the design stage, whereas it can be applied to existing buildings only when the resistances of both the internal and external surfaces, as

well as the thickness and the thermal conductivity of each layer, are known [16]. In this section, the relevant studies on theoretical method are described, including Asdrubali et al. [50], Ficco et al. [16], Pérez-Bella et al. [51], and Lucchi [42].

Asdrubali et al. [50] reported the results of a field measurement campaign on thermal transmittance conducted in various buildings located in Umbria, Italy. Field measurements of the thermal permeability of six walls were conducted, and the results were compared with the values provided by the manufacturer for the materials' thermal properties to evaluate actual wall performance. Field measurements consistently showed higher values compared to the calculated values. The authors presented various reasons for the discrepancy between the measured and calculated values. First, manufacturers often exaggerate the performance data of building materials for marketing purposes. Second, the thermal performance of building components and materials is typically assessed under controlled laboratory conditions. Third, the materials cannot be fully installed in the actual building. Last, external conditions can affect the measurements. However, the verification of the above factors affecting the accuracy has not been conducted.

Ficco et al. [16] proposed a method of estimating the uncertainty (λ_i) related to the ISO 6946 method due to the possible significant difference in the design U-value from the actual U-value. Given the rectangular probability distribution of thermal conductivity, ranging from the minimum ($\lambda_{i,min}$) to the maximum ($\lambda_{i,max}$) values of thermal conductivity, the uncertainty can be expressed as Equation (4). When characterizing the composition of the wall, the relative uncertainty of thermal conductivity was estimated to be 3%. However, theoretical methods may face challenges if technical details about the wall's composition are unavailable or if an endoscope cannot be used.

$$\lambda_i = \frac{\lambda_{i,max} - \lambda_{i,min}}{2\sqrt{3}} \tag{4}$$

Pérez-Bella et al. [51] presented the conductivity correction factor (CCF) tailored to external environmental conditions for each provincial capital in Spain. The CCF can be employed to calculate the designed thermal conductivity of building materials at different locations, using standard conductivity values specified in building regulations under controlled environmental conditions. A comparison of the thermal results of various façade configurations with those calculated using the method described by ISO 10456:2007 [52] for each material showed a discrepancy of less than 1%. Because that study was only conducted in major cities in Spain, further studies under different climatic conditions are necessary.

Lucchi [42] presented the results of a field campaign conducted on several historical stone buildings, each distinguished by their heritage values, historical dates, and varying uses. The results of their study are as follows: First, the U-value calculated using ISO 6946 [25] method was higher than the U-value determined using the measurement method. Second, problems arose when setting the range of thermal performance due to the diversity of the stones. Third, the thickness and ratio of air gaps or voids significantly influenced the assessment of the thermal performance of building structures. Lucchi reported in a follow-up study [41] that the U-value of historical stone walls can be accurately determined through HFM measurements. This shows that there is a limit to the utility of the theoretical method because the actual and theoretical U-values differ for older buildings.

In this section, several studies that employed a theoretical approach to evaluate the thermal performance of buildings were reviewed. The theoretical method was compared primarily with the field-measurement method, but most field measurements were higher than the theoretical values. Previous studies explain this difference as follows: First, manufacturers often overestimate performance data for building materials due to marketing purposes. Second, the thermal performance of building components and materials is typically assessed under controlled laboratory conditions. Third, the materials cannot be fully installed in actual buildings. Fourth, external conditions such as rain and wind can affect the measurements. Fifth, the performance of the insulation can change over time. Therefore,

appropriate information about the composition and thermal properties of the materials is required to obtain reliable results. Despite these limitations, this approach is used in several countries as evidence of meeting the national energy efficiency standard [53]. Although field measurements may not be possible, estimating the thermal performance of a building through calculations before conducting field measurement is relatively straightforward.

5. Active Measurement (In Situ)

This section describes the active method, in which the thermal performance of the building envelope is diagnosed by conducting a measurement campaign. As these methods measure the current thermal performance of the building envelope, uncertainties related to building aging or deterioration of the outer shell insulation performance may be avoided. However, this approach requires information on the cost of equipment, long-term measurement due to measurement errors, and data analysis. The methods involved in this category are as follows:

- Heat flow meter (HFM) method;
- Simple hot box–HFM (SHB-HFM) method;
- Thermometric (THM) method;
- Quantitative infrared thermography (QIRT) method.

5.1. Heat Flow Meter (HFM) Method

The HFM method, which involves a non-destructive test to determine the building envelope's U-value in situ, has been the most commonly used method of studying U-values in recent years. It requires an adequate heat flow, which is achieved by maintaining a minimal temperature difference between the indoor and outdoor environments [22]. This method is appropriate for building components that have opaque layers perpendicular to the direction of heat flow and that exhibit minimal lateral heat transfer [54].

This is a standardized experimental method, first introduced as an ISO 9869 standard in 1994 [54], and then technically modified as ISO 9869-1:2014 in 2014 [55]. According to the standard, the U-value is derived directly from the heat flow rate and temperatures on the sides of the element under steady-state conditions. To perform the measurement, an HFM plate, two ambient temperature sensors (T_e and T_i), and a data logger are required (Figure 3). To measure the heat flow rate as recommended by the standard, measuring the heat flow rate requires positioning at least one HFM on the surface of the element closest to the more stable temperature and employing a data logger along with two ambient temperature sensors for data analysis.

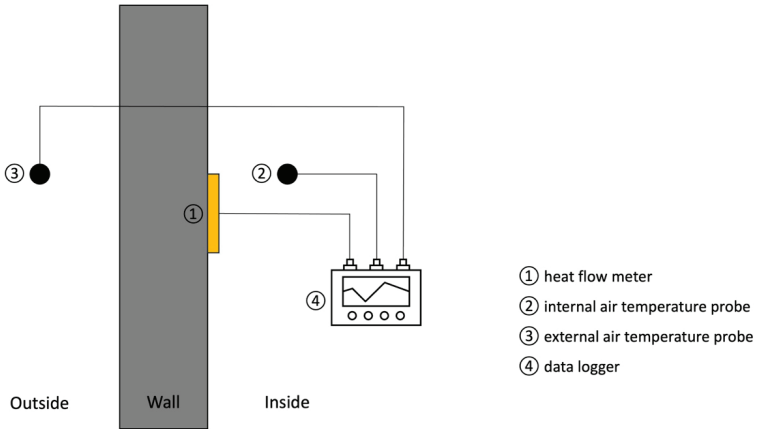

Figure 3. Schematic of the HFM method. Figures were resketched from Teni et al. [22].

According to established standards [54], measurement data must be recorded continuously or at fixed intervals throughout a monitoring period of complete days (n). The test period must be maintained for at least 72 h, and the error rate between the heat flow rate at the end of the measurement and that 24 h before the end of the period must not differ by more than 5%. Finally, the error rate between the heat flow rate calculated during the first two-thirds of the entire measurement period and that calculated at the end of the measurement period must be less than 5%.

Because it is difficult to satisfy the steady-state conditions during in situ measurements, the standard [54] proposes the calculation of the U-value through the average method and the dynamic method. The average method involves a prolonged monitoring period, utilizing the average instantaneous heat flow value and the average temperature difference between the external and internal air, as detailed in Equation (4) [23]. In Equation (5), q_j is the heat flux passing through the unit area of the sample W/m^2, and $T_{in,j}$ and $T_{out,j}$ are the indoor and outdoor ambient temperatures [K], respectively, at time j.

$$U = \frac{\sum_{j=1}^{n} q_j}{\sum_{j=1}^{n} (T_{in,j} - T_{out,j})} \tag{5}$$

The dynamic method, as outlined in Equation (6), is more advanced and intricate compared to the average method because it incorporates the heat equation and several parameters to account for fluctuations in temperature and heat flow rate [42]. However, several studies [56–64] have shown that, when using the dynamic method, the analysis can be more time-consuming and complex but is less sensitive to the measurement period and provides more accurate results. In Equation (5), Λ is thermal conductance (W/m^2k), and $T_{s,in,i}$ and $T_{s,out,i}$ are the indoor and outdoor surface temperatures at time t_i (i ranges from 1 to N) [K]. $\dot{T}_{s,in,i}$ and $\dot{T}_{s,out,i}$ are the respective time derivatives of the indoor and outdoor surface temperatures. The variable β_n is an exponential function of the time constant τ_n, while K_1, K_2, P_n, and Q_n are dynamic characteristics of the wall that depend on the time constant τ_n.

$$\begin{aligned} q_i \left[\tfrac{W}{m^2}\right] &= \Lambda(T_{s,in,i} - T_{s,out,i}) + \mathrm{K}_1 \dot{\mathrm{T}}_{s,in,i} - \mathrm{K}_2 \dot{\mathrm{T}}_{s,out,i} \\ &+ \sum_n P_n \sum_{j=i-p}^{i-1} \mathrm{T}_{s,in,j} (1-\beta_n)\beta_n (i-j) \\ &+ \sum_n Q_n \sum_{j=i-p}^{i-1} \mathrm{T}_{s,out,j} (1-\beta_n)\beta_n (i-j) \end{aligned} \tag{6}$$

In this section, the relevant studies on the heat flow meter (HFM) method are described, including Asdrubali et al. [50], Walker and Pavía [65], Bros Williamson [66], Ficco et al. [16], Gori and Elwell [67], Ahmad et al. [68], Evangelisti et al. [69,70], Gaspar et al. [71], Richard O'Hegarty et al. [72], Choi et al. [73], and Suh et al. [74].

Asdrubali et al. [50] conducted thermal transmittance field measurements at some buildings in Umbria, Italy, not under laboratory conditions. By conducting field measurements of the thermal transmittance of walls, the values obtained from the manufacturers' data on material properties were compared with the real-world performance of the walls. The results indicate that the calculated values typically overestimate the actual thermal transmittance. However, the verification of the cause of the difference in the U-value was not conducted.

Walker and Pavía [65] investigated the field thermal performance of seven insulation alternatives applied to historical brick walls, employing both field and laboratory methods. The experiment confirmed that the field measurement U-value of walls with insulation was higher than the calculated value. The thermal conductivity value provided by the manufacturer led to an error of 13–25% in the wall U-value estimation compared to the field

measurement value. However, no research has been conducted on a method for accurate measurement of the U-value.

Bros Williamson et al. [66] analyzed building performance and annual energy demand in two adjacent houses (a control house [CH] and a passive house [PH]) over a three-year occupancy period. Monitoring and field measurements showed that the actual performance of the house differed from the calculated performance: the CH (13–65%) and PH (10–20%) values were larger than the theoretical values. However, studies on the analysis of U-value measurement results have not been conducted.

Ficco et al. [16] focused on field measurement U-values with commercial thermometers in various measurement conditions and envelope components. In their paper, the authors presented the results of an experimental campaign designed to evaluate both the metrological performance of HFMs and the impact of ambient conditions. The field U-value was compared with the value estimated based on design data and field analysis. The test results had error margins of 2% to 55% (average 13%) in winter and 62% to 264% (average 152%) in summer compared with the heat flux values analyzed through endoscopy. This shows good behavior of the HFM when performing the test according to ISO 9869. However, studies on measuring the HFM with high accuracy according to the season have not been conducted.

Gori and Elwell [67] emphasized the significance of error analysis for gaining strong insight into the actual thermal behavior of buildings based on field measurements. Their paper investigates the impact of systematic measurement uncertainties on the thermophysical properties of building elements (e.g., R-values and U-value) through two long-term case studies: a solid wall and a cavity wall. The analysis indicated that, as anticipated, the relative error grows when the gap between the average internal and external temperatures narrows. In their paper, error derivation considering the use of dynamic and optimization methods was applied to provide an appropriate error estimate even when the mean temperature difference between the indoor and outdoor was significantly below 10 °C. This helps to narrow the performance gap, as reducing the temperature difference between the indoor and outdoor during field measurements results in a U-value estimation with moderate errors. However, the method proposed in this study has not yet been evaluated in the field.

Ahmad et al. [68] performed field measurements to evaluate the thermal performance of building's two outer walls, constructed from reinforced precast concrete panels. The measurements were conducted in accordance with the standard procedures specified in international standards. As a result of the measurements, it was found that south-, east-, and west-facing walls had a higher heat flux compared with north-facing walls, and that the orientation of the wall may affect the heat flux by more than 37.3%. The thermal performance of the wall shows that its thermal transmittance is influenced by both the wall's orientation and the local weather conditions. However, the method for determining a reliable U-value based on the wall's orientation and external climatic conditions has not been discussed.

In a study by Evangelisti et al. [69], the HFM method was applied to determine the U-value of the north–south walls of buildings. The authors reported an error rate of 18% to 60% compared with the theoretical U-value (60% in southern winter and 18% in northern winter). In that study, the error rate was reduced to between 1% and 15% in the absence of insolation using only data from the same time zone (15% in southern winter and 1% in northern winter). This indicates that the error rate is high when measuring U-values in unstable environmental conditions. An accurate estimate of the contribution of field-measurement uncertainty (e.g., from measurement season or insolation) is needed.

Gaspar et al. [71] calculated and compared the discrepancy between the theoretical heat flow rate and values obtained using both the average and dynamic methods. When the environmental conditions for field measurements were optimal, the error rate was 5% for the average method and 1% for the dynamic method. If the measurement environment was not optimal, the error rate was 20% for the average method; when the dynamic method was used, the fit with the theoretical value improved significantly, with an error rate less than

10%. In addition, multiple studies [60,63,75–78] of dynamic methods have been conducted in recent years, but more are needed to confirm the limitations of the proposed method.

Richard O'Hegarty et al. [72] conducted an on-site monitoring study of the U-value of highly insulated building envelopes. The study revealed that the design U-value for these highly insulated envelopes was not being achieved in practice. Over 90% of the tested buildings performed below the expected standard. Among the 10 on-site tests of building envelopes designed with a U-value below 0.3, only one site exhibited better-than-expected performance. Additionally, the discrepancies between the measured and design U-values ranged from 10% to 297%. Therefore, further research is required to identify the key factors contributing to the gap between the on-site and design U-values of highly insulated building envelopes.

Evangelisti et al. [70] evaluated the thermal performance of a building by installing heat flux meters (HFMs) on the northern and northwestern walls. HFMs are generally placed on the northern side to avoid solar radiation, but the study was conducted because not all walls have the optimal orientation for on-site measurements. The experiments were carried out on a building constructed in the 1960s. The results showed a difference of 10.45% on the northern side, 92.14% on the northwestern side, and 56.12% when nighttime data from the northwestern side was used, compared to the design values. These results indicate the effects of prolonged exposure to solar radiation over approximately 60 years, as well as the degradation of the physical properties of the walls due to climatic variability. Thus, further research comparing the performance of new and aged wall materials is needed to investigate the variability in values.

Choi et al. [73] investigated the causes of discrepancies between the design and on-site R-values of highly insulated building walls. Winter measurements showed that using the average method, which incorporates additional internal wall temperature and heat flux data, resulted in a 9.12% difference from the design values. The study identified inconsistencies between the surface heat flux and the heat passing through the walls as the main source of error. The authors proposed a new method, the extended averaging method, which yielded highly accurate results with an error rate of just 0.6%. However, this method is not non-destructive, and further research on its applicability is required.

Suh et al. [74] aimed to improve the energy performance of historical buildings for sustainable use. Since the target building was registered as national cultural heritage, the scope of construction was limited, and simulation programs were used to implement various scenarios. As part of the process to verify the reliability of the simulation program, the thermal performance of the building envelope was measured on site. The difference between the simulated and measured values for the building's exterior walls was found to be 1.52%, indicating close agreement. However, due to structural and safety concerns, there were limitations in directly measuring the U-values of the roof and internal walls.

In this section, several studies evaluating the U-value of a building using an HFM are reviewed. In optimal conditions, a high-accuracy value can be obtained when measuring the U-value in the field with an HFM, but the measurement time is relatively long and the error rate is high under non-optimal conditions. Studies conducted to date indicate that the accuracy of HFM measurements is influenced by several factors: measurement season (temperature gradient) [50,68,71,79,80], measurement wall position (solar radiation) [81,82], experimental period [79], and data post-processing [61,67,71,79,83]. Further studies are needed for high-accuracy U-value determination under non-optimal conditions.

To evaluate the field applicability of the HFM method, the results of previous studies of its accuracy and measurement period are summarized in Table 1. The deviation between the results obtained using the HFM method and the comparison method value (U_C)) can be calculated as an absolute value using Equation (7):

$$Deviation\ (\%) = \left| \frac{U_{HFM} - U_C}{U_C} \right| \times 100 \quad (7)$$

Table 1. Summary of studies on U-value assessment of building walls using the HFM method.

Author (Year)	Measurement Method	Comparison Method	Deviation [%]	Test Period	Building Information
Asdrubali et al. (2014) [50]	HFM, average method	Theoretical method: ISO 6946	14–43%, average 23%	Heating season 2010 and 2013 At least 7 days	Six buildings constructed using green architecture techniques
Ficco et al. (2015) [16]	HFM, average method	Theoretical method: ISO 6946	winter 1–70%, average 24% summer 45–142%, average 90%	Winter and Summer 3–168 h	Six different buildings in Italy completed between 1965 and 2015
	HFM, average method	Endoscopic analysis and core samplings	winter 2–55%, average 13% summer 62–264%, average 152%		
Walker and Pavia (2015) [65]	HFM, average method	Theoretical method: provider values	13–25%	June 2014 to April 2015	Brick building in Dublin completed in 1805
Gaspar et al. (2016) [71]	HFM, average method	Theoretical method: ISO 6946	2–20%, average 9%	December 2015 to April 2016 72 h	Three buildings in Catalonia, Spain, completed in 1960, 1992, and 2007
	HFM, dynamic method	Theoretical method: ISO 6946	1–10%, average 3%		
Bros Williamson et al. (2016) [66]	HFM method	Theoretical method: ISO 6946	10–65%, average 27%	First winter in 2012 and 2014 14–21 days	A residential building in the UK completed in 2012
Lucchi (2017) [42]	HFM, average method	Tabulated design method: Standard UNI TS 11300-1:2014	7.7–46.5%	Two winter seasons 7–14 days	Fourteen old brick buildings in Italy
Lucchi (2017) [41]	HFM, average method	Theoretical method: ISO 6946	3–54%	Two winter seasons 7–14 days	Ten brick buildings in the Lombardy region, representing northern Italy
Evangelisti et al. (2020) [69]	HFM, average method	Theoretical method: ISO 6946	2–60%, average 1–11%	February 2019 7–18 days	Buildings in Italy characterized by high-insulation walls and solar-shading systems
Gaspar et al. (2021) [84]	HFM, dynamic method	Theoretical method: ISO 6946	1–6%	June and October 2016 144–168 h	Buildings in Spain completed in 1960 and 2005
Richard O'Hegarty et al. (2021) [72]	HFM, average method	Theoretical method: ISO 6946	10~297%	August 2019~February 2021 more than 72 h	A total of 13 tests at 7 different sites in Ireland
Evangelisti et al. (2022) [70]	HFM, average method	Theoretical method: ISO 6946	10.45% (north), 92.14% (north-west)	January 2019, 4 days (north) April 2019, 7 days (north-west)	Educational buildings in Italy from the 1960s
Choi et al. (2023) [73]	HFM, average method	Theoretical method: ISO 6946	9.12%	November to December 2021 13 days	Specially designed and constructed for this research in May 2021

Table 1. *Cont.*

Author (Year)	Measurement Method	Comparison Method	Deviation [%]	Test Period	Building Information
Lee et al. (2024) [85]	HFM, average method	Theoretical method: ISO 6946	5.63~9.97% average 7.01%	June 2022~May 2023 7 days, 86 sets	Specially designed and constructed for this research in May 2021
	HFM, dynamic method	Theoretical method: ISO 6946	5.85~37.83% average 12.81%		
	HFM method, extended average	Theoretical method: ISO 6946	2.57~6.86% average 4.02%		
Suh et al. (2024) [74]	HFM, average method	Theoretical method: DesignBuilder	1.52%	72 h	Campus buildings in Seoul, South Korea, constructed in 1924

5.2. Simple Hot Box–HFM (SHB-HFM) Method

Field-based U-value measurement should be conducted under a thermal gradient greater than 10 °C between indoor and outdoor temperatures (conditions that can cause heat exchange) [16,67]. The TCB-HFM method [86–89], an approach that can more easily determine and control the thermal gradient between indoor and outdoor environments, was proposed by Chinese studies. This method, which combines the advantages of the HBM and HFM, controls the internal air temperature by installing a hot box on the inner surface of the wall (appropriate for the season). The box heats the indoor air in winter and cools it during summer. Recently, a research team in China developed the SHB-HFM method, which is a simpler than TCB-HFM method [90].

The SHB-HFM method combines the HFM principle and the advantages of the TCB-HFM method. A temperature gradient is created by heating without cooling, and the hot box is placed on a warm surface [91]. The SHB is placed on the interior side of the wall during winter and on the exterior side during summer. Because the TCB-HFM method requires an air conditioner, which is not required for the SHB-HFM method, the latter is less expensive and simpler to use. The components needed to use the SHB-HFM method include an SHB, HFM plate, ambient temperature sensor, surface temperature sensor, and data loggers (Figure 4).

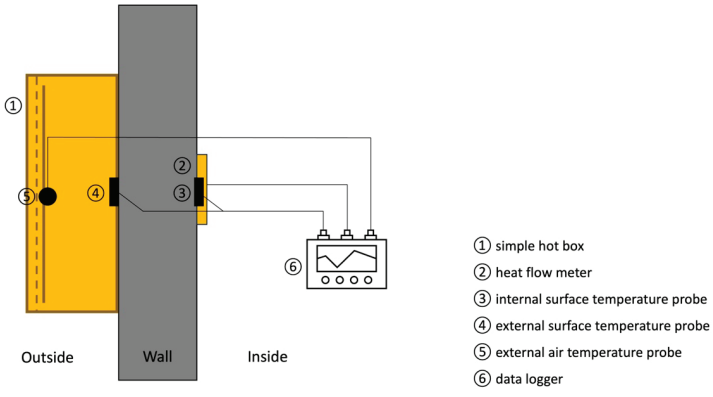

Figure 4. Schematic of the SHB-HFM method. Figures were resketched from Teni et al. [22].

According to Atsonios et al. [81], SHB measurement equipment should be installed on the surface of a wall without heat bridges, and a thermocouple measuring the indoor air temperature should be placed in the center of the SHB. The surface temperature sensor should be placed evenly on either side of the HFM plate. The optimum temperature

difference during measurement is 20 °C or greater. This represents a main advantage of the SHB-HFM method, as it achieves a condition that is challenging to attain with the traditional HFM method. The measurement uses data after 24 h of heating the inside of the box.

The data analysis method of SHB-HFM is similar to the average method used in the HFM method, as expressed in Equation (5). Equation (8) is used for the SHB-HFM method. The measurement should continue for at least 72 h but can be shorter if stable conditions can be guaranteed. In Equation (8), h_{out} is the outdoor heat transfer coefficient, and h_{in} is the indoor heat transfer coefficient, both measured in W/m^{2}K. $T_{s,in,j}$ and $T_{s,out,j}$ are the respective inner and outer surface temperatures [K] at time j, and q_j is the conductive heat flux [W/m^2] at time j.

$$U = \left(\frac{1}{h_{out}} + \frac{\sum_{j=1}^{n}\left(T_{s,in,j} - T_{s,out,j}\right)}{\sum_{j=1}^{n} q_j} + \frac{1}{h_{in}}\right)^{-1} \quad (8)$$

Meng et al. [90] proposed a new method called SHB-HFM because a simple and accurate field measurement method was needed to test the wall U-value when determining the energy efficiency of Chinese buildings. To evaluate the reliability and adaptability of the SHB-HFM method, the experiment was conducted under very unfavorable climatic conditions. Throughout the measurement period, the weather varied with rainy days, cloudy days, and clear days, and the ambient temperature fluctuated. Despite the harsh testing conditions, the SHB-HFM method measured the wall heat transmittance rate with an error of only 4% to 7% of the design value, demonstrating that the method offers adequate testing accuracy. The authors confirmed that box size has a significant effect on the test accuracy, and that properly enlarging the box size improves the field test accuracy. Meng et al. [91] conducted a numerical study on wall temperature distribution for U-value field measurements using SHB-HFM and proposed the optimal dimensions for the hot box. They confirmed that increasing the temperature difference in the wall from 10 °C to 30 °C reduced the average error by up to 4.4% to 7.5%. In addition, the multi-factor coupled regression formula for determining the minimum box dimension enables quick identification of the optimal dimensions, ensuring measurement accuracy while being portable and minimizing selection uncertainty. The optimal hot box dimensions were 0.75 m for 120 mm walls, 0.90 m for 180 mm walls, 1.05 m for 240 mm walls, and 1.45 m for 360 mm walls. However, since this proposed formula is relatively new, further studies are expected to be needed to verify the accuracy.

Roque et al. [92], who considered the need for further academic research on the SHB-HFM method, conducted field measurements on historical buildings in Viseu in northern Portugal. The authors obtained results with an error rate of 1.4% to 4.3% compared with the U-value calculated through the analysis of the field wall. Due to the heterogeneity of the analyzed "tabique" wall, variations in temperature and heat flux measurements were observed depending on the placement of the measuring device on the wall. These differences can affect the final result. Therefore, if the heterogeneous factors or shapes are not known, the measured values should be interpreted carefully by overlapping thermocouples and heat flux meters. It seems that further studies are needed on the interpretation of the field measurement values according to the components of the wall.

Francesco Nicoletti et al. [93] conducted a study on various methods for measuring the thermal performance of building envelopes on-site. Among these, the SHB-HFM method was used, showing relatively high accuracy with results ranging from 0.3% to 7.5% in winter and 1.9% to 13% in summer. This method also offered the advantages of a shorter testing period and the ability to obtain measurements during the summer. However, its reliability decreased when the insulation was located on the side opposite to the sensor. Since the location of the insulation cannot be known in advance, further research on this issue is required.

This section reviewed studies evaluating the thermal performance of buildings using the SHB-HFM method. Teni et al. [22] note that the SHB-HFM method is relatively new and has been studied for a limited range of wall types. Despite reports of high accuracy in existing studies, there are still concerns regarding the method's reliability and applicability, indicating a need for more case studies.

To evaluate the field applicability of the SHB-HFM method, the results of previous studies of the accuracy and measurement period are summarized in Table 2. The deviation between the results obtained using the SHB-HFM method and the comparison method value (U_C) can be calculated as an absolute value using Equation (9):

$$U_{SHB-HFM} - U_C = \left| \frac{U_{SHB-HFM} - U_C}{U_C} \right| \times 100 \quad (9)$$

Table 2. Summary of studies on U-value assessment of building walls using the SHB-HFM method.

Author (Year)	Measurement Method	Comparison Method	Deviation [%]	Test Period	Building Information
Meng et al. (2015) [90]	SHB–HFM method	Theoretical method	4–7%, average 5.97%	August 2013 192 h	A newly built two-story rural building located in China
Meng et al. (2017) [91]	SHB–HFM method	Theoretical method	4.4–7.5%	August 2013 192 h	A newly built two-story rural building located in China
Roque et al. (2020) [92]	SHB–HFM method	Endoscopic analysis and core samplings	1.4–4.3%	Winter 120 h	Tabique buildings located in the northern region of Portugal, constructed in late 19th century or early 20th century
Francesco Nicoletti et al. (2023) [93]	SHB–HFM method	Theoretical method	0.3~7.5% (winter) 1.9~13% (summer)	January 2019, 5~7 days (winter) July 2019, 4~9 days (summer)	A total of eight masonry walls, which are differentiated by various thermal characteristics

5.3. Thermometric (THM) Method

The THM method is a relatively new and straightforward approach to collecting field measurements of U-values. It is also called the temperature measurement method [94] or air–surface temperature ratio (ASTR) method [95]. The methodology, based on Newton's law of cooling, posits that heat transfer rate is directly proportional to both the temperature difference between an object and its environment and the surface area [96].

The THM method is a non-standard method, but it is widely used by experts and has been verified in recently published studies [94,95,97,98]. To perform the measurement, two ambient temperature sensors, a surface temperature sensor, and a data logger are required (Figure 5). Like other methods, the THM method also requires a temperature difference of 15 °C or greater when performing the measurement [50,68,71,79,80]. The measurement period must meet the same criteria as in the HFM method [99]. Regarding the data measurement interval, further research is needed to determine the optimal test period. In previous studies [94,95,97,98], acquisition intervals of 5, 15, and 30 min were used.

Equation (10) is used in the THM method. A key distinction between the THM and HFM methods is that the THM method does not involve measuring the heat flux through the wall. In Equation (10), h_{in} is the internal heat transfer coefficient.

$$U = \frac{h_{in}(T_{in} - T_{s,in})}{T_{in} - T_{out}} \quad (10)$$

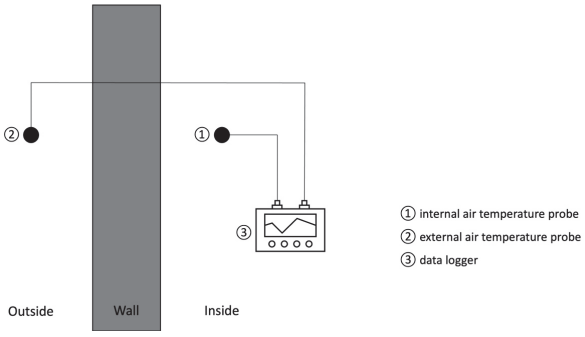

Figure 5. Schematic of the THM method. Figures were resketched from Teni et al. [22].

Buzatu et al. [98] compared the U-values obtained using THM measurement procedures and theoretical calculation methods according to MC 001/2009. The authors reported that the TBM method results in discrepancies of 44.19% and 40.18% between the theoretical and measured U-values. This difference could be due to unknown layers within the wall or inaccuracies in the thermal conductivity values of the component materials. The THM method was used primarily to obtain U-value measurements, but no in-depth analysis of the reliability and applicability of this method was performed. Therefore, further studies are needed for field application.

Andújar Márquez et al. [97] developed a measuring instrument that calculates the U-value for many measurements of the U-value in a short time. This is the most necessary condition in the actual field. The developed device calculates the U-value using three temperature measurements: the outside of the wall, the inside of the wall, and the surface of the inside of the wall. This device is modular, expandable, and wireless, allowing it to take multiple measurements simultaneously according to the user's needs. In order to evaluate the accuracy of the developed system, it was compared with the U-value of the HFM method measured by reflecting ISO 9869. A reliable result with an error rate of less than 2% was obtained. However, since this method is applied to the building where the energy retrofitting has been completed, it is considered that additional accuracy verification of the developed method in the unrenovated building is necessary.

Bienvenido-Huertas et al. [94] studied the applicability of the THM method through eight case studies conducted in areas of the Mediterranean climate (Csa). The results indicate that the THM method performs more efficiently in winter compared to summer, with relative uncertainties varying from 6% to 13%. They found that obtaining reliable results during warm seasons was challenging. Due to the typical nature of the Mediterranean climate, achieving records with a temperature difference of 10 °C or higher between the internal and external environments is particularly challenging. Therefore, they found that the thermal gradient of 5 °C can be considered in tests conducted in warm climate regions, but the larger the difference, the less the uncertainty and more representative values can be obtained. However, further studies are needed on methods for evaluating U-values in warm climate types, since no studies have been conducted.

Kim et al. [95] propose the air–surface temperature ratio (ASTR) method as an in situ approach for measuring the U-value of existing buildings. The wall U-values were measured in situ using both the heat flow meter (HFM) method, as per ISO 9869-1, and the air–surface temperature ratio (ASTR) method. A comparison was made between the results obtained from the HFM and ASTR methods, and the relative error rates and measurement accuracy were analyzed. The mean relative measurement errors for the HFM and ASTR methods were found to be ±3.21%. Measurements taken over both short durations of one day and extended periods of seven days or more showed average error rates of about ±2.63%. These results are within the acceptable tolerance range. However, in this study, only winter measurement campaigns were conducted, and experimental campaigns in

summer were not conducted. Therefore, it is considered that further research on summer measurement is necessary.

Evangelisti et al. [100] studied the heat flux meter (HFM) and air–surface temperature ratio (ASTR) methods. The results obtained by testing the HFM method during the summer were compared with theoretical values and those from a previous measurement campaign conducted on the same building during the winter. The deviation from the winter measurements was found to be between 0.51% and 4%, indicating reliable results. When the ASTR method was compared based on these measurements, the deviation ranged from 37.2% to 143.7%. This outcome reflects differences in internal heat transfer coefficients under various conditions. Therefore, further research is needed to investigate heat transfer coefficients across different scenarios.

Evangelisti et al. [70] evaluated the thermal performance of the aged exterior walls of a building envelope through on-site measurements. Simultaneous measurements were conducted using both the heat flux meter (HFM) and temperature-based (TB) methods. The results obtained from the HFM method during winter were compared with the measurements from the TB method conducted in April. When using data from the entire measurement period, the error rate ranged from 0.52% to 32.6%, while using only nighttime data resulted in error rates of 76.26% to 127.43%. This demonstrated that the TB method does not require a 10 °C temperature difference. However, further research is needed on the effects of wind speed on heat transfer.

In this section, the research results evaluating the thermal performance of buildings through the THM method are reviewed. The THM method is fast, simple, and inexpensive compared with the HFM method, and it produces a similar degree of accuracy to the HFM method (Table 3). However, because few studies have evaluated the THM method in real-world environments, an evaluation of its accuracy is necessary. In addition, because the data used are different for each study, additional studies are needed to establish common criteria for the THM method.

To evaluate the field applicability of the THM method, the results of previous studies of its accuracy and measurement period are summarized in Table 3. The presented deviation between the results obtained using the THM method and the comparison method value (U_C) can be calculated as an absolute value using Equation (11):

$$U_{THM} - U_C = \left| \frac{U_{THM} - U_C}{U_C} \right| \times 100 \quad (11)$$

Table 3. Summary of studies on U-value assessment of building walls using the THM method.

Author (Year)	Measurement Method	Comparison Method	Deviation [%]	Test Period	Building Information
Andújar Márquez et al. (2017) [97]	THM method	HFM method	2%	Summer and winter, 4 days	-
Bienvenido-Huertas et al. (2018) [94]	THM method	Theoretical method: ISO 6946	Winter: 4–37% Summer:7–62% Autumn: 19–83%	Summer, winter, and autumn	Eight buildings from different architectural periods located in Seville and Cadiz, Spain
Kim et al. (2018) [95]	ASTR method	HFM method	0.3–5%	November to December 2015 7–14 days	Four buildings located in South Korea, constructed in the late 20th century
Evangelisti et al. (2019) [100]	ASTR method	HFM method	37.2~143.7%	Summer	Educational buildings in Italy from the 1960s
Evangelisti et al. (2022) [70]	THM method	Theoretical method: ISO 6946	North: 0.5~32.4% North-west: 76.3~127.4%	January 2019, 4 days (north) April 2019, 7 days (north-west)	Educational buildings in Italy

5.4. Quantitative Infrared Thermography (QIRT) Method

Infrared thermography has conventionally been employed for the qualitative analysis of building envelopes [101–104]. This method is used for various purposes, including detecting thermal anomalies (e.g., variations in thermal conductivities and moisture presence) [105–109], locating thermal bridges [110–112], and identifying air infiltration [105,110,113,114]. However, due to the challenges associated with the HFM method, techniques for measuring U-values using infrared thermography have been developed [23]. Due to the simplicity of thermal imaging, numerous studies over the past decade have focused on assessing heat flow rates, leading to the establishment of the ISO 9869-2:2018 [99] standard for measuring the heat flow rate of building frames. However, the method remains under investigation, and a universal equation for determining U-values has yet to be established [49].

Recent research is focused on developing and analyzing a method for calculating U-values using thermal imaging, which can be categorized into two types based on the measurement location: internal and external.

To perform the measurement, a calibrated infrared camera, a hot-wire anemometer, and two ambient temperature sensors are required (Figure 6). Infrared cameras should be placed 1.5 m from the wall of measurement, and the hot-wire anemometer should be placed 0.1 m from the wall [115,116].

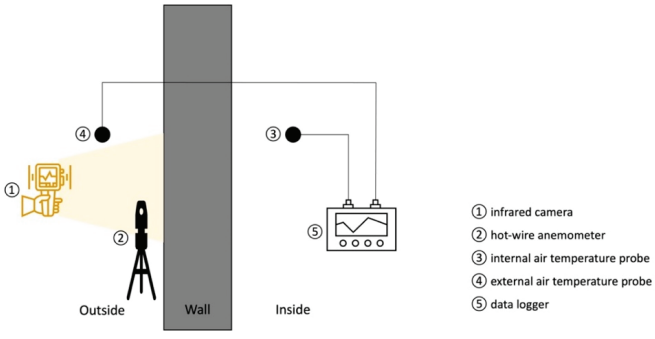

Figure 6. Schematic of the QIRT method.

This method requires specific conditions. An indoor and outdoor temperature difference of 15 °C or greater should be maintained for 3 to 4 h before conducting the test [117]. Measurements should be conducted in winter because it is difficult to achieve a strong temperature gradient in summer [116,117]. During measurements, the wind speed should be less than 1 m/s [118]. Measurements should be carried out during the early-morning hours when solar radiation is not a factor [119].

Since instantaneous measurements can yield non-representative results [120], test should be conducted over a period of 2 to 3 h [116]. Extending the test duration can reduce uncertainty in the results, although there is ongoing debate regarding the optimal interval between thermogram acquisition. Previous studies (Table 4) used collection intervals of 1 [116], 15 [104], 20 [117], and 30 [121] min. At least 10 instantaneous measurements should be performed to achieve useful estimates of the uncertainty [103].

In 2008, Madding [104] conducted a study of R-value measurement in the wall of a building using infrared imaging. Equation (12), which can calculate the U-value using internal convection and radiation as expressed by the linear Stefan–Boltzmann law, was proposed:

$$U = \frac{4\varepsilon\sigma\left(\frac{T_{s,in}+T_{ref}}{2}\right)^3\left(T_{s,in}-T_{ref}\right)+h_{in}\left(T_{s,in}-T_{in}\right)}{T_{in}-T_{out}} \quad (12)$$

where ε (without dimension) is the wall emissivity, σ is the Stefan–Boltzmann constant of $5.67 \cdot 10^{-8}$ W/(m^2 K^4), and T_{ref} (K) is the apparent reflected temperature. When the temperature difference between the indoor and outdoor environments was kept around 15 °C, an R-value within 12% of the calculated value was achieved. This emphasizes the importance of time and temperature changes during data collection and R-value measurement and implies that statistical accuracy can be improved by selecting the correct time zone and performing the measurement.

$$U = \frac{4\varepsilon\sigma {T_{s,in}}^3 \left(T_{s,in} - T_{ref}\right) + h_{in}(T_{s,in} - T_{in})}{T_{in} - T_{out}} \quad (13)$$

A similar method was proposed by Fokides and Kalogiro (2011) [117]. The formula presented in their research employed Equation (13) but with the third power applied solely to the surface temperature, rather than to the mean inner surface temperature and the reflected temperature. The measurements were conducted in five dwellings in Cyprus during August 2009 and February 2010. The study found that the percentages of absolute deviations between the theoretical and measured U-values between 10% and 20% were acceptable. However, the two results were measured in the laboratory, and verification under real-world conditions is necessary.

In 2010, Albatici et al. [122] developed a testing method using external measurements by thermal imaging cameras and the thermal balance relationship for the outside of the wall. An external convection coefficient was determined from the Jurges correlation as published by Watanabe. In Equation (14), ν (m/s) is the local wind speed. In the study, the ratio of deviation between the theoretical equation and the proposed equation was relatively high, ranging from 27% to 31%.

$$U = \frac{\varepsilon\sigma\left({T_{s,out}}^4 - {T_{out}}^4\right) + 3.8054\nu(T_{s,out} - T_{out})}{T_{in} - T_{out}} \quad (14)$$

Dall'O' et al. (2013) [123] adopted an alternative thermal balance equation that factored in the equivalence between the heat flux from convection exchanged with the external surroundings and the heat flux through the wall. They used h_{out} from the convective correlation published by Watanabe but did not simplify the equation, resulting in Equation (15). An error of 1.5% to 154% (36% on average) was obtained. The results were highly influenced by the measurement time zone and weather.

$$U = \frac{(5.8 + 3.8054\nu)(T_{s,out} - T_{out})}{T_{in} - T_{out}} \quad (15)$$

In the two aforementioned studies, the authors proposed the following conditions for obtaining accurate field measurements: no solar radiation (3 to 4 a.m.); wind speed of less than 1 m/s to avoid convection; indoor temperature remains the same for 48 h before measurement; and the indoor and outdoor temperature difference is maintained at 15 °C for heat exchange. The authors indicate that the proposed method is applicable only during winter due to the specific conditions mentioned later.

Albatici et al. [124] conducted a study of the U-values of opaque building elements in the field using Equation (14). Infrared thermal imaging technology was previously proposed by those authors. The resulting error rate was between 8% and 20% compared with values measured by the HFM method. It turned out that conducting the survey while focusing solely on walls facing north and east yielded more accurate outcomes. However, although the method produces reliable results for heavy constructions, further research is required for light and super-insulated walls. In addition, it is thought that analysis of environmental variables is necessary to perform reliable measurements.

Tejedor et al. [116,125] present a method for determining the field U-value using the QIRT method. As a result of comparing and analyzing the measured and theoretical

U-values calculated using the proposed method, the deviation was 1.24% to 3.97%. In addition, this proposed method can provide measurements at a temperature difference of 7 °C, unlike the recently developed QIRT method. However, as this study was also based on indoor measurements, further research in external conditions is warranted.

In Choi and Ko [126], the U-values obtained through theoretical equations and Equations (12)–(15) using QIRT suggested in previous studies were compared with field measurements. The following error rates were obtained: 10–27% for Equation (12), 11–29% for Equation (13), 10–44% for Equation (14), and 7–19% for Equation (15). These relatively large deviations are thought to result from the use of different parameters in the equations and the omission of the thermal storage effect. Therefore, a study is needed to completely characterize the influence of the number of various mediators on the results obtained through long-term measurements in the actual environment. In addition, since this study was conducted in winter, it seems that summer research is also necessary.

Bienvenido-Huertas et al. [127] conducted a comparative study on the expression of heat transfer rates through various external convective heat transfer coefficients (ECHTCs) for quantitative analysis using infrared thermography (IRT). A total of 46 wind-speed-related correlations were analyzed, with accuracy ranging from 0% to 150%. The study indicates that there is a lack of research analyzing the vast number of correlations for ECHTCs based on wind speed and dimensionless numbers. Further research is needed to analyze the internal convective heat transfer coefficient in relation to heat transfer methods.

Milad Mahmoodzadeh et al. [128] studied the application of external IRT for the quantitative analysis of the thermal performance of building envelopes. On-site measurements of a test building on a university campus in Canada showed differences between the design values and measurements ranging from 5.88% to 12.5%. The study demonstrated that the surface and outdoor temperature measurements taken using an IR camera had the greatest impact on the uncertainty of the results. Further research is required to enhance the accuracy of environmental data measured by thermal cameras. Additionally, this could enable large-scale quantitative assessments of building envelopes in much shorter timeframes using unmanned aerial vehicles (UAVs) rather than handheld thermal cameras.

Rodríguez et al. [129] conducted a study to overcome the typical physical limitations of conventional building inspection methods by using UAVs equipped with infrared thermography (IR) cameras. The study used the IRT method simultaneously with the THM method, and the results showed differences ranging from 4.3% to 29.1%. The authors concluded that for accurate evaluations, U-value measurements need to be stable and consistent over an extended period. The framework proposed in the study overcomes the limitations of inspecting difficult-to-access areas, such as high roofs or exterior walls, which are challenging to assess with traditional methods. However, the limitation of not being able to evaluate certain areas with a single measurement highlights the need for further research.

Zhang et al. [130] proposed a field testing protocol for evaluating heat transfer through building exterior walls using UAV-IRT. The effectiveness of the protocol was validated through field tests on two buildings. When compared to the U-values measured using the HFM method, the error rates ranged from 18% to 45% for case 1 and from 3% to 24% for case 2. The study found that the error rates increased as the drone's testing distance increased, which led to a decrease in wall temperature and heat transfer rates compared to the HFM values. Additionally, the decline in image quality due to the drone's flight speed and outdoor wind speed also contributed to the error rates. Therefore, further research is needed to improve the accuracy of U-value assessments in on-site evaluations using UAVs.

In this section, several studies assessing the thermal performance of buildings using QIRT were reviewed. The QIRT method was compared with the theoretical value or the HFM measurement value, and the error range was relatively wide, at 0–286%. In the overall error range, the accuracy in winter was relatively stable, at 2–68%, compared to 10–286% in summer. The data measurement and analysis of the QIRT method are simpler than those of other field measurement methods but require specific environmental conditions: a constant

indoor and outdoor temperature difference, winter measurement period, wind speed less than 1 m/s, and a time frame without solar radiation. However, these conditions have limitations when applied to field measurements. A thermal image calculation formula that can be used without limitation of measurement conditions is necessary to analyze the environmental variables that affect accuracy.

To evaluate the field applicability of the QIRT method, the results of previous studies of its accuracy and measurement period are summarized (Table 4). The deviation between the results obtained with the QIRT method and the comparison method value (U_C) was calculated as an absolute value using Equation (16):

$$U_{\mathrm{QIRT}} - U_C = \left| \frac{U_{\mathrm{QIRT}} - U_C}{U_C} \right| \times 100 \tag{16}$$

Table 4. Summary of studies on U-value assessment of building walls using the QIRT method.

Author (Year)	Measurement Method	Comparison Method	Deviation [%]	Test Period	Building Information
Dall'O et al. (2013) [123]	QIRT method	Theoretical method	1.5–154%, average 36%	January 2013	Fourteen buildings located in Milan, completed between 18,800 and 2009
Tzifa et al. (2014) [103]	QIRT method	Theoretical method: ISO 6946	Winter 2–68%, average 29% Summer 10–286%, average 97%	January to February 2011	An educational building located in Athens, Greece
Albatici et al. (2015) [124]	QIRT method	Theoretical method: ISO 6946	0–43%, average 22%	November 2010 to March 2011 November 2011 to March 2012 November 2012 to March 2013	Buildings in Italy specifically designed for research, featuring five types of walls
	QIRT method	HFM method	5–29%, average 19%		
Nardi et al. (2015) [17]	QIRT method	Theoretical method: ISO 6946	4–46%, average 20%	72–144 h	Buildings in Italy designed for three different purposes
	QIRT method	HFM method	1–48%, average 17%		
Nardi et al. (2016) [121]	QIRT method: in a guarded hot box	Theoretical method: ISO 6946	0–96%, average 22%	February 2013 7–18 days	Walls reproducing typical 1970s Italian building stock
	QIRT method: in a guarded hot box	HFM method	0–77%, average 18%		
Tejedor et al. (2017) [116]	QIRT method	Theoretical method: ISO 6946	4–20%, average 12%	January and February 2016	Two typical types of Spanish walls from different periods
	QIRT method	HFM method	13–27%, average 20%		
Tejedor et al. (2018) [125]	QIRT method	Theoretical method: ISO 6946	0.2–9%, average 4%	January to February 2017	An educational building located in Spain
Choi and Ko (2017) [126]	QIRT method	Theoretical method: ISO 6946	7~44%	January to February 2016 27 days	Residential building in South Korea

Table 4. *Cont.*

Author (Year)	Measurement Method	Comparison Method	Deviation [%]	Test Period	Building Information
Bienvenido-Huertas et al. (2019) [127]	QIRT method	Theoretical method: ISO 6946	0~150%	Scheduled date for the lowest external temperature	Most representative building in Spain
Milad Mahmoodzadeh et al. (2022) [128]	QIRT method	Theoretical method: ISO 6946	5.88~12.5%	Different days with varying exterior and interior conditions	Representative of low-rise Canadian west coast construction
Rodríguez et al. (2024) [129]	QIRT method	THM method	4.3~29.1%	Summer and winter 3 days	Educational buildings in Spain built in 2001
Zhang et al. (2024) [130]	QIRT method	HFM method-Average	20~46% (case 1) 3~24% (case 2)	December 2020	Residential buildings in Harbin built in 1985 (case 1) and 2014 (case 2)
	QIRT method	HFM method-Dynamic	18~45% (case 1) 3~24% (case 2)		

6. Discussion

This section explores the limitations of existing active measurements methods. A comparison of accuracy, test period, measurement parameters, and methods related to the measurement equipment is presented in Table 5. The characteristics of each method can be derived based on the comparisons. The factors of comparison are described in detail below.

Table 5. Comparison of active measurement methods presented in this paper.

Method	Accuracy	Test Period	Measurement Parameter	Equipment Required for Measurement
HFM	Winter 1–70% Summer 45–264%	Min. 3 days Max. 21 days	Heat flux Air temperature (internal and external)	Heat flow meter Air temperature probe Data logger
SHB-HFM	0.3–13%	Min. 3 days	Heat flux Surface temperature (internal and external) Air temperature (external)	Simple hot box Heat flow meter Surface temperature probe Air temperature probe Data logger
THM	Winter 0.3–37% Summer 7–143.7%	Less than 1 day	Air temperature (internal and external) Surface temperature (internal)	Air temperature probe Data logger
QIRT	Winter 0–154% Summer 10–286%	Min. 3 nights	Air temperature (internal and external) Surface temperature (internal or external) Emissivity Wind speed	Infrared camera Hot wire anemometer Air temperature probe Data logger

The accuracy of each method is evaluated based on the minimum and maximum deviations. The accuracy of all methods can be influenced by measurement conditions and the properties of the envelope components, which can strongly influence the field thermal perfusion. Several studies have been conducted on some methods, but only a limited number are available for others. Therefore, the presented results represent the accuracy obtained in the conducted studies. It was more difficult to achieve the minimum temperature difference for performance measurements during the summer, and there was a difference in accuracy according to the wall position.

Finally, the measurement parameters required to determine the U-value in each method were established and included indoor temperature, outdoor temperature, wall temperature, wall heat flow, wind speed, and emissivity.

Additional details are provided in Table 5 so that researchers can choose the appropriate measurement method according to parameters such as measurement season, measurement time, and data post-processing method. In addition, further research is needed on how to overcome the limitations of the existing methods analyzed.

7. Conclusions

Improving the energy efficiency of existing buildings is a crucial aspect of any effort to achieve sustainability goals in the building sector in response to the threats posed by global warming [131]. One approach to enhancing building efficiency is to reduce heat acquisition or loss by increasing the insulation performance of the building envelope [11–13]. To achieve this, it is necessary to gauge the current insulation performance of the building. Therefore, this review was conducted to evaluate the methods suitable for assessing the U-value of building envelopes.

More than 100 publications of various types published in the last 20 years were reviewed. They present an overview of the importance of determining the U-value of the building envelope and the methods used. Building envelope thermal performance is the most important thermal and physical property affecting energy performance [15–18], and the best-developed method was evaluated. These methods are analogous with coeval building assessments, theoretical calculations, and the HFM, SHB-HFM, THM, and QIRT methods. The theoretical formulations for each method, necessary equipment and materials, equipment installation, data collection, and the results of previous studies were then discussed.

The measurement methods described above (Table 5) determine how they should be applied to specific situations. A passive method evaluates the building envelope's performance using a technical document or database for the envelope or an estimate based on a similar configuration. It is used to approximate the thermal performance of a building through calculation before field measurements, even though field measurement may not be possible or may not be required. Active methods can provide more representative values; however, they are influenced by numerous factors, with environmental conditions being the most important. In situ measurements should maintain a stable measurement environment, such as zero rainfall, low wind speed, no solar radiation or other radiation sources that can affect the wall of interest, and a minimum temperature gradient.

This review found that, despite extensive research efforts, there remain problems to be solved regarding the limitations of field measurements. The main problems are as follows:

1. In situ measurements under summer conditions are limited, and existing seasonal constraints remain to be addressed.
2. It is a necessity to provide a shorter test duration to enable more measurements to be performed in a given time.
3. The limitations of the measurement time and orientation of the measurement wall were not overcome because field measurements were not performed under conditions affected by solar radiation.
4. Most of the studies were conducted in indoor spaces, but further studies are needed on how to determine U-values through outdoor measurements.

To solve this problem, an integrated approach using artificial intelligence (AI) and field measurements has recently been proposed [132,133]. However, AI tools are not yet mature, and additional robust datasets and tests for model design are needed. In addition, an approach that combines thermal imaging and drones has been proposed to measure large spaces outside the building. However, the limited accuracy of thermal imaging measurement has yet to be overcome, and research is needed to solve this problem. Additional research is needed to shorten the measurement time by combining thermal

imaging and drones with in-depth analysis of the potential to apply AI to field measurement methods of U-values. Future studies should involve the following elements:

1. Analysis of factors affecting accuracy in U-value determination by the QIRT method outdoors.
2. Development of field application of the QIRT method regardless of an unstable environment through in-depth AI analysis (e.g., seasonal impact, measurement time zone, or solar radiation effect by measurement orientation).
3. Development of a rapid and accurate method of determining U-values by photographing the exterior wall using a drone equipped with a thermal imaging camera.
4. Verification of field application accuracy of a combination of thermal imaging and drone-mounted cameras.

Author Contributions: All authors contributed to the study conception and design. Conceptualization, methodology, conducting the literature search, writing—original draft preparation, and writing—review and editing were performed by A.S., Y.K. and S.H. Conceptualization, funding acquisition, supervision, and writing—review and editing were performed by M.S. and S.L. All authors have read and agreed to the published version of the manuscript.

Funding: This work was supported by the Korea Agency for Infrastructure Technology Advancement (KAIA) grant funded by the Ministry of Land, Infrastructure and Transport (Grant RS-2022-00141900).

Data Availability Statement: Data generated or analyzed during this study are available from the corresponding author upon reasonable request.

Conflicts of Interest: The authors declare no conflicts of interest.

References

1. UN Environment Programme. *2021 Global Status Report for Buildings and Construction: Towards a Zero-Emission, Efficient and Resilient Buildings and Construction Sector*; UN Environment Programme: Nairobi, Kenya, 2021.
2. Maierhofer, D.; Röck, M.; Saade, M.R.M.; Hoxha, E.; Passer, A. Critical life cycle assessment of the innovative passive nZEB building concept 'be 2226' in view of net-zero carbon targets. *Build. Environ.* **2022**, *223*, 109476. [CrossRef]
3. Ebel, R.E.; Croissant, M.P.; Masih, J.R.; Calder, K.E.; Thomas, R.G. International energy outlook: US department of energy. *Wash. Q.* **1996**, *19*, 70–99. [CrossRef]
4. Lucon, O.; Ürge-Vorsatz, D.; Ahmed, A.; Akbari, H.; Bertoldi, P.; Cabeza, L.; Eyre, N.; Gadgil, A.; Harvey, L.; Jiang, Y. *Buildings Climate Change 2014: Mitigation of Climate Change IPCC Working Group III Contribution to AR5*; Cambridge University Press: Cambridge, UK, 2014.
5. Zhang, Y.; Bai, X.; Mills, F.P.; Pezzey, J.C. Rethinking the role of occupant behavior in building energy performance: A review. *Energy Build.* **2018**, *172*, 279–294. [CrossRef]
6. Asif, M. Growth and sustainability trends in the buildings sector in the GCC region with particular reference to the KSA and UAE. *Renew. Sustain. Energy Rev.* **2016**, *55*, 1267–1273. [CrossRef]
7. Coates, G.J. The sustainable urban district of Vauban in Freiburg, Germany. *Int. J. Des. Nat. Ecodynamics* **2013**, *8*, 265–286. [CrossRef]
8. Ismail, A.M.; Ramirez-Iniguez, R.; Asif, M.; Munir, A.B.; Muhammad-Sukki, F. Progress of solar photovoltaic in ASEAN countries: A review. *Renew. Sustain. Energy Rev.* **2015**, *48*, 399–412. [CrossRef]
9. Scarlat, N.; Dallemand, J.-F.; Monforti-Ferrario, F.; Banja, M.; Motola, V. Renewable energy policy framework and bioenergy contribution in the European Union—An overview from National Renewable Energy Action Plans and Progress Reports. *Renew. Sustain. Energy Rev.* **2015**, *51*, 969–985. [CrossRef]
10. Ajagekar, A.; You, F. Quantum computing and quantum artificial intelligence for renewable and sustainable energy: A emerging prospect towards climate neutrality. *Renew. Sustain. Energy Rev.* **2022**, *165*, 112493. [CrossRef]
11. Iwaro, J.; Mwasha, A. The impact of sustainable building envelope design on building sustainability using Integrated Performance Model. *Int. J. Sustain. Built Environ.* **2013**, *2*, 153–171. [CrossRef]
12. Harish, V.; Kumar, A. A review on modeling and simulation of building energy systems. *Renew. Sustain. Energy Rev.* **2016**, *56*, 1272–1292. [CrossRef]
13. Luo, Y.; Zhang, L.; Bozlar, M.; Liu, Z.; Guo, H.; Meggers, F. Active building envelope systems toward renewable and sustainable energy. *Renew. Sustain. Energy Rev.* **2019**, *104*, 470–491. [CrossRef]
14. LaFrance, M. *Technology Roadmap: Energy Efficient Building Envelopes*; IEA: Paris, France, 2013.
15. Desogus, G.; Mura, S.; Ricciu, R. Comparing different approaches to in situ measurement of building components thermal resistance. *Energy Build.* **2011**, *43*, 2613–2620. [CrossRef]

16. Ficco, G.; Iannetta, F.; Ianniello, E.; Alfano, F.R.d.A.; Dell'Isola, M. U-value in situ measurement for energy diagnosis of existing buildings. *Energy Build.* **2015**, *104*, 108–121. [CrossRef]
17. Nardi, I.; Ambrosini, D.; De Rubeis, T.; Sfarra, S.; Perilli, S.; Pasqualoni, G. A comparison between thermographic and flow-meter methods for the evaluation of thermal transmittance of different wall constructions. *J. Phys. Conf. Ser.* **2015**, *655*, 012007. [CrossRef]
18. Zheng, K.; Cho, Y.K.; Wang, C.; Li, H. Noninvasive Residential Building Envelope R-Value Measurement Method Based on Interfacial Thermal Resistance. *J. Archit. Eng.* **2016**, *22*, A4015002. [CrossRef]
19. Kirimtat, A.; Krejcar, O. A review of infrared thermography for the investigation of building envelopes: Advances and prospects. *Energy Build.* **2018**, *176*, 390–406. [CrossRef]
20. Lucchi, E. Applications of the infrared thermography in the energy audit of buildings: A review. *Renew. Sustain. Energy Rev.* **2018**, *82*, 3077–3090. [CrossRef]
21. Tardy, F. A review of the use of infrared thermography in building envelope thermal property characterization studies. *J. Build. Eng.* **2023**, *75*, 106918. [CrossRef]
22. Teni, M.; Krstić, H.; Kosiński, P. Review and comparison of current experimental approaches for in-situ measurements of building walls thermal transmittance. *Energy Build.* **2019**, *203*, 109417. [CrossRef]
23. Bienvenido-Huertas, D.; Moyano, J.; Marín, D.; Fresco-Contreras, R. Review of in situ methods for assessing the thermal transmittance of walls. *Renew. Sustain. Energy Rev.* **2019**, *102*, 356–371. [CrossRef]
24. *ISO 7345*; Thermal Performance of Buildings and Building Components—Physical Quantities and Definitions. ISO: Geneva, Switzerland, 2018. Available online: https://cdn.standards.iteh.ai/samples/65000/62f3bede7e394297acf7484026c7d505/ISO-7345-2018.pdf (accessed on 5 May 2024).
25. *ISO 6946:2017*; Building Components and Building Elements—Thermal Resistance and Thermal Transmittance—Calculation Methods. European Committee for Standardization: Brussels, Belgium, 2017.
26. ASHRAE. ASHRAE Terminology. Available online: https://terminology.ashrae.org/ (accessed on 5 May 2024).
27. Snow, D.A. *Plant Engineer's Reference Book*; Elsevier: Amsterdam, The Netherlands, 2001.
28. Muresan, A.A.; Attia, S. Energy efficiency in the Romanian residential building stock: A literature review. *Renew. Sustain. Energy Rev.* **2017**, *74*, 349–363. [CrossRef]
29. Economidou, M.; Atanasiu, B.; Despret, C.; Maio, J.; Nolte, I.; Rapf, O.; Laustsen, J.; Ruyssevelt, P.; Staniaszek, D.; Strong, D. Europe's buildings under the microscope. In *A Country-by-Country Review of the Energy Performance of Buildings*; BPIE: Siromanipur, India, 2011.
30. Ascione, F.; Bianco, N.; De Masi, R.F.; Mauro, G.M.; Musto, M.; Vanoli, G.P. Experimental validation of a numerical code by thin film heat flux sensors for the resolution of thermal bridges in dynamic conditions. *Appl. Energy* **2014**, *124*, 213–222. [CrossRef]
31. Ascione, F.; Ceroni, F.; De Masi, R.F.; de'Rossi, F.; Pecce, M.R. Historical buildings: Multidisciplinary approach to structural/energy diagnosis and performance assessment. *Appl. Energy* **2017**, *185*, 1517–1528. [CrossRef]
32. Nardi, I.; Lucchi, E.; de Rubeis, T.; Ambrosini, D. Quantification of heat energy losses through the building envelope: A state-of-the-art analysis with critical and comprehensive review on infrared thermography. *Build. Environ.* **2018**, *146*, 190–205. [CrossRef]
33. Li, X.; Yao, R.; Liu, M.; Costanzo, V.; Yu, W.; Wang, W.; Short, A.; Li, B. Developing urban residential reference buildings using clustering analysis of satellite images. *Energy Build.* **2018**, *169*, 417–429. [CrossRef]
34. Tardioli, G.; Kerrigan, R.; Oates, M.; O'Donnell, J.; Finn, D.P. Identification of representative buildings and building groups in urban datasets using a novel pre-processing, classification, clustering and predictive modelling approach. *Build. Environ.* **2018**, *140*, 90–106. [CrossRef]
35. Cesaratto, P.G.; De Carli, M. A measuring campaign of thermal conductance in situ and possible impacts on net energy demand in buildings. *Energy Build.* **2013**, *59*, 29–36. [CrossRef]
36. Aksoezen, M.; Daniel, M.; Hassler, U.; Kohler, N. Building age as an indicator for energy consumption. *Energy Build.* **2015**, *87*, 74–86. [CrossRef]
37. Ballarini, I.; Corgnati, S.P.; Corrado, V. Use of reference buildings to assess the energy saving potentials of the residential building stock: The experience of TABULA project. *Energy Policy* **2014**, *68*, 273–284. [CrossRef]
38. TABULA Database. Available online: https://episcope.eu/welcome (accessed on 24 February 2024).
39. Basaglia, A.; Cianchino, G.; Cocco, G.; Rapone, D.; Terrenzi, M.; Spacone, E.; Brando, G. An automatic procedure for deriving building portfolios using the Italian "CARTIS" online database. *Structures* **2021**, *34*, 2974–2986. [CrossRef]
40. Wardhana, K.; Hadipriono, F.C. Study of recent building failures in the United States. *J. Perform. Constr. Facil.* **2003**, *17*, 151–158. [CrossRef]
41. Lucchi, E. Thermal transmittance of historical stone masonries: A comparison among standard, calculated and measured data. *Energy Build.* **2017**, *151*, 393–405. [CrossRef]
42. Lucchi, E. Thermal transmittance of historical brick masonries: A comparison among standard data, analytical calculation procedures, and in situ heat flow meter measurements. *Energy Build.* **2017**, *134*, 171–184. [CrossRef]
43. Siviour, J. Experimental U-values of some house walls. *Build. Serv. Eng. Res. Technol.* **1994**, *15*, 35–36. [CrossRef]
44. Lucchi, E. *Diagnosi Energetica Strumentale Degli Edifici*; Dario Flaccovio Editore: Palermo, Italy, 2012.
45. Xu, Y.; Sun, D.a.; Zeng, Z.; Lv, H. Effect of aging on thermal conductivity of compacted bentonites. *Eng. Geol.* **2019**, *253*, 55–63. [CrossRef]

46. Pontinha, A.D.R.; Mäntyneva, J.; Santos, P.; Durães, L. Thermomechanical performance assessment of sustainable buildings' insulating materials under accelerated ageing conditions. *Gels* **2023**, *9*, 241. [CrossRef]
47. Villarejo, P.; Gámez, R.; Santamaría-López, Á. Building renovation passports in Spain: Integrating exiting instruments for building conservation, renovation and heritage protection. *Energy Policy* **2021**, *157*, 112506. [CrossRef]
48. Jensen, P.A.; Maslesa, E. Value based building renovation–A tool for decision-making and evaluation. *Build. Environ.* **2015**, *92*, 1–9. [CrossRef]
49. Nardi, I.; Lucchi, E. In Situ Thermal Transmittance Assessment of the Building Envelope: Practical Advice and Outlooks for Standard and Innovative Procedures. *Energies* **2023**, *16*, 3319. [CrossRef]
50. Asdrubali, F.; D'Alessandro, F.; Baldinelli, G.; Bianchi, F. Evaluating in situ thermal transmittance of green buildings masonries—A case study. *Case Stud. Constr. Mater.* **2014**, *1*, 53–59. [CrossRef]
51. Pérez-Bella, J.M.; Dominguez-Hernandez, J.; Cano-Sunen, E.; del Coz-Diaz, J.J.; Rabanal, F.P.A. A correction factor to approximate the design thermal conductivity of building materials. Application to Spanish façades. *Energy Build.* **2015**, *88*, 153–164. [CrossRef]
52. *ISO 10456*; Building Materials and Products—Hygrothermal Properties—Tabulated Design Values and Procedures for Determining Declared and Design Thermal Values. International Organization for Standardization: Geneva, Switzerland, 2007.
53. Rodríguez-Soria, B.; Domínguez-Hernández, J.; Pérez-Bella, J.M.; del Coz-Díaz, J.J. Review of international regulations governing the thermal insulation requirements of residential buildings and the harmonization of envelope energy loss. *Renew. Sustain. Energy Rev.* **2014**, *34*, 78–90. [CrossRef]
54. *ISO 9869:1994*; Thermal Insulation: Building Elements: In-Situ Measurement of Thermal Resistance and Thermal Transmittance. ISO: Geneva, Switzerland, 1994.
55. *ISO 9869-1:2014*; Thermal Insulation—Building Elements—In-Situ Measurement of Thermal Resistance and Thermal Transmittance: Isolation Thermique—Éléments de Construction—Mesurage In Situ de la Résistance Thermique et du Coefficient de Transmission Thermique. Heat Flow Meter Method. Méthode Du Fluxmètre. ISO: Geneva, Switzerland, 2014.
56. Aittomäki, A. *Determination of the Overall Heat Transfer Coefficient of Multilayer Structures under Non-Steady-State Conditions*; CIB Session Working paper; CIB: Hongkong, China, 1972.
57. Roulet, C.; Gass, J.; Marcus, I. In-situ U-value measurement: Reliable results in shorter time by dynamic interpretation of measured data. *ASHRAE Trans* **1987**, *108*, 1371–1379.
58. Anderlind, G. Multiple regression analysis of in situ thermal measurements—Study of an attic insulated with 800 mm loose fill insulation. *J. Therm. Insul. Build. Envel.* **1992**, *16*, 81–104. [CrossRef]
59. Norlén, U. Estimating thermal parameters of outdoor test cells. *Build. Environ.* **1990**, *25*, 17–24. [CrossRef]
60. Jiménez, M.J.; Madsen, H.; Andersen, K.K. Identification of the main thermal characteristics of building components using MATLAB. *Build. Environ.* **2008**, *43*, 170–180. [CrossRef]
61. Jiménez, M.; Porcar, B.; Heras, M. Application of different dynamic analysis approaches to the estimation of the building component U value. *Build. Environ.* **2009**, *44*, 361–367. [CrossRef]
62. Gutschker, O. Parameter identification with the software package LORD. *Build. Environ.* **2008**, *43*, 163–169. [CrossRef]
63. Baker, P.H.; Van Dijk, H. PASLINK and dynamic outdoor testing of building components. *Build. Environ.* **2008**, *43*, 143–151. [CrossRef]
64. Naveros, I.; Bacher, P.; Ruiz, D.; Jiménez, M.; Madsen, H. Setting up and validating a complex model for a simple homogeneous wall. *Energy Build.* **2014**, *70*, 303–317. [CrossRef]
65. Walker, R.; Pavía, S. Thermal performance of a selection of insulation materials suitable for historic buildings. *Build. Environ.* **2015**, *94*, 155–165. [CrossRef]
66. Bros-Williamson, J.; Garnier, C.; Currie, J.I. A longitudinal building fabric and energy performance analysis of two homes built to different energy principles. *Energy Build.* **2016**, *130*, 578–591. [CrossRef]
67. Gori, V.; Elwell, C.A. Estimation of thermophysical properties from in-situ measurements in all seasons: Quantifying and reducing errors using dynamic grey-box methods. *Energy Build.* **2018**, *167*, 290–300. [CrossRef]
68. Ahmad, A.; Maslehuddin, M.; Al-Hadhrami, L.M. In situ measurement of thermal transmittance and thermal resistance of hollow reinforced precast concrete walls. *Energy Build.* **2014**, *84*, 132–141. [CrossRef]
69. Evangelisti, L.; Guattari, C.; Vollaro, R.D.L.; Asdrubali, F. A methodological approach for heat-flow meter data post-processing under different climatic conditions and wall orientations. *Energy Build.* **2020**, *223*, 110216. [CrossRef]
70. Evangelisti, L.; Guattari, C.; Fontana, L.; Vollaro, R.D.L.; Asdrubali, F. On the ageing and weathering effects in assembled modular facades: On-site experimental measurements in an Italian building of the 1960s. *J. Build. Eng.* **2022**, *45*, 103519. [CrossRef]
71. Gaspar, K.; Casals, M.; Gangolells, M. A comparison of standardized calculation methods for in situ measurements of façades U-value. *Energy Build.* **2016**, *130*, 592–599. [CrossRef]
72. O'Hegarty, R.; Kinnane, O.; Lennon, D.; Colclough, S. In-situ U-value monitoring of highly insulated building envelopes: Review and experimental investigation. *Energy Build.* **2021**, *252*, 111447. [CrossRef]
73. Choi, D.-S.; Lee, Y.-J.; Moon, J.-H.; Kim, Y.-S.; Ko, M.-J. Estimating in-situ R-value of highly insulated building walls based on the measurement of temperature and heat flux inside the wall. *Energies* **2023**, *16*, 5714. [CrossRef]
74. Suh, W.D.; Yuk, H.; Park, J.H.; Jo, H.H.; Kim, S. Sustainable use of historic campus buildings: Retrofit technology to improve building energy performance considering preservation of interior finishing material. *Energy Build.* **2024**, *320*, 114620.

75. Deconinck, A.-H.; Roels, S. Comparison of characterisation methods determining the thermal resistance of building components from onsite measurements. *Energy Build.* **2016**, *130*, 309–320. [CrossRef]
76. Naveros, I.; Ghiaus, C.; Ruíz, D.; Castaño, S. Physical parameters identification of walls using ARX models obtained by deduction. *Energy Build.* **2015**, *108*, 317–329. [CrossRef]
77. Biddulph, P.; Gori, V.; Elwell, C.A.; Scott, C.; Rye, C.; Lowe, R.; Oreszczyn, T. Inferring the thermal resistance and effective thermal mass of a wall using frequent temperature and heat flux measurements. *Energy Build.* **2014**, *78*, 10–16. [CrossRef]
78. Gori, V.; Marincioni, V.; Biddulph, P.; Elwell, C.A. Inferring the thermal resistance and effective thermal mass distribution of a wall from in situ measurements to characterise heat transfer at both the interior and exterior surfaces. *Energy Build.* **2017**, *135*, 398–409. [CrossRef]
79. Gaspar, K.; Casals, M.; Gangolells, M. Review of criteria for determining HFM minimum test duration. *Energy Build.* **2018**, *176*, 360–370. [CrossRef]
80. Hoffmann, C.; Geissler, A. The prebound-effect in detail: Real indoor temperatures in basements and measured versus calculated U-values. *Energy Procedia* **2017**, *122*, 32–37. [CrossRef]
81. Atsonios, I.A.; Mandilaras, I.D.; Kontogeorgos, D.A.; Founti, M.A. A comparative assessment of the standardized methods for the in-situ measurement of the thermal resistance of building walls. *Energy Build.* **2017**, *154*, 198–206. [CrossRef]
82. Tadeu, A.; Simoes, N.; Simões, I.; Pedro, F.; Škerget, L. In-situ thermal resistance evaluation of walls using an iterative dynamic model. *Numer. Heat Transf. Part A Appl.* **2015**, *67*, 33–51. [CrossRef]
83. Cesaratto, P.G.; De Carli, M.; Marinetti, S. Effect of different parameters on the in situ thermal conductance evaluation. *Energy Build.* **2011**, *43*, 1792–1801. [CrossRef]
84. Gaspar, K.; Casals, M.; Gangolells, M. Influence of HFM thermal contact on the accuracy of in situ measurements of façades' U-value in operational stage. *Appl. Sci.* **2021**, *11*, 979. [CrossRef]
85. Lee, Y.-J.; Moon, J.-H.; Choi, D.-S.; Ko, M.-J. Application of the Heat Flow Meter Method and Extended Average Method to Improve the Accuracy of In Situ U-Value Estimations of Highly Insulated Building Walls. *Sustainability* **2024**, *16*, 5687. [CrossRef]
86. Tian, S. Study on In-Situ Measurement Method of Heat Transfer Coefficient of Building Envelop. Master's Thesis, Xi'an University of Architecture and Technology, Xi'an, China, 2006.
87. Pan, L.; Chen, B.; Fang, Z.; Han, B.; Zhen, Y. Measurement of thermal resistance of building enclosures by means of the heat box method, Build. *Energy Environ.* **2005**, *2*, 74–77.
88. Pan, L.; Chen, B.; Fang, Z.; Zhen, Y. Field measurement and data processing method of envelope's thermal resistance, Build. *Energy Environ.* **2005**, *6*, e84.
89. Zhu, X.; Li, L.; Yin, X.; Zhang, S.; Wang, Y.; Liu, W.; Zheng, L. An in-situ test apparatus of heat transfer coefficient for building envelope. *Build. Energy Effic.* **2012**, *256*, 57–60.
90. Meng, X.; Gao, Y.; Wang, Y.; Yan, B.; Zhang, W.; Long, E. Feasibility experiment on the simple hot box-heat flow meter method and the optimization based on simulation reproduction. *Appl. Therm. Eng.* **2015**, *83*, 48–56. [CrossRef]
91. Meng, X.; Luo, T.; Gao, Y.; Zhang, L.; Shen, Q.; Long, E. A new simple method to measure wall thermal transmittance in situ and its adaptability analysis. *Appl. Therm. Eng.* **2017**, *122*, 747–757. [CrossRef]
92. Roque, E.; Vicente, R.; Almeida, R.M.; da Silva, J.M.; Ferreira, A.V. Thermal characterisation of traditional wall solution of built heritage using the simple hot box-heat flow meter method: In situ measurements and numerical simulation. *Appl. Therm. Eng.* **2020**, *169*, 114935. [CrossRef]
93. Nicoletti, F.; Cucumo, M.A.; Arcuri, N. Evaluating the accuracy of in-situ methods for measuring wall thermal conductance: A comparative numerical study. *Energy Build.* **2023**, *290*, 113095. [CrossRef]
94. Bienvenido-Huertas, D.; Rodríguez-Álvaro, R.; Moyano, J.J.; Rico, F.; Marín, D. Determining the U-value of façades using the thermometric method: Potentials and limitations. *Energies* **2018**, *11*, 360. [CrossRef]
95. Kim, S.-H.; Kim, J.-H.; Jeong, H.-G.; Song, K.-D. Reliability field test of the air–surface temperature ratio method for in situ measurement of U-values. *Energies* **2018**, *11*, 803. [CrossRef]
96. Cengel, A. *Heat Transfer*; McGraw-Hill: New York, NY, USA, 2003.
97. Andújar Márquez, J.M.; Martínez Bohórquez, M.Á.; Gómez Melgar, S. A new metre for cheap, quick, reliable and simple thermal transmittance (U-Value) measurements in buildings. *Sensors* **2017**, *17*, 2017. [CrossRef] [PubMed]
98. Buzatu, G.-C.; Stan-Ivan, F.-E.; Mircea, P.-M.; Manescu, L.-G. Thermal transmittance determination for different components of buildings. In Proceedings of the 2017 International Conference on Optimization of Electrical and Electronic Equipment (OPTIM) & 2017 Intl Aegean Conference on Electrical Machines and Power Electronics (ACEMP), Brasov, Romania, 25–27 May 2017; pp. 227–232.
99. *ISO 9869-2:2018*; Thermal Insulation—Building Elements—In-Situ Measurement of Thermal Resistance and Thermal Transmittance—Part 2: Infrared Method for Frame Structure Dwelling. ISO: Geneva, Switzerland, 2018.
100. Evangelisti, L.; Guattari, C.; Asdrubali, F. Comparison between heat-flow meter and Air-Surface Temperature Ratio techniques for assembled panels thermal characterization. *Energy Build.* **2019**, *203*, 109441. [CrossRef]
101. Kato, S.; Kuroki, K.; Hagihara, S. Method of in-situ measurement of thermal insulation performance of building elements using infrared camera. In Proceedings of the 6th International Conference on Indoor Air Quality, Ventilation & Energy Conservation in Buildings-IAQVEC, Sendai, Japan, 28–31 October 2007.

102. Albatici, R.; Tonelli, A. On site evaluation of U-value of opaque building elements: A new methodology. In *Towards Zero Energy Buildings*; University College Dublin: Dublin, Ireland, 2008; pp. 1–8.
103. Tzifa, V.; Papadakos, G.; Papadopoulou, A.G.; Marinakis, V.; Psarras, J. Uncertainty and method limitations in a short-time measurement of the effective thermal transmittance on a building envelope using an infrared camera. *Int. J. Sustain. Energy* **2017**, *36*, 28–46. [CrossRef]
104. Madding, R. Finding R-values of stud frame constructed houses with IR thermography. *Proc. InfraMation* **2008**, *2008*, 261–277.
105. Gonçalves, M.D. Commissioning of exterior building envelopes of large buildings for air leakage and thermal anomalies using infrared thermography and other diagnostic tools. In Proceedings of the Workshop on Building and Ductwork Airtightness Design, Implementation, Control and Durability: Feedback from Practice and Perspectives, Washington, DC, USA, 18–19 April 2013.
106. Kilic, G. Using advanced NDT for historic buildings: Towards an integrated multidisciplinary health assessment strategy. *J. Cult. Herit.* **2015**, *16*, 526–535. [CrossRef]
107. Kominsky, J.; Luckino, J.; Martin, T. *Passive Infrared Thermography—A Qualitative Method for Detecting Moisture Anomalies in Building Envelopes*; Tedford & Pond: Hartford, CT, USA, 2007; pp. 1–11.
108. Barreira, E.; Almeida, R.; Delgado, J. Infrared thermography for assessing moisture related phenomena in building components. *Constr. Build. Mater.* **2016**, *110*, 251–269. [CrossRef]
109. Grinzato, E.; Bison, P.G.; Marinetti, S. Monitoring of ancient buildings by the thermal method. *J. Cult. Herit.* **2002**, *3*, 21–29. [CrossRef]
110. Taylor, T.; Counsell, J.; Gill, S. Energy efficiency is more than skin deep: Improving construction quality control in new-build housing using thermography. *Energy Build.* **2013**, *66*, 222–231. [CrossRef]
111. Hopper, J.; Littlewood, J.R.; Taylor, T.; Counsell, J.A.; Thomas, A.M.; Karani, G.; Geens, A.; Evans, N.I. Assessing retrofitted external wall insulation using infrared thermography. *Struct. Surv.* **2012**, *30*, 245–266. [CrossRef]
112. Taileb, A.; Dekkiche, H. Infrared imaging as a means of analyzing and improving energy efficiency of building envelopes: The case of a LEED gold building. *Procedia Eng.* **2015**, *118*, 639–646. [CrossRef]
113. Kalamees, T. Air tightness and air leakages of new lightweight single-family detached houses in Estonia. *Build. Environ.* **2007**, *42*, 2369–2377. [CrossRef]
114. Lerma, C.; Barreira, E.; Almeida, R.M. A discussion concerning active infrared thermography in the evaluation of buildings air infiltration. *Energy Build.* **2018**, *168*, 56–66. [CrossRef]
115. Kylili, A.; Fokaides, P.A.; Christou, P.; Kalogirou, S.A. Infrared thermography (IRT) applications for building diagnostics: A review. *Appl. Energy* **2014**, *134*, 531–549. [CrossRef]
116. Tejedor, B.; Casals, M.; Gangolells, M.; Roca, X. Quantitative internal infrared thermography for determining in-situ thermal behaviour of façades. *Energy Build.* **2017**, *151*, 187–197. [CrossRef]
117. Fokaides, P.A.; Kalogirou, S.A. Application of infrared thermography for the determination of the overall heat transfer coefficient (U-Value) in building envelopes. *Appl. Energy* **2011**, *88*, 4358–4365. [CrossRef]
118. Lehmann, B.; Wakili, K.G.; Frank, T.; Collado, B.V.; Tanner, C. Effects of individual climatic parameters on the infrared thermography of buildings. *Appl. Energy* **2013**, *110*, 29–43. [CrossRef]
119. Van De Vijver, S.; Steeman, M.; Van Den Bossche, N.; Carbonez, K.; Janssens, A. The influence of environmental parameters on the thermographic analysis of the building envelope. In Proceedings of the 12th International Conference on Quantitative InfraRed Thermography (QIRT 2014), Bordeaux, France, 7–11 July 2014.
120. Kisilewicz, T.; Wróbel, A. Quantitative infrared wall inspection. In Proceedings of the 10th Edition of the Quantitative InfraRed Thermography—International Conference, Québec, QC, Canada, 27–30 July 2010; pp. 27–30.
121. Nardi, I.; Paoletti, D.; Ambrosini, D.; De Rubeis, T.; Sfarra, S. U-value assessment by infrared thermography: A comparison of different calculation methods in a Guarded Hot Box. *Energy Build.* **2016**, *122*, 211–221. [CrossRef]
122. Albatici, R.; Tonelli, A.M. Infrared thermovision technique for the assessment of thermal transmittance value of opaque building elements on site. *Energy Build.* **2010**, *42*, 2177–2183. [CrossRef]
123. Dall'O', G.; Sarto, L.; Panza, A. Infrared screening of residential buildings for energy audit purposes: Results of a field test. *Energies* **2013**, *6*, 3859–3878. [CrossRef]
124. Albatici, R.; Tonelli, A.M.; Chiogna, M. A comprehensive experimental approach for the validation of quantitative infrared thermography in the evaluation of building thermal transmittance. *Appl. Energy* **2015**, *141*, 218–228. [CrossRef]
125. Tejedor, B.; Casals, M.; Gangolells, M. Assessing the influence of operating conditions and thermophysical properties on the accuracy of in-situ measured U-values using quantitative internal infrared thermography. *Energy Build.* **2018**, *171*, 64–75. [CrossRef]
126. Choi, D.S.; Ko, M.J. Comparison of various analysis methods based on heat flowmeters and infrared thermography measurements for the evaluation of the in situ thermal transmittance of opaque exterior walls. *Energies* **2017**, *10*, 1019. [CrossRef]
127. Bienvenido-Huertas, D.; Bermúdez, J.; Moyano, J.; Marín, D. Comparison of quantitative IRT to estimate U-value using different approximations of ECHTC in multi-leaf walls. *Energy Build.* **2019**, *184*, 99–113. [CrossRef]
128. Mahmoodzadeh, M.; Gretka, V.; Lee, I.; Mukhopadhyaya, P. Infrared thermography for quantitative thermal performance assessment of wood-framed building envelopes in Canada. *Energy Build.* **2022**, *258*, 111807. [CrossRef]

129. Rodríguez, M.V.; Melgar, S.G.; Márquez, J.M.A. Evaluation of aerial thermography for measuring the thermal transmittance (U-value) of a building façade. *Energy Build.* **2024**, *324*, 114874. [CrossRef]
130. Zhang, D.; Zhan, C.; Chen, L.; Wang, Y.; Li, G. An in-situ detection method for assessing the thermal transmittance of building exterior walls using unmanned aerial vehicle–infrared thermography (UAV-IRT). *J. Build. Eng.* **2024**, *91*, 109724. [CrossRef]
131. European Commission. *A Roadmap for Moving to a Competitive Low Carbon Economy in 2050: Communication from the Commission to the European Parliament, the Council, the European Economic and Social Committee and the Committee of the Regions*; Publications Office of the European Union: Luxembourg, 2011.
132. Sadhukhan, D.; Peri, S.; Sugunaraj, N.; Biswas, A.; Selvaraj, D.F.; Koiner, K.; Rosener, A.; Dunlevy, M.; Goveas, N.; Flynn, D. Estimating surface temperature from thermal imagery of buildings for accurate thermal transmittance (U-value): A machine learning perspective. *J. Build. Eng.* **2020**, *32*, 101637. [CrossRef]
133. Patel, D.; Estevam Schmiedt, J.; Röger, M.; Hoffschmidt, B. A Model Calibration Approach to U-Value Measurements with Thermography. *Buildings* **2023**, *13*, 2253. [CrossRef]

MDPI AG
Grosspeteranlage 5
4052 Basel
Switzerland
Tel.: +41 61 683 77 34

Buildings Editorial Office
E-mail: buildings@mdpi.com
www.mdpi.com/journal/buildings

Academic Open
Access Publishing

mdpi.com

ISBN 978-3-7258-2564-6